



Project Sagebrush Phase 2

D. Finn¹
K. L. Clawson¹
R. M. Eckman¹
R. G. Carter¹
J. D. Rich¹
B. R. Reese¹
S. A. Beard¹
M. Brewer¹
D. Davis¹
D. Clinger¹
Z. Gao²
H. Liu²

NOAA/ Air Resources Laboratory/Field Research Division¹
Idaho Falls, Idaho

Laboratory for Atmospheric Research²
Washington State University

Air Resources Laboratory (ARL)
College Park, MD 20740

August, 2017

Project Sagebrush Phase 2

D. Finn¹
K. L. Clawson¹
R. M. Eckman¹
R. G. Carter¹
J. D. Rich¹
B. R. Reese¹
S. A. Beard¹
M. Brewer¹
D. Davis¹
D. Clinger¹
Z. Gao²
H. Liu²

NOAA/ Air Resources Laboratory
Field Research Division¹
Idaho Falls, Idaho

Laboratory for Atmospheric Research²
Washington State University

Air Resources Laboratory (ARL)
College Park, MD 20740

August, 2017



**UNITED STATES
DEPARTMENT OF COMMERCE**

Wilbur Ross
Secretary

**NATIONAL OCEANIC AND
ATMOSPHERIC ADMINISTRATION**

Benjamin Friedman
Under Secretary for Oceans
and Atmosphere/Acting Administrator

**Office of Oceanic and
Atmospheric Research**

Craig McLean
Assistant Administrator
Oceanic & Atmospheric
Research

NOTICE

This report was prepared as an account of work sponsored by an agency of the United States Government. Neither the United States Government nor any agency thereof, or any of their employees, makes any warranty, expressed or implied, or assumes any legal liability or responsibility for any third party's use, or the results of such use, of any information, apparatus, product, or process disclosed in this report, or represents that its use by such third party would not infringe on privately owned rights. Mention of a commercial company or product does not constitute an endorsement by NOAA/OAR. Use of information from this publication concerning proprietary products or tests of such products for publicity or advertising is not authorized.

TABLE OF CONTENTS

NOTICE	ii
TABLE OF CONTENTS	iii
FIGURES	vii
TABLES	xxii
ABSTRACT	xxiii
INTRODUCTION	1
EXPERIMENTAL PLAN	7
Grid 3 Dispersion Array and Release	8
Wind Direction Analysis	8
Bag Sampling	9
Fast Response Tracer Gas Analyzers	11
Meteorological Equipment	11
IOP Summaries	13
THE SF ₆ TRACER RELEASE SYSTEM	15
Accuracy	16
SF ₆ Release Summary	16
SF ₆ Release Quality Control	22
Data File Format	23
BAG SAMPLING	25
Description of Equipment	25
Description of Bag Sampling Grid	26
Sampler Cartridge Analysis	27
Sampler Handling and Chain of Custody	30
Potential Sampling Artifacts	34
Quality Control Procedures and Measurement Quality Objectives	35
Final Bag Sampler Data Files and Format	76
Final Data File Quality Control Flags	77
FAST RESPONSE TRACER ANALYZERS	79
Instrument Description	79
Calibration and Concentration Determination	81

MLOD/MLOQ	82
Quality Control (QC)	83
METEOROLOGICAL MEASUREMENTS	91
Grid 3 Tower (GRI)	91
NOAA ARLFRD	95
Sonic Anemometers	95
Experimental Setup	95
Quality Control	96
Data File Formats	98
Other Grid 3 Tower Measurements	103
Configuration	103
Quality Control	103
Data File Formats	104
WSULAR	105
Sonic Anemometers	105
Experimental Setup	105
Quality Control	105
Data File Formats	106
Other Measurements	110
Experimental Setup	110
Quality Control	110
Data File Formats	110
Meteorological Towers on Sampling Grid	111
Experimental Setup	111
Quality Control	111
Data File Formats	112
Sodars	113
Experimental Setup	113
Quality Control	114
Data File Formats	114
Radar Wind Profiler and RASS	114
Experimental Setup	114
Quality Control	115
Data File Formats	116
Flux Station	116
Experimental Setup	116
Quality Control	118
Data File Formats	118
Radiosondes	120
Experimental Procedures	120
Quality Control	121
Data Files and Results	123
Ceilometer	126

NOAA/INL Mesonet	126
Configuration	126
Quality Control	127
Data File Formats	127
SUMMARY OF INDIVIDUAL IOPs	129
Introduction	129
IOP1	131
Date/Time and General Description	131
Wind Speed and Direction Quality Assurance	132
Turbulence	133
Wind and Turbulence Profiles	138
Radiosonde Results	145
Bag Sampling Results	147
Fast Response Results	156
IOP2	159
Date/Time and General Description	159
Wind Speed and Direction Quality Assurance	160
Turbulence	165
Wind and Turbulence Profiles	167
Radiosonde Results	174
Bag Sampling Results	176
Fast Response Results	185
IOP3	188
Date/Time and General Description	188
Wind Speed and Direction Quality Assurance	189
Turbulence	194
Wind and Turbulence Profiles	196
Radiosonde Results	203
Bag Sampling Results	205
Fast Response Results	214
IOP4	217
Date/Time and General Description	217
Wind Speed and Direction Quality Assurance	218
Turbulence	223
Wind and Turbulence Profiles	225
Radiosonde Results	232
Bag Sampling Results	234
Fast Response Results	243
IOP5	246
Date/Time and General Description	246
Wind Speed and Direction Quality Assurance	247
Turbulence	253
Wind and Turbulence Profiles	255

	Radiosonde Results	262
	Bag Sampling Results	264
	Fast Response Results	277
IOP6	280
	Date/Time and General Description	280
	Wind Speed and Direction Quality Assurance	281
	Turbulence	287
	Wind and Turbulence Profiles	289
	Radiosonde Results	297
	Bag Sampling Results	299
	Fast Response Results	310
IOP7	312
	Date/Time and General Description	312
	Wind Speed and Direction Quality Assurance	313
	Turbulence	319
	Wind and Turbulence Profiles	321
	Radiosonde Results	328
	Bag Sampling Results	330
	Fast Response Results	344
IOP8	347
	Date/Time and General Description	347
	Wind Speed and Direction Quality Assurance	348
	Turbulence	354
	Wind and Turbulence Profiles	356
	Radiosonde Results	363
	Bag Sampling Results	365
	Fast Response Results	377
	PRELIMINARY DISCUSSION	381
	REFERENCES	389

FIGURES

Figure 1. Map of southeast Idaho showing the Idaho National Laboratory and surrounding terrain. A star indicates the location of the tracer studies.	1
Figure 2. Google Earth image of the Grid 3 area showing sampling arcs and other features. ...	3
Figure 3. Photo from Grid 3 tower looking northeast along the radial road at 55° azimuth through the tracer sampling array. The release site is near the center of the photo, the command center (COC) tower and wind profiler installation (PRO) are visible in the right center of the photo, and the ridge to the northeast of the release is visible in the upper left.	3
Figure 4. Photo of the Grid 3 tower.	4
Figure 5. Configuration of PSB2 field tracer experiments. The labels are defined in the text. Daytime tests utilized the 100, 200, and 400 m arcs from the 276 to 126 degrees azimuth plus the 800 m arc. Nighttime tests utilized only the 100, 200, and 400 m arcs from 312 to 162 degrees azimuth.	7
Figure 6. Photo of bag sampler mounting.	9
Figure 7. The SF ₆ release system inside the cargo trailer including the SF ₆ bottles, mass flow controller, computer data acquisition and control system, and electronic scales under the bottles.	15
Figure 8. Photo of the cargo trailer where the release system was housed on location at the Grid 3 facility.	15
Figure 9. SF ₆ release rate for IOP1.	18
Figure 10. SF ₆ release rate for IOP2.	18
Figure 11. SF ₆ release rate for IOP3.	19
Figure 12. SF ₆ release rate for IOP4.	19
Figure 13. SF ₆ release rate for IOP5.	20
Figure 14. SF ₆ release rate for IOP6.	20
Figure 15. SF ₆ release rate for IOP7.	21
Figure 16. SF ₆ release rate for IOP8.	21
Figure 17. Bag sampler with cover and cartridge removed.	25
Figure 18. Sampler cartridge.	25
Figure 19. Bag sampler with sampler cartridge installed.	26
Figure 20. ATGASs in lab.	27
Figure 21. ATGASs in lab with computer.	28
Figure 22. Schematic of sample loop fill with column 1 (pre-column) in the back-flush position.	29
Figure 23. Schematic of injection to column 1 (pre-column) and on to column 2 (main column).	29
Figure 24. Timewand.	30
Figure 25. Sampler servicing procedure A: Placing a sampler at a location.	31
Figure 26. Sampler servicing procedure B: Retrieving a sampler.	31
Figure 27. Sampler servicing procedure C: Replacing a cartridge.	32
Figure 28. Example of Sampler Servicing Record. This was from cartridge removal after Test 1.	33

Figure 29. Photo cartridge cleaning apparatus.	38
Figure 30. Comparison between measured and NIST-certified standard concentrations for all lab control (CCV) samples.	46
Figure 31. Graph of rerun against original values for all laboratory duplicates.	49
Figure 32. Plot of field control sample results.	52
Figure 33a. Graph of field duplicate samples by IOP with included linear regressions.	54
Figure 33b. Graph of field duplicate samples by day and night and distance with included linear regressions.	55
Figure 34. Results from the very cold temperature (first) pink box test. Red traces are for the early 1300 h start samplers and black traces are for the late 1330 h start samplers.	57
Figure 35. Results from cold temperature (second) pink box test. Red traces are for the early 1030 h start samplers and black traces are for the late 1130 h start samplers.	58
Figure 36. Example of Raw Data Summary sheet.	62
Figure 37. Example of first page from quality control sheets.	63
Figure 38. Example of last page from quality control sheets.	64
Figure 39. Example of chromatogram and calibration curve check sheet.	65
Figure 40. Example of laboratory notebook page.	66
Figure 41. Example of data package Data Verification sheet.	67
Figure 42. Example of Analysis Summary sheet.	68
Figure 43. Example of bubble/dot plot for examining consistency of concentrations between neighboring locations and identifying suspicious values.	72
Figure 44. Example of cartridge time series plots used for identifying suspicious values.	73
Figure 45. Example of output from program used to assign flags to values in final data sets and final check for possible errors.	74
Figure 46. NOAA mobile, fast response, tracer gas analyzer installed in the passenger seat of a van. A calibration box is visible in the foreground. The microcontroller that collects the data and runs automated calibrations is attached to the top of the instrument.	80
Figure 47. Operating checklist for fast response analyzers.	85
Figure 48. An example of a fast response analyzer settings record.	86
Figure 49. Example of a fast response analyzer QC sheet.	89
Figure 50. Schematic representation of the 62 m Grid 3 tower instrumentation. All anemometers mounted transverse to prevailing winds on booms extending from the tower. Barometric pressure, rain gauge, and soil flux not shown. CV represents cups and vanes, Temp is temperature and humidity, Son is 3-D sonic anemometer, and Rad is solar radiation. . .	94
Figure 51. Photo of an R. M. Young Ultrasonic 81000 (left) and a Gill Windmaster Pro (right) used during PSB2.	95
Figure 52. An Acumen data collection bridge (white device inside) was used to collect data from the sonic anemometers.	96
Figure 53. 30 m command center meteorological tower (COC).	112
Figure 54. Photo of the ASC sodar, collocated with the radar wind profiler at PRO.	113
Figure 55. Photo of the radar wind profiler (PRO) and RASS.	115
Figure 56. Photo of the flux station.	117
Figure 57. Photo of radiosonde release.	121

Figure 58. Example balloon profile data diagram from IOP1, Launch 1, with atmospheric pressure (green), relative humidity (orange), air temperature (blue), balloon ascent rate (black), wind speed (red), and radiosonde height AGL (black) plotted as a function of time after launch. The time stamp is the start of the ascent in UTC.	123
Figure 59. Example thermodynamic (Stueve) diagram diagram from IOP1, Launch 1, with relative humidity (orange), air temperature (blue), wind direction (black), and wind speed (red) plotted as a function of geopotential height MSL. The time stamp is the start of the ascent in UTC.	124
Figure 60. Example tephigram from IOP1, Launch 1, with air temperature (blue), wet bulb temperature (red) and dew point temperature (orange) plotted on a temperature/potential temperature graph. The time stamp is the start of the ascent in UTC..	124
Figure 61. Example Skew-T diagram from IOP1, Launch 1, with air temperature (blue) and dew point temperature (orange) plotted on a temperature/pressure graph. The time stamp is the start of the ascent in UTC.	125
Figure 62. Example emagram from IOP1, Launch 1, with air temperature (blue) and dew point temperature (orange) plotted on a temperature/pressure graph. The time stamp is the start of the ascent in UTC.	125
Figure 63. Example altitude diagram from IOP1, Launch 1, with wind speed (red), relative humidity (orange), temperature (blue), and wind direction (black) plotted as a function of height. The time stamp is the start of the ascent in UTC..	126
Figure 64. Incoming solar radiation and classification of stability conditions using the Pasquill-Gifford Solar Radiation Delta T (srdt) and σ_0 (sigt) methods (EPA 2000c) during IOP1. Classes A, B, C, and D are designated 1, 2, 3, and 4, respectively.	131
Figure 65. Time series of near surface wind speed and direction measurements during IOP1. In the legend, location is specified in upper case, the measurement type in lower case (cv = cup and vane, son = sonic), and the measurement height numerically.	133
Figure 66. Time series of wind speed and direction measurements at heights between 9 and 30 m agl during IOP1. Legend notations described in caption of Fig. 65.	134
Figure 67. Time series of wind speed and direction measurements at heights above 30 m agl during IOP1. Legend notations described in caption of Fig. 65.	135
Figure 68. Time series from GRI and COC showing cup anemometer and wind vane measurements of U , wind direction, standard deviation of wind direction σ_0 , and temperature during IOP1. The locations are designated 'xxxxy' where xxx = tower and yy = measurement height..	136
Figure 69. Time series of near surface turbulence (sonic) measurements during IOP1. The GRI and COC are σ_0 wind vane measurements (cv) in degrees converted to radians for purposes of comparison. Notation before and after underscore designates location and height, respectively.	137
Figure 70. Profiles of U , wind direction, standard deviation of wind direction σ_0 , and aspirated temperature from cup anemometers and wind vanes during IOP1 at GRI and COC. Each profile is designated 'xxxhrmn' where xxx = tower and hrmn = start time of 10-minute interval.	139

Figure 71. Profiles of U , wind direction, σ_v/U ($\sim\sigma_\theta$), and σ_w/U ($\sim\sigma_\phi$) from sonic anemometers at GRI during IOP1. The legend specifies the start time of the 10-minute interval (hrmn).	140
Figure 72. Profiles of turbulent kinetic energy (TKE), standard deviation in vertical wind speed σ_w , virtual temperature, and friction velocity u_* from sonic anemometers at GRI during IOP1. The legend specifies the start time of the 10-minute interval (hrmn).	141
Figure 73. Time-height cross-section of wind speed and direction at sodar (SOD) during IOP1. Legend represents m s^{-1}	142
Figure 74. Time-height cross-section of wind speed and direction at wind profiler (PRO) during IOP1. Legend represents m s^{-1}	143
Figure 75. Time-height cross-section of σ_w at sodar (SOD) during IOP1. Legend represents m s^{-1}	144
Figure 76. Time-height cross-section of TKE at sodar (SOD) during IOP1. Legend represents $\text{m}^2 \text{s}^{-2}$	144
Figure 77. Time-height cross-section of virtual temperature at the RASS during IOP1. Temperatures are in degrees C.	145
Figure 78. Potential temperature profile from radiosonde probe, IOP1. Pre-test launch bold, post-test launch dotted.	146
Figure 79. Specific humidity profile from radiosonde probe, IOP1. Pre-test launch bold, post-test launch dotted.	146
Figure 80. Color-coded normalized ($F^*\chi/Q$ ppt s g^{-1}) concentrations at 1 m agl for bags 1-6 during IOP1. The number in () is bag number.	148
Figure 81. Color-coded normalized ($F^*\chi/Q$ ppt s g^{-1}) concentrations at 1 m agl for bags 7-12 during IOP1. The number in () is bag number.	149
Figure 82. Color-coded measured SF_6 concentrations (ppt) at 1 m agl for bags 1-6 during IOP1. The number in () is bag number.	150
Figure 83. Color-coded measured SF_6 concentrations (ppt) at 1 m agl for bags 7-12 during IOP1. The number in () is bag number.	151
Figure 84. Cross-sections of normalized concentration along the arcs for bags 1-6 during IOP1.	152
Figure 85. Cross-sections of normalized concentration along the arcs for bags 7-12 during IOP1.	153
Figure 86. Cross-sections of measured SF_6 concentration along the arcs for bags 1-6 during IOP1.	154
Figure 87. Cross-sections of measured SF_6 concentration along the arcs for bags 7-12 during IOP1.	155
Figure 88. Vertical profiles of measured SF_6 concentration at the mobile tower during IOP1.	156
Figure 89. Locations of fast response analyzers during IOP1.	157
Figure 90. Fast response concentration time series during IOP1.	158
Figure 91. Incoming solar radiation and classification of stability conditions using the Pasquill-Gifford Solar Radiation Delta T (srdt) and σ_θ (sigt) methods (EPA 2000c) during IOP2. Classes A, B, C, and D are designated 1, 2, 3, and 4, respectively.	159

Figure 92. Time series of near surface wind speed and direction measurements during IOP2. In the legend, location is specified in upper case, the measurement type in lower case (cv = cup and vane, son = sonic), and the measurement height numerically.	161
Figure 93. Time series of wind speed and direction measurements at heights between 9 and 30 m agl during IOP2. Legend notations described in caption of Fig. 92.	162
Figure 94. Time series of wind speed and direction measurements at heights above 30 m agl during IOP2. Legend notations described in caption of Fig. 92.	163
Figure 95. Time series from GRI and COC showing cup anemometer and wind vane measurements of U , wind direction, standard deviation of wind direction σ_θ , and temperature during IOP2. The locations are designated 'xxxxy' where xxx = tower and yy = measurement height.	164
Figure 96. Time series of near surface turbulence (sonic) measurements during IOP2. The GRI and COC are σ_θ wind vane measurements (cv) in degrees converted to radians for purposes of comparison. Notation before and after underscore designates location and height, respectively.	166
Figure 97. Profiles of U , wind direction, standard deviation of wind direction σ_θ , and aspirated temperature from cup anemometers and wind vanes during IOP2 at GRI and COC. Each profile is designated 'xxxhrmn' where xxx = tower and hrmn = start time of 10-minute interval.	168
Figure 98. Profiles of U , wind direction, σ_v/U ($\sim\sigma_\theta$), and σ_w/U ($\sim\sigma_\phi$) from sonic anemometers at GRI during IOP2. The legend specifies the start time of the 10-minute interval (hrmn). . .	169
Figure 99. Profiles of turbulent kinetic energy (TKE), standard deviation in vertical wind speed σ_w , virtual temperature, and friction velocity u_* from sonic anemometers at GRI during IOP2. The legend specifies the start time of the 10-minute interval (hrmn).	170
Figure 100. Time-height cross-section of wind speed and direction at sodar (SOD) during IOP2. Legend represents m s^{-1}	171
Figure 101. Time-height cross-section of wind speed and direction at wind profiler (PRO) during IOP2. Legend represents m s^{-1}	172
Figure 102. Time-height cross-section of σ_w at sodar (SOD) during IOP2. Legend represents m s^{-1}	173
Figure 103. Time-height cross-section of TKE at sodar (SOD) during IOP2. Legend represents $\text{m}^2 \text{s}^{-2}$	173
Figure 104. Time-height cross-section of virtual temperature at the RASS during IOP2. Temperatures are in degrees C.	174
Figure 105. Potential temperature profile from radiosonde probe, IOP2. Pre-test launch bold, post-test launch dotted.	175
Figure 106. Specific humidity profile from radiosonde probe, IOP2. Pre-test launch bold, post-test launch dotted.	175
Figure 107. Color-coded normalized ($F^*\chi/Q \text{ ppt s g}^{-1}$) concentrations at 1 m agl for bags 1-6 during IOP2. The number in () is bag number.	177
Figure 108. Color-coded normalized ($F^*\chi/Q \text{ ppt s g}^{-1}$) concentrations at 1 m agl for bags 7-12 during IOP2. The number in () is bag number.	178

Figure 109. Color-coded measured SF_6 concentrations (ppt) at 1 m agl for bags 1-6 during IOP2. The number in () is bag number.	179
Figure 110. Color-coded measured SF_6 concentrations (ppt) at 1 m agl for bags 7-12 during IOP2. The number in () is bag number.	180
Figure 111. Cross-sections of normalized concentration along the arcs for bags 1-6 during IOP2.	181
Figure 112. Cross-sections of normalized concentration along the arcs for bags 7-12 during IOP2.	182.
Figure 113. Cross-sections of measured SF_6 concentration along the arcs for bags 1-6 during IOP2.	183
Figure 114. Cross-sections of measured SF_6 concentration along the arcs for bags 7-12 during IOP2.	184
Figure 115. Vertical profiles of measured SF_6 concentration at the mobile tower during IOP2.	185
Figure 116. Locations of fast response analyzers during IOP2.	186
Figure 117. Fast response concentration time series during IOP2.	187
Figure 118. Incoming solar radiation and classification of stability conditions using the Pasquill-Gifford Solar Radiation Delta T (srdt) and σ_θ (sigt) methods (EPA 2000c) during IOP3. Classes A, B, C, and D are designated 1, 2, 3, and 4, respectively.	188
Figure 119. Time series of near surface wind speed and direction measurements during IOP3. In the legend, location is specified in upper case, the measurement type in lower case (cv = cup and vane, son = sonic), and the measurement height numerically.	190
Figure 120. Time series of near surface wind speed and direction measurements at heights between 9 and 30 m agl during IOP3. Legend notations described in caption of Fig. 119.	191
Figure 121. Time series of near surface wind speed and direction measurements at heights above 30 m agl during IOP3. Legend notations described in caption of Fig. 119.	192
Figure 122. Time series from GRI and COC showing cup anemometer and wind vane measurements of U , wind direction, standard deviation of wind direction σ_θ , and temperature during IOP3. The locations are designated 'xxxxy' where xxx = tower and yy = measurement height.	193
Figure 123. Time series of near surface turbulence (sonic) measurements during IOP3. The GRI and COC are σ_θ wind vane measurements (cv) in degrees converted to radians for purposes of comparison. Notation before and after underscore designates location and height, respectively.	195
Figure 124. Profiles of U , wind direction, standard deviation of wind direction σ_θ , and aspirated temperature from cup anemometers and wind vanes during IOP3 at GRI and COC. Each profile is designated 'xxxhrmn' where xxx = tower and hrmn = start time of 10-minute interval.	197
Figure 125. Profiles of U , wind direction, σ_v/U ($\sim\sigma_\theta$), and σ_w/U ($\sim\sigma_\phi$) from sonic anemometers at GRI during IOP3. The legend specifies the start time of the 10-minute interval (hrmn).	198

Figure 126. Profiles of turbulent kinetic energy (TKE), standard deviation in vertical wind speed σ_w , virtual temperature, and friction velocity u_* from sonic anemometers at GRI during IOP3. The legend specifies the start time of the 10-minute interval (hrmn).	199
Figure 127. Time-height cross-section of wind speed and direction at sodar (SOD) during IOP3. Legend represents $m\ s^{-1}$	200
Figure 128. Time-height cross-section of wind speed and direction at wind profiler (PRO) during IOP3. Legend represents $m\ s^{-1}$	201
Figure 129. Time-height cross-section of σ_w at sodar (SOD) during IOP3. Legend represents $m\ s^{-1}$	202
Figure 130. Time-height cross-section of TKE at sodar (SOD) during IOP3. Legend represents $m^2\ s^{-2}$	202
Figure 131. Time-height cross-section of virtual temperature at the RASS during IOP3. Temperatures are in degrees C.	203
Figure 132. Potential temperature profile from radiosonde probe, IOP3. Pre-test launch bold, post-test launch dotted.	204
Figure 133. Specific humidity profile from radiosonde probe, IOP3. Pre-test launch bold, post-test launch dotted.	204
Figure 134. Color-coded normalized ($F^*\chi/Q\ ppt\ s\ g^{-1}$) concentrations at 1 m agl for bags 1-6 during IOP3. The number in () is bag number.	206
Figure 135. Color-coded normalized ($F^*\chi/Q\ ppt\ s\ g^{-1}$) concentrations at 1 m agl for bags 7-12 during IOP3. The number in () is bag number.	207
Figure 136. Color-coded measured SF_6 concentrations (ppt) at 1 m agl for bags 1-6 during IOP3. The number in () is bag number.	208
Figure 137. Color-coded measured SF_6 concentrations (ppt) at 1 m agl for bags 7-12 during IOP3. The number in () is bag number.	209
Figure 138. Cross-sections of normalized concentration along the arcs for bags 1-6 during IOP3.	210
Figure 139. Cross-sections of normalized concentration along the arcs for bags 7-12 during IOP3.	211
Figure 140. Cross-sections of measured SF_6 concentration along the arcs for bags 1-6 during IOP3.	212
Figure 141. Cross-sections of measured SF_6 concentration along the arcs for bags 7-12 during IOP3.	213
Figure 142. Vertical profiles of measured SF_6 concentration at the mobile tower during IOP3.	214
Figure 143. Locations of fast response analyzers during IOP3.	215
Figure 144. Fast response concentration time series during IOP3.	216
Figure 145. Incoming solar radiation and classification of stability conditions using the Pasquill-Gifford Solar Radiation Delta T (srdt) and σ_θ (sigt) methods (EPA 2000c) during IOP4. Classes A, B, C, and D are designated 1, 2, 3, and 4, respectively.	217
Figure 146. Time series of near surface wind speed and direction measurements during IOP4. In the legend, location is specified in upper case, the measurement type in lower case (cv = cup and vane, son = sonic), and the measurement height numerically.	219

Figure 147. Time series of near surface wind speed and direction measurements at heights between 9 and 30 m agl during IOP4. Legend notations described in caption of Fig. 146.	220
Figure 148. Time series of near surface wind speed and direction measurements at heights above 30 m agl during IOP4. Legend notations described in caption of Fig. 146.	221
Figure 149. Time series from GRI and COC showing cup anemometer and wind vane measurements of U , wind direction, standard deviation of wind direction σ_θ , and temperature during IOP4. The locations are designated ‘xxxxyy’ where xxx = tower and yy = measurement height.	222
Figure 150. Time series of near surface turbulence (sonic) measurements during IOP4. The GRI and COC are σ_θ wind vane measurements (cv) in degrees converted to radians for purposes of comparison. Notation before and after underscore designates location and height, respectively.	224
Figure 151. Profiles of U , wind direction, standard deviation of wind direction σ_θ , and aspirated temperature from cup anemometers and wind vanes during IOP4 at GRI and COC. Each profile is designated ‘xxxhrmn’ where xxx = tower and hrmn = start time of 10-minute interval.	226
Figure 152. Profiles of U , wind direction, σ_v/U ($\sim\sigma_\theta$), and σ_w/U ($\sim\sigma_\phi$) from sonic anemometers at GRI during IOP4. The legend specifies the start time of the 10-minute interval (hrmn).	227
Figure 153. Profiles of turbulent kinetic energy (TKE), standard deviation in vertical wind speed σ_w , virtual temperature, and friction velocity u_* from sonic anemometers at GRI during IOP4. The legend specifies the start time of the 10-minute interval (hrmn).	228
Figure 154. Time-height cross-section of wind speed and direction at sodar (SOD) during IOP4. Legend represents m s^{-1}	229
Figure 155. Time-height cross-section of wind speed and direction at wind profiler (PRO) during IOP4. Legend represents m s^{-1}	230
Figure 156. Time-height cross-section of σ_w at sodar (SOD) during IOP4. Legend represents m s^{-1}	231
Figure 157. Time-height cross-section of TKE at sodar (SOD) during IOP4. Legend represents $\text{m}^2 \text{s}^{-2}$	231
Figure 158. Time-height cross-section of virtual temperature at the RASS during IOP4. Temperatures are in degrees C.	232
Figure 159. Potential temperature profile from radiosonde probe, IOP4. Pre-test launch bold, post-test launch dotted.	233
Figure 160. Specific humidity profile from radiosonde probe, IOP4. Pre-test launch bold, post-test launch dotted.	233
Figure 161. Color-coded normalized ($F^*\chi/Q$ ppt s g^{-1}) concentrations at 1 m agl for bags 1-6 during IOP4. The number in () is bag number.	235
Figure 162. Color-coded normalized ($F^*\chi/Q$ ppt s g^{-1}) concentrations at 1 m agl for bags 7-12 during IOP4. The number in () is bag number.	236
Figure 163. Color-coded measured SF_6 concentrations (ppt) at 1 m agl for bags 1-6 during IOP4. The number in () is bag number.	237

Figure 164. Color-coded measured SF_6 concentrations (ppt) at 1 m agl for bags 7-12 during IOP4. The number in () is bag number.	238
Figure 165. Cross-sections of normalized concentration along the arcs for bags 1-6 during IOP4	239
Figure 166. Cross-sections of normalized concentration along the arcs for bags 7-12 during IOP4.	240
Figure 167. Cross-sections of measured SF_6 concentration along the arcs for bags 1-6 during IOP4.	241
Figure 168. Cross-sections of measured SF_6 concentration along the arcs for bags 7-12 during IOP4.	242
Figure 169. Vertical profiles of measured SF_6 concentration at the mobile tower during IOP4	243
Figure 170. Locations of fast response analyzers during IOP4.	244
Figure 171. Fast response concentration time series during IOP4.	245
Figure 172. Incoming solar radiation and classification of stability conditions using the Pasquill-Gifford Solar Radiation Delta T (srdt) and σ_θ (sigt) methods (EPA 2000c) during IOP5. Classes D, E, and F are designated 4, 5, and 6, respectively.	246
Figure 173. Time series of near surface wind speed and direction measurements and Brunt-Väisälä frequency N during IOP5. In the legend, location is specified in upper case, the measurement type in lower case (cv = cup/vane, son = sonic), and the measurement height numerically.	249
Figure 174. Time series of near surface wind speed and direction measurements at heights between 9 and 30 m agl during IOP5. Legend notations described in caption of Fig. 173.	250
Figure 175. Time series of near surface wind speed and direction measurements at heights above 30 m agl during IOP5. Legend notations described in caption of Fig. 173.	251
Figure 176. Time series from GRI and COC showing cup anemometer and wind vane measurements of U , wind direction, standard deviation of wind direction σ_θ , and temperature during IOP5. The locations are designated 'xxxxyy' where xxx = tower and yy = measurement height.	252
Figure 177. Time series of near surface turbulence (sonic) measurements during IOP5. The GRI and COC are σ_θ wind vane measurements (cv) in degrees converted to radians for purposes of comparison. Notation before and after underscore designates location and height, respectively.	254
Figure 178. Profiles of U , wind direction, standard deviation of wind direction σ_θ , and aspirated temperature from cup anemometers and wind vanes during IOP5 at GRI and COC. Each profile is designated 'xxxhrmn' where xxx = tower and hrmn = start time of 10-minute interval.	256
Figure 179. Profiles of U , wind direction, σ_v/U ($\sim\sigma_\theta$), and σ_w/U ($\sim\sigma_\phi$) from sonic anemometers at GRI during IOP5. The legend specifies the start time of the 10-minute interval (hrmn).	257
Figure 180. Profiles of turbulent kinetic energy (TKE), standard deviation in vertical wind speed σ_w , virtual temperature, and friction velocity u_* from sonic anemometers at GRI during IOP5. The legend specifies the start time of the 10-minute interval (hrmn).	258

Figure 181. Time-height cross-section of wind speed and direction at sodar (SOD) during IOP5. Legend represents m s^{-1} .	259
Figure 182. Time-height cross-section of wind speed and direction at wind profiler (PRO) during IOP5. Legend represents m s^{-1} .	260
Figure 183. Time-height cross-section of σ_w at sodar (SOD) during IOP5. Legend represents m s^{-1} .	261
Figure 184. Time-height cross-section of TKE at sodar (SOD) during IOP5. Legend represents $\text{m}^2 \text{s}^{-2}$.	261
Figure 185. Time-height cross-section of virtual temperature at the RASS during IOP5. Temperatures are in degrees C.	262
Figure 186. Potential temperature profile from radiosonde probe, IOP5. Pre-test launch bold, post-test launch dotted.	263
Figure 187. Specific humidity profile from radiosonde probe, IOP5. Pre-test launch bold, post-test launch dotted.	263
Figure 188. Color-coded normalized ($F^*\chi/Q \text{ ppt s g}^{-1}$) concentrations at 1 m agl for bags 1-6 during IOP5. The number in () is bag number.	266
Figure 189. Color-coded normalized ($F^*\chi/Q \text{ ppt s g}^{-1}$) concentrations at 1 m agl for bags 7-12 during IOP5. The number in () is bag number.	267
Figure 190. Color-coded measured SF_6 concentrations (ppt) at 1 m agl for bags 1-6 during IOP5. The number in () is bag number.	268
Figure 191. Color-coded measured SF_6 concentrations (ppt) at 1 m agl for bags 7-12 during IOP5. The number in () is bag number.	269
Figure 192. Cross-sections of normalized concentration along the arcs for bags 1-6 during IOP5.	270
Figure 193. Cross-sections of normalized concentration along the arcs for bags 7-12 during IOP5.	271
Figure 194. Cross-sections of measured SF_6 concentration along the arcs for bags 1-6 during IOP5.	272
Figure 195. Cross-sections of measured SF_6 concentration along the arcs for bags 7-12 during IOP5.	273
Figure 196. Vertical concentration profiles at the arc position given in the legend for (bags) 1-6 during IOP5.	274
Figure 197. Vertical concentration profiles at the arc position given in the legend for (bags) 7-12 during IOP5.	275
Figure 198. Vertical concentration profiles for the 100 m towers at the annotated arc position and times given in the legends during IOP5.	276
Figure 199. Vertical concentration profiles for the 200 m and mobile towers at the annotated arc position and times given in the legends during IOP5.	277
Figure 200. Locations of fast response analyzers during IOP5.	278
Figure 201. Fast response concentration time series during IOP5.	279
Figure 202. Incoming solar radiation and classification of stability conditions using the Pasquill-Gifford Solar Radiation Delta T (srdt) and σ_θ (sigt) methods (EPA 2000c) during IOP5. Classes D, E, and F are designated 4, 5, and 6, respectively.	280

Figure 203. Time series of near surface wind speed and direction measurements and Brunt-Väisälä frequency N during IOP6. In the legend, location is specified in upper case, the measurement type in lower case (cv = cup/vane, son = sonic), and the measurement height numerically.	283
Figure 204. Time series of near surface wind speed and direction measurements at heights between 9 and 30 m agl during IOP6. Legend notations described in caption of Fig. 203.	284
Figure 205. Time series of near surface wind speed and direction measurements at heights above 30 m agl during IOP6. Legend notations described in caption of Fig. 203.	285
Figure 206. Time series from GRI and COC showing cup anemometer and wind vane measurements of U , wind direction, standard deviation of wind direction σ_θ , and temperature during IOP6. The locations are designated ‘xxxxy’ where xxx = tower and yy = measurement height.	286
Figure 207. Time series of near surface turbulence (sonic) measurements during IOP6. The GRI and COC are σ_θ wind vane measurements (cv) in degrees converted to radians for purposes of comparison. Notation before and after underscore designates location and height, respectively.	288
Figure 208. Profiles of U , wind direction, standard deviation of wind direction σ_θ , and aspirated temperature from cup anemometers and wind vanes during IOP6 at GRI and COC. Each profile is designated ‘xxxhrmn’ where xxx = tower and hrmn = start time of 10-minute interval.	290
Figure 209. Profiles of U , wind direction, σ_w/U ($\sim\sigma_\theta$), and σ_w/U ($\sim\sigma_\theta$) from sonic anemometers at GRI during IOP6. The legend specifies the start time of the 10-minute interval (hrmn).	291
Figure 210. Profiles of turbulent kinetic energy (TKE), standard deviation in vertical wind speed σ_w , virtual temperature, and friction velocity u_* from sonic anemometers at GRI during IOP6. The legend specifies the start time of the 10-minute interval (hrmn).	292
Figure 211. Time-height cross-section of wind speed and direction at sodar (SOD) during IOP6. Legend represents m s^{-1}	293
Figure 212. Profiles of low-level jet 0300 to 0600 h during IOP6.	294
Figure 213. Time-height cross-section of wind speed and direction at wind profiler (PRO) during IOP6. Legend represents m s^{-1}	295
Figure 214. Time-height cross-section of σ_w at sodar (SOD) during IOP6. Legend represents m s^{-1}	296
Figure 215. Time-height cross-section of TKE at sodar (SOD) during IOP6. Legend represents $\text{m}^2 \text{s}^{-2}$	296
Figure 216. Time-height cross-section of virtual temperature at the RASS during IOP6. Temperatures are in degrees C.	297
Figure 217. Potential temperature profile from radiosonde probe, IOP6. Pre-test launch bold, post-test launch dotted.	298
Figure 218. Specific humidity profile from radiosonde probe, IOP6. Pre-test launch bold, post-test launch dotted.	298
Figure 219. Color-coded normalized ($F^*\chi/Q$ ppt s g^{-1}) concentrations at 1 m agl for bags 1-6 during IOP6. The number in () is bag number.	300

Figure 220. Color-coded normalized ($F^*\chi/Q$ ppt s g ⁻¹) concentrations at 1 m agl for bags 7-12 during IOP6. The number in () is bag number.	301
Figure 221. Color-coded measured SF ₆ concentrations (ppt) at 1 m agl for bags 1-6 during IOP6. The number in () is bag number.	302
Figure 222. Color-coded measured SF ₆ concentrations (ppt) at 1 m agl for bags 7-12 during IOP6. The number in () is bag number.	303
Figure 223. Cross-sections of normalized concentration along the arcs for bags 1-6 during IOP6.	304
Figure 224. Cross-sections of normalized concentration along the arcs for bags 7-12 during IOP6.	305
Figure 225. Cross-sections of measured SF ₆ concentration along the arcs for bags 1-6 during IOP6.	306
Figure 226. Cross-sections of measured SF ₆ concentration along the arcs for bags 7-12 during IOP6.	307
Figure 227. Vertical concentration profiles at the arc position given in the legend for (bags) 1-6 during IOP6. All concentrations were at or near background.	308
Figure 228. Vertical concentration profiles at the arc position given in the legend for (bags) 7-12 during IOP6. All concentrations were at or near background.	309
Figure 229. Locations of fast response analyzers during IOP6.	310
Figure 230. Fast response concentration time series during IOP6.	311
Figure 231. Incoming solar radiation and classification of stability conditions using the Pasquill-Gifford Solar Radiation Delta T (srdt) and σ_θ (sigt) methods (EPA 2000c) during IOP7. Classes D, E, and F are designated 4, 5, and 6, respectively.	312
Figure 232. Time series of near surface wind speed and direction measurements and Brunt-Väisälä frequency N during IOP7. In the legend, location is specified in upper case, the measurement type in lower case (cv = cup/vane, son = sonic), and the measurement height numerically.	315
Figure 233. Time series of near surface wind speed and direction measurements at heights between 9 and 30 m agl during IOP7. Legend notations described in caption of Fig. 232.	316
Figure 234. Time series of near surface wind speed and direction measurements at heights above 30 m agl during IOP7. Legend notations described in caption of Fig. 232.	317
Figure 235. Time series from GRI and COC showing cup anemometer and wind vane measurements of U , wind direction, standard deviation of wind direction σ_θ , and temperature during IOP7. The locations are designated 'xxxxyy' where xxx = tower and yy = measurement height.	318
Figure 236. Time series of near surface turbulence (sonic) measurements during IOP7. The GRI and COC are σ_θ wind vane measurements (cv) in degrees converted to radians for purposes of comparison. Notation before and after underscore designates location and height, respectively.	320
Figure 237. Profiles of U , wind direction, standard deviation of wind direction σ_θ , and aspirated temperature from cup anemometers and wind vanes during IOP7 at GRI and COC. Each profile is designated 'xxxhrmn' where xxx = tower and hrmn = start time of 10-minute interval.	322

Figure 238. Profiles of U , wind direction, σ_v/U ($\sim\sigma_\theta$), and σ_w/U ($\sim\sigma_\phi$) from sonic anemometers at GRI during IOP7. The legend specifies the start time of the 10-min interval (hrmn)...	323
Figure 239. Profiles of turbulent kinetic energy (TKE), standard deviation in vertical wind speed σ_w , virtual temperature, and friction velocity u_* from sonic anemometers at GRI during IOP7. The legend specifies the start time of the 10-min interval (hrmn).	324
Figure 240. Time-height cross-section of wind speed and direction at sodar (SOD) during IOP7. Legend represents m s^{-1} .	325
Figure 241. Time-height cross-section of wind speed and direction at wind profiler (PRO) during IOP7. Legend represents m s^{-1} .	326
Figure 242. Time-height cross-section of σ_w at sodar (SOD) during IOP7. Legend represents m s^{-1} .	327
Figure 243. Time-height cross-section of TKE at sodar (SOD) during IOP7. Legend represents $\text{m}^2 \text{s}^{-2}$.	327
Figure 244. Time-height cross-section of virtual temperature at the RASS during IOP7. Temperatures are in degrees C.	328
Figure 245. Potential temperature profile from radiosonde probe, IOP7. Pre-test launch bold, post-test launch dotted.	329
Figure 246. Specific humidity profile from radiosonde probe, IOP7. Pre-test launch bold, post-test launch dotted.	329
Figure 247. Color-coded normalized ($F^*\chi/Q$ ppt s g^{-1}) concentrations at 1 m agl for bags 1-6 during IOP7. The number in () is bag number.	333
Figure 248. Color-coded normalized ($F^*\chi/Q$ ppt s g^{-1}) concentrations at 1 m agl for bags 7-12 during IOP7. The number in () is bag number.	334
Figure 249. Color-coded measured SF_6 concentrations (ppt) at 1 m agl for bags 1-6 during IOP7. The number in () is bag number.	335
Figure 250. Color-coded measured SF_6 concentrations (ppt) at 1 m agl for bags 7-12 during IOP7. The number in () is bag number.	336
Figure 251. Cross-sections of normalized concentration along the arcs for bags 1-6 during IOP7.	337
Figure 252. Cross-sections of normalized concentration along the arcs for bags 7-12 during IOP7.	338
Figure 253. Cross-sections of measured SF_6 concentration along the arcs for bags 1-6 during IOP7.	339
Figure 254. Cross-sections of measured SF_6 concentration along the arcs for bags 7-12 during IOP7.	340
Figure 255. Vertical concentration profiles at the arc position given in the legend for (bags) 1-6 during IOP7.	341
Figure 256. Vertical concentration profiles at the arc position given in the legend for (bags) 7-12 during IOP7.	342
Figure 257. Vertical concentration profiles for the 100 m towers at the annotated arc position and times given in the legends during IOP7.	343
Figure 258. Vertical concentration profiles for the 200 m and mobile towers at the annotated arc position and times given in the legends during IOP7.	344
Figure 259. Locations of fast response analyzers during IOP7.	345

Figure 260. Fast response concentration time series during IOP7.	346
Figure 261. Incoming solar radiation and classification of stability conditions using the Pasquill-Gifford Solar Radiation Delta T (srdt) and σ_θ (sigt) methods (EPA 2000c) during IOP8. Classes D, E, and F are designated 4, 5, and 6, respectively.	347
Figure 262. Time series of near surface wind speed and direction measurements and Brunt-Väisälä frequency N during IOP8. In the legend, location is specified in upper case, the measurement type in lower case (cv = cup/vane, son = sonic), and the measurement height numerically.	350
Figure 263. Time series of near surface wind speed and direction measurements at heights between 9 and 30 m agl during IOP8. Legend notations described in caption of Fig. 262.	351
Figure 264. Time series of near surface wind speed and direction measurements at heights above 30 m agl during IOP8. Legend notations described in caption of Fig. 262.	352
Figure 265. Time series from GRI and COC showing cup anemometer and wind vane measurements of U , wind direction, standard deviation of wind direction σ_θ , and temperature during IOP8. The locations are designated 'xxxxyy' where xxx = tower and yy = measurement height.	353
Figure 266. Time series of near surface turbulence (sonic) measurements during IOP8. The GRI and COC are σ_θ wind vane measurements (cv) in degrees converted to radians for purposes of comparison. Notation before and after underscore designates location and height, respectively.	355
Figure 267. Profiles of U , wind direction, standard deviation of wind direction σ_θ , and aspirated temperature from cup anemometers and wind vanes during IOP8 at GRI and COC. Each profile is designated 'xxxhrmn' where xxx = tower and hrmn = start time of 10-min interval.	357
Figure 268. Profiles of U , wind direction, σ_v/U ($\sim\sigma_\theta$), and σ_w/U ($\sim\sigma_\phi$) from sonic anemometers at GRI during IOP8. The legend specifies the start time of the 10-min interval (hrmn). . .	358
Figure 269. Profiles of turbulent kinetic energy (TKE), standard deviation in vertical wind speed σ_w , virtual temperature, and friction velocity u_* from sonic anemometers at GRI during IOP8. The legend specifies the start time of the 10-min interval (hrmn).	359
Figure 270. Time-height cross-section of wind speed and direction at sodar (SOD) during IOP8. Legend represents m s^{-1}	360
Figure 271. Time-height cross-section of wind speed and direction at wind profiler (PRO) during IOP8. Legend represents m s^{-1}	361
Figure 272. Time-height cross-section of σ_w at sodar (SOD) during IOP8. Legend represents m s^{-1}	362
Figure 273. Time-height cross-section of TKE at sodar (SOD) during IOP8. Legend represents $\text{m}^2 \text{s}^{-2}$	362
Figure 274. Time-height cross-section of virtual temperature at the RASS during IOP8. Temperatures are in degrees C.	363
Figure 275. Potential temperature profile from radiosonde probe, IOP8. Pre-test launch bold, post-test launch dotted.	364
Figure 276. Specific humidity profile from radiosonde probe, IOP8. Pre-test launch bold, post-test launch dotted.	364

Figure 277. Color-coded normalized ($F^*\chi/Q$ ppt s g ⁻¹) concentrations at 1 m agl for bags 1-6 during IOP8. The number in () is bag number.	366
Figure 278. Color-coded normalized ($F^*\chi/Q$ ppt s g ⁻¹) concentrations at 1 m agl for bags 7-12 during IOP8. The number in () is bag number.	367
Figure 279. Color-coded measured SF ₆ concentrations (ppt) at 1 m agl for bags 1-6 during IOP8. The number in () is bag number.	368
Figure 280. Color-coded measured SF ₆ concentrations (ppt) at 1 m agl for bags 7-12 during IOP8. The number in () is bag number.	369
Figure 281. Cross-sections of normalized concentration along the arcs for bags 1-6 during IOP8.	370
Figure 282. Cross-sections of normalized concentration along the arcs for bags 7-12 during IOP8.	371
Figure 283. Cross-sections of measured SF ₆ concentration along the arcs for bags 1-6 during IOP8.	372
Figure 284. Cross-sections of measured SF ₆ concentration along the arcs for bags 7-12 during IOP8.	373
Figure 285. Vertical concentration profiles at the arc position given in the legend for (bags) 1-6 during IOP8.	374
Figure 286. Vertical concentration profiles at the arc position given in the legend for (bags) 7-12 during IOP8.	375
Figure 287. Vertical concentration profiles for the 100 m towers at the annotated arc position and times given in the legends during IOP8.	376
Figure 288. Vertical concentration profiles for the 200 m and mobile towers at the annotated arc position and times given in the legends during IOP8.	377
Figure 289. Locations of fast response analyzers during IOP8.	378
Figure 290. Fast response concentration time series during IOP8.	379
Figure 291. Mean absolute values of field duplicate %RPD with standard deviations by distance for (a) PSB1 daytime, PSB2 daytime, and PSB2 nighttime and (b) PSB2 10, 20, and 30 min results. IOPs 4 and 6 have been omitted to minimize the effects of including ambient background samples. Error bars slightly offset to avoid overwrite.	382
Figure 292. TKE fluctuation intensity ($\sigma_{TKE}/\langle TKE \rangle$) for 10-min records at the near surface sonic anemometers.	384
Figure 293. σ_w fluctuation intensity ($\sigma(\sigma_w)/\langle \sigma_w \rangle$) for 10-min records at the near surface sonic anemometers.	385
Figure 294. Ten-minute average 2 m wind speed and direction at GRI and COC as a function of Brunt-Väisälä frequency N	387

TABLES

Table 1. IOP Summary.	13
Table 2. Point source release summary for all IOPs. ‘MFC’ is the flow rate measured by the mass flow controller. ‘Scale’ is the difference in mass of the SF ₆ cylinder between the start and end of the release.	17
Table 3. Arc and arc angle location of field duplicate, field control, and field blank samplers. .	27
Table 4. Measurement quality objectives (MQO) for the bag sampling Data Quality Indicators..	36
Table 5. ATGAS analytical ranges.	39
Table 6. Summary of project instrument sensitivity and low end instrument bias.	42
Table 7. Summary of all laboratory control (CCV) results.	45
Table 8. Summary of results for lab background checks (room air).	47
Table 9. Summary of RPD results for laboratory duplicates.	48
Table 10. Field blank results for each test.	50
Table 11. Combined ATGAS field control results expressed in terms of standard concentration and IOP number.	51
Table 12. Summary of field duplicate sampler results.	53
Table 13. Estimates of MLOQ using field duplicates, field blanks, and field controls.	70
Table 14. Summary of data completeness by IOP with contribution to analyses by individual GC.	75
Table 15. Method Limit of Detection (MLOD) and Method Limit of Quantitation (MLOQ) for fast response analyzers.	83
Table 16. Meteorological instrumentation used during PSB2.	92
Table 17. Summary of radiosonde launch dates, times, durations, and calculated variables. .	122
Table 18. Meteorological conditions during IOP1.	132
Table 19. Meteorological conditions during IOP2.	160
Table 20. Meteorological conditions during IOP3.	189
Table 21. Meteorological conditions during IOP4.	218
Table 22. Meteorological conditions during IOP5.	247
Table 23. Ceilometer estimates of boundary layer heights during IOP5.	264
Table 24. Meteorological conditions during IOP6.	281
Table 25. Ceilometer estimates of boundary layer heights during IOP6.	299
Table 26. Meteorological conditions during IOP7.	313
Table 27. Ceilometer estimates of boundary layer heights during IOP7.	330
Table 28. Meteorological conditions during IOP8.	348

ABSTRACT

The Field Research Division of the Air Resources Laboratory of the National Oceanic and Atmospheric Administration, in collaboration with the Laboratory for Atmospheric Research at Washington State University, conducted a series of tracer field experiments at the Idaho National Laboratory. The emphasis of these tracer experiments was plume dispersion in low wind speed conditions. Four tests were conducted during the daytime in unstable conditions in July and August of 2016. Four additional tests were conducted in October at nighttime in the very stable boundary layer. The field study was designated Project Sagebrush Phase 2 (PSB2), the second in a series that began with PSB1 in October, 2013.

Each experimental period consisted of a continuous 2.5 h SF₆ point source tracer release from 1.5 m agl with consecutive 10 min average bag sampling over the last 2 h of the tracer release period. Sampling resources were limited. The main motivation was to provide good resolution of the plume at a minimum of three downwind distances and allow for some vertical sampling when possible. Bag sampling was done across 210° of arc at 100, 200, and 400 m downwind at 6° spacing. The daytime tests also included sampling along 90° of arc at 800 m and one mobile tower up to 25 m agl. The nighttime tests did not use the 800 m arc but deployed samplers on the mobile tower as well as four additional fixed towers. The bag sampling was complemented by four fast response tracer analyzers and an extensive suite of meteorological measurements of wind, turbulence, and temperature in the horizontal and vertical.

This PSB2 study provides a dataset with a unique combination of higher resolution (10 min) time-averaged bag sampling, fast response tracer sampling, and extensive meteorological measurements for examining plume dispersion in low wind conditions in an open terrain setting. This is particularly the case for analyzing plume structure and dispersion in the very stable boundary layer.

Wind directions were such that not all of the eight tests (Intensive Observation Periods) were successful due to the 210° arc limitation. Daytime IOPs 1 and 2 and nighttime IOPs 5 and 7 were largely successful with relatively minimal plume truncation (edge effects) with respect to the sampling arcs. These should provide good cases for testing plume models and IOPs 5 and 7 are particularly interesting for what they indicate about horizontal dispersion in the very stable boundary layer. IOPs 3 and 8 were more qualified successes. IOPs 4 and 6 had severe edge effects although some useful data can probably be gleaned from them.

A key result from PSB2 regards the uncertainty in tracer measurements. It was found that measurement uncertainty related to plume stochastic factors increases with decreasing downwind distance from the source and is about twice as large in the very stable boundary layer as it is during the daytime. This result has implications on how to account for uncertainties in mean concentration and the probability distribution of concentration in plume dispersion models.

This page is intentionally left blank.

INTRODUCTION

The Air Resources Laboratory's Field Research Division (ARLFRD), part of the National Oceanic and Atmospheric Administration (NOAA), in collaboration with the Laboratory for Atmospheric Research at Washington State University (WSULAR), conducted a set of tracer releases at the Idaho National Laboratory (INL, Fig. 1) during July, August, and October 2016. This is the second in a series of new tracer experiments called Project Sagebrush to study dispersion from continuous sources in flat terrain using technologies not available during older tracer studies from the 1950s and 1960s. These older studies have continued to be used in model development largely due to the expenses associated with conducting comprehensive tracer releases. The initial Project Sagebrush study in 2013 is called phase 1 (PSB1). Results from the five experiments in PSB1 are reported in Finn et al. (2015, 2016). The 2016 results reported here represent Project Sagebrush phase 2 (PSB2).

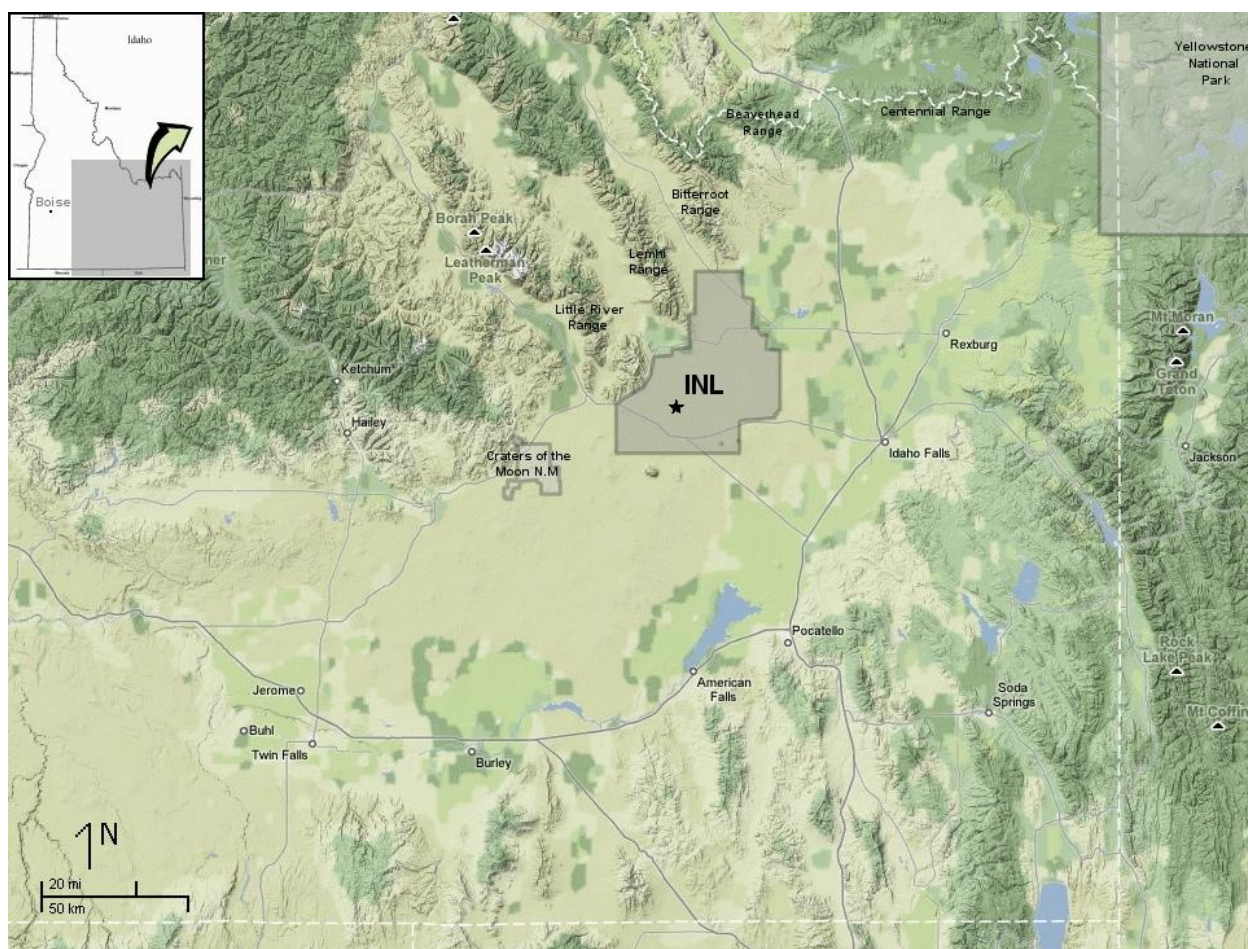


Figure 1. Map of southeast Idaho showing the Idaho National Laboratory and surrounding terrain. A star indicates the location of the tracer studies.

The motivations for conducting Project Sagebrush are developed in Finn et al. (2015) and the science objectives are restated here:

1. Improve the understanding of short-range dispersion from continuous near-surface releases in nearly flat terrain using modern meteorological sensors and tracer technology.
2. Improve the understanding of concentration fluctuations within continuous plumes.
3. Assess the overall repeatability and applicability of individual tracer studies by comparing the new tracer results to classical tracer experiments.
4. Develop improved parameterizations linking plume widths to observed boundary-layer structure.
5. Develop improved dispersion models for both mean concentrations and concentration fluctuations.
6. Provide a new high-quality data set for testing and validating existing dispersion models.

The emphasis of PSB2 was on making tracer measurements in light winds, both in very unstable conditions during the daytime and very stable conditions at night. Relatively few tracer experiments for the measurement of plume dispersion have been conducted in light wind conditions, particularly in low wind speed, nighttime conditions. The tracer study reported by Sagendorf and Dickson (1974) remains one of the most relied upon sources of information for nighttime dispersion in low wind conditions.

Four tracer tests were conducted during the day in light wind conditions in July and August 2016. Four additional tests were conducted at night in light winds during October 2016. Details of the individual experiments are given in the Experimental Plan and IOP Summary chapters. In the light wind conditions targeted for PSB2, placing tracer samplers in full circles around the source would be ideal to eliminate the need to forecast wind directions prior to a release. However, providing adequate spacing in full circles would require more samplers than were available in ARLFRD's inventory. Also, even at low speeds the wind at the experiment site tends to channel along the southwest-northeast axis of the valley where the releases took place (Fig. 1).

Given the available number of tracer samplers and the expected wind channeling, the PSB2 sampler arcs were restricted to 210° with 6° spacing between samplers. This limitation is worth note given the considerable difficulty in accurately forecasting wind direction in light wind conditions. The combination of highly variable wind directions and restricted sampling arcs sometimes resulted in experimental periods where parts of the plume were not being measured. Some of the consequences of this will be described further in later chapters.

The following description of the INL Grid 3 experimental site (Fig. 2) is adopted in large part from Finn et al. (2015). The INL is located across a broad, relatively flat plain on the western edge of the Snake River Plain in southeast Idaho (Fig 1). Elevations across the INL are

approximately 1500 m above mean sea level (MSL). Several parallel mountain chains with peaks exceeding 3000 m MSL dominate the western side of the plain. These chains are separated by a series of tributary valleys that feed into the Snake River Plain. The mountains and benches forming the eastern side of the plain are somewhat lower in elevation, with mountain peaks at roughly 2200 m MSL. Several tributary valleys also feed into the plain from the east, but they are not as regularly spaced as those to the west.

The site offers relatively uniform aerodynamic characteristics across the Grid 3 area (Fig. 3). The terrain is basically flat but has some slight topographic undulations. The canopy is mostly



Figure 2. Google Earth image of the Grid 3 area showing sampling arcs and other features.



Figure 3. Photo from Grid 3 tower looking northeast along the radial road at 55° azimuth through the tracer sampling array. The release site is near the center of the photo, the command center (COC) tower and wind profiler installation (PRO) are visible in the right center of the photo, and the ridge to the northeast of the release is visible in the upper left.

sagebrush and grass. The Grid 3 tall tower (GRI), located 200 m southwest of the tracer release point and center of the sampling array, has routine wind measurements at 2, 10, 15, 45, and 61 m above the ground (Fig. 4). Wind profiles from this tower in near-neutral conditions have been used in a statistical algorithm to estimate the roughness length z_0 at the tracer facility. For southwest winds common during the day the median z_0 is 3 cm, with a 90% probability interval of 2.5–3.5 cm. For northeast winds common at night the median z_0 is 3.8 cm with a 90% probability interval of 3.3–4.4 cm. The slightly higher roughness length for northeast winds may be due to the old river channels and low terrain undulations to the northwest and northeast of the facility. Estimates of the displacement height d were also computed from the Grid 3 profiles, but the values are not significantly different from zero. A small displacement height of a few centimeters probably exists but is not detectable with the current observations on the tower.



Figure 4. Photo of the Grid 3 tower.

GRI has been in continuous operation for decades. Analyses of data from this tower showed that the near-surface wind usually blows parallel to the axis of the Snake River Plain, with southwest winds common during the day and northeast winds at night. Hence, although the INL is within a few km of complex terrain, the tracer facility usually has a relatively flat, uniform fetch extending many tens of kilometers upwind. The boundary layer under such conditions is expected to be close to equilibrium. Two INL building complexes are located about 1.6 km from the tracer facility and are the closest potential flow obstructions of note. One is

nearly south at a true azimuth of 165° (INTEC) and the other almost west at 255° (ATR). The low terrain undulations to the northwest, the low ridge to the northeast (< 3 m relief), and the INTEC and ATR facilities are the only possible terrain interferences. Wind rose analysis prior to PSB2 indicated these facilities are usually not a factor except perhaps for winds out of the WSW. GRI provided vertical profiles of wind, turbulence, fluxes, and temperature during PSB2.

Faint traces of old stream channels are visible in Fig. 2. These channels create only very minor topographic variations. They could have a minor influence on the air flow over the tracer facility when winds have more of a westerly component. The streaks of lighter vegetation with a southwest-northeast orientation in Fig. 2 are burn scars from wildfires. Fires typically kill the darker sagebrush and leave lighter-colored grasses as the dominant vegetation until the sagebrush can recover.

For moderate to strong winds, predicting the wind directions is an easier task because the higher wind speeds are more likely to be associated with the common southwest daytime/north-northeast nighttime wind pattern (Clawson et al, 2007). However, it was a much more difficult task to reliably predict the direction and timing of wind shifts in light wind conditions. Some details of the analysis that was used to determine the timing of sampling and location of the sampling array are described in the Wind Direction Analysis section of the Experimental Plan chapter.

For summer daytime conditions, the lightest winds tend to occur in late morning to early afternoon after nocturnal northeast winds have subsided but before any increase in wind speed associated with the heating-induced southwest winds of mid-late afternoon. However, determining the exact timing of this shift in wind direction is tricky.

For October nighttime conditions, the historical wind rose data indicate a bimodal distribution with both southwest and northeast modes well represented, and it was a matter of predicting which mode would prevail on a given night. The southwest mode tended to prevail in the presence of a weak pressure gradient that overrode nighttime down-valley flows.

A decision was made to array the samplers along arcs that emphasized the northeast quadrant (southwest winds) with respect to the tracer release location for both the daytime and nighttime tests. The daytime sampling arcs ranged from 276° through north to 126° azimuth to try to optimize the increased likelihood of winds from southeast to southwest directions in light wind conditions. The nighttime sampling arcs ranged from 312° through north to 162° azimuth. The choice of a northeast sampling array for nighttime tests was driven by the analysis that southwest winds near the surface tended to occur when winds aloft were weaker. Furthermore, the temperature differences between tower levels indicated that southwest flows tended to occur in the most strongly stable conditions.

The Grid 3 area on the INL was selected for Project Sagebrush for several reasons (Figs. 2 and 3). It was originally designed to conduct transport and dispersion tracer studies in the 1950s. Numerous tracer and other atmospheric studies have been conducted at Grid 3 since that

time (Start et al. 1984; Sagendorf and Dickson 1974; Garodz and Clawson 1991, 1993; Clawson et al. 2009; Finn et al. 2010). Conducting Project Sagebrush at Grid 3 allows ARLFRD to include valuable knowledge from previous work gained over the years. Deployment of the experiment to the INL had the added benefits of simplifying logistics, minimizing some of the costs, and the availability of meteorological measurements already in place at the INL.

EXPERIMENTAL PLAN

Eight tracer release tests, or Intensive Observational Periods (IOPs), were conducted as part of PSB2. Four of these occurred between July 26 and August 5, 2016 in unstable, low wind speed daytime conditions. An additional set of four tests occurred between October 13 and October 26 in very stable, low wind speed nighttime conditions. For reasons elaborated below, the study domain was located primarily on the northeast quadrant of the Grid 3 dispersion array with the idea that winds during the measurement periods would be mainly from southerly through westerly directions. Figure 2 shows a Google Earth image of the study area. Figure 5 is a more detailed schematic image showing the configuration of PSB2.

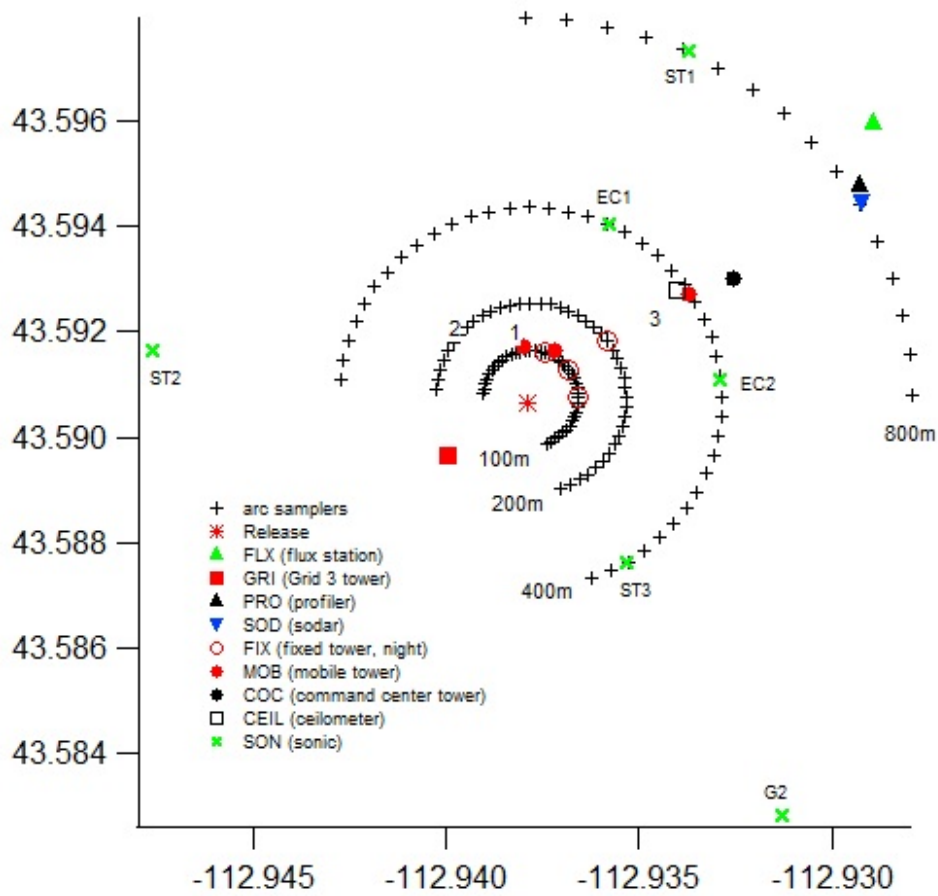


Figure 5. Configuration of PSB2 field tracer experiments. The labels are defined in the text. Daytime tests utilized the 100, 200, and 400 m arcs from 276 to 126 degrees azimuth plus the 800 m arc. Nighttime tests utilized only the 100, 200, and 400 m arcs from 312 to 162 degrees azimuth.

Grid 3 Dispersion Array and Release

Tracer sampling arcs are visible in Fig. 2 around the center (release) point of the Grid 3 dispersion array. The arcs at 100, 200, 400, and 800 m from the source are labeled, but arcs of varying length (degrees) are also present at 50, 1000, 1600, and 3200 m. The arcs were surveyed and marked at 1° intervals to facilitate the placement of tracer samplers. For the daytime tests, bag sampling was conducted over 210° of arc at 6° intervals from 276° azimuth to 126° azimuth on the 100, 200, and 400 m arcs and from 0° to 90° azimuth on the 800 m arc. For the nighttime tests, bag sampling was conducted over 210° of arc at 6° intervals from 312° azimuth to 162° azimuth on the 100, 200, and 400 m arcs.

Continuous releases of SF₆ tracer gas at a constant rate were made from a point source at the center of the Grid 3 dispersion array for each IOP during PSB2. The releases began one-half hour prior to the start of sampling on the dispersion array to establish a quasi-steady state SF₆ concentration field across the array. The release then continued at a constant rate for the two-hour duration of the sampling in the IOP. Release rates were set based upon preliminary calculated estimates of concentrations at different distances and the anticipated atmospheric stability conditions.

Wind Direction Analysis

As noted in the Introduction, only a limited number of bag samplers were available (nominally 151). This required choices to be made between the number of arcs utilized, the total arc length sampled, the number of samplers allocated to each arc, the arc distance between each sampler, the number to be used for measuring vertical tower concentration profiles, and the number needed for quality control purposes. Ideally, if sufficient samplers were available, sampling could be conducted on several full 360° arcs, but this was not possible without making sacrifices on the number of arcs. For this reason, it was necessary to select an arc length that would allow for the maximum number of arcs that would still hopefully optimize the ability to measure the full plume spread in light wind conditions.

This called for a detailed analysis of historical wind speed and wind direction data for the months and times of day anticipated for the tracer release tests. For the daytime tests sampling arcs of 210° from 276° to 126° azimuth with early afternoon releases in July and August were chosen. The nighttime analysis was more difficult due to a number of confounding factors. Principal among these is the fact that nighttime wind roses at Grid 3 tend to be distinctly bimodal with both southwest and northeast modes well represented (Clawson et al, 2007). After considerable deliberation, sampling arcs of 210° from 312° to 162° azimuth with early morning releases ahead of sunrise were selected. The time of day and months for both the daytime and nighttime releases was dictated mainly by considerations for the realization of maximal unstable/stable conditions and minimal wind speeds.

Bag Sampling

The bag sampling measurements were the most essential feature of the experiment. Nominally, 150 samplers were deployed for each IOP with one held in reserve for possible contingencies. For the daytime IOPs, 36 samplers were placed along each of the 100, 200, and 400 m arcs. They were mounted atop plastic boxes at 1 m agl and stabilized from toppling in the wind by hooking the carrying handle over the metal post marking the sampling location (Fig. 6). They were placed at 6° intervals from 276° azimuth to 126° azimuth (i.e., 276, 282, ..., 120, 126°). An additional 16 samplers were deployed on the 800 m arc at 6° intervals from 0° azimuth to 90° azimuth (i.e., 0, 6, ..., 84, 90°). For the nighttime IOPs, 36 samplers were placed along each of the 100, 200, and 400 m arcs at 6° intervals from 312° azimuth to 162° azimuth (i.e., 312, 306, ..., 156, 162°).



Figure 6. Photo of bag sampler mounting.

A mobile tower was available for vertical sampling during PSB2. For the daytime IOPs, bag samplers were deployed on this tower at 1, 5, 10, 15, 20, and 25 m heights at locations on the 100 m arc. These are shown on Fig. 5 as MOB (for mobile tower) sites 1 (IOPs 1 and 2) and 2 (IOPs 3 and 4). Due to the anticipated rapidity of vertical dispersion in unstable daytime conditions, it was assumed that the tower would only be useful relatively close in to the source. For that reason, the only daytime vertical sampling was conducted by MOB on the 100 m arc.

For the nighttime IOPs, MOB was moved to site 3 on the 400 m arc shown on Fig. 5 with sampling at the same heights. Additionally, bag samplers were deployed on four fixed towers (FIX) on the 100 and 200 m arcs. Three of these towers were 10 m tall and located on the 100 m arc. Samplers were placed at 1, 3, 6, and 9 m heights on these towers. The fourth 15 m fixed

tower was on the 200 m arc. Samplers were placed at the same levels as the 10 m towers together with an additional 12 m level. These locations are also shown in Fig. 5.

Bag sampler locations were designated with a 4-digit code with the 2-character prefix 'LC'. The first digit represents the arc or tower location (1 = 100 m, 2 = 200 m, 4 = 400 m, 8 = 800 m, 5 = a tower sampler). For the arc samplers, digits 2-4 specified the azimuth in degrees. For example, Location LC2006 would be an arc sampler located on the 200 m arc at 6° azimuth. Quality control (QC) was integral to the experimental plan and called for the use of blank, control, and duplicate samplers. The number 5 was added to the second digit to designate a duplicate sampler. For example, the duplicate collocated with LC2006 was LC2506. There were 4 duplicate samplers on each of the 100, 200, and 400 m arcs and 2 duplicate samplers on the 800 m arc for a total of 12 per IOP (14 daytime).

Field blank and field control samples were designated with '9' in the first digit with digits 2-4 designating azimuth. The field blank and control sample designations did not indicate arc but these were documented ahead of time and included in the electronic record. For example, LC9042 was the only blank or control sampler located on any of the arcs at 42° azimuth and was specified to be a field control. There was 1 field blank and field control, each, on the 100, 200, and 400 m arcs for all IOPs.

For tower samplers, the second digit identified the tower and digits 3 and 4 specified the sampling height (agl). The second digit designations are:

- 0 – mobile (MOB) tower
- 1 – fixed (FIX) 10 m tower at 17.5° on the 100 m arc
- 5 – fixed 10 m tower at 53.5° on the 100 m arc
- 8 – fixed 10 m tower at 89.5° on the 100 m arc
- 9 – fixed 15 m tower at 53.5° on the 200 m arc

For the mobile tower, digits 3 and 4 '01', '02', '03', '04', '05', and '06' represent the 1, 5, 10, 15, 20, and 25 m heights, respectively. For the fixed towers, digits 3 and 4 '01', '02', '03', '04', and '05' represent the 1, 3, 6, 9, and 12 m heights. For example, LC5502 would designate the 3 m agl sampler on the fixed 10 m tower at 53.5° on the 100 m arc.

The SF₆ samplers operated by pumping air into Tedlar bags with each of the 12 bags being filled sequentially for 10 min over the 2 h IOP sampling period. Thus, the analysis of the bags provided 10-min average concentrations. Tracer concentrations from 2 parts per trillion volume (pptv) to 1 parts per million volume (ppmv) could be analyzed. A complete discussion of bag sampler operation, timing, analysis, and QC can be found in the Bag Sampling chapter.

Fast Response Tracer Gas Analyzers

Four fast response SF₆ analyzers were deployed during PSB2. These were mounted in vehicles and driven to a bag sampling location on the sampling arcs. The primary purpose of the fast response analyzers was to measure concentration fluctuations at about 1 Hz. Ideally, the fast response analyzers would remain at a fixed location to measure the concentration probability density distribution at specific points within the tracer plume. The collection of extended time series would make possible the analysis of concentration fluctuation intensities and probability distributions containing information about large excursions from the mean. However, due to the large variability observed in the wind directions, it was sometimes necessary to perform mobile reconnaissance traverses along the arcs to try to identify where the plume was at a given time.

The analyzer vehicles were generally driven to locations near the plume centerline while avoiding instrument “railing” artifacts where the concentration levels were higher than the analyzer could quantify. Sampling was done through an inlet line extending outside the vehicle. The inlet was usually collocated with a bag sampler location at 1 m agl. If a post or other support was not available for the inlet line at a location, the inlet was hung outside the vehicle at about 1.5 m agl. Nominally, the fast response analyzers had a dynamic range from a few tens pptv to about 10,000 pptv, depending on the characteristics of the individual analyzer. Some of the analyzers were equipped with a dilution system that made it possible to measure concentrations up to about 20,000 pptv. While the analyzer vehicles often remained at a fixed position to measure concentration fluctuations, they were sometimes repositioned due to wind direction shifts or the need to better optimize the location of the analyzer in the plume.

To ensure data quality, a complete QC program was followed during operation of the fast response, real-time analyzers. A more complete description of the fast response analyzer operations can be found in the Fast Response Tracer Analyzer chapter.

Meteorological Equipment

Every effort was made to fully characterize the conditions and structure of the boundary layer during PSB2 for the purpose of identifying all possible meteorological factors controlling tracer dispersion. This included:

- Wind speed and direction variations in the horizontal and vertical
- Vertical profiles of turbulence and turbulent fluxes
- Temperature profiles
- Horizontal homogeneity of the turbulence field
- Soil temperatures, moisture, and heat fluxes
- Solar radiation, net radiation, and energy balance
- Barometric pressure

To this end, ARLFRD, in collaboration with WSULAR, used a broad array of meteorological instrumentation and measurements during PSB2 (Fig. 5):

1. 62 m Grid 3 tower (GRI) – cup and vane anemometers at 5 levels; 3-d sonic anemometers at 6 levels, aspirated air temperature at 5 levels, relative humidity, solar radiation, barometric pressure, soil heat flux at 2 levels
2. Six 3-d sonic anemometers (SON) arrayed across the field site at nighttime to investigate horizontal homogeneity (1 daytime)
3. 30 m Command Center (COC) meteorological tower – cup anemometers and wind vanes at 3 levels
4. SoDAR (SOD) at 800 m (winds at 30-200 m)
5. 915 MHz radar wind profiler (PRO in Fig. 5) and Radio Acoustic Sounding System (RASS) at about 800 m (winds up to 2.9 km height, temperatures up to about 1 km height; both usually much less)
6. Radiosondes before and after each IOP, released from near MOB site 3
7. Flux station (FLX) at about 900 m on the dispersion array – 3-d sonic anemometer, infrared gas analyzer, solar radiation, four-component net radiometer, air temperature/humidity, barometric pressure, soil temperature at 2 levels, soil moisture, soil heat flux at 4 locations
8. 33 other (in addition to Grid 3 tower) meteorological stations of the NOAA/INL mesonet
9. Ceilometer (CEIL)

A complete description of the meteorological instrumentation, measurements, QC procedures, and data file formats can be found in the Meteorological Measurements chapter.

IOP Summaries

A brief summary of IOP test dates and times, release rates, meteorological conditions, and atmospheric stability is listed in Table 1. More comprehensive discussions of each IOP and sampling period are given later in individual chapters.

Table 1. IOP Summary.

IOP	Date	Start Time (MST)	Release Rate (g s^{-1})	Stability			Meteorological Summary
				z/L (3.7)	z/L (9)	Ri_b	
1	26-Jul-16	1200	0.1922	-0.30	-0.58	-1.59	Hot and dry with light and variable winds. Some cloudiness in second hour.
2	27-Jul-16	1130	0.1460	-0.23	-0.50	-0.61	Hot, dry, and clear with U mainly $2\text{--}4 \text{ m s}^{-1}$.
3	04-Aug-16	1300	0.1218	-0.22	-0.81	-2.36	Warm and dry with clear skies and light and variable winds.
4	05-Aug-16	1230	0.1466	-0.36	-0.38	-1.25	Warm and dry with cirrus gradually building during the second hour. Mainly NE winds up to $2\text{--}3 \text{ m s}^{-1}$.
5	13-Oct-16	0400	0.0147	0.85	4.34	0.82	Mostly clear and cold with mainly NW winds about 1 m s^{-1} near the surface and NE winds above that.
6	20-Oct-16	0400	0.0120	1.30	0.75	0.19	Mostly clear and cold with mainly NW winds about 1 m s^{-1} near the surface and NE winds above that.
7	21-Oct-16	0400	0.0120	2.69	1.96	1.13	Mostly clear and cold with variable winds $< 1 \text{ m s}^{-1}$ near the surface and NE winds above that.
8	26-Oct-16	1830	0.0119	1.57	0.50	0.51	Mostly clear and cool with variable winds $1\text{--}2 \text{ m s}^{-1}$.

This page intentionally left blank.

THE SF₆ TRACER RELEASE SYSTEM

The SF₆ tracer release system was custom built for PSB2 at the ARLFRD office in Idaho Falls, ID. The system was placed in a cargo trailer to simplify deployment, provide a reasonably controlled environment for operation, and to simplify removal of the release system when the field deployment was complete. The complete release system (Fig. 7) was entirely self-contained in the cargo trailer (Fig. 8) and only required a 115 VAC 20 ampere power source. This was provided from an adjacent power pole.

The ARLFRD tracer release system was engineered to release a constant amount of SF₆ from a single point source at the center of the Grid 3 tracer facility. Each SF₆ point source release during PSB2 lasted a total of 2.5 hours. The first half-hour of each release period was dedicated to obtaining steady-state dispersion conditions over the entire sampling area before sampling began. Each release then continued at the initial release rate for the next two hours for the actual 2 h long tracer sampling period.

During all SF₆ releases, the gaseous tracer flowed from a cylinder containing SF₆ through the mass flow controller,



Figure 7. The SF₆ release system inside the cargo trailer including the SF₆ bottles, mass flow controller, computer data acquisition and control system, and electronic scales under the bottles.



Figure 8. Photo of the cargo trailer where the release system was housed on location at the Grid 3 facility.

through a visible flow meter, and into a garden hose. The outlet end of the garden hose served as the dissemination point. The garden hose outlet was placed at a height of 1.5 m agl attached to a tower at the center of the sampling grid. It was oriented horizontally to avoid imparting any vertical momentum to the tracer. A heater was used to maintain constant pressure in the SF₆ cylinder and to assist with the vaporization of the liquid SF₆. The SF₆ tracer was provided in K-size cylinders by Concorde Specialty Gases. The certified concentration of the liquid SF₆ was $\geq 99.9\%$.

The heart of the SF₆ tracer release system was the thermal mass flow controller (Hastings Teledyne, Model HFC-203). The mass flow controller was responsible for monitoring and controlling the tracer leaving the SF₆ cylinder. During a release, a voltage was applied to the mass flow controller that was proportional to a given SF₆ flow rate. This voltage could be manually controlled to obtain any desired release rate between a set range. The voltage and the flow rate from the mass flow controller were continuously monitored and recorded with a datalogger.

Accuracy

The mass flow controller was calibrated at the factory and subsequently double-checked outdoors at our office in Idaho Falls. Calibration was needed to correlate the tracer flow rate to the applied voltage. Several verification tests were conducted after the factory calibration to ensure proper functioning of the mass flow controller.

SF₆ Release Summary

All 8 of the PSB2 tracer releases took place at the center of the sampling grid. The target SF₆ release rates for the daytime IOPs ranged from 0.128 to 0.190 g s⁻¹. The target release rates for the nighttime IOPs were about an order of magnitude less (Table 2). These release rates were selected in order to provide measurable tracer concentrations within the dynamic sampling ranges of the bag and fast response samplers at all sampling distances. The gas chromatographs used to measure the bag sample concentrations can handle a very wide range of concentrations, so they are capable of handling almost any release rate. However, the fast response analyzers have a much more limited range and, in particular, are subject to a clipping of the higher concentration peaks (see Fast Response Analyzer chapter). This somewhat limits the usefulness of such data, since it is not known what the maximum concentrations were, just that they exceeded a certain concentration.

Full details of the tracer dissemination, including release date and time, target release rate, actual average release rate from the mass flow meter, and the total mass of SF₆ released for each period are listed in Table 2. Actual release rates differed only slightly from the target release rates. The actual release rates were either the same or very close to the targeted rates for all IOPs with one exception. The measured release rate during IOP3 varied from the target rate by 5% with a relatively larger standard deviation. The relative standard deviations for all other IOPs were very small or zero. The low standard deviations indicated very steady flow rates

throughout the entire 2.5 h continuous release periods. Graphs of the release rates, together with the cumulative amount of SF₆ tracer released during each test are shown in Figs. 9-16. The total amount of SF₆ tracer material that was disseminated during PSB2 was 5,968.1 g.

Table 2. Point source release summary for all IOPs. ‘MFC’ is the flow rate measured by the mass flow controller. ‘Scale’ is the difference in mass of the SF₆ cylinder between the start and end of the release.

Test	Date (2016)	Start Time (MST)	End Time (MST)	Total SF ₆ Release Scale (g)	Total SF ₆ Release MFC (g)	Correction (Scale/ MFC)	Target Release Rate (g s ⁻¹)	Measured 2-hr Release Rate (g s ⁻¹)	Release Rate Standard Deviation (g s ⁻¹)	Release Rate Error (%)
1	26-Jul	11:30	14:00	1,728.9	1,796.301	0.9625	0.190	0.1922	0.0079	1.16
2	27-Jul	11:00	13:30	1,313.8	1,350.105	0.9731	0.146	0.1460	2.39e-14	0.00
3	04-Aug	12:30	15:00	1,145.8	1,170.227	0.9791	0.128	0.1218	0.0258	5.09
4	05-Aug	12:00	14:30	1,319.7	1,350.401	0.9773	0.146	0.1466	0.0000	0.41
5	13-Oct	03:30	06:00	137.0	135.040	1.0145	0.015	0.0147	0.0028	2.04
6	20 Oct	03:30	06:00	107.6	107.996	0.9963	0.012	0.0120	0.0000	0.00
7	21 Oct	03:30	06:00	108.0	108.010	0.9999	0.012	0.0120	0.0000	0.00
8	26-Oct	18:00	20:30	107.3	107.946	0.9940	0.012	0.0119	0.0000	0.84

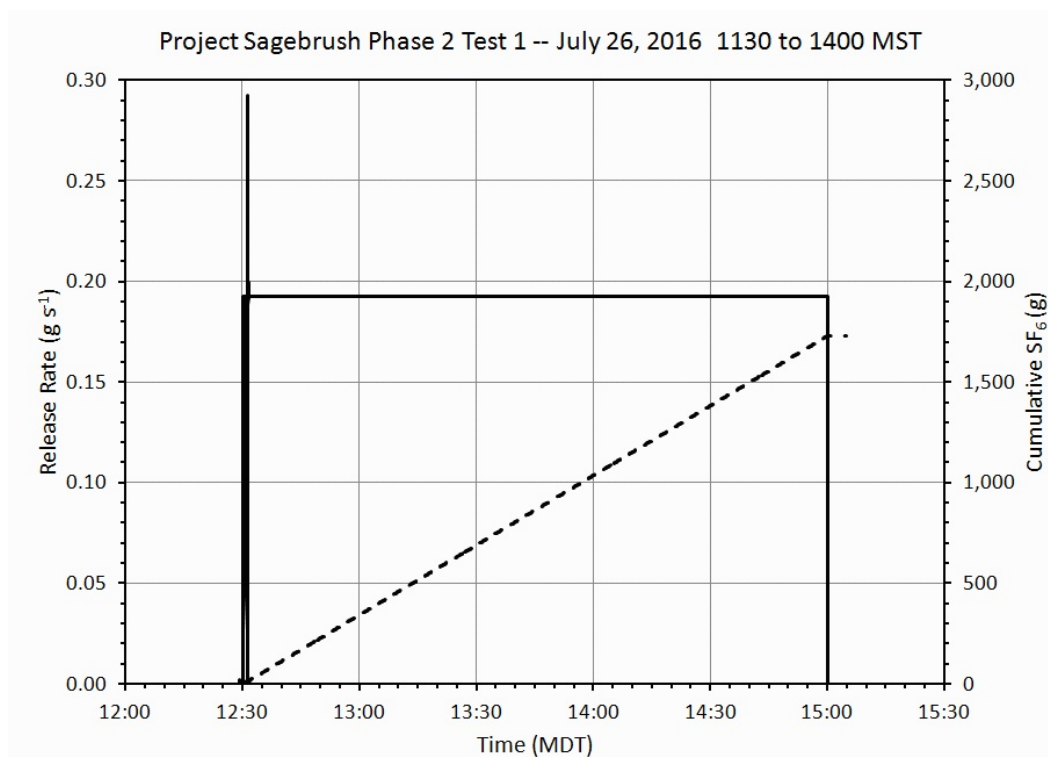


Figure 9. SF_6 release rate for IOP1.

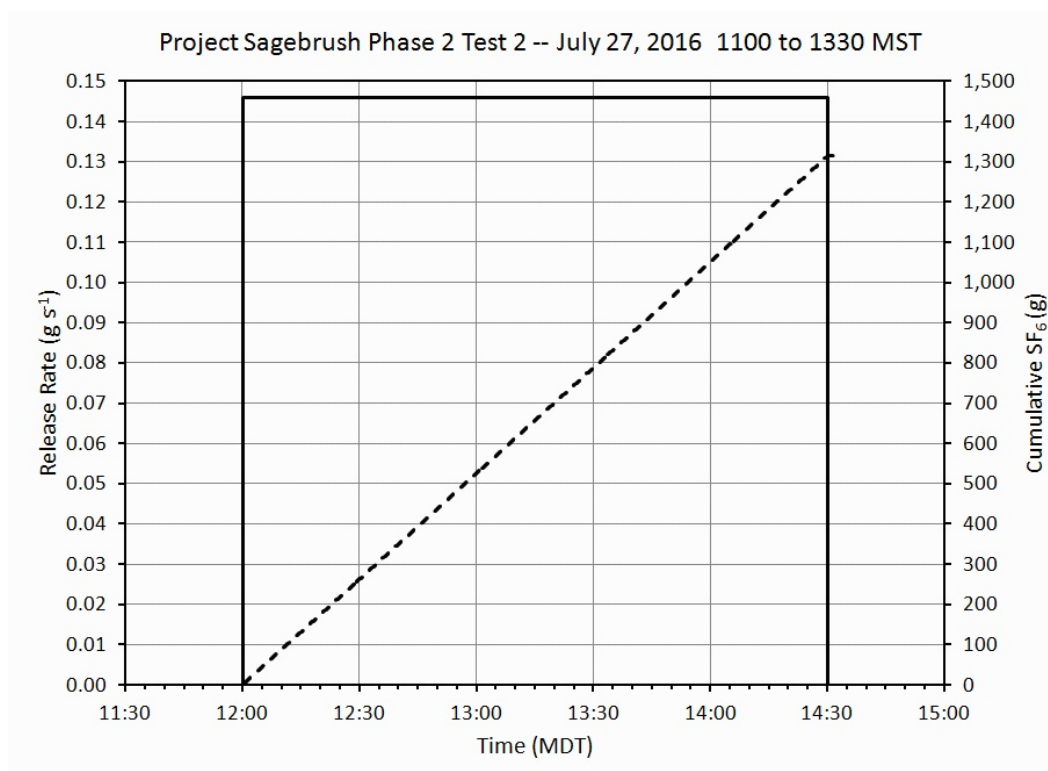


Figure 10. SF_6 release rate for IOP2.

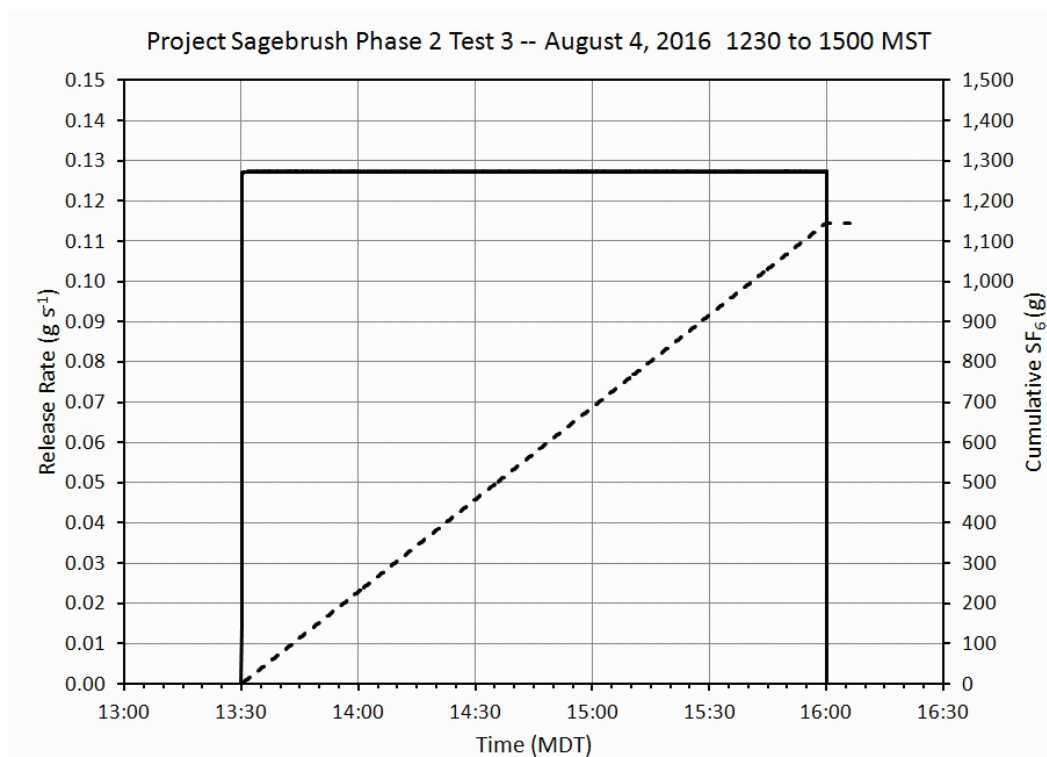


Figure 11. SF_6 release rate for IOP3.

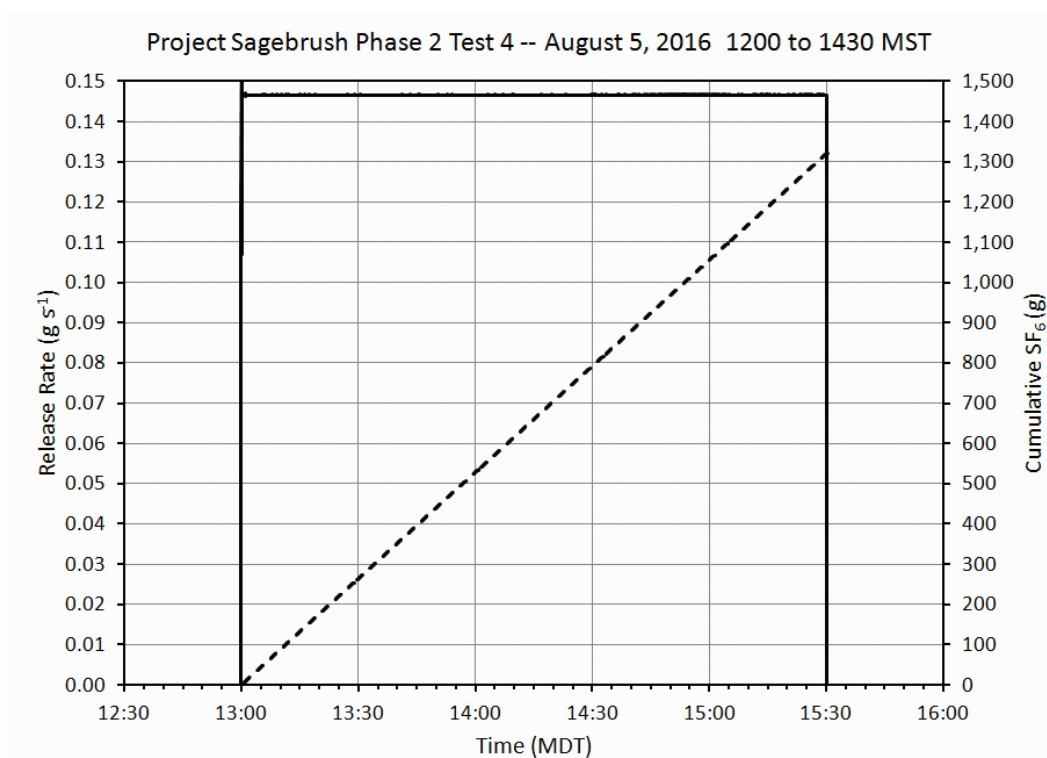


Figure 12. SF_6 release rate for IOP4.

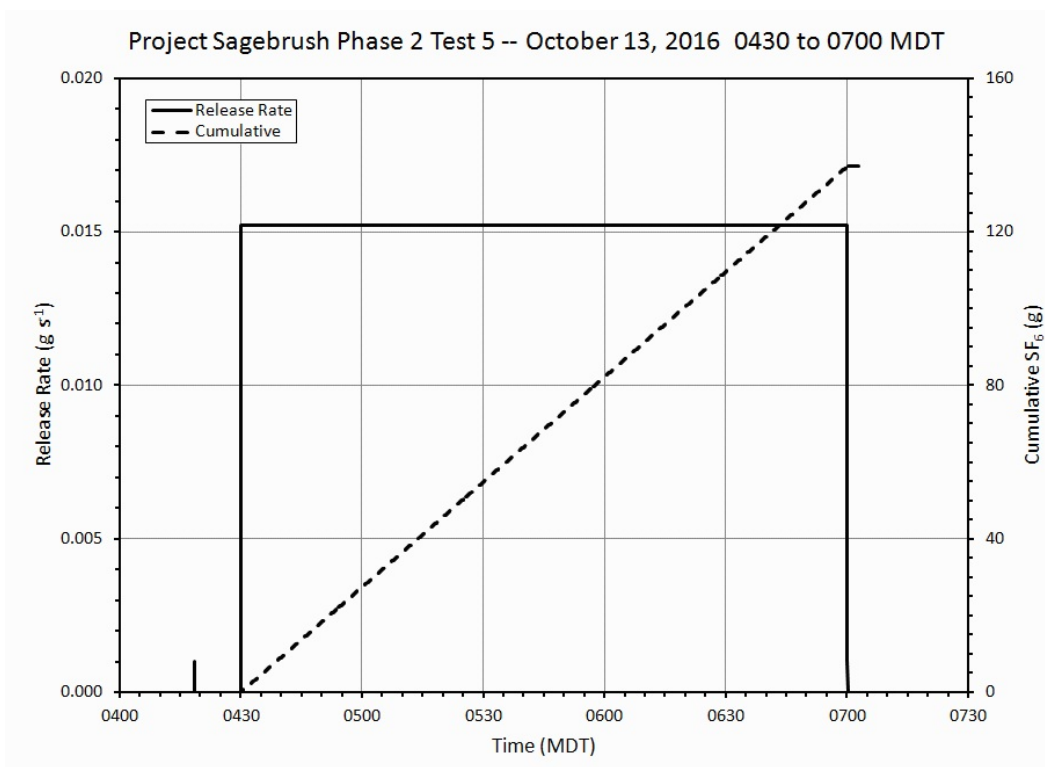


Figure 13. SF_6 release rate for IOP5.

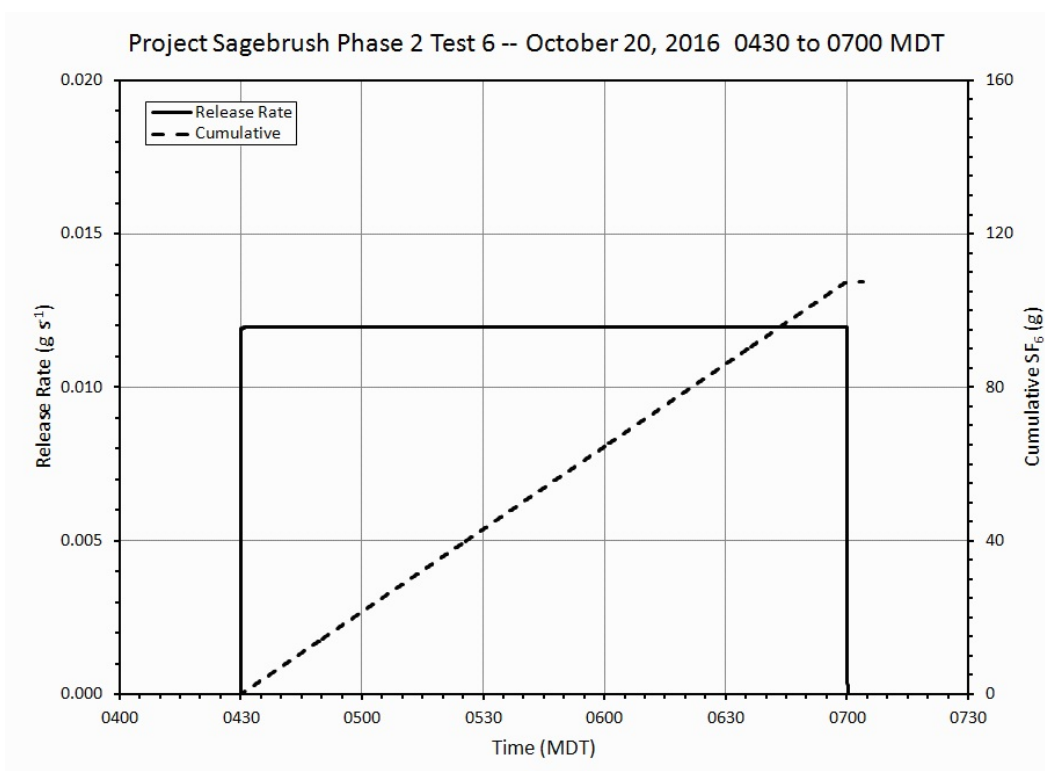


Figure 14. SF_6 release rate for IOP6.

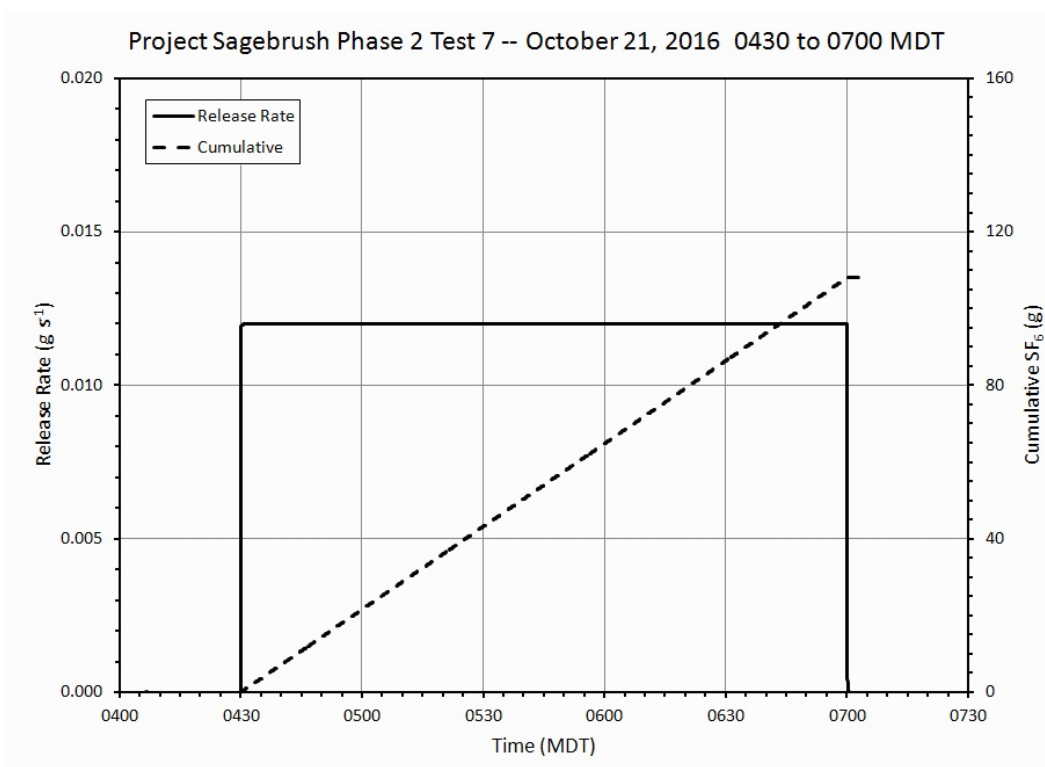


Figure 15. SF_6 release rate for IOP7.

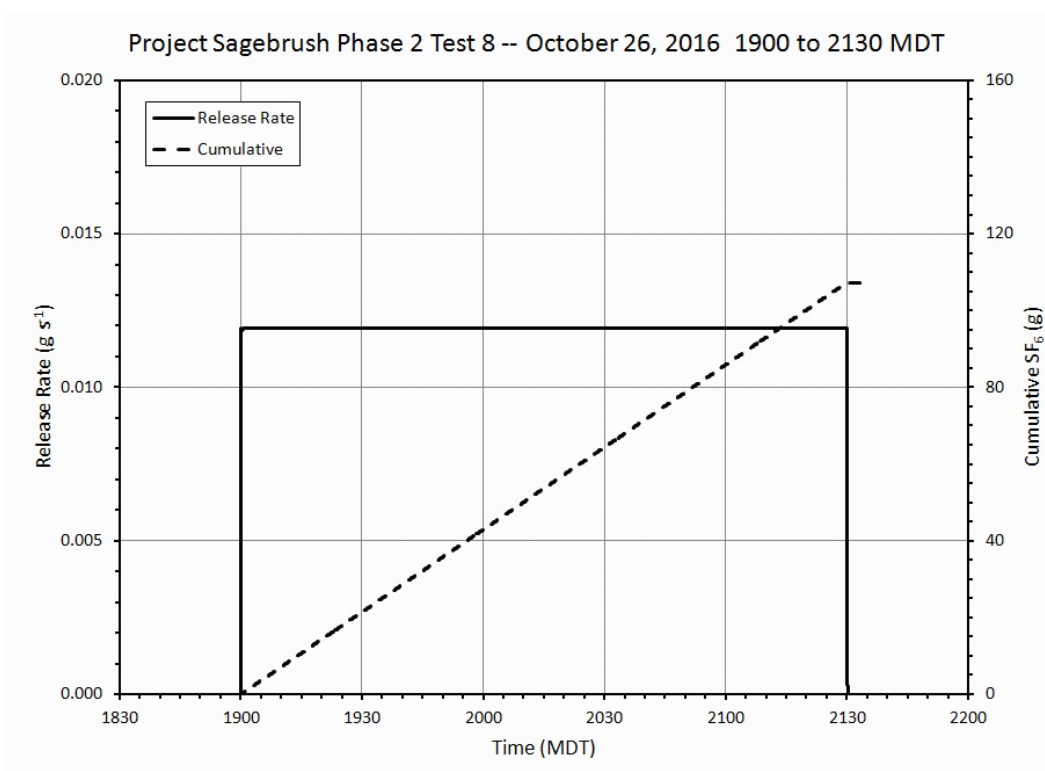


Figure 16. SF_6 release rate for IOP8.

SF₆ Release Quality Control

The quality control program for the SF₆ tracer release consisted of the 8 steps outlined below:

1. Pre-project preparation.
2. Pre-test procedures.
3. Monitoring of key operational parameters during the test.
4. Post-test procedures.
5. Post-test data screening and processing.
6. Verification of all calculations and data by a second analyst.
7. Identification of data problems and setting of QC flags.
8. Review of final data files.

1. Pre-project preparation.

Before the experiment, the SF₆ release mechanism was constructed and thoroughly tested to ensure all systems were in good working order. Prior to the release system construction, the mass flow controller was calibrated at the factory and again at the FRD office/laboratory facility to correlate the actual flow rate with the indicated flow rate. After construction, the system was tested from end to end for flow accuracy. The release system released 99.9% pure SF₆ without dilution.

2. Pre-test procedures.

On the day of a test, the release system operator was required to follow established procedures for preparing the release mechanism. These procedures were based on the experience of previous tracer projects. The procedure included checking for loose connections, visually inspecting the release line, calibrating the scale, setting the clock, setting the mass flow controller output to zero, and verifying that data was recording on the computer. These actions were recorded in the release logbook.

3. Monitoring of key operational parameters during the test.

During the test, the mass flow controller and weight of the SF₆ bottle were monitored for a stable and correct flow rate. These values were recorded approximately every 10 minutes in the release logbook. The release system operator was able to adjust the flow rate on the release mechanism if necessary. Note: The mass flow meter was accurate enough that it did not require additional adjustment after initial setting at the beginning of each test.

4. Post-test procedures.

After a test was complete, the release system operator followed end-of-release procedures for shutting down the release mechanism and collecting the data. Weight loss from the SF₆ bottle(s) was recorded in the release logbook. Release data that had been recorded on the computer was backed up onto a compact memory stick and returned to the FRD office for processing.

5. Post-test data screening and processing.

Once the memory stick was returned to FRD, the data was uploaded onto the network for processing. Release rate data was graphed and reviewed for any spikes or anomalies in the recorded data that would indicate deviations from a stable flow rate. Release rate data from the mass flow controller was compared to the actual weight of the released tracer, as measured by the scales, to ensure that the flow rate was within five percent of the mass flow set point. The mass flow output data was adjusted (corrected) to match the total amount released using the precision balance scale data.

6. Verification of all calculations and data by a second analyst.

The plots of the new data were reviewed and verified by a second analyst.

7. Identification of data problems and setting of QC flags.

The release logbook entries and the plots of the data were carefully reviewed by the data analysts. No problems were found. If any problems had been found, they would have been annotated with the appropriate flag and recorded in the final data files. The data flags would indicate unstable or varying flows, spikes in the release rate, or missing data.

8. Review of final data files.

The data files were carefully reviewed for any problems.

Data File Format

The one second readings from the mass flow controllers are provided in data files on the CD accompanying this report. The files are named 'Test # Release.xlsx, where “#” is the IOP test number. The files contain 10 columns:

1. TIMESTAMP	month/day/year hh:mm:ss (note: MDT)
2. RECORD	record number
3. Grams_sec_out	g s ⁻¹ released
4. PSI_Mass_input	
5. Gas_Temp_C	

6. Set_Grams_sec	release setpoint g s^{-1}
7. FlowRate	
8. Cumulative	cumulative grams released, uncorrected
9. Corrected_Grams_Out	corrected release rate, g s^{-1}
10. Corrected Cumulative	cumulative grams released, corrected

There are additional calculated quantities in the file in the columns to the right summarizing the release.

BAG SAMPLING

Description of Equipment

Stationary time-integrated sampling of SF_6 for PSB2 was performed using programmable bag samplers. These samplers acquired time-sequenced air samples in bags that were subsequently analyzed for the concentration of the SF_6 tracer. The samplers collected 12 samples by sequentially pumping air into each of 12 individual Tedlar® bags. The integrated sampling time for each bag in the study was 10 minutes. This allowed each sampler to cover the full 2 h release during each IOP.



Figure 17. Bag sampler with cover and cartridge removed.

The bag sampler housing is constructed from durable double-wall polypropylene manufactured by Mills Industries Inc. and measures 61 cm x 41 cm x 33 cm (Fig. 17). There were 151 of these samplers available. The mounting of the sampler was shown previously in Fig. 6. The other component of the bag sampler assembly is a cardboard sampler cartridge (Fig. 18). The sampler boxes contain 12 microprocessor-controlled



Figure 18. Sampler cartridge.

air pumps designed to start sequentially filling the bags at a time and duration specified for each bag. The sampling period for each bag and the delays between each bag can be independently specified to create a sampling program customized for each situation. The cartridge box contains 12 Tedlar® bags. Prior to deployment, a sample cartridge was placed into each sampler box (Fig. 19) and connected by R-3603 tubing to the sampler pumps.



Figure 19. Bag sampler with sampler cartridge installed.

With its cover in place (Fig. 6), each sampler box and sampler cartridge assembly had a total mass of approximately 4 kg and was powered by a single D-cell battery. The microprocessor and air pump components of the sampler design have been used successfully in field experiments for many years and are known to be free of artifacts (e.g. Clawson et al. 2004, 2005, 2009). The material used for the bag sampler housing represents an improved design that was extensively tested for reliability and potential sampling artifacts in 2007 and found to be free of artifacts.

Description of Bag Sampling Grid

A total of 108 primary bag samplers were deployed on the 100, 200, and 400 m sampling arcs (36 per arc) shown in Fig. 5 during each IOP. For the daytime IOPs 1-4, these were arrayed across 210° of arc from 276° to 126° azimuth at 6° intervals. In addition, 16 samplers were deployed on the 800 m arc from 0° to 90° azimuth (the only section of this arc available for use). For the nighttime IOPs 5-8, the 36 samplers on each arc were arrayed across 210° of arc from 312° to 162° azimuth. The arc samplers were mounted atop plastic boxes and secured in place with bungee cords attached to metal fence posts. Sample inlet tubes were at about 1 m agl. The locations of each bag sampler were specified by (1) latitude and longitude and (2) distance of the arc from the release location at the center of the arc array and azimuth (angle in degrees clockwise from north along each arc). IOPs 1-4 also included sampling on the mobile tower (MOB) at sites 1 (100 m arc at 24° azimuth) and 2 (100 m arc at 352° azimuth) in Fig. 5 at 1, 5, 10, 15, 20, and 25 m agl. IOPs 5-8 included sampling at the mobile tower at MOB site 3 (400 m arc at 57° azimuth) on Fig. 5 at the same heights. In addition, IOPs 5-8 included sampling at the four fixed tower sites (FIX) shown on Fig. 5. Three of these towers were 10 m tall and located at 17.5°, 53.5°, and 89.5° azimuths from the source on the 100 m arc. They had samplers located at

1, 3, 6, and 9 m agl. The fourth fixed tower was at 53.5° on the 200 m arc and had a sampler at 12 m agl in addition to the same levels as on the other fixed towers.

Quality control samplers were also deployed. This included 14 field collocated duplicates, 3 field controls, and 3 field blanks for the daytime IOPs 1-4. The same was done for the nighttime IOPs 5-8 but only 12 field duplicates were used since the 800 m arc was not used. The arc angle positions of these QC samplers are listed in Table 3.

Table 3. Arc and arc angle location of field duplicate, field control, and field blank samplers.

Arc (m)	Arc Angle Position (degrees)		
	Duplicate	Control	Blank
100	30, 36, 54, 78	42	84
200	6, 12, 24, 66	78	30
400	24, 36, 48, 66	60	12
800	18, 78		

Sampler Cartridge Analysis

Sample cartridges were analyzed at the Tracer Analysis Facility (TAF) in Idaho Falls, ID. The TAF hosts four gas chromatographs (GC, numbered 1-4), each housed within its own autosampler module and connected to a computer with the master data acquisition system. The complete configuration with GC, autosampler, and data acquisition system is called an Automated Tracer Gas Analysis System (ATGAS) (Figs. 20, 21). A dedicated small black handheld computer, visible atop each GC in Figs. 20 and 21, was used to set the operational parameters on each ATGAS.

Each GC housed two Supelco 60/80 Molecular Sieve-5A columns (5' x 1/4" and 2' x 1/4"), a 10-port sample valve, and a sample loop. These columns were maintained at 65°C inside their respective ovens. Two columns (pre-column and main column) were used to reduce analysis time and to vent interfering species that can damage the columns and detector (i.e. oxygen). After the SF₆ sample was injected onto and eluted by the first 2-foot (610 mm) pre-column (Fig. 22), the gas flow was switched to back-flush the



Figure 20. ATGASs in lab.

pre-column while the sample loop was filled with the next sample (Fig. 23). The SF_6 continued on to the main 5-foot (1520 mm) column where further separation occurred before being passed to the detector. Detection of SF_6 was accomplished using a Valco Instrument Co., Inc., Model 140BN electron capture detector (ECD) containing 5 millicuries of Ni-63. The ECD operating temperature was kept at 170°C. The ECDs and columns were protected by a Supelco High Capacity Gas Purifier tube



Figure 21. ATGASs in lab with computer.

heated inside an oven to remove oxygen, water, carbon monoxide and carbon dioxide in the carrier gas as well as a Supelcarb HC hydrocarbon trap to remove organic impurities. Ultra high purity (UHP) nitrogen served as the carrier gas and filtered compressed air was used as the valve actuator gas. Concentration ranges from 2 pptv to about 1 ppmv have been analyzed using this methodology.

All fittings associated with the GCs were leak checked prior to the start of the project. Any leaks identified were corrected. One of the GCs (GC2) exhibited drift and erratic response problems when analyzing samples for IOPs 1 and 2. The detector for GC2 was replaced with a rebuilt detector on August 2, 2016 for the analysis of subsequent IOPs and the performance was then significantly more stable. It is suspected that erratic performance was due to leaks in the detector itself. The Valco 140BN detector on GC4 was replaced by a SRI 110 detector between the analyses for IOPs 4 and 5. The design of the SRI 110 detector is the same as the Valco 140BN but the controller box is included as a module with the detector rather than being a separate unit. The SRI 110 detector generally performed well, although it was somewhat less sensitive to low concentrations as will be described later.

The ATGAS computer software (Carter, 2003) was developed in-house and was used to analyze the tracer gas chromatograms, calculate concentrations, and perform quality control functions. The software incorporates a history file system that records all operations performed on each ATGAS.

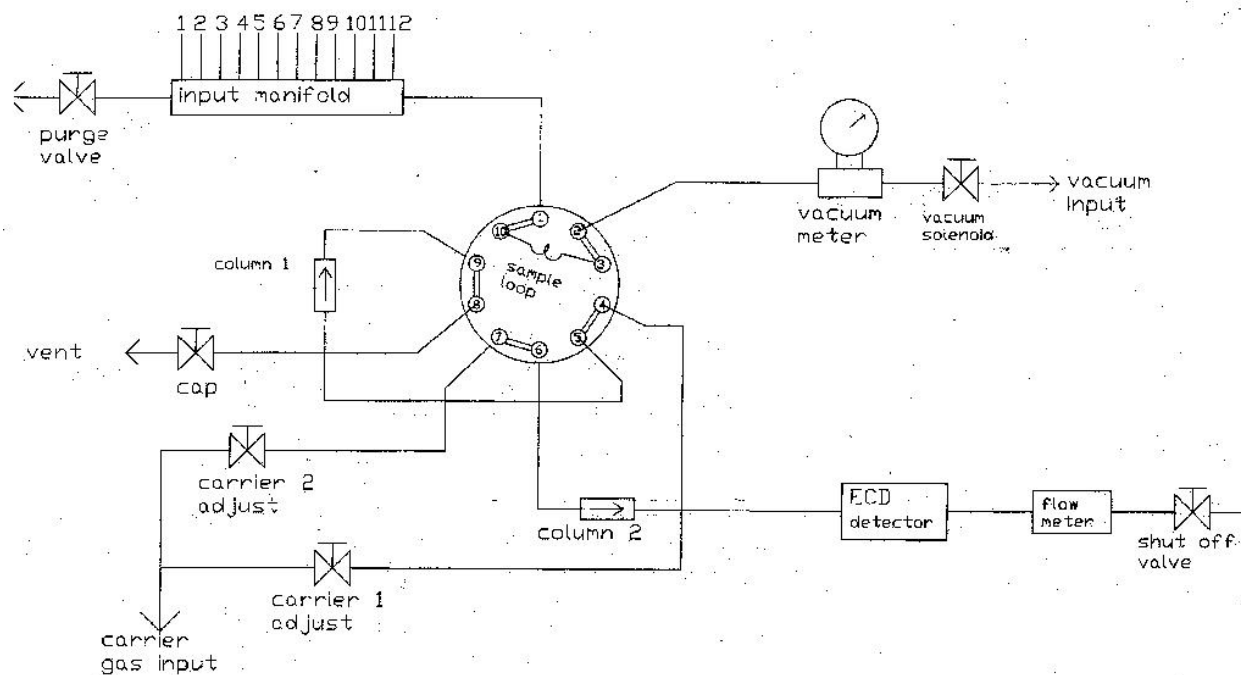


Figure 22. Schematic of sample loop fill with column 1 (pre-column) in the back-flush position.

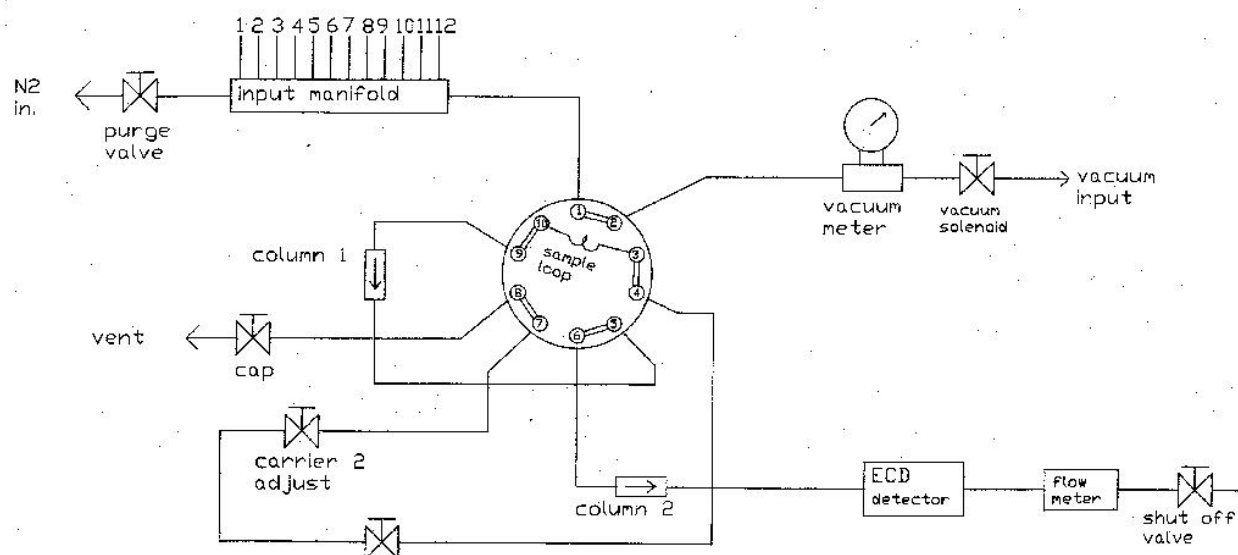


Figure 23. Schematic of injection to column 1 (pre-column) and on to column 2 (main column).

Sampler Handling and Chain of Custody

A history file in the master ATGAS computer maintained a complete, comprehensive record for each sampler cartridge. The scheme for maintaining the comprehensive history file was based upon unique bar coded serial numbers attached to both samplers and sample cartridges and the use of bar code scanners. In addition, prior to the start of the project, each field sampling location was identified and tagged with a location number that consisted of a weatherproof bar code label. These were affixed to the metal fence posts installed at each sampling location. A file with a list of the locations was uploaded to the ATGAS computer in the TAF. The bar code labels for the samplers, cartridges, and locations were used to automatically generate a chain of custody record for each sample.

In preparation for each test, a sample cartridge was placed inside each sampler and then transported to the field. Samplers were deployed at each location, the tubing was connected, clips were opened, and a sampling program downloaded into the memory of each sampler's microprocessor. The latter was accomplished with the use of a small hand-held computer (Videx Timewand II) shown in Fig. 24. This device also serves as a bar code scanner. The Timewands were programmed with sample start and stop times for each bag prior to each test using a dedicated laptop computer in the TAF. They were then used in the field to scan the location number, sampler number, and cartridge number bar codes, after which they downloaded the sampling program. The complete field download records were later retrieved from the Timewands and transferred into the history file on the ATGAS computer in the TAF prior to the start of cartridge analysis.

Details of these field sampling servicing procedures are shown in Figs. 25, 26, and 27. These procedures were developed after years of prior field experience. Personnel responsible for deploying the samplers in the field received classroom and hands-on training in Idaho Falls prior to the experiment. It was also required that handwritten Sampler Servicing Record sheets be completed in the field for each removed or installed cartridge (Fig. 28). These records were created to provide the TAF analyst with details of potential problems pertaining to each cartridge and sample bag. In combination with the history



Figure 24. Timewand.

Sampler Procedure A: Placing a Sampler at a Location

1. Place the cartridge in the sampler and
 - connect the tubes securely and in the correct order
 - open the clips, making sure that the tubing is fully opened and the clip slides easily on the tube. Press on the tube with a finger or blunt end of a pen if necessary.
 2. On the Sampler Servicing Record Sheet, fill in the
 - Location number
 - Sampler number
 - Time (available by pressing "+" on the Time Wand)
 - Cartridge installed
 3. Check the sampler inlet tubes to be sure they have not been pushed back into the sampler.
 4. Make sure there is a battery in the sampler. If you need to insert one, do so carefully so that the battery clips are not damaged.
 5. Plug the Time Wand II cord into the sampler. Verify that the right LED is blinking.
 6. With the Time Wand II, scan the sampler serial number, the cartridge serial number, and the location serial number. These may be scanned in any order. Make sure you use the **correct location number** for each sampler. The Time Wand II will now download the program into the sampler. The left LED will light to indicate a successful download. Make sure the left LED is on before removing the cable!
- NOTE: **In emergencies only**, the serial numbers may be entered with the keypad. (Type the 6-digit code and then press the "=" key.) Since this is very error prone, do not use this method unless there is absolutely no other way!
7. Disconnect the Time Wand II.
 8. Record any problems on the Sampler Servicing Record Sheet. **If there are problems noted, place a mark on the metal bracket in the cartridge with a Sharpie permanent marker** so that lab analyst will know to check the Sampler Servicing Record Sheet.
 9. Place the lid on the sampler and put it on the hanger.

Figure 25. Sampler servicing procedure A: Placing a sampler at a location.

Sampler Procedure B: Retrieving a Sampler

1. Retrieve the sampler from the hanger and remove the lid.
2. On the Sampler Servicing Record Sheet, fill in the
 - Location number
 - Sampler number
 - Cartridge Removed
 - Time (available by pressing "+" on the Time Wand)
3. Verify that the cartridge was connected correctly and the bags were filled. Record any problems on the Sampler Servicing Record Sheet. **If there are problems noted, place a mark on the metal bracket in the cartridge with a permanent marker** so that lab analyst will know to check the Sampler Servicing Record Sheet.
4. Close the clips on the cartridge.
5. Disconnect the tubes.
6. Cartridge may now be removed from the sampler or transported in the sampler.

Figure 26. Sampler servicing procedure B: Retrieving a sampler.

Sampler Procedure C: Replacing a Cartridge

1. Retrieve the sampler from the hanger and remove the lid.
2. On the Sampler Servicing Record Sheet, fill in the
 - Location number
 - Sampler number
 - Cartridge Removed
 - Time (available by pressing "+" on the Time Wand)
3. Verify that the cartridge was connected correctly and the bags were filled. Record any problems on the Sampler Servicing Record Sheet. **If there are problems noted, place a mark on the metal bracket in the cartridge with a permanent marker** so that lab analyst will know to check the Sampler Servicing Record Sheet.
4. Close the clips on the cartridge.
5. Disconnect the tubes and remove the cartridge.
6. Plug the Time Wand II cord into the sampler. Verify that the right LED is blinking.
7. With the Time Wand II, scan the sampler serial number and the sampler flush code **FL0406**. The sampler will now run each pump for about 4 seconds to flush the pump and the tubes.

NOTE: **In emergencies only**, the numbers may be entered with the keypad. (Type the 6-digit code and then press the "=" key.) Since this is very error prone, do not use this method unless there is absolutely no other way!
8. Place the new cartridge in the sampler and when the pumps have finished running:
 - connect the tubes securely and in the correct order
 - open the clips, making sure that the tubing is fully opened and the clip slides easily on the tube. Press on the tube with a finger or blunt end of a pen if necessary.
9. On the Sampler Servicing Record Sheet, fill in the
 - Cartridge installed
10. Check the sampler inlet tubes to be sure they have not been pushed back into the sampler.
11. If you have been instructed to replace the battery, do so carefully so that the battery clips are not damaged.
13. With the Time Wand II, scan the sampler serial number, the cartridge serial number, and the location serial number. These may be scanned in any order. Make sure you use the **correct location number** for each sampler. The Time Wand II will now download the program into the sampler. The left LED will light to indicate a successful download. Make sure the left LED is on before removing the cable!
14. Disconnect the Time Wand II.
15. Record any problems on the Sampler Servicing Record Sheet. **If there are problems noted, place a mark on the metal bracket in the cartridge with a Sharpie permanent marker** so that lab analyst will know to check the Sampler Servicing Record Sheet.
16. Place the lid on the sampler and put it on the hanger.

Figure 27. Sampler servicing procedure C: Replacing a cartridge.

Sampler Servicing Record Sheet

Each line represents a single visit to a sampler location. Each sheet represents a single traverse of a sampler route. Start a new sheet each time you start your sampler route.

Project: Sage Route: 1600 m Date: 10/2/13
 IOP(s): 1 TimeWand: _____ Name: Jason + Dennis

Location	Sampler	Cartridge Removed	Time	Cartridge Installed	Comments or Problems
LC 6004	GF 206	SN 1196	1830	SN	Bags a little flat (O.k.)
LC 6007	GF 84	SN 4367		SN	O.k.
LC 6010	GF 101	SN 5028		SN	O.k.
LC 6110	GF 41	SN 000 0120		SN	O.k. (little light)
LC 6013	GF 63	SN 0105		SN	O.k.
LC 6015	GF 16	SN 1031		SN	O.k. #9 click wants to open
LC 6019	GF 314	SN 4373		SN	O.k. (little light)
LC 6022	GF 208	SN 1212	1841	SN	#3 + 10 little low (O.k.)
LC 6025	GF 318	SN 1259		SN	O.k. (little light)
LC 6028	GF 30	SN 0389		SN	O.k.
LC 6031	GF 17	SN 0177		SN	#1 Low
LC 6031	GF 312	SN 0031		SN	Looks Good
LC 6034	GF 85	SN 0042		SN	#6 Flat
LC 6134	GF 26	SN 1299	1851	SN	OK
LC 6037	GF 998	SN 1275		SN	OK
LC 6040	GF 212	SN 0231		SN	OK
LC 6043	GF 102	SN 0085		SN	OK
LC 6046	GF 57	SN 1169		SN	OK
LC 6049	GF 999	SN 4364		SN	OK
LC 6052	GF 319	SN 4317		SN	OK
LC 6152	GF 87	SN 0310		SN	OK
LC 6055	GF 36	SN 4307	1903	SN	OK
LC 6058	GF 22	SN 4359		SN	OK
LC 9658	GF 263	SN 1264		SN	OK
LC 6061	GF 996 996	SN 0112		SN	#10 Low a few others low too
LC 6064	GF 207	SN 4388		SN	OK

Sampler 996 #'s on outside ~~are~~ are transposed ⁽⁹⁶⁶⁾ need fixed.

Figure 28. Example of Sampler Servicing Record. This was from cartridge removal after Test 1.

files, these records were invaluable as a reference for sample check-in and later for QC flagging of data. The Sampler Servicing Records were given to the laboratory analyst after sampler collection and delivery were performed. All record sheets were organized and placed in a binder for future reference.

The sample cartridges were transported back to the TAF at the completion of each IOP and analyzed within a few days of sampling. They were all checked in prior to analysis using a bar code scanner. During this process each bag was inspected and the following flags were entered into the computer for each bag:

- B = Too big (overfilled)
- G = Good
- L = Low
- F = Flat
- D = Damaged clip or bag
- I = Improper hookup (tubes crossed, clip open, etc.)

These flags were used later for querying, sorting and generating final QC flags as well as for monitoring sampler performance and checking for mistakes by field personnel.

Each cartridge was again scanned when it was attached to the ATGAS prior to analysis. This linked the GC identity and the acquired chromatogram and calculated concentration data to the computerized data previously collected in the field that specified the project identification, test number, grid location number, grid location coordinates, sampling start time, the sample time per bag, and sampling type (primary or quality control sample). The record also included the cartridge check-in record and cleaning records. Thus a complete computer-generated chain of custody is available for each bag sample as well as automatically linking all field, chromatogram, concentration, and quality control data into one comprehensive data record that could be readily reviewed. This minimized the possibility of errors caused by mistakes in manually recording, copying, or entering of location information and provided an invaluable source of information in the event of a discrepancy or a question about the data.

Potential Sampling Artifacts

Latex tubing was used in the past but it was found to be very susceptible to degradation, cracking, and having tubes pinched off even with the clips open. R-3603 tubing has been found to be largely immune to that type of problem. However, with continued usage, it was found that the R-3603 tubing has the potential to be associated with a different set of sampling artifacts. Foremost among these is how the tubes sometimes fail to completely seal when the clip is closed. This was relatively infrequent but it did call for attention to making sure clips were fully closed to ensure the tube was pinched closed. If the clips were open slightly, sample bags could be corrupted during the line purge cycle prior to the start of the analysis on the gas chromatograph. It is believed that this was almost always identified and the data flagged accordingly but the data user should be aware that there could be instances where this is not the

case. There could be some instances where a bag sample was slightly diluted during the purge cycle resulting in an indeterminate lowering of the concentration. The available lines of evidence involving the replication of sampling and analyses indicate that, while some samples might have been affected, the overall picture provided by the concentrations and their areal distribution should be an accurate representation.

Another observation unique to PSB2 was the often large differences measured between collocated field duplicates during the nighttime IOPs. Previous experience with duplicate sampling in earlier tracer field studies demonstrated consistently good agreement between the concentrations measured in the collocated bag samplers. However, that experience was mainly during daytime tests. Temperatures were generally near or below freezing during the PSB2 nighttime tests. It was conjectured that this observation was possibly due to cold temperature related leaks in the air pumps and/or tubing fittings. Step 16 in the Quality Control Procedures section below describes results of follow up testing regarding this observation.

Quality Control Procedures and Measurement Quality Objectives

The following are detailed descriptions of the quality control and quality assurance methods followed for the sampling, analysis, and reporting of the PSB2 time-integrated bag sampler tracer data. Protocols established in the Environmental Protection Agency's (EPA) Guidance for Data Quality Assessment (U.S. EPA 2000a), the general requirements for the competence of calibration and testing laboratories of International Standards Organization/IEC Guide 25 (ISO 1990), the quality systems established by the National Environmental Laboratory Accreditation Conference (U.S. EPA 2000b), and the Department of Defense Quality Systems Manual for Environmental Laboratories (DOD 2002) provided a basis for quality assurance and quality control procedures followed during analysis. Instrument and method limits of detection (ILOD/MLOD) were calculated based upon 40 CFR Part 136, Appendix B and the American Chemical Society (ACS) Committee on Environmental Improvement's paper titled, "Principles of Environmental Analysis" (Keith et al. 1983). ACS principles relative to detection limit calculations in 40 CFR Part 136, Appendix B are documented in "Revised Assessment of Detection and Quantitation Approaches" (EPA 2004). Although our research-based automated analysis of tracer gases has no specified method performance or regulatory criteria, compliance with the established quality control procedures stated above were followed, where applicable, to provide high quality data that is both accurate and reliable.

The laboratory procedures followed were designed to ensure meeting the stated Measurement Quality Objectives (MQO) for the project shown in Table 4. This table will be referenced as the results for each procedural step are described.

Table 4. Measurement quality objectives (MQO) for the bag sampling Data Quality Indicators.

Data Quality Indicator	Objectives (MQO)	How Determined
Instrument Sensitivity	Instrument Limit of Detection (ILOD) < 4 pptv	Lab blanks and low concentration calibration checks
Instrument precision	RSD ¹ < 10%	CCV
Between Instrument Precision	RSD ¹ < 10%	Room Air (Lab background)
Low End Instrument Bias	<1 pptv	Lab blanks
Instrument Precision	RPD ² < 5%	Lab duplicates above MLOQ
	RSD < 10%	Lab controls above MLOQ
Instrument Accuracy	RPD ³ < 20% (< 50 ppt)	Required by calibration check and recalibration protocol
	RPD ³ < 10% (< 50 ppt)	
Low End Method Bias ⁴	< MLOQ ⁵	Field Blanks
Method Sensitivity	Method Limit of Detection (MLOD) < 12 pptv	May be calculated from field blanks, low concentration field controls, field duplicates, or background samples
Method Precision	RPD ² < 15%	Field duplicates above MLOQ
	RSD < 15%	Field Controls
Completeness %	90%	Percentage of samples producing good measurements

¹ RSD is relative standard deviation: standard_deviation/average

² RPD is relative percent difference: for duplicates is (measure_1 – measure_2)/average_of_1&2

³ RPD is relative percent difference: for known concentrations is (measure – actual)/actual

⁴ “Method” is entire sampling method including sampling and analysis.

⁵ Method Limit of Quantitation

Quality control issues pertaining to procedures for sample handling in the field and chain of custody were described in the previous section. Pre-project and laboratory QC procedures are described below and consisted of the following 22 steps:

1. Pre-project maintenance of bag samplers.
2. Testing of all sample bags.
3. Pre-project cleaning and analysis checks of all sample bags.
4. Development of analysis protocols for the expected sample concentration ranges.
5. Use of a written standard operating procedure (SOP).
6. Pre-project calculation of instrument limit of detection (ILOD) and instrument limit of quantitation (ILOQ).

7. Holding time studies.
8. Daily calibration of the ATGAS.
9. Initial ATGAS Calibration Verification (ICV).
10. Continuing ATGAS Calibration Verification (CCV) and analysis of laboratory controls.
11. Atmospheric background checks of SF₆ at the tracer analysis facility (TAF).
12. Analysis of laboratory (instrument) blanks.
13. Analysis of laboratory duplicates.
14. Analysis of field blanks.
15. Analysis of field controls.
16. Analysis of field duplicates.
17. Software quality control checks.
18. Data verification.
19. Post-project determination of MLOD and MLOQ.
20. Final data review.
21. Data handling.
22. Summary of Data Completeness.

1. Pre-project maintenance of the bag samplers.

Prior to deployment to the field, each of the 151 bag samplers was tested to ensure proper operation in the field and to ensure the collection of an adequate sample volume. This mainly involved checking the function of the microprocessor and pumps and the battery voltages.

2. Testing of all sample bags.

Experience has shown that almost all leaks in sample bags occurred around the fitting used for attachment to the sample tubing. This problem was rectified prior to PSB2 by permanently sealing the seam between the fitting and the bag in all sample bags using Pliobond 30. Previously, bags had been checked for leaks using the procedure detailed in Clawson et al. (2004, 2005, 2009). The bag sealing resulted in a lower failure rate during both PSB1 and PSB2 than had been achieved by the leak checking procedure of the past (Finn et al. 2015).

3. Pre-project cleaning and analysis checks of all sample bags.

After the bags were leak checked but prior to deployment to the field, all bags in the sampler cartridges were cleaned. The bags were cleaned by repeatedly filling them with UHP nitrogen and then evacuating them on the cartridge cleaning apparatus seen in Fig. 29. The apparatus consisted of a nitrogen tank and vacuum connected to a system that fills and evacuates the sample bags by changing valves. Up to 72 bags in 6 cartridges could be cleaned at one time. The computer mounted underneath the cleaning apparatus was used to create cartridge cleaning records or the cartridges were scanned as clean before entering the lab after cleaning. The laptop

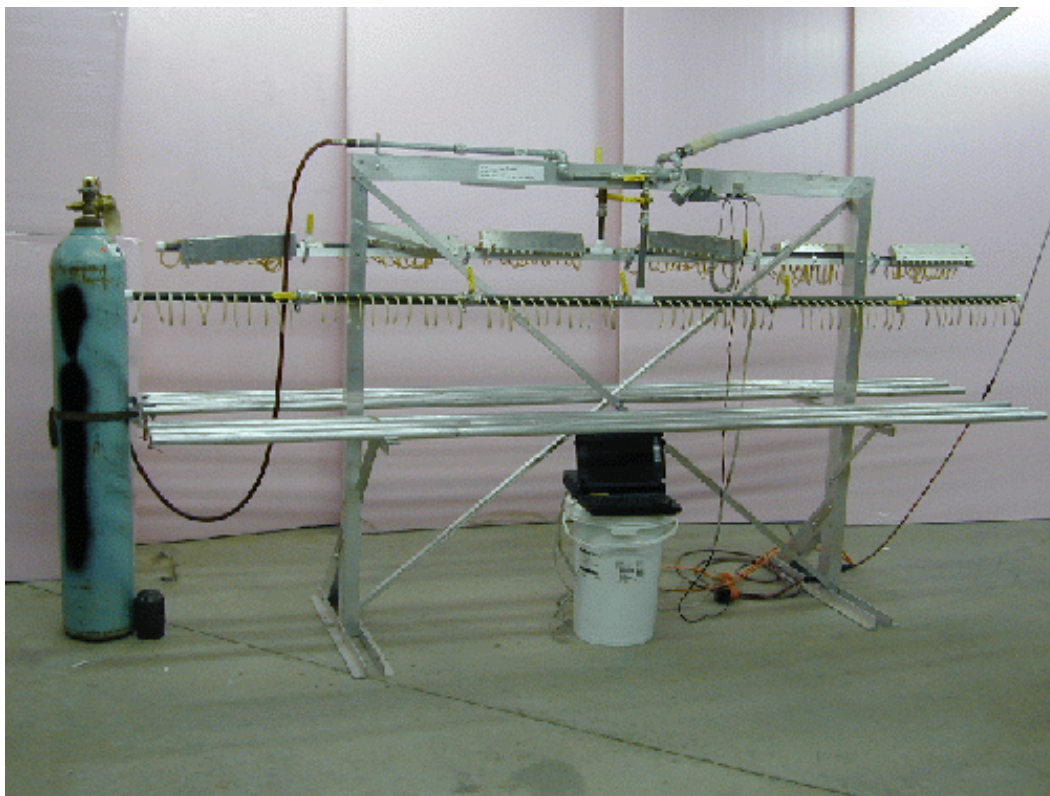


Figure 29. Cartridge cleaning apparatus.

computer used to record the cartridge cleaning records failed part way through the project. Cartridges were then scanned as clean when entering the lab. This information was then uploaded into the ATGAS history file. An 8-step cleaning protocol was used to clean the bags:

1. Connect all tubes to the cleaning machine.
2. Open all clips.
3. Make sure the cleaning machine valves are set so that nitrogen can flow into all connected cartridges.
4. Evacuate bags.
5. Fill all bags with nitrogen and then evacuate. Repeat until all bags have been evacuated 5 times.
6. Fill all bags with nitrogen for analysis.
7. Scan all cartridge bar codes with the bar code scanner and upload the data to the ATGAS PC.
8. After analysis, place the cartridges back on the cleaning machine, evacuate the nitrogen, disconnect the tubes and wait 30 seconds before closing clips. Prior to this step, air samples from the vicinity of the cleaning machine were checked for any anomalous background concentrations of SF_6 that could corrupt the bags during equilibration.

This protocol was developed after extensive testing to ensure that bags containing concentrations in the expected high range of up to 150,000 pptv or more could be cleaned to less than background levels. After cleaning, the bags were filled with UHP nitrogen and analyzed to ensure there was no contamination from previous tests or from long-term storage. Any bags with a concentration greater than 5 pptv were re-cleaned and re-analyzed. Less than 10 out of over 10,000 bags exceeded the 5 pptv threshold and had to be re-cleaned and re-analyzed. None were greater than 10 pptv after the initial cleaning and the vast majority were below the instrument limit of detection and within 0.1-0.2 pptv of zero. All bags were stored evacuated until their use (item 8 above).

4. Development of analysis protocols for the expected sample concentration ranges.

Analysis protocols were developed to optimize instrument performance, accuracy and efficiency during the project. In particular, each GC was configured to optimize the detection of the lowest possible concentrations in line with the expectation that the planned tracer release rates would result in mostly low to moderate concentrations and relatively fewer very high concentrations. Larger volume sample loops were selected in anticipation of measuring mostly lower concentrations. However, smaller volume sample loops were also evaluated to characterize the dynamic range available for measuring high concentrations on each GC in the event these were encountered. Analysis parameters were adjusted to account for the magnitude of concentration ranges that were expected. One set of parameters dealt with the worst case scenario carryover issue resulting from measuring extremely low concentration samples immediately following extremely high concentration samples. Nitrogen purge and vacuum times and the number of purge-vacuum cycles of the GC were set to ensure no carryover of high concentrations. Other parameters controlling the timing of the injection, switch to back-flush, and total length of the analysis cycle were set to ensure that oxygen and other contaminants were back-flushed before reaching the ECD to avoid any interferences. Electron capture detector attenuation adjustments were also tested at different concentration levels to provide quick adjustments to the instruments in the case of unexpected concentration ranges. The minimum dynamic ranges determined prior to the start of the project for the operational parameters used during PSB2 are given in Table 5.

Table 5. ATGAS analytical ranges.

ATGAS	Loop Volume	Calibrated Range	Number of Standards
1	1 ml	ILOD-75,100 pptv	19
2	1 ml	ILOD-142,300 pptv	22
3	500 ul	ILOD-210,700 pptv	23
4	1 ml	ILOD-52,600 pptv	18

5. Use of a written standard operating procedure (SOP).

A written SOP entitled, “Standard Operating Procedure for Sampling and Analysis of Sulfur Hexafluoride Using Programmable Integrating Gas Samplers (PIGS) and Automated Tracer Gas Analysis Systems (ATGAS)” was used by all personnel performing SF₆ analysis so that all analyses were performed consistently. The SOP contained the following sections:

1. Scope and Application.
2. Summary of Method.
3. Health and Safety Warnings.
4. Interferences.
5. Personnel Qualifications.
6. Equipment and Supplies.
7. ATGAS Setup.
8. Sample Collection.
9. Cartridge Check-In.
10. Analysis Preparation.
11. Analysis.
12. Sample Handling and Holding Times.
13. Data Analysis and Calculations.
14. Quality Control and Quality Assurance.
15. Data and Records Management.
16. Trouble-shooting.
17. References.

6. Pre-project calculation of instrument limit of detection (ILOD) and instrument limit of quantitation (ILOQ).

Prior to the start of the project, the ILOD and ILOQ were established for each ATGAS to provide information on instrument performance. The ILOD is the instrument’s limit of detection and is defined as the lowest concentration that can be determined to be statistically different from zero. It is a measure of instrument sensitivity and based upon the specific instrument’s ability to differentiate a low level concentration standard from instrument noise. One bag filled with a low level standard was analyzed on each of the 12 autosampler ports on each ATGAS. The analysis at each port was preceded by the analysis of a higher concentration standard of at least 10,000 pptv to evaluate any possible carryover effects. The ILOD was calculated as three times the standard deviation of a low level standard that was analyzed twelve times. The ILOQ is the instrument’s limit of quantitation and is defined as the lowest concentration that can be determined within 30% of the actual concentration. The ILOQ was calculated as ten times the standard deviation of the same low level standard analyzed 12 times. Since using different concentrations will yield different ILOD and ILOQs, the analyst selected the lowest concentration standard to meet as many of the following criteria as possible:

- Has a relative standard deviation (RSD), i.e., the standard deviation divided by the mean multiplied by 100 of less than 15%.
- Has a signal to noise (S/N; the mean divided by the standard deviation) between 3 and 10 (a higher value does not invalidate the result; rather it indicates that a lower concentration standard can be used).
- Has a percent recovery (analyzed value divided by the certified value multiplied by 100) between 90% and 110%.

Results for the pre- and post-project estimation of ILOD and ILOQ for each ATGAS are shown in Table 6. While some of the recoveries were slightly outside of specification, all initial pre-project ILOD were less than 1 pptv and much less than the stated measurement quality objective (MQO) of less than 4 pptv outlined in Table 4. The maximum initial ILOQ was 3.02 pptv for GC4. No carryover effects were observed.

7. Holding time studies.

Holding time studies are determinations of the length of time a sample can be held in its container before the sample concentration changes appreciably. Holding time studies are conducted whenever the method or sampling container is changed in any way prior to commencement of a project. These studies are used to determine what effect degradation of the materials will have on sample results. Knowledge of the length of time the samples can be held will help in planning the analysis schedule for the samples in the field. Holding time studies on the Tedlar sample bags performed in 2004 showed no appreciable change in sample concentration for up to six months if stored indoors and away from temperature extremes. Artifact studies on the Pliobond-sealed bag sample fittings and R-3603 tubing were performed in 2011 and early 2013 and showed no evidence of sample contamination or bag leakage. All samples were initially analyzed within a week of sampling for this project.

8. Daily calibration of the ATGAS.

In order to quantify the concentration of the samples, each of the four ATGASs was calibrated at the beginning of each analysis day using up to 20 NIST-traceable SF₆ standards. The number of standards used was dependent upon the expected concentration ranges for that day and the range available to each ATGAS as they were configured for this experiment. Each ATGAS was configured to optimize the ability to detect very low concentrations, principally by choice of a sufficiently large sample loop. This low end optimization had the effect of restricting the ability to quantify higher concentrations without changing sample loops. The analytical ranges for each ATGAS used during PSB2 are shown in Table 5. Differences relate to sample loop size and the specific performance characteristics of each ATGAS. GCs 2 and 3 could analyze samples at concentrations higher than their stated ranges, if necessary. This was necessary in a few cases.

Table 6. Summary of project instrument sensitivity and low end instrument bias.

Pre-Project (3.11 pptv)					1	
	GC1	GC2	GC3	GC4		
Number	12	12	12	12		
Mean	3.44	3.22	2.80	3.41		
Recovery	110.6	103.5	89.9	109.8		
S.D.	0.087	0.091	0.27	0.30		
RSD	2.54	2.83	9.52	8.84		
S/N	39.4	35.3	10.5	11.3		
ILOD	0.26	0.27	0.80	0.91		
ILOQ	0.87	0.91	2.66	3.02		
Lab Blank						
	GC1	GC2	GC3	GC4 (1-4)	GC (5-8)	
Number	198	206	212	108	92	
Mean	0.003	0.003	-0.657	0	-0.121	
S.D.	0.043	0.029	0.708	0.100	0.379	
ILOD	0.128	0.086	2.125	0.301	1.138	
ILOQ	0.426	0.286	7.083	1.005	3.793	
Lab Control (pptv)						
	GC1 (3.11)	GC2 (3.11)	GC3 (3.11)	GC3 (10.1)	GC4 (10.1)	All (3.11)
Number	147	124	151	141	137	422
Mean	3.14	3.22	3.03	10.17	9.90	3.13
Recovery%	101.1	100.3	97.4	100.7	98.0	100.8
S.D.	0.185	0.41	0.60	1.01	1.22	0.44
RSD%	5.9	7.8	19.8	10.0	12.3	14.1
S/N	17.0	12.9	5.1	10.0	8.1	7.1
ILOD	0.56	1.24	1.80	3.04	3.7	1.33
ILOQ	1.85	4.12	6.00	10.13	12.2	4.42
Post-Project (pptv)						
	GC1 (3.11)	GC2 (3.11)	GC2 (3.11)	GC4 (10.1)		
Number	12	12	12	12		
Mean	3.25	3.14	3.20	3.12		
Recovery%	106.6	112.1	97.3	105.4		
S.D.	0.095	0.15	0.16	0.26		
RSD	2.92	4.78	5.00	8.33		
S/N	34.21	20.93	20.00	12.00		
ILOD	0.285	0.45	0.48	0.78		
ILOQ	0.95	1.50	1.60	2.60		

The commonly used calibration standards ranged from 3.11 pptv to 75,100 pptv and covered most of the range of field sample concentrations encountered. In general, the nighttime IOPs had higher concentrations and therefore required broader, higher analytical ranges. Over the course of the project, three standards were depleted and replaced by standards with similar concentrations. The 504 pptv standard was replaced with a 505 pptv standard, the 9,730 pptv standard was replaced with a 10,010 pptv standard, and the 10.1 pptv standard was replaced with a 9.95 pptv standard. The latter happened late in the project and was used mainly in follow up testing. Some standards were getting low by the end of the project but it was not necessary to replace them. The UHP air zero point used in the calibration contained a slight trace of SF₆ as demonstrated by the very small peaks often seen in the chromatograms. Concentrations of samples were calculated using a point-to-point fit calibration of the standards. The calibration curve was examined for "wild fits" and error messages were displayed in the event of the occurrence of some anomaly so that the analyst could more closely examine the calibration curve and decide if it was appropriate to use.

9. Initial ATGAS calibration verification (ICV).

After each calibration was completed and reviewed, the curve was validated by analyzing the same calibration standards as if they were field samples. This validation demonstrated that sample concentrations within the calibration range could be quantified correctly. The recoveries were required to be within $\pm 7\%$ of the certified value ($\pm 12\%$ for standards < 50 pptv) or the standards were re-analyzed. If the recoveries still did not meet the acceptance limits, the bags were refilled and analyzed again. If the recoveries were still not acceptable, the instrument was re-calibrated and ICV was attempted again.

10. Continuing ATGAS calibration verification (CCV) and laboratory controls.

The validity of the ATGAS instrument calibration curves were regularly checked by re-analyzing calibration standards as if they were field samples. This procedure, called continuing calibration verification (CCV), was performed to provide evidence that instrument drift had not caused the calibration to be unable to correctly quantify sample results within the MQO acceptance levels. Standards were chosen to cover the concentration range of samples that had been analyzed since the last calibration verification. The standards were required to have a recovery of $\pm 10\%$ of the certified value ($\pm 20\%$ for < 50 pptv) for the CCV to be considered valid (Table 4). If any of the standards were not within the acceptance window, the instrument was re-calibrated and the curves were re-validated. All data within the unacceptable concentration range, from the point of the last acceptable CCV, were flagged and re-analyzed.

There was a tendency for the responses of the GCs to become more stable with continued operation but all of them exhibited some susceptibility to drift of the calibration, especially in the first few hours of operation. The frequency of CCVs ranged from less than 1 to about 3 h depending on the GC and how long it had been in operation with a relatively stable calibration for any given day. In general, calibration checks were done more frequently in the first few hours of operation and less frequently after that if the GC was exhibiting stable behavior.

Recalibrations were usually done if the response had drifted significantly ($>$ about 6-8%) as there was a tendency that once drift had commenced it often continued and raised the prospect of performing analyses that would have to be redone due to violating the MQO requirements of $\pm 10\%$ (> 50 ppt) or $\pm 20\%$ (< 50 ppt). Furthermore, the intent was to keep all results within 10%. Following any recalibration, responses were often stable within $\pm 5\%$ for the remainder of the day. In some cases it was not necessary to recalibrate after the initial calibration although it was common for GCs 2 and 3 to be recalibrated once a few hours into the day and then remain stable for an extended period of time. GCs 1 and 4 were the most susceptible to problematic calibration drift but they sometimes had stable calibrations. Considerable time was spent in calibration and recalibration of the GCs to ensure achieving MQO. There was also some analysis time lost due to the necessity to rerun some sets of sample cartridges due to failure to achieve the requisite CCV recoveries.

The CCV serve as laboratory control samples and measures of instrument precision and instrument accuracy (Table 4). Results for the combined laboratory control samples (CCV) are summarized in Table 7. All CCV data are included except for when a failed CCV was repurposed to be a new calibration. In such cases those records were eliminated. Excepting the 3.11 pptv standard, all of the RSD were below the 10% limit specified in the MQOs and indicated good instrument precision. The higher RSD result for the 3.11 pptv standards arises from the relative lack of low end sensitivity for GCs 3 and 4. In fact, GC4 often had trouble detecting the 3.11 pptv peak. That explains the decision to eventually omit the 3.11 standard as part of the calibration curve for GC4. The lack of low end sensitivity in GC3 was less acute but it still contributed to an increase in RSD at 3.11 pptv. The lack of sensitivity to such low concentrations was not critical in that ambient background concentrations of SF_6 were much higher, generally around 8-9 pptv. The agreement between the measured and actual NIST-certified standard values is also shown in Fig. 30. Excepting a few outliers, there is good agreement. The overall slope (1.002) indicates no appreciable bias and the Pearson's r correlation value of 0.9996 shows excellent precision. The average recoveries are indicative of excellent accuracy across the full range of concentrations used and are easily within the $100 \pm 10\%$ (or $\pm 20\%$) requirement.

Table 7. Summary of project laboratory control (CCV) results.

Concentration						
Actual	Measured (Avg.)	S.D.	Avg. % Recovery	RSD %	S/N	#
0	-0.005	2.23				558
3.11	3.12	0.44	100.8	14.1	7.1	422
10.1	10.11	0.91	100.1	9.0	11.1	540
19.19	19.67	1.22	102.4	6.2	16.1	516
35.1	34.90	2.11	99.4	6.0	16.6	501
88.7	89.70	3.54	101.2	3.9	25.3	500
301	302.60	19.60	100.5	6.5	15.5	487
504	509.00	27.90	101.0	5.5	18.2	269
505	511.70	23.70	101.3	4.6	21.6	199
799	806.50	50.30	100.9	6.2	16.0	459
1,550	1,582.40	106.40	102.1	6.7	14.9	442
3,140	3,182.60	170.80	101.4	5.4	18.6	423
4,980	5,073.40	269.40	101.9	5.3	18.8	388
8,270	8,364.90	275.50	101.1	3.3	30.4	301
9,730	9,912.40	343.40	103.0	3.5	28.9	103
10,010	10,213.40	315.90	102.0	3.1	32.3	155
16,370	16,571.90	618.70	101.2	3.7	26.8	239
21,720	21,790.60	1,015.10	100.3	4.7	21.5	150
36,900	36,997.80	783.70	100.3	2.1	47.2	102
52,600	52,434.60	1,646.00	99.7	3.1	31.9	78
75,100	75,394.80	1,005.50	100.4	1.3	75.0	28
90,100	90,540.80	982.60	100.5	1.1	92.1	17
103,600	103,019.00	758.00	99.4	0.7	135.9	7
142,300	143,822.00	1019.40	101.1	0.7	141.1	2

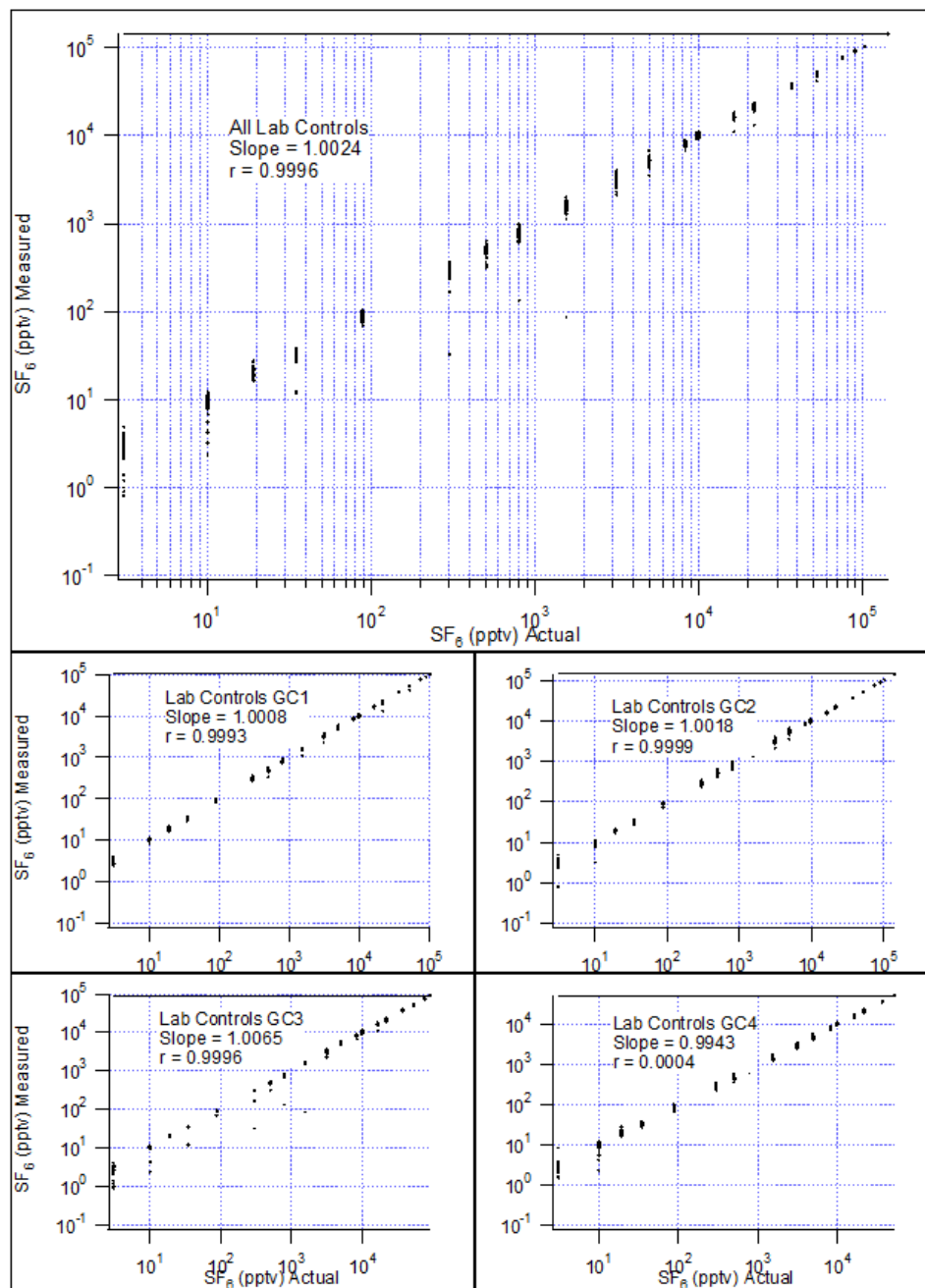


Figure 30. Comparison between measured and NIST-certified standard concentrations for all lab control (CCV) samples.

11. Atmospheric background checks of SF_6 at the tracer analysis facility (TAF).

A background atmospheric check of SF_6 in the TAF consisted of analyzing three samples of the room air in the TAF, after calibration but prior to running regular samples, on each GC every analysis day,. This information was used to determine if there was any leakage in the analysis system when compared to the instrument blanks that were subsequently analyzed. The

data provided for an inter-comparison between GCs that were being used on the same day to check the between instrument precision. The results were also used to reveal discrepancies between GCs to indicate a problem that otherwise might go undetected. The results shown in Table 8 indicate that, with the possible exception of GC1, there was good precision between the four GCs. The average concentration for all background checks was 9.8 pptv with a standard deviation of 1.7 pptv. The RSD specification was not satisfied with all RSD greater than the 10% MQO specified in Table 4 (“Between Instrument Precision”). The primary reason for this is that there were a few days where the ambient room air had slightly elevated SF₆ concentrations, usually in the 10-20 pptv range. This was above the nominal ambient background that was usually about 8-10 pptv, thus the larger standard deviations and RSD. The slightly elevated concentrations were found to be a transient phenomenon, when present, and the results could vary by GC depending on the timing of the room air analyses. In the absence of any transient elevated background, the agreement between GCs was even better than indicated in Table 8.

Table 8. Summary of results for lab background checks (room air).

RoomAir	#	Mean	S.D.	RSD
GC1	57	10.72	2.38	22.2
GC2	60	9.66	1.32	13.7
GC3	55	9.81	1.29	13.2
GC4	53	9.14	1.15	12.5
All	225	9.84	1.71	17.3

12. Laboratory (instrument) blanks.

A laboratory or instrument blank was analyzed on each ATGAS each analysis day to verify that there was no contamination or leaks within the analysis system as compared to the background checks analyzed that day, that there was no carry-over from previously analyzed high concentration standards, and to ensure carrier gas purity. The blank sample consisted of a cartridge of 12 bags that were each filled with ultra high purity (UHP) nitrogen. The concentration results of all bags were required to be less than the lowest calibration standard and close to a concentration of 0 pptv. If the concentration of one or more of the bags was higher than the acceptable range, the bag was re-filled and re-analyzed. If the concentration still was not within acceptable limits, the instrument was re-calibrated and re-verified or the samples were flagged and re-analyzed. If there were still indications of contamination, the problem was identified and fixed before analysis continued.

The laboratory blank results for each ATGAS and its corresponding ILOD and ILOQ are included in Table 6. The average results indicate no contamination or leakage problems within any of the ATGASs as well as no carryover issues and meet the MQO of <4 pptv (Table 4). The larger standard deviation for GC3 reflects its sensitivity to the effect of very small changes in baseline on the peak integration at very low level concentrations.

13. Laboratory duplicates.

Analyses of laboratory duplicates were performed each day to provide evidence of instrument precision. Each day at least one primary field bag sampler cartridge was analyzed in duplicate on each ATGAS. Days during which the TAF was in operation for longer hours, an attempt was made to run at least two lab duplicates. The sample cartridge had an initial analysis and was then set aside for a second, duplicate analysis 3 hours or more later to ensure an appropriate estimation of instrument precision over time. The cartridges used for this duplicate analysis were selected to encompass as much variation and range of concentration as possible within the concentration range bracketed by the calibration curve for each ATGAS. The mean of the absolute value of the relative percent differences (RPD) is

$$\text{RPD} = (100 * (\text{measure\#1} - \text{measure\#2}) / \text{average}(\#1 \text{ and } \#2))$$

The MQO objective was for $\text{RPD} < 5\%$ (Table 4). Any result not within the acceptable limits was flagged and re-analyzed. If the result was still not within acceptable limits, the analysis was terminated until the ATGAS precision could be re-established.

The $|\text{RPD}|$ laboratory duplicate results are shown in Table 9. GCs 1, 2, and 3 showed good precision over time and satisfied the MQO objective for lab duplicates. GC4 did not satisfy the RPD MQO objective suggesting a greater tendency for temporal drift in response that was not fully accounted for by routine CCV and re-calibrations. A regression analysis of the laboratory duplicates is shown in Fig. 31.

Table 9. Summary of RPD results for laboratory duplicates.

GC	#	Mean % RPD	Mean $ \text{RPD} $
1	160	1.08	2.25
2	212	-0.03	1.84
3	209	0.06	2.10
4 (IOPs 1-4)	59	2.10	5.58
4 (IOPs 5-8)	65	-2.01	6.20

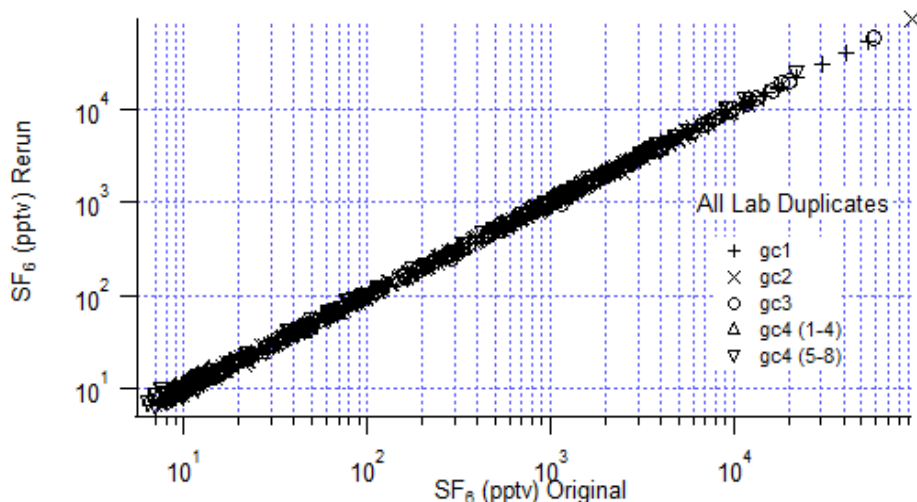


Figure 31. Graph of rerun values against original values for all laboratory duplicates.

14. Field blanks.

Field (method) blanks were sampled and analyzed to indicate if there was any contamination or leakage introduced by any part of a bag sample's history from sampling, handling, and transport through to the final analysis. For example, isolated instances of high concentrations of SF_6 in the field blanks could indicate holes in the sampling bag, clips not properly closed, wrong location number, or other operational problems. Consistently high concentrations would indicate a sampling method that could not measure null concentrations accurately.

Three field blank samplers were deployed during each IOP, one per arc as shown in Table 3. A field blank consisted of a sampler containing a cartridge filled with ultra high purity (UHP) nitrogen. Each sampler was deployed at its designated location and collocated with a regular sampler with the tubes connected and clips left open. Software requirements of the sampling program made it necessary for the pump on the first bag to turn on for one short pulse. However, after that, all pumps were left off and there was no additional filling of any of the bags. At the end of each test, the clips on the blank cartridges were closed and the cartridges were collected, transported, and stored along with all the regular sample cartridges. With the exception of the special sampling program, the field blanks were treated identically to the regular samples.

A summary of the results is presented in Table 10. The means and standard deviations for IOPs 1, 2, and 4 are all near zero and very low indicating no contamination or sample handling problems. The means for IOPs 3, 6, and 8 are fairly low but hint at the possibility of slight contamination or other artifact. The much larger means for IOPs 5 and 7 are believed to represent sample contamination due to infiltration of high concentration plume into some of the bag samples. The highest measured blank was 13.7 pptv during IOP5. During these IOPs, high

Table 10. Field blank results for each test.

IOP	#	Mean	S.D.	MLOQ
1	36	0.02	0.06	0.6
2	35	-0.17	0.36	3.6
3	36	0.19	1.41	14.1
4	36	0.00	0.00	0.0
5	36	2.79	3.74	37.4
6	36	0.15	0.54	5.4
7	35	0.79	1.38	13.8
8	36	0.12	0.70	7.0

concentrations were measured at many locations on the bag sampling array for extended periods of time. It is possible that small amounts of tracer diffused into the sample bags past the pump seals and through the open, unclipped tubing. This contamination issue will be discussed below in detail in step 16 of this section (field duplicates). Despite this, these results suggest that the influence of high concentration plumes on low concentration bags was still minimal as even IOPs 5 and 7 were generally well below ambient background concentrations.

The consequences of these observations are considered more fully in the determination of final MLOQ for the project results (step 19 below). Briefly, the field blank results adversely affected some of the project MQOs (Table 4) in that they indicated an MLOQ sometimes greater than the nominal MLOQ.

15. Field controls.

Three field control samplers were deployed during each IOP, one per arc (Table 3). The cartridge for each control sampler was filled with NIST-traceable tracer concentrations ranging from 14.79 pptv to 5170 pptv. Bags 1-3 contained 14.79 pptv, bags 4-6 contained 283.9 pptv, bags 7-9 contained 1571 pptv, and bags 10-12 contained 5170 pptv. Each sampler was deployed at its designated location and collocated with a regular sampler with the tubes connected and clips left open. Software requirements of the sampling program made it necessary for the pump on the first bag to turn on for one short pulse. However, after that, all pumps were left off and there was no additional filling of any of the bags. At the end of each test, the clips on the control cartridges were closed and the cartridges were collected, transported, and stored along with all the regular sample cartridges. With the exception of the special sampling program, the field controls were treated identically to the regular samples.

The field control samplers served two primary purposes. First, they checked for any biases or inaccuracies introduced during the sampling, handling, and storage of the samples. Second, recall that the standards used to calibrate the GCs (up to 210,700 pptv) were all NIST traceable. The tracer concentrations used to fill the control bags also came from NIST-traceable standards but they were different from those used in the calibration of the ATGASs. As a consequence, the field control samples serve as a semi-independent measure of quality control of the overall process, essentially a method audit.

The results for the field control samples expressed in terms of the individual IOPs are shown in Table 11. While many of the results were quite good, there were some significant problems identified with the field control samples.

Table 11. Combined ATGAS field control results expressed in terms of standard concentration and IOP number.

	IOP1	IOP2	IOP3	IOP4	IOP5	IOP 6	IOP 7	IOP 8	All
14.79 pptv									
#	9	8	9	9	9	9	6	9	68
Mean	15.26	14.96	14.83	14.98	17.0	15.31	15.32	14.96	15.33
S.D.	0.26	0.27	0.54	0.45	4.14	0.28	0.75	0.48	1.63
Avg. Recovery	1.03	1.01	1.00	1.01	1.15	1.04	1.04	1.01	1.04
Mean RPD %	3.2	1.2	0.3	1.3	14.9	3.5	3.6	1.1	3.7
Mean RPD %	3.3	1.5	2.8	2.7	15.4	3.5	4.7	2.6	4.6
RSD %	1.7	1.8	3.7	3.0	24.4	1.8	4.9	3.2	10.6
S/N	58.6	56.1	27.3	33.1	4.1	55.5	20.4	31.0	9.4
283.9 pptv									
#	9	9	9	8	9	9	6	9	68
Mean	282.3	300.6	300.4	300.6	297.3	295.2	298.8	295.9	296.2
S.D	20.9	4.1	7.0	5.5	6.6	26.7	6.2	2.3	13.8
Avg. Recovery	0.99	1.06	1.06	1.06	1.05	1.04	1.05	1.04	1.04
Mean RPD %	-0.6	5.9	5.8	5.9	4.7	4.0	5.2	4.2	4.3
Mean RPD %	6.6	5.9	5.8	5.9	4.7	8.5	5.2	4.2	5.9
RSD %	7.4	1.4	2.3	1.8	2.2	9.1	2.1	0.8	4.7
S/N	13.5	72.5	42.9	54.7	45.1	11.0	48.1	128.3	21.4
1571 pptv									
#	9	9	9	8	9	9	6	9	68
Mean	1,468.1	1,546.9	1,524.2	1,513.7	1,524.3	1,531.9	1,215.8	1,105.5	1,437.0
S.D.	148.3	20.9	26.0	73.1	18.8	78.7	394.8	355.5	236.0
Avg. Recovery	0.93	0.98	0.97	0.96	0.97	0.98	0.77	0.70	0.91
Mean RPD %	-6.6	-1.5	-3.0	-3.6	-3.0	-2.5	-22.6	-29.6	-8.5
Mean RPD %	6.6	1.8	3.0	3.7	3.0	4.2	22.6	29.6	8.8
RSD %	10.1	1.35	1.7	4.8	1.2	5.1	32.5	32.2	16.4
S/N	9.9	74.1	58.7	20.7	81.1	19.5	3.1	3.1	6.1
5170 pptv									
#	9	9	9	9	9	9	6	9	69
Mean	4,259.4	5,075.9	4,861.5	5,022.6	4,893.5	5,091.0	3,362.1	4,376.6	4,672.5
S.D.	1,611.4	138.7	124.2	78.2	145.2	117.1	1,339.0	885.4	892.3
Avg. Recovery	0.82	0.98	0.94	0.97	0.95	0.98	0.65	0.85	0.90
Mean RPD %	-17.6	-1.8	-6.0	-2.85	-5.35	-1.5	-35.0	-15.3	-9.6
Mean RPD %	17.6	2.7	6.0	2.85	5.35	2.25	35.0	15.3	9.8
RSD %	37.8	2.7	2.55	1.6	3.0	2.3	39.8	20.2	19.1
S/N	2.6	36.6	39.1	64.2	33.7	43.5	2.5	4.9	5.2

First, the lower recoveries for the 1571 and 5170 pptv standards in IOP1 can be attributed to an operational oversight. An improper size tubing fitting was in place at the time these standards were filled and there was insufficient time to locate the correct fittings prior to the IOP1 deployment. The size discrepancy resulted in an incomplete seal and slight dilution of some of the noted sample bags during filling.

Second, the number of samples for the 283.9 and 1571 pptv standards was 8 instead of 9 in IOP4 due to an operator error during bag filling.

Third, one of the control sample cartridges was mistakenly set to run as a regular sample during IOP7. This operator error in the field resulted in further filling bags that were already filled with their respective control standard concentrations. This corrupted the control samples at that site and explains the drop from 9 to 6 for the number run during IOP7. The regular sampler that was collocated with the control sampler was programmed to run as the control sample. As a consequence, the pumps failed to run and the bags were flat thus voiding the results from that regular sampler as well.

Fourth, and perhaps most significantly, the recoveries for the 1571 and 5170 pptv standards for the control samples in IOPs 7 and 8 are poor and anomalously low. The corresponding RSD and RPD are similarly very poor. The cause of this is not certain but it might be related to cold temperature sampling artifacts. The MQO objectives for the 14.79 pptv standard in IOP5 were not met, possibly for the same reason. A review of Table 11 suggests that the failures to meet MQO objectives were biased toward the nighttime IOPs. The potential cold temperature sampling artifacts are discussed in greater detail in the following section (step 16) in the context of field duplicate discrepancies.

There are a few other values where MQO objectives were not met but the list above is the most noteworthy. Figure 32 illustrates the often poor agreement between the control standard concentrations and their measured concentrations, especially for the 1571 and 5170 pptv control standards.

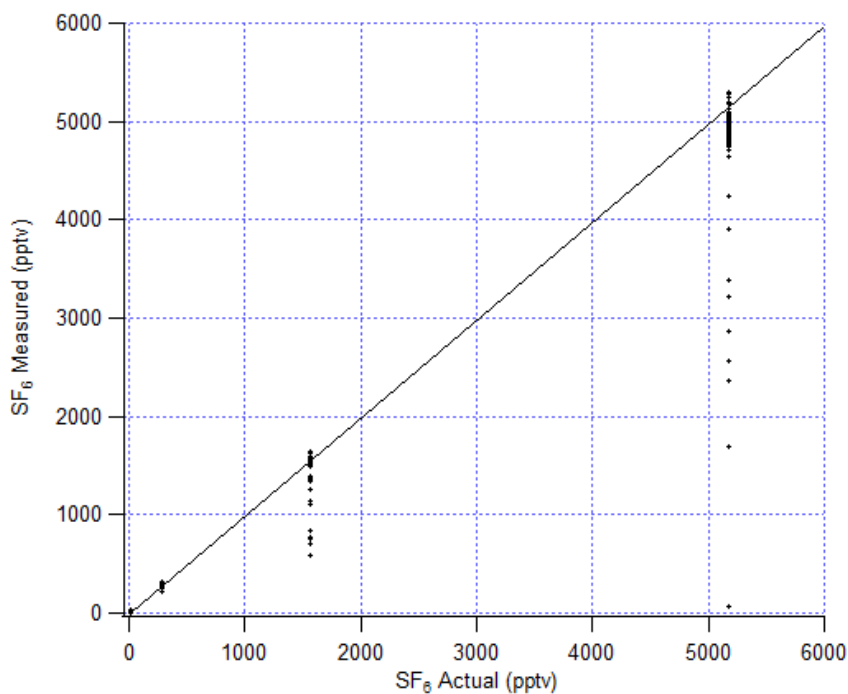


Figure 32. Plot of field control sample results.

16. Field duplicates.

Fourteen field duplicate samplers were deployed for each daytime IOP and 12 for each nighttime IOP during PSB2 (Table 3). The duplicate samplers were handled identically to the primary samplers with which they were collocated. Both samplers were mounted at the same height and affixed to the same post. The sample inlets for the two samplers faced opposite directions from the mounting post with inlet separation between samplers being a little more than 1 m. A summary of the results is provided in Table 12.

A salient feature of Table 12 is the much different |RPD| results between the daytime and nighttime IOPs. For the daytime, only IOP1 failed to meet the MQO objective of $|RPD| < 15\%$. In contrast, only IOP6 met the |RPD| objective for the nighttime IOPs. In fact, the remaining IOPs were significantly higher than the objective. The high nighttime |RPD| values resulted in the overall (“All”) MQO objectives not being met. That was true for all distances. However, a distinct pattern emerges when the data are broken down by distance and day or night. First, the discrepancy between duplicate samplers was much higher at night than during the day. The daytime |RPD| mostly satisfied the MQO objective while the nighttime |RPD| were generally significantly greater than the MQO objective. Second, there appears to be a distinct trend in both the daytime and nighttime |RPD| with decreasing values at increasing downwind distance.

The field duplicate results are also shown graphically in Figs. 33a and 33b. From Fig. 33b it's apparent that all of the field duplicate results for IOPs 4 and 6 were mainly background concentrations near or below MLOQ which probably explains their superior |RPD| results in Table 12. It can also be seen that the scatter for IOP7 is particularly large. In Fig. 33b it can be seen that the correlation coefficient is higher for every daytime downwind distance than the corresponding nighttime distances.

Table 12. Summary of field duplicate sampler results.

Test	Number	Avg. % RPD	Avg. % RPD
1	130	-2.3	18.0
2	141	-3.4	13.8
3	129	1.9	12.7
4	143	-1.7	6.4
5	141	-7.6	33.0
6	140	-1.7	9.3
7	140	-17.3	44.0
8	140	6.5	32.1
All	1,104	-3.3	21.3
All 100 m	378	-2.9	24.3
All 200 m	365	-4.5	22.2
All 400 m	361	-2.3	17.1
All 100 m Day	190	-3.1	15.6
All 200 m Day	177	0.6	12.2
All 400 m Day	175	-1.2	9.2
All 100 m Night	188	-2.8	33.1
All 200 m Night	187	-8.8	31.1
All 400 m Night	185	-2.9	24.1

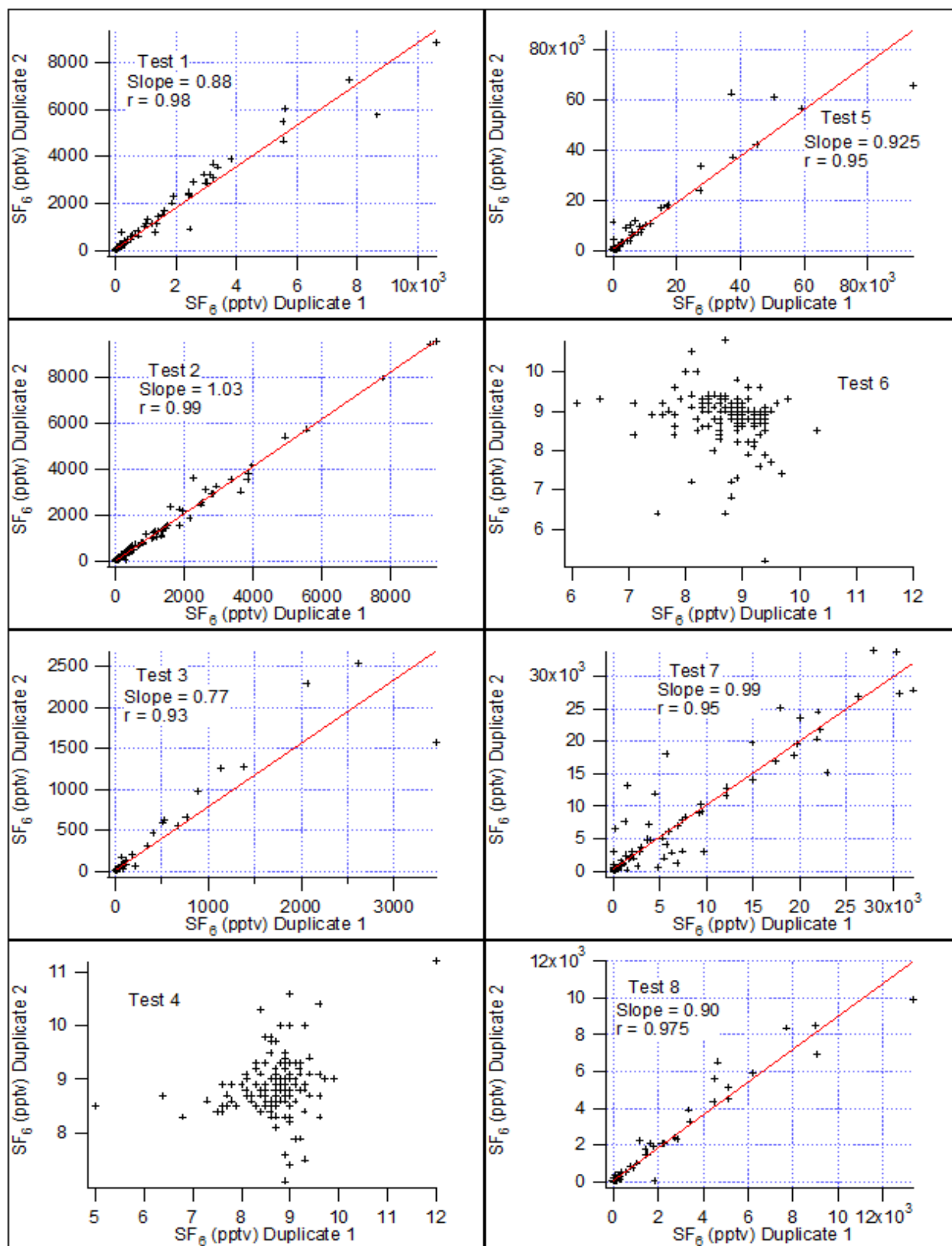


Figure 33a. Graph of field duplicate samples by IOP with included linear regressions.

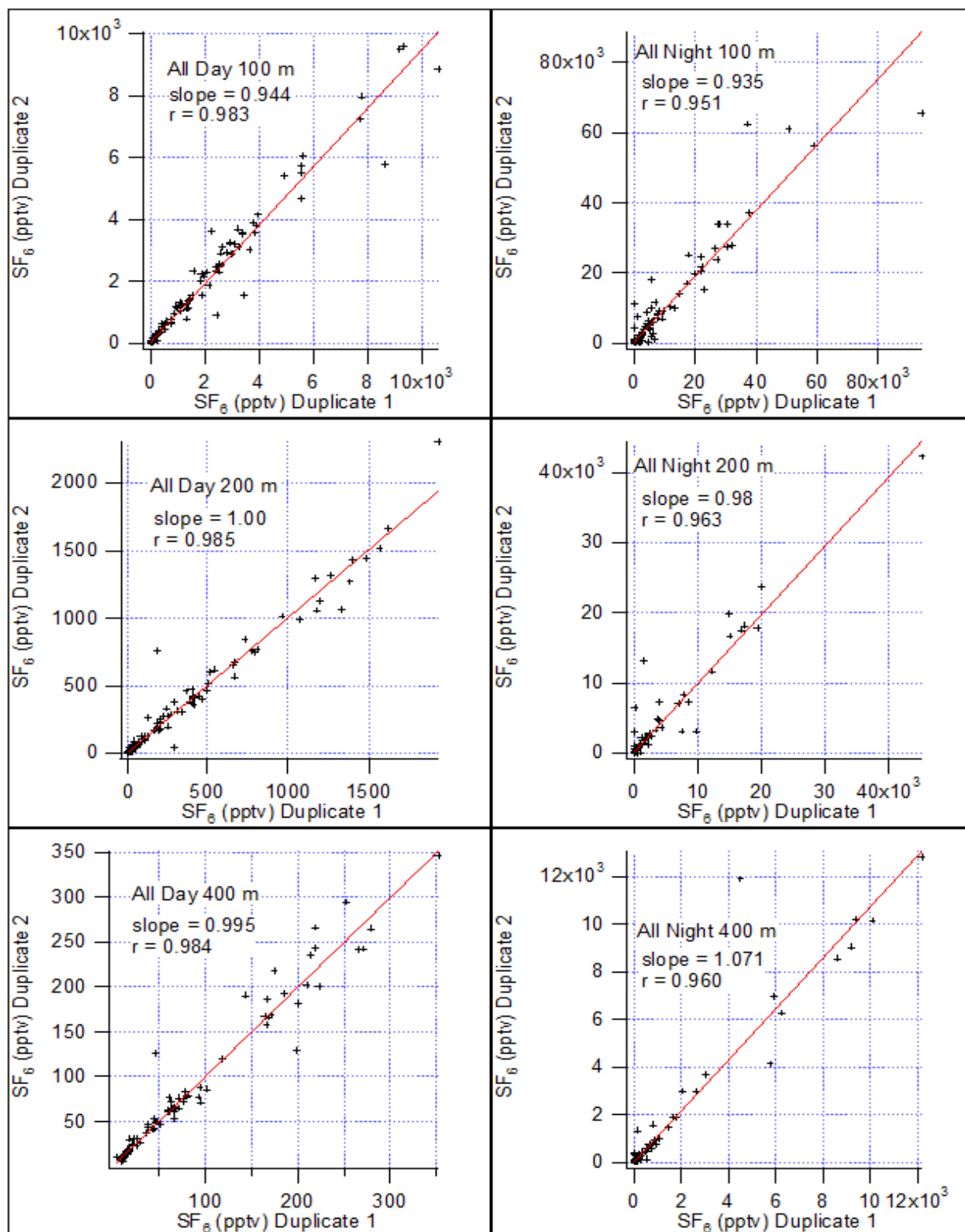


Figure 33b. Graph of field duplicate samples by day and night and distance with included linear regressions.

These observations suggest two possible explanations. First, the turbulent mixing processes during the daytime are more effective at mixing than during nighttime at the scale of the separation of the colocated duplicate sampler inlets. Furthermore, as would be expected, the plume becomes more thoroughly mixed with increasing downwind distance during the day and night. Second, it is a possibility that the day and night differences might be at least partly attributable to a sampling artifact related to colder temperatures. It is possible that both explanations contributed to the observed discrepancies.

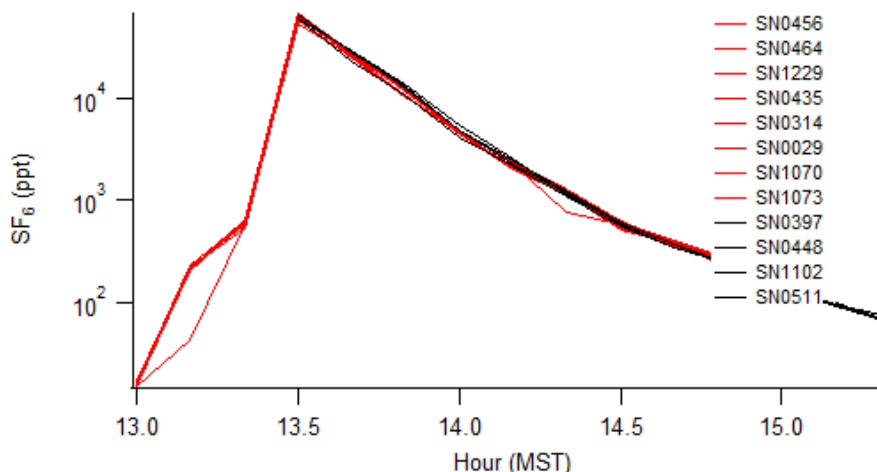
Two experiments were conducted after the project was completed that attempted to identify if the observed field duplicate discrepancies were due to a sampling artifact or whether they were possibly explained by physical mixing processes. A “pink box” measuring 8’x4’x4’ was constructed of Styrofoam. Samplers with their sample cartridges were placed into the box and programmed to collect 10-min average samples over a 2 h period bracketing a one-time bolus injection of SF₆ into the box volume. The purpose of the box was to expose the samplers to a sustained high concentration atmosphere that gradually dissipated over time through small seams or gaps in the box. A fan inside the box was used to ensure that the box atmosphere was well mixed.

The first experiment was conducted in very cold conditions with light ambient winds. Samplers and cartridges were equilibrated to an ambient temperature of -12.2 C (10 F) then programmed and enclosed inside the pink box at 1115 h. Twelve samplers were placed in the box in 4 stacks with 3 samplers each with inlet tubes facing both toward and away from the center of the box. The pump rate was increased to 300 strokes per bag in an attempt to counter the tendency of pump and battery efficiency to decrease in colder temperatures. Eight samplers were programmed to begin sampling at 1300 h with 4 starting a half hour later at 1330 h. The SF₆ injection was done at 1330 h. Therefore, there were 3 bags in each of 8 samplers that sampled ambient air prior to the injection. The temperature at time of injection was -10 C (14 F). Samplers were retrieved at about 1540 h with a temperature of -6.7 C (20 F). It was observed at that time that the bags were very full, in several cases bulging and well beyond optimally full.

During preparation, when the tubing from the pumps was being connected to the sample cartridge tubing, it was observed that the tubing attached to the pump was looser than expected compared to our experience with use of the samplers in warmer conditions. In fact, the pump tubing was inadvertently pulled off the pump barb fitting twice. It was also observed that the seal on the pump tubing barb visibly shifted when the tubing was flexed. These observations suggest that the seal on the pump tube barb might be less effective at very cold temperatures.

The results for the first test are shown in Fig. 34. Logarithmic scaling is used to highlight the fact that the bags that ran prior to the injection at 1330 h had concentrations much higher than the expected ambient concentrations of about 8-9 pptv. The bag 3 concentrations, just prior to the injection, had concentrations up to 649 pptv. All of the early start samplers followed a very similar pattern with increasing concentrations from bag 1 to bag 3. Bag 1 concentrations ranged from 15 to 17 pptv. This result suggests that there was a sampling artifact in this test that

adversely affected and corrupted the concentrations in the early bags. There was no apparent evidence of post-injection corruption since all of the results follow the same pattern with a gradual decrease from the high concentrations at injection.



From earlier testing it is known that the pumps can potentially leak at cold

Figure 34. Results from the very cold temperature (first) pink box test. Red traces are for the early 1300 h start samplers and black traces are for the late 1330 h start samplers.

temperatures. Thus, when the pump is off and supposedly closed in cold temperatures, there is a possibility that ambient air might infiltrate through the pump and into the sample bags through the open, unclipped tubing. The observations of the looser pump tubing and very full bags together with the ramp in concentrations for bags 1-3 suggested there might be an additional factor as well. From these observations it was speculated that the overly full bags pushing on each other could have resulted in flexing of the tubing which might have promoted leaks around the pump tube seal in the cold temperatures. The effects of squeezing from the overfull bags would be felt most acutely at bag 3, less at bag 2, and least at bag 1. This first test left some questions unanswered and raised additional questions so a second pink box experiment was conducted.

The second experiment was conducted in temperatures that were similar to those during the nighttime tests IOPs 5-7. This was generally below freezing by a few degrees but not as cold as the first pink box test. Winds were again light. Ten minute average sampling was again used. Fifteen samplers were enclosed in the pink box. Two samplers began sampling 1 h before injection with a pump rate of 280 strokes per bag (down from 300); 2 samplers began sampling 1 h before injection with a pump rate of 250 strokes per bag; 2 samplers began sampling at the time of injection with the 280 pump rate; and 2 samplers began sampling at the time of injection with the 250 pump rate. All 8 of these samplers had the standard tubing and connections. In Fig. 35 the high and low pump rates are denoted 'hi' and 'lo', respectively, while the early and late starts are shown in red and black, respectively. An additional 4 samplers had early starts but had different configurations of tubing and connectors. In Fig. 35 'dbl' represents a different connector between the pump and cartridge tubing, the r1000 and r3603 represent pump tubing with different i.d. and wall thickness, and 'ww' and 'wow' represent with and without wire to tighten the seal around the pump tube barb. The three additional samplers were used for an unrelated set of tests.

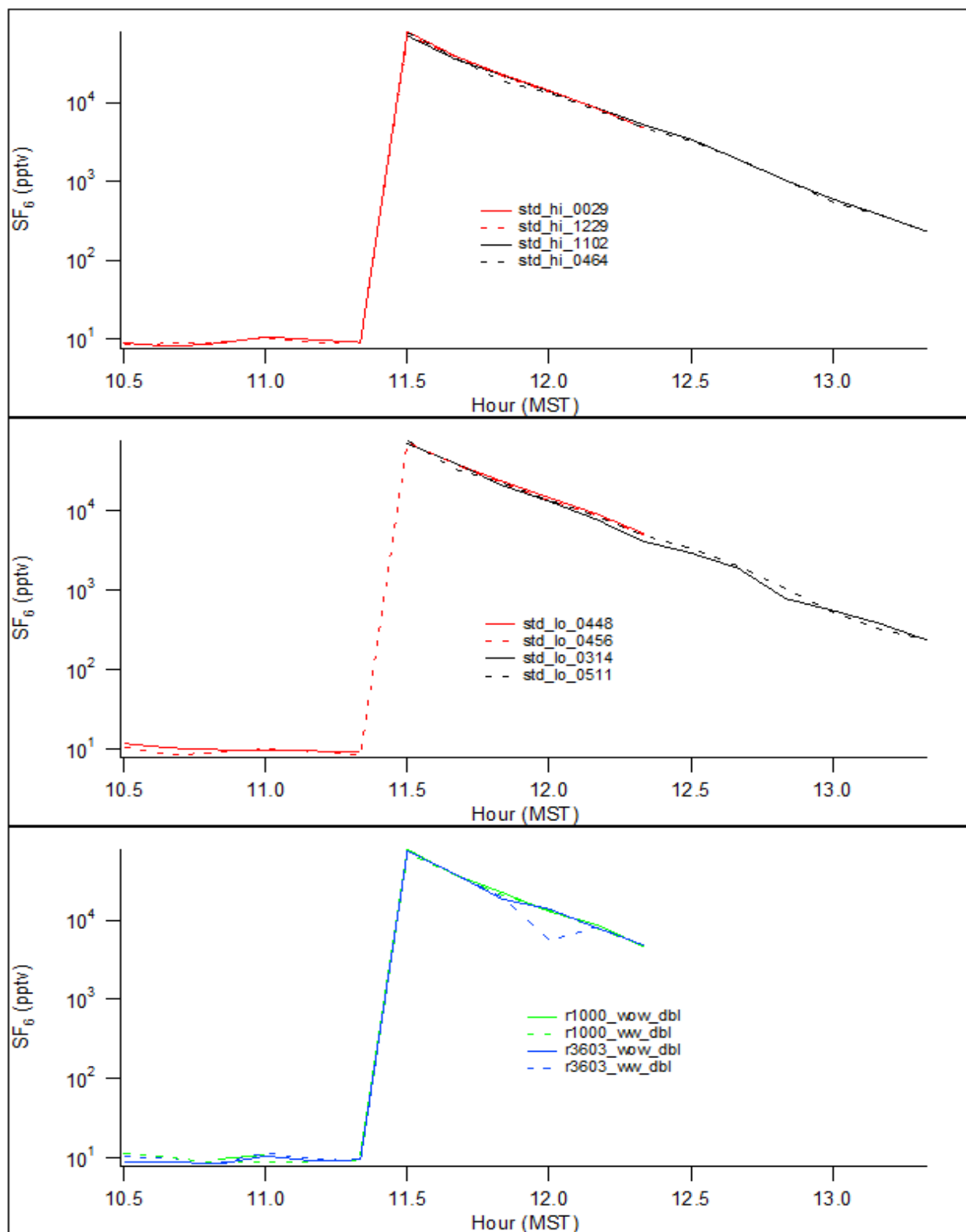


Figure 35. Results from cold temperature (second) pink box test. Red traces are for the early 1030 h start samplers and black traces are for the late 1130 h start samplers.

Sampling began at 1030 h with the delayed start and SF₆ injection at 1130 h. Temperatures were -6.7 C (20 F) at 0953 h prior to the test and gradually increased to -1.1 C (30 F) by 1330 h at the end of the experiment. While a few bags failed to sample and were flat, all other bags had adequate sample volume and none were excessively full, even for the high pump rate samplers.

The main takeaway from this second experiment is that there is no evidence for a cold temperature artifact such as was seen in the early bags in the first pink box experiment. All of the samples taken prior to the injection had ambient concentrations generally 8-10 pptv. It is not known whether this might have been due to the reduction in pump rates, so that the bags were not overfull, together with the somewhat warmer temperatures. There is no evidence that the sampler configurations featuring different tubing, connectors, or wiring had any appreciable effect on the results.

It should be emphasized that most of the nighttime IOPs were conducted in temperatures similar to the second pink box experiment and bag fullness was generally similar to or less than the second pink box experiment. If the duplicate discrepancies were related to pump leaks, they didn't manifest themselves in the second experiment. The field blank results provide evidence that there was probably infiltration when the sampler was exposed to sustained high level concentrations for a long enough time. That might be attributable to leakage past the pump but there is no strong evidence that this was a major problem as blank values were never more than a few pptv. Thus, it is not at all clear that the field duplicate discrepancies are due in any significant way to a systemic sampling artifact. That might be the case but the evidence for it is sketchy.

Another factor to consider here is the tube closure issue mentioned in the Description of Equipment section at the start of this (Bag Sampling) chapter. That is the collocated duplicate discrepancies might be attributable, at least in part, to tubing not being completely closed at the clip. In that event, gas could potentially infiltrate into or out of a bag while awaiting analysis or be corrupted during the line purge cycle on the GC. As mentioned there, it would not be surprising if some of the discrepancies were attributable to this but evidence that this would account for the consistency and magnitude of the discrepancies is sparse at best. Problems caused by improper tube closure should be nearly random and distributed across all IOPs. The differences between day and night and the consistency of the decrease in the discrepancies with distance during both day and night argue against a random problem such as improper tube closures. Rather, they suggest the data might be pointing to a real phenomenon. It might be worth noting that consistent field duplicate discrepancies of these magnitudes were generally not observed in previous field studies (e.g., Finn et al. 2015). However, most of those experiments were conducted in warmer temperatures and at larger downwind distances.

In summary, the field duplicate results suggest two things. One is that they might be pointing to the effects of real turbulent mixing phenomena at varying scales and distances in stable and unstable conditions. Second, at a minimum, they should be used as an estimate of the

uncertainty in the measurements. After allowing for the known errors associated with the field control sampling, those results could also be used to help make estimates of uncertainty.

17. Software quality control checks.

Several important quality checks were built into the software to efficiently aid the TAF analyst in ensuring that the ATGAS instruments were functioning correctly during analysis.

- Since the concentration is dependent upon the temperature of the ATGAS ovens, it is critical that oven temperatures do not fluctuate widely during analysis. Temperature acceptance limits were set ($\pm 2^{\circ}\text{C}$) and the software produced a pop-up window to alert the analyst in case of unacceptable oven temperature readings. All samples obtained using the incorrect oven temperatures were re-analyzed.
- To check for instrument drift, the software alerted the analyst to validate the calibration curve when more than three hours had elapsed from the last CCV. The analyst had the option of overriding the alert or checking the calibration and re-starting the 3-hour clock. This option was never exercised except on a few occasions near the end of the analysis day when only 1-2 more cartridges required analysis. Even then this was only done on ATGASs that had previously been exhibiting consistently stable response for extended periods of time during that day.
- In order to verify the calibration curve in the area of interest and to save time, the software produced on the computer screen a record of the highest and lowest concentrations measured since the last CCV. The analyst had only to re-analyze calibration samples within that range. However, the complete calibration range was routinely done to most fully evaluate the current status of instrument response and performance.
- Several data flags were shown immediately on the computer screen to aid the analyst in deciding whether the data for each bag was “good” or re-analysis was necessary. For example, the low pressure flag alerted the operator to a problem with the analysis that was almost invariably due to pinched tubing restricting sample flow.
- The software kept track of which ATGAS field duplicate was analyzed on and directed the analyst to use the same GC for the duplicate cartridge. This helped to quantify the variability of the field analysis without adding the extra variability of analyzing on a separate ATGAS. Field duplicate sample cartridges with concentrations exceeding the maximum calibrated concentration on a particular GC were moved to a GC with a higher calibrated range.
- The software alerted the analyst if any calibration points did not meet pre-determined acceptance criteria. The analyst could then review the calibration curve to determine the acceptable course of action.

18. Data verification.

Data verification was performed to ensure that the samples met all QC acceptance limits and that all samples had been analyzed for that particular test. Transcription and calculation errors were reduced by automated data reduction techniques such as automated flagging of results outside acceptable limits, raw data summary sheets (Fig. 36), auto-generated quality control sheets (Fig. 37 and 38), auto generation of chromatogram plots including calibration curves (Fig. 39), and electronic transfer of data from the ATGASs to Excel spreadsheets. The analyst and at least one other person familiar with the data analysis process reviewed all data packages. All data packages were batch processed per run on each ATGAS. All data packages included the raw data sheets, quality control sheets that summarized the results of all QC data generated for that batch, plots of all chromatograms and calibration curves, a copy of the laboratory notebook pages for that analysis (Fig. 40), and a data verification sheet (Fig. 41) to ensure the verifier checked all QC parameters. Software produced an Analysis Summary (Fig. 42) that was utilized to ensure that there was at least one acceptable result for each bag for each location that was downloaded for each IOP. Any samples noted by the software were re-analyzed and the Analysis Summary report was re-run until all samples had been analyzed or a justifiable reason had been determined for a missing sample. Cartridges were not cleaned for reuse until all available samples had been analyzed, the verification completed, and all QC checks done.

131015	1035	SN0397	SAGE13	2	58	3	1	14304.62	65	653.	0	0	G	
131015	1036	SN0397	SAGE13	2	59	4	1	84.44	65	653.	0	0	G	
131015	1037	SN0397	SAGE13	2	60	5	1	912.44	65	653.	0	0	G	
131015	1038	SN0397	SAGE13	2	61	6	1	311.52	65	653.	0	0	G	
131015	1040	SN0397	SAGE13	2	62	7	1	22023.60	65	653.	0	0	G	
131015	1041	SN0397	SAGE13	2	63	8	1	3692.82	65	653.	0	0	G	
131015	1042	SN0397	SAGE13	2	64	9	1	16482.13	65	653.	0	0	G	
131015	1043	SN0397	SAGE13	2	65	10	1	11621.93	65	653.	0	0	G	
131015	1044	SN0397	SAGE13	2	66	11	1	15636.64	65	653.	0	0	G	
131015	1045	SN0397	SAGE13	2	67	12	1	32469.91	65	653.	0	0	G	
131015	1049	SN0289	SAGE13	2	68	1	1	1225.11	65	653.	0	0	G	
131015	1050	SN0289	SAGE13	2	69	2	1	347.32	66	653.	0	0	G	
131015	*1051*	SN0289*	SAGE13	2	70*	3	1*	17.10*	65	652.	0	3	F	**** unusable
131015	1052	SN0289	SAGE13	2	71	4	1	162.98	66	653.	0	0	G	
131015	1053	SN0289	SAGE13	2	72	5	1	52.92	66	653.	0	0	G	
131015	1054	SN0289	SAGE13	2	73	6	1	101.49	66	653.	0	0	G	
131015	1055	SN0289	SAGE13	2	74	7	1	8.51	65	652.	0	0	G	
131015	1056	SN0289	SAGE13	2	75	8	1	8.55	65	652.	0	0	G	
131015	1057	SN0289	SAGE13	2	76	9	1	8.96	65	652.	0	0	G	
131015	1058	SN0289	SAGE13	2	77	10	1	8.39	65	653.	0	0	G	
131015	1059	SN0289	SAGE13	2	78	11	1	8.53	66	653.	0	0	G	
131015	1100	SN0289	SAGE13	2	79	12	1	8.64	65	653.	0	0	(L)	low bag
131015	1105	SN4383	SAGE13	2	80	1	1	7.92	66	653.	0	0	G	fdp
131015	1106	SN4383	SAGE13	2	81	2	1	7.93	65	653.	0	0	G	fdp
131015	1107	SN4383	SAGE13	2	82	3	1	3006.30	65	653.	0	0	G	fdp
131015	1108	SN4383	SAGE13	2	83	4	1	81.52	65	653.	0	0	G	fdp
131015	1109	SN4383	SAGE13	2	84	5	1	1019.18	65	652.	0	0	G	fdp
131015	1110	SN4383	SAGE13	2	85	6	1	15.42	65	653.	0	0	G	fdp
131015	1111	SN4383	SAGE13	2	86	7	1	4791.56	65	652.	0	0	G	fdp
131015	1112	SN4383	SAGE13	2	87	8	1	853.01	65	652.	0	0	G	fdp
131015	1113	SN4383	SAGE13	2	88	9	1	26366.36	65	652.	0	0	G	fdp
131015	1115	SN4383	SAGE13	2	89	10	1	9346.58	65	652.	0	0	G	fdp
131015	1116	SN4383	SAGE13	2	90	11	1	10919.11	65	652.	0	0	G	fdp
131015	1117	SN4383	SAGE13	2	91	12	1	45963.54	65	652.	0	0	G	fdp
131015	1121	SN4329	SAGE13	2	92	1	1	10.47	65	652.	0	0	G	
131015	1122	SN4329	SAGE13	2	93	2	1	56.15	65	652.	0	0	G	
131015	1123	SN4329	SAGE13	2	94	3	1	40.29	65	652.	0	0	G	
131015	1124	SN4329	SAGE13	2	95	4	1	203.30	66	652.	0	0	G	
131015	1125	SN4329	SAGE13	2	96	5	1	62.75	65	652.	0	0	G	
131015	1126	SN4329	SAGE13	2	97	6	1	69.57	65	652.	0	0	G	
131015	1127	SN4329	SAGE13	2	98	7	1	446.45	65	652.	0	0	G	
131015	1128	SN4329	SAGE13	2	99	8	1	10.06	65	652.	0	0	G	
131015	1129	SN4329	SAGE13	2	100	9	1	8.61	65	652.	0	0	G	
131015	1130	SN4329	SAGE13	2	101	10	1	7.92	65	652.	0	0	G	
131015	1131	SN4329	SAGE13	2	102	11	1	8.55	65	652.	0	0	G	
131015	1132	SN4329	SAGE13	2	103	12	1	8.56	66	652.	0	0	G	
131015	1137	SN4343	SAGE13	2	104	1	1	4425.70	65	652.	0	0	G	
131015	1138	SN4343	SAGE13	2	105	2	1	1017.25	66	652.	0	0	G	
131015	1139	SN4343	SAGE13	2	106	3	1	142.95	66	652.	0	0	G	
131015	1140	SN4343	SAGE13	2	107	4	1	162.84	66	652.	0	0	G	
131015	1141	SN4343	SAGE13	2	108	5	1	408.26	66	652.	0	0	G	
131015	1142	SN4343	SAGE13	2	109	6	1	488.85	65	652.	0	0	G	
131015	1143	SN4343	SAGE13	2	110	7	1	38.70	66	652.	0	0	G	
131015	1144	SN4343	SAGE13	2	111	8	1	715.22	65	652.	0	0	G	
131015	1145	SN4343	SAGE13	2	112	9	1	34.68	66	652.	0	0	G	
131015	1146	SN4343	SAGE13	2	113	10	1	9.30	65	652.	0	0	G	
131015	1147	SN4343	SAGE13	2	114	11	1	9.78	65	652.	0	0	G	
131015	1148	SN4343	SAGE13	2	115	12	1	9.53	65	652.	0	0	G	
131015	1153	SN0007	SAGE13	2	116	1	1	9.21	66	652.	0	0	G	
131015	1154	SN0007	SAGE13	2	117	2	1	8.01	66	652.	0	0	G	

Figure 36. Example of Raw Data Summary sheet.

National Oceanic and Atmospheric Administration
Air Resources Laboratory Field Research Division
Quality Control Sheets

Analyst: Dennis Finn et. al.
Date: 10/16/2013
Project: SAGE13
GC# 1
Parameter: SF6
Data file: GL131016.r01

Verified by: Roger B. Carter

Date: 23 Oct 2013

Calibration Verification (±7%; <50 ±12%)			Lab Blank		Calibration Check (±10%; <50 ±20%)		Background Level	
Bag	True Value	Result	%Recovery	area	Bag	Result	Bag	Result
#01	0.00	0.56	?	686	#01	0.00	#01	10.268
#02	3.11	3.39	109	2974	#02	0.00	#02	10.316
#03	10.10	10.37	103	10965	#03	0.00	#03	10.058
#04	19.19	19.77	103	22180	#04	0.00	Average	10.214
#05	35.10	35.04	100	33412	#05	0.00	Sample	
#06	88.70	87.98	99	116748	#06	0.00	Min=	0.00
#07	301.00	297.95	99	450292	#07	0.00	Max=	51066.39
#08	504.00	500.72	99	736517	#08	0.00	Temperature	
#09	818.00	822.40	101	1093385	#09	0.00	Min=	62.6
#10	1550.00	1556.80	100	1684523	#10	0.00	Max=	67.4
#11	3110.00	3070.56	99	2307952	#11	0.00		
#12	5220.00	5213.41	100	2951101	#12	0.00		
#01	8300.00	8292.34	100	3564852				
#02	9730.00	9736.86	100	3876774				
#03	16370.00	16663.88	102	4793330				
#04	21720.00	21817.29	100	5350192				
#05	36900.00	37147.07	101	7161377				
#06	52600.00	51719.08	98	8810498				
#07	75100.00	74834.21	100	10969928				

Final Calibration Verification (±10%; <50 ±20%) Comments/Corrective Actions

Bag True Value Result %Recovery

#01	0.00	0.20	?
#02	3.11	3.21	103
#03	10.10	10.33	102
#04	19.19	19.85	103
#05	35.10	35.58	101
#06	88.70	90.92	102
#07	301.00	305.47	101

SN0378 #06 was low

SN0378 #08 was low

SN1265 #09 should be re-run

SN1265 #10 should be re-run

SN1265 #8 should be re-run

Figure 37. Example of first page of quality control sheet.

#07	75100.00	75798.70	101	10505549	52600.00	53943.86	103
					75100.00	76633.05	102

Final Calibration Verification(±10%; <50 ±20%) Comments/Corrective Actions

Bag True Value Result %Recovery

#01	0.00	-0.37	?
#02	3.11	3.15	101
#03	10.10	9.66	96
#04	19.19	17.89	93
#05	35.10	33.12	94
#06	88.70	85.39	96
#07	301.00	292.01	97
#08	504.00	494.74	98
#09	818.00	825.60	101
#10	1550.00	1632.51	105
#11	3110.00	3279.07	105
#12	5220.00	5484.06	105
#01	8300.00	8379.71	101
#02	9730.00	9816.35	101
#03	16370.00	16746.16	102
#04	21720.00	22060.15	102
#05	36900.00	35925.72	97
#06	52600.00	52720.06	100
#07	75100.00	73595.19	98

Duplicates

cart	Bag	Result 1	Result 2	RPD
SN0203	#01	10074.35	10291.76	-2.1
SN0203	#02	11150.15	11397.22	-2.2
SN0203	#03	3430.90	3504.70	-2.1
SN0203	#04	11137.65	11522.75	-3.4
SN0203	#05	14273.24	14722.13	-3.1
SN0203	#06	6227.48	6405.37	-2.8
SN0203	#07	20973.62	21356.79	-1.8
SN0203	#08	18979.41	19477.15	-2.6
SN0203	#09	16407.46	17464.74	-6.2
SN0203	#10	23266.80	23634.66	-1.6
SN0203	#11	939.91	965.06	-2.6
SN0203	#12	2976.72	3057.99	-2.7
SN0238	#01	3067.30	3194.99	-4.1
SN0238	#02	1725.45	1851.00	-7.0

Figure 38. Example of last page from quality control sheets.

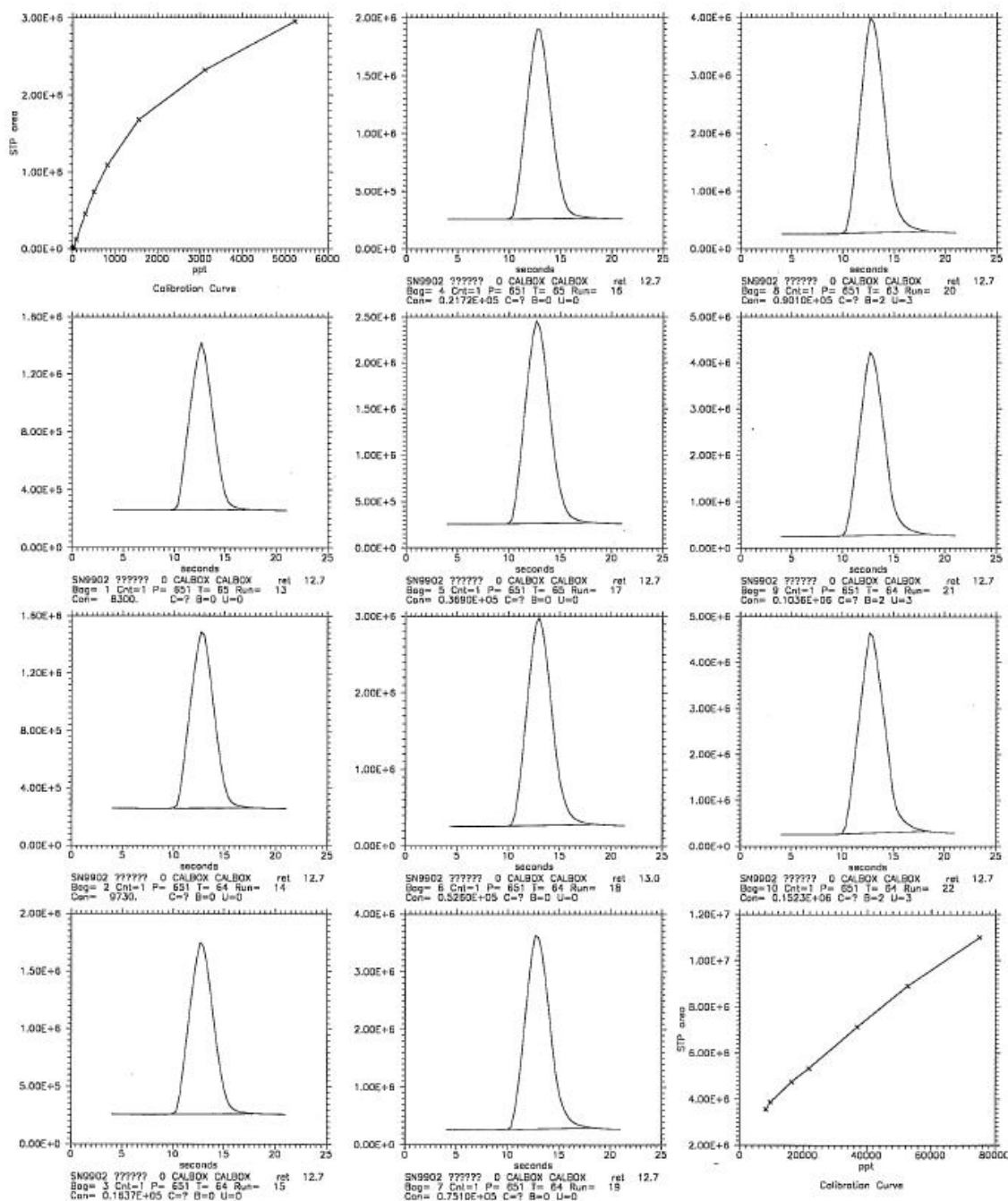


Figure 39. Example of chromatogram and calibration curve check sheet.

10/22/13

Test 4

Extended warm up

FILE NAME	92131622.R1	C1-SETTING	35
PROJECT ID	Sage 13	C2-SETTING	17
CARRIER PRESS. (PSI)	30	PURIFIER PRESS. (PSI)	30%
DETECTOR TEMP °C	170	OVEN TEMP °C	65
ATTENUATION	212	BASELINE ADJ.	161
DETECTOR FLOW	110	SAMPLE LOOP	1ml

Cal

Chk

1.	zero	0.9	0	0	0	0	0	0
2.	3.11	125 ^{rerun} =97	92	106	104	106	111	102
3.	10.1	110	100	99	(74) ^{refill} =105	106	100	97
4.	19.19	106	105	98	102	106	100	98
5.	35.1	102	104	101	102	104	100	100
6.	88.7	102	105	102	104	106	101	100
7.	301	102	108	101	104	107	101	101
8.	504	102	109	100	103	105	101	100
9.	818	102	110	101	107	108	103	100
10.	1550	102	111*	101	106	108	102	101
11.	3140	103	111*	102	105	107	102	101
12.	4980	103	111*	101	104	107	101	102
13.	8270	102		99	102	98	101	100
14.	9730	103		101	104	107	101	99
15.	16370	103		99	102	105	101	80 ^{refill} =100
16.	21720	102		102	104	106	100	100
17.	36900	103		102	105	107	101	93
18.	52600	102		101	102	104	102	101
V = 0.0210 0.0220 0.0224 0.0232 0.0242 0.0244 0.0245								

Lab Blank - all zeros

Room Air - 8.3, 8.2, 7.9

"b. 2" didn't run, rerun

Lab dupe - SN0399

Fail chk, rerun all > 818 ppt
after recal

SN4410 b. 5, 2

SN1243 b. 2

SN0399 b. 2

Figure 40. Example of laboratory notebook page.

Quality Control Verification Sheet

Date: 23 Oct 2013
 Verifier: Roger Cuto-
 Data File: 61131016.P01
 Project: SAGEB

YES	NO	NA
<input checked="" type="checkbox"/>	<input type="checkbox"/>	<input type="checkbox"/>
Data package contains complete and legible:		
Chromatograms		
Raw data		
Logbookcopy		
QC sheet		
<input checked="" type="checkbox"/>	<input type="checkbox"/>	<input type="checkbox"/>
The same data file is on the raw data sheet, logbook copy, QC sheet and chromatograms.		
<input checked="" type="checkbox"/>	<input type="checkbox"/>	<input type="checkbox"/>
A complete set of calibration checks, that cover the range of sample concentrations, were analyzed at the end of the run.		
<input checked="" type="checkbox"/>	<input type="checkbox"/>	<input type="checkbox"/>
All pressures are acceptable. Any low-pressure bugs have been re-analyzed if not marked at flat.		
<input checked="" type="checkbox"/>	<input type="checkbox"/>	<input type="checkbox"/>
The chromatograms show no anomalies.		
<input checked="" type="checkbox"/>	<input type="checkbox"/>	<input type="checkbox"/>
The calibration curve shows no anomalies.		
<input checked="" type="checkbox"/>	<input type="checkbox"/>	<input type="checkbox"/>
All flagged samples have been re-analyzed unless the sample is no longer usable.		
<input checked="" type="checkbox"/>	<input type="checkbox"/>	<input type="checkbox"/>
All data that has "bad analysis flags" has been marked as unusable and re-analyzed if possible.		
<input checked="" type="checkbox"/>	<input type="checkbox"/>	<input type="checkbox"/>
The background level was reported. The background level is greater than the lab blank indicating there is no leakage within the system.		
<input checked="" type="checkbox"/>	<input type="checkbox"/>	<input type="checkbox"/>
All data greater than 10% higher than the highest calibration standard is flagged as an estimate and has been re-analyzed.		
<input checked="" type="checkbox"/>	<input type="checkbox"/>	<input type="checkbox"/>
All data less than 10% lower than the lowest calibration standard is flagged as an estimate and has been re-analyzed.		
<input checked="" type="checkbox"/>	<input type="checkbox"/>	<input type="checkbox"/>
All anomalies reported on the logbook copies are reported on the QC sheet and the data has been flagged appropriately.		
<input checked="" type="checkbox"/>	<input type="checkbox"/>	<input type="checkbox"/>
All the data has been transferred correctly from the raw data to the QC sheet.		
<input checked="" type="checkbox"/>	<input type="checkbox"/>	<input type="checkbox"/>
Calibration curve verification was within 7% of the true value. (12% for concentrations less than 50ppb) Any anomalies are noted.		
<input checked="" type="checkbox"/>	<input type="checkbox"/>	<input type="checkbox"/>
Lab blanks were analyzed and were less than the lowest calibration standard.		
<input checked="" type="checkbox"/>	<input type="checkbox"/>	<input type="checkbox"/>
Recoveries for the calibration checks were within $\pm 10\%$ (20% for concentrations less than 50ppb) or the instrument was re-calibrated and the samples within the invalid ranges were re-analyzed.		
<input checked="" type="checkbox"/>	<input type="checkbox"/>	<input type="checkbox"/>
Duplicates were analyzed and were within $\pm 10\%$ RPD (20% for concentrations less than 50ppb). Those not meeting the acceptable range were re-analyzed.		
<input checked="" type="checkbox"/>	<input type="checkbox"/>	<input type="checkbox"/>
The Min. and Max. even temperatures were within $\pm 2^\circ\text{C}$ of the temperature set point.		
<input checked="" type="checkbox"/>	<input type="checkbox"/>	<input type="checkbox"/>
Data is usable as noted		
<input checked="" type="checkbox"/>	<input type="checkbox"/>	<input type="checkbox"/>

Verifier Comments: Data ok when noted run and flag sets complete.

SN4409 b.10 did not run
 SN1042 runs 491-495 flag as est.

Figure 41. Example of data package Data Verification sheet.

Analysis Summary for SAGE13 test 1 tracer:SF6
start year=2013 start month= 9
estimated results accepted as good.
12-NOV-13 17:16:39

Cartridges downloaded, but analysis NOT complete
SN0030 LC8061 2
SN4312 LC1020 5

Flat, damaged, or incorrectly connected bags that are NOT analyze
d

Locations downloaded but NOT listed as project locations

Project locations NOT downloaded

LC2004
LC2007
LC2010
LC2013
LC2016
LC2019
LC2022
LC2025
LC2028
LC2031
LC2034
LC2037
LC2040
LC2043
LC2046
LC2049
LC2052
LC2055
LC2058
LC2061
LC2064
LC2067
LC2070
LC2073
LC2076
LC2079
LC2082
LC2085
LC2116
LC2131
LC2155
LC2173

SN0030 10/2 Varsam
10/3 Check, Analyze (1) L L FGGGLGGGG
10/10 Clean
10/18 Varsam
10/24 Check Analyze (3)
SN4312 10/2 Varsam
10/3 Check, Analyze (1) 5 L, 11 I
10/8 Clean
10/11 Varsam
10/22 Check, Analyze (3)

clip was open
flag set
flat?

clip open
e-purge
flag set
flat?

DF 11/14

Figure 42. Example of Analysis Summary sheet.

19. Post-project determination of ILOD, ILOQ, MLOD, and MLOQ.

ILOD and ILOQ were previously defined in the quality control procedures (step 6 above). In that section a procedure was described for obtaining a preliminary pre-project estimate of the ILOD and ILOQ using a very low concentration calibration standard. These results were reported in Table 6. There are additional ways to estimate ILOD and ILOQ. These include the use of laboratory blanks and the low level laboratory control standards used for calibration and CCV. These alternative determinations together with a post-project repeat of the initial procedure are also shown in Table 6. In general, all of the various estimates for ILOD were low and well below the stated MQO of 4 pptv. The lab blank estimate of ILOD for GC3 was relatively high at 2.1 pptv. As noted earlier, this is due to the sensitivity of GC3 to the effect of very small changes in baseline on the peak integration at very low concentrations. Similarly, the ILOD estimate for GC3 based on lab control (CCV) results was also elevated at 3.04 pptv. The other exception was for the ILOD on GC4 (3.7 pptv) based on the lab control results. This was based on the 10.1 pptv standard, instead of the 3.11 pptv standard, since the detection of the lower concentration standard by GC4 was erratic.

The method limit of detection (MLOD) and method limit of quantitation (MLOQ) are estimates of the lowest field concentration level that can be determined with some degree of certainty. Unlike ILOD and ILOQ, MLOD and MLOQ incorporate all the sources of variability and uncertainty introduced during each phase of the sampling, handling, and analysis. The MLOD is defined as the lowest field concentration measurement that can be determined to be statistically different from zero. It is based upon the method's ability to differentiate a low-level concentration standard from the combined effects of instrument and method noise. The MLOD and MLOQ are calculated exactly the same as ILOD and ILOQ except that method variability is factored into the determination by using results from samples that have been put through the rigors of field sampling. The MLOD is calculated as 3 times the standard deviation of a low level standard. The MLOQ is defined as the lowest concentration that can be determined within 30% of the actual concentration. The MLOQ is calculated as 10 times the standard deviation of the same low level standard.

Table 13. Estimates of MLOQ using field duplicates, field blanks, and field controls.

Field Duplicates	IOP1	IOP2	IOP3	IOP4	Day Avg.	IOP5	IOP6	IOP7	IOP8	Night Avg.	All Avg.
Count (dup<12)	23	7	58	142	230	57	141	8	19	229	455
Mean	0.20	-0.27	0.42	-0.14	0.03	0.03	-0.10	-0.79	0.31	-0.05	-0.01
S.D.	1.15	1.20	1.17	0.75	0.96	1.27	1.21	0.92	1.78	1.28	1.13
MLOQ	11.5	12.0	11.7	7.5	9.6	12.7	12.1	9.2	17.8	12.8	11.3
Count (dup<20)	34	19	94	143	290	68	141	16	73	298	588
Mean	0.02	-0.44	0.28	-0.14	0.00	0.09	-0.10	-1.29	0.43	0.01	0.00
S.D.	1.5	1.7	1.28	0.75	1.13	2.43	1.21	2.27	3.57	2.35	1.85
MLOQ	15	17	12.8	7.5	11.3	24.3	12.1	22.7	35.7	23.5	18.5
Field Blanks											Combined
Count	36	36	36	36	144	35	36	35	36	142	286
Mean	0.02	-0.17	0.19	0.00	0.01	2.79	0.15	0.79	0.12	0.95	0.48
S.D.	0.06	0.36	1.41	0.00	0.73	3.74	0.54	1.38	0.70	2.28	1.75
MLOQ	0.6	3.6	14.1	0.0	7.3	37.4	5.4	13.8	7.0	22.8	17.5
Field Controls (14.79 ppt)											
Count	9	8	9	9	35	9	9	6	9	33	68
Mean	15.3	15.0	14.8	15.0	15.0	17.0	15.3	15.3	15.0	15.7	15.3
S.D.	0.26	0.27	0.54	0.45	0.42	4.14	0.28	0.75	0.48	2.27	1.63
MLOQ	2.7	2.7	5.4	4.5	4.2	41.4	2.8	7.5	4.8	22.7	16.3

There are several ways to attempt to estimate MLOD and MLOQ. These include field blanks, low concentration field controls, and field duplicates. Ambient background samples of all regular field samples can also be used to estimate MLOQ. However, these samples do not incorporate all sources of variability observed during experiments. Specifically, background samples, by definition, were not exposed to the higher level concentrations measured by many of the samplers that were strongly impacted by the tracer plume. Sampler cartridges located on parts of the grids that were heavily impacted by the tracer plume were seen to occasionally have their lower concentration bags affected (e.g., some of the field blank bags). There is also the problem of setting a cutoff value separating truly background samples from those that were slightly influenced by the plume. For these reasons, the ambient background method was not calculated. Estimates of MLOQ were made using each of the other methods. Table 13 summarizes the results of the analysis for the estimate of MLOQ.

Estimates of MLOQ using the field duplicates technique provided estimates ranging by IOP from 7.5 to 17.8 pptv for duplicate pairs less than 12 pptv with an overall IOP average of 11.3 pptv. Again, there was a notable difference between the overall day and night results (9.6

and 12.8, respectively). For duplicate pairs less than 20 pptv estimates of MLOQ ranged from 7.5 to 35.7 pptv by IOP with a much larger discrepancy between day and night. Estimates of MLOQ using field blanks ranged from zero to 37.4 pptv with an overall average of 17.5 pptv. The overall average is skewed by the results of IOPs 3, 5, and 7. The result for IOP3 is dominated by one value of 8.4 pptv with the other 35 values being zero. IOPs 5 and 7 had several non-zero blank values resulting, again, in a much higher estimate of MLOQ for the overall nighttime average. That is likely due to the fact that IOPs 5 and 7 had the highest measured concentrations during PSB2 and they occurred over much of the sampling array. All of the estimates of MLOQ by the field controls were < 7.5 pptv with the exception of IOP5 (41.4 pptv). Again, it is possible this higher result is due to a sampling artifact.

The significant differences in MLOQ results suggest using different values for day and night. For reasons given earlier, it is preferable to use the lowest practicable concentrations for the calculation of MLOQ. That would discount the estimates of MLOQ using duplicate pairs <20 pptv and recommend the usage of duplicate pairs <12 pptv. The daytime average MLOQ based on field duplicates is then 9.6 pptv. Excepting the one outlier field blank value in IOP3 all of the daytime blank results are < 5 pptv. The daytime MLOQ based on the low control standard is similarly low. Thus, a case can be made for a daytime MLOQ not to exceed about 9-10 pptv. A daytime MLOQ was selected to be 9 pptv. That is consistent with MLOQ determined in past studies and very near what appears to be the current ambient global background for SF₆.

The nighttime assessment is more problematic. The average nighttime MLOQ by field duplicates, field blanks, and low control standard is 12.8, 22.8, and 22.7 pptv, respectively. In this nighttime analysis, the field blank result will be given lesser weight as it emphasizes the variability around zero due to the infiltration of small quantities of tracer. The effect of tracer infiltration suggested by the field blanks would be small on any samples near ambient background levels of 8-10 pptv and increasingly negligible as concentrations increased. The maximum blank value was 13.7 pptv in IOP5 and very few values exceeded 5 pptv. All of the nighttime estimates of MLOQ by field control standard are low except for IOP5 (41.4 pptv) and the overall nighttime average is 16.3 pptv. Based on the stated assumption and the overall results for the field duplicates and control samples an argument can be made for a nighttime MLOQ in the range of roughly 12-16 pptv. The decision was somewhat arbitrary but a value of 15 pptv was selected as the final nighttime MLOQ.

While an argument could be made for a higher daytime MLOQ, and an even better argument might be made for a higher nighttime MLOQ, the final MLOQ were determined to be 9 and 15 pptv for daytime and nighttime samples, respectively. All daytime values (IOPs 1-4) less than 9 pptv and all nighttime values (IOPs 5-8) less than 15 pptv have been flagged as estimates in the final database.

20. Final data review.

All field data were verified to make sure there was a result for every location, cartridge, and sample bag and that all results were flagged appropriately. The following examples of verification plots and summaries were chosen to illustrate the diligence with which each data point is reviewed. Every quality control sheet (Figs. 36-38) for each data package was reviewed to ensure proper flagging of final data. Bubble/dot plots (Fig. 43) were created and reviewed to ensure all data were reasonable and consistent with respect to the overall concentration pattern and the nearby neighbors of each bag sample. Any suspicious data point was traced back through the analysis and deployment records to determine if it was indeed a valid result. The sampler servicing records (e.g., Fig. 28), maintained by all field sampler deployment personnel for noting any problems, were used to check any outliers or anomalies in the data. Cartridge time history plots (Fig. 44) as well as individual chromatograms (Fig. 39) were also reviewed to determine any suspicious data points. Any suspicious data point was traced back through the

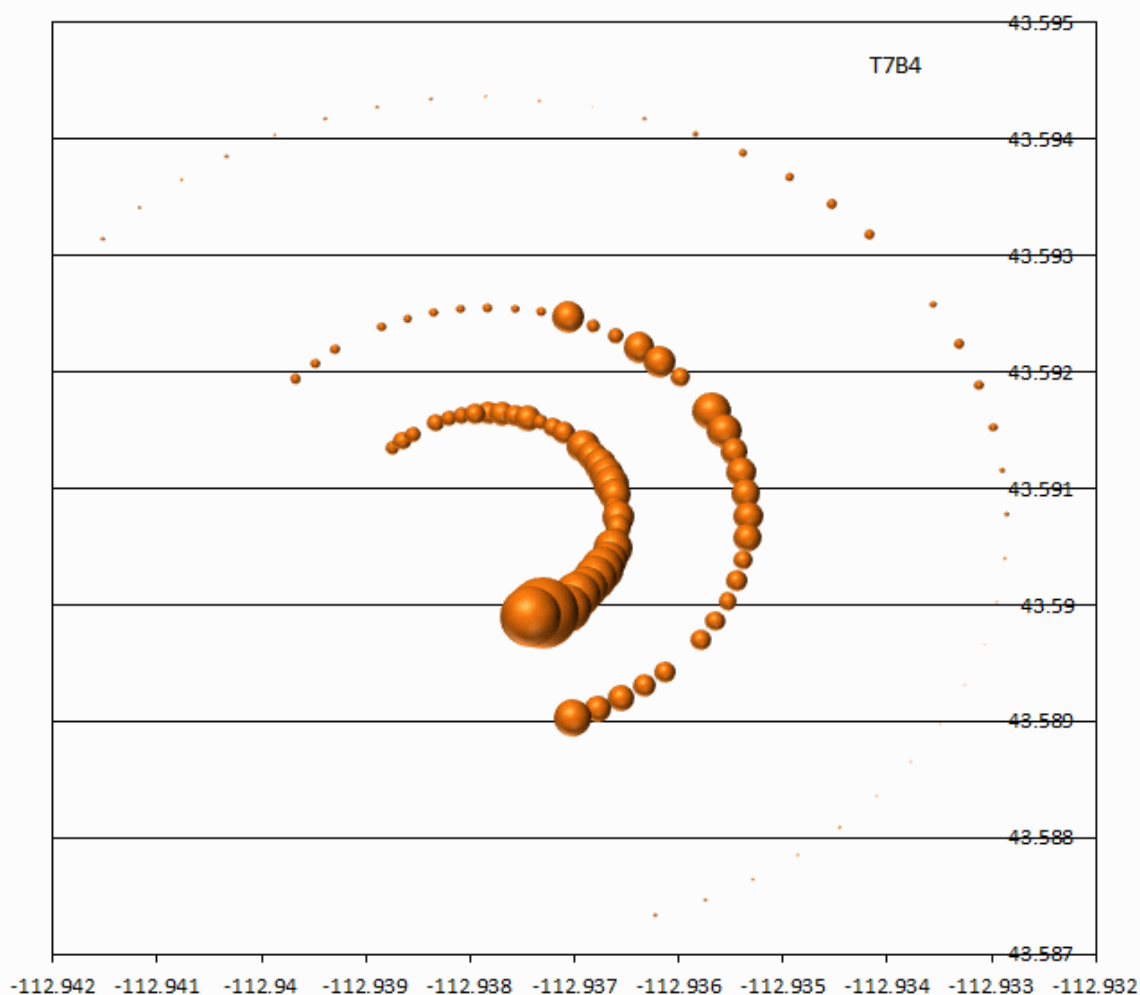


Figure 43. Example of bubble/dot plot for examining consistency of concentrations between neighboring locations and identifying suspicious values.

analysis and deployment records, sometimes with the aid of the master history file, to determine if it was indeed a valid result. All field QC was scrutinized. All suspicious data were rerun and/or flagged as appropriate.

The finalized data set was then analyzed using a program used to determine if all flags were added correctly and if a primary sampler result could be replaced by a more reliable duplicate result. Any results appearing on this sheet were verified and changes to the data base were made as necessary (Fig. 45).

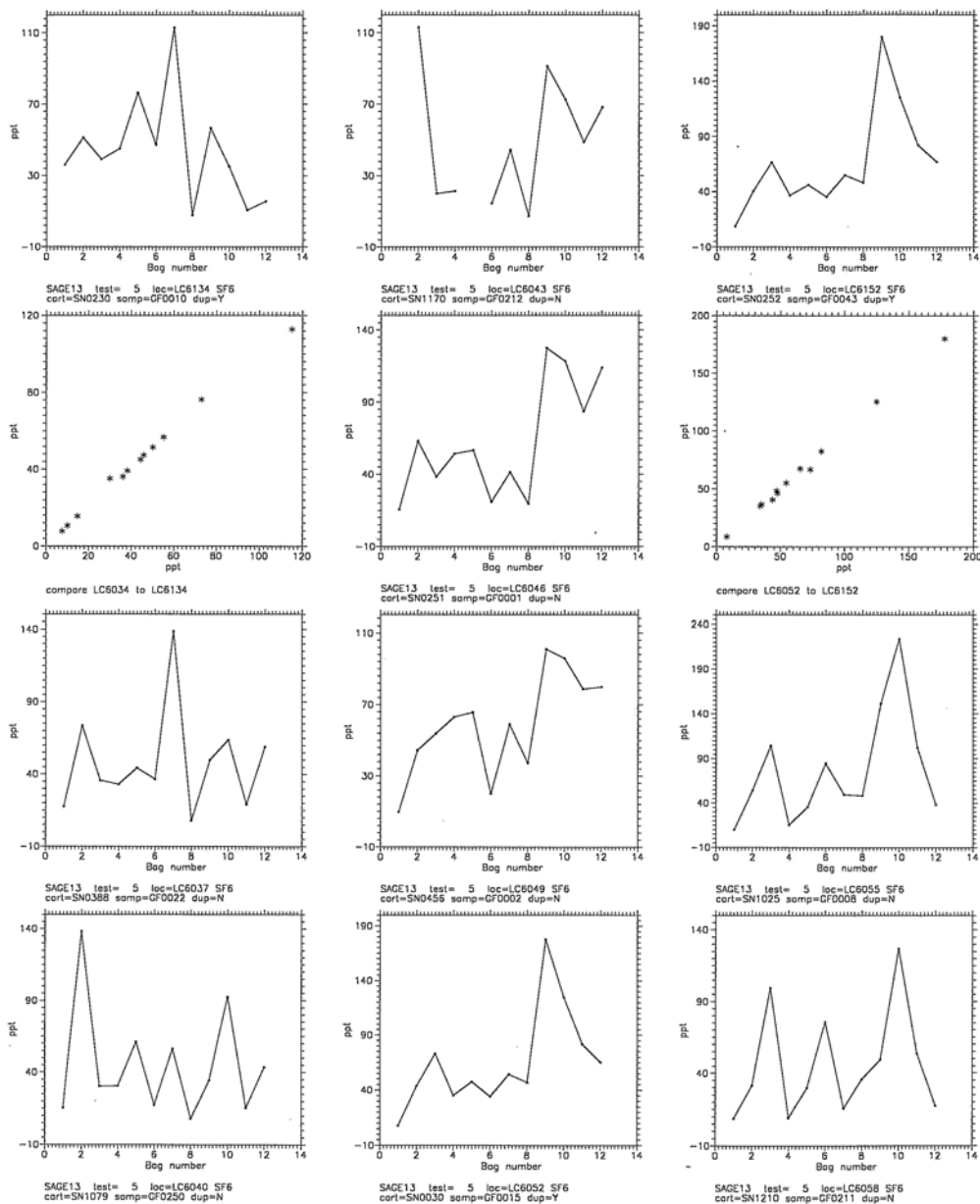


Figure 44. Example of cartridge time series plots used for identifying suspicious values.

Test3_1.Log

SBMAGIC version 1.5, 12-Dec-2013
 Run on 13-Jan-2014 at 12:11
 TEST = 3

Missing value on duplicate sampler	3	LC3055	2	- replace w. 3055 b2; reset flag
Missing value on duplicate sampler	3	LC3076	2	- replace w. 3176 b2; reset flag
Missing value on duplicate sampler	3	LC8025	1	- set as est. due to possibility clip not closed during purge
NO CHECK IN FLAG. ASSUMED GOOD	3	LC8055	1	
NO CHECK IN FLAG. ASSUMED GOOD	3	LC8055	2	
NO CHECK IN FLAG. ASSUMED GOOD	3	LC8055	3	
NO CHECK IN FLAG. ASSUMED GOOD	3	LC8055	4	
NO CHECK IN FLAG. ASSUMED GOOD	3	LC8055	5	
NO CHECK IN FLAG. ASSUMED GOOD	3	LC8055	6	
NO CHECK IN FLAG. ASSUMED GOOD	3	LC8055	7	
NO CHECK IN FLAG. ASSUMED GOOD	3	LC8055	8	
NO CHECK IN FLAG. ASSUMED GOOD	3	LC8055	9	
NO CHECK IN FLAG. ASSUMED GOOD	3	LC8055	10	
NO CHECK IN FLAG. ASSUMED GOOD	3	LC8055	11	
NO CHECK IN FLAG. ASSUMED GOOD	3	LC8055	12	
Missing value on duplicate sampler	3	LC8085	7	- replace w. 8185 b7; reset flag
POSSIBLE CONTROL		LC8046		

----- SAMPLE COUNTS -----
 Samples analyzed on GC1= 392
 Samples analyzed on GC2= 297
 Samples analyzed on GC3= 476
 Samples analyzed on GC4= 371
 Samples not analyzed = 0

Total samples= 1536
 OK samples= 1486
 Flag 3 samples= 23
 Flag 4 samples= 24
 Flag 5 samples= 3

Figure 45. Example of output from program used to assign flags to values in final data set and final check for possible errors.

21. Data handling.

All results were printed on hard copy as a backup in case of loss of the data files and to aid in the data verification process. The data packages were filed for future reference and to be readily available during the project for immediate review. Backup copies of the raw ATGAS data were made occasionally and at the end of the project to prevent total loss of data in the case of a computer failure. All final QC and sample results were printed on hard copy and placed in a binder to be stored with any reference materials in the project archive.

22. Summary of Data Completeness and Contribution by GC

Table 14 summarizes bag sampling data completeness for each test as well as for the entire project. The MQO of 90% (Table 4) was exceeded in every case. GC3 ran the highest fraction of the total number of samples. This was due to its wide analytical range available without resorting to sample loop changes, the shortest analytical cycle time, and relatively consistent stable operation that minimized the need to recalibrate or rerun samples. GC2 ran the next most samples. It had a slower cycle time than GC3 but had the most stable operation once the detector was replaced between IOPs 2 and 3. GCs 1 and 4 were overall the least productive, primarily due to greater difficulty in sustaining stable calibrations, but also longer cycle times than GC3. Regardless of GC, however, data had to be bracketed by satisfactory ICV and CCV recovery criteria to be acceptable.

Table 14. Summary of data completeness by IOP with contribution to analyses by individual GC.

GC	IOP								Total
	1	2	3	4	5	6	7	8	
1	458	323	215	421	310	409	326	408	2,870
2	225	367	550	421	466	374	441	420	3,264
3	576	567	600	433	485	455	434	444	3,994
4	301	303	195	285	299	334	371	300	2,388
Total	1,560	1,560	1,560	1,560	1,572	1,572	1,572	1,572	12,528
Valid	1,512	1,523	1,543	1,534	1,501	1,487	1,480	1,547	12,127
Flag3 (see below)	2	4	0	1	13	12	6	14	52
Flag4	46	33	17	25	58	61	86	11	337
Flag5	0	0	0	0	0	9	0	0	9
Flag6	5	2	5	1	5	3	7	1	29
Not Analyzed	0	0	0	0	12	0	0	0	12
Completeness%	96.7	97.6	98.9	98.3	95.4	94.6	94.1	98.4	96.8

Final Bag Sampler Data Files and Format

The final bag sample tracer data files provided with this report contain 12 columns:

1. test (IOP) number
2. bag number (1-12)
3. begin time (yyyymmdd)
4. start time (hhmmss)
5. sampling period (seconds)
6. dist (distance from release point in meters)
7. angle (angle in degrees along respective arc from north)
8. agl (meters, above ground level)
9. longitude
10. latitude
11. concentration (SF₆ pptv)
12. quality control flag

The files are in csv format with fixed width fields. The data files are named 'SAGE16Sampler##.csv' where '##' is the number of the Individual IOP test. The bag sampling Readme file accompanying this report summarizes the contents of this chapter on the bag sampling.

A supplemental set of tracer data files containing field duplicate analyses is also provided. This was not customarily included in the databases for past field studies. They are included here because of the sometimes large differences observed in collocated field duplicate sampling during PSB2 and the potential significance of these differences on interpretation of the data and any attempts to estimate uncertainty in the measurements. These files are named 'SAGE16##DUP.csv' where '##' is the IOP number. There are 12 columns in these files:

- | | | |
|-----|-----------|---|
| 1. | Project | SAGE16 |
| 2. | Test | IOP number |
| 3. | Loc. 1 | Location identification of primary sampler |
| 4. | Cart. 1 | Sample cartridge at Loc. 1 |
| 5. | Sampler 1 | Sampler at Loc. 1 |
| 6. | Loc. 2 | Location identification of duplicate sampler collocated with Loc. 1 |
| 7. | Cart. 2 | Sample cartridge at Loc. 2 |
| 8. | Sampler 2 | Sampler at Loc. 2 |
| 9. | Bag | Bag number |
| 10. | Concen. 1 | Concentration at Loc. 1 |
| 11. | Concen. 2 | Concentration at Loc. 2 |
| 12. | RPD | Calculated relative % difference |

Some of the files contain additional information in the next few columns related to sample reruns attempting to confirm the original result for selected field duplicate pairs.

Final Data File Quality Control Flags

All of the data in the main files were flagged with one of seven possible quality flags: These are:

- 0 > MLOQ; good data to be used without qualification.
- 1 < MLOD (4 pptv)
- 2 < MLOQ (9 pptv day or 15 pptv night) and > MLOD. Treat as an estimate.
- 3 missing – field problem (check in was F, I, or B), also missing analyses are included here; data values set equal to -999.
- 4 missing – lab problem; data values set equal to -999.
- 5 estimate because of laboratory problem, data values set equal to -999.
- 6 possibly suspect based on spatial/temporal comparisons with nearby results but for which there is no other basis to believe there is a problem with the sample

Flag '1' applies primarily to anomalously low ambient samples. Ambient background samples were generally in the range from 7-10 pptv. Values less than 5 pptv were preemptively designated with '-999' since anything less than 5 pptv for an ambient sample is unlikely.

Flag '2' applies primarily to ambient background samples and those samples that were affected by the plume but still had concentrations below the MLOQ. Flag '3' was applied to any data that was suspect due to field-related problems. This includes improperly connected bags, clips in the open position when they were checked in before laboratory analysis, flat bags, and overfilled bags. Flat bags, or low bags with suspect values, were the most common problem in this category. The reasons for flat bags include the sampling program failed to download from the Timewand into the sampler, the sampler failed to function properly, or the operator forgot to open the clips. In some cases operator error was the cause of the failure of the sampling program to download correctly. Flags '4' and '5' were applied to any data that was suspect due to problems with the laboratory analysis. An example of this was clips being open during the purge cycle of the analysis resulting in bag-filling and sample dilution.

This page left intentionally blank.

FAST RESPONSE TRACER ANALYZERS

Four vehicle mounted fast response SF₆ analyzers were deployed for Project Sagebrush Phase 2. These provided tracer concentration measurements with a response time of approximately one second. The output from these analyzers is provided in a set of data files. The file names and format are described at the end of this chapter.

Instrument Description

The FRD fast response SF₆ analyzers are based on a modified Precision Tracer Gas Analyzer (model TGA-4000) manufactured by Scientech Inc. of Pullman, Washington. Modifications include a different plumbing system, a computer controlled calibration system, an integrated global positioning system (GPS), an automatic cleaning system, and a built in microcontroller with a CompactFlash™ card for data storage as shown in Fig. 46. The TGA-4000 measures atmospheric SF₆ concentrations with a response time of about 1 s (Benner and Lamb 1985). The rapid response time and mobile nature of the analyzers make them ideally suited for the determination of plume widths and structure. They have been utilized to determine both cross and along wind diffusion parameters commonly used in transport and dispersion models and Gaussian plume models (Clawson et al. 2004, 2005).

The TGA-4000 uses a tritium based electron capture detector (ECD) to detect the SF₆. The ECD is very sensitive to halogenated compounds such as chloro-fluorocarbons and SF₆ as well as oxygen. Oxygen interferes with the ECD operation and is therefore removed from the sample prior to introducing it into the ECD. This is done by reacting the oxygen with hydrogen in a catalytic reactor and removing the resultant water through a semi-permeable membrane.

The instrument limit of detection (ILOD) of the TGA-4000 is about 10 parts per trillion by volume (pptv) under optimal laboratory conditions. However, under field operations, the method limit of detection (MLOD) can be significantly higher. Calculations of MLODs and actual values for this experiment are discussed below.

The maximum concentration measurement capability is about 10,000 pptv, but can be doubled with the aid of a dilution system. The dilution system mixes the incoming sample air with an equal quantity of ultrapure air and reduces the concentration in the instrument to half what is in the sample air. However, using the dilution system also doubles the method limit of detection (MLOD) and method limit of quantitation (MLOQ). (This is discussed in more detail in the description of the data quality flags at the end of this chapter.)

The analyzer output signal along with instrument temperatures and status were collected at the rate of 2 Hz and stored on a CompactFlash™ card. The signal was simultaneously displayed on a hand held screen for operator interpretation and control. Using this display, operators performed real-time calculations of tracer concentrations and communicated details of plume location, concentrations, and structure to the test director.



Figure 46. NOAA mobile, fast response, tracer gas analyzer installed in the passenger seat of a van. A calibration box is visible in the foreground. The microcontroller that collects the data and runs automated calibrations is attached to the top of the instrument.

During IOPs 1-4, the analyzers were driven to a programmable bag sampler location and remained parked next to the sampler with the analyzer inlet as close to the sampler as practical. The analyzer and the sampler performed co-located measurements. The analyzers generally stayed parked at the same sampler the entire IOP with only a few exceptions when the analyzer was moved to a new location. It was anticipated that the conditions during IOPs 5-8 would require the analyzers to move much more frequently, so GPS units were added to provide location information during these IOPs.

Calibration and Concentration Determination

Calibration of a fast response analyzer was accomplished by allowing it to sample calibration mixtures with known concentrations of SF₆ and recording the output corresponding to each concentration. SF₆ concentrations of sample air are then determined by linearly interpolating between the calibration concentrations whose output values bracket the sample output. The calibration functions are all controlled by the built in microcontroller when initiated by the operator.

The SF₆ calibration standards were stored in Tedlar® bags identical to those used in the bag samplers which were described in a previous section of this report. The bags were connected to the analyzer sample stream by a series of electrically operated three-way valves. The computer switched the sample stream from outside air to a given calibration mixture by activating the corresponding valve. Eight calibration standards were used ranging in concentration from ultrapure air (0 pptv) to over 10,000 pptv SF₆. The calibration standards were manufactured by Scott-Marrin, Inc. of Riverside CA and had a manufacturer listed concentration uncertainty of ±5% and were NIST traceable. A full set of eight calibration standards were run on each analyzer both before the release began and after sampling was completed. Operators also ran calibration verification sets during the IOPs as needed.

All of the calibration standards were made by mixing small amounts of SF₆ with ultrapure air. Consequently, the analyzer response to any calibration concentration had to be calculated as a difference between the response to the calibration gas and the response to ultrapure air. This was done by running ultrapure air through the analyzer before and after the calibration gas. The automated calibration system ran the ultrapure air standard, then ran two or three calibration standards, then the ultrapure air standard, then two or three calibration standards, then the ultrapure air standard, etc. until all calibrations were completed. The ultrapure air signal corresponding to each calibration was then determined by linearly interpolating between the bracketing ultrapure air standards. This was subtracted from the response to the calibration standard to determine the analyzer response due to the SF₆ present in the standard.

Operators typically ran two or three calibration sets during an IOP. The responses from all runs of the same calibration standard were averaged together. Sample concentrations were then determined by interpolating between these averages. In cases where sensitivity drift was a

problem, concentrations were determined using only calibrations that were run close to the same time as the measurements.

MLOD/MLOQ

Two quantities that are useful for evaluating instrument performance are the method limit of detection (MLOD) and the method limit of quantitation (MLOQ). The MLOD is the lowest concentration level that can be determined to be statistically different from a blank or a 0 pptv SF₆ sample (Keith et. al. 1983). The MLOQ is typically defined to be the level at which the concentration may be determined with an accuracy of $\pm 30\%$. The recommended values for these are 3σ for MLOD and 10σ for MLOQ, where σ is the standard deviation for measurements made on blanks or low concentration standards (Keith et. al. 1983). The MLOD differs from the instrument limit of detection (ILOD) in that it includes all variability introduced by the sampling method. MLOD/MLOQ are used in this report because they are calculated from the variability observed during actual sampling operations.

Since the analyzer was measuring continuously, every point may be viewed as a measurement of a blank so long as it was sampling clean air. The standard deviation of the baseline signal then estimates σ . Ideally, this standard deviation should be calculated during actual sampling conditions; i.e. in the vehicle parked on the sampling grid.

A second method of determining the MLOD and MLOQ is to calculate the standard deviation of the instrument's response to a calibration gas. This deviation may then be used as σ in the MLOD/MLOQ calculations.

Both methods were used for the real-time analyzers. After data collection for an IOP was completed, the data analyst followed a written procedure and calculated each instrument's MLOD and MLOQ from the baseline noise and from the variation of instrument response to each calibration gas used during the testing. The procedure called for comparing the MLOD from the lowest concentration calibration with a signal to noise ratio between 3 and 10 with the MLOD from the baseline calculation. The larger of these two values was generally selected as the instrument MLOD for that IOP. However, other factors such as the number of calibrations available for the calibration variation calculation, consistency of the calculated numbers from different calibration concentrations, instrument response to low concentrations of tracer, and availability of good calibrations in the MLOD range were also considered. In some cases, adjustments were made or another value selected. Every effort was made to ensure that the selected MLOD accurately represented instrument performance. However, the procedure was designed to favor higher MLOD estimates since an overestimate is preferable to an underestimate. Setting the MLOD too low allows some data to be flagged as valid when it should not be and is unacceptable by FRD standards. The MLOD/MLOQs for each instrument and each IOP are listed in Table 15.

Table 15. Method Limit of Detection (MLOD) and Method Limit of Quantitation (MLOQ) for fast response analyzers.

		Analyzer A	Analyzer B	Analyzer C	Analyzer D
IOP 1	MLOD	15.2	7.7	7.0	9.4
	MLOQ	45.4	25.7	23.4	31.4
IOP 2	MLOD	15.3	9.4	7.2	8.9
	MLOQ	51.0	31.3	23.9	29.6
IOP 3	MLOD	12.8	10.0	10.4	na*
	MLOQ	42.6	33.3	34.8	na*
IOP 4	MLOD	11.0	8.9	11.0	10.2
	MLOQ	36.7	29.6	36.6	34.0
IOP 5	MLOD	10.5	8.7	30.5	7.8
	MLOQ	35.1	28.9	101.5	26.1
IOP 6	MLOD	7.3	5.3	28.7	4.7
	MLOQ	24.3	17.6	95.7	15.7
IOP 7	MLOD	6.6	10.2	53.0	8.7
	MLOQ	22.0	34.0	177.0	29.1
IOP 8	MLOD	7.1	9.0	44.0	2.5
	MLOQ	23.7	30.0	147.0	8.3

* no tracer was detected, so MLOD/MLOQ values were not set.

Quality Control (QC)

The quality control (QC) procedure for the real-time analyzers included 12 steps that ensure the real-time analyzer data was as reliable as possible. During field operations, operators were required to follow written checklists that included all QC steps. A written procedure was also followed during post-IOP processing. The QC steps were:

1. Pre-project preparation.
2. Monitoring of key operational parameters during the study.
3. Daily instrument calibrations.
4. Real-time monitoring of QC parameters during testing.
5. Operator logging of all measurements.
6. Post-IOP screening of calibrations.
7. Post-IOP determination of MLOD/MLOQ.

8. Post-IOP screening of data.
9. Verification of all calculations and data by a second analyst.
10. Identification of data problems and setting of QC flags.
11. Verification and conversion of position information.
12. Creation and review of final data files.

1. Pre-project preparation.

Before the experiment, each analyzer was thoroughly tested to be sure that all systems were in good working order. Any necessary repairs were made. The analyzers were then conditioned by running them for several weeks, which was required for optimum performance. During this period, each one was adjusted to provide the best response to the range of concentrations expected during the study.

Operator training occurred the week before field deployment. Dedicated binders were prepared for each analyzer that contained all procedures, phone numbers, safety and Nuclear Regulatory Commission (NRC) requirements. All operators were trained on the operation of the analyzers, including troubleshooting and data handling. They were each required to complete hands-on training plus attend a training class at the FRD office in Idaho Falls, ID.

2. Monitoring of key operational parameters.

Analyzer operators were expected to follow a standard operating checklist (Fig. 47) which included operating and QC instructions. The checklist instructed them to fill out a Settings Record as they ran the real-time analyzers (Fig. 48). They recorded 17 instrument parameters at key times during the operation. These included gas pressures, flow rates, analyzer component temperatures, electrometer settings, etc. The Settings Record, constructed in table form, contained several days of entries. These sheets were reviewed for any large changes in the parameters that could indicate a problem with the analyzer. Any changes were investigated and the required maintenance was performed. Each analyzer operator also maintained a dedicated logbook during each IOP and recorded the measured SF₆, location of the analyzer, and any problems with the analyzer. Analyzers were run between IOPs to ensure optimum instrument performance.

TGA-4000 Operating Checklist		Aug 27, 2013
Initial Setup		
___	Check gas and electrical connections	
___	Remove caps from EX. 1 (Dryer-pump) & EX. 2 (Detector)	
___	Remove cover from sample inlet AND make sure inlet is properly connected to the TGA.	
___	Verify that the sample valve is in Nitrogen position	
___	Turn on Nitrogen tank and record primary pressure on Settings Record	
___	Turn Dryer Nitrogen on (yellow valve on back of TGA)	
___	Use large flowmeter to verify that Nitrogen flows are within these ranges. If they are not, set Nitrogen flows by adjusting regulator pressure (Do NOT exceed 40 psi!)	
	EX. 1 (Dryer-Pump): >140 on large flowmeter (but NOT against the top stop)	
___	EX. 2 (Detector): 15 to 60 on large flowmeter__ Record Nitrogen delivery pressure and flows on Settings Record	
___	Disconnect flowmeter!	
Detector Cleaning	(If the detector was cleaned less than 18 hours ago AND it has been purged continuously with Nitrogen since the cleaning, skip cleaning)	
___	Verify that sample valve is in Nitrogen position and methanol bottle is not empty	
___	Attach capture bottle to EX.2 (Detector) and note the level of methanol in the bottle	
___	Turn black valve to METHANOL FLUSH (back of TGA)	
___	Wait until 25 to 30cc of methanol flow into the capture bottle (about 2 minutes)	
___	Turn black valve to NITROGEN SYSTEM	
___	After 1 to 2 minutes, remove capture bottle and dispose of waste methanol	
Startup		
___	Main power on	
___	Dryer on	
___	Pump on	
___	Verify that the red Hydrogen valve is off	
___	Turn on Hydrogen tank and record primary pressure on Settings Record	
___	Wait for DTEMP to reach 80 °C	
___	Turn on the red Hydrogen valve and observe reactor temperature (RTEMP) increase	
___	Record Hydrogen delivery pressure on Settings Record (must be <40 psi ; usually 30-35 psi)	
___	Insert Compact Flash card and power on data system	
___	If GPS is not installed, check and set date and time.	
___	Wait for RTEMP to reach operating levels (190-210 °C) DO NOT EXCEED 220 °C!	
___	Wait for signal to stabilize	
___	Switch sample valve to sample position	
___	Wait for signal to stabilize	
___	Determine O ₂ break through by reducing H ₂ controller SLOWLY. (instructions in binder)	
___	Increase H ₂ two units above break through; record sample and H ₂ settings on Settings Record	
___	Wait for signal to stabilize	
___	Adjust signal to about 0 volts with the lower potentiometer and record zero, gain, period, and RTEMP on Settings Record	
Calibration (Dilution system must be OFF!)		
___	Connect the cal module to a calibration box and verify that the bags are not empty	
___	Check the connections on the cal module electrical cable	
___	Wait for 2 minutes of stable base line	
___	Use the Cal Bag switches to select desired bags (usually all), then press "Cal Start"	
___	Verify that each bag runs properly - pressing "Cal Start" again will stop cal's if there is a problem	
___	Record calibration slope on Settings Record	
___	Wait for baseline to stabilize, then press "Calculate LOD" on status screen and record LOD on the Settings Record	
___	Record recoveries from status screen Cal List in notebook (skip for 1st cal set)	
Dilution Setup	(Skip this section if you do not have a dilution system)	
___	Turn on Ultrapure Air tank and record pressures on Settings Record (delivery should be <20psi; typically 10 psi)	
___	Remove rain cup from the inlet and attach the small flowmeter	
___	Carefully observe flow rate	
___	Open dilution valve and adjust dilution controller until the flowmeter shows ½ of original flow rate. Be as accurate as possible!	
___	Disconnect flowmeter and replace rain cup	
___	Verify that the dilution light is on and the display indicates that dilution is on	
___	Close dilution valve and record controller setting on Settings Record	
Operation Notes	During operation try to:	
•	Tape inlet on co-located sampler with rain cup near sampler inlets.	
•	Keep vehicle temperature as constant as possible.	
•	Do calibrations before and after each test and every few hours if test schedule permits.	
•	Use the dilution system when needed. Check dilution flow rates every few hours if possible.	
•	Switch to Nitrogen position while fueling vehicle, if you suspect outside air is heavily contaminated, or if there are any problems of any kind.	
•	Turn Reactor on to stabilize RTEMP if it drifts out of allowable range.	
•	Write everything in the notebook.	
•	Mark all peaks on the display.	
Shutdown		
___	Switch sample valve to Nitrogen position	
___	Turn off the red Hydrogen valve and the Hydrogen tank	
___	Reactor off	
___	After about 1 minute, turn off data system. Compact Flash card may now be removed.	
___	Record Nitrogen and Hydrogen pressures on Settings Record (Use a second line)	
___	Turn off dilution valve and Ultrapure air tank	
___	Wait until RTEMP is <100 °C	
___	Dryer off	
___	Pump off	
___	Main power off	
___	Dryer Nitrogen off (yellow valve on back of TGA)	
___	Cap EX. 1 (Dryer-Pump) and put inlet cover on sample inlet or plug TGA inlet	
___	Clean detector (no exceptions!) (follow instructions for Detector Cleaning above)	
___	If TGA will be used within 18 hours, leave Nitrogen flowing through the detector at a reduced rate of ¼ to ½ of normal to conserve Nitrogen.	
___	If TGA will not be used within 18 hours, then turn off Nitrogen at tank and cap EX. 2	
___	Give Compact Flash card and copies of notebook pages to data processor	

Figure 47. Operating checklist for fast response analyzers.

TGA-4000 Settings Record

TGA number: 7 Cal Module: _____ Sep. 2008

date	time	N ₂ primary	N ₂ delivery	EX.1 flow	EX.2 flow	H ₂ primary	H ₂ delivery	sample controller	H ₂ controller	zero	gain	period	RTEMP	cal slope	LOD	Air primary	Air delivery	dilution controller
9/27	9:25	1400	15	145	77	1580	38	142	67	173	8	0	195			1740	7	
		1210	15			1580												
9/30	10:50	1210	16			1570	36	144	66	172	8	0	199					
		1250	1150			1510	32											
10/2	8:30	1100	16					145	75									
10/3	12:53	1100	15	145	73	1500	35	144	66	172	8	0	193	1422	11ppt	1800	12	49.5
10/3	18:00	900	14			1450	35											
10/4	11:00	800	14	143	66	1320	36	140	65.5	176	8	0	202					
		1530	650	14		1300	37											
10/5	7:07	1800	16	145	75	1300	35	140	67	177	8	0	207	1288	8ppt	1740	14	51
10/5	16:27	1600	16			1100	35											
10/7/13	11:39	1480	14	145	75	1080	36	140	66	176	8	0	205	1397	11ppt	1600	10	48.5
10-9-12	10:23	1100	14	142	62	870	36	138	67	168	8	0	198					
		1350	Adjusted Sample back to 440. RT5 MP had dropped to 190															
		1443	920			870												

Figure 48. An example of a fast response analyzer Settings Record.

3. Daily instrument calibrations.

All analyzers were calibrated at the beginning and end of each IOP. If time permitted, multiple calibrations were run before the IOP started. These helped identify response drift and were used in MLOD/MLOQ calculations.

4. Real-time monitoring of QC parameters during testing.

After the first set of calibrations was completed, the calibration curve was checked every time additional calibrations were performed. This was done by treating the new calibrations as unknowns and calculating their concentration based on the calibration curve generated from the first set of calibrations. The results were recorded and examined for possible problems. The analyzer also calculated and displayed an MLOD from the baseline noise. Operators were required to display and record this value after every set of calibrations. If large variations in MLOD or calibration recoveries were observed, the cause was investigated and corrected.

5. Operator logging of all measurements.

To help ensure that noise spikes, analyzer adjustments, and extraneous features were not reported as valid measurements, operators were required to mark all SF₆ peaks on the computer using the software marking function. They also recorded details of each peak, e.g., time, concentration, location, together with other pertinent observations in a notebook. Any signals that could be mistaken for SF₆ were also recorded in the notebooks.

6. Post-IOP screening of calibrations.

After an IOP was completed, the analyzer operators delivered their logbook and a CompactFlash™ card containing all data for the IOP to the data analyst. The entire data file including the calibrations was then carefully reviewed by the data analyst. To ensure that concentration calculations were as accurate as possible, any calibration points with problems such as significant baseline drift, contamination, accidental instrument adjustments, etc., were identified and eliminated. The recovery for each calibration was calculated and examined. This was done by treating the calibration as an unknown and calculating the concentration using the calibration curve. The recovery was defined as the calculated concentration divided by the actual concentration converted to a percent. The recoveries for all calibrations above the MLOQ were expected to be between 80% and 120%. If they were not, they were re-examined for problems and the logbook entries were reviewed. In cases where the calibrations showed evidence of significant sensitivity drift during the IOP, the calibrations could be divided into several groups, typically an “early” group and a “late” group. Each group was used to calculate concentrations for peaks within the time frame they encompassed. If the calibrations still failed to meet the recovery limits, all data in the concentration ranges that were out-of-limits were flagged as estimates.

7. Post-IOP determination of MLOD/MLOQ.

The MLOD and MLOQ were determined for each analyzer for each day's operation. These values define the lower limit of valid measurements. Concentrations below these levels are flagged with appropriate QC flags so users of the data are aware of its limitations. The MLOD and MLOQ were calculated by two methods: calculations based on the baseline noise and calculations based on the variation in response to calibrations of the same concentration. The data analyst then compared these two calculations and selected the instrument MLOD/MLOQ following the guidelines in a written FRD procedure. Typically, the value calculated from the lowest concentration calibration with a signal to noise ratio in the 3 to 10 range was compared to the value calculated from the baseline noise and the larger of the two selected. However, other factors such as number of calibrations available, instrument problems, behavior on other calibration levels, instrument response to low tracer concentrations, etc. were considered in the selection. A more complete discussion of this calculation was included in a previous section of this chapter.

8. Post-IOP screening of data.

After an IOP, the data analyst reviewed the peaks marked by the operators and compared them with the notebook log to ensure that marked peaks were above the MLOD and that they were not false peaks caused by extraneous factors such as altitude changes, bumps, interfering chemicals in the air, etc. The peaks were checked for correct identification of instrument baseline on leading and trailing sides of each peak. (Note that the baseline was always subtracted off of the peak, so the measurements are **above background** concentrations. The programmable bag samplers measure the total concentration which includes the background.) The entire data set was examined for possible peaks that may have been missed. Once necessary corrections were made, the peaks were converted to concentrations, plotted and reviewed.

9. Verification of all calculations and data by a second analyst.

During steps 5 through 8, the data analyst generated a QC sheet (Fig. 49), plots of the calibrations curves, results from the MLOD/MLOQ calculations, and plots of all peaks. The QC sheet was annotated with notes explaining problems that were identified, corrective actions taken, and justification for all data processing decisions that were made by the analyst. A second person familiar with the data processing procedures reviewed and verified this entire data package. If any errors were discovered or if the verifier did not agree with the decisions made, the problems were discussed with the data analyst and a resolution agreed on and implemented.

10. Identification of data problems and setting of QC flags.

The operator logbooks and concentration plots were carefully reviewed for any anomalies that required QC flags to be set. The review focused specifically on instrument over range, dilution system usage that was not detected, and starting or stopping of the dilution system during a peak. Any other problems were also noted. From this review, a list of flags that needed to be set was generated. These were combined with the data during the generation of final data files.

11. Verification and conversion of position information.

During IOPs 1-4, the analyzers were co-located with a bag sampler. The location number of this bag sampler was recorded by the operator. The known latitude and longitude of the sampler location were inserted in the final file. For IOPs 5-8, it was anticipated that the analyzers would move more frequently, so they were equipped with GPS units. The GPS latitude and longitude were included without modification in the final files. Gaps in the GPS positions were filled in using sampler locations recorded by the operators where possible.

12. Creation and review of final data files.

Final data files were generated in a three step process. First, the software used to review the data and generate the QC sheets was used to create a data file for each analyzer on each IOP. This software automatically adds most of the quality flags. Then, additional flags identified in

NOAA ARLFRD TGA-4000 Quality Control Sheet

Try 1, Final

version: v07-2.1
file: .\T0091310.05A
TGA: 9
start time = 5-Oct-13 09:02:06

operator: S. Beard

data analyst: R. Carter

verified by: D. Finn

analysis date: 30 Oct 2013

verify date: 7 Mar 2014

	analyst	verifier
All calibration recoveries are within +/-20%	<u>yes</u> no	<u>yes</u> no
LOQ < 150 ppt	<u>yes</u> no	<u>yes</u> no
RMS error (as percent of range center) < 10%	<u>yes</u> no	<u>yes</u> no
Data is usable as is	<u>yes</u> no	<u>yes</u> no
IF data is not usable as is, it could be		
usable with corrective actions noted below	yes no	yes no

All < 41.3 should be Flagged.

limit of detection (LOD) = 12.5 ppt
limit of quantitation (LOQ) = 41.3 ppt
(LOD/LOQ calculated from baseline variations.)

Center Ocal should be Flagged.

Calibrations recalculated as unknowns:

(UHP air (0.0) results are "change since previous 0.0")

cal	true	result	%recovery	result	%recovery
#	value	using 1st	using 1st	using all	using all
		cal set	cal set	cals ave.	cals ave.
0	0.0	-0.0		-0.0	
1	35.1	35.1	100.0	34.7	98.9
2	504.0	504.0	100.0	515.2	102.2
3	0.0	-16.7		-16.5	
4	1550.0	1550.0	100.0	1594.7	102.9
5	3110.0	3110.0	100.0	3198.1	102.8
6	0.0	-81.1		-80.3	
7	5220.0	5220.0	100.0	5404.4	103.5
8	8300.0	8300.0	100.0	8293.0	99.9
9	9730.0	9730.0	100.0	9584.8	98.5
10	0.0	-276.3		-273.3	
11	0.0	-103.4		-102.2	
12	0.0	-9.8		-9.7	
13	35.1	35.8	102.0	35.5	101.0
14	504.0	482.9	95.8	493.2	97.9
15	0.0	5.7		5.7	
16	1550.0	1467.8	94.7	1507.7	97.3
17	3110.0	2899.7	93.2	3000.5	96.5
18	0.0	-55.9		-55.3	
19	5220.0	5001.1	95.8	5109.4	97.9
20	8300.0	8324.1	100.3	8310.9	100.1
21	9730.0	10050.4	103.3	9875.2	101.5
22	0.0	-192.7		-190.6	

Calibration curve errors (for all calibrations averaged):

	RMS error	percent of range center
all cals	96.75 ppt	2.0%
< 2330	31.77 ppt	2.7%
> 2330	134.35 ppt	2.2%

comments/corrective actions:

Figure 49. Example of a fast response analyzer QC sheet.

step 10 were added to these files. Finally, a custom computer program was used to insert latitudes and longitudes and re-format the files into their final form.

After the final data files were created, they were carefully reviewed for any problems. Each of the data files were read into a spreadsheet and the concentration and flags plotted versus time. The concentrations were compared to the earlier peak plots to verify that all the peaks were included at the correct time. The QC flags were checked visually by plotting and by computer programs that listed start and stop times for each flag and the range of concentrations for each flag. These lists were then compared with the lists generated earlier in the QC process. Any problems were fixed and the files regenerated using the updated information. The process was repeated until no discrepancies were found.

METEOROLOGICAL MEASUREMENTS

An extensive array of meteorological instrumentation was used to measure the boundary layer in the Project Sagebrush study area during PSB2. Most of it was provided by ARLFRD but it included contributions from WSULAR. The primary tall tower designated GRI is 62.3 m in height. Other site designations are:

COC – 30.5 m command center meteorological tower located within the tracer sampling array at approximately 499 m, 60° azimuth

ASC – permanent Atmospheric Systems Corp. sodar on the 800 m arc

ART – mobile Atmospheric Research & Technology sodar near TOW on 3200 m arc

PRO – permanent radar wind profiler plus RASS on the 800 m arc

G2 – NOAA sonic anemometer at 30 m on GRI

EC1 – WSULAR eddy correlation station at 400 m, 25° azimuth

EC2 – WSULAR eddy correlation station at 400 m, 85° azimuth

ST1 – WSULAR sonic anemometer at 800 m, 25° azimuth

ST2 – WSULAR sonic anemometer at 800 m, 277° azimuth

ST3 – WSULAR sonic anemometer at 400 m, 150° azimuth

FLX – NOAA flux station, within tracer sampling array about 900 m NE of release point

CEIL – Ceilometer at approximately 400 m, 54° azimuth

Table 16 provides a listing of the meteorological instruments used during PSB2. The locations of the instrumentation are shown on Figs. 2-5. Data from the NOAA/INL Mesonet stations are included in the PSB2 database in addition to measurements from the instrumentation listed in Table 16. Quality control procedures are described for each instrument as well as the formats of their respective data files.

Grid 3 Tower (GRI)

GRI was of particular significance due to its close proximity to the tracer dispersion grid and the extensive suite of meteorological measurements that were made there (Table 16). This tower is located approximately 200 m southwest of the test area release location (Figs. 2 and 5). Figure 50 is a schematic representation of the instrumentation on the Grid 3 tower. The GRI tower (Figs. 4, 50) has been collecting measurements since the early 1960s. The tower provided important data about the overall meteorological conditions during the project. Of particular importance are the vertical profiles of wind, temperature, and turbulence it afforded. The permanent NOAA INL Mesonet cup anemometer and wind vane measurements and the temperature measurements were mounted on booms extending at 155 degrees from GRI. The array of sonic anemometers deployed on GRI during PSB2 was mounted on booms extending a uniform distance from the tower at 335 degrees.

Table 16. Meteorological instrumentation used during PSB2.

Type	Instrument		Location		
	Make	Model	Arc Distance	Arc Angle	Height (m)
<u>Grid 3 Tower (GRI) [43.5897N, 112.939933W]</u>			200 m	235 deg	62.3 m
Wind Speed	Met One Inc.	010C			2, 9.96, 15.31, 45.1, 60.05 m
Wind Direction	Met One Inc.	020C			2, 9.96, 15.31, 45.1, 60.05 m
Air Temperature/RH	Vaisala	HMP45C			1.47 m
Air Temperature Aspirated	Met One Inc.	076B			10.7, 14.9, 45, 59.6 m
Solar Radiation	LI-COR	LI200X			60.35 m
Barometric Pressure	Setra Systems	270			1.75 m
Rain Gauge	Friez Engineering	7405H			1 m
Data Logger	Campbell Scientific	CR23X			
3d Sonic Anemometer (R2)	R.M. Young	Ultrasonic 81000			2 m
3d Sonic Anemometer (R9)	R.M. Young	Ultrasonic 81000			3.7 m
3d Sonic Anemometer (R1)	R.M. Young	Ultrasonic 81000			9 m
3d Sonic Anemometer (R3)	R.M. Young	Ultrasonic 81000			16.5 m
3d Sonic Anemometer (R6)	R.M. Young	Ultrasonic 81000			30 m
3d Sonic Anemometer (R5)	R.M. Young	Ultrasonic 81000			60 m
Soil Moisture/ Temperature	Stevens	Hydra Probe II			5, 10, 20, 50, 100 cm
<u>100 Foot Tower (COC) [43.593N, 112.933W]</u>			499	60	
Wind Speed	Met One Inc.	010C			2, 10, 30 m
Wind Direction	Met One Inc.	020C			2, 10, 30 m
Data Logger	Campbell Scientific	CR23X			
<u>Horizontal Sonic Array (EC1, EC, ST1, ST2, ST3 deployed IOPs 5-8 only)</u>					
3d Sonic Anemometer (G2)	Gill	Windmaster Pro	1000	150	3.1 m
<u>[43.58283N, 112.931306W]</u>					
3d Sonic Anemometer [EC1]	Campbell Scientific	CSAT3B	400	25	2.97 m
<u>[43.59403N, 112.935778W]</u>					
IRGA (close path)	LICOR	LI-7200			2.97 m
Net Radiation	Kipp & Zonen	CNR4			2.7 m
Air Temperature/RH (x2)	Rotronic	HC2S3			1.5, 2.97 m
Rain Gauge	Texas Electronics	TE525			1.5 m
Soil Surface Temperature	Apogee	SI-111			2.1m
Soil Heat Flux Plates (x2)	Hukseflux	HFP01			5 cm
Soil Temperature (x2)	Campbell Scientific	109SS			2.5, 5 cm
Soil Moisture	Campbell Scientific	CS616			2.5 cm
Data Logger	Campbell Scientific	CR3000			
3d Sonic Anemometer [EC2]	Campbell Scientific	CSAT3	400	85	3.14 m
<u>[43.59108N, 112.932889W]</u>					
IRGA (open path)	LICOR	LI-7500A			3.14m
Net Radiation	Kipp & Zonen	CNR2			2.9 m
Air Temperature/RH (x2)	Rotronic	HC2S3			1.6, 3.14 m
Soil Heat Flux Plates (x2)	Hukseflux	HFP01			5 cm
Soil Temperature (x2)	Campbell Scientific	109SS			2.5, 5 cm
Soil Moisture	Campbell Scientific	CS616			2.5 cm
Data Logger	Campbell Scientific	CR5000			

Table 16 continued. Meteorological instrumentation used during PSB2.

Type	Instrument		Location		
	Make	Model	Arc Distance	Arc Angle	Height (m)
3d Sonic Anemometer [ST1] [43.597306N, 112.933722W]	Campbell Scientific	CSAT3B	800	25	3.0 m
Air Temperature/RH Data Logger	Rotronic Campbell Scientific	HC2S3 CR6			3.0 m
3d Sonic Anemometer [ST2] [43.587396N, 112.935306W]	Campbell Scientific	CSAT3B	400	150	3.05
Air Temperature/RH Data Logger	Rotronic Campbell Scientific	HC2S3 CR6			3.05 m
3d Sonic Anemometer [ST3] [43.591639N, 112.945278W]	Campbell Scientific	CSAT3	800	277	2.89 m
Air Temperature/RH Data Logger	Rotronic Campbell Scientific	HC2S3 CR5000			2.89 m
Remote Sensors					
Radar Wind Profiler (PRO) [43.59473N, 112.9293W]	Radian	LAP-3000	828	~56	
RASS [43.59473N, 112.9293W]	Radian	LAP-3000	828	~56	
SoDAR (ASC) [43.59443N, 112.9292W]	ASC	4000	816	~57	
Radiosonde releases	GRAW Radiosondes		~400	~55	
Ceilometer [43.591278N, 112.9368236W]	Vaisala	CL31	~400	~54	
Flux Station (FLX) [43.59586N, 112.9288W]			916	51	
Net Radiometer	Kipp & Zonen	NR-LITE-L			2.5 m
Air Temperature/RH	Visalia	HMP45C			1.5 m
Barometric Pressure	Visalia	PTB101B			1 m
Solar Radiation	LI-COR	LI200X-L			2.5 m
3d Sonic Anemometer	Gill	1210R3			3.2 m
IRGA (open path)	LI-COR	LI7500			2.54 m
Soil Temperature	Campbell Scientific	TCAV-L			2, 6 cm
Soil Moisture	Campbell Scientific	CS616			2.5 cm
Soil Heat Flux Plates (x4)	Hukseflux	HFP01SC			8 cm

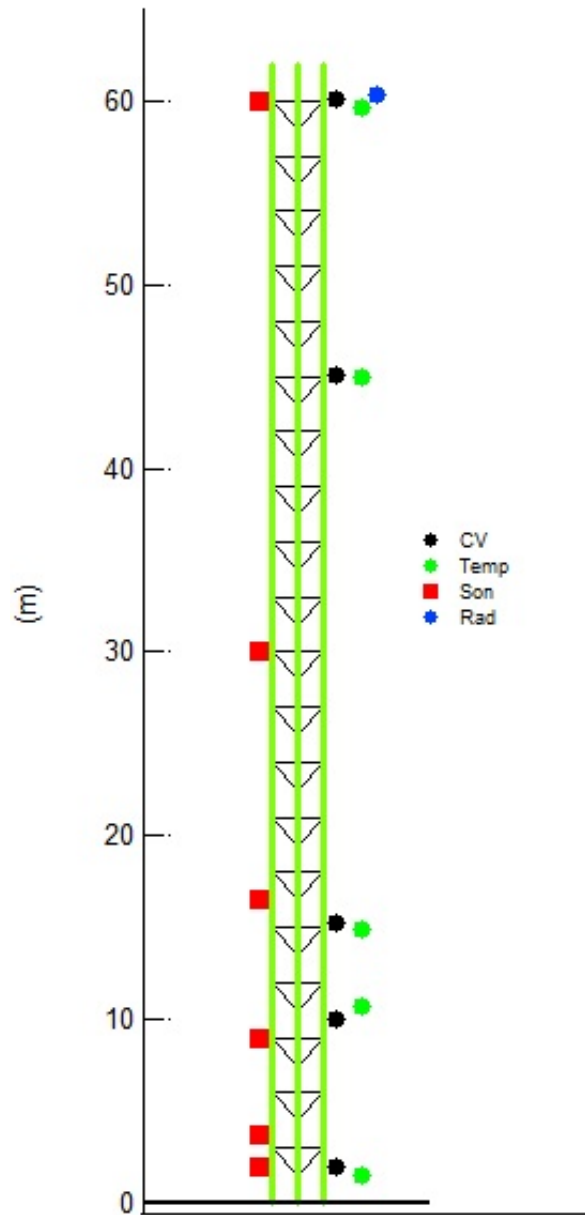


Figure 50. Schematic representation of the 62 m Grid 3 tower instrumentation. All anemometers mounted transverse to the prevailing winds on booms extending from the tower. Barometric pressure, rain gauge, and soil heat flux not shown. CV represents cups and vanes, Temp is temperature/humidity, Son is 3-D sonic anemometer, and Rad is solar radiation.

NOAA ARLFRD

Sonic Anemometers

Experimental Setup

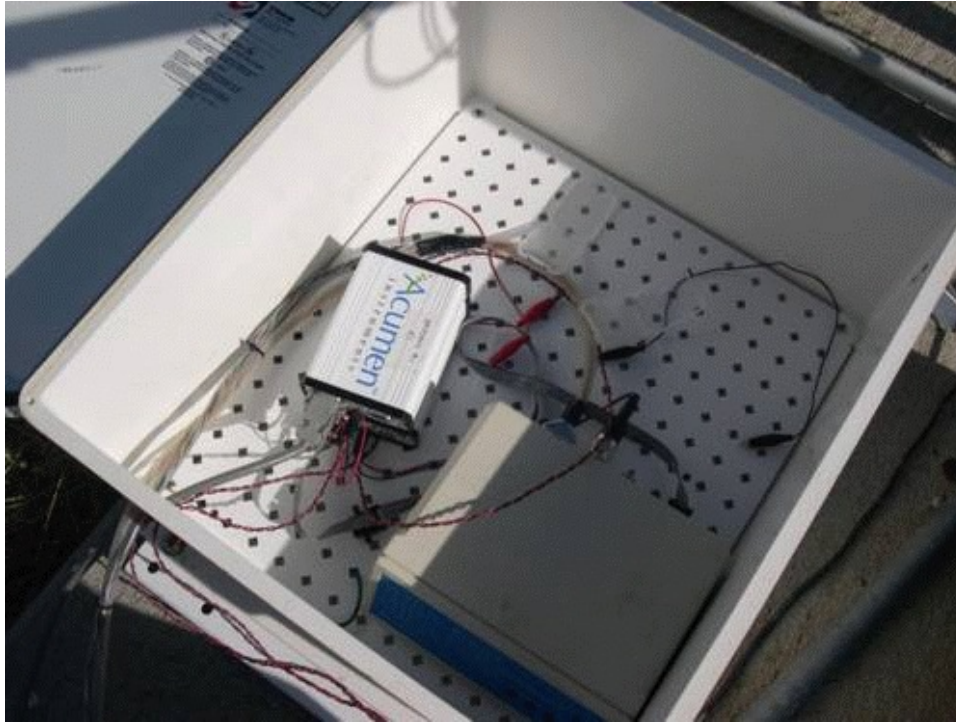
Sonic anemometers were deployed during the study to measure the turbulence field driving the tracer dispersion in the horizontal and vertical. The sonics measured the turbulence by taking high frequency (10 Hz) measurements of the 3-d wind field and temperature (u , v , w , t). A 3-d sonic anemometer “sample” consisted of transmitting sound back and forth across the measurement volume of the anemometer. The delay between transmission and receipt of a sound pulse in both directions along the 3 axes of the anemometer yields wind speed and direction in 3 dimensions. Virtual temperature was also derived from the speed of sound across the sonic sampling volume.

For measurements of the vertical turbulence profile on GRI, ARLFRD deployed six 3-d sonic anemometers during the study. These were R. M. Young Model 81000 Ultrasonic anemometers installed at 2, 3.7, 9, 16.5, 30, and 60 m agl. The 2 and 3.7 m sonics were mounted on tripods near the tower. The sonics from 9 m agl upwards were mounted on booms extending the same distance from the tower on a 335° azimuth. Power was supplied to the sonics and all other instrumentation on GRI by gel cell batteries. The batteries on GRI were continuously charged by AC line power. One Gill Windmaster Pro sonic anemometer (G2) was installed on a tripod at 3.1 m agl on the 1000 m arc at 150° azimuth. A close up picture of a Windmaster Pro and an Ultrasonic 81000 sonic anemometer can be seen in Fig. 51.

The ARLFRD sonic data were continuously recorded for the duration of the experimental period at 10 Hz on a compact flash card inserted into an Acumen Serial Data Collection Bridge (Fig. 52). The data bridge was configured manually with a laptop computer with the sonic



Figure 51. A closeup picture of an R. M. Young Ultrasonic 81000 (left) and a Gill Windmaster Pro (right) used during PSB2.



designation at the start of its filename (e.g., R1, G2). A GPS unit was also used to verify, and synchronize if needed, the correct time in the data bridge. The sonic data were recorded in an ASCII text file. The compact flash cards were gathered and returned to ARLFRD for processing and data archival at regular intervals during the experimental period.

Figure 52. An Acumen data collection bridge (white device inside box) is used to collect data from the sonic anemometers.

Quality Control

Once the flash cards were returned to ARLFRD, the data was uploaded onto the network for processing. The 10 Hz data was parsed into both 10-minute and 30-minute files containing nominally 6000 and 18,000 observations, respectively, for the entire PSB2 experimental period. Means, variances, covariances, and other calculations were made on these 10 and 30-min data files.

The 10-min averaging time was selected to match with the 10-min averaging period of the SF₆ tracer sampling period. The longer 30-min averaging period included for some of the measurements in the database better accounts for nonstationarity effects in the flow and provides a more robust statistical measurement of the turbulent fluxes. If necessary, the data was rotated into the correct meteorological coordinate system prior to processing (60 degrees, Gill sonic anemometer only).

Data collected from the seven ARLFRD sonic anemometers were subjected to a comprehensive quality control and processing software package based upon the schemes detailed in Vickers and Mahrt (1997). That package included spike detection, 2-coordinate rotation to zero out the mean vertical and crosswind wind speeds and calculate the streamwise mean wind, range checks, amplitude resolution tests, dropout tests, Haar transform stationarity (discontinuity) tests, checks for excessive skewness and kurtosis, tests for relative systematic flux sampling error (RSET), tests for random flux sampling error (RFET), tests for flux

variations associated with mesoscale motions (RNT), and tests for alongwind relative nonstationarity (RNU), crosswind relative nonstationarity (RNV), and vector wind relative nonstationarity (RNS).

The most common problem with sonic anemometer measurements is spiking in which large, random, very brief, and infrequent electronic signal noise is recorded. Spikes were detected based upon the criteria of Vickers and Mahrt (1997), with slight modification. This entailed identifying 3 or less consecutive points exceeding the mean \pm a multiple of the standard deviation for a 5-min (3000 point) moving average. The thresholds used were 4.0 standard deviations for u , v , w , and t . For w , the standard deviation threshold was adjusted to 4.5 if it was nighttime with temperatures below freezing. This was done to account for nocturnal periods often characterized by low and very intermittent turbulence. Spikes were replaced recursively by the mean of the nearest non-spike values on either side of the spike. The spike replacement routine was repeated for up to 11 passes through the record or until no spikes were detected. The threshold increased by 0.1 with each pass. The quality control data files provide information on both the total number of passes through the record and the cumulative number of spikes detected in all passes. If the total number of spikes detected for any channel exceeded 0.5% of the total record on any pass, the record was flagged accordingly. Final calculations were done using the despiked output files. These calculations included both the uncorrected and corrected mean and flux quantities as well as a suite of quality control parameters.

The resulting despiked sonic anemometer data sets were plotted and reviewed by the data analyst for consistency and accuracy by comparing results with other measurements for the duration of each IOP plus one hour before and after each IOP. This included the following comparisons:

- Time series comparisons in the horizontal between all wind speed and direction measurements in the study area, where available, at 2 m; at 10 m; at 15 m; at 30 m; at 45 m; and at 60 m. These comparisons included the sonic anemometers, cup anemometer and wind vanes at GRI and COC, and the ASC sodar. Heights were compared if they were close. For example, 2 m cup and vane results at GRI and COC were compared with sonic results at 3 m (e.g., G2, EC1) and 40 m results for the ASC sodar were compared to 45 m anemometer results at GRI.
- Vertical profile comparisons between sonic anemometer measurements and cup anemometer and wind vane measurements on GRI.

The cup anemometers and wind vanes on GRI were calibrated to rigorous standards. Like the other meteorological towers in the NOAA/INL Mesonet, a detailed and comprehensive data quality assurance program is performed on GRI on a routine basis. The instrumentation, quality control, calibration, and maintenance procedures at GRI meet the generally accepted requirements and guidelines set out in DOE (2004, 2005), ANSI/ANS-3.11 (2015), and ANSI/ANS-3.2 (2006). To help follow these guidelines, the quality assurance program uses an excellent set of software tools to display trended meteorological data. This enhances the data

quality evaluations and makes them more efficient. The quality control program consisted of both manual and automated processes. Every 5 min period for each parameter was plotted for missing or spiked data. Data were also screened for electronic noise, non-working aspirators that affect air temperature and relative humidity values, orientation errors in the wind direction, stalled wind sensors, rime icing that degrade wind speeds, and other erroneous values caused by maintenance, bird droppings, etc. Plotting the data allows the meteorologist to identify and flag any of the problems in the database and, if needed, a technician is notified to quickly fix the problem. Calibrations of all instrumentation are completed on a semi-annual basis.

The results for these comparisons are included in sets of graphs in each IOP summary (see Summary of Individual IOPs section).

The plots of the new data sets were reviewed and verified by a second analyst. If any problems or errors were discovered, the two analysts had to agree upon and implement a resolution. An error in the G2 sonic anemometer was identified and corrected between IOPs 2 and 3. It was found that the G2 Acumen had been initially programmed in MDT whereas all the other instrumentation was in MST. Wind speeds at the 2, 10, and 30 m heights for COC were also found to be anomalously high in the initial review for IOP4. It was found that the maximum 5-minute gusts instead of the mean 5-minute wind speeds had been incorporated into the review plots for that IOP. This was corrected and then good agreement was found. No other problems or errors were discovered in the measurements of wind speed and direction in any of the anemometer data sets. The protocols used to generate the data sets described below were derived from Vickers and Mahrt (1997).

Data File Formats

There are 7 ARLFRD files containing 10-min average processed data, six for the sonic anemometers on GRI and one for the G2 sonic for each IOP. The data files are summaries of the measurements and calculated quantities for each 24 h period encompassing an IOP test. Each file is in CSV format. The data filenames are specified as 'PSB2data_FRD_IOPx_XX_yy_###min.csv' where 'x' is the IOP test number, 'XX' is the identity of the sonic anemometer specified in Table 16 (e.g., G2, R1), 'yy' is the agl measurement height, and '###' is the averaging period (10 or 30 minutes). There are corresponding quality control 10-min average files with the filenames 'PSB2qc_FRD_IOPx_XX_yy_###min.csv'. The quality control files contain a listing of quality control parameter values and flags for each period. Data from the G2 sonic was unavailable for IOP4.

There are a total of 14 FRD files containing 30-min average processed data. Seven of these are 'data' files and seven are 'qc' files, one pair for each sonic anemometer. Each file contains two blocks of data, one covering the daytime IOPs and one covering the nighttime IOPs.

Some data have been automatically flagged out with '-9999' due to flags set in the 'qc' files, columns 4-7 and 24-27. These are for excessive number of spikes or min/max values exceeding certain thresholds, respectively. Temporal gaps with missing data are also flagged '-9999'. The corresponding 'data' and 'qc' files contain matching records by row. The temperatures reported are virtual sonic temperatures.

The column header designations for the data summary files are:

1. XXMMDDYYHRMN, 'XX' is the identity of the sonic anemometer, 'MM' is the month, 'DD' is the day, 'YY' is the year, and 'HRMN' is the starting hour and minute of the 10 or 30 minute averaging period for that row
2. KNT Data points in interval
3. VECWD Vector Wind Direction (despiked) [degrees azimuth]
4. SCALWS Mean Scalar Wind Speed (despiked) [m+1 s-1]
5. SCALWSr Mean Scalar Wind Speed (raw) [m+1 s-1]
6. VECWS Mean Vector Wind Speed (despiked) [m+1 s-1]
7. USPD_rot Mean Vector Wind Speed (despiked, rotated/streamwise)[m+1 s-1]
8. VN Mean north vector [m+1 s-1]
9. VE Mean east vector {m+1 s-1}
10. UVAR U Variance (despike,detrend,unrotated) [m+2 s-2]
11. VVAR V Variance (despike,detrend,unrotated) [m+2 s-2]
12. WVAR W Variance (despike,detrend,unrotated) [m+2 s-2]
13. UVAR_rot U Variance (despike,detrend,rotated) [m+2 s-2]
14. VVAR_rot V Variance (despike,detrend,rotated) [m+2 s-2]
15. WVAR_rot W Variance (despike,detrend,rotated) [m+2 s-2]
16. SIGMAT Sigma (theta), horizontal [radians]
17. SIGMAP Sigma (phi), vertical [radians]
18. UV_rot u'v' momentum flux (despike,detrend,rotated) [m+2 s-2]
19. UW_rot u'w' momentum flux (despike,detrend,rotated) [m+2 s-2]
20. VW_rot v'w' momentum flux (despike,detrend,rotated) [m+2 s-2]
21. WTBAR_rot w'T' sensible heat flux (despike,detrend,rotated) [m+1 K+1 s-1]
22. USTR_rot u* (despike,detrend,rotated) [m+1 s-1]
23. OLEN_rot Obukhov Length (despike,detrend,rotated) [m-1]
24. TAVG Mean Virtual Sonic Temperature (despiked) [C]
25. TSDEV Standard deviation temperature (despike,detrend) [C]
26. UAVGr Mean U Component Wind Speed (raw) [m+1 s-1]
27. VAVGr Mean V Component Wind Speed (raw) [m+1 s-1]
28. WAVGr Mean W Component Wind Speed (raw) [m+1 s-1]
29. USDEVr Standard Deviation U (raw) [m+1 s-1]
30. VSDEVr Standard Deviation V (raw) [m+1 s-1]
31. WSDEVr Standard Deviation W (raw) [m+1 s-1]
32. USTR u* (despike,detrend,unrotated) [m+1 s-1]
33. UV u'v' momentum flux (despike,detrend,unrotated) [m+2 s-2]
34. UW u'w' momentum flux (despike,detrend,unrotated) [m+2 s-2]

35. VW	v'w' momentum flux (despike,detrend,unrotated) [m+2 s-2]
36. WTBAR	w'T' sensible heat flux (despike,detrend) [m+1 K+1 s-1]
37. UT	u'T' advective heat flux (despike,detrend) [m+1 K+1 s-1]
38. OLEN	Obukhov Length (despike,detrend) [m-1]
39. UAVG	Mean U Component Wind Speed (despiked) [m+1 s-1]
40. VAVG	Mean V Component Wind Speed (despiked) [m+1 s-1]
41. WAVG	Mean W Component Wind Speed (despiked) [m+1 s-1]
42. TAVGr	Mean Virtual Sonic Temperature (raw) [C]
43. TSDEVr	Standard deviation temperature (raw) [C]
44. skwU	Skewness U
45. skwV	Skewness V
46. skwW	Skewness W
47. skwT	Skewness T
48. kurU	Kurtosis U
49. kurV	Kurtosis V
50. kurW	Kurtosis W
51. kurT	Kurtosis T

In the description below, a cycle refers to a single pass through a single record for the specified variable during the despiking process. The column headers for the quality control parameter file are:

1. XXMMDDYYHRMN, 'XX' is the identity of the sonic anemometer, 'MM' is the month, 'DD' is the day, 'YY' is the year, and 'HRMN' is the starting hour and minute of the 10 or 30 minute averaging period for that row
2. Number of observations in the averaging period
3. Flag=1 if number of observations is more than 100 outside of nominal 10 Hz value for the averaging period (10-minutes, 5900-6100; 30-minutes, 17900-18100)
4. Flag=1 if number of spikes in u is greater than 0.5% of observations for any single cycle
5. Flag=1 if number of spikes in v is greater than 0.5% of observations for any single cycle
6. Flag=1 if number of spikes in w is greater than 0.5% of observations for any single cycle
7. Flag=1 if number of spikes in T is greater than 0.5% of observations for any single cycle
8. Total (cumulative) number of spikes detected in u after 'lpknt_U' cycles through record
9. Total (cumulative) number of spikes detected in v after 'lpknt_V' cycles through record
10. Total (cumulative) number of spikes detected in w after 'lpknt_W' cycles through record
11. Total (cumulative) number of spikes detected in T after 'lpknt_T' cycles through record

12. lpknt_U, number of cycles through u record to eliminate all spikes. The maximum number of cycles allowed is 11.
13. lpknt_V, number of cycles through v record to eliminate all spikes.
14. lpknt_W, number of cycles through w record to eliminate all spikes.
15. lpknt_T, number of cycles through T record to eliminate all spikes.
16. flgRES_U, number of times >70% of bins in 1000 point moving window amplitude resolution test are empty for u
17. flgRES_V, number of times >70% of bins in 1000 point moving window amplitude resolution test are empty for v
18. flgRES_W, number of times >70% of bins in 1000 point moving window amplitude resolution test are empty for w
19. flgRES_T, is number of times >70% of bins in 1000 point moving window amplitude resolution test re empty for T
20. flgDRP_U, number of times >15% of points in u record fall in same bin for 1000 point moving window
21. flgDRP_V, number of times >15% of points in v record fall in same bin for 1000 point moving window
22. flgDRP_W, number of times >15% of points in w record fall in same bin for 1000 point moving window
23. flgDRP_T, number of times >15% of points in T record fall in same bin for 1000 point moving window
24. flgABS_U, number of points in u record $> 30 \text{ m s}^{-1}$ (check after despiking)
25. flgABS_V, number of points in v record $> 30 \text{ m s}^{-1}$ (check after despiking)
26. flgABS_W, number of points in w record $> |5 \text{ m s}^{-1}|$ (check after despiking)
27. flgABS_T, number of points in T record, $T > 45\text{C}$ or $T < -30\text{C}$ (check after despiking)
28. flgHT1_U, number of “soft” Haar transform threshold exceedances for mean u (2x threshold)
29. flgHT1_V, number of “soft” Haar transform threshold exceedances for mean v (2x threshold)
30. flgHT1_W, number of “soft” Haar transform threshold exceedances for mean w (2x threshold)
31. flgHT1_T, number of “soft” Haar transform threshold exceedances for mean T (2x threshold)
32. flgHT2_U, number of “soft” Haar transform threshold exceedances for standard deviation u (2x threshold)
33. flgHT2_V, number of “soft” Haar transform threshold exceedances for standard deviation v (2x threshold)
34. flgHT2_W, number of “soft” Haar transform threshold exceedances for standard deviation w (2x threshold)
35. flgHT2_T, number of “soft” Haar transform threshold exceedances for standard deviation T (2x threshold)
36. flgHT3_U, number of “hard” Haar transform threshold exceedances for mean u (3x threshold)

37. flgHT3_V, number of “hard” Haar transform threshold exceedances for mean v (3x threshold)
38. flgHT3_W, number of “hard” Haar transform threshold exceedances for mean w (3x threshold)
39. flgHT3_T, number of “hard” Haar transform threshold exceedances for mean T (3x threshold)
40. flgHT4_U, number of “hard” Haar transform threshold exceedances for standard deviation u (3x threshold)
41. flgHT4_V, number of “hard” Haar transform threshold exceedances for standard deviation v (3x threshold)
42. flgHT4_W, number of “hard” Haar transform threshold exceedances for standard deviation w (3x threshold)
43. flgHT4_T, number of “hard” Haar transform threshold exceedances for standard deviation T (3x threshold)
44. flgSKW_U, flag=1 for $|u \text{ skewness}| > 1$; flag=2 for $|u \text{ skewness}| > 2$
45. flgSKW_V, flag=1 for $|v \text{ skewness}| > 1$; flag=2 for $|v \text{ skewness}| > 2$
46. flgSKW_W, flag=1 for $|w \text{ skewness}| > 1$; flag=2 for $|w \text{ skewness}| > 2$
47. flgSKW_T, flag=1 for $|T \text{ skewness}| > 1$; flag=2 for $|T \text{ skewness}| > 2$
48. flgKUR_U, flag=1 for u kurtosis < -1 or u kurtosis > 2 ; flag=2 for u kurtosis < -2 or u kurtosis > 5
49. flgKUR_V, flag=1 for v kurtosis < -1 or v kurtosis > 2 ; flag=2 for v kurtosis < -2 or v kurtosis > 5
50. flgKUR_W, flag=1 for w kurtosis < -1 or w kurtosis > 2 ; flag=2 for w kurtosis < -2 or w kurtosis > 5
51. flgKUR_T, flag=1 for T kurtosis < -1 or T kurtosis > 2 ; flag=2 for T kurtosis < -2 or T kurtosis > 5
52. flgRNU, RN alongwind relative nonstationarity test for u; flag=1 for RNU > 0.5
53. flgRNV, RN crosswind relative nonstationarity test for v; flag=1 for RNV > 0.5
54. flgRNS, RN vector wind relative nonstationarity test wind speed; flag=1 RNS >0.5
55. flgRSET, flag=1 for relative systematic flux sampling error test (RSE) > 0.5
56. RSET, value for RSE
57. flgRFET, flag=1 for random flux sampling error (RFET) test value > 0.25
58. flgRNT, flag=1 for flux trends associated mesoscale motions (RNT) value > 0.25
59. RFET, value for RFET
60. RNT, value for RNT

Finally, there is a group of text files containing the raw, unprocessed 10 Hz data for the ARLFRD sonic anemometer measurements. They are reported in a series of data records of 4 hours each. The data covers one hour before the IOP tracer measurement period to one hour after the tracer measurements. There is one file per sonic anemometer per IOP. The filenames are 'PSB2_SS_htm_IOPn.txt' where 'SS' is the sonic designation (e.g., R1, G2), 'htm' is the agl height of the sonic in meters, and 'n' is the number of the IOP. There is no file for the G2 sonic for IOP4.

The R.M. Young sonic files (SS=R#) have the following columns:

1. Date (mm/dd/yy)
2. Time (hh:mm:ss)
3. U wind component (m s^{-1})
4. V wind component (m s^{-1})
5. W wind component (m s^{-1})
6. T (deg C)

For sonics R1 and R9 the date has a 4-digit instead of 2-digit year. The G2 sonic (SS=G2) has the same date and time columns as the R.M. Young sonics. The next three numeric fields are U, V, and W (m s^{-1}). The next column is the speed of sound in air (C_air). For sonic G2 in IOPs 1 and 2, the times reported for the raw, unprocessed data are MDT but the data represents the same time period as the other sonics. This is the only exception to the use of MST in all other data sets.

Other Grid 3 Tower Measurements

Configuration

In addition to the six 3-d sonic anemometers listed above, ARLFRD also made measurements with the permanently installed instrumentation on GRI that relates to its function as a Mesonet station. These other measurements include wind speed and wind direction at 2, 10, 15.3, 45.1, and 60 m heights using Met One cup anemometers (Model 010C) and vanes (Model 020C); aspirated air temperature at heights of 1.5, 10.7, 14.9, 45, and 59.6 m; and measurements of solar radiation, relative humidity, precipitation, atmospheric pressure, and soil temperatures and moisture at five levels (5, 10, 20, 50, 100 cm depths) (Table 16).

In addition to the obvious importance of wind speed and direction, the wind speed, temperature gradient (ΔT), and net radiation measurements permitted the determination of the Pasquill stability class using the Solar Radiation Delta-T (SRDT) method described in EPA (2000c).

Quality Control

As noted earlier, a detailed and comprehensive data quality assurance program is performed at GRI and the other meteorological towers in the NOAA/INL Mesonet on a routine basis (see above).

The GRI wind speed and direction data sets were plotted and reviewed by the data analyst for consistency and accuracy by comparing results with other measurements for the duration of each IOP plus one hour before and after each test. This includes the same comparisons described in detail above for the despiked sonic anemometer data. The results for these comparisons are included in sets of graphs for each IOP in the Summary of Individual IOPs chapter.

Data File Formats

There are eight NOAA/INL Mesonet files for GRI in PSB2 that provide the non-sonic anemometer data. Each covers the 24 h day encompassing the IOP test days (July 26 and 27; August 4 and 5; October 13, 20, 21, and 26). The filenames are 'PSB2_GRI_IOP#_10min.csv' where '#' specifies the number of the IOP. The time listed for each record is the *end* time for the 10-min period. All times are MST. Missing values are indicated by '-999'. The column headers are:

- 1: year
- 2: month
- 3: day
- 4: hour (MST, end time of the 5-minute interval)
- 5: minute (end time of the 5-minute interval)
- 6: 2m Wind Speed, [m s^{-1}]
- 7: 2m Wind Gust, [m s^{-1}]
- 8: 2m Wind Direction, [deg]
- 9: 2SD, standard deviation wind direction at 2m, [deg]
- 10: 10m Wind Speed, [m s^{-1}]
- 11: 10m Wind Gust, [m s^{-1}]
- 12: 10m Wind Direction, [deg]
- 13: 10SD, standard deviation wind direction at 10m, [deg]
- 14: 15m Wind Speed, [m s^{-1}]
- 15: 15m Wind Gust, [m s^{-1}]
- 16: 15m Wind Direction, [deg]
- 17: 15SD, standard deviation wind direction at 15m, [deg]
- 18: 45m Wind Speed, [m s^{-1}]
- 19: 45m Wind Gust, [m s^{-1}]
- 20: 45m Wind Direction, [deg]
- 21: 45SD, standard deviation wind direction at 45m, [deg]
- 22: Top Wind Speed, wind speed at 60m, [m s^{-1}]
- 23: Top Wind Gust, wind direction at 60m, [m s^{-1}]
- 24: Top Wind Direction, wind direction at 60m, [deg]
- 25: TopSD, standard deviation wind direction at 60m, [deg]
- 26: 2m Temp C, air temperature at 1.5 m, [deg C]
- 27: 10m Temp C, air temperature at 10.7 m, [deg C]
- 28: 15m Temp C, air temperature at 14.9 m, [deg C]
- 29: 45m Temp C, air temperature at 45.0 m, [deg C]
- 30: TopT C, air temperature at 59.6 m, [deg C]
- 31: 2m RH%, relative humidity at 2 m, [%]
- 32: Solar Rad, solar radiation, [W m^{-2}]
- 33: BP, barometric pressure, [in. Hg]
- 34: Rain, [inches]
- 35: 5cm Soil Moisture, [fractional]

36. 10cm Soil Moisture, [fractional]
37. 20cm Soil Moisture, [fractional]
38. 50cm Soil Moisture, [fractional]
39. 100cm Soil Moisture, [fractional]
40. 5cm Soil Temperature, [deg C]
41. 10cm Soil Temperature, [deg C]
42. 20cm Soil Temperature, [deg C]
43. 50cm Soil Temperature, [deg C]
44. 100cm Soil Temperature, [deg C]

WSULAR

Sonic Anemometers

Experimental Setup

WSULAR installed five 3-d Campbell Scientific CSAT3 or CSAT3B sonic anemometers at the 'EC' and 'ST' locations indicated on Fig. 5 during the month of October. Thus they were in place for all of the nighttime IOPs. Besides the GRI, COC, and G2 sonic measurements, the 'EC' and 'ST' sites provided most of the information about the homogeneity of the wind and turbulence fields in the horizontal during IOPs 5-8. At the 'EC' sites the CSAT3X anemometers were collocated with LICOR infrared gas analyzers (IRGAs) for the measurement of the fluxes of latent heat, water vapor, and carbon dioxide.

The WSULAR 3-d sonic data were continuously recorded for the duration of the experimental period at 10 Hz on a compact flash card installed in Campbell Scientific data loggers, one for each 3-d sonic and IRGA pair. Five and 30 min averages were also automatically calculated and stored in separate files on the data loggers.

Quality Control

The WSULAR 3-d sonic data and LICOR data were processed following algorithms described in Vickers and Mahrt (1997). This included calculations of means, standard deviations, and covariances for 10 and 30 min averages and quality control tests for spike detection, checks for excessive skewness and kurtosis, and time lag tests for the LICOR measurements. These calculations were both pre and post rotation.

Data collected from the WSULAR sonic anemometers were evaluated using protocols similar to those described for the ARLFRD sonic anemometers. Data were also plotted and reviewed by the analyst for consistency and accuracy by comparing results with other measurements for the duration of each IOP plus one hour before and after each test. This included the following comparisons:

- All wind speed, direction, and turbulence measurements in the horizontal at about 3 m, where available. These comparisons included the sonic anemometer G2 and the cup anemometer and wind vane measurements at 2 m on GRI and COC.

Data File Formats

There are a total of 40 files containing processed WSULAR sonic data, 10 files per nighttime IOP (IOPS 5-8). There are five 10 min and five 30 min average files for each of the IOPs, one set each for the EC1, EC2, ST1, ST2, and ST3 sites. Each file contains data for a 24 h period encompassing the corresponding IOP. The data filenames are 'PSB2data_WSU_IOPn_id#_xxm_yymin.csv' where 'n' is the designation of the IOP, 'id' represents the tower type designation (EC=eddy correlation, ST=sonic only), '#' represents the site identification number for that tower type, and 'xx' represents the measurement height (m agl), and 'yy' is the averaging period in minutes. The two 'EC' sites include data from a collocated LICOR. Missing values are indicated by '-9999'. The column header designations for these sonic data files are:

- 1: date, yyyy is the year, mm is the month, dd is the day, [yyyymmdd]
- 2: time, hh:mm is the middle of the 10 or 30 minute averaging period, e.g. 00:00-00:30
-> 00:15, [hh:mm]
- 3: decimal_day, decimal day of year, [#]
- 4: U_star, Friction velocity, [m s^{-1}]
- 5: WS, Wind speed, [m s^{-1}]
- 6: WD, Wind direction, [deg]
- 7: Temp_air, Air temperature, [K]
- 8: RH, Relative humidity, [%]
- 9: u_unrot, Mean unrotated u, [m s^{-1}]
- 10: v_unrot, Mean unrotated v, [m s^{-1}]
- 11: w_unrot, Mean unrotated w, [m s^{-1}]
- 12: u_rot, Mean rotated u, [m s^{-1}]
- 13: v_rot, Mean rotated v, [m s^{-1}]
- 14: w_rot, Mean rotated w, [m s^{-1}]
- 15: Ts_avg, Mean sonic temperature, [K]
- 16: c_avg, Mean CO_2 concentration, [mg m^{-3}]
- 17: q_avg, Mean H_2O concentration, [g m^{-3}]
- 18: p_avg, Mean pressure from LiCor, [kPa]
- 19: u_unrot_SD, Standard deviation of unrotated u, [m s^{-1}]
- 20: v_unrot_SD, Standard deviation of unrotated v, [m s^{-1}]
- 21: w_unrot_SD, Standard deviation of unrotated w, [m s^{-1}]
- 22: u_SD, Standard deviation of rotated u, [m s^{-1}]
- 23: v_SD, Standard deviation of rotated v, [m s^{-1}]
- 24: w_SD, Standard deviation of rotated w, [m s^{-1}]
- 25: Ts_SD, Standard deviation of sonic temperature, [K]
- 26: c_SD, Standard deviation of CO_2 concentration, [mg m^{-3}]

- 27: q_SD, Standard deviation of H2O concentration, [g m⁻³]
- 28: P_SD, Standard deviation of air pressure, [kPa]
- 29: uv_unrot, Covariance of unrotated u and v, [m² s⁻²]
- 30: uw_unrot, Covariance of unrotated u and w, [m² s⁻²]
- 31: uTs_unrot, Covariance of unrotated u and sonic temperature, [K m s⁻¹]
- 32: uc_unrot, Covariance of unrotated u and CO₂ concentration, [mg m⁻² s⁻¹]
- 33: uq_unrot, Covariance of unrotated u and H2O concentration, [g m⁻² s⁻¹]
- 34: vw_unrot, Covariance of unrotated v and w, [m² s⁻²]
- 35: vTs_unrot, Covariance of unrotated v and sonic temperature, [K m s⁻¹]
- 36: vc_unrot, Covariance of unrotated v and CO₂ concentration, [mg m⁻² s⁻¹]
- 37: vq_unrot, Covariance of unrotated v and H2O concentration, [g m⁻² s⁻¹]
- 38: wTs_unrot, Covariance of unrotated w and sonic temperature, [K m s⁻¹]
- 39: wc_unrot, Covariance of unrotated w and CO₂ concentration, [mg m⁻² s⁻¹]
- 40: wq_unrot, Covariance of unrotated w and H2O concentration, [g m⁻² s⁻¹]
- 41: uv, Covariance of rotated u and v, [m² s⁻²]
- 42: uw, Covariance of rotated u and w, [m² s⁻²]
- 43: uTs, Covariance of rotated u and sonic temperature, [K m s⁻¹]
- 44: uc, Covariance of rotated u and CO₂ concentration, [mg m⁻² s⁻¹]
- 45: uq, Covariance of rotated u and H2O concentration, [g m⁻² s⁻¹]
- 46: vw, Covariance of rotated v and w, [m² s⁻²]
- 47: vTs, Covariance of rotated v and sonic temperature, [K m s⁻¹]
- 48: vc, Covariance of rotated v and CO₂ concentration, [mg m⁻² s⁻¹]
- 49: vq, Covariance of rotated v and H2O concentration, [g m⁻² s⁻¹]
- 50: wTs, Covariance of rotated w and sonic temperature, [K m s⁻¹]
- 51: wc, Covariance of rotated w and CO₂ concentration, [mg m⁻² s⁻¹]
- 52: wq, Covariance of rotated w and H2O concentration, [g m⁻² s⁻¹]
- 53: cTs, Covariance of CO₂ concentration and sonic temperature, [K m s⁻³]
- 54: qTs, Covariance of H2O concentration and sonic temperature, [K m s⁻³]
- 55: cq, Covariance of CO₂ concentration and H2O concentration, [g m⁻³ mg m⁻³]
- 56: Ruv, Correlation coefficient of rotated u and v, [#]
- 57: Ruw, Correlation coefficient of rotated u and w, [#]
- 58: RuTs, Correlation coefficient of rotated u and sonic temperature, [#]
- 59: Ruc, Correlation coefficient of rotated u and CO₂ concentration, [#]
- 60: Ruq, Correlation coefficient of rotated u and H2O concentration, [#]
- 61: Rvw, Correlation coefficient of rotated v and w, [#]
- 62: RvTs, Correlation coefficient of rotated v and sonic temperature, [#]
- 63: Rvc, Correlation coefficient of rotated v and CO₂ concentration, [#]
- 64: Rvq, Correlation coefficient of rotated v and H2O concentration, [#]
- 65: RwTs, Correlation coefficient of rotated w and sonic temperature, [#]
- 66: Rwc, Correlation coefficient of rotated w and CO₂ concentration, [#]
- 67: Rwq, Correlation coefficient of rotated w and H2O concentration, [#]
- 68: RcTs, Correlation coefficient of CO₂ concentration and sonic temperature, [#]
- 69: RqTs, Correlation coefficient of H2O concentration and sonic temperature, [#]
- 70: Rcq, Correlation coefficient of CO₂ concentration and H2O concentration, [#]

- 71: Tlag_c, Lag time between sonic and LiCor CO₂, [s]
- 72: Tlag_q, Lag time between sonic and LiCor H₂O, [s]
- 73: spike_u, Number of spikes detected and points exceeding absolute limits in u (± 50 m/s), [#]
- 74: spike_v, Number of spikes detected and points exceeding absolute limits in v (± 50 m/s), [#]
- 75: spike_w, Number of spikes detected and points exceeding absolute limits in w (± 10 m/s), [#]
- 76: spike_Ts, Number of spikes detected and points exceeding absolute limits in sonic temperature (-20 ~ 50 C), [#]
- 77: spike_c, Number of spikes detected and points exceeding absolute limits in CO₂ concentration (200 ~ 1000 mg / m³), [s]
- 78: spike_q, Number of spikes detected and points exceeding absolute limits in H₂O concentration (0 ~ 30 g / m³), [s]
- 79: n_missing, Number of missing values for sonic anemometer (CSAT diagnostic code > 63), [#]
- 80: Skw_u_unrot, Skewness of unrotated u, [#]
- 81: Skw_v_unrot, Skewness of unrotated v, [#]
- 82: Skw_w_unrot, Skewness of unrotated w, [#]
- 83: Skw_u, Skewness of rotated u, [#]
- 84: Skw_v, Skewness of rotated v, [#]
- 85: Skw_w, Skewness of rotated w, [#]
- 86: Skw_Ts, Skewness of sonic temperature, [#]
- 87: Skw_c, Skewness of CO₂ concentration, [#]
- 88: Skw_q, Skewness of H₂O concentration, [#]
- 89: Kur_u_unrot, Kurtosis of unrotated u, [#]
- 90: Kur_v_unrot, Kurtosis of unrotated v, [#]
- 91: Kur_w_unrot, Kurtosis of unrotated w, [#]
- 92: Kur_u, Kurtosis of rotated u, [#]
- 93: Kur_v, Kurtosis of rotated v, [#]
- 94: Kur_w, Kurtosis of rotated w, [#]
- 95: Kur_Ts, Kurtosis of sonic temperature, [#]
- 96: Kur_c, Kurtosis of CO₂ concentration, [#]
- 97: Kur_q, Kurtosis of H₂O concentration, [#]

There is also a group of text files containing the raw, unprocessed 10 Hz data from the WSULAR EC1, EC2, ST1, ST2, and ST3 stations. There are a total of 20 files in the project database. Each file has a 4 h record that includes the two hours of each IOP tracer sampling period plus one hour before and after at each station. The filenames are xx#_2016mmdd.DAT where 'xx#' designates the EC or ST site number, 'mm' is the month, and 'dd' is the day. Please note that the sonics were not oriented to true north. The EC1, EC2, ST1, ST2, and ST3 were oriented at 319°, 324°, 311°, 313°, and 314°, respectively.

The column header designations for the EC1 are:

1. TIMESTAMP, TS time stamp
2. RECORD, RN, record
3. Ux_3m, m/s, wind speed of u component
4. Uy_3m, m/s, wind speed of v component
5. Uz_3m, m/s, wind speed of w component
6. Ts_3m, C, sonic temperature
7. diag_csats_3m, unitless, Sonic diagnostic value
8. mco2_3m, umol/mol, CO2 dry mole mixing ratio inside the Li-7200 sensor cell
9. mh2o_3m, mmol/mol, H2O dry mole mixing ratio inside the Li-7200 sensor cell
10. co2, mg/m³, CO2 density (concentration) inside the Li-7200 sensor cell
11. h2o, g/m³, H2O density (concentration) inside the Li-7200 sensor cell
12. Press_Li7200_3m, kPa, Pressure measured in LI-7550
13. agc_3m, %, Li-7200 diagnostic value
14. AirTC_3m, Deg C, Air temperature at same height with the EC system
15. RH_3m, %, Relative humidity at same height with the EC system

The column header designations for the EC2 are:

1. TIMESTAMP, TS, time stamp
2. RECORD, RN, record
3. Ux, m/s, wind speed of u component
4. Uy, m/s, wind speed of v component
5. Uz, m/s, wind speed of w component
6. Ts, degC, sonic temperature
7. diag_csats, unitless, Sonic diagnostic value
8. co2, mg/m³, CO2 density (concentration) inside the Li-7500 sensor cell
9. h2o, g/m³, H2O density (concentration) inside the Li-7500 sensor cell
10. Press_Li7500, kPa, Pressure measured in LI-7550
11. diag_irga, unitless, Li-7500 diagnostic value
12. AirTC, Deg C, Air temperature at same height with the EC system
13. RH, %, Relative humidity at same height with the EC system

The column header designations for the ST1, ST2, and ST3 are:

1. TIMESTAMP, TS, time stamp
2. RECORD, RN, record
3. Ux, m/s, wind speed of u component
4. Uy, m/s, wind speed of v component
5. Uz, m/s, wind speed of w component
6. Ts, degC, sonic temperature
7. diag_csats, unitless, Sonic diagnostic value

8. AirTC, deg C, Air temperature at same height with the Sonic
9. RH, %, Relative humidity at same height with the Sonic

Other Measurements

Experimental Setup

In addition to the measurements on the five 3-d sonic anemometers and two IRGAs, WSULAR also made a suite of other measurements at the two 'EC' sites. Measurements of non-aspirated air temperature and relative humidity were made using Rotronic HC2S3 sensors. Radiation measurements at these two sites included net shortwave, net longwave, and net radiation. Soil temperatures were measured at 2.5 and 5 cm depths, soil water content at 2.5 cm, soil heat flux at 5 cm.

Quality Control

The air temperature, relative humidity, net radiation, air pressure, and soil heat flux data sets were plotted and reviewed by the data analyst. Problems were identified with much of this data from EC1 so data from this station is not provided for these measurements.

Data File Formats

There are two files that provide these additional, non-sonic anemometer measurements by WSULAR, one for 10 min averages and one for 30 min averages for IOPs 5-8. The filenames are 'EC2_RM_Data_xxmin.csv' where the 'xx' represents the averaging period. The files cover the period from 5 October to 30 October for station EC2. These data are unavailable from EC2. Missing values are indicated by '-999'. The column headers, description, and units are:

- 1: date, yyyy is the year, mm is the month, dd is the day, [yyyymmdd]
- 2: time, hh:mm is the middle of the 10 or 30 minute averaging period, e.g. 00:00-00:30
-> 00:15, [hh:mm]
- 3: decimal_day, decimal day of year, [#]
- 4: NetSW_Avg, Net shortwave radiation, [W m^{-2}]
- 5: NetLW_Avg, Net longwave radiation, [W m^{-2}]
- 6: NetRad_Avg, Net radiation, [W m^{-2}]
- 7: AirTC_Avg, Air temperature at 3.14 m, [deg C]
- 8: RH_Avg, Relative humidity at 3.14 m, [%]
- 9: AirTC_2_Avg, Air temperature at 1.6 m, [deg C]
- 10: RH_2_Avg, Relative humidity at 1.6 m, [%]
- 11: T109_C_1_Avg, Soil temperature at 2.5 cm, [deg C]
- 12: T109_C_2_Avg, Soil temperature at 5 cm, [deg C]
- 13: VW_Avg, Soil water content at 2.5 cm, [fraction]
- 14: shf_3_Avg, Soil heat flux at 5 cm, [W m^{-2}]
- 15: shf_4_Avg, Soil heat flux at 5 cm, [W m^{-2}]

Meteorological Towers on Sampling Grid

Experimental Setup

A 30.5 m open lattice aluminum meteorological tower purchased from Triex (model T-15) was located at approximately 499 m arc distance and 60 degrees arc angle during PSB2. This was the '100 foot' meteorological tower linked to the command center and thus is designated COC. Met One Instruments Inc. cup anemometers (Model 010C) and wind vanes (Model 020C) were used to measure the wind speed and direction at 2, 10, and 30 m heights. A picture of this tower is shown in Fig. 53.

Data from the tower was collected with a Campbell Scientific CR23X data logger and recorded in 1 s and 5 min averages. The 1-sec averages were transferred by direct line back to the command center during IOPs where the project manager was able to monitor the current winds from a graphical display on a computer. This information was used to advise the TGA operators where to expect the tracer along the grid sampling arcs and to assist with positioning. The 1 s data are available in the project database.

Quality Control

The cup anemometer and wind vane on COC were calibrated to rigorous standards. The instrumentation selection criteria, quality control, calibration, and maintenance procedures at COC were the same as those at GRI and met the generally accepted requirements and guidelines set out in DOE (2004, 2005), ANSI/ANS-3.11 (2015), and ANSI/ANS-3.2 (2006).

The wind speed and direction data sets for the COC tower was plotted and reviewed by the data analyst for consistency and accuracy by comparing results with other measurements for the duration of each test plus one hour before and after each test. This included the following comparisons:

- All wind speed and direction measurements in the horizontal at 2, 10, and 30 m, where available. These comparisons included the sonic anemometers and cup anemometers and wind vanes at GRI and the ASC sodar. In some cases heights were compared if they were close. For example, 2 m cup and vane results at GRI and COC were compared with sonic results at 3 m (e.g., G2, EC1).

The results for these comparisons are included in the Summary of Individual IOPs chapter.

Data File Formats

For COC there are eight raw 1-sec files and eight processed 10 min average files in the final PSB2 project database. Each raw file covers the 24-hour day encompassing the IOP test days (July 26 and 27, August 4 and 5, and October 13, 20, 21, and 26). The processed files cover a 4 h period from 1 h prior to the start of bag sampling to 1 h after bag sampling ended.

The filenames for the raw files are 'PSB2_COC_IOP#_1sec.csv' where the '#' specifies the number of the IOP. The filenames for the processed files are 'PSB2_COC_IOP#_10min.csv'. The time listed for each record is the start time for the 10-min period. All times are MST. Missing values are indicated by '-999'. The column headers for the 1-sec files are:

- 1: Date and Time (MST) [MM/DD/YYYY HR:MN] where HR:MN is hour and minute at the end of each second
- 2: Sequential record number
- 3: Wind speed at 2 m [m s^{-1}]
- 4: Wind speed at 10 m [m s^{-1}]
- 5: Wind speed at 30 m [m s^{-1}]
- 6: Wind direction at 2 m [degrees]



Figure 53. 30 m command center meteorological tower (COC).

- 7: Wind direction at 10 m [degrees]
- 8: Wind direction at 30 m [degrees]

The column headers for the 10 min average files are:

- 1: Hour (decimal hour MST start time of 10 min average)
- 2: Wind speed at 2 m [m s^{-1}]
- 3: Wind speed at 10 m [m s^{-1}]
- 4: Wind speed at 30 m [m s^{-1}]
- 5: Wind direction at 2 m [deg]
- 6: Wind direction at 10 m [deg]
- 7: Wind direction at 30 m [deg]
- 8: Standard deviation horizontal wind direction σ_θ at 2 m [deg]
- 9: Standard deviation horizontal wind direction σ_θ at 10 m [deg]
- 10: Standard deviation horizontal wind direction σ_θ at 30 m [deg]

Sodars

Experimental Setup

A minisodar is a remote sensing device that measures vertical profiles of wind speed and direction in the lowest levels of the atmosphere. It has a vertical range of as low as 15 m up to 200 m maximum with a height resolution of as small as 5 m. The height range and resolution during PSB2 were set at 30 to 200 m and at 10 m, respectively. One sodar was deployed on the tracer dispersion grid during PSB2.

An Atmospheric Systems Corporation ASC4000 minisodar was located at a permanent site designated as ‘SOD’ at about 800 m arc distance, 57 degrees arc angle (Figs. 2 and 5). A picture of this sodar can be seen in Fig. 54. Data from the ASC4000 was averaged at 10-min intervals and transmitted by radio link back to the ARLFRD office. Computer times on the minisodars were regularly checked and synched to the official internet time. Power to the ASC4000 was supplied by AC line power.

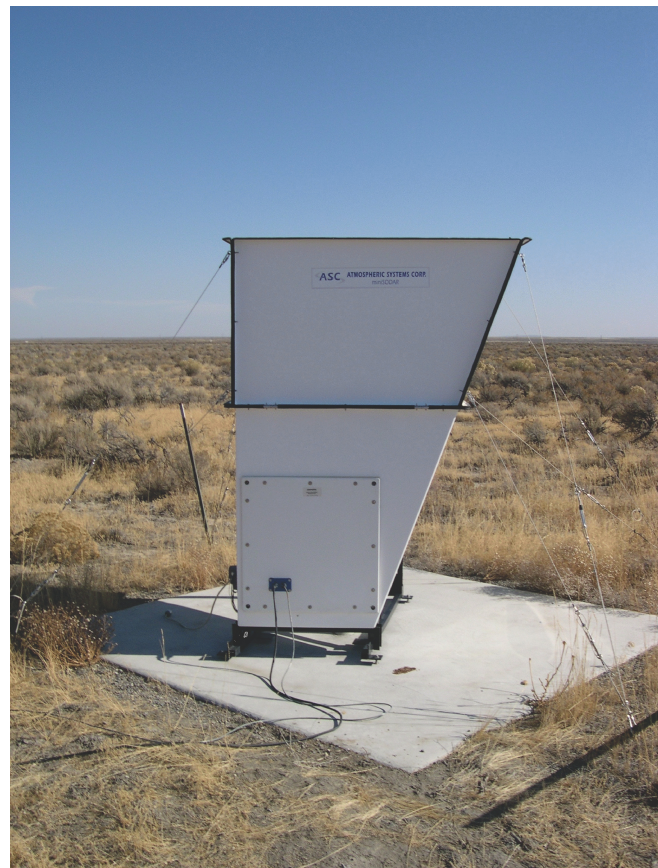


Figure 54. Photo of the ASC sodar, collocated with radar wind profiler at PRO.

Quality Control

Data was automatically screened for acceptance or rejection by proprietary internal algorithms using criteria based primarily on signal-to-noise ratio and number of acceptable values during the averaging period. Rejected data were specified as missing values. ARLFRD used the software program called SodarView for the ASC. The wind speed and direction data sets for the ASC and ART sodars were plotted and reviewed by the data analyst for consistency and accuracy by comparing results with other measurements for the duration of each test plus one hour before and after each test. This included the following comparisons:

- All wind speed and direction measurements in the horizontal at 30 m (sonic R6 and cup and vane on GRI, cup and vane on COC), 40 m (cup and vane on GRI), 60 m (sonic R5 and cup and vane on GRI), and 160 m (PRO), where available.

The results for these comparisons are included for each IOP in the Summary of Individual IOPs chapter. Most comparisons were good with the exception of PRO at 160 m. Data was either sparse or unavailable at one or both of PRO and SOD. PRO appeared to sometimes have a low U bias relative to SOD.

Data File Formats

Eight files for the ASC4000 sodar are included in the PSB2 project database, one for each of the IOP test days. Each file contains 10 min averages covering the 24 h period of the day. The files are designated 'PSB2_SOD_IOP#.csv' where '#' specifies the IOP test number. The times listed are MST (hh:mm:ss) for the start time of the 10 min averaging period. The notation in the column headers follows: ws = wind speed, wd = wind direction, w = mean vertical wind speed, sdw = standard deviation in w, sdu = standard deviation in u, sdv = standard deviation in v. Wind speeds and standard deviations are in units of m s^{-1} and the wind direction is in degrees. The number following (30, 40, ..., 200) is the height of the measurement in meters. Flagged or missing values are designated by '9999' for wind direction and '99.99' for everything else. The sodar's internal algorithms determined which points were missing. No further QC or processing was done.

Radar Wind Profiler and RASS

Experimental Setup

A 500 W, 915 MHz radar wind profiler (PRO) with Radio Acoustic Sounding System (RASS) measured boundary layer wind and air temperature profiles during PSB2. This system has operated continuously at its location on the tracer dispersion grid at about 800 m arc distance and 56 degrees arc angle since 1992 (Figs. 2 and 5). The radar wind profiler with RASS (Fig. 55) provides highly-resolved round-the-clock data for mixing layer characteristics above the sounding site. The radar wind profiler was configured to take measurements at 28 levels

covering a vertical range from 159 to 2895 m with vertical resolution set at 101 m. Remotely sensed measurements include wind speed and direction. The RASS was configured to take measurements of temperature with a vertical resolution of 105 m covering the range 165 to 1633 m agl.

Quality Control

The wind profiler data were retrieved and stored in the ARLFRD database similarly to the Mesonet data. The system has a built-in automatic quality control algorithm from the manufacturer. Data was flagged as -950 for any data points identified as suspect.

Data was often sparse but the available comparisons of U for PRO, SOD, and the top of the GRI suggest the 159 m U at PRO were sometimes biased low with respect to the other measurements. Wind directions at the 159 m level at PRO were usually roughly consistent with the wind directions at the upper levels of SOD but varied by IOP. Details of these comparisons are shown in the Summary of Individual IOPs chapter.



Figure 55. Photo of the radar wind profiler and RASS.

Data File Formats

The data for the wind profiler and RASS are archived in their original files. There is one wind profiler and one RASS file for each of the IOPs. Each file covers the 24 h period encompassing each of the IOPs. The file notation is 'GRI6mmdd.zzz' where the '6' represents the year 2016, the 'mm' represents the month, and the 'dd' represents the day. The 'zzz' file extension is W2B for the wind profiler data and T2B for the RASS data.

Wind data were collected for 25 minute intervals twice each hour at 5 to 30 min past the hour and at 35 to 60 min past the hour. The first, second, third, and fourth columns contain a QC code, the measurement height (m agl), wind speed (m s^{-1}), and wind direction (deg), respectively. Each half hour block is separated by an hour and minute (hrmn) timestamp designating the start time (MST) of the measurement interval. For example, '0235' represents the measurement from 2:35 to 3:00 AM. The '28' is the number of measurement levels.

The temperature data were collected for 5 min intervals twice each hour from zero to 5 min past the hour and from 30 to 35 min past the hour. The first, second, and third columns contain a QC code, the measurement height (m agl), and virtual temperature (TV, deg C), respectively. The hour and minute (hrmn, MST) starting time of each 5-min measurement interval is given at the start of each half hour record block. For example, '0030' represents the measurements from time period 12:30 to 12:35 AM.

The QC code '0' indicates valid data and records with '-950' represent failed consensus. The data codes are listed in the header text of each file along with date, location, Julian day, and other information. Data recovery for the RASS was often poor.

A supplemental file named 'PSB2_RadarProfiler_AllIOPs.csv' contains data reformatted from the raw wind profiler files (W2B) for the 4 h periods encompassing each IOP. Wind speed (m/s) is specified with 'ws' and wind direction (degrees) is specified with 'wd'. The number appended to the 'ws' and 'wd' represents the height level of the measurement. Levels 1 through 28 represent the measurement heights of 159, 261, 362, 463, 565, 666, 767, 868, 970, 1071, 1172, 1274, 1375, 1476, 1578, 1679, 1780, 1882, 1983, 2084, 2186, 2287, 2388, 2490, 2591, 2692, 2794, and 2895 m agl, respectively. Missing values are designated by '-950'.

Flux Station

Experimental Setup

The energy flux station (Fig. 56) is a permanent installation designed to measure how the shrub-steppe habitat of the INL interacts with the global energy cycle. It has been operational since 2000. For PSB2 it provided an additional site for the evaluation of horizontal homogeneity as well as a means of determining energy balance.

A suite of measurements were made on two separate towers at the flux station and in the soil subsurface. Measurements of net radiation, air temperature, relative humidity, barometric pressure, and solar radiation are made on one tripod tower. A Gill Model 1210R3 sonic anemometer and an open path LI-7500 infrared gas analyzer (IRGA) are mounted on the other tripod tower. This tower is used to measure the fluxes of momentum, sensible heat, latent heat and carbon dioxide. The anemometer and IRGA are mounted at heights of 3.2 and 2.54 m, respectively. The subsurface sensors make measurements of soil temperature (2 and 6 cm), soil moisture (2.5 cm), and soil heat flux (8 cm). The soil heat flux plates represent varying degrees of vegetation cover. Additional measurements include net radiation, air temperature/RH, solar radiation, and barometric pressure. The energy flux station is located approximately 500 m NE of the command center (about 900 m NE of the release location). Full details on instrumentation are provided in Table 16.



Figure 56. Photo of the flux station.

Quality Control

The data from the energy flux station is being provided on an as is basis and caution is advised in use of the data. Similarly, no quality control review was performed on the soil temperature and heat flux measurements.

Data File Formats

Data from the energy flux station is provided in two sets of files.

There eight 5-minute average files that include all of the measurements made on the first (non-sonic) tower and in the soil subsurface, one for each test day. These data files are in comma separated variable (CSV) format with fixed length fields. They are named 'PSB2_FluxStation_Tower1_IOPn.csv' where 'n' is the IOP number. The columns in the file are:

- 1: Year
- 2: Month
- 3: Day
- 4: Hour (MST)
- 5: Minute
- 6: Battery Voltage
- 7: Air Temperature at 2 m (deg C)
- 8: Relative Humidity at 2 m (%)
- 9: Solar Radiation (W m^{-2})
- 10: Soil Temperature Location A at 2 cm (deg C)
- 11: Pressure (mb)
- 12: Net Radiation (W m^{-2})
- 13: Soil Moisture, 2.5 cm (% by volume)
- 14: Soil Heat Flux, Plate 1, 8 cm (W m^{-2})
- 15: Soil Heat Flux, Plate 2, 8 cm (W m^{-2})
- 16: Soil Temperature Location B at 6 cm (deg C)
- 17: Soil Heat Flux, Plate 3, 8 cm (W m^{-2})
- 18: Soil Heat Flux, Plate 4, 8 cm (W m^{-2})

The second set of files contain data processed from the sonic anemometer and LI-7500 IRGA. They include half hour summary files that were automatically generated by the Licor SmartFlux EddyPro system. There are eight of these, one for each test day. A subset of the data extracted from these half hour summary records is provided in the project database for the days encompassing each of the IOPs. These include the more basic meteorological, flux, and quality control data. The complete files contain more comprehensive records with 189 total fields and are available upon request. The filenames are 'PSB2_FluxStation_Tower2_IOPn.csv'. The column headers for data in the subset files are:

1. filename
2. date [yyyy-mm-dd]
3. time [HH:MM]
4. DOY [ddd]
5. daytime [1=daytime]
6. Tau [#]
7. qc_Tau [#]
8. H [kg+1m-1s-2]
9. qc_H [#]
10. LE [W+1m-2]
11. qc_LE [#]
12. co2_flux [$\text{\AA}\mu\text{mol}+1\text{s}-1\text{m}-2$]
13. qc_co2_flux [#]
14. h2o_flux [mmol+1s-1m-2]
15. qc_h2o_flux [#]
16. ch4_flux
17. qc_ch4_flux [#]
18. co2_molar_density [$\text{\AA}\mu\text{mol}+1\text{s}-1\text{m}-2$]
19. co2_mole_fraction [$\text{\AA}\mu\text{mol}+1\text{mol}_a-1$]
20. co2_mixing_ratio [$\text{\AA}\mu\text{mol}+1\text{mol}_d-1$]
21. h2o_molar_density
22. h2o_mole_fraction [mmol+1mol_a-1]
23. h2o_mixing_ratio [mmol+1mol_d-1]
24. ch4_molar_density
25. ch4_mole_fraction [$\text{\AA}\mu\text{mol}+1\text{mol}_a-1$]
26. ch4_mixing_ratio [$\text{\AA}\mu\text{mol}+1\text{mol}_d-1$]
27. sonic_temperature [K]
28. air_temperature [K]
29. air_pressure [Pa]
30. air_density [kg+1m-3]
31. air_heat_capacity [J+1kg-1K-1]
32. air_molar_volume [m+3mol-1]
33. ET [mm]
34. water_vapor_density [[kg+1m-3]
35. e [Pa]
36. es [Pa]
37. specific_humidity [kg+1kg-1]
38. RH [%]
39. VPD [Pa]
40. Tdew [K]
41. u_unrot [m+1s-1]
42. v_unrot [m+1s-1]
43. w_unrot [m+1s-1]
44. u_rot [m+1s-1]

45.	v_rot	[m+1s-1]
46.	w_rot	[m+1s-1]
47.	wind_speed	[m+1s-1]
48.	wind_dir	[\hat{A}°]
49.	u*	[m+1s-1]
50.	TKE	[m+2s-2]
51.	L	[m]
52.	z-d/L	[#]
53.	bowen_ratio	[#]
54.	T*	[K]
55.	u_spikes	[#]
56.	v_spikes	[#]
57.	w_spikes	[#]
58.	ts_spikes	[#]
59.	co2_spikes	[#]
60.	h2o_spikes	[#]
61.	ch4_spikes	[#]
62.	u_var	[m+2s-2]
63.	v_var	[m+2s-2]
64.	w_var	[m+2s-2]
65.	ts_var	[K+2]
66.	co2_var	-
67.	h2o_var	-
68.	ch4_var	-
69.	none_var	-
70.	w/ts_cov	[m+1s-1K+1]
71.	w/co2_cov	-
72.	w/h2o_cov	-
73.	w/ch4_cov	-
74.	co2_mean	-
75.	h2o_mean	-

Radiosondes

Experimental Procedures

Radiosonde launches (Fig. 57) were performed before and after each test period from near the command center. The first balloon of a test period was launched approximately 15-min before the samplers were set to begin sampling the tracer plume. The second balloon was launched approximately 15 min after the end of the sampling period. Data from all launches were recorded during ascent through balloon burst and continued through descent until the signal could no longer be acquired. A summary of the radiosonde launches is given in Table 17.

The radiosonde system used was the GRAW model GS-H ground station (GRAW Radiosondes GmbH & Co. KG, Nuernberg, Germany) with GRAWMET software version 5.9.2.4, in conjunction with the GRAW digital radiosonde model DFM-09. A 200-gram balloon supplied the lift. The balloons were intentionally under-inflated to slow the balloon ascent in order to maximize the number of measurements in the boundary layer during balloon ascent. A target ascent rate of 4 m s^{-1} was selected. An average ascent rate of 4.3 m s^{-1} was achieved, which is only slightly less than the minimum ascent rate of 4.6 m s^{-1} requested by the National Weather Service (NWS).

Quality Control

The data are provided on an as is basis. The only data available for any kind of comparison are the wind speed and direction data from PRO and temperature data from the RASS and that comparison is limited. There are some comments on comparisons between the radiosonde and PRO data for individual IOPs in the Summary of Individual IOPs chapter.



Figure 57. Photo of releasing the radiosonde.

Table 17. Summary of radiosonde launch dates, times, durations and calculated variables.

Ascent																	Average			Mixing		
Test #	Date	Launch #	Launch Time MDT	End Time MDT	Duration HH:MM	LCL hPa	CCL hPa	LI	SI	K- index	S- index	TT- index	Ko- index	Freezing		Tropopause hPa	Tropopause m	Highest Point hPa	Highest Point m	Ascent Rate m s ⁻¹	Pot. Spec. Temp Hum	
														Level hPa	Level m							
1	7/26/2016	1	19:18	20:47	1:29	525.4	520.9	-1	-1	22	32	51	-75	579.0	4,750	213.0	11,938	33.5	23,622	4.6	4786 4609	
1	7/26/2016	2	21:08	22:22	1:14	515.3	511.8	0	0	20	30	50	-78	578.8	4,757	207.0	12,126	44.8	21,811	4.7	4071 4200	
2	7/27/2016	1	18:36	20:20	1:44	545.2	500.7	3	3	23	30	44	-59	554.5	5,112	121.0	15,591	24.4	25,709	4.2	2792 1713	
2	7/27/2016	2	20:38	22:23	1:45	518.6	476.1	4	3	19	26	44	-65	560.5	5,032	123.0	15,490	29.5	24,491	4.5	2992 2992	
3	8/4/2016	1	20:07	21:39	1:32	542.9	455.4	7	7	3	11	36	-37	578.4	4,728	120.1	15,576	32.9	23,767	4.7	1601 660	
3	8/4/2016	2	22:02	23:34	1:32	499.9	439.4	214	6	9	17	38	-59	573.7	4,793	125.4	15,503	34.8	23,368	4.4	1655 1622	
4	8/5/2016	1	19:39	21:15	1:36	509.5	471.0	3	N/A	N/A	N/A	N/A	N/A	586.2	4,618	131.4	15,013	34.5	23,431	4.6	3127 5869	
4	8/5/2016	2	21:36	23:07	1:31	499.7	387.2	210	N/A	N/A	N/A	N/A	N/A	586.7	4,598	125.6	15,285	32.8	23,766	5.1	3942 5188	
5	10/13/2016	1	10:54	11:56	1:02	808.9	532.4	20	18	-1	13	23	27	675.4	3,387	191.4	12,290	50.6	20,547	5.1	night night	
5	10/13/2016	2	13:06	14:19	1:13	813.0	517.5	22	19	-3	11	21	28	673.3	3,412	196.7	12,133	41.8	21,759	4.6	night night	
6	10/20/2016	1	10:56	N/A	N/A	N/A	N/A	N/A	N/A	N/A	N/A	N/A	N/A	N/A	N/A	N/A	N/A	N/A	N/A	N/A	N/A	night night
6	10/20/2016	2	13:06	14:12	1:06	850.0	566.5	20	16	-7	8	27	22	N/A	N/A	177.7	12,840	49.3	20,767	4.9	night night	
7	10/21/2016	1	10:58	12:11	1:13	836.4	505.4	23	20	1	13	20	29	673.8	3,438	171.5	13,093	43.9	21,462	4.6	night night	
7	10/21/2016	2	13:06	14:17	1:11	834.1	491.6	25	22	-2	9	17	21	671.4	3,456	168.4	13,193	46.4	21,108	4.6	night night	
8	10/27/2016	1	1:30	2:36	1:06	757.9	664.9	4	3	23	34	44	-7	636.3	3,918	154.7	13,719	53.1	20,257	4.8	night night	
8	10/27/2016	2	3:39	4:49	1:10	814.7	655.7	7	7	17	24	39	7	637.3	3,902	154.6	13,729	90.0	17,025	4.5	night night	

Data Files and Results

The height of the mixed layer was estimated using the profiles of potential temperature and specific humidity. These estimates are discussed in their respective IOP summary. The profiles of potential temperature and specific humidity usually provided unambiguous estimates of mixing depth for the daytime IOPs. That was not the case for the nighttime IOPs.

Summary graphs of the radiosonde data were automatically generated by the software for each launch and are provided in the project database. These graphs are: 1) profile data diagram, 2) thermodynamic (Stueve) diagram, 3) tephigram, 4) skew-T diagram, 5) emagram, 6) altitude diagram, 7) balloon track, and 8) hodograph. Examples of several of these graphs from launch 1 of IOP1 are shown in Figs. 58-63.

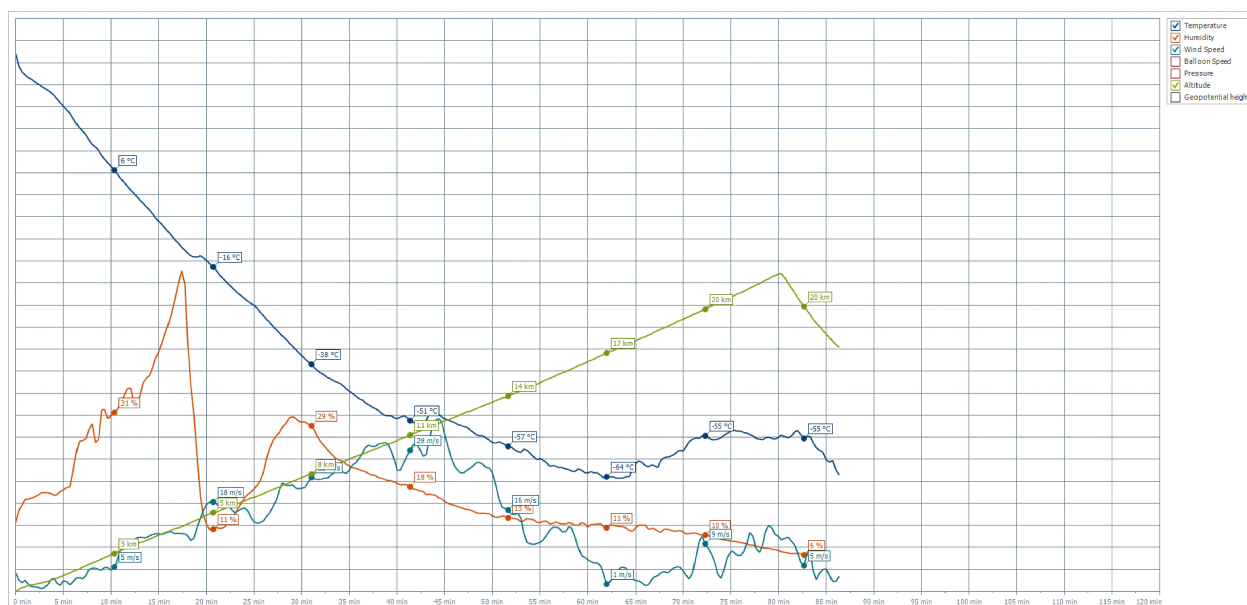


Figure 58. Example balloon profile data diagram from IOP1, Launch 1, with atmospheric pressure (green), relative humidity (orange), air temperature (blue), balloon ascent rate (black), wind speed (red), and radiosonde height AGL (black) plotted as a function of time after launch. The time stamp is the start of the ascent in UTC.

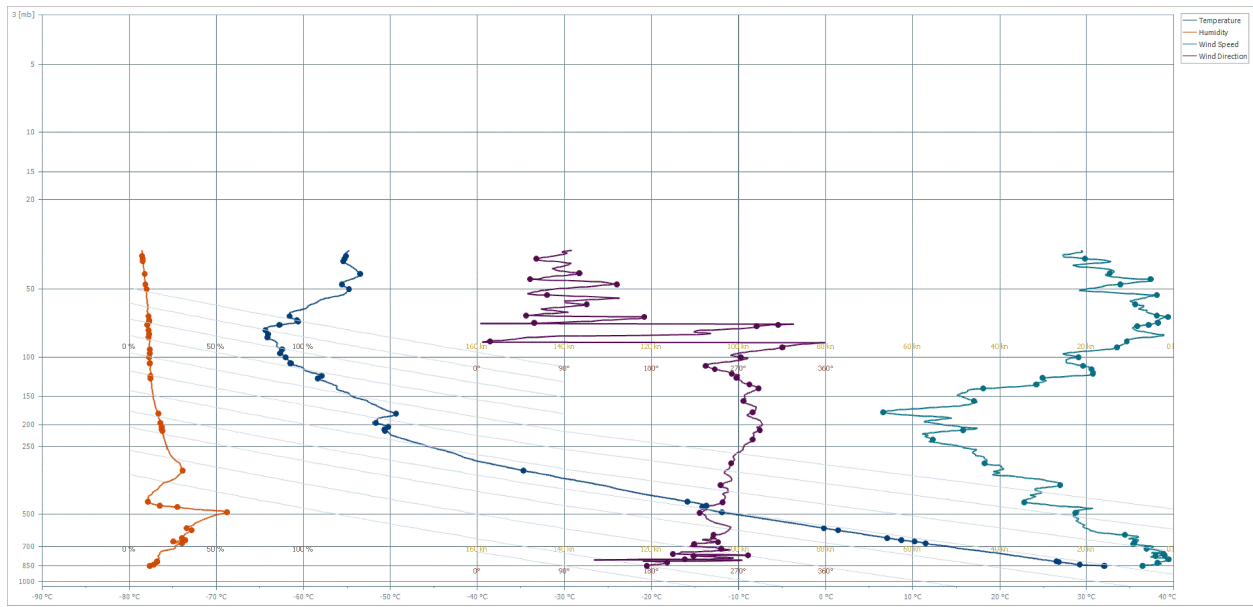


Figure 59. Example thermodynamic (Stueve) diagram from IOP1, Launch 1, with relative humidity (orange), air temperature (blue), wind direction (black), and wind speed (red) plotted as a function of geopotential height MSL. The time stamp is the start of the ascent in UTC.

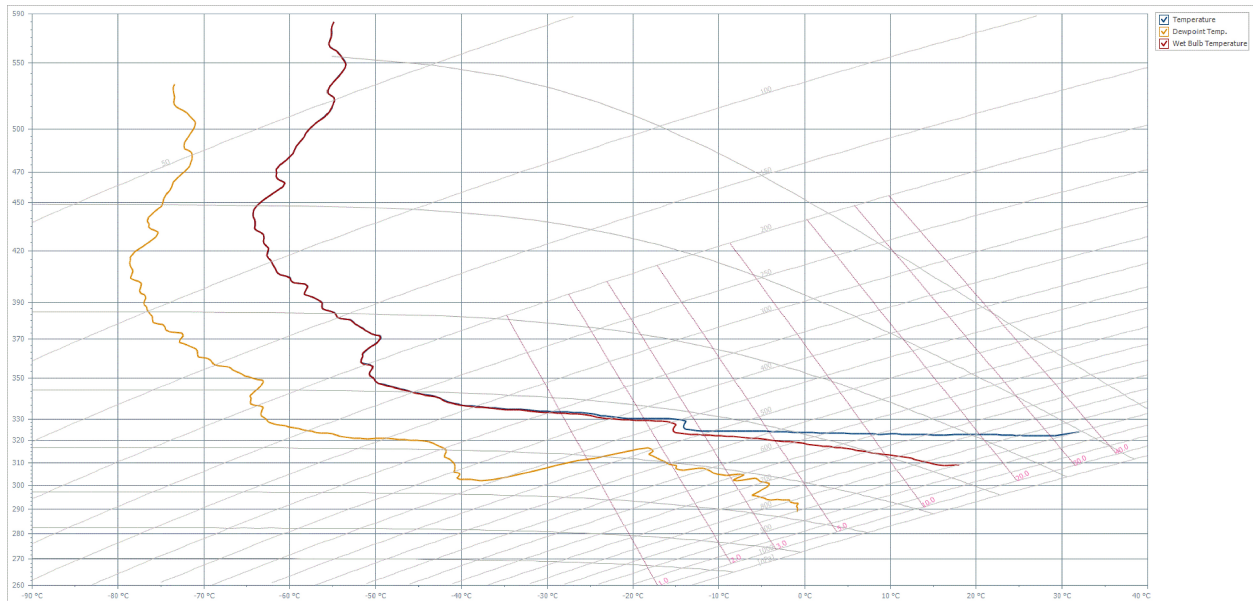


Figure 60. Example tephigram from IOP1, Launch 1, with air temperature (blue), wet bulb temperature (red) and dew point temperature (orange) plotted on a temperature/potential temperature graph. The time stamp is the start of the ascent in UTC.

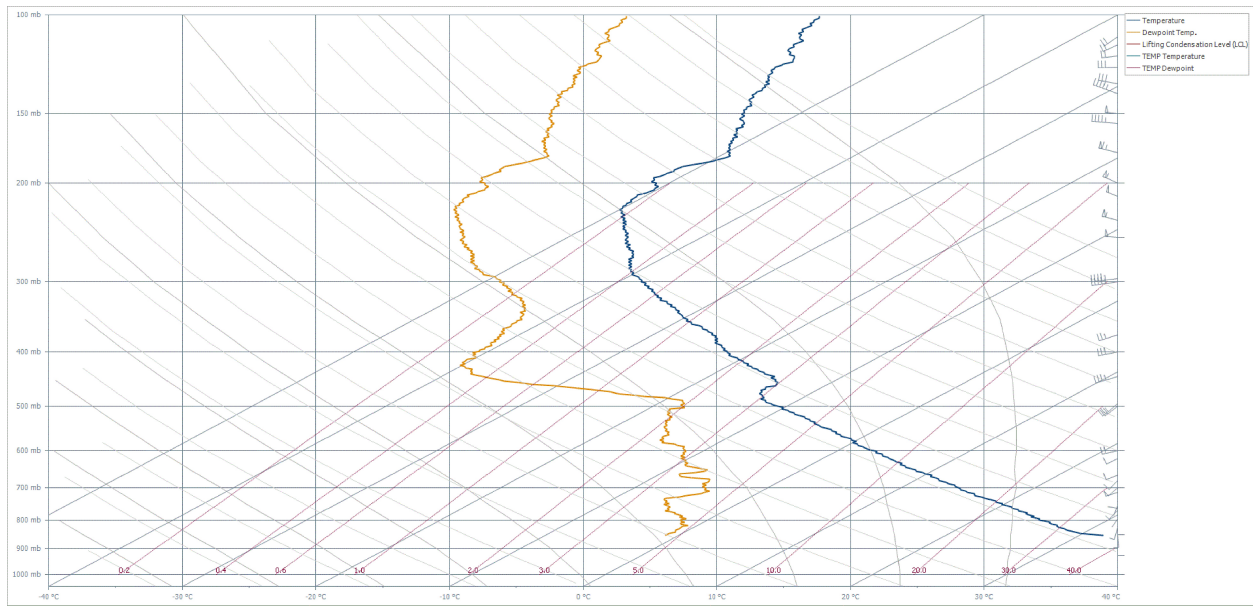


Figure 61. Example Skew-T diagram from IOP1, Launch 1, with air temperature (blue) and dew point temperature (orange) plotted on a temperature/pressure graph. The time stamp is the start of the ascent in UTC.

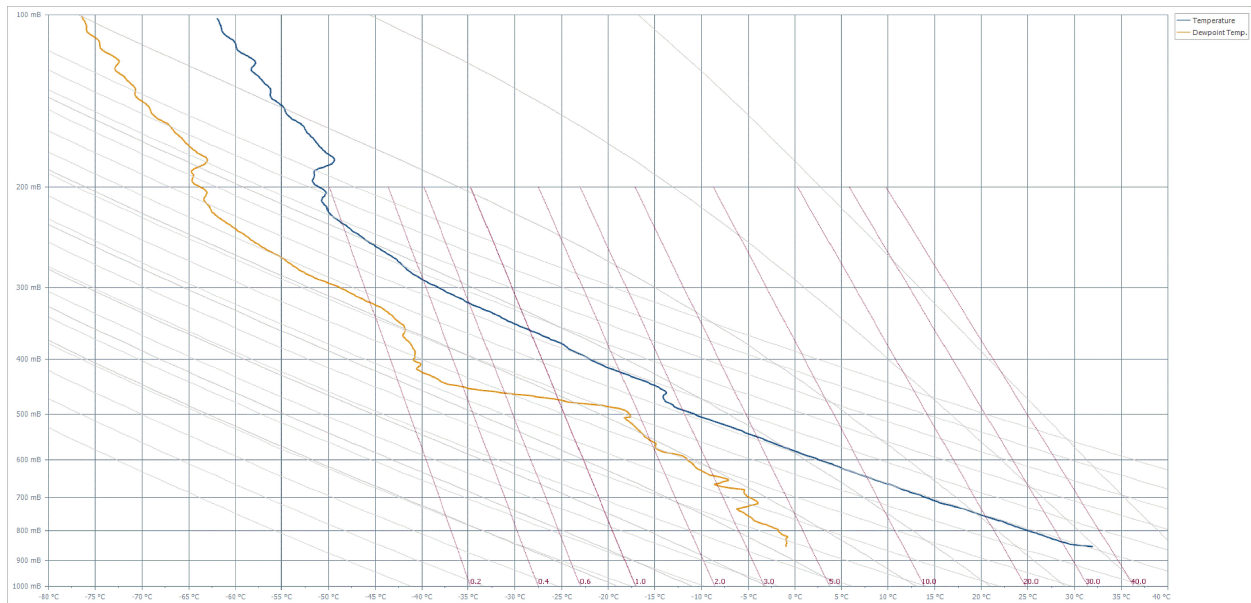


Figure 62. Example emagram from IOP1, Launch 1, with air temperature (blue) and dew point temperature (orange) plotted on a temperature/pressure graph. The time stamp is the start of the ascent in UTC.

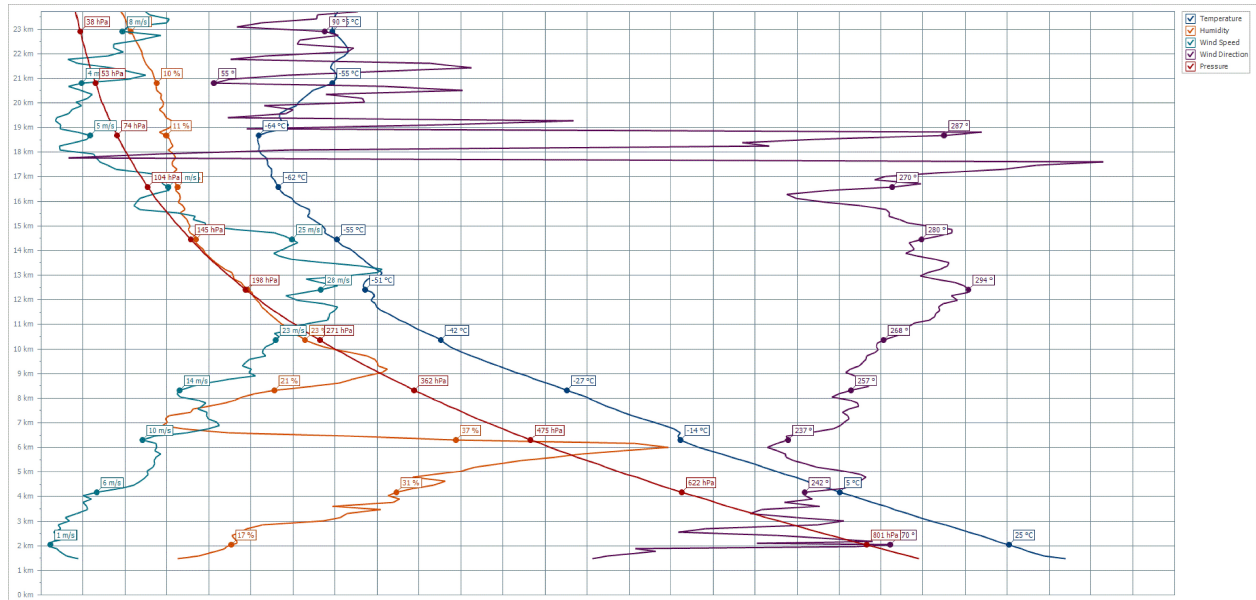


Figure 63. Example altitude diagram from IOP1, Launch 1, with wind speed (red), relative humidity (orange), temperature (blue), and wind direction (black) plotted as a function of height. The time stamp is the start of the ascent in UTC.

Ceilometer

A Vaisala CL31 ceilometer was deployed by WSULAR near the mobile tower during IOPs 5-8 at a little less than 400 m distance at approximately 54° azimuth (Fig. 5). Tables of the measurement of ‘BL_Height1’ for the 4 h periods covering IOPs 5-7 are included in the Summary of Individual IOPs chapter. No data is available for IOP8. The data for IOPs 5-7 for 10 and 30 min averaging periods are provided on an as is basis in the files ‘IOPn_Ceil.csv’ where ‘n’ is the test number.

NOAA/INL Mesonet

Configuration

ARLFRD has maintained a large network of (presently) 34 meteorological stations or towers across the Eastern Snake River Plain that includes the INL and the local test area at Grid 3. This network provided a complete historical archive of wind speed, wind direction, air temperature, and other data. This database served as the source for graphical wind rose analyses by month of the year and hour of the day. These analyses have guided the optimization of the experimental field configuration to maximize the frequency of winds across the tracer sampling grid from the appropriate direction with the desired range of speeds.

The Mesonet data were collected in Campbell Scientific CR23X data loggers and recorded as averages, totals, or extremes for 5 min periods. Wind speed, wind direction, air temperature, relative humidity, and solar radiation were measured every 1-sec and averaged over the 5 min periods. Precipitation was totaled for the same 5-minute interval. The maximum and minimum 1-min averages were used as the maximum and minimum air temperatures for each 5-min period. A 3 s average wind gust is selected as the maximum of a 3 s running average of wind speed. Data was collected and transmitted every 5 min by a radio link back to the FRD office and eventually onto the Internet. The project manager was able to access the Mesonet data in the command center during the test via Internet connection.

Quality Control

The cup anemometers and wind vane measurements, as well as all other measurements, on GRI, COC, and the NOAA/INL Mesonet were all calibrated to the rigorous standards described previously.

Data File Formats

Files in this section contain subsets of data from the NOAA/INL Mesonet towers near the location of PSB2. The mesonet data is broken up into 3 different files containing 5-min averages for each day. The first file contains 'PSB2_RING1_IOP#_5min' stations that are within a 10 miles radius from Grid 3. The '#' designates the IOP. The nine ring 1 stations include the stations 690, BAS, DEA, GRI, LOS, NRF, PBF, RWM, and TRA. The second file for each day is called 'PSB2_RING2_IOP#_5min' and contains stations that are between 10-20 miles radius from Grid 3. Those 10 stations are ARC, ATO, BIG, EBR, HOW, LOF, ROV, SAN, SUM, and TAB. A third file is called 'PSB2_TOWER_IOP#_5min' and contains the additional data for the 3 tall towers. Those 3 tall towers include GRI, EBR, and LOF. All files are archived in csv format.

There are corresponding sets of 10 and 30 min average files. They have the same naming convention except with a '10min' or '30min' preceding the IOP designation.

The first record in each file is a header record. The first four columns in each header record are the year, month, day of month, and time in hhmm format for the end of the listed time period for the data record. Times listed are Mountain Standard Time (MST) at the *end* of the averaging period. The following columns in the header record describe the location, height, description of the measurement, and the units of the measurement. The general format of these column headers is 'NNN ##M MMMM Units' or 'NNN ##M FFFF' where 'NNN' is a 3-character site identifier (tower code), '##' is the height of the measurement (agl, m), 'MMMM' is a description of the measurement, 'FFFF' is a quality flag code, and 'Units' specifies the units of the measurement. The measurement and flag fields are always paired in successive columns. Additional details are provided in the accompanying ReadMe file.

The tower code, latitude, longitude, elevation and facility or location name of each of the mesonet stations are listed below:

Tower Code	Latitude (deg N)	Longitude (deg W)	Elevation (ft MSL)	Facility or Location Name
690	43.532598	112.947757	4,950	Central Facilities Area Building 690
ABE	42.954968	112.824550	4,392	Aberdeen
ARC	43.624522	113.297087	5,290	Arco
ATO	43.443700	112.812400	5,058	Atomic City
BAS	43.677557	113.006053	4,900	Base of Howe Peak
BIG	43.294095	113.181607	5,200	Cox's Well
BLK	43.189867	112.333300	4,520	Blackfoot
BLU	44.074897	112.842082	5,680	Blue Dome
CRA	43.429115	113.538265	5,996	Craters of the Moon
DEA	43.624868	113.059840	5,108	Dead Man Canyon
DUB	44.242393	112.201815	5,465	Dubois
EBR	43.594138	112.651713	5,143	Materials and Fuels Complex
FOR	43.019833	112.412068	4,452	Fort Hall
GRI	43.589718	112.939855	4,897	Grid 3/INTEC
HAM	44.007535	112.238845	4,843	Hamer
HOW	43.784113	112.977358	4,815	Howe
IDA	43.504078	112.050117	4,709	Idaho Falls
KET	43.547555	112.326315	5,190	Kettle Butte
LOF	43.859793	112.730253	4,790	Specific Manufacturing Capability
LOS	43.548538	113.008460	4,983	Lost River Rest Area
MIN	42.804510	113.589783	4,285	Minidoka
MON	44.015378	112.535885	4,797	Montevieu
NRF	43.647887	112.911193	4,847	Naval Reactor Facility
PBF	43.547477	112.869697	4,910	Critical Infrastructure Test Range Complex
RIC	43.058408	114.134670	4,315	Richfield
ROB	43.742210	112.125752	4,760	Roberts
ROV	43.720590	112.529560	5,008	Rover
RWM	43.503362	113.046030	5,025	Radioactive Waste Management Complex
SAN	43.779632	112.758165	4,820	Sand Dunes
SUG	43.896578	111.737600	4,895	Sugar City
SUM	43.396300	113.021800	7,576	Big Southern Butte Summit
TAB	43.318700	112.691875	4,730	Taber
TER	43.841650	112.418305	4,792	Terreton
TRA	43.584612	112.968653	4,937	Reactor Technology Complex

Summary of Individual IOPs

Introduction

The tracer data concentrations will be represented graphically in several ways. The first is map plan views. The second is cross-sectional representations of concentrations along the arcs. The third is a set of vertical profiles of concentration measurements on the towers. Finally, there is a set of representations of the fast response analyzer results. In most cases, the log of the concentrations will be shown due to the often very wide range. In some cases the actual values were used where the range in a graph was small and the concentrations generally at or near background levels.

The map presentations of the 10-min average bag sampling results for the individual IOPs shows colored markers for each ground-based 1 m agl sampling location. These provide an overall spatial and temporal representation of the plume. There are two sets of maps with dots at each location based upon (1) the measured SF₆ concentration (χ) in parts per trillion by volume (ppt) and (2) the normalized concentration χ/Q (ppt s g⁻¹). The first is intended to provide the reader with a sense of the actual measured concentrations while the second provides a basis for comparison of results between IOPs independent of the release rate Q . It was decided not to use concentration contouring to represent the plumes as the plume concentrations were often highly irregular.

Given the often very large measured SF₆ concentrations and the low Q , the normalized values were often very large in magnitude and somewhat unwieldy to work with. For this reason, the daytime normalized results were multiplied by an adjustment factor $F = 0.01$. Despite the fact that the nighttime Q were about one-tenth of the daytime Q , the measured nighttime SF₆ concentrations were generally larger by about an order of magnitude. For this reason the nighttime normalized results were multiplied by $F = 0.001$.

The color code for the markers, day and night, of SF₆ concentrations is:

	<u>ppt</u>
Gray	< 15
Purple	15-100
Blue	100-500
Green	500-2500
Olive	2500-5000
Orange	5000-10000
Red	> 10000

The color code for the normalized concentrations $F^*\chi/Q$ is:

	$F^*(\text{ppt s g}^{-1})$
Gray	< 1
Purple	1-5
Blue	5-25
Green	25-100
Olive	100-250
Orange	250-500
Red	> 500

The selection of these bins and the use of F had the effect that coloration of the markers on each map set for a given IOP were often the same or similar between the measured concentration and normalized map types. In all cases, gray represents ambient background concentrations and purple low level concentrations greater than background. It will be seen that the overall levels of concentrations during the nighttime IOPs were often about an order of magnitude greater than the daytime IOPs. Even after a larger adjustment by F , the coloration associated with the normalized nighttime plumes was skewed toward reds and oranges relative to the daytime results.

The interpretation of concentrations on the arc cross-sections is straight forward. Cross-sections of both the SF_6 (ppt) and normalized (χ/Q) concentrations are shown. The χ/Q results shown in the cross-sections were *not* adjusted by an F so that direct comparisons of normalized concentrations across IOPs can be made.

Vertical concentration profiles showing the temporal evolution at each tower are shown. The nighttime IOPs featured tracer measurements on an additional four towers. Therefore, for the nighttime IOPs, the vertical concentration profiles from each tower are grouped together for each 10-min averaging period. This is intended to provide a sense of how the plume was behaving in the vertical across the array at a given time.

The fast response concentration time series are also color coded according to the flag values listed in the Fast Response Tracer Analyzer chapter. Flags 1, 2, and 5 (values < MLOQ) are shown in gray. Flag 0 (good values) is shown in green. Code 3 (> 115% of highest calibration) is shown in orange. Code 9 (measurement problem and/or > 130% of highest calibration) is shown in blue. Code 4 (overranged, railed) is shown in purple. The remaining codes were designated 'NaN' and were not plotted. Red traces for IOPs 5-8 are independent of any code and indicate periods when the analyzer was on the move between fixed locations.

The fast response analyzers measure the tracer concentration above background and the bag samplers measure total concentration including background.

For the daytime IOPs, IOPs 1 and 2 provide the best overall cases for analysis. Truncation at one or both edges of the plume was much more common during IOPs 3 and 4. For

the nighttime IOPs, IOPs 5 and 7 should be interesting case studies. Edge effects were present during these IOPs but most of the plume subtended the sampling arcs most of the time. The first hour of IOP8 could be an interesting study although conditions deteriorated during the second hour. IOP6 was rather severely affected by truncation.

IOP1

Date/Time and General Description

IOP1 was conducted on 26 July from 1200-1400 MST (1300-1500 MDT). Conditions were hot and dry with light and variable winds throughout the IOP. Skies were clear and sunny during the first hour of the measurement period with some cloudiness during the second hour. Overall conditions were unstable and highly non-stationary in both time and space. Estimates of stability based on traditional Pasquill-Gifford (P-G) schemes were mainly class A during the first hour and class C during the second hour (Fig. 64). Estimates of mean z/L from GRI ranged from -0.30 to -0.58 with a bulk Richardson number (Ri_b) of -1.59. The tracer plume mostly tracked across the bag sampler array although it was common for one or both limbs of the plume to be truncated at the edge of the array. A summary of the meteorological conditions during IOP1 are shown in Table 18. The SF_6 release rate was 0.192 g s^{-1} (Table 2). The fast response analyzers were located on the 100, 200, 400, and 800 m arcs at 42, 36, 36, and 30 degrees azimuth, respectively. Their positions were fixed for the duration of the IOP.

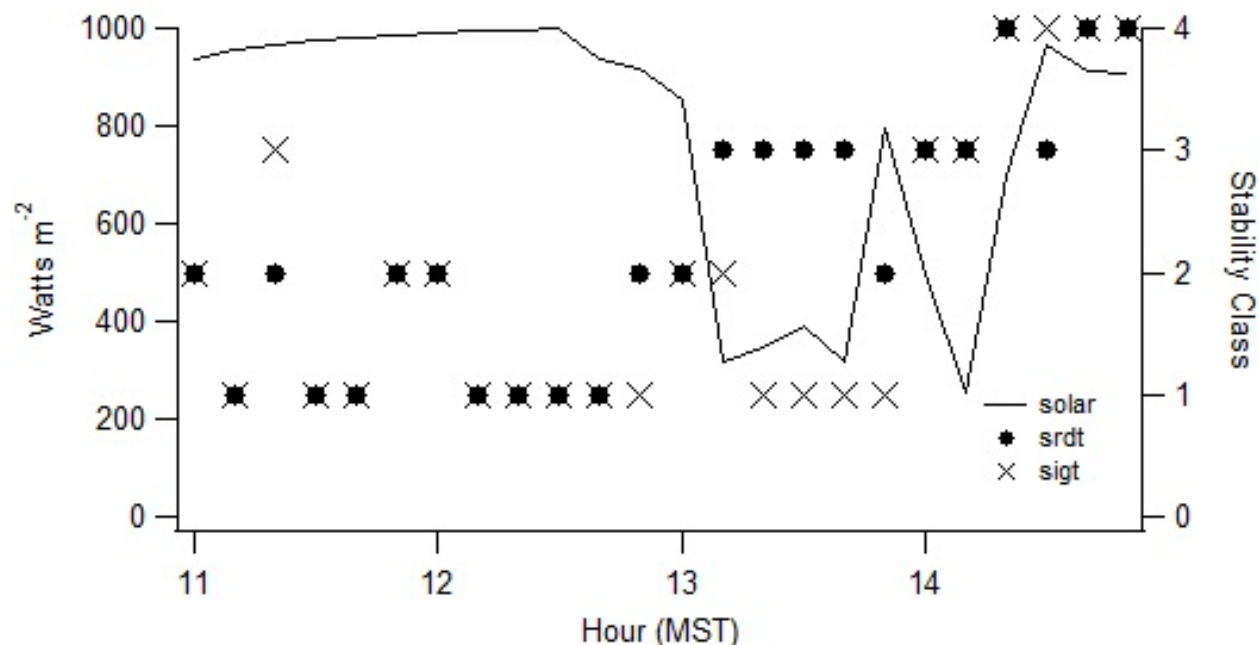


Figure 64. Incoming solar radiation and classification of stability conditions using the Pasquill-Gifford Solar Radiation Delta T (srdt) and σ_0 (sigt) methods (U.S. EPA 2000c) during IOP1. Classes A, B, C, and D are designated 1, 2, 3, and 4, respectively.

Table 18. Meteorological conditions during IOP1.

	COC				GRI						GRI			Solar
	U (m s ⁻¹)		WD (deg)		U (m s ⁻¹)		WD (deg)		σ_θ (deg)		L	L	degC	W m ⁻²
Bag	2m	10m	2m	10m	2m	10m	2m	10m	2m	10m	3.7m	9m	2m	
1	2.0	2.5	67.3	67.9	2.6	3.1	169.7	168.3	34.3	21.4	-10.1	-23.9	32.1	992.5
2	2.4	3.2	82.8	86.9	2.2	2.3	103.4	100.7	43.5	37.3	-5.1	-0.9	32.1	996.5
3	2.9	3.5	143.3	147.0	1.5	1.6	106.4	81.3	72.5	66.0	-51.6	-70.1	32.7	996.0
4	2.2	2.3	271.2	264.3	1.8	2	69.5	75.7	39.4	35.8	-0.6	-8.9	32.4	999.0
5	1.6	1.9	92.8	97.2	1.3	1.7	111.5	113.6	66.2	59.1	-4.6	-4.1	32.4	936.0
6	2.0	2.4	203.9	178.5	1.6	2.0	126.5	120.4	65.7	46.2	-28.8	-21.0	32.7	916.5
7	2.6	3.3	185.0	186.3	2.5	3.0	197.9	195.0	52.7	55.3	-4.6	-5.5	33.8	853.5
8	2.5	3.1	170.3	169.0	2.4	3.0	196.9	191.8	51.6	48.9	-7.0	-15.9	32.8	316.4
9	1.6	1.9	224.8	220.9	1.6	1.9	168.8	166.8	31.3	24.7	-5.3	-6.7	32.5	346.3
10	2.1	2.3	305.3	300.4	0.7	1.1	149.1	152.3	39.6	34.3	-10.3	-7.3	32.5	388.8
11	2.5	3.4	247.6	244.1	1.6	1.9	258.7	258.6	41.8	55.0	NaN	-13.4	32.3	317.9
12	2.0	2.4	209.1	201.6	2.3	2.8	233.9	233.4	28.1	25.9	-5.9	-9.6	33.1	792.9
Avg. L											-12.17	-15.62		
z/L											-0.30	-0.58		
Ri _b												-1.59		

Wind Speed and Direction Quality Assurance

Figures 65-67 show wind speed and direction time series comparisons for a sequence of measurement heights during IOP1. In Fig. 65, the near surface measurement of U was consistent at all stations except for a deviation at COC in the last hour after tracer sampling had ceased. Wind directions at all three sites shown (GRI, COC, G2) varied considerably in the horizontal but there was good agreement between all 3 anemometers at GRI. Wind speeds were light throughout the tracer release period although U began to increase at the end of the period at GRI and G2. The wind speed and direction comparisons between 9 and 30 m agl showed a similar pattern with consistent wind speed measurements but variability in wind direction in the horizontal (Fig. 66). That includes the sodar measurements at 30 m agl. Much the same can be said for the upper level measurements although there is insufficient data available from the sodar (SOD) and radar profiler (PRO) to make any realistic comparison (Fig. 67). Other than the poor data recovery for SOD and PRO at 160 m agl, there is little evidence of a systematic measurement problem. Any of the observed variability or discrepancies are likely attributable to non-stationarity and horizontal inhomogeneity in the wind field.

Figure 68 shows time series measurements for cup anemometers and wind vanes only (excluding sonics) at all heights on the two towers during IOP1. There was a large variation in wind direction with σ_θ often in excess of 40°, especially near the surface.

Turbulence

The available near surface turbulence measurements are mostly consistent with some exceptions (Fig. 69). These include the apparent high bias in measurements of σ_ϕ (σ_w/U) at G2 relative to those at GRI and the sharp excursion in TKE at G2 during the second hour. The drop in sensible heat flux $\langle wT \rangle$ during the second hour is consistent with the decrease in solar radiation at that time (Table 18).

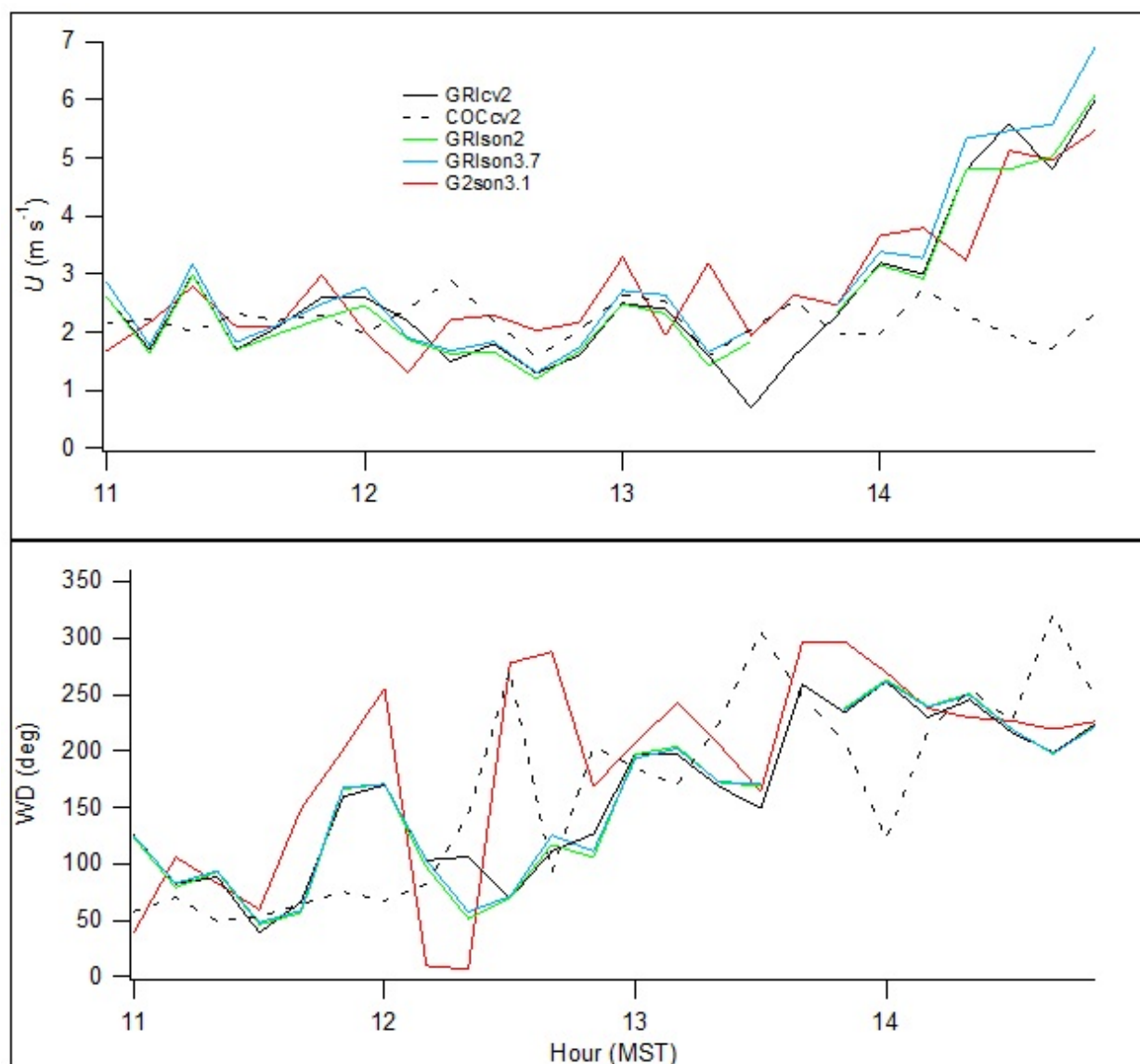


Figure 65. Time series of near surface wind speed and direction measurements during IOP1. In the legend, location is specified in upper case, the measurement type in lower case (cv = cup and vane, son = sonic), and the measurement height numerically.

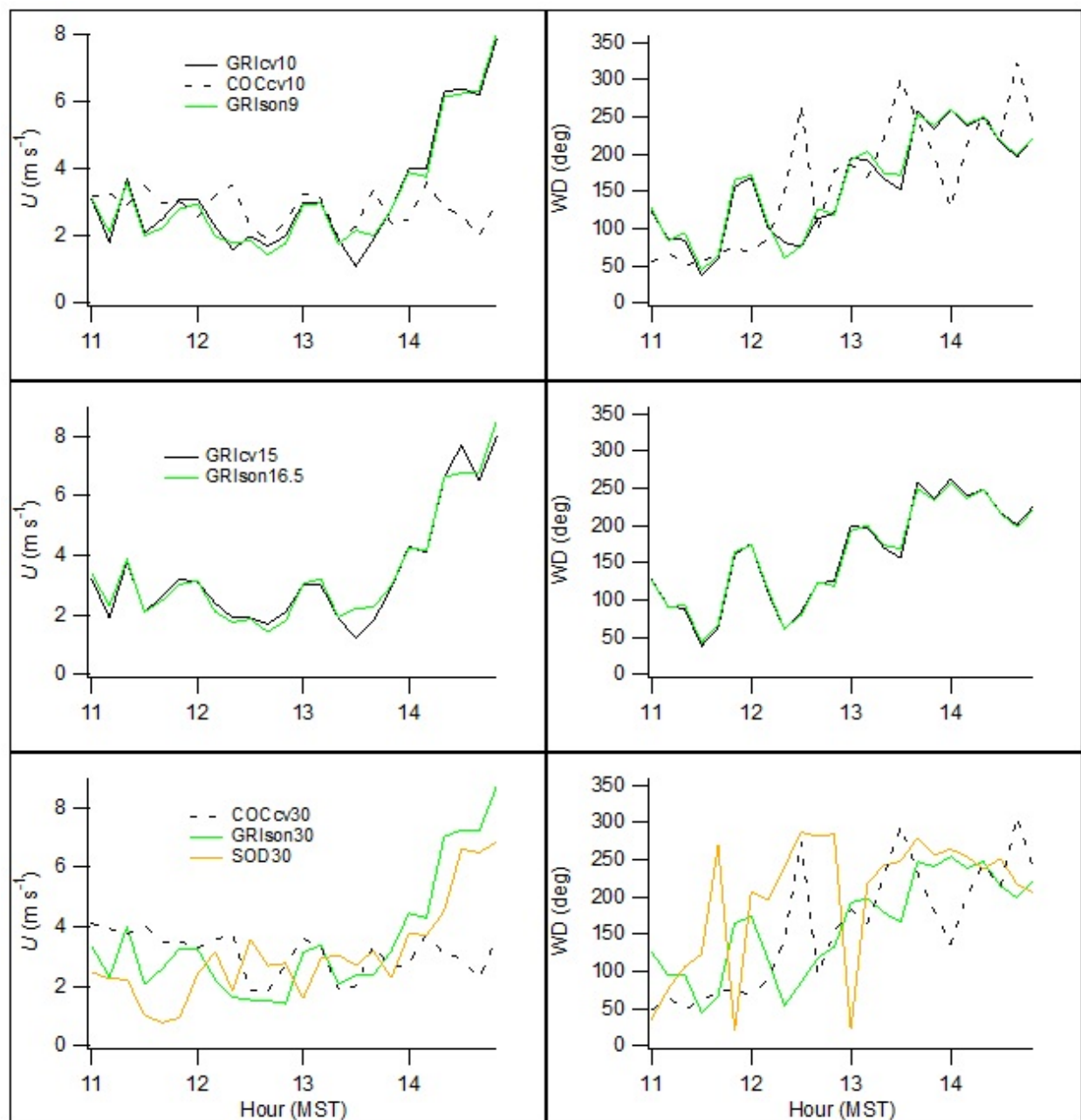


Figure 66. Time series of wind speed and direction measurements at heights between 9 and 30 m agl during IOP1. Legend notations described in caption of Fig. 65.

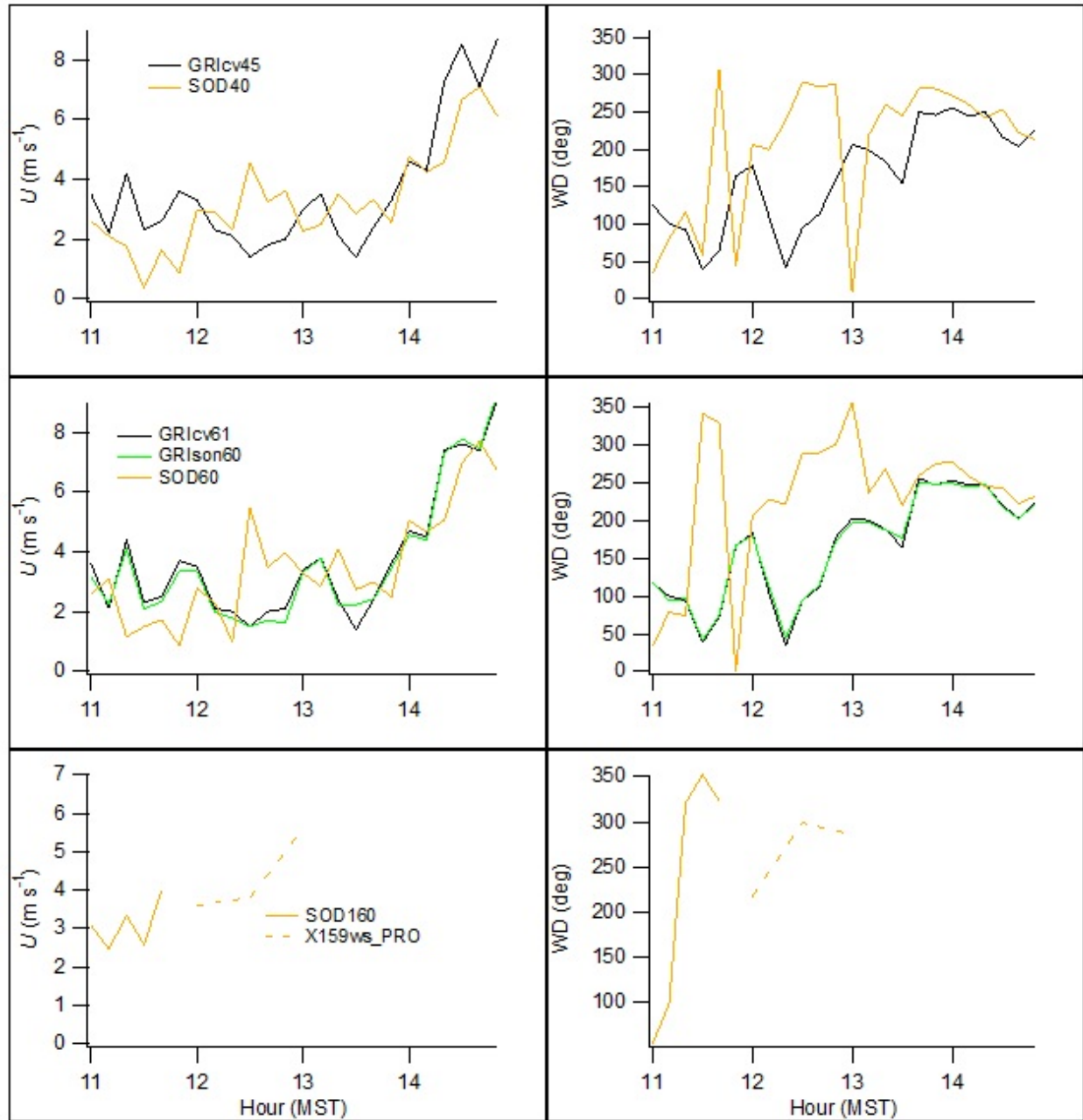


Figure 67. Time series of wind speed and direction measurements at heights above 30 m agl during IOP1. Legend notations described in caption of Fig. 65.

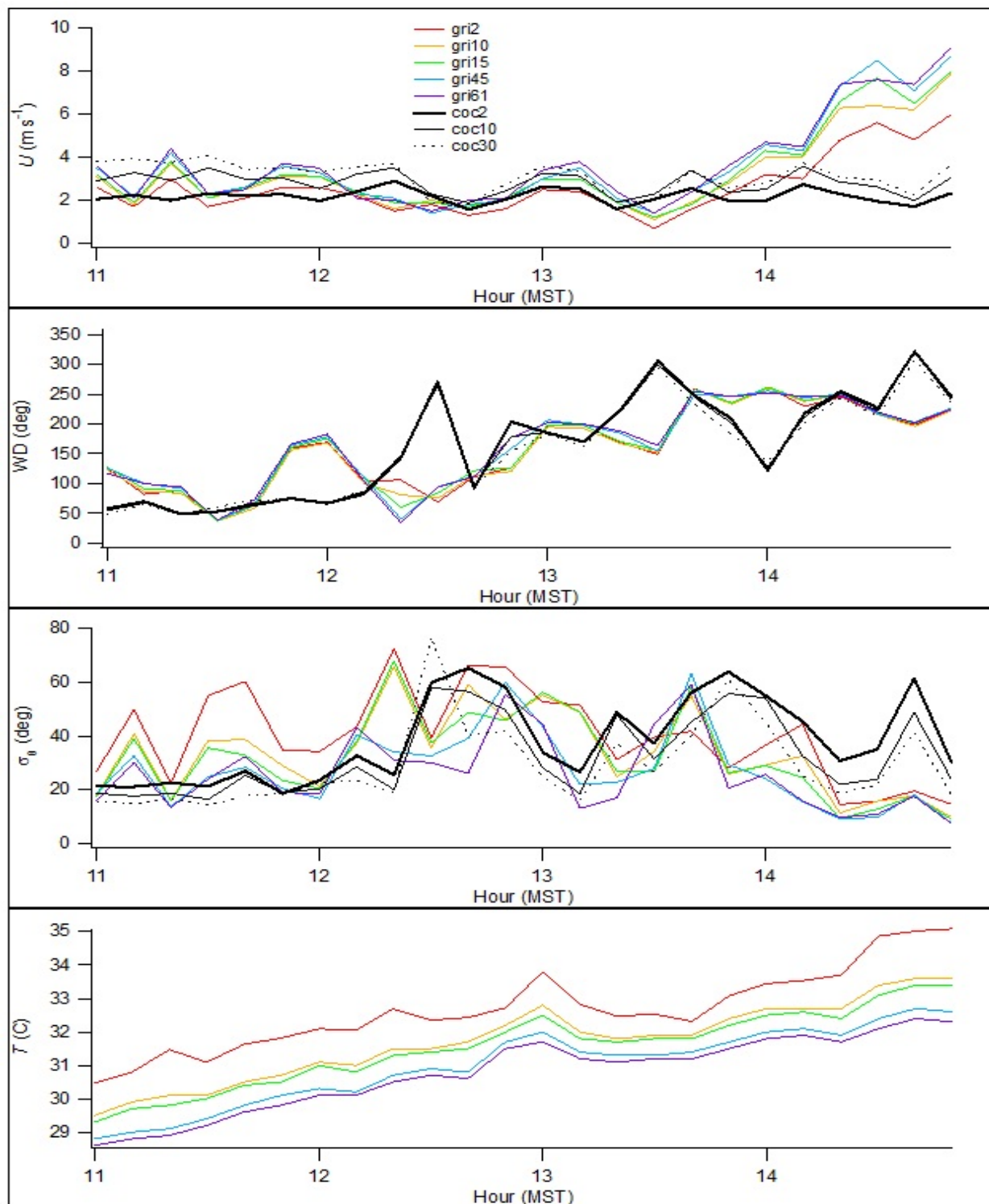


Figure 68. Time series from GRI and COC showing cup anemometer and wind vane measurements of U , wind direction, standard deviation of wind direction σ_0 , and temperature during IOP1. The locations are designated 'xxxx' where xxx = tower and yy = measurement height.

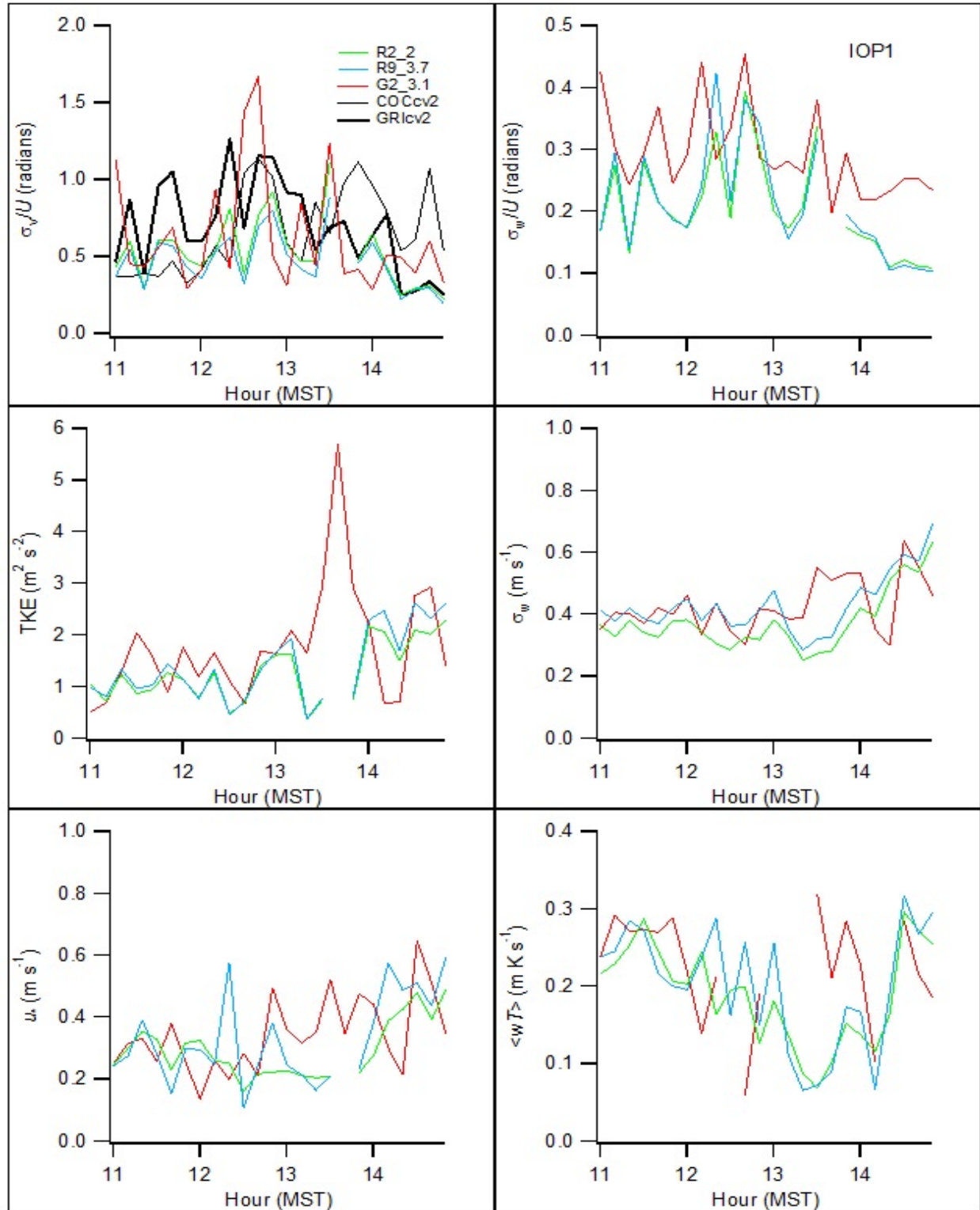


Figure 69. Time series of near surface turbulence (sonic) measurements during IOP1. The GRI and COC are σ_θ wind vane measurements (cv) in degrees converted to radians for purposes of comparison. Notation before and after underscore designates location and height, respectively.

Wind and Turbulence Profiles

Figure 70 shows profiles of the non-sonic measurements at GRI and COC during IOP1. Wind directions were mostly uniform in the vertical within a given profile but the direction was constantly shifting at each 10-minute interval. Wind speed and temperature profiles were consistent with the strong daytime surface heating. The σ_θ were very large and exhibited large variation in both time and in the vertical.

Figures 71 and 72 show profiles of the sonic turbulence measurements at GRI. Profiles of U and wind direction were well behaved and generally consistent with the non-sonic measurements in Fig. 70 with similar ranges of speed and directional variability. The measurements of σ_v/U and σ_w/U were large, as would be expected for low wind speed conditions during daytime. However, the σ_θ from the non-sonic measurements tended to range higher than the corresponding σ_v/U measured by the sonics. They tended to be relatively uniform in the vertical with the exception of anomalous deviations in both measures at the R3 anemometer at 16.5 m agl. In Fig. 72 the friction velocity measurements exhibit considerable variation in time and in the vertical.

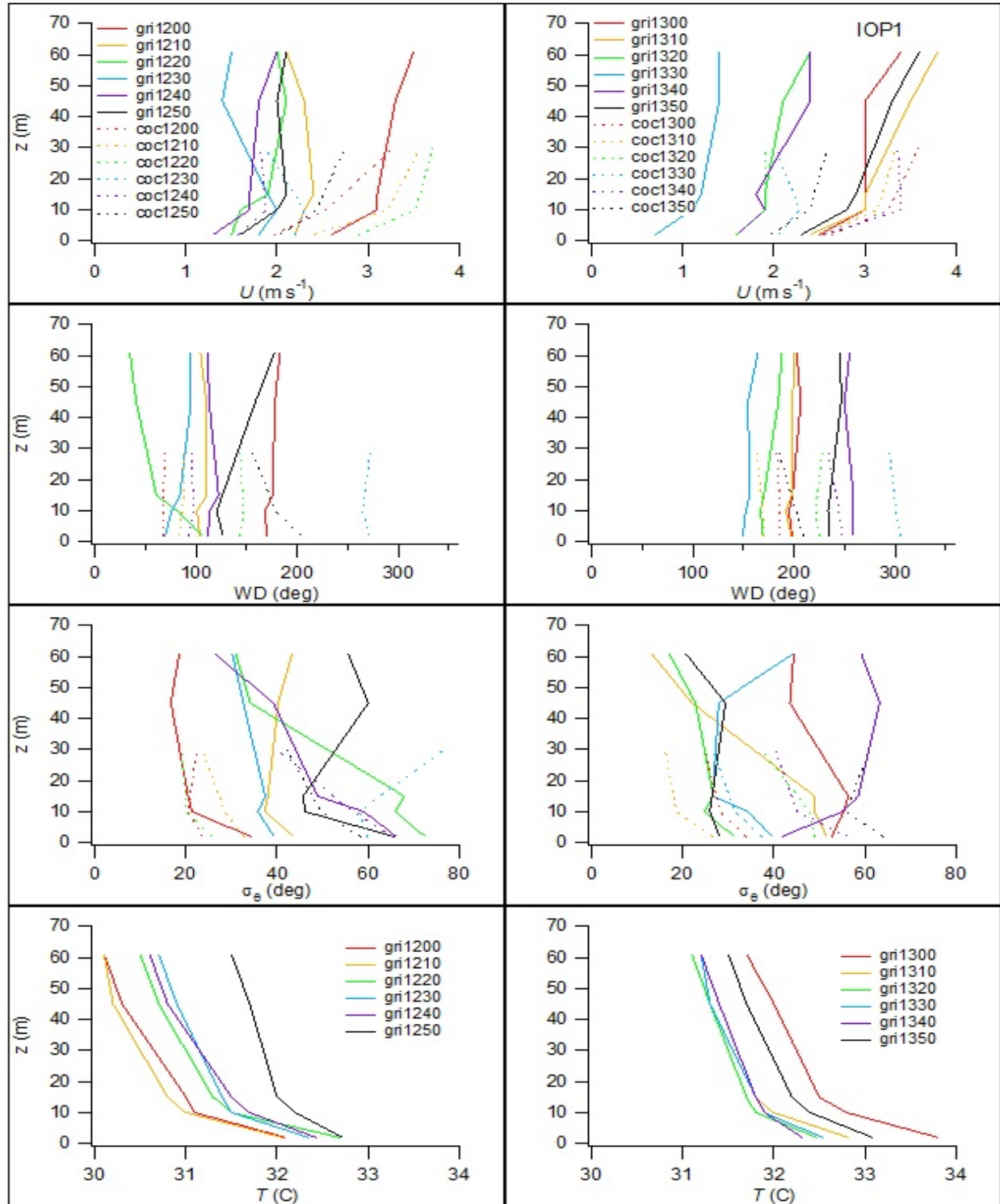


Figure 70. Profiles of U , wind direction, standard deviation of wind direction σ_θ , and aspirated temperature from cup anemometers and wind vanes during IOP1 at GRI and COC. Each profile is designated 'xxxhrmn' where xxx = tower and hrmn = start time of 10-minute interval.

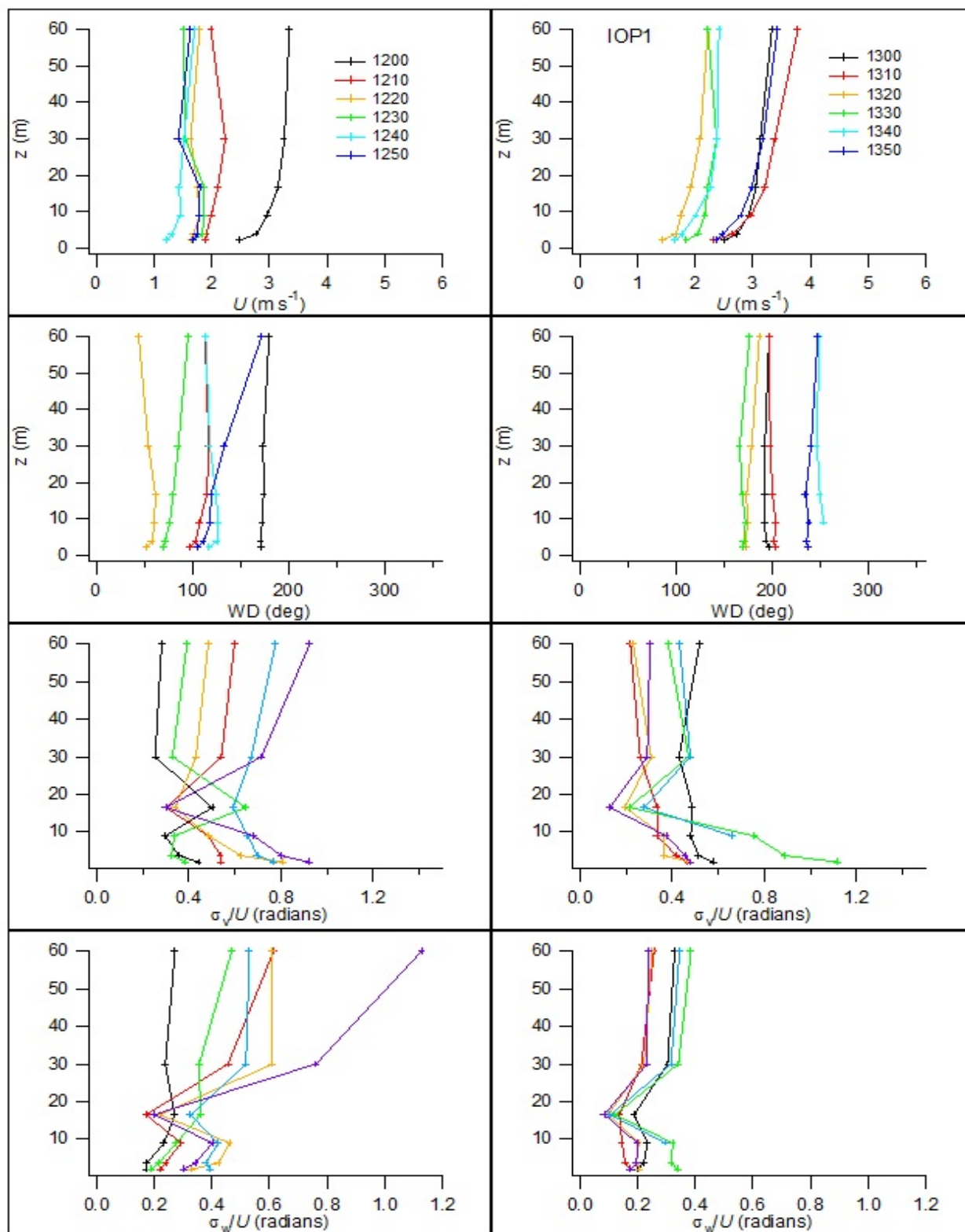


Figure 71. Profiles of U , wind direction, σ_v/U ($\sim\sigma_\theta$), and σ_w/U ($\sim\sigma_\phi$) from sonic anemometers at GRI during IOP1. The legend specifies the start time of the 10-minute interval (hrmn).

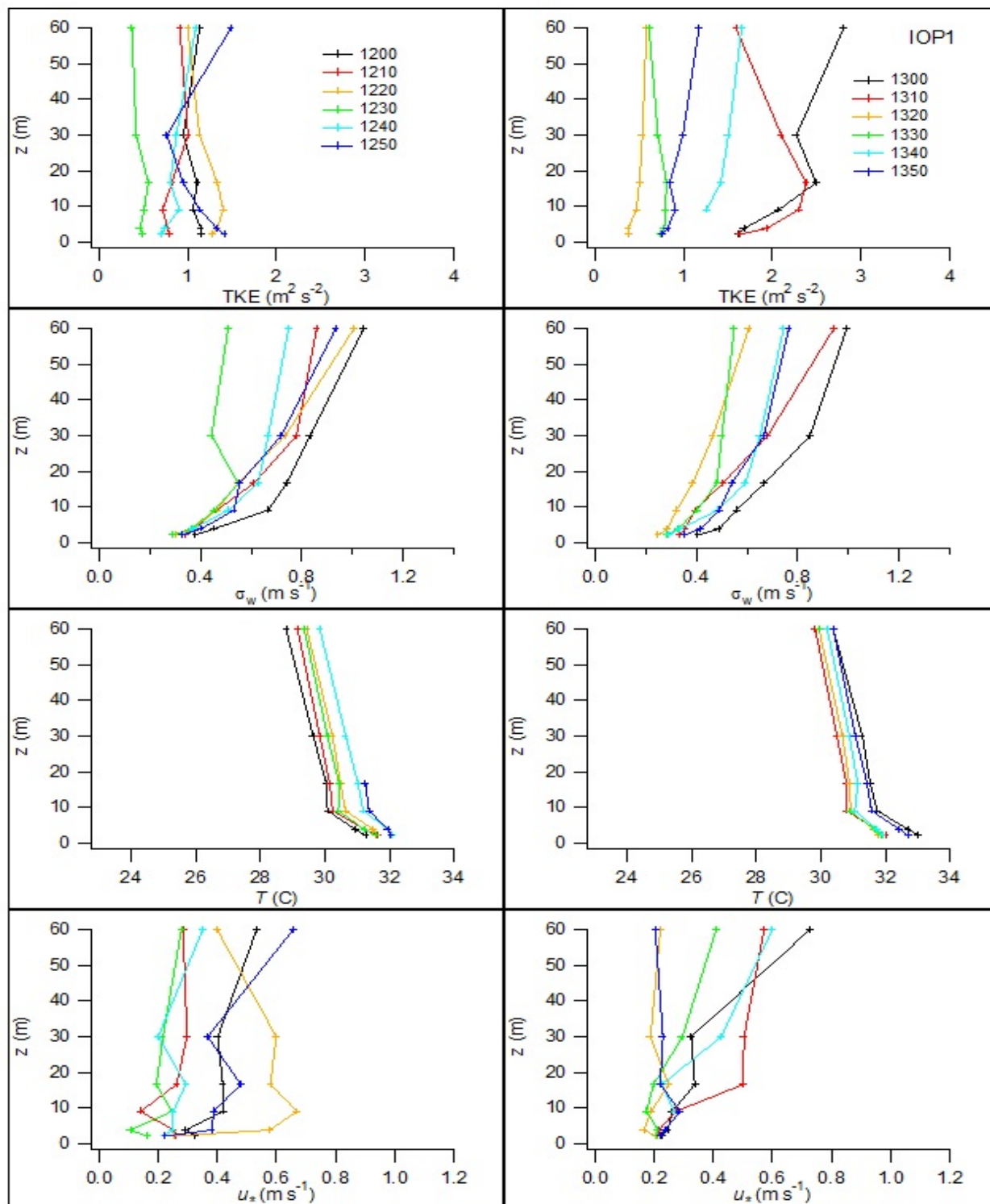


Figure 72. Profiles of turbulent kinetic energy (TKE), standard deviation in vertical wind speed σ_w , virtual temperature, and friction velocity u_* from sonic anemometers at GRI during IOP1. The legend specifies the start time of the 10-minute interval (hrmn).

Figures 73 and 74 show time-height representations of wind speed and direction for SOD and PRO, respectively, during IOP1. Wind directions at SOD were southerly during the first half hour of the tracer measurement period then mainly westerly after 1230 h. The U were mostly in the 2-4 m s^{-1} range. The U were roughly consistent with the U measured at GRI (Figs. 70, 71) but the GRI wind directions tended to be rotated counterclockwise a few tens of degrees relative to SOD. Data recovery at PRO was relatively sparse after 1300 h. The wind directions in the PRO profiles exhibited considerable variability with time and height. A comparison between PRO and the radiosonde results is complicated by the fact that the radiosonde data starts at 1.5 km and data recovery at PRO is limited above that height. The U measured by PRO tended to be somewhat higher than those measured by the radiosonde and the profiles show more variability (see project database for radiosonde data). The available upper level wind direction data for PRO indicating southwest winds aloft is consistent with the radiosonde data.

Figures 75 and 76 show SOD time-height representations of σ_w and TKE, respectively, during IOP1. The σ_w profiles exhibit a roughly periodic pattern, possibly due to thermals. The timing of the peaks of σ_w for SOD appear to lag the timing of the σ_w peaks at GRI by 10 minutes, especially after 1300 h. The large σ_w peak at 1230 h in Fig. 75 does not have an apparent

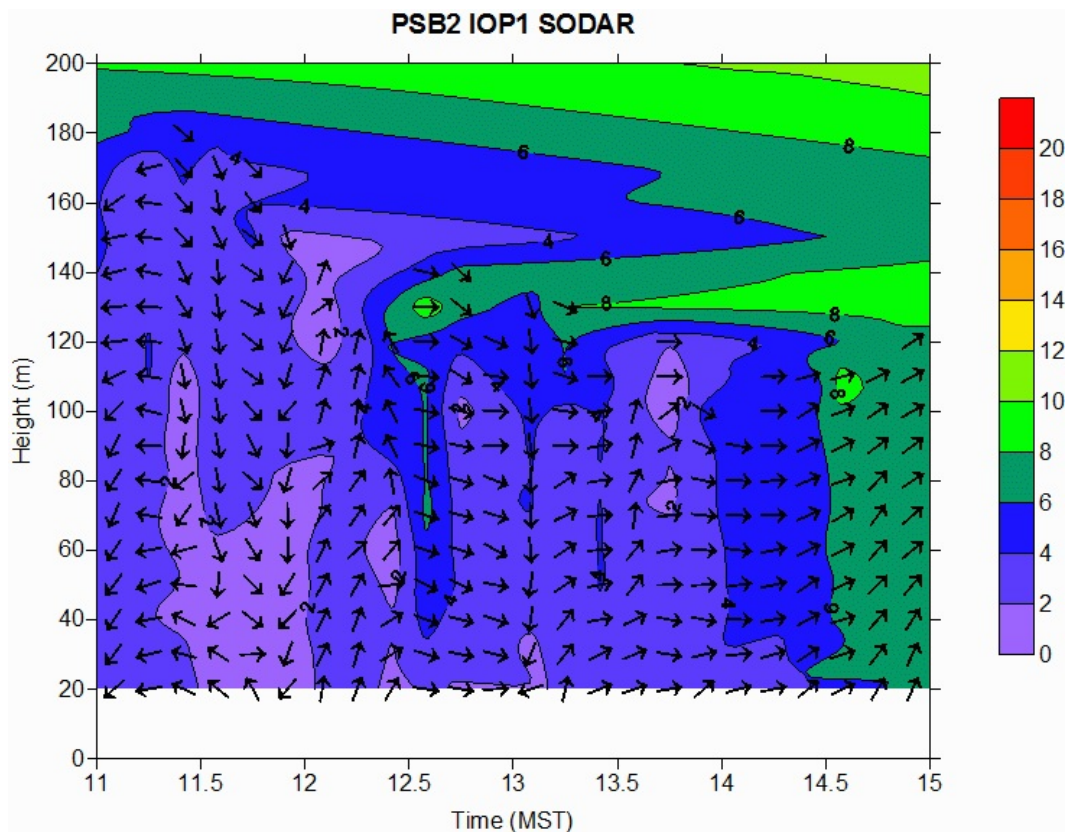


Figure 73. Time-height cross-section of wind speed and direction at sodar (SOD) during IOP1. Legend represents m s^{-1} .

contemporary match to the distinctly higher σ_w in Fig. 72 but the measurements are separated by about 1 km. The magnitudes of σ_w measured by sonic tended to run higher than those measured by SOD at the same height (Figs. 72, 75). The SOD TKE measurements exhibited a similar pattern to that seen for σ_w . The overall magnitudes of TKE measured by SOD (Fig. 76) and sonic (Fig. 72) were similar. The TKE high observed at SOD after 1300 h was matched by some higher GRI TKE profiles at the same time (Fig. 72). Figure 77 shows time-height temperature profiles from the RASS.

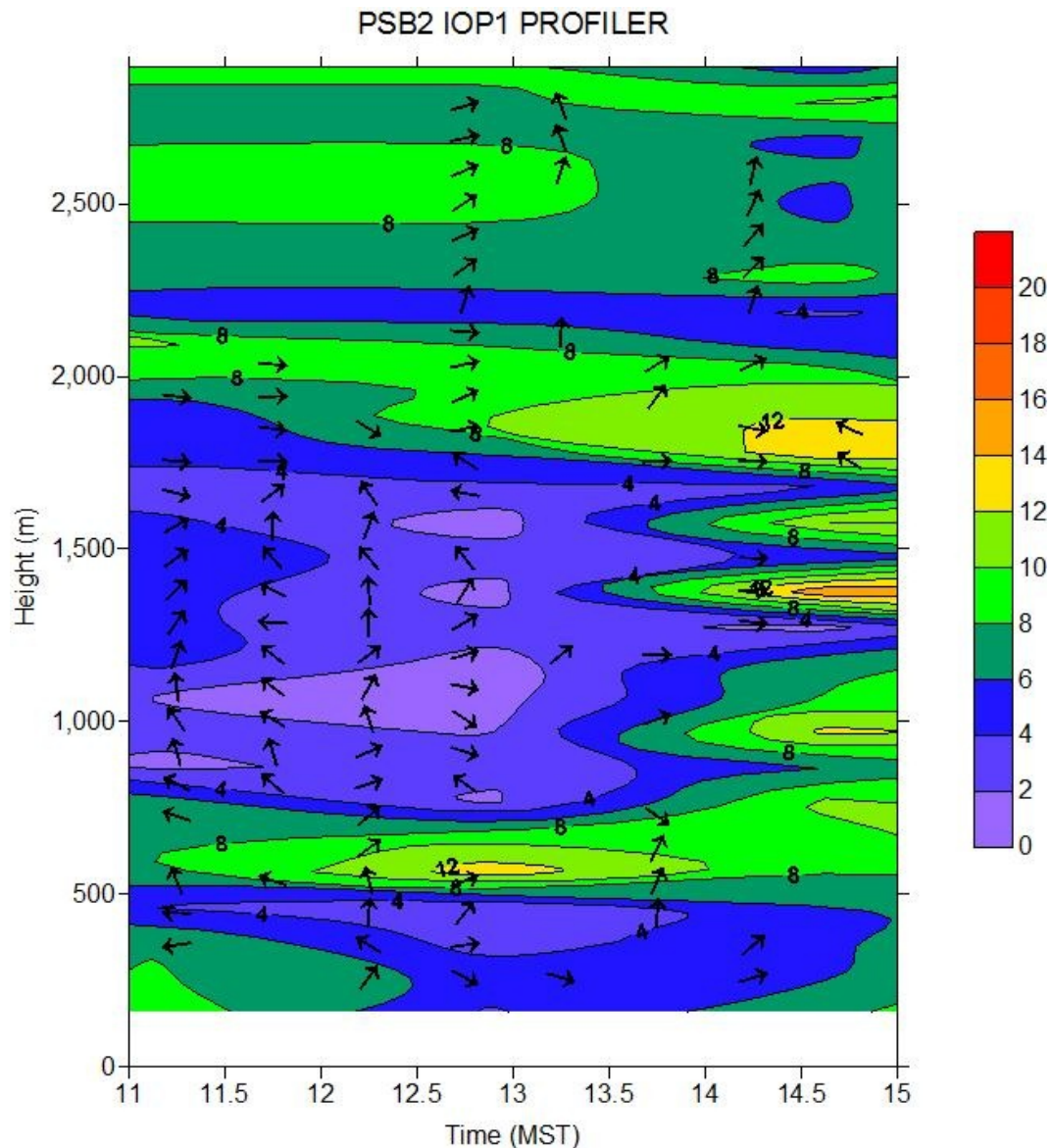


Figure 74. Time-height cross-section of wind speed and direction at wind profiler (PRO) during IOP1. Legend represents m s^{-1} .

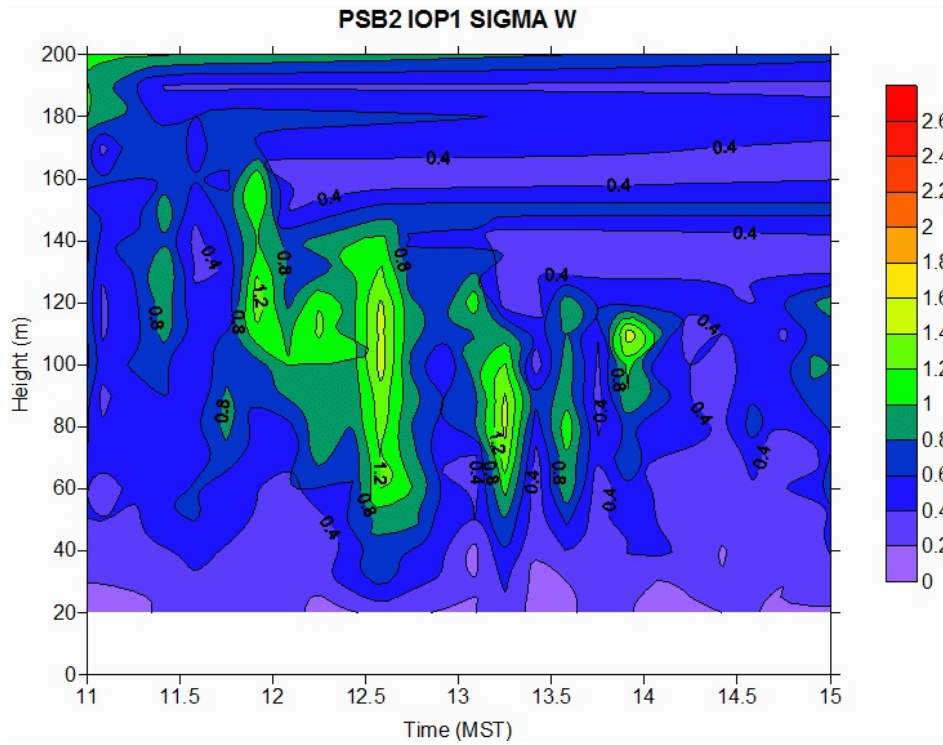


Figure 75. Time-height cross-section of σ_w at sodar (SOD) during IOP1. Legend represents m s^{-1} .

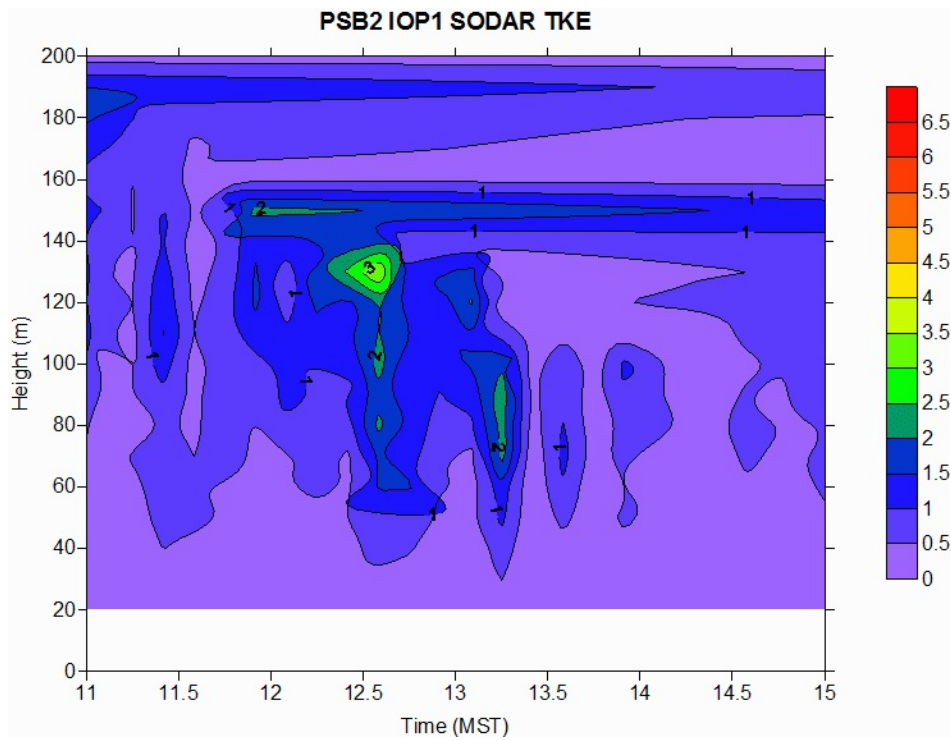


Figure 76. Time-height cross-section of TKE at sodar (SOD) during IOP1. Legend represents $\text{m}^2 \text{s}^{-2}$.

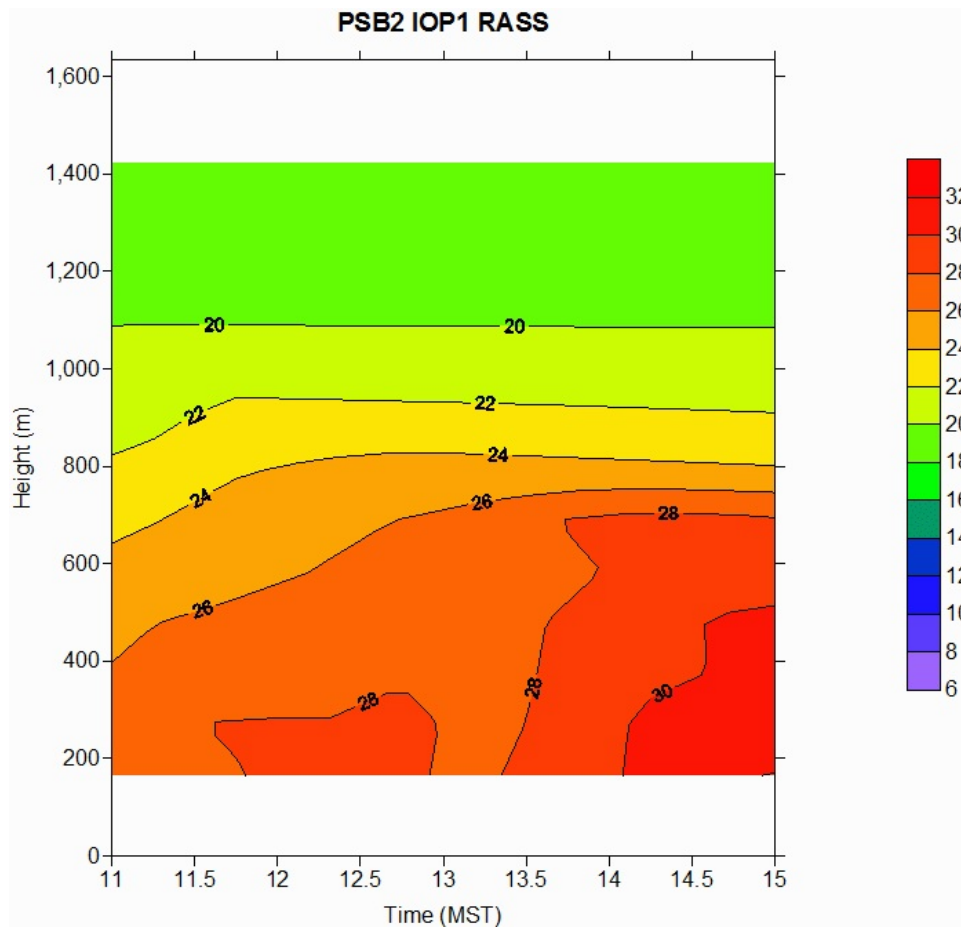


Figure 77. Time-height cross-section of virtual temperature at the RASS during IOP1. Temperatures are in degrees C.

Radiosonde Results

Pre and post-IOP radiosonde profiles of potential temperature and specific humidity for IOP1 are shown in Figs. 78 and 79. Selection of a pre-test mixing height from this data is somewhat ambiguous. There appears to have been several layers present including a major boundary at about 4000 m. However, by the end of the experiment these transient layers had disappeared and an estimate of about 4000 m agl for the post-test mixing height is unambiguous.

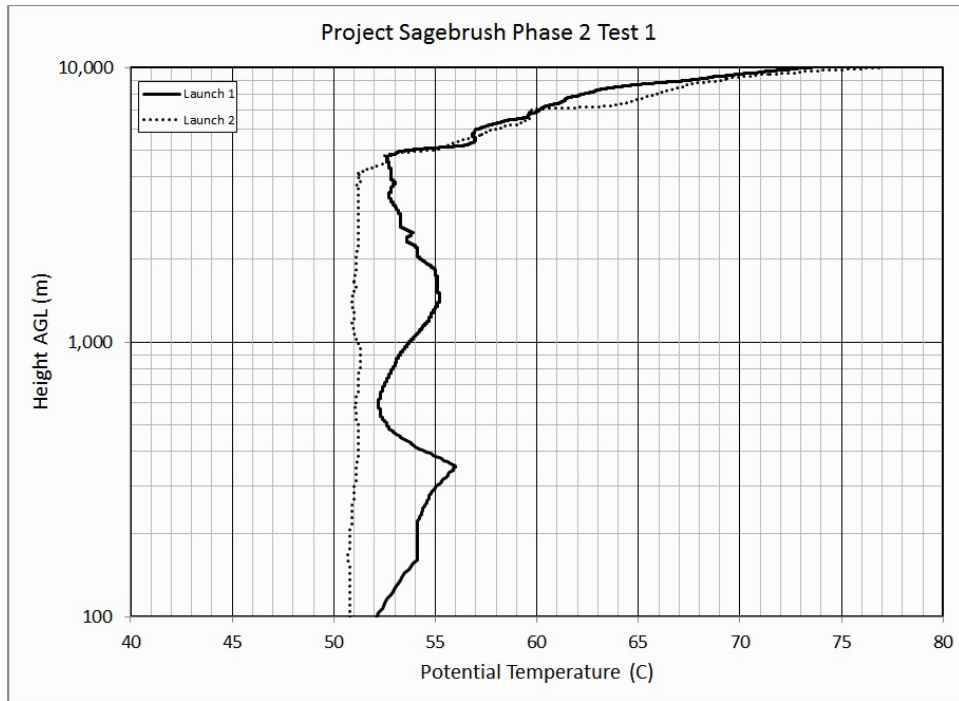


Figure 78. Potential temperature profile from radiosonde probe, IOP1. Pre-test launch bold, post-test launch dotted.

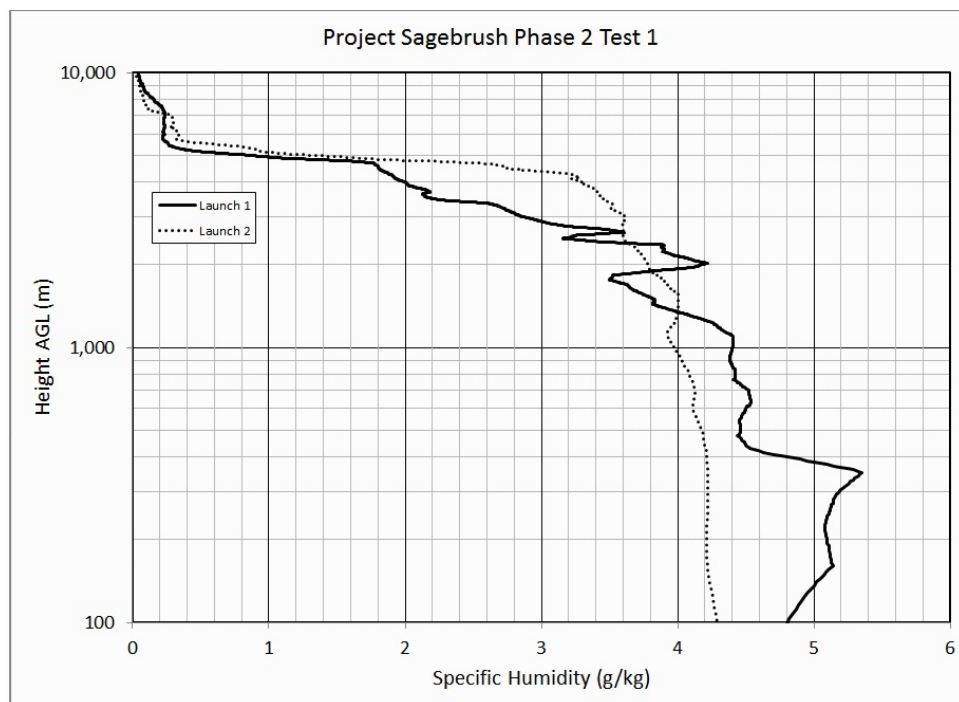


Figure 79. Specific humidity profile from radiosonde probe, IOP1. Pre-test launch bold, post-test launch dotted.

Bag Sampling Results

Figures 80 and 81 and Figures 82 and 83 show the 10-min average normalized and actual, respectively, color-coded plan view concentration maps for IOP1 bag sampling at 1 m agl. Figures 84 and 85 and Figures 86 and 87 show the 10-min average normalized and actual concentrations, respectively, along each of the arcs.

There were some 10-min periods during which the plume appeared to be largely contained within the confines of the 210° sampling arcs for all distances (e.g., bags 1, 8, 9, and perhaps 12). It's also fair to say that most of the plume was usually confined to range of the sampling arcs. However, most of the plumes showed some evidence of edge effects where one or both limbs of the plume were truncated before reaching baseline. Truncation was most pronounced on the 100 m arc and less of an issue on the 200 and 400 m arcs. Edge effects are also apparent on the 800 m arc although concentrations were often small enough such that the plume was not well defined there.

The plume was roughly centered on the sampling array early in the IOP then rotated counterclockwise into mainly the northwest part of the array. Near the end of the first hour the plume rotated clockwise into mainly the northeast part of the array. These observations are consistent with the observations of wind direction at GRI and COC (Figs. 65, 66, 68; Table 18). Plume morphology tended toward the development of a central, often multi-peaked composite. These peaks were crudely Gaussian in form except during periods of transition in wind direction. The plume was more smeared out and very irregular at these times. When a main peak was present, it usually subtended about 90-150° of arc or more at 100 m and the margins of the plume were relatively sharp. The subtended range generally decreased with increasing downwind distance.

Figure 88 shows the vertical concentration profiles up to 25 m agl from the mobile tower located on the 100 m arc at 24° azimuth (red dot 1, Fig. 5). Most of the profiles exhibit a relatively uniform concentration with height, especially during the first hour. The second hour exhibits greater variation in vertical concentration with some profiles suggesting liftoff of the vertical plume centerline and others with maxima closer to the surface. No concentration measurements were obtained from the 25 m level during IOP1 so the picture is incomplete. However, it is likely that some portion of the plume exceeded 25 m.

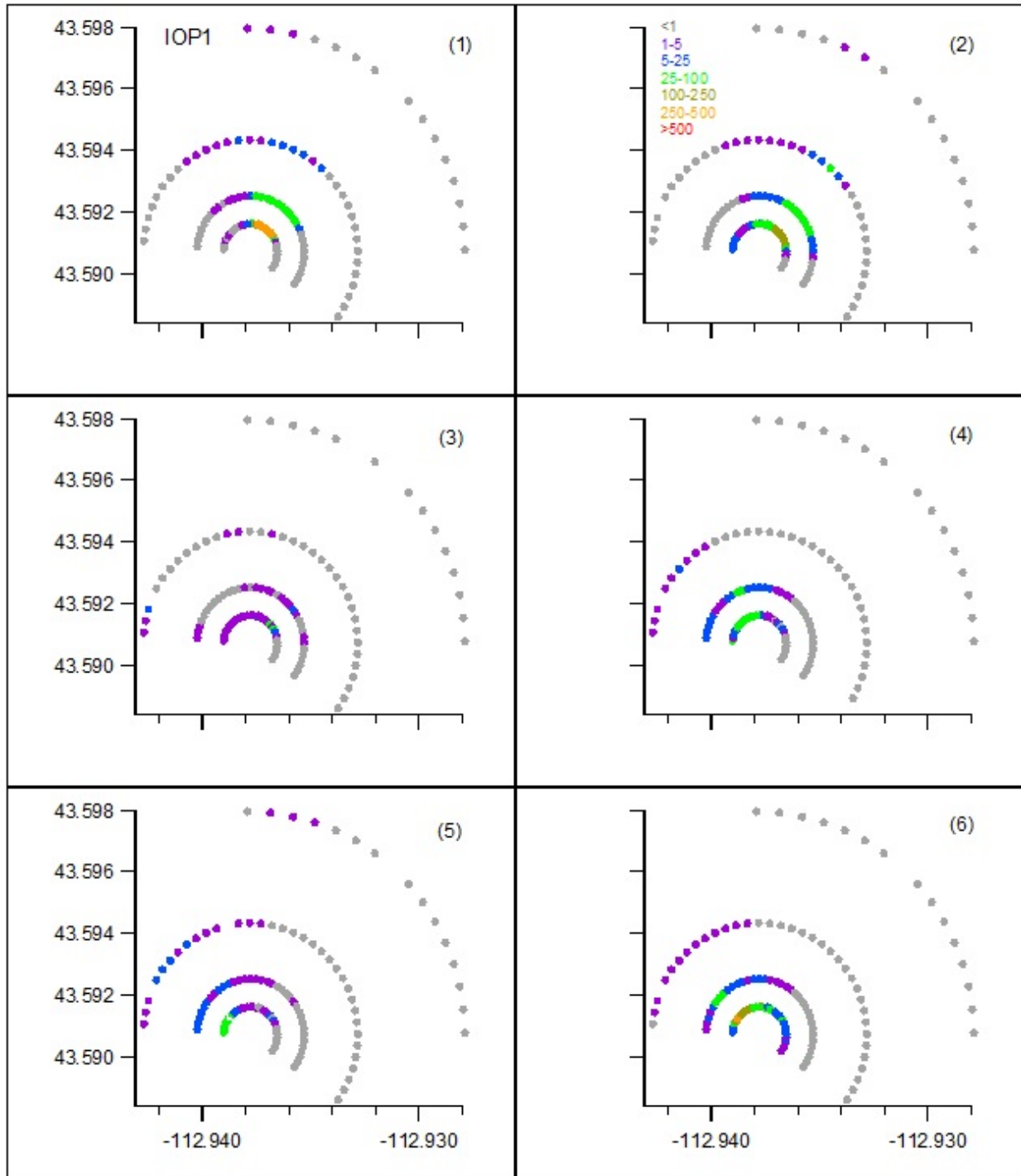


Figure 80. Color-coded normalized ($F^*\chi/Q$ ppt s g⁻¹) concentrations at 1 m agl for bags 1-6 during IOP1. The number in () is bag number.

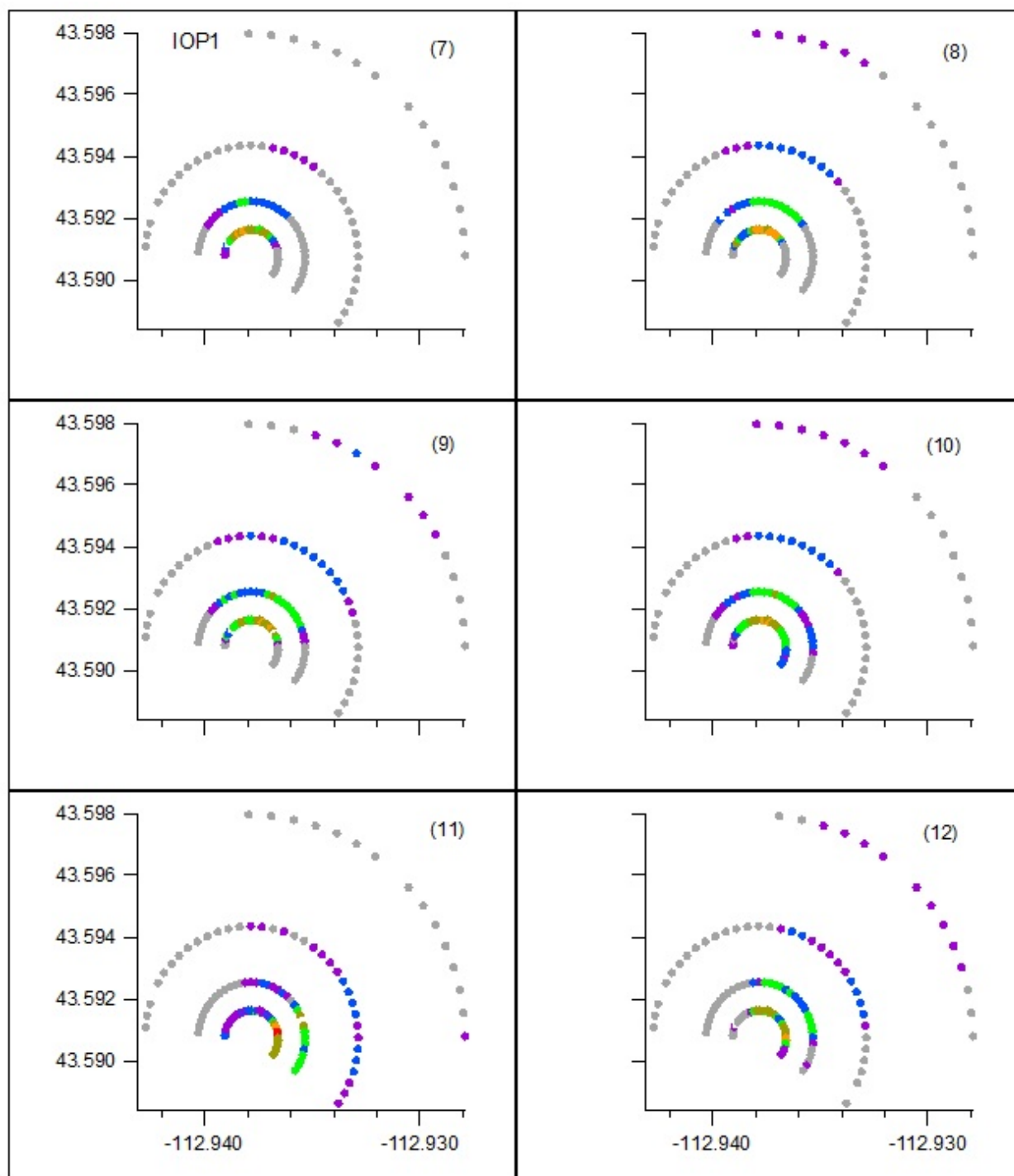


Figure 81. Color-coded normalized ($F^*\chi/Q$ ppt s g^{-1}) concentrations at 1 m agl for bags 7-12 during IOP1. The number in () is bag number.

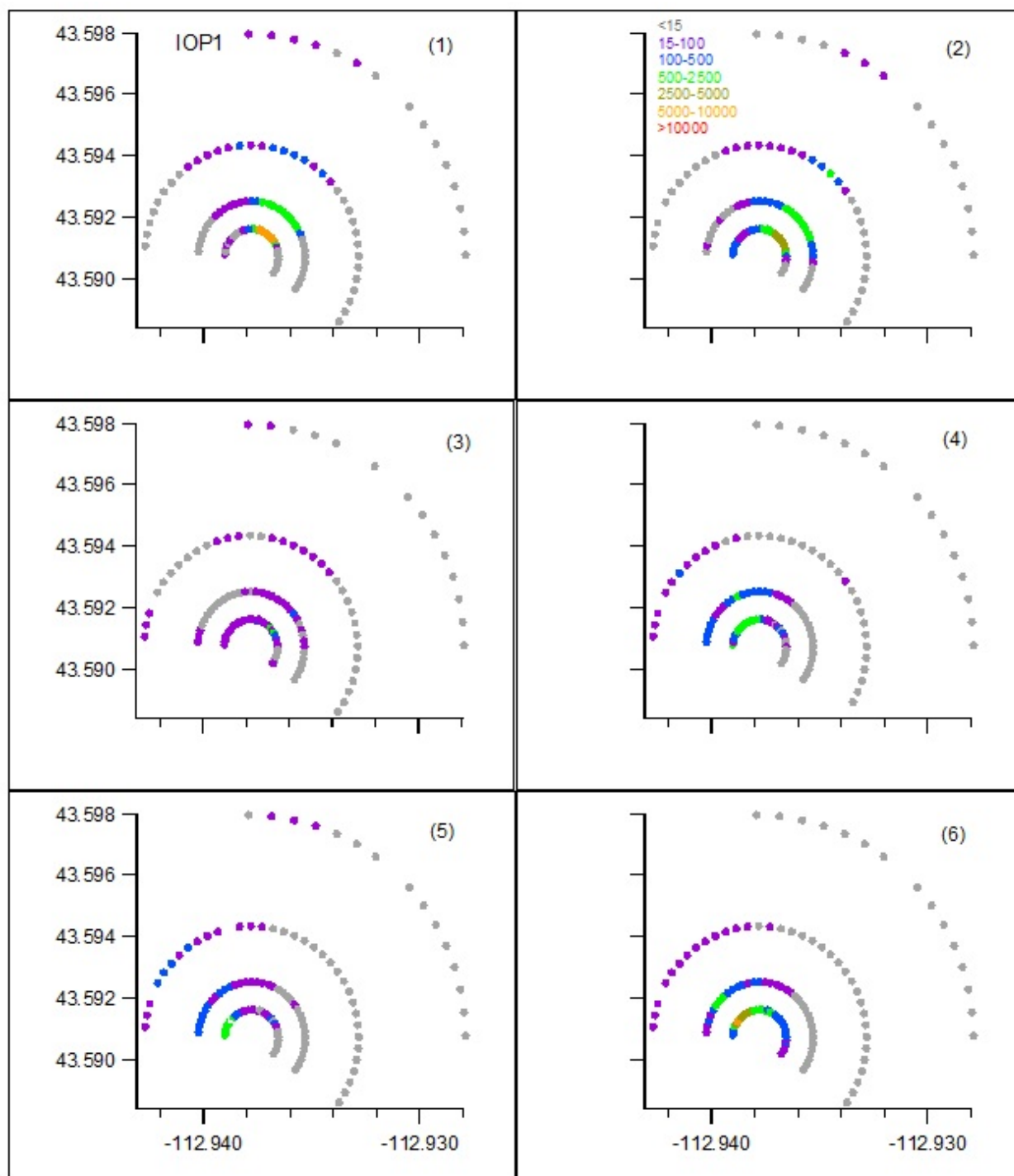


Figure 82. Color-coded measured SF_6 concentrations (ppt) at 1 m agl for bags 1-6 during IOP1. The number in () is bag number.

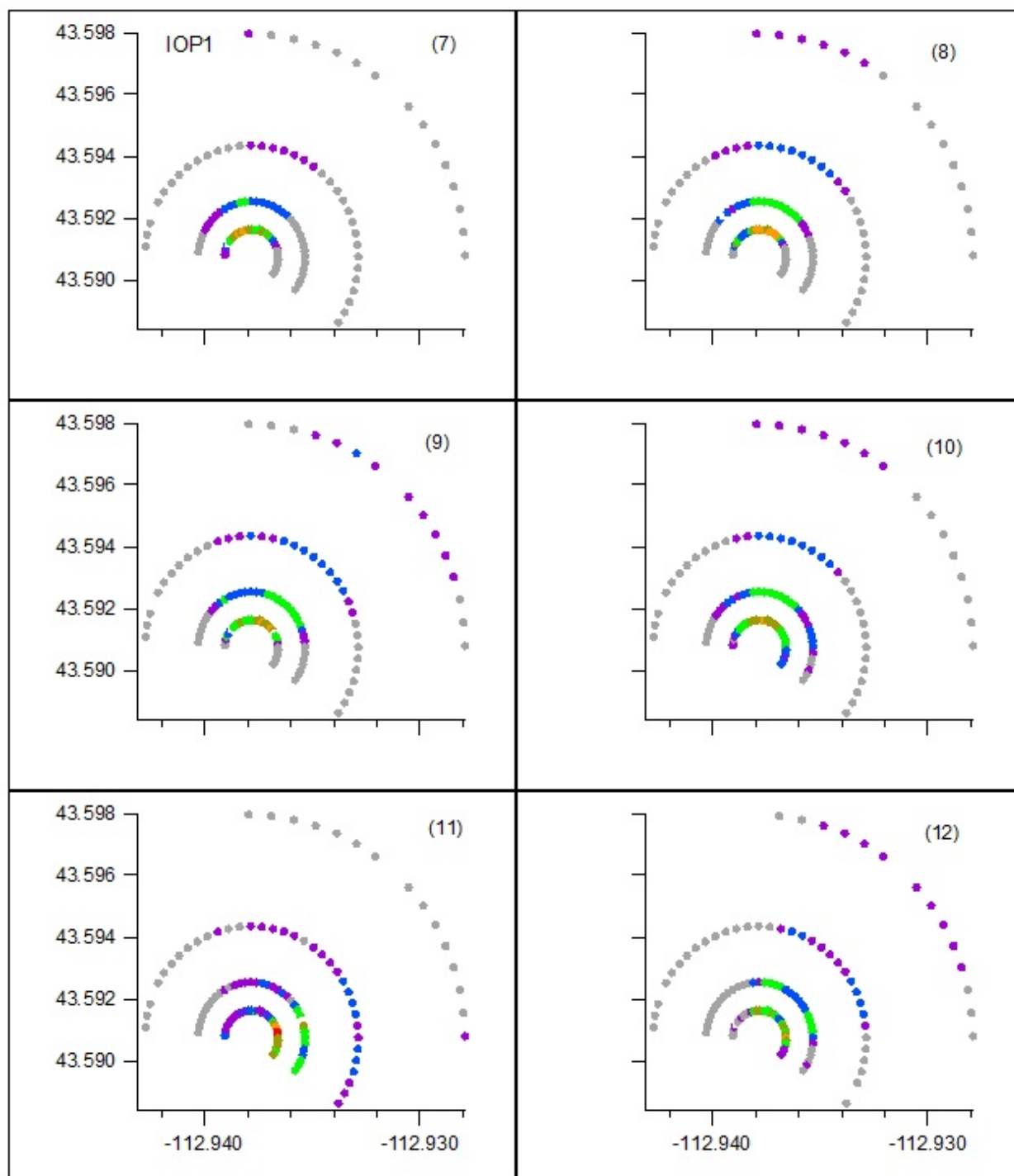


Figure 83. Color-coded measured SF_6 concentrations (ppt) at 1 m agl for bags 7-12 during IOP1. The number in () is bag number.

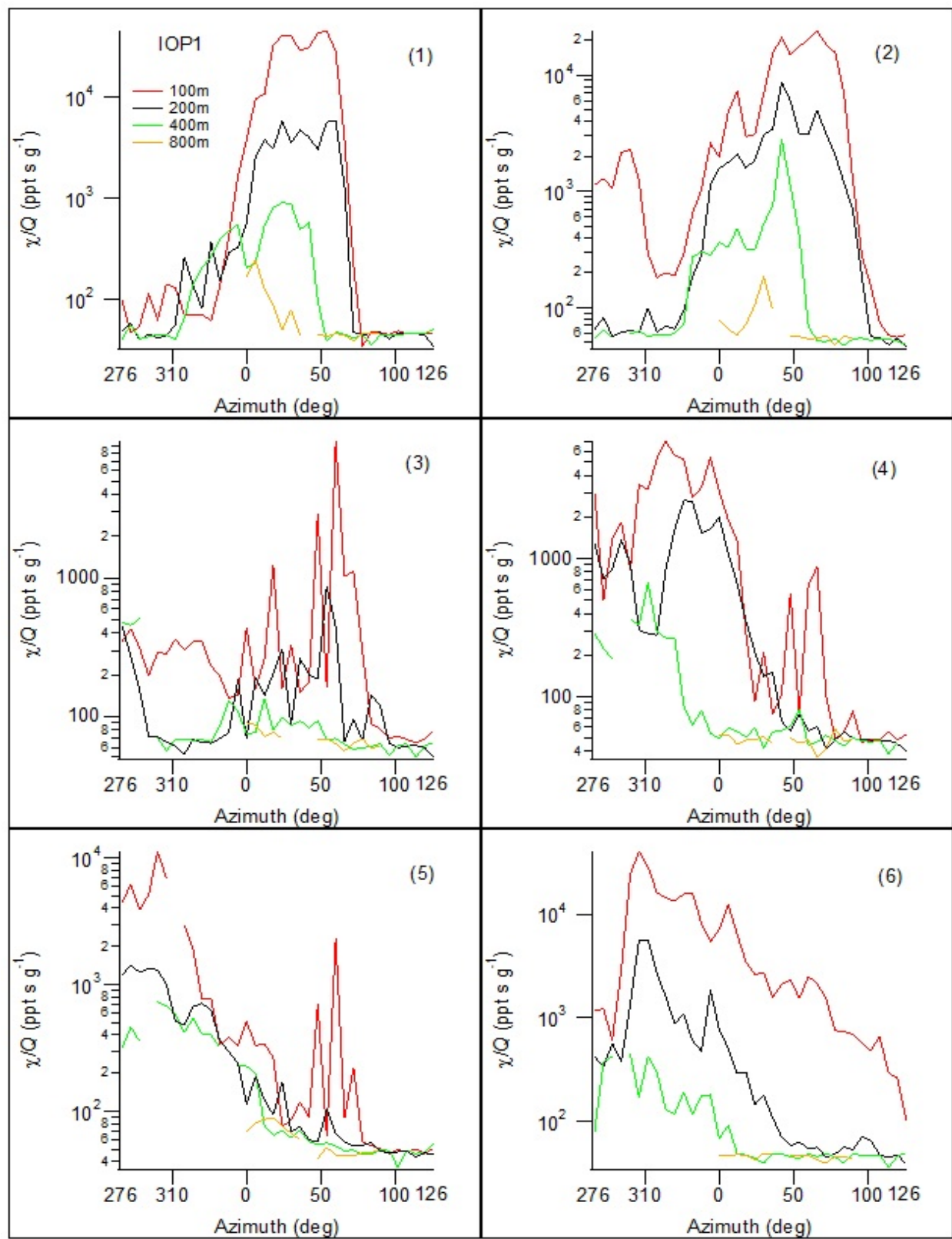


Figure 84. Cross-sections of normalized concentration along the arcs for bags 1-6 during IOP1.

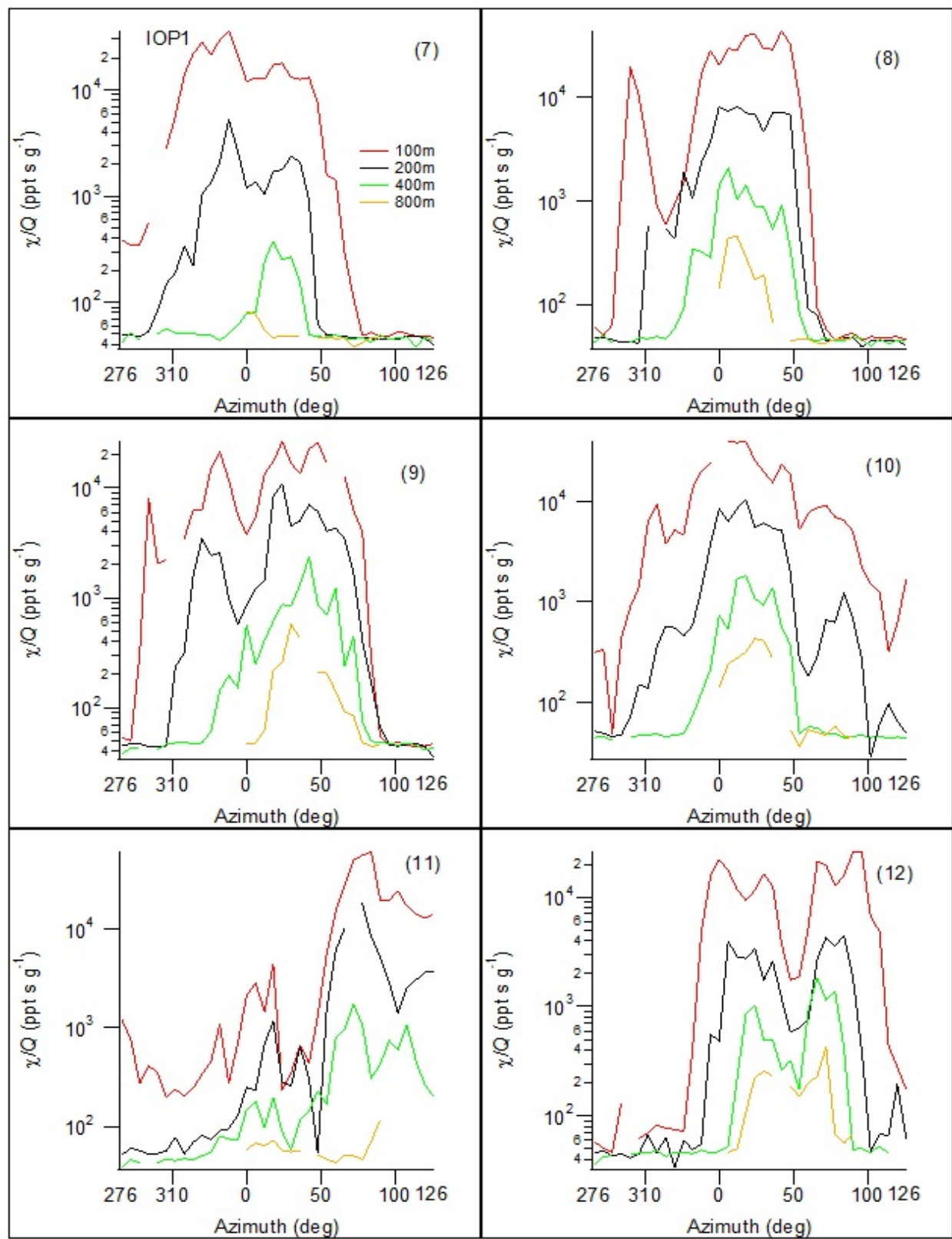


Figure 85. Cross-sections of normalized concentration along the arcs for bags 7-12 during IOP1.

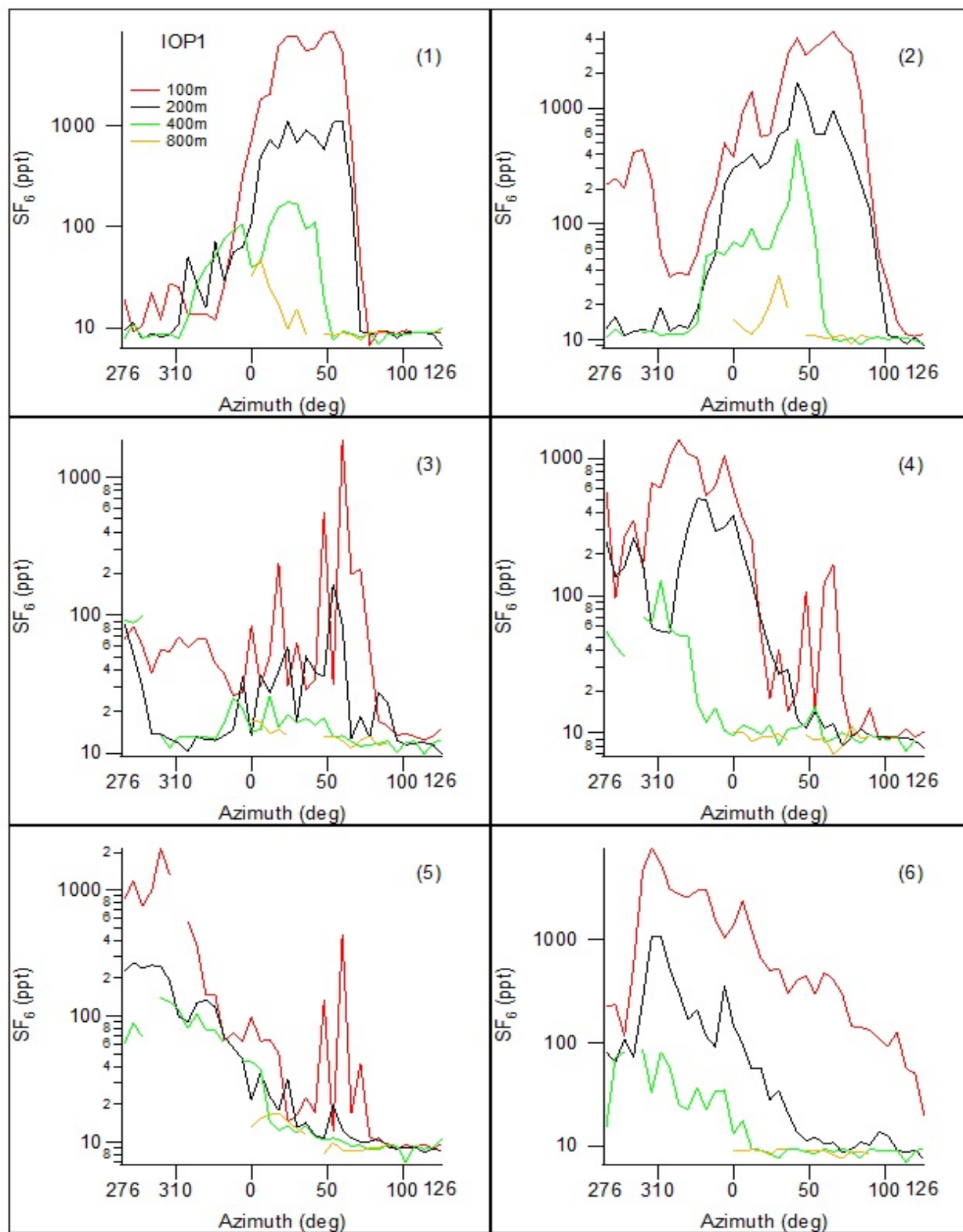


Figure 86. Cross-sections of measured SF_6 concentration along the arcs for bags 1-6 during IOP1.

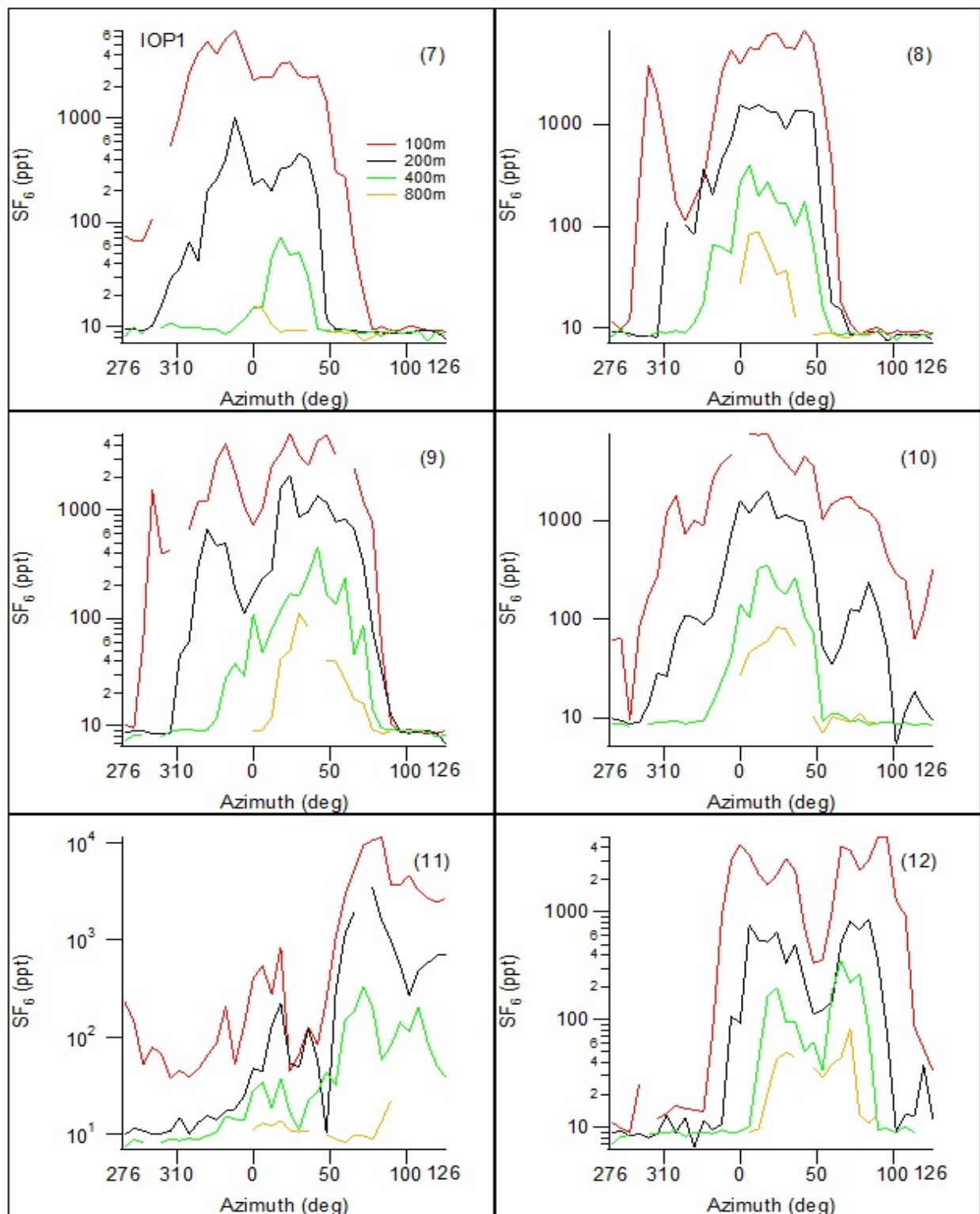


Figure 87. Cross-sections of measured SF_6 concentration along the arcs for bags 7-12 during IOP1.

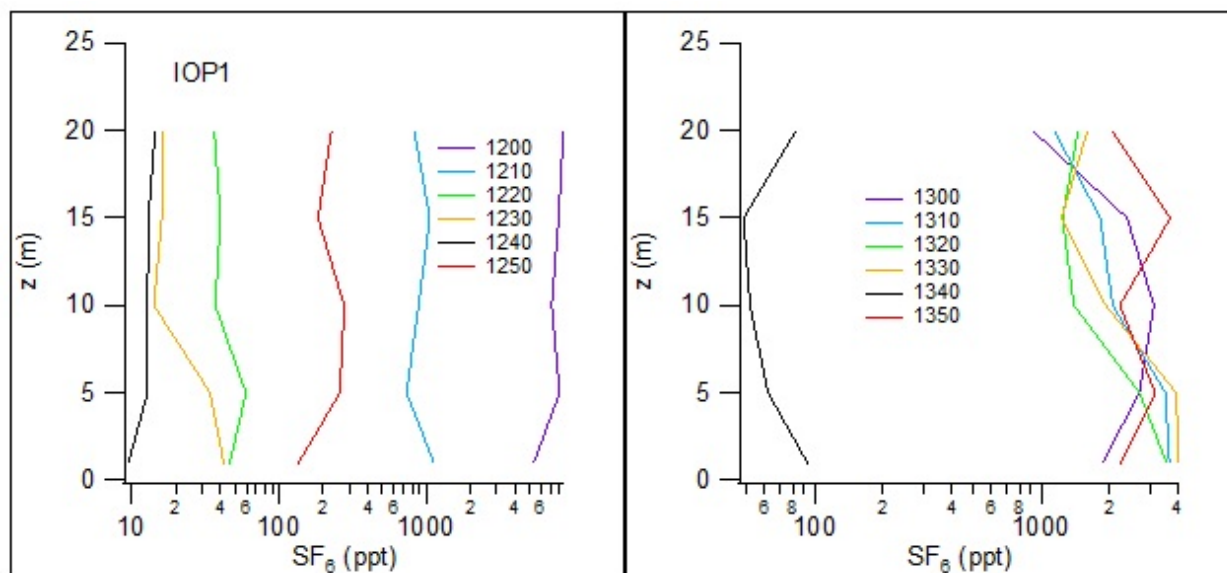


Figure 88. Vertical profiles of measured SF_6 concentration at the mobile tower during IOP1.

Fast Response Results

The locations of the fast response analyzers during IOP1 are shown in Fig. 89. The corresponding concentration time series are shown in Fig. 90. The color coding of the time series was described in the Introduction to this section.

Part of the record for the first hour is missing but the available fast response records indicate only sporadic, weak concentrations during that time. Given the location of the fast response analyzers, that is consistent with the bag sampling results for the part of the record that is available (Figs. 80 and 82). During the second hour the plume was more consistently over the northeastern part of the sampling array where the fast response analyzers were located. During that time the plume was commonly measured on all of the arcs. However, the measurements were characterized by being highly variable and intermittent with often rapid increases from background to peak values followed by rapid drops in concentration back to background or near background concentrations. The peaks were sometimes railed (overranged), especially on the 100 m arc at analyzer A. The character of the time series suggests that the plume was probably relatively narrow at any given time and, with frequent shifts in wind direction, resulted in the very intermittent time series observed. Thus the bag sampling averaging likely represents a smoothing of a much more fluctuating signal with large peak:mean ratios.

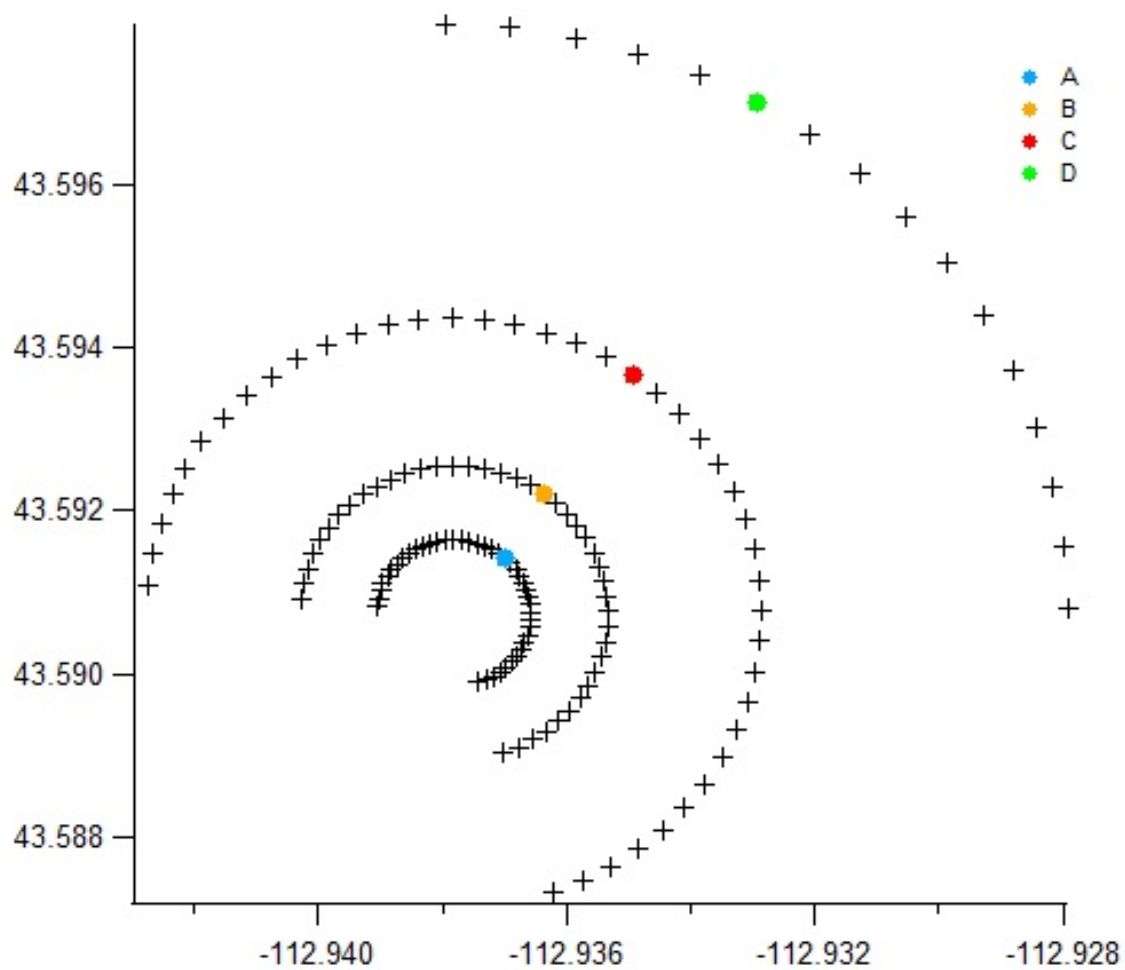


Figure 89. Locations of fast response analyzers during IOP1.

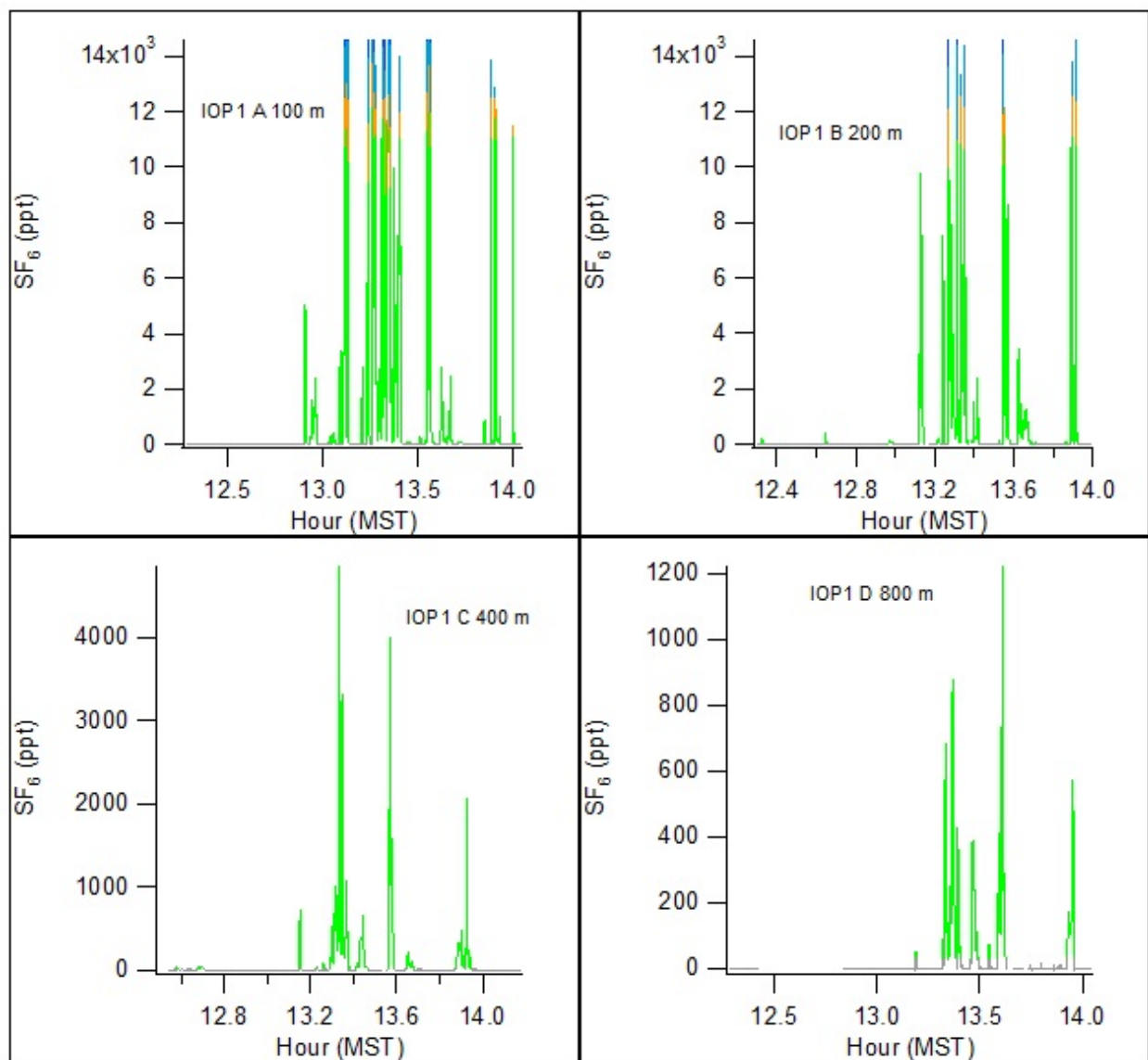


Figure 90. Fast response concentration time series during IOP1.

IOP 2

Date/Time and General Description

IOP2 was conducted on 27 July from 1130-1330 MST (1230-1430 MDT). Conditions were hot and dry with wind speeds near 3 m s^{-1} over most of the IOP. Skies were clear and sunny throughout the experimental period. Overall conditions were unstable and highly non-stationary in both time and space. Estimates of stability based on traditional Pasquill-Gifford (P-G) schemes were mainly class B with some class A and C (Fig. 91). Estimates of mean z/L from GRI ranged from -0.23 to -0.50 with a Ri_b of -0.61. The tracer plume was mostly confined to the bag sampling array although wind directions sometimes advected part of the plume away from the sampler array. A summary of the meteorological conditions during IOP2 are shown in Table 19. The SF_6 release rate was 0.146 g s^{-1} (Table 2). The fast response analyzers were located on the 100, 200, 400, and 800 m arcs, all at 18 degrees azimuth. Their positions were fixed for the duration of the IOP.

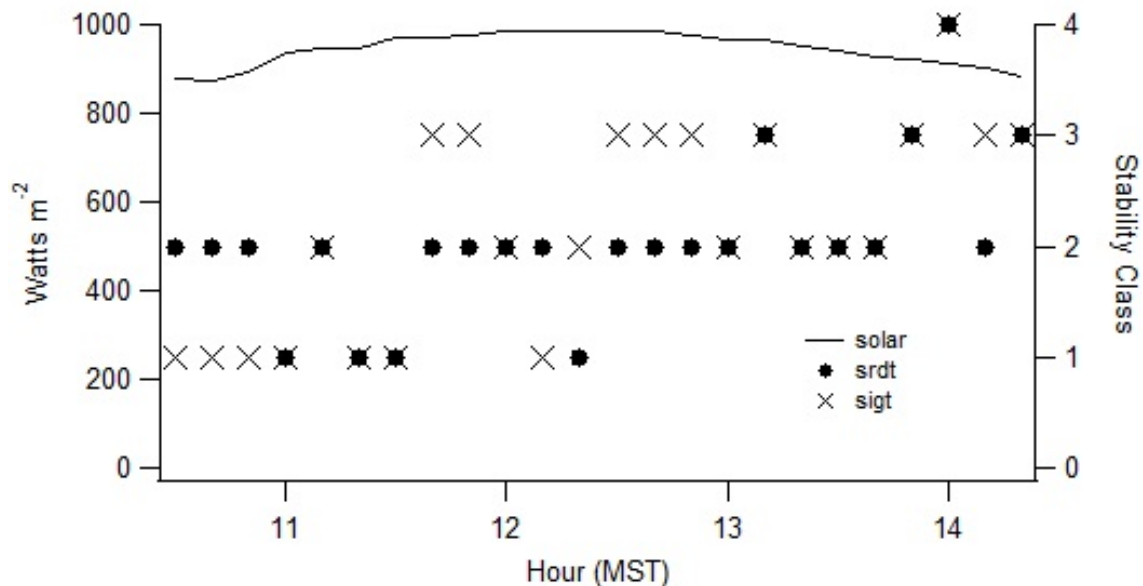


Figure 91. Incoming solar radiation and classification of stability conditions using the Pasquill-Gifford Solar Radiation Delta T (srdt) and σ_0 (sigt) methods (U.S. EPA 2000c) during IOP2. Classes A, B, C, and D are designated 1, 2, 3, and 4, respectively.

Table 19. Meteorological conditions during IOP2.

Bag	COC				GRI						GRI			Solar W m ⁻²
	U (m s ⁻¹)		WD (deg)		U (m s ⁻¹)		WD (deg)		σ_θ (deg)		L	L	degC	
	2m	10m	2m	10m	2m	10m	2m	10m	2m	10m	3.7m	9m	2m	
1	1.3	1.5	111.5	121.6	2.2	2.6	167.5	169.3	34.8	33.2	-8.5	-10.3	30.6	970.0
2	2.0	2.4	133.0	138.6	3.3	4.2	200.5	199.3	29.2	28.9	-6.3	-3.3	31.8	972.5
3	1.9	2.4	229.9	229.7	3.5	4.2	186.6	186.5	26.8	24.5	-15.3	-13.8	31.7	976.5
4	1.9	2.5	180.4	180.4	2.3	2.8	258.1	261.8	33.6	22.2	-27.8	-38.0	31.3	985.0
5	1.9	2.5	195.0	194.0	1.2	1.8	133.5	138.5	60.8	57.5	-19.7	NaN	31.2	986.0
6	3.2	4.2	189.0	186.4	2.5	3.0	224.9	218.7	34.7	35.2	-22.7	-29.6	31.9	984.0
7	2.5	3.2	197.2	201.0	3.4	4.2	216.2	212.1	22.5	19.2	-16.5	-10.6	32.1	983.0
8	3.0	3.8	177.2	177.7	3.6	4.5	213.9	213.5	26.2	23.9	-16.5	-16.2	32.5	984.5
9	4.1	5.4	198.3	197.0	3.3	4.0	209.8	207.9	18.4	14.9	-15.6	-18.3	32.5	975.5
10	2.0	2.5	207.9	213.7	2.7	3.0	250.3	244.0	43.0	41.8	-5.7	-23.3	32.2	964.5
11	2.4	3.0	319.4	313.2	3.9	5.1	237.7	236.5	23.2	22.9	-11.2	-6.8	33.1	964.5
12	2.5	3.0	194.2	188.9	2.8	3.6	216.7	216.7	46.0	47.6	-27.5	-27.2	32.7	952.0
Avg. L											-16.11 -17.95			
z/L											-0.23 -0.50			
Ri _b											-0.61			

Wind Speed and Direction Quality Assurance

Figures 92-94 show wind speed and direction time series comparisons for a sequence of measurement heights during IOP2. In Fig. 92, the near surface measurement of U showed some horizontal variation between sites, with the COC station being the most inconsistent with respect to the other stations. Wind directions at all three sites were consistent within a few tens of degrees during most of the experimental period. Wind speeds were approximately 3 m s⁻¹ most of the time with a gradual increase over time. The wind speed and direction measurements between 9 and 30 m agl were mostly consistent throughout the period (Fig. 93). COC had some differences relative to GRI at the 10 m level and both COC and SOD had periods with large deviations in wind direction relative to GRI. The sodar measurements at 30 m agl were largely consistent with GRI. For the 45 and 60 m levels the measurements of U were consistent between GRI and SOD but there were some differences in wind direction (Fig. 94). There is insufficient data available from the sodar (SOD) and radar profiler (PRO) at 160 m agl to make any reliable assessment. Other than the poor data recovery for SOD and PRO at 160 m agl, there is little evidence of a systematic measurement problem. Any of the observed variability or discrepancies are likely attributable to non-stationarity and horizontal inhomogeneity in the wind field.

Figure 95 shows time series measurements for cup anemometers and wind vanes only (excluding sonics) at all heights on the two towers during IOP2. Again, there were differences

between GRI and COC with U and σ_0 at COC tending to be less than and greater than GRI, respectively, and some periods with wind direction differences.

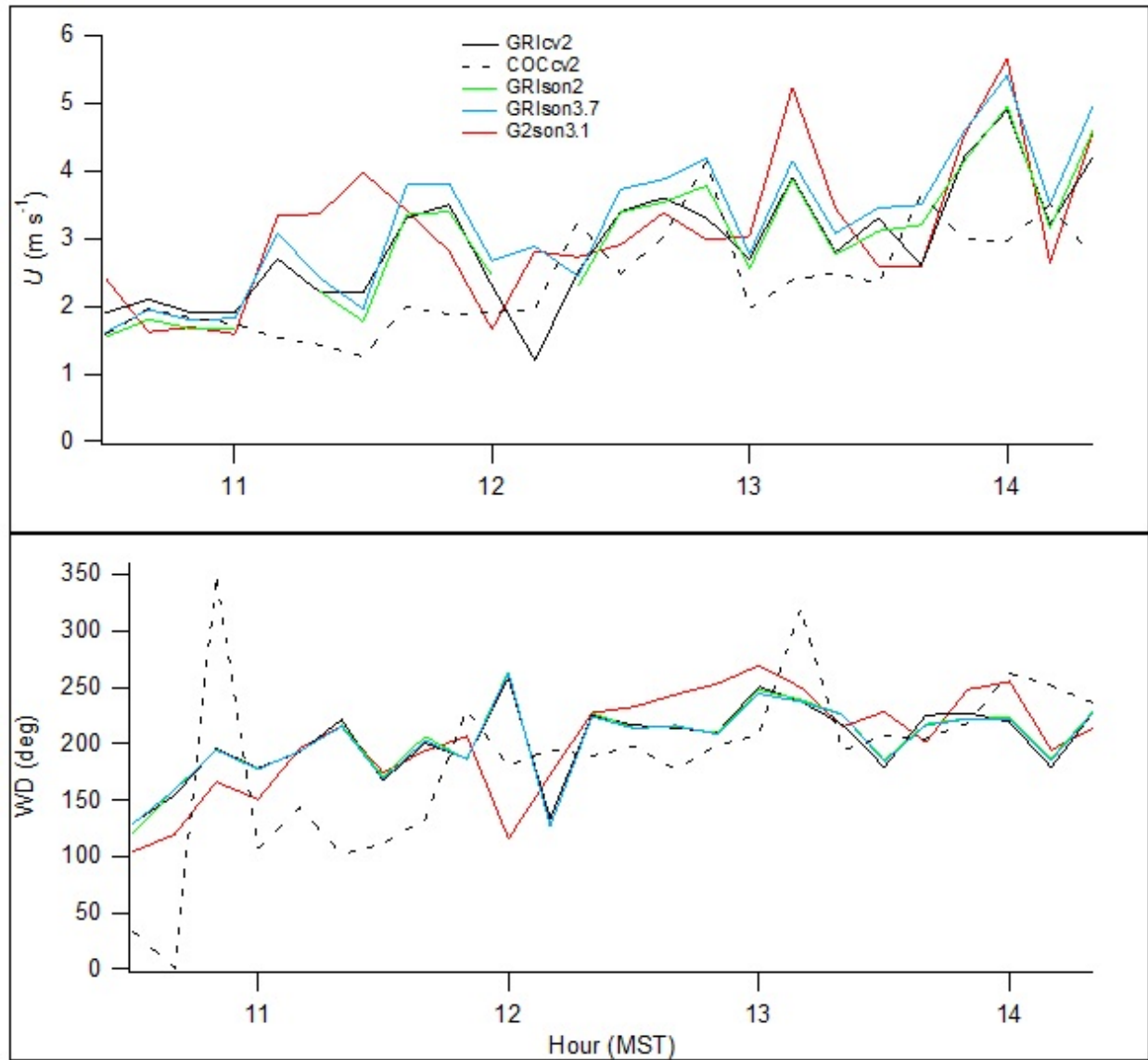


Figure 92. Time series of near surface wind speed and direction measurements during IOP2. In the legend, location is specified in upper case, the measurement type in lower case (cv = cup and vane, son = sonic), and the measurement height numerically.

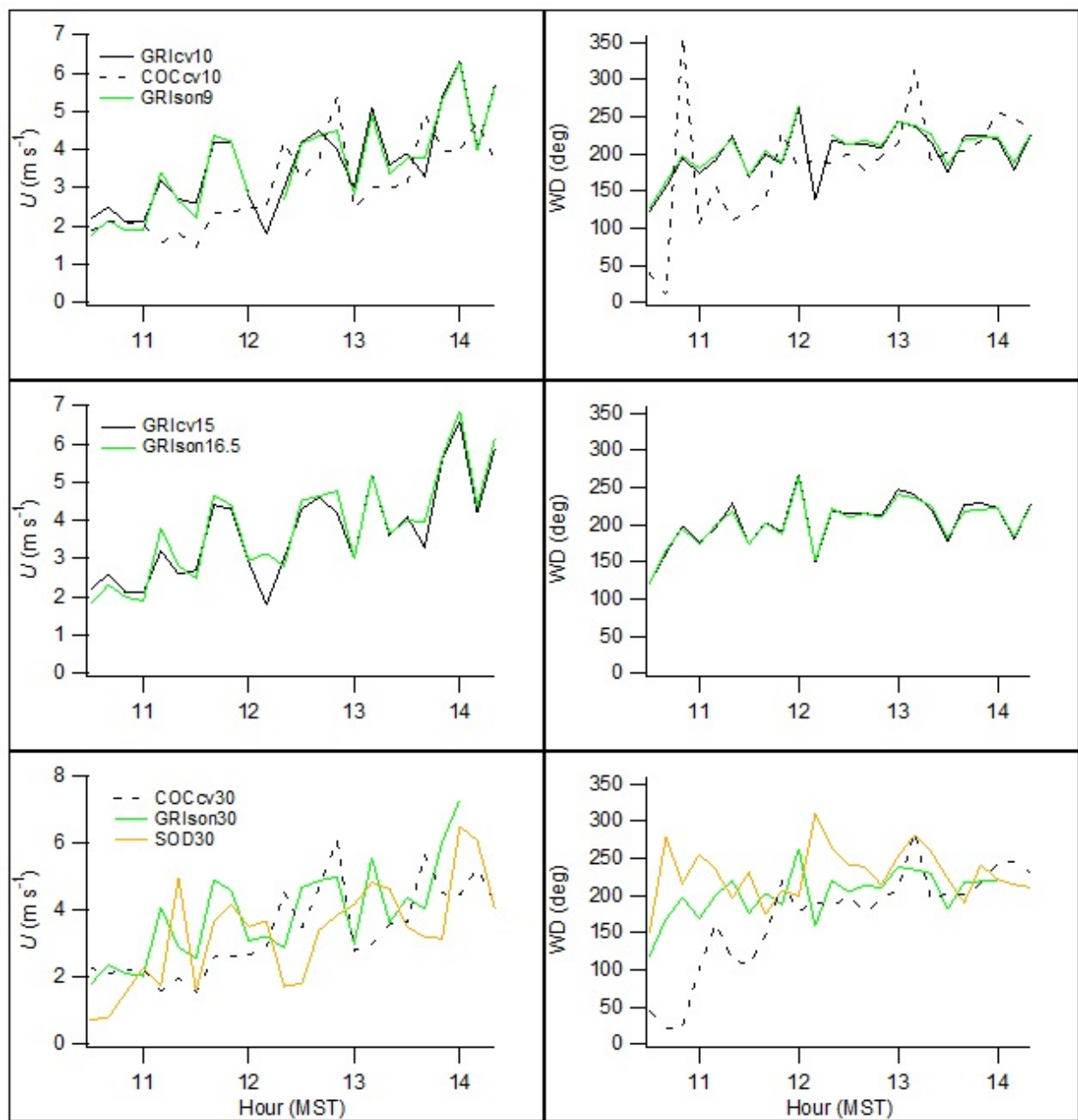


Figure 93. Time series of wind speed and direction measurements at heights between 9 and 30 m agl during IOP2. Legend notations described in caption of Fig. 92.

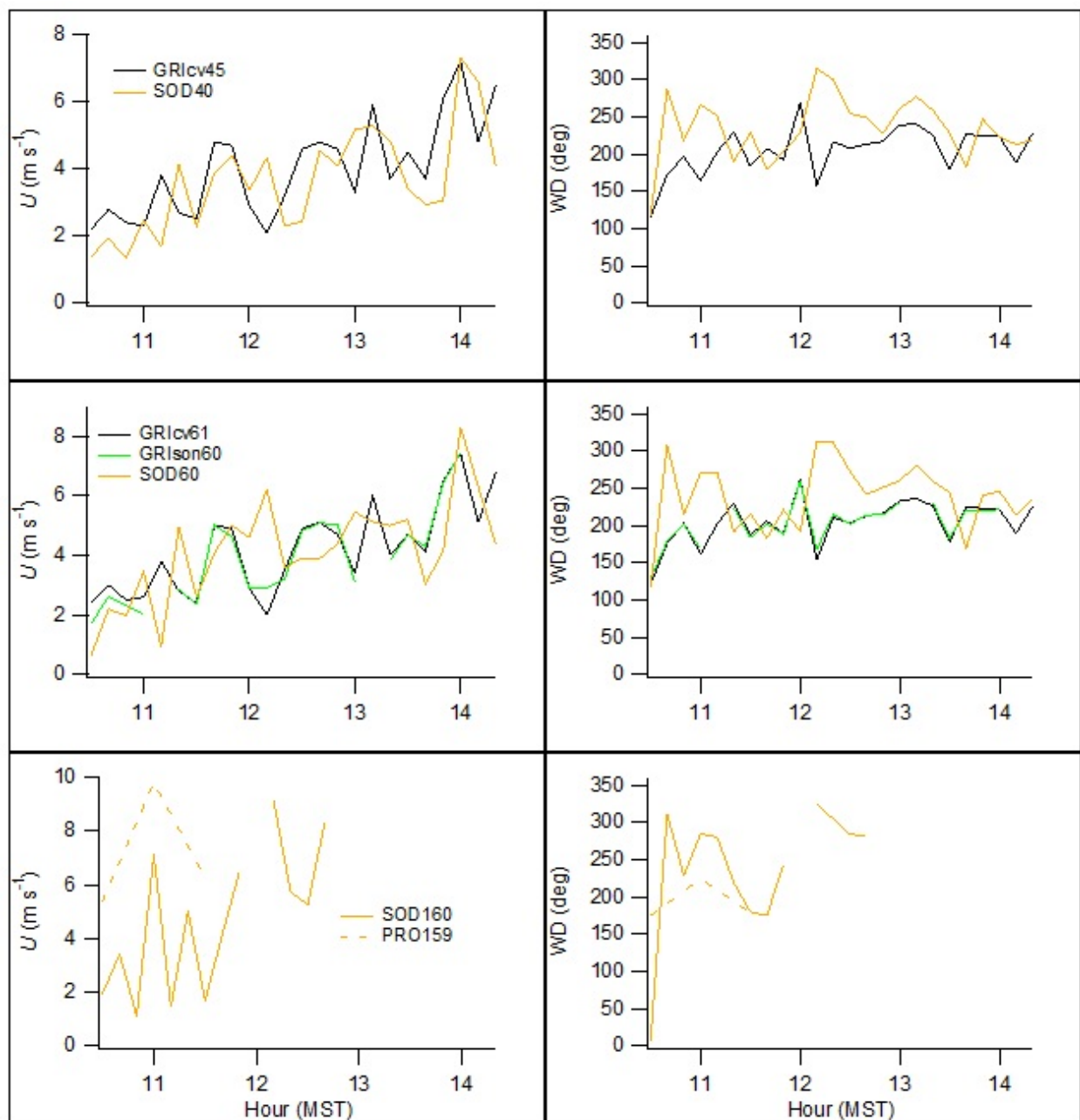


Figure 94. Time series of wind speed and direction measurements at heights above 30 m agl during IOP2. Legend notations described in caption of Fig. 92.

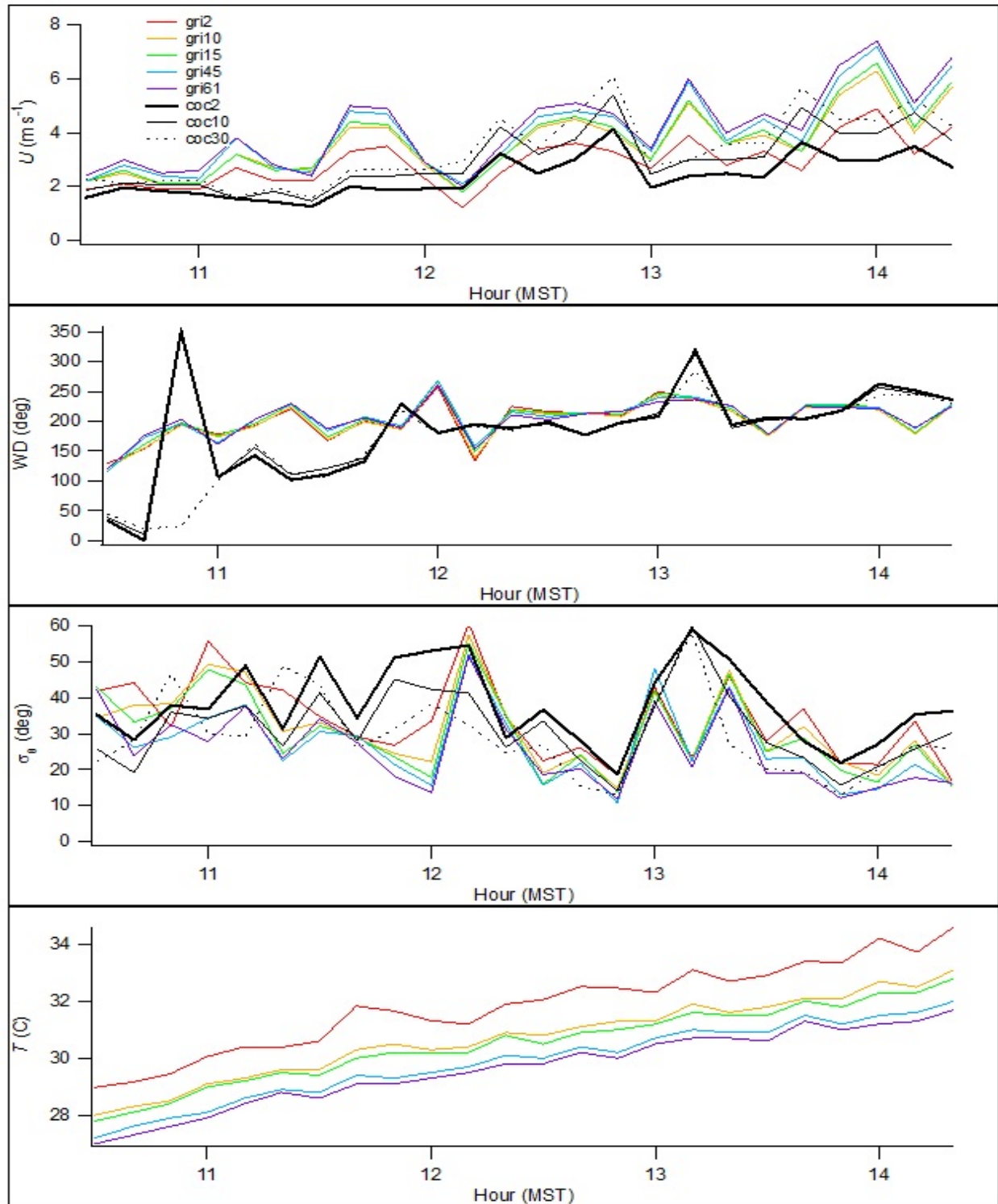


Figure 95. Time series from GRI and COC showing cup anemometer and wind vane measurements of U , wind direction, standard deviation of wind direction σ_0 , and temperature during IOP2. The locations are designated 'xxxy' where xxx = tower and yy = measurement height.

Turbulence

The available near surface turbulence measurements are mostly consistent with some exceptions (Fig. 96). These include the apparent high bias in measurements of σ_ϕ (σ_w/U) at G2 relative to those at GRI and the sharp excursions in σ_v/U and σ_w/U at R2 and R9 on GRI shortly after 1200 h. G2 has a smaller excursion in TKE.

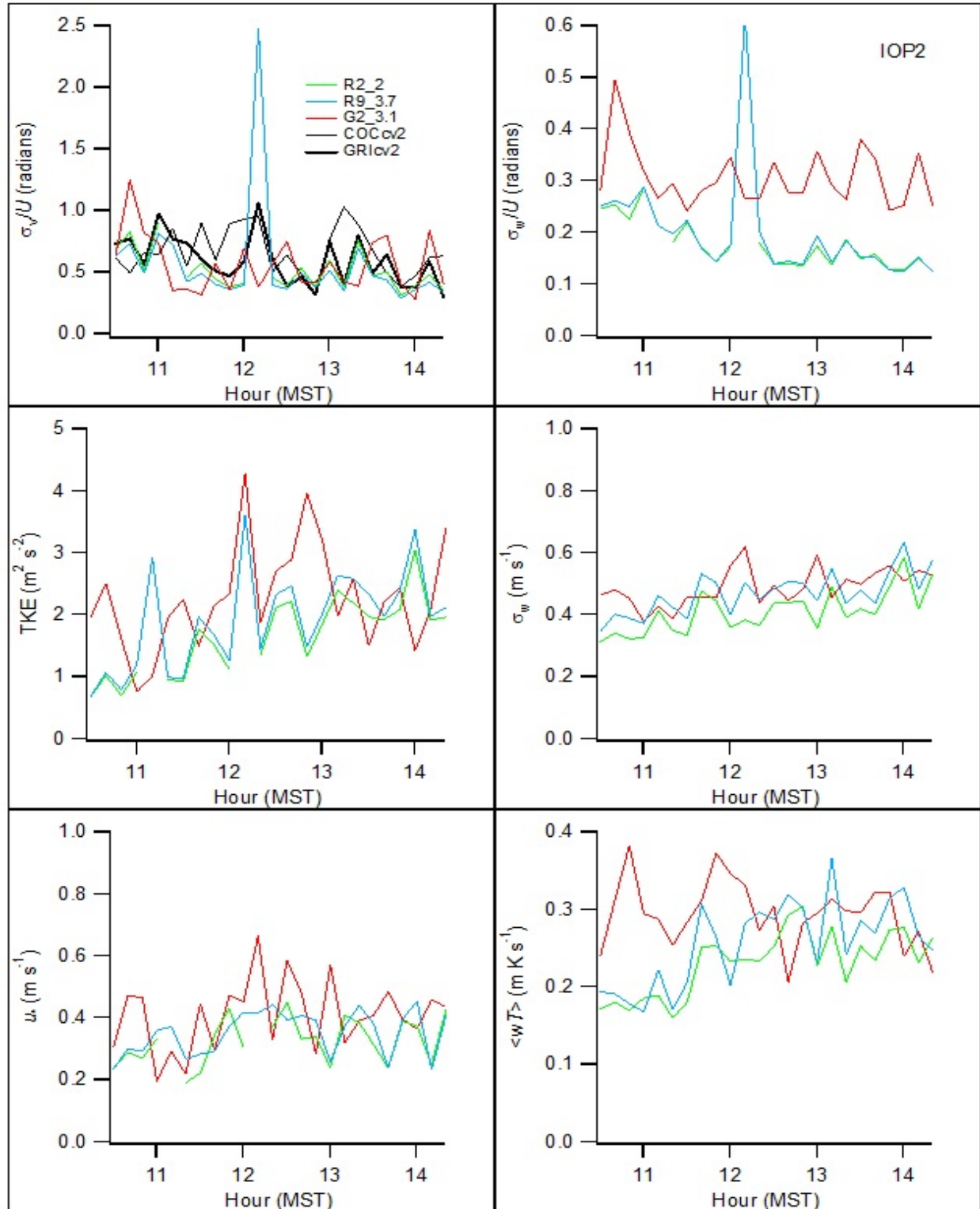


Figure 96. Time series of near surface turbulence (sonic) measurements during IOP2. The GRI and COC are σ_0 wind vane measurements (cv) in degrees converted to radians for purposes of comparison. Notation before and after underscore designates location and height, respectively.

Wind and Turbulence Profiles

Figure 97 shows profiles of the non-sonic measurements at GRI and COC during IOP2. Wind directions were mostly uniform in the vertical within a given profile but the direction was shifting a lot at each 10-minute interval during the first half of the experiment. An increase in U from generally a little less than 3 m s^{-1} to a little more than 3 m s^{-1} midway through the experiment corresponded to a reduction in the variability of wind direction. All profiles were generally well behaved and consistent with the strong daytime surface heating.

Figures 98 and 99 show profiles of the sonic turbulence measurements at GRI during IOP2. Wind speeds and directions were generally consistent with the non-sonic measurements in Fig. 97 with similar ranges of speed and directional variability. The measurements of σ_v/U showed less variability than the corresponding measurements of σ_θ by wind vane. Similar to Fig. 97, the profiles were generally well behaved and absent any significantly anomalous deviations. In Fig. 99 the friction velocity measurements often exhibited considerable variation in time and in the vertical.

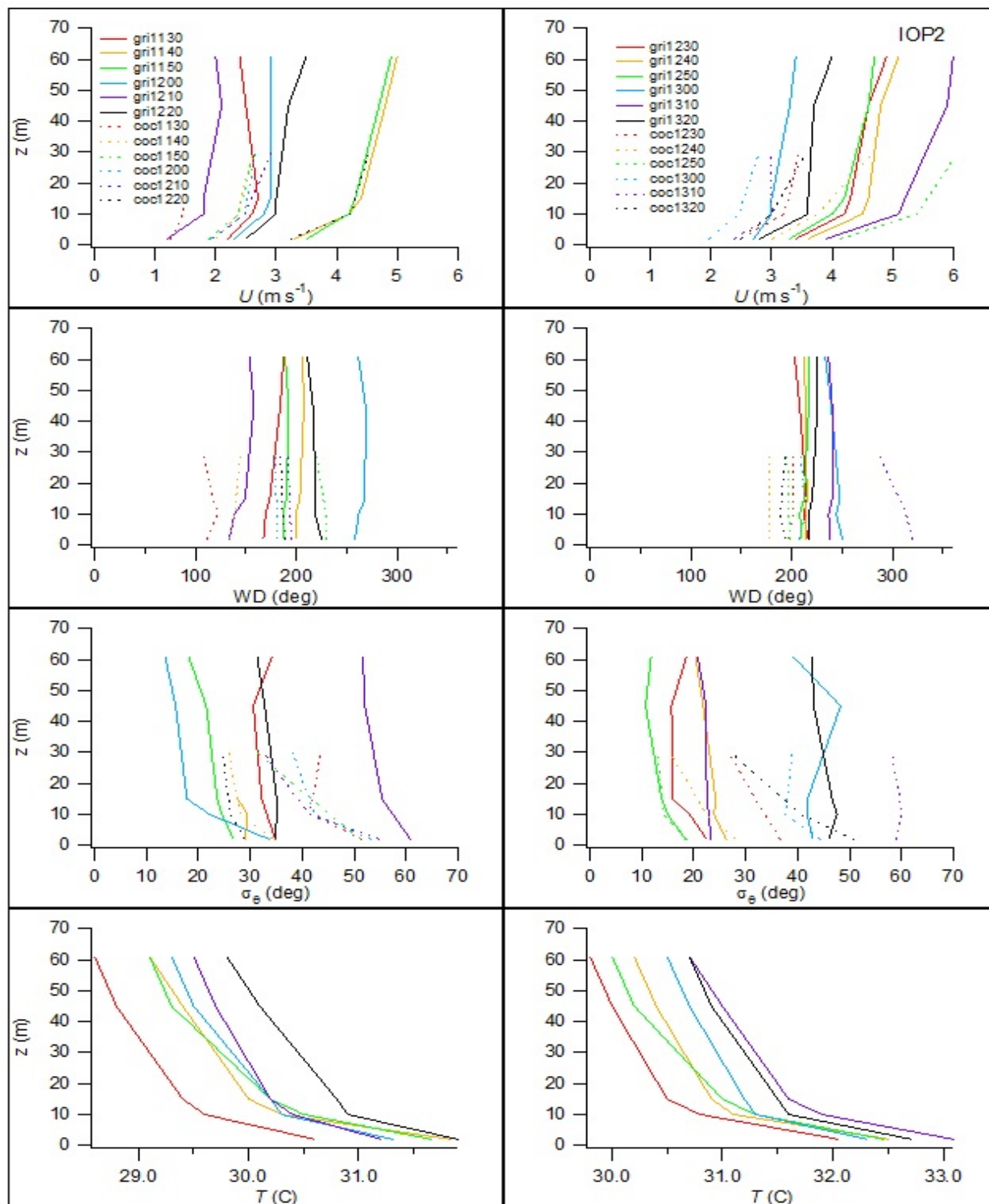


Figure 97. Profiles of U , wind direction, standard deviation of wind direction σ_θ , and aspirated temperature from cup anemometers and wind vanes during IOP2 at GRI and COC. Each profile is designated ‘xxxhrmn’ where xxx = tower and hrmn = start time of 10-minute interval.

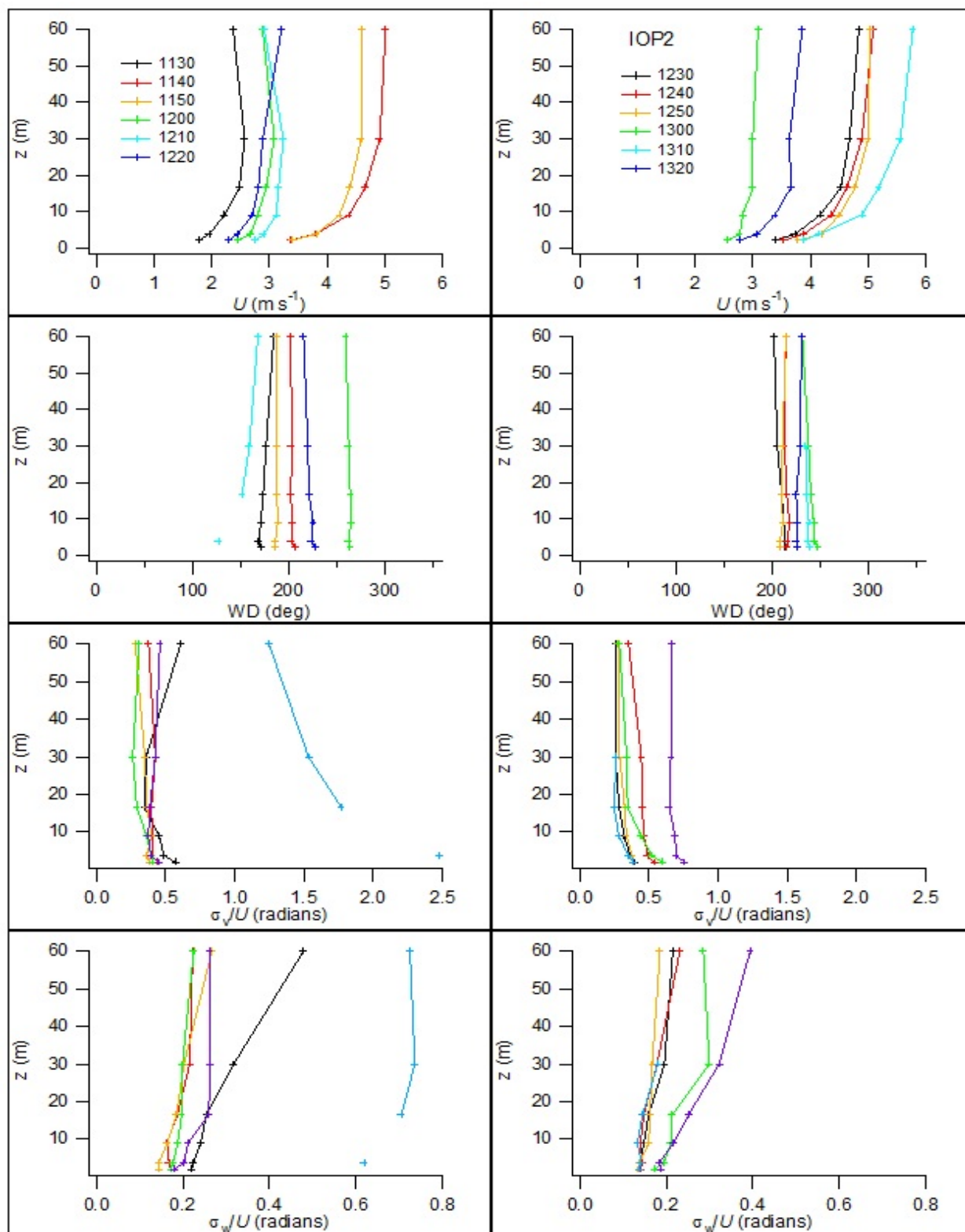


Figure 98. Profiles of U , wind direction, σ_v/U ($\sim\sigma_\theta$), and σ_w/U ($\sim\sigma_\phi$) from sonic anemometers at GRI during IOP2. The legend specifies the start time of the 10-minute interval (hrmn).

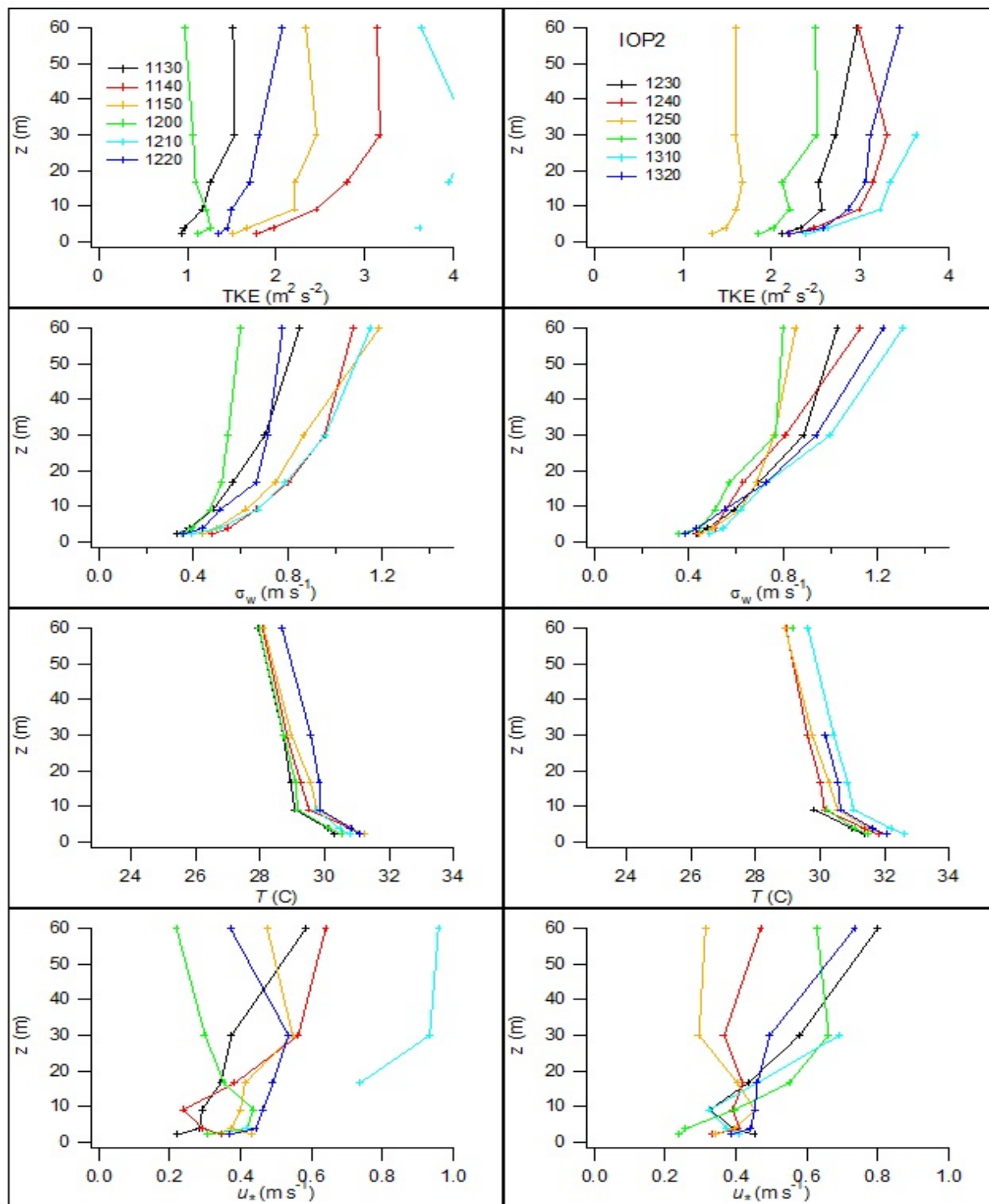


Figure 99. Profiles of turbulent kinetic energy (TKE), standard deviation in vertical wind speed σ_w , virtual temperature, and friction velocity u_* from sonic anemometers at GRI during IOP2. The legend specifies the start time of the 10-minute interval (hrmn).

Figures 100 and 101 show time-height representations of wind speed and direction for SOD and PRO, respectively, during IOP2. Wind directions at SOD were mainly southerly during the first half hour of the tracer measurement period then mainly westerly after 1210 h. There was a 10-min incursion of northwest winds between 1210-1220 h. By comparison, wind directions at GRI (Figs. 97, 98) were also mainly southerly during the first hour, then southwesterly during the second hour. A west-northwest wind direction profile is indicated at GRI between 1200-1210 h. The U were mostly in the $2\text{--}4\text{ m s}^{-1}$ range then $> 4\text{ m s}^{-1}$ in the last half hour. This is consistent with the GRI results in Figs. 97 and 98. Data recovery at PRO was sparse, including above 1.5 km where it could be compared to the radiosonde profiles. The available U and wind direction data at PRO were roughly consistent with the radiosonde profiles (not shown, see project database).

Figures 102 and 103 show SOD time-height representations of σ_w and TKE, respectively, during IOP2. The σ_w profiles exhibit an episodic pattern, possibly due to thermals. Two prominent σ_w highs occurred just after 1200 h and 1330 h. The timing of the peaks of σ_w for SOD does not appear to have a clear correlation in the σ_w results for GRI but, again, the measurements are separated by 1 km. The magnitudes of σ_w measured by sonic at GRI were roughly similar in magnitude to those measured at SOD but tended to be slightly higher (Figs. 99, 102). The SOD

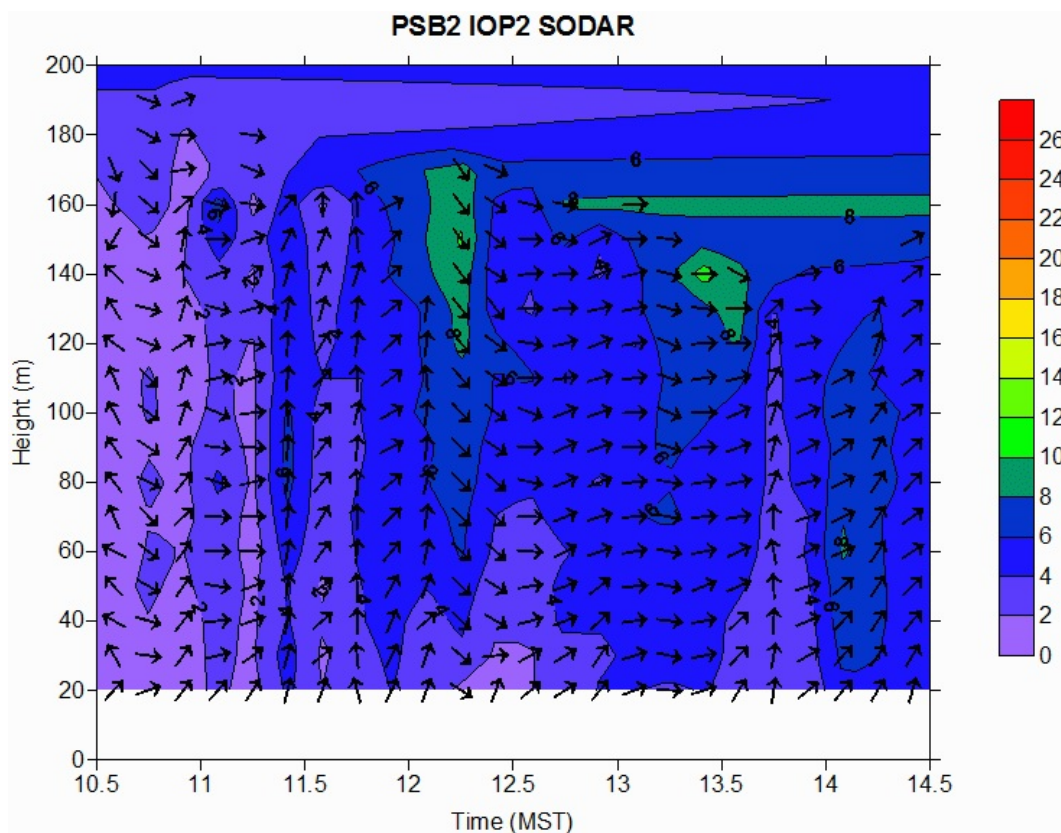


Figure 100. Time-height cross-section of wind speed and direction at sodar (SOD) during IOP2. Legend represents m s^{-1} .

TKE measurements exhibited a similar pattern to that seen for σ_w . The overall magnitudes of TKE measured by SOD (Fig. 103) were generally significantly lower than those measured by sonic at GRI (Fig. 99). Like σ_w , there is little clear correspondence in the timing between the TKE maxima observed at SOD and those observed at GRI. Figure 104 shows time-height temperature profiles from the RASS.

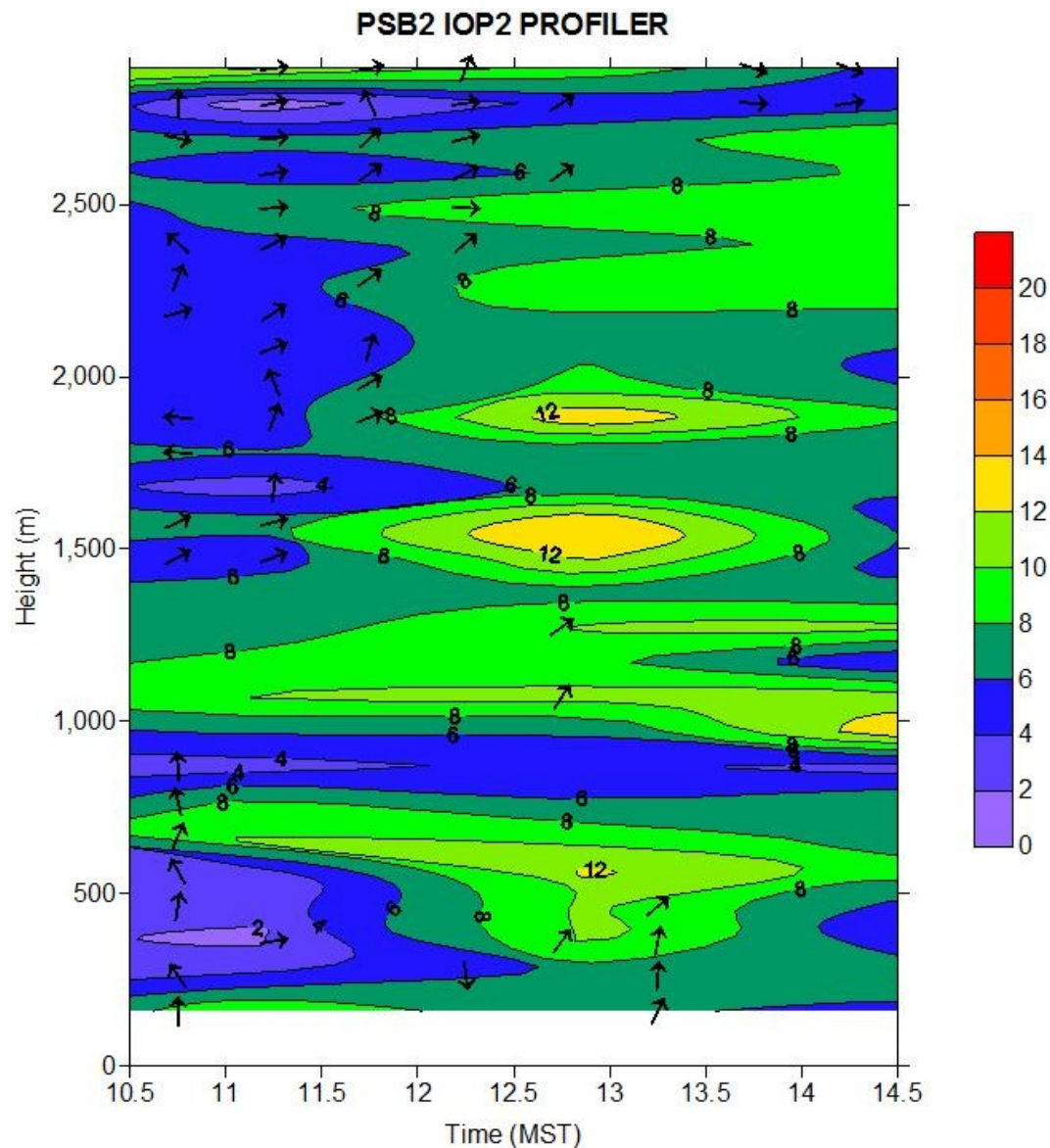


Figure 101. Time-height cross-section of wind speed and direction at wind profiler (PRO) during IOP2. Legend represents m s^{-1} .

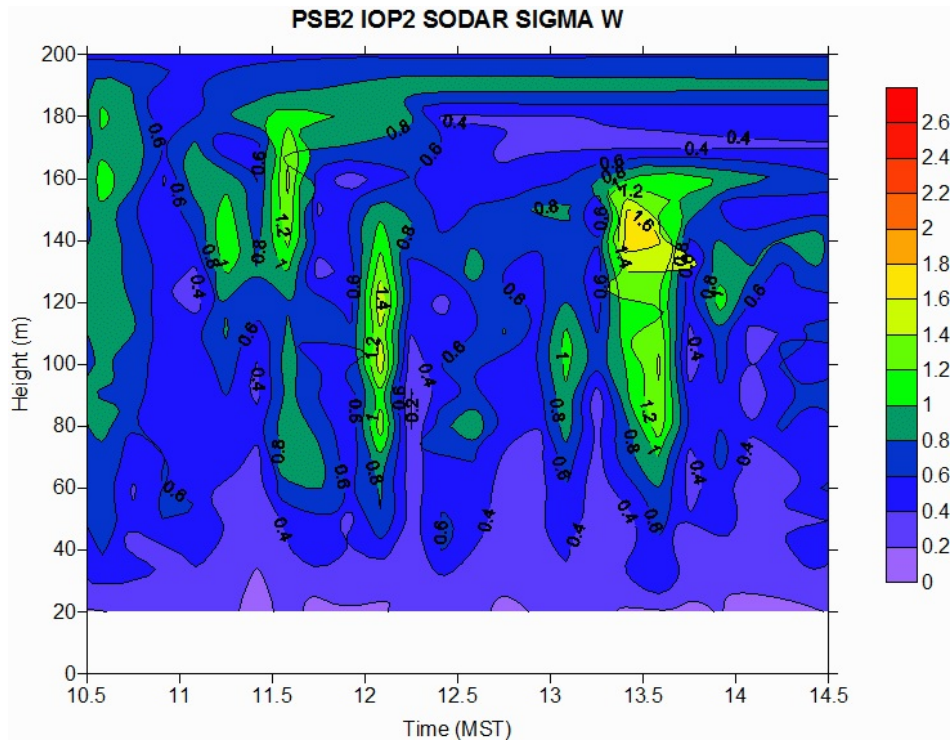


Figure 102. Time-height cross-section of σ_w at sodar (SOD) during IOP2. Legend represents m s^{-1} .

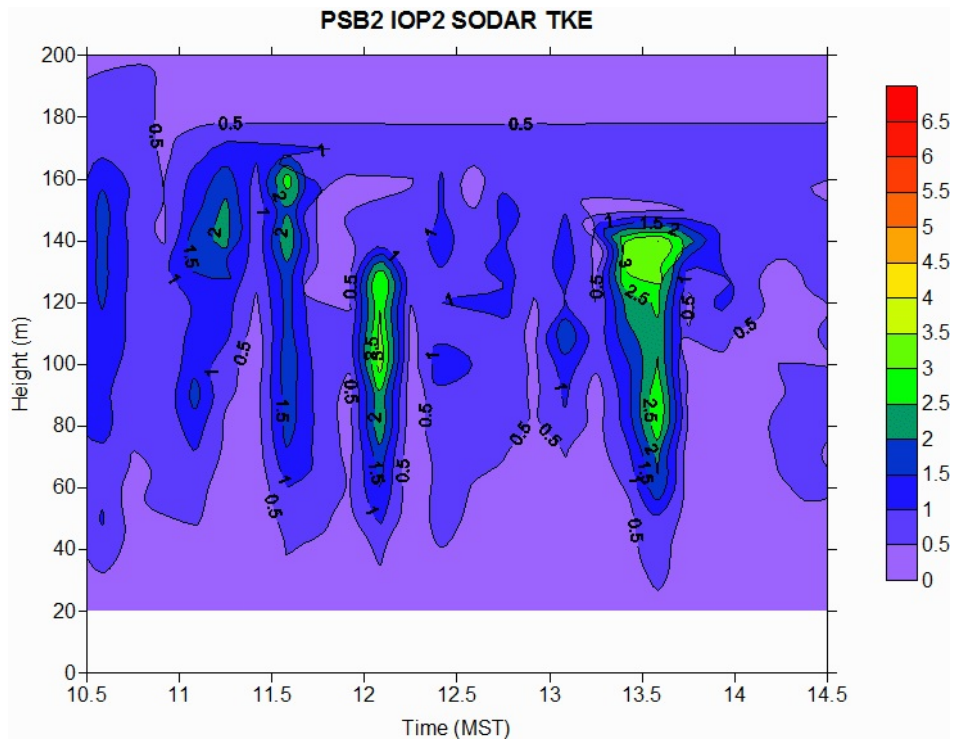


Figure 103. Time-height cross-section of TKE at sodar (SOD) during IOP2. Legend represents $\text{m}^2 \text{s}^{-2}$.

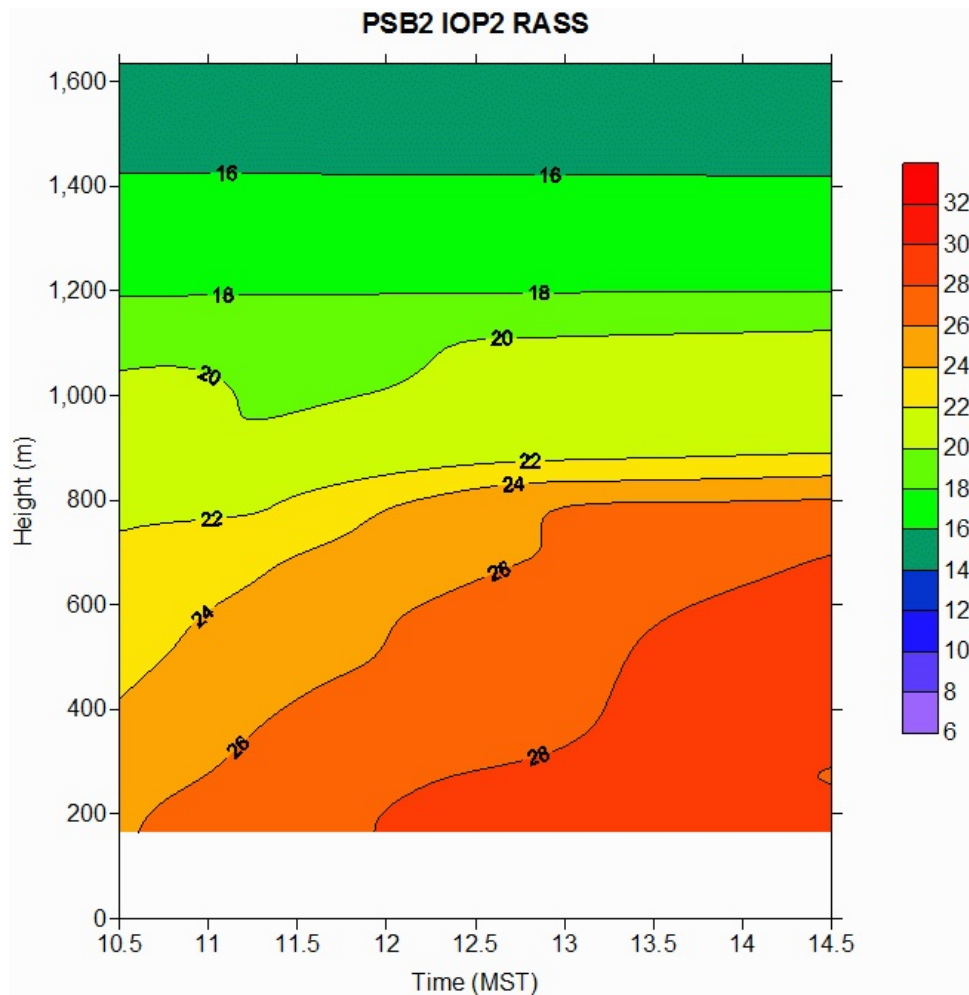


Figure 104. Time-height cross-section of virtual temperature at the RASS during IOP2. Temperatures are in degrees C.

Radisonde Results

Pre and post-IOP radiosonde profiles of potential temperature and specific humidity for IOP2 are shown in Figs. 105 and 106. The potential temperature profile suggests a pre-test mixing height of about 3000 m agl while a pre-test estimate based on the specific humidity profile appears to be either 2000 or 3000 m. The post-test potential temperature profile is a little more ambiguous but an estimate of 3000 m still looks reasonable. That would be consistent with a more definitive post-test estimate of 3000 m from the specific humidity profile.

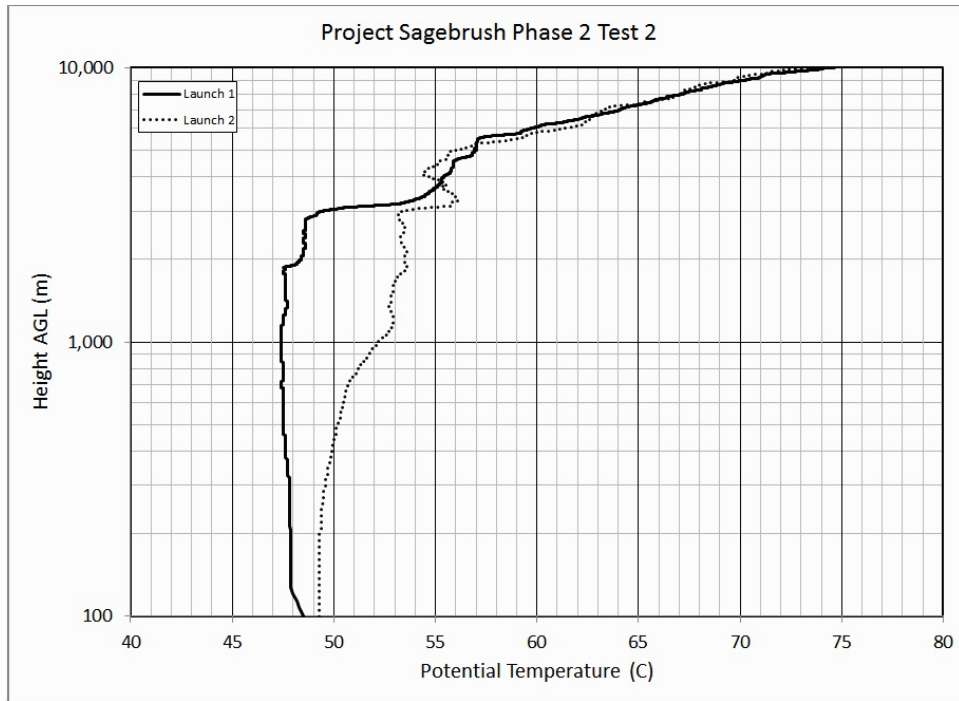


Figure 105. Potential temperature profile from radiosonde probe, IOP2. Pre-test launch bold, post-test launch dotted.

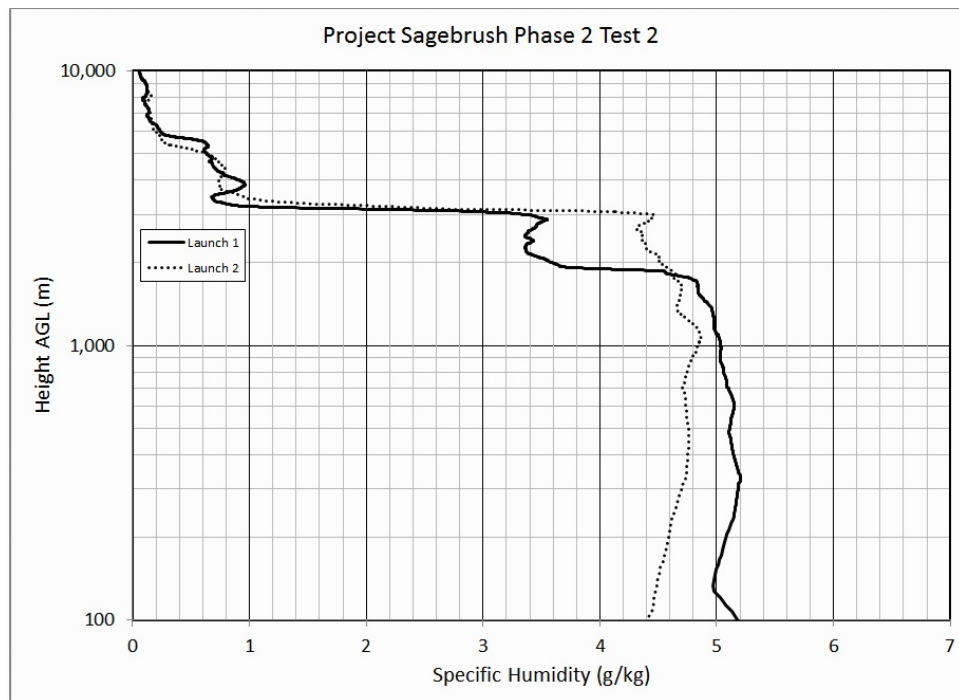


Figure 106. Specific humidity profile from radiosonde probe, IOP2. Pre-test launch bold, post-test launch dotted.

Bag Sampling Results

Figures 107 and 108 and Figures 109 and 110 show the 10-min average normalized and actual, respectively, color-coded plan view concentration maps for IOP2 bag sampling at 1 m agl. Figures 111 and 112 and Figures 113 and 114 show the 10-min average normalized and actual concentrations, respectively, along each of the arcs.

For the most part, the plume appeared to be centered or nearly centered and largely confined within the confines of the 210° sampling arcs throughout the IOP. However, some truncations of the plume occurred such as bags 4, 5, 10, and 11, mainly on the 100 m arc but also some on the 200 m arc in bags 4 and 5. The western limb of the 800 m arc also showed plume truncation in several bags. These observations are consistent with the observations of wind direction at GRI and COC (Figs. 92, 93, 95; Table 19). Plume morphology tended toward the development of a central, often multi-peaked composite. These peaks were crudely Gaussian in form except during periods of transition in wind direction. The plume was more smeared out and very irregular at these times. When a main peak was present, it usually subtended about 100-160° of arc at 100 m and the margins of the plume were relatively sharp. The subtended range generally decreased with increasing downwind distance.

Figure 115 shows the vertical concentration profiles up to 25 m agl from the mobile tower located on the 100 m arc at 24° azimuth (red dot 1, Fig. 5). During the first half hour several of the profiles exhibit a relatively uniform concentration with height. However, by the second hour, the concentration profiles mostly show maxima near the surface and decreasing concentration with height. While the overall shapes of the profiles are relatively well defined, it is again clear that the upper limb of the plume generally exceeded the upper 25 m measurement level.

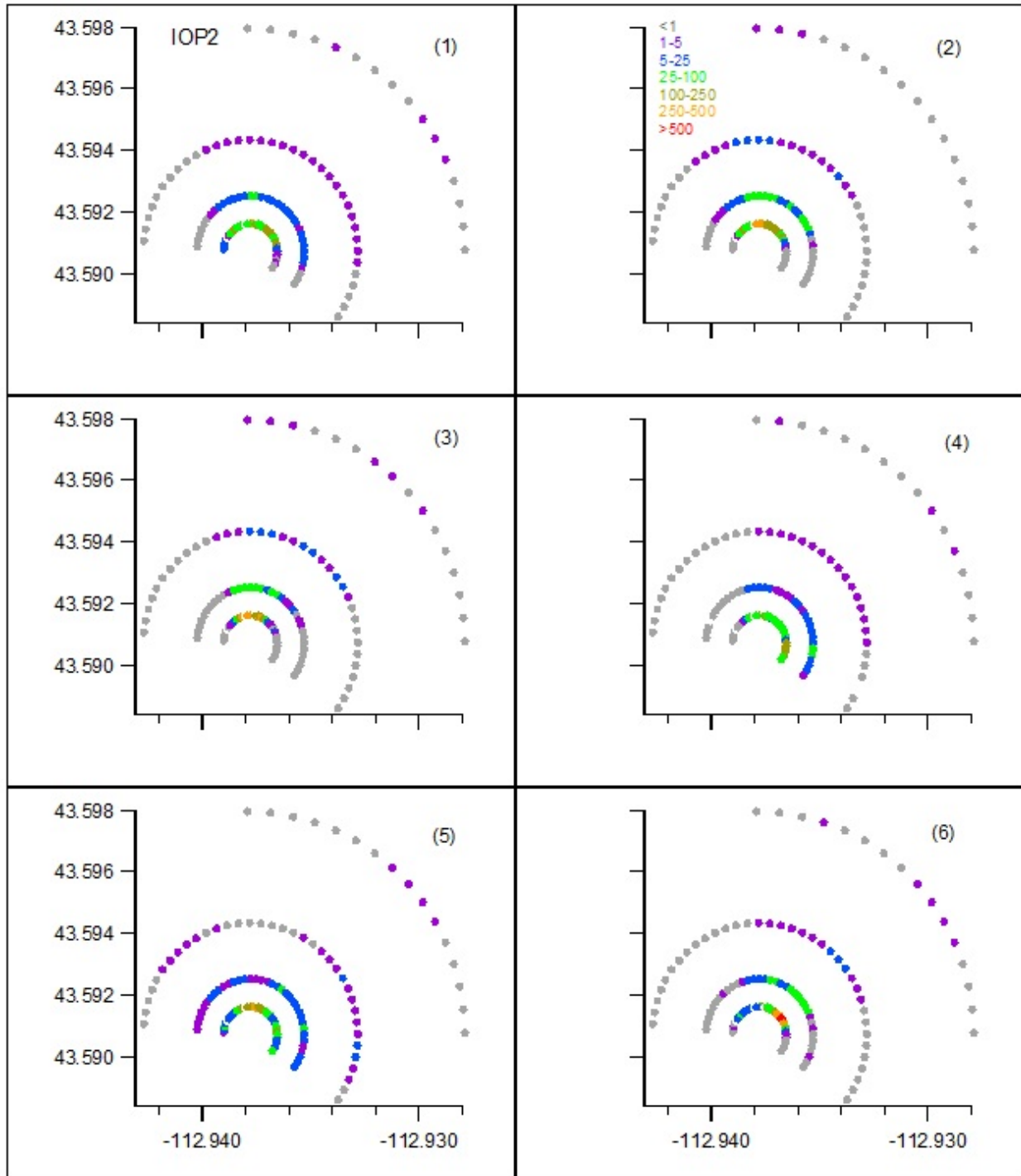


Figure 107. Color-coded normalized ($F^*\gamma/Q$ ppt s g^{-1}) concentrations at 1 m agl for bags 1-6 during IOP2. The number in () is bag number.

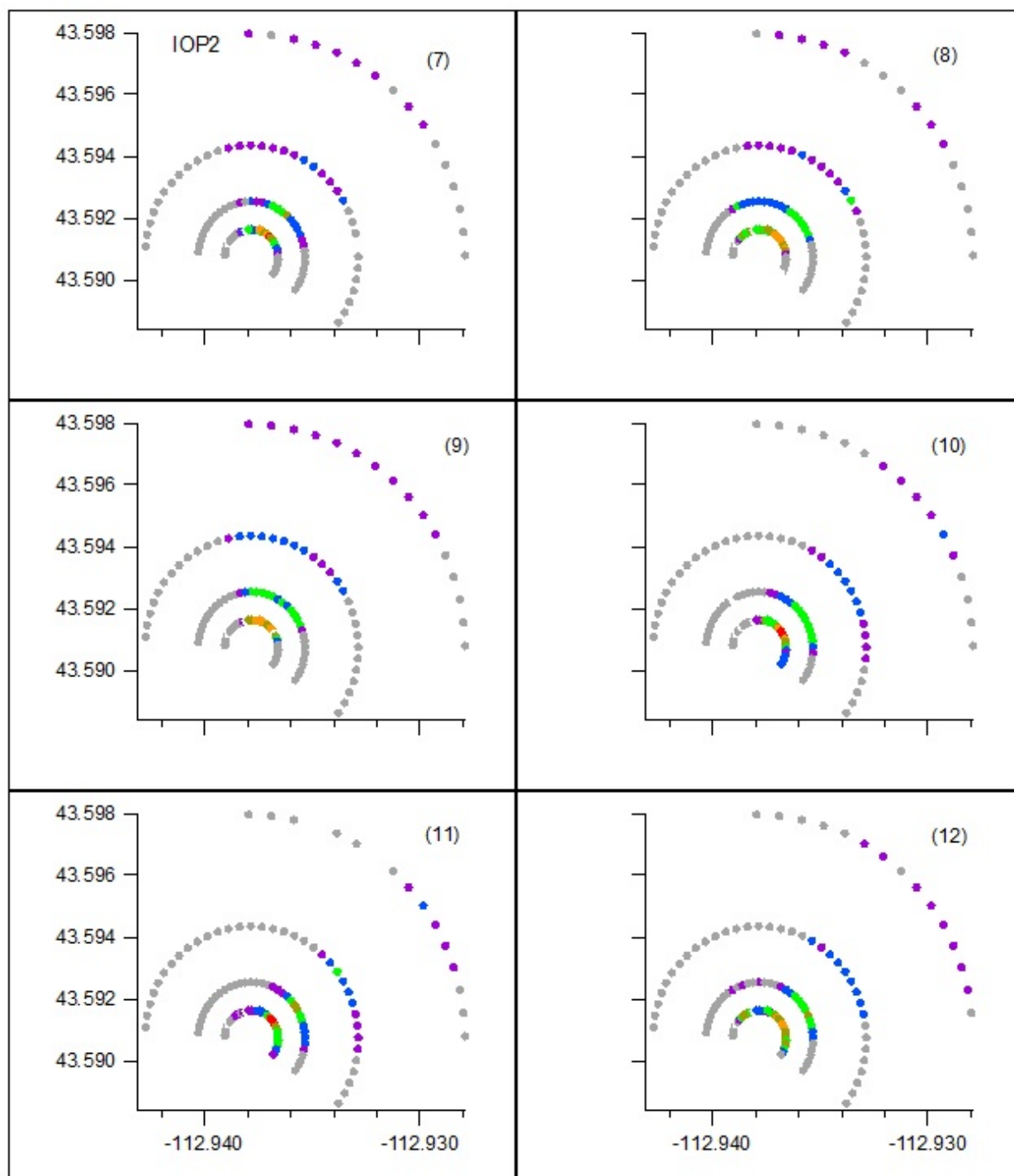


Figure 108. Color-coded normalized ($F^*\chi/Q$ ppt s g^{-1}) concentrations at 1 m agl for bags 7-12 during IOP2. The number in () is bag number.

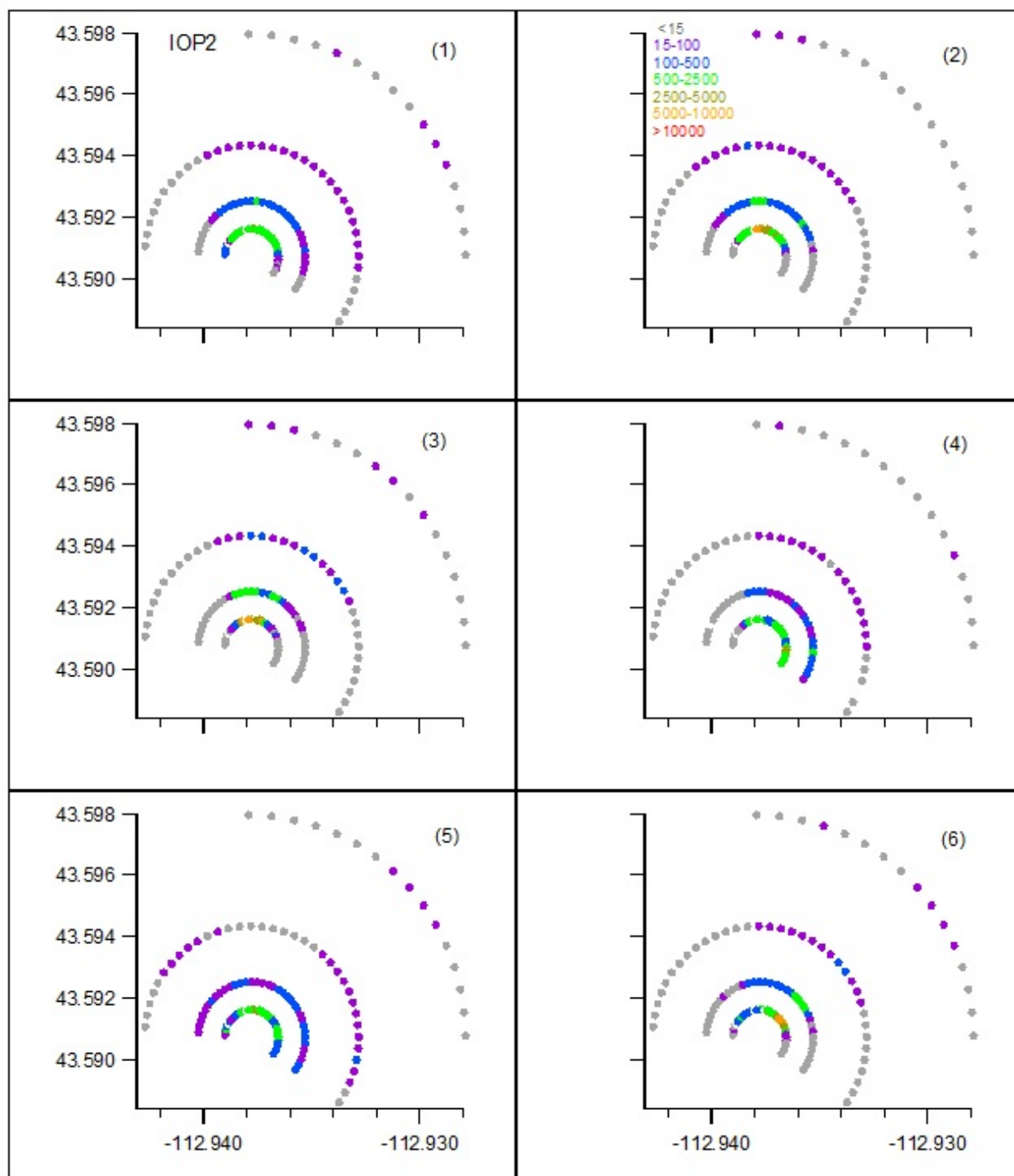


Figure 109. Color-coded measured SF_6 concentrations (ppt) at 1 m agl for bags 1-6 during IOP2. The number in () is bag number.

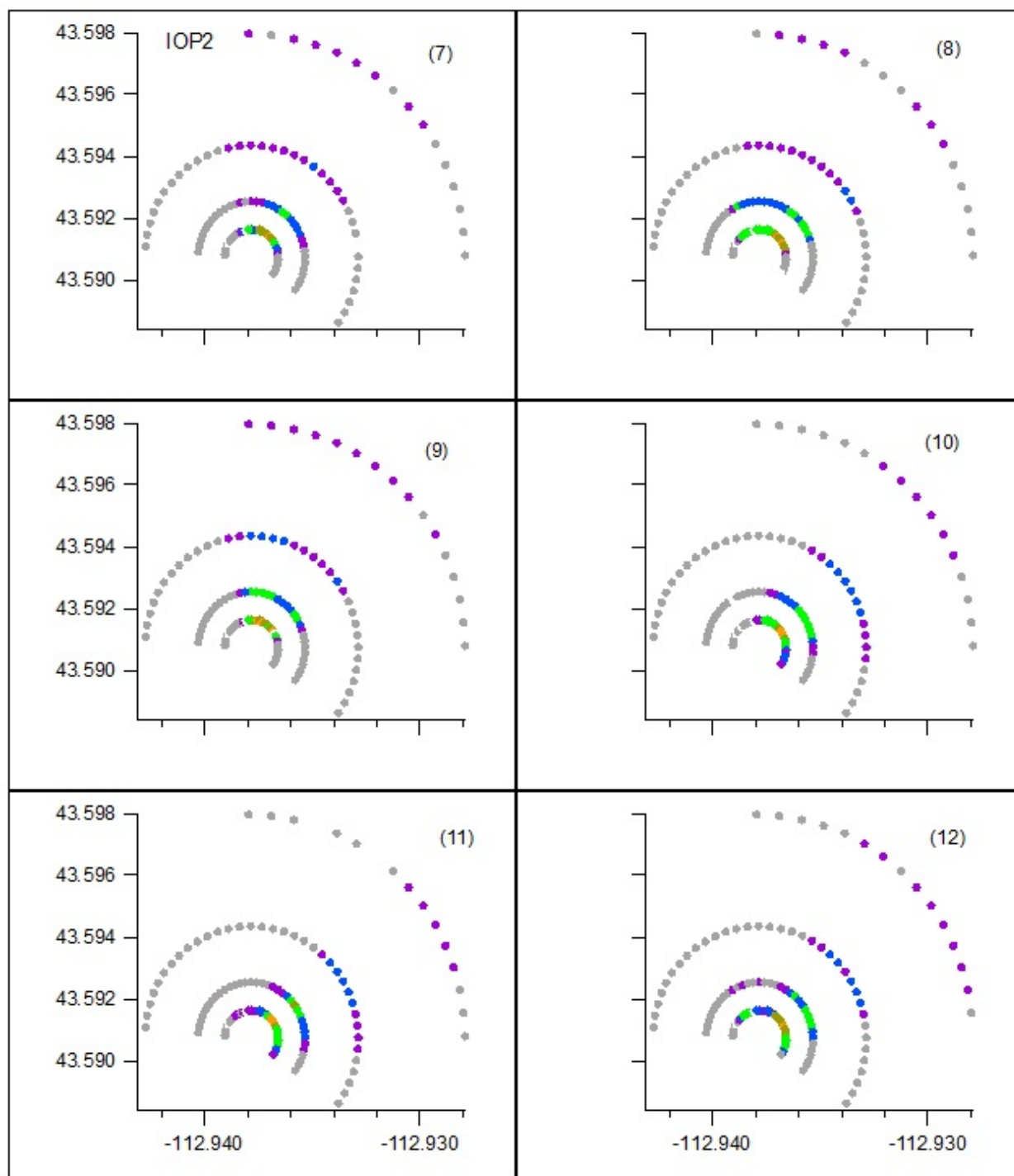


Figure 110. Color-coded measured SF_6 concentrations (ppt) at 1 m agl for bags 7-12 during IOP2. The number in () is bag number.

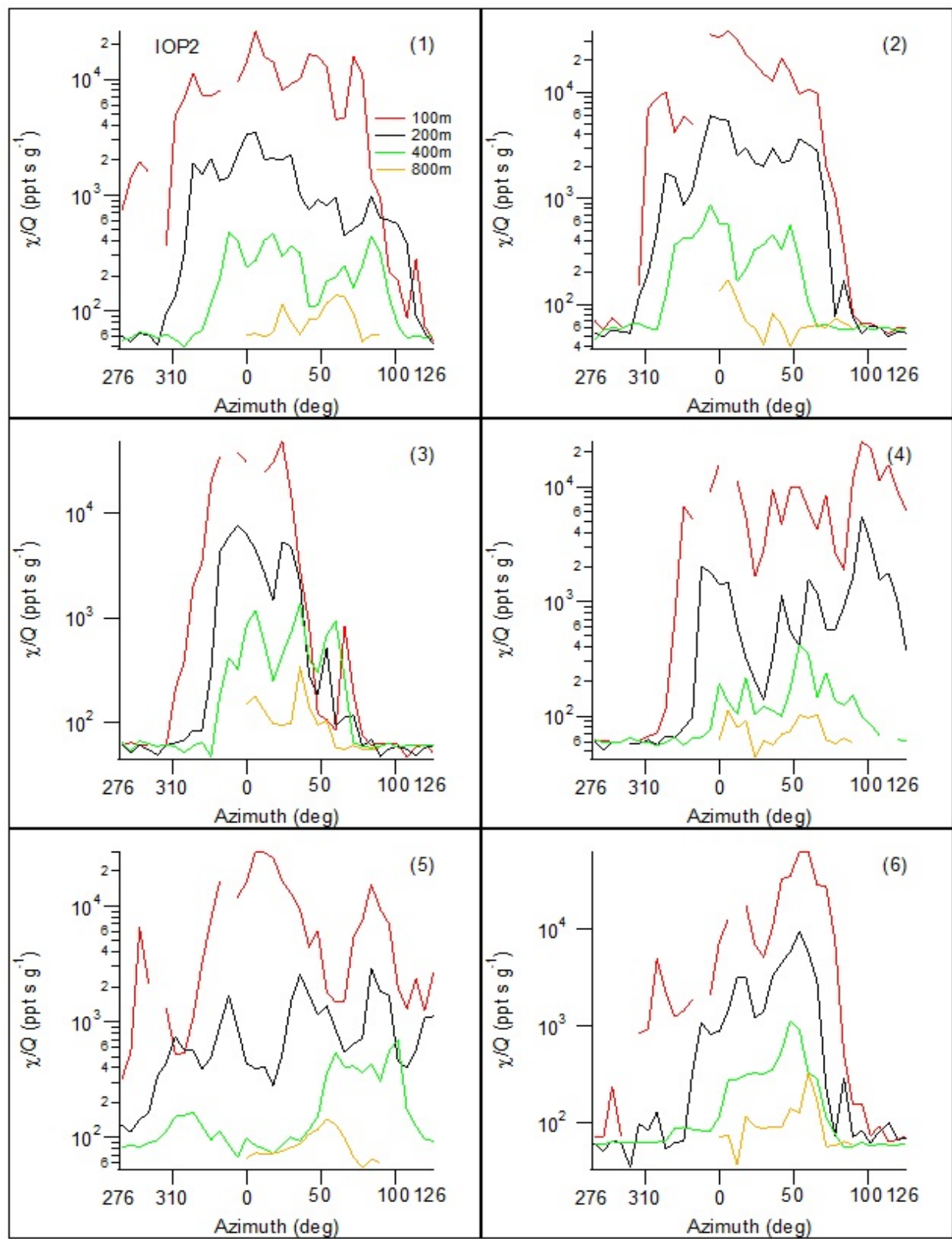


Figure 111. Cross-sections of normalized concentration along the arcs for bags 1-6 during IOP2.

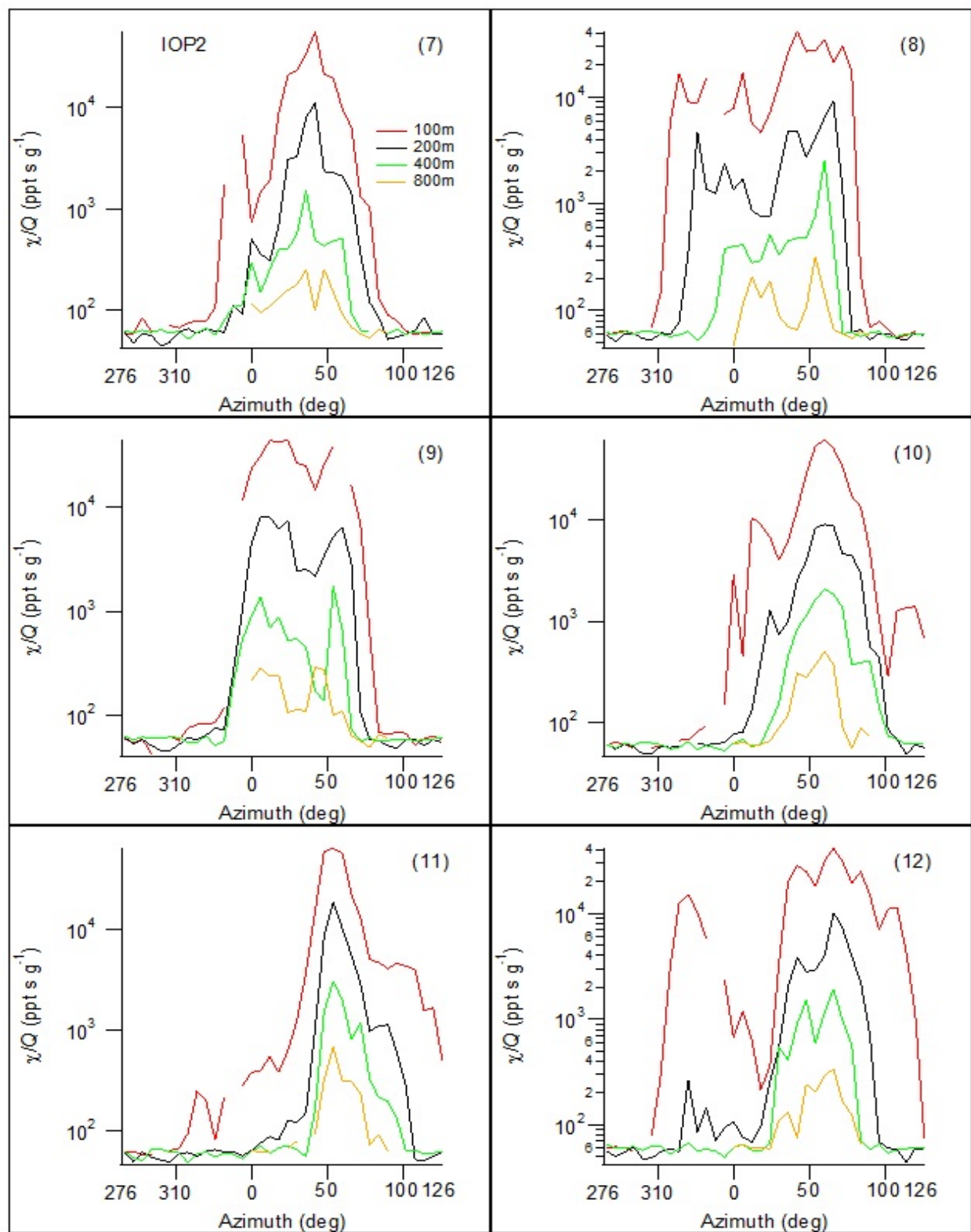


Figure 112. Cross-sections of normalized concentration along the arcs for bags 7-12 during IOP2.

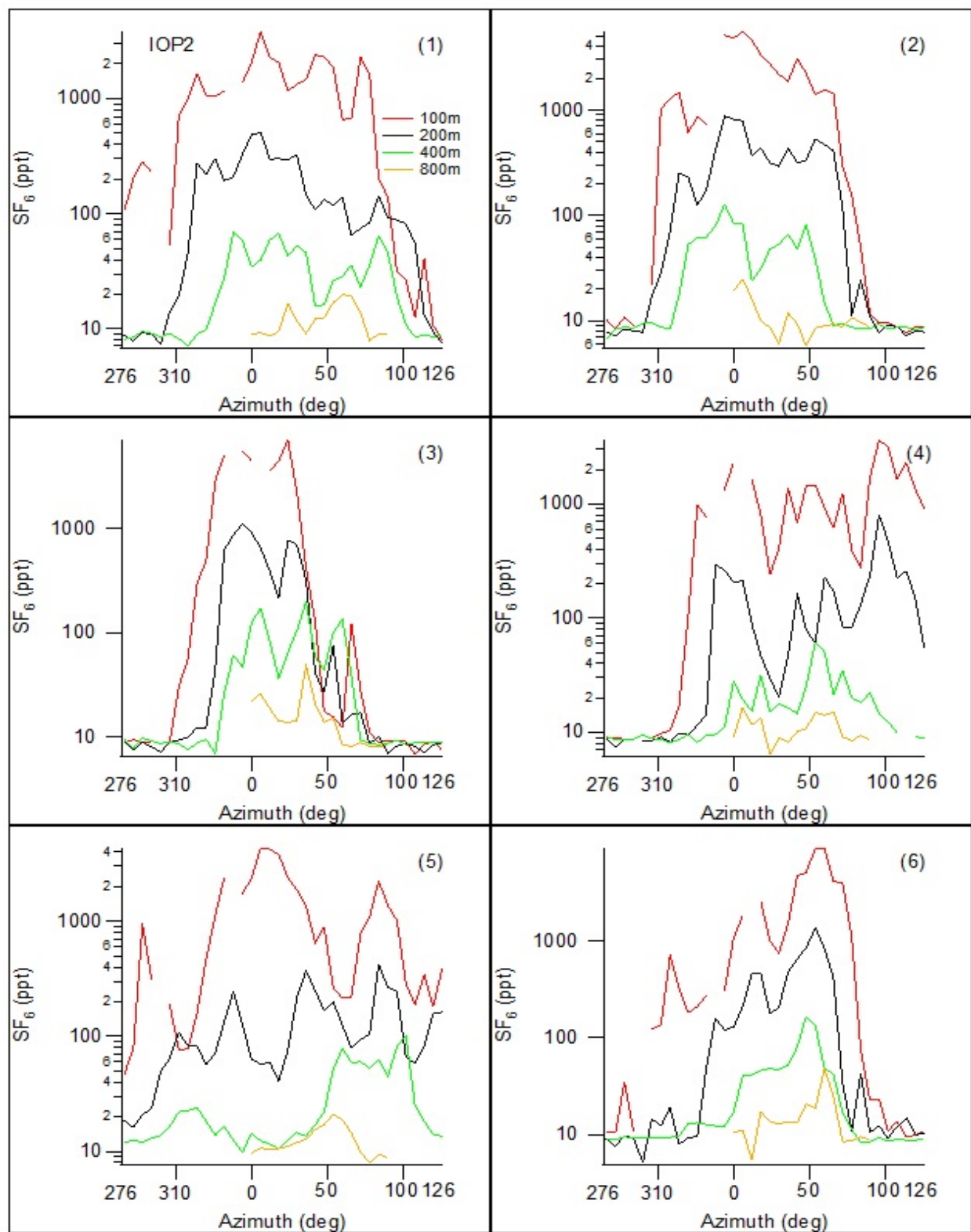


Figure 113. Cross-sections of measured SF_6 concentration along the arcs for bags 1-6 during IOP2.

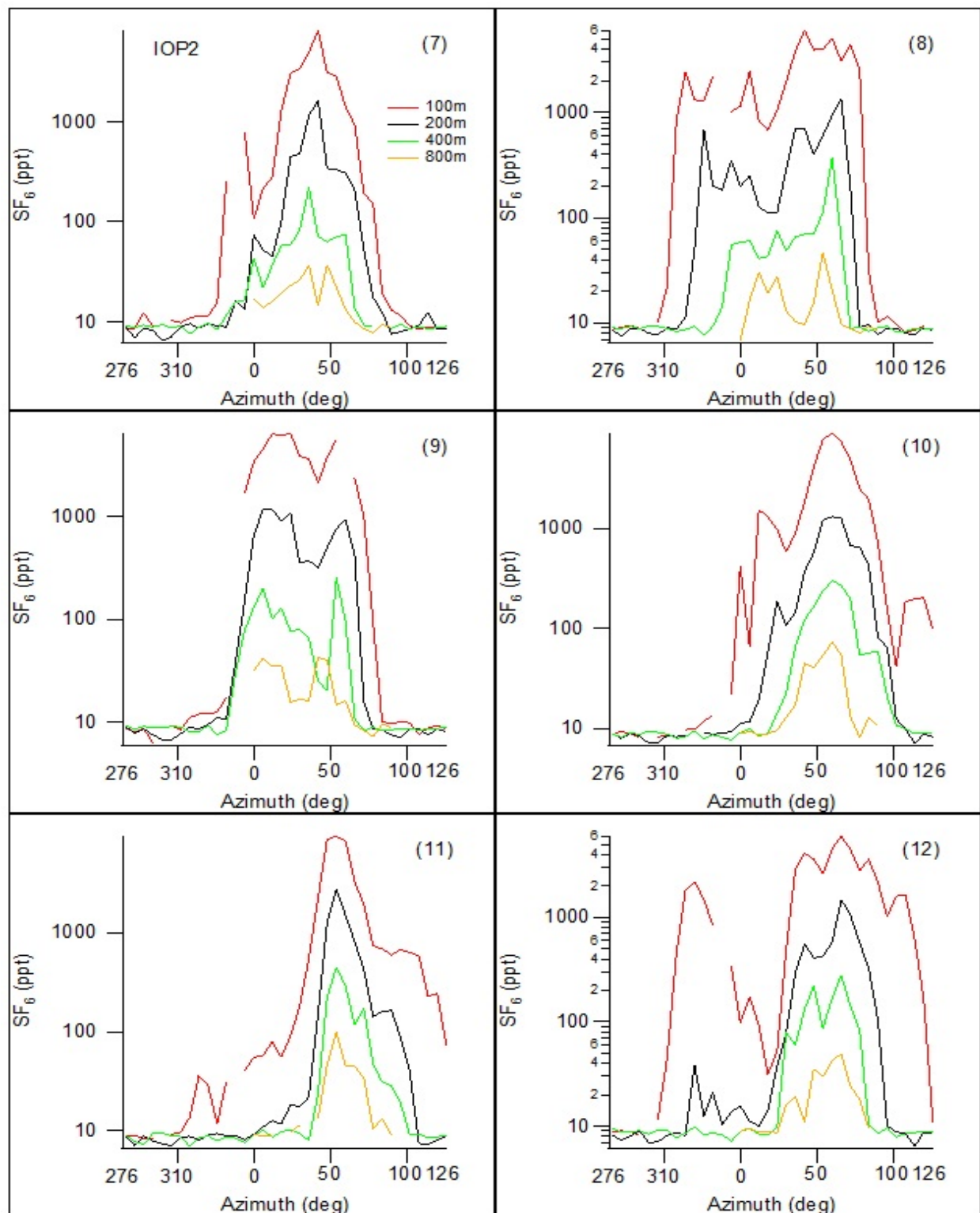


Figure 114. Cross-sections of measured SF_6 concentration along the arcs for bags 7-12 during IOP2.

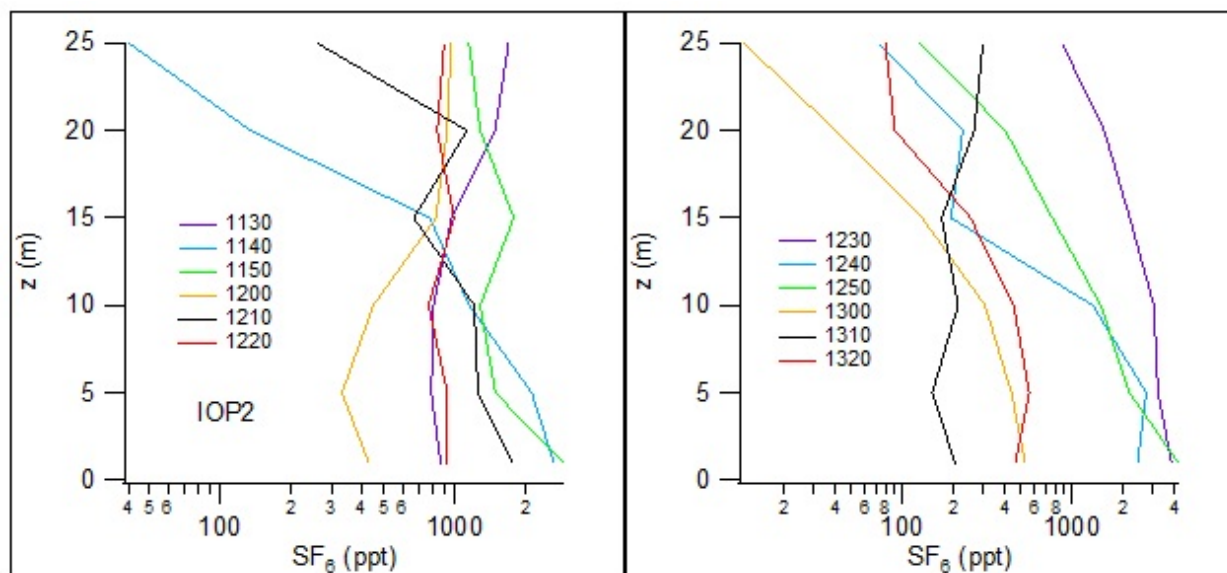


Figure 115. Vertical profiles of measured SF_6 concentration at the mobile tower during IOP2.

Fast Response Results

The locations of the fast response analyzers during IOP2 are shown in Fig. 116. The corresponding concentration time series are shown in Fig. 117. The color coding of the time series was described in the Introduction to this section.

The analyzers were more or less continuously in the plume from 1130-1300 h. There was little SF_6 detected after that at any of the analyzers. This is basically consistent with the bag sampling (Figs. 107-114) and wind direction (Figs. 92, 93, 95; Table 19) results. Wind directions gradually shifted from mostly south-southwest to more southwesterly over the course of the IOP. By the last half hour the analyzer positions at 18° azimuth put them near the western margin of the plume, not in the plume like was generally the case prior to that. Like IOP1, the measurements were characterized by being highly variable and intermittent with often rapid increases from background to peak values followed by rapid drops in concentration back to background or near background concentrations. The peaks were sometimes railed (overranged), especially on the 100 m arc at analyzer A. The character of the time series suggests that the plume was probably relatively narrow at any given time and, with frequent shifts in wind direction, resulted in the very intermittent time series observed. Thus the bag sampling averaging likely represents a smoothing of a much more fluctuating signal with large peak:mean ratios.

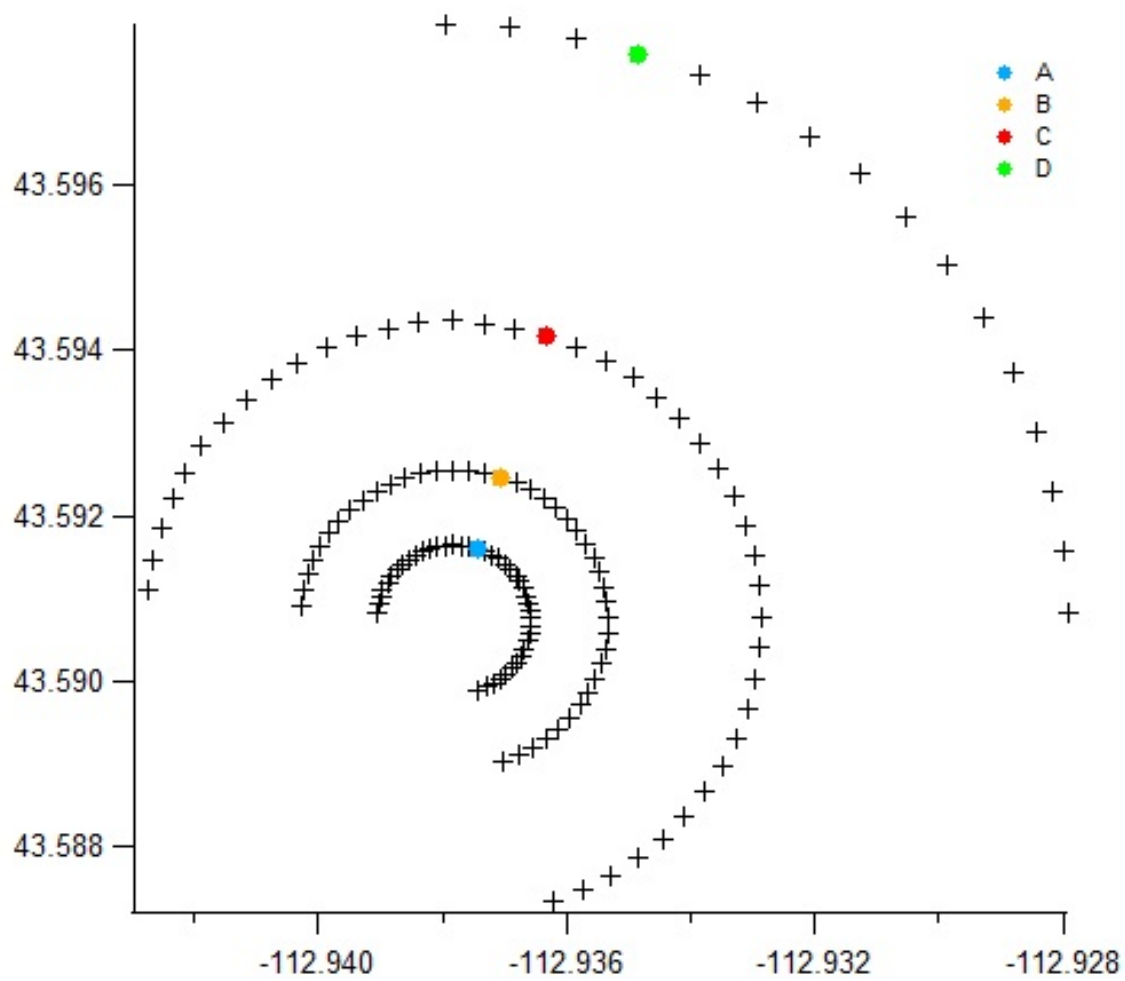


Figure 116. Locations of fast response analyzers during IOP2.

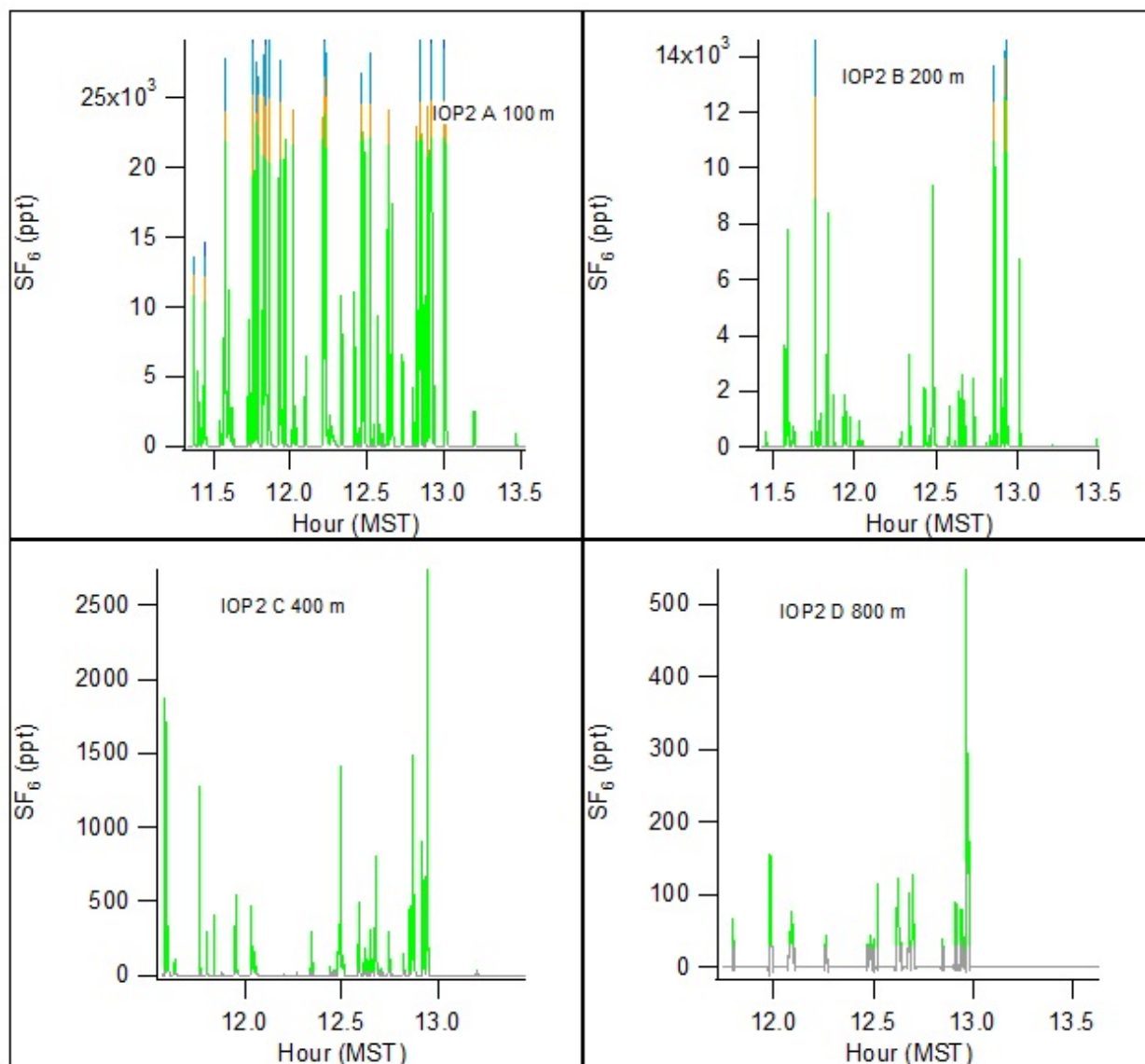


Figure 117. Fast response concentration time series during IOP2.

IOP 3

Date/Time and General Description

IOP3 was conducted on 04 August from 1300-1500 MST (1400-1600 MDT). Conditions were warm and dry with clear skies and light and very variable winds throughout the IOP. Overall conditions were unstable and highly non-stationary in both time and space. Estimates of stability based on traditional Pasquill-Gifford (P-G) schemes were all class A during the first hour and a mix of class A and B in the second hour (Fig. 118). Estimates of mean z/L from GRI ranged from -0.22 to -0.81 with a Ri_b of -2.36. A summary of the meteorological conditions during IOP3 are shown in Table 20. There was considerable variation in wind direction, both in time and space (compare GRI and COC in Table 20). One consequence was that the 210° sampling arcs, in general, failed to fully measure the plumes. While the tracer plumes never entirely missed the 210° sampling arcs, it was common for about half of the plume to be truncated at the western margin of the bag sampling array. The SF_6 release rate was 0.122 g s^{-1} (Table 2). Three of the fast response analyzers were located on the 100, 200, and 400 m arcs at 342° azimuth. The fourth analyzer was located due north on the 800 m arc. All positions were fixed for the duration of the IOP.

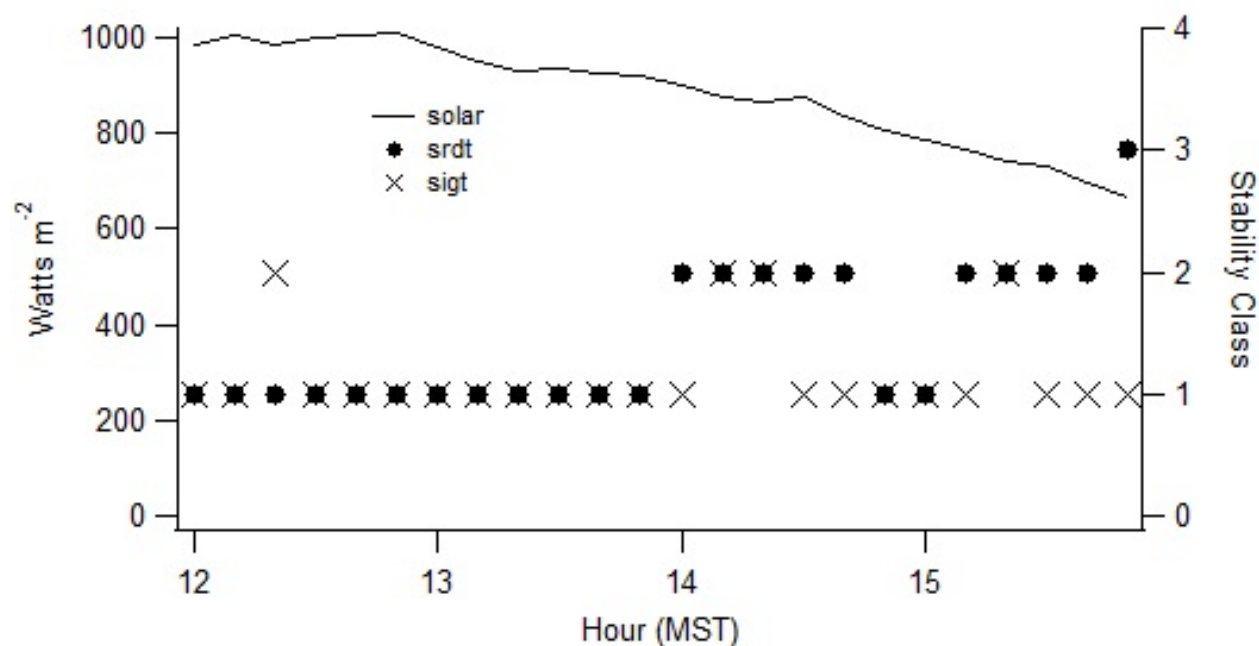


Figure 118. Incoming solar radiation and classification of stability conditions using the Pasquill-Gifford Solar Radiation Delta T (srdt) and σ_θ (sigt) methods (EPA 2000c) during IOP3. Classes A, B, C, and D are designated 1, 2, 3, and 4, respectively.

Table 20. Meteorological conditions during IOP3.

Bag	COC				GRI						GRI			Solar
	U (m s ⁻¹)		WD (deg)		U (m s ⁻¹)		WD (deg)		σ_θ (deg)		L	L	degC	W m ⁻²
	2m	10m	2m	10m	2m	10m	2m	10m	2m	10m	3.7m	9m	2m	
1	1.6	1.7	301.3	292.6	1.8	2.0	67.0	49.1	67.5	61.2	-0.8	-1.6	26.5	981.5
2	1.3	1.6	353.4	330.0	1.9	1.9	20.5	23.0	52.3	34.8	-13.5	-20.0	26.0	950.5
3	2.3	2.6	109.6	116.3	1.2	1.6	94.0	91.1	47.5	37.7	-9.8	-4.9	26.5	930.5
4	2.0	2.5	89.6	121.0	2.3	2.6	132.2	126.8	33.7	26.4	-3.8	-4.4	27.2	935.0
5	2.1	2.2	35.4	40.7	0.1	0.7	126.4	158.3	82.5	81.2	-3.7	-0.6	27.4	923.0
6	1.5	1.6	41.9	44.1	1.6	1.7	192.2	193.0	35.7	39.9	-6.4	-11.0	28.2	920.5
7	1.8	2.1	67.4	73.9	1.5	2.0	104.7	108.5	64.1	47.4	-5.3	-2.9	27.9	899.0
8	1.9	2.2	145.9	162.2	3.3	3.1	250.3	269.8	49.0	52.1	NaN	NaN	28.2	878.0
9	1.8	2.0	195.6	201.1	2.7	3.5	180.8	193.8	44.9	46.8	NaN	NaN	28.8	868.0
10	1.5	1.8	130.0	128.9	2.5	2.9	182.8	182.5	49.0	43.5	-6.8	-22.1	28.5	873.5
11	1.8	2.2	215.3	224.0	2.1	2.4	207.4	206.7	37.5	31.9	-8.5	-1.9	28.8	837.0
12	2.0	2.2	151.1	169.6	0.2	0.6	74.4	98.4	72.2	69.2	-106.5	-41.2	28.5	807.0
Avg. L											-16.51 -11.06			
z/L											-0.22 -0.81			
Ri _b											-2.36			

Wind Speed and Direction Quality Assurance

Figures 119-121 show wind speed and direction time series comparisons for a sequence of measurement heights during IOP3. In Fig. 119, the near surface measurement of U showed some variation with the largest differences relative to the other stations being associated with the 2 m cup anemometer at GRI. Wind directions varied significantly between the three sites over most of the experimental period. Wind speeds were generally about 2 m s⁻¹. A similar pattern of observations held for the wind speed and direction measurements between 9 and 30 m agl (Fig. 120). There were some large differences in wind direction between sites and lesser, more irregular differences in the measurement of U . The measurement of U by SOD appears to have had a slight low bias. The weak low U bias at SOD also appears to be present at 45 m agl but is not apparent at 60 m (Fig. 121). The overall pattern of wind direction variation at GRI and SOD at 30 and 45 m was similar, however, the actual wind direction differences at any specific time were often large. There is insufficient data available from the sodar (SOD) and radar profiler (PRO) at 160 m agl to make any assessment. Other than the poor data recovery for SOD and PRO at 160 m agl, there is little evidence of a systematic measurement problem. Any of the observed variability or discrepancies are likely attributable to non-stationarity and horizontal inhomogeneity in the wind field.

Figure 122 shows time series measurements for cup anemometers and wind vanes only (excluding sonics) at all heights on the two towers during IOP3. Measurements of U during the

first half of the experiment were similar between GRI and COC. However, during the second half, GRI tended to fluctuate about 2 m s^{-1} while COC remained relatively constant. Variations in wind direction were large, both in magnitude and between sites. Wind directions were consistent within a site but the variations between GRI and COC were generally large. The measured σ_θ were generally in excess of 40° , especially at the lower measurement levels.

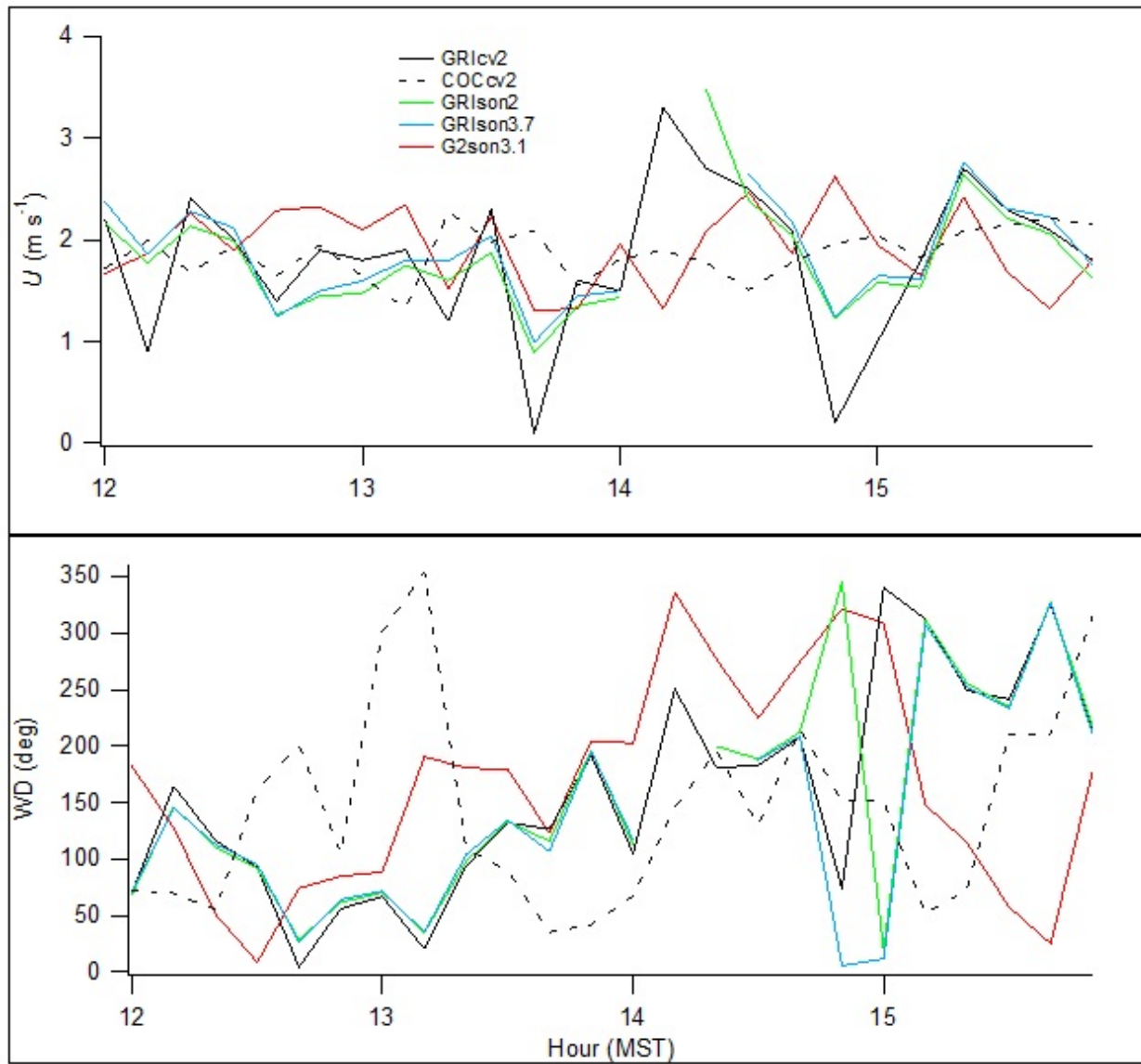


Figure 119. Time series of near surface wind speed and direction measurements during IOP3. In the legend, location is specified in upper case, the measurement type in lower case (cv = cup and vane, son = sonic), and the measurement height numerically.

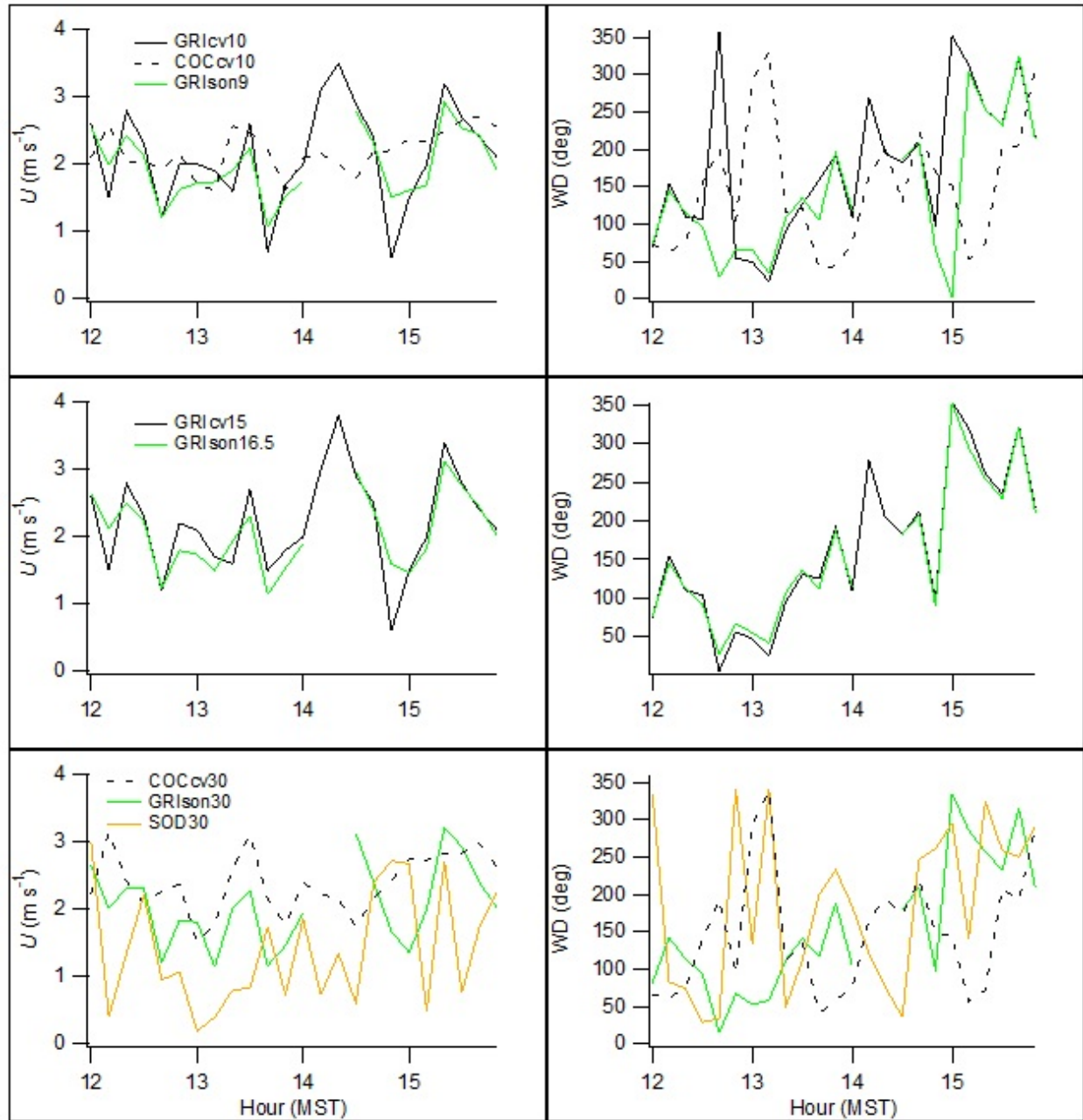


Figure 120. Time series of wind speed and direction measurements at heights between 9 and 30 m agl during IOP3. Legend notations described in caption of Fig. 119.

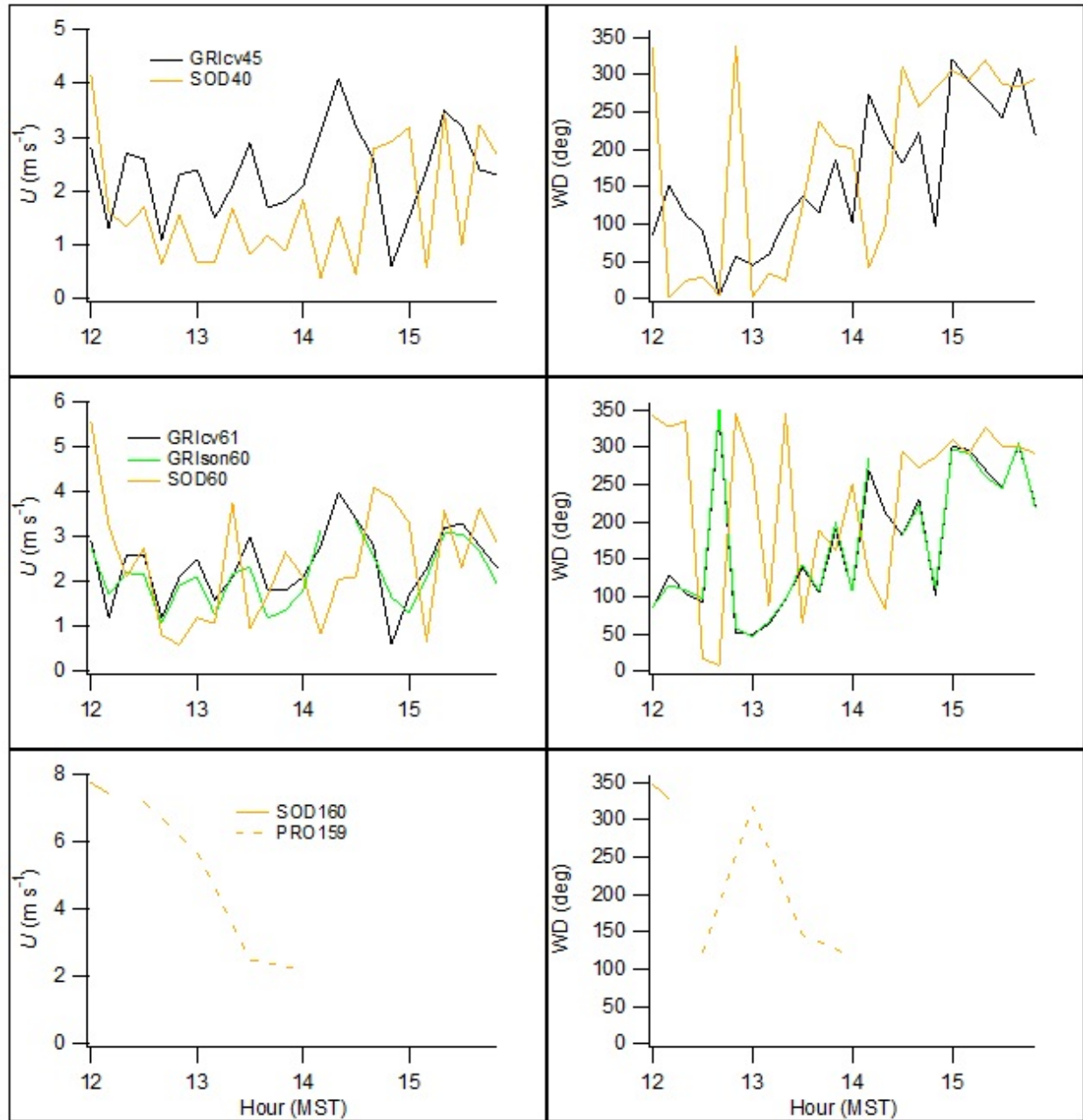


Figure 121. Time series of wind speed and direction measurements at heights above 30 m agl during IOP3. Legend notations described in caption of Fig. 119.

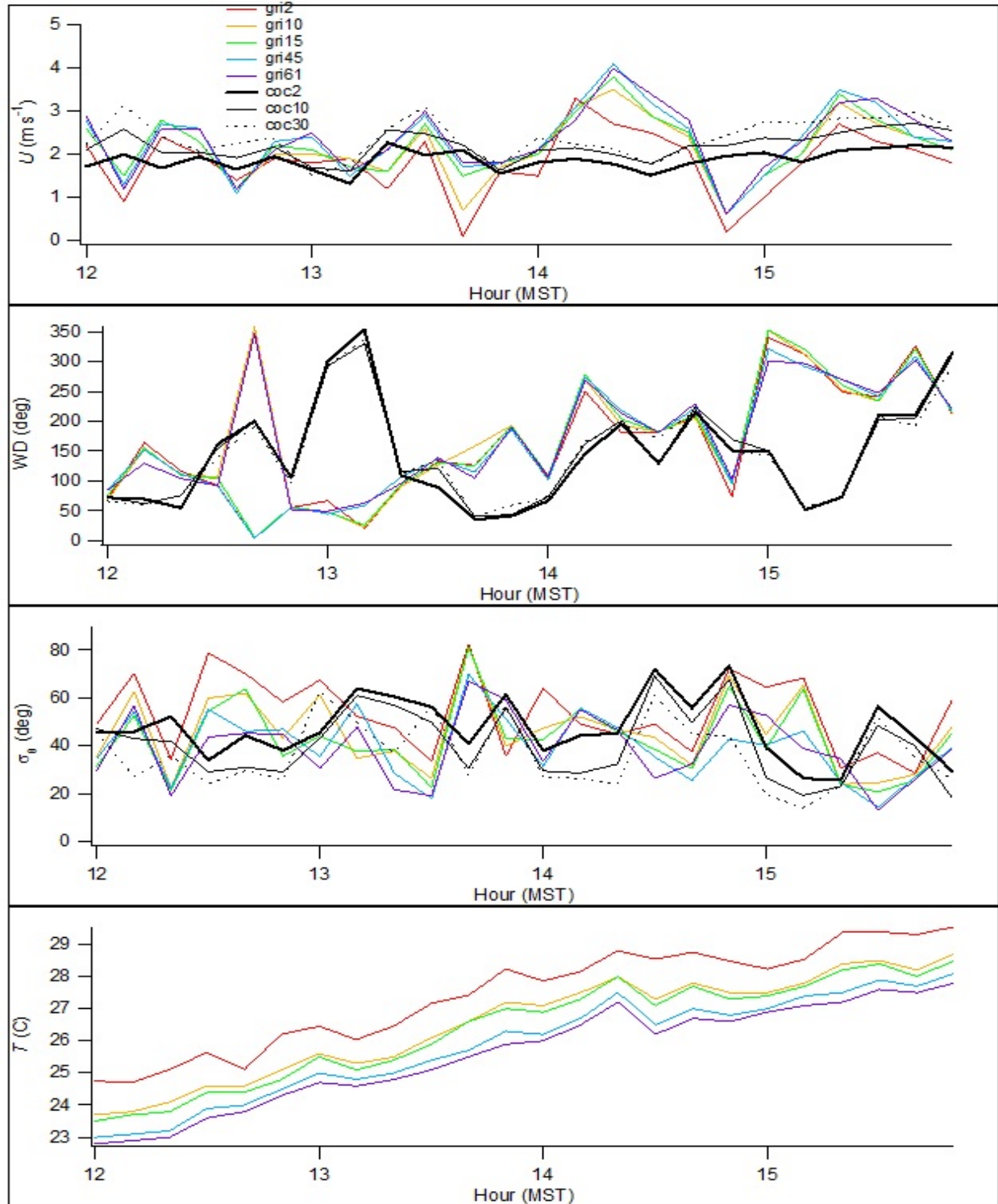


Figure 122. Time series from GRI and COC showing cup anemometer and wind vane measurements of U , wind direction, standard deviation of wind direction σ_0 , and temperature during IOP3. The locations are designated 'xxxxy' where xxx = tower and yy = measurement height.

Turbulence

The available near surface turbulence measurements exhibited considerable variation between sites (Fig. 123). Some of this variation was expressed as sharp excursions, especially for anemometers R2 and R9. This was particularly the case for σ_v/U and σ_w/U and is likely due to sensitivity to the sometimes very low U . At other times the variations were expressed as sustained shifts in magnitude between sites such as seen for TKE, σ_w , and u_* .

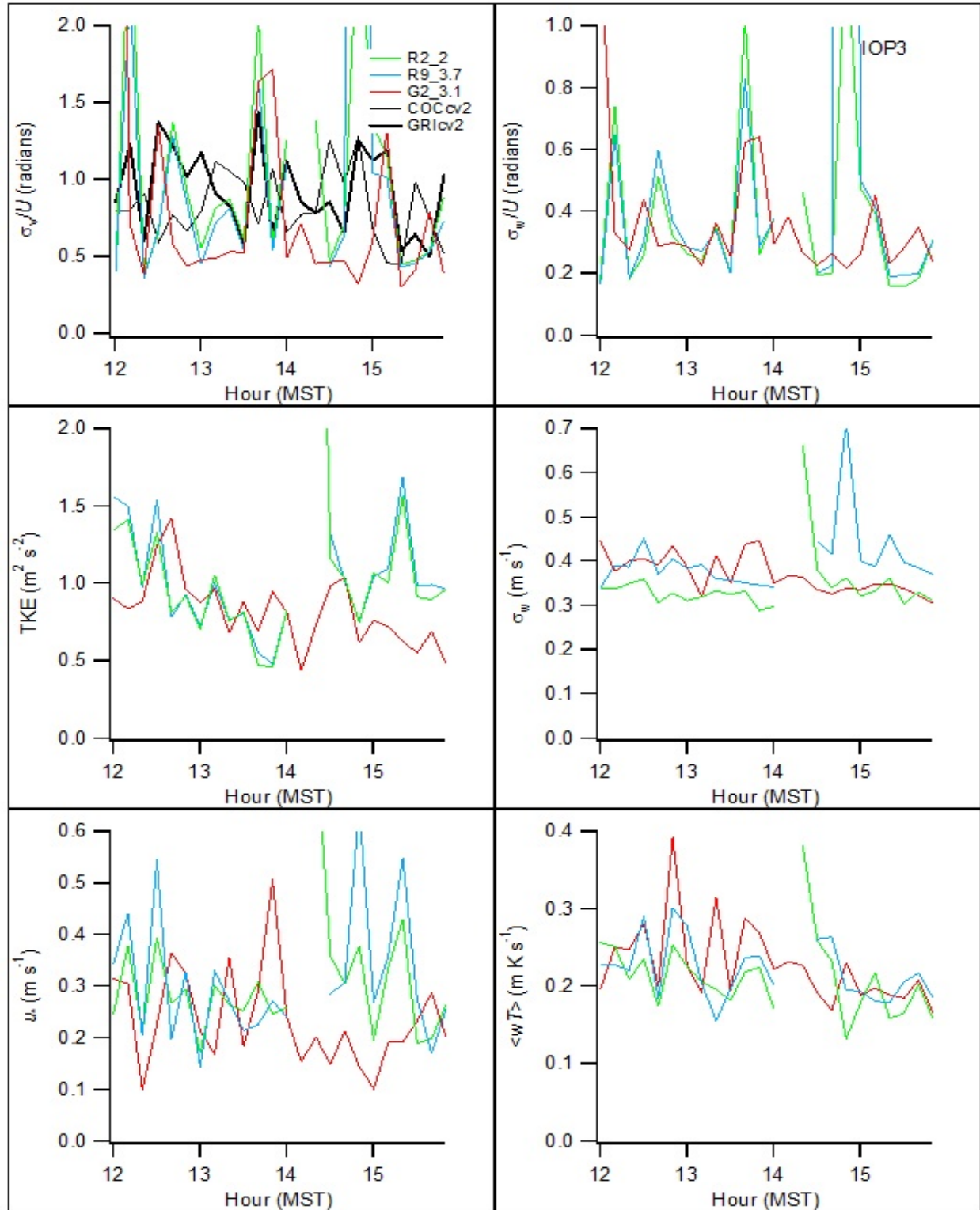


Figure 123. Time series of near surface turbulence (sonic) measurements during IOP3. The GRI and COC are σ_θ wind vane measurements (cv) in degrees converted to radians for purposes of comparison. Notation before and after underscore designates location and height, respectively.

Wind and Turbulence Profiles

Figure 124 shows profiles of the non-sonic measurements at GRI and COC during IOP3. Wind directions tended to be uniform in the vertical within a given profile but large shifts in direction occurred throughout the experiment. Wind speeds ranged mostly from 1 to 3 m s⁻¹. Most of the profiles were well behaved although there is some evidence of weakly anomalous deviations or vertical gradients, especially for σ_θ .

Figures 125 and 126 show profiles of the sonic turbulence measurements at GRI during IOP3. Wind directions showed large variation like that seen in Fig. 124. Wind speeds in Fig. 125 tend to be a little higher than U in Fig. 124. The σ_v/U and σ_w/U were large in magnitude, consistent with the results in Fig. 124, but also exhibited the effects of the low U in the form of profiles being shifted right to larger magnitudes and the presence of some extreme anomalies.

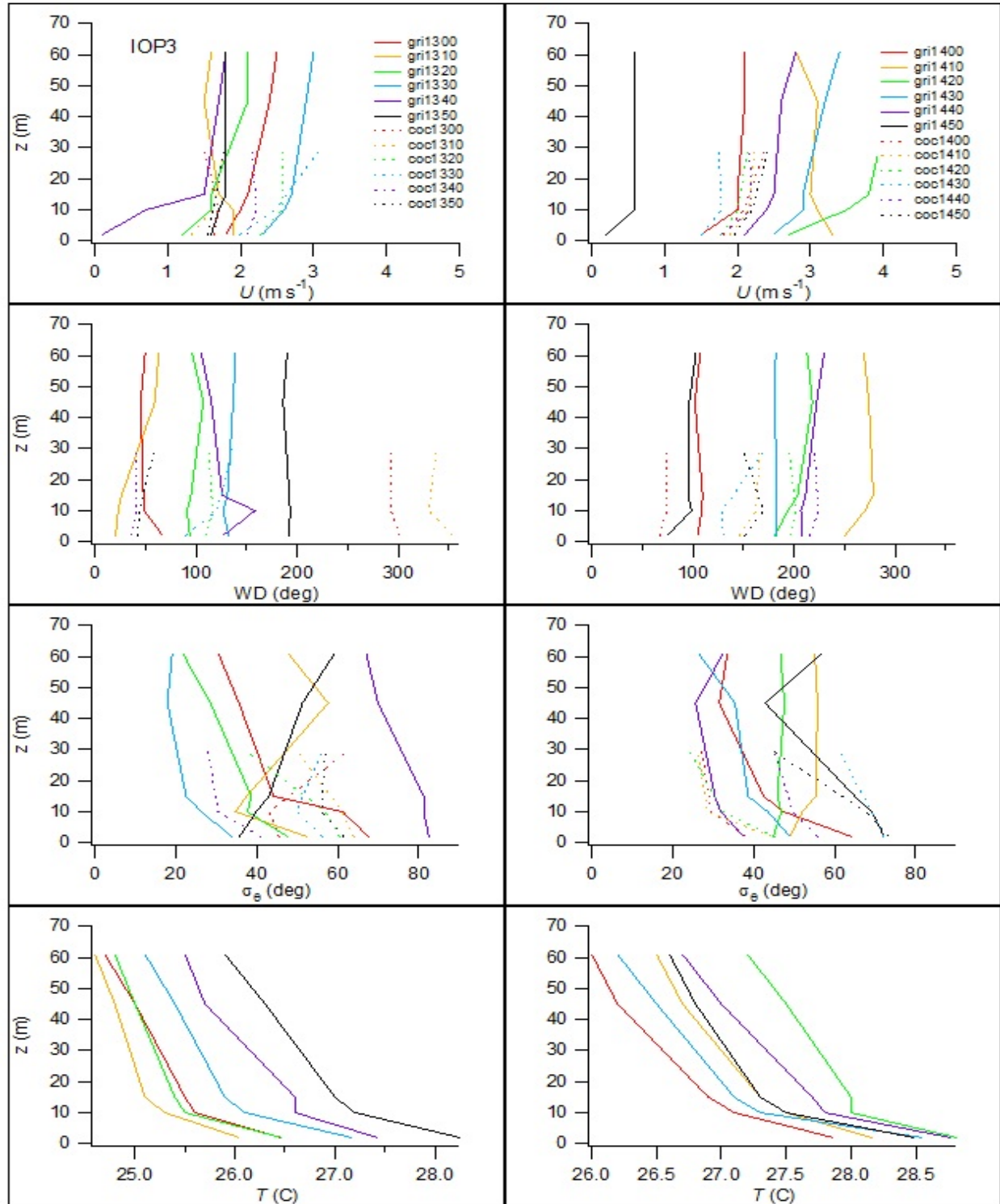


Figure 124. Profiles of U , wind direction, standard deviation of wind direction σ_{θ} , and aspirated temperature from cup anemometers and wind vanes during IOP3 at GRI and COC. Each profile is designated 'xxxhrmn' where xxx = tower and hrmn = start time of 10-minute interval.

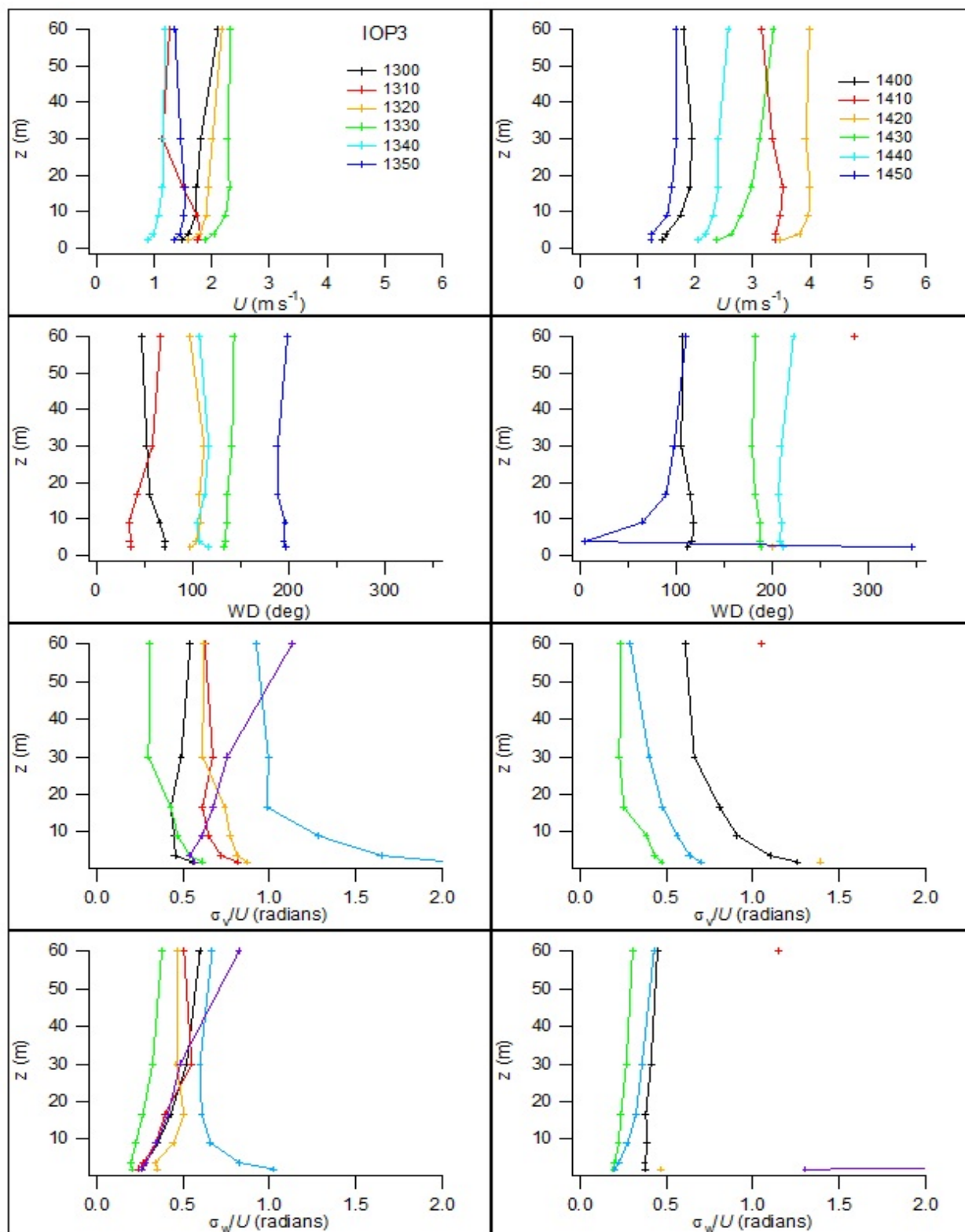


Figure 125. Profiles of U , wind direction, σ_v/U ($\sim\sigma_\theta$), and σ_w/U ($\sim\sigma_\phi$) from sonic anemometers at GRI during IOP3. The legend specifies the start time of the 10-minute interval (hrmn).

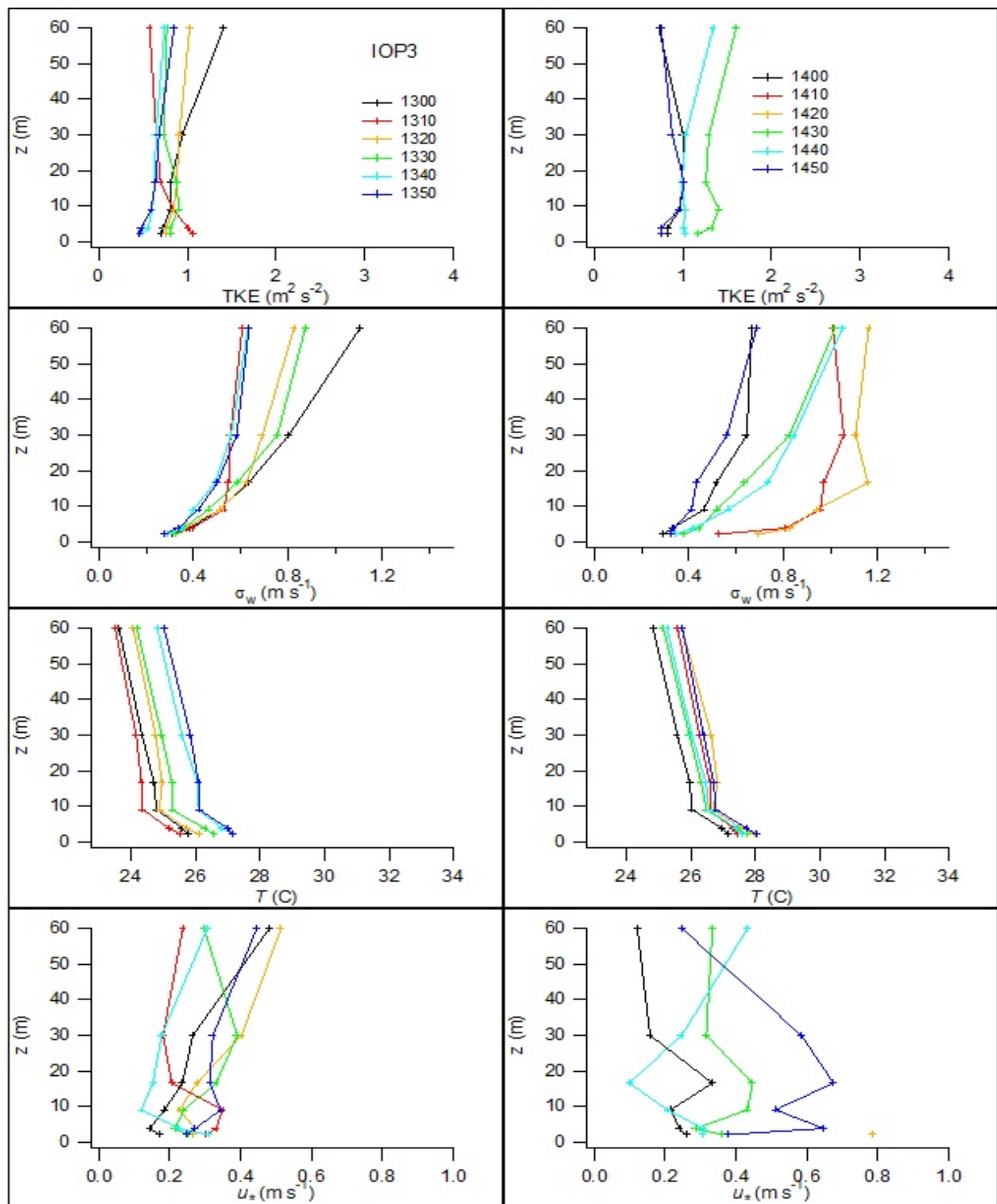


Figure 126. Profiles of turbulent kinetic energy (TKE), standard deviation in vertical wind speed σ_w , virtual temperature, and friction velocity u_* from sonic anemometers at GRI during IOP3. The legend specifies the start time of the 10-minute interval (hrmn).

Figures 127 and 128 show time-height representations of wind speed and direction for SOD and PRO, respectively, during IOP3. Wind speeds and directions at SOD were light and variable throughout the test period. That is entirely consistent with the observations at GRI (Figs. 124, 125). Wind speeds at SOD increased slightly and directions stabilized somewhat from westerly near the end of the tracer measurement period at 1500 h. A similar increase in U was observed at GRI but it was slightly earlier there, mainly 1410-1440 h. Data recovery at PRO was relatively good. These also showed generally low U and variable wind directions throughout the profiles and the test.

Figures 129 and 130 show SOD time-height representations of σ_w and TKE, respectively, during IOP3. The σ_w profiles exhibit a roughly periodic pattern, possibly associated with thermals. This pattern is most apparent above the levels measured at GRI and obscured below that. The magnitudes of σ_w measured by sonic at GRI were similar to or higher than those measured by SOD at comparable heights (Figs. 126, 129). The SOD TKE measurements exhibited an episodic pattern similar to that seen for σ_w . The overall magnitudes of TKE measured by GRI sonic (Fig. 126) were generally a few tenths greater than those measured by SOD (Fig. 130). The concentration of higher σ_w and TKE values at about 120 m agl might represent, in part, measurement artifacts near the top of the profiles. Figure 131 shows time-height temperature profiles from the RASS.

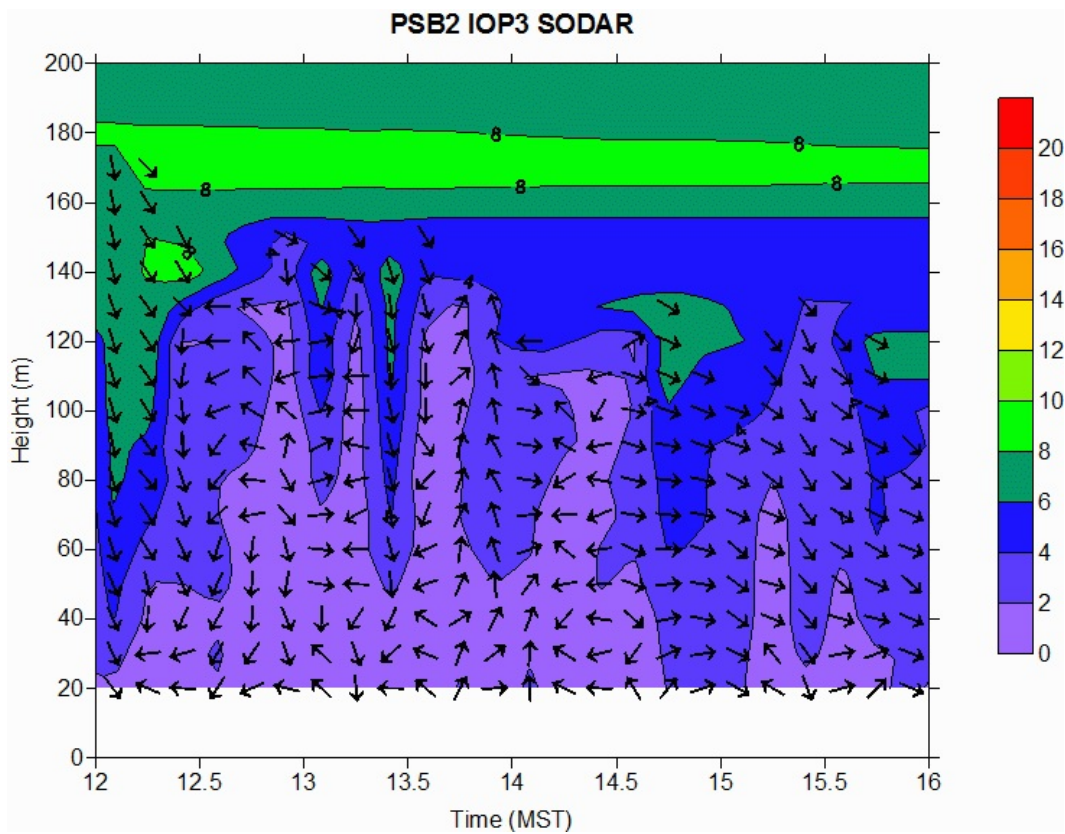


Figure 127. Time-height cross-section of wind speed and direction at sodar (SOD) during IOP3. Legend represents m s^{-1} .

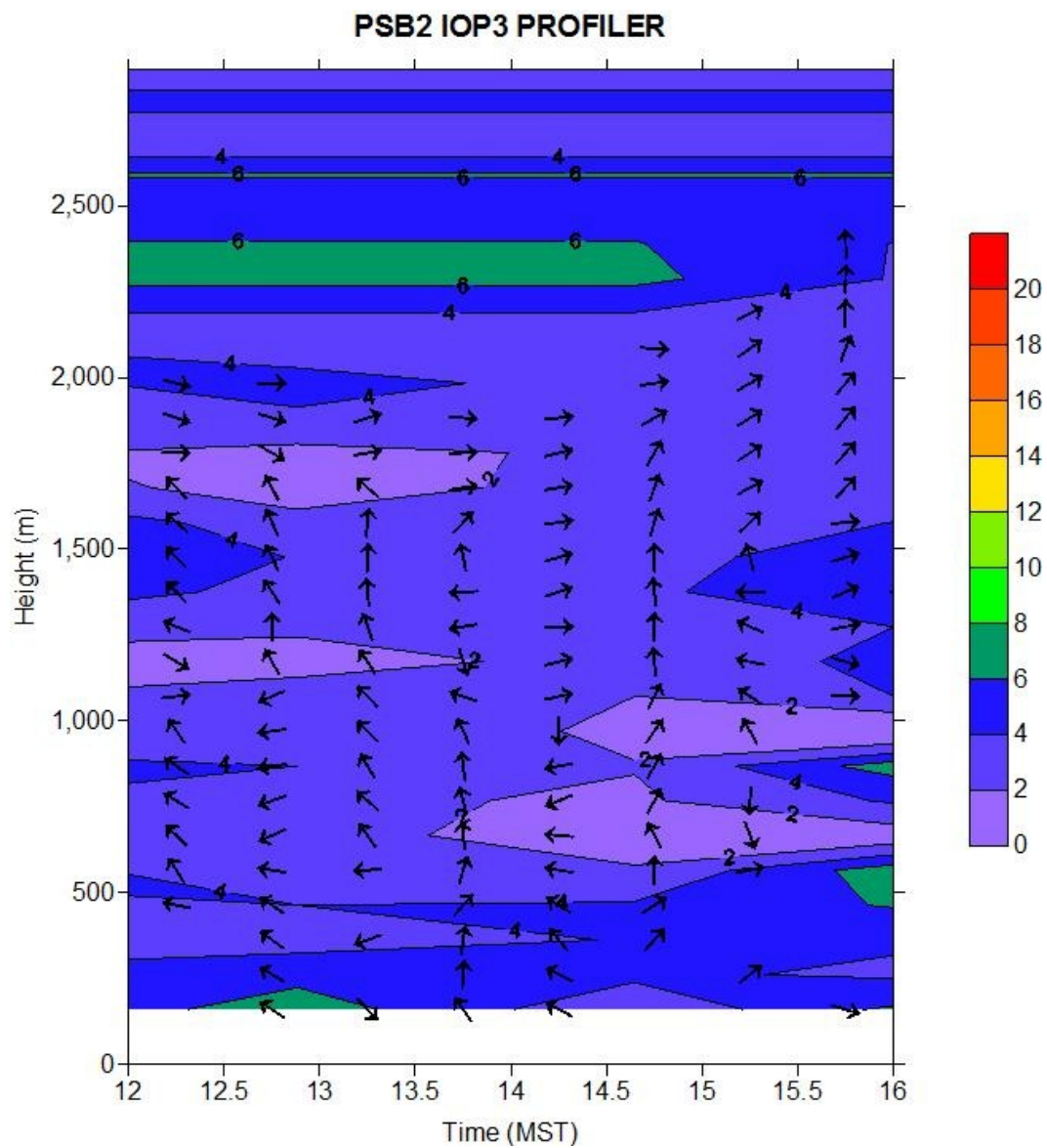


Figure 128. Time-height cross-section of wind speed and direction at wind profiler (PRO) during IOP3. Legend represents m s^{-1} .

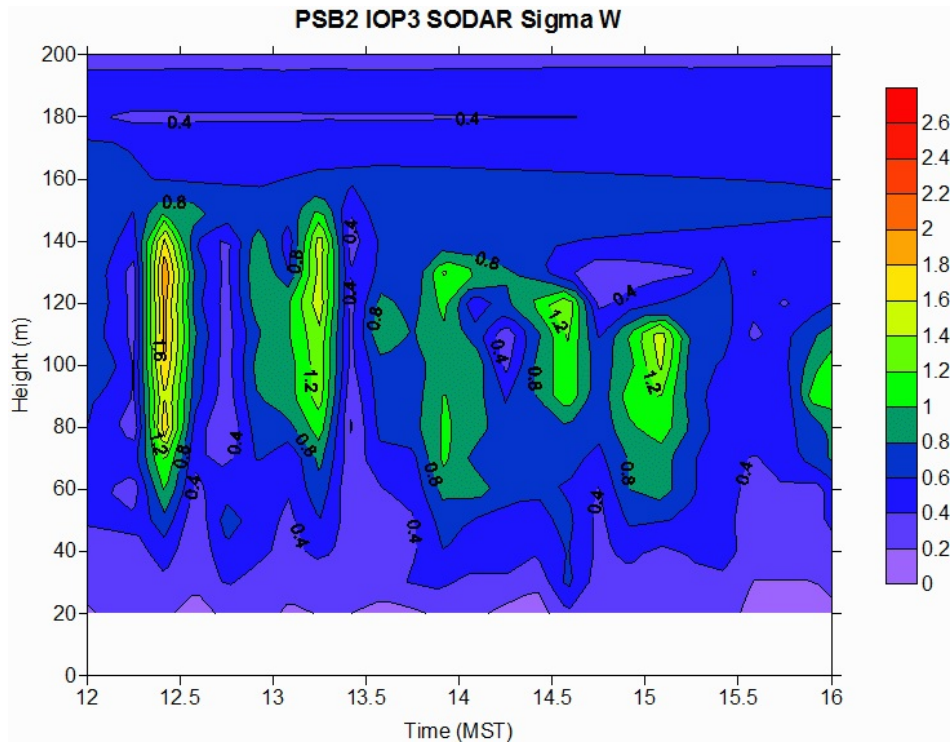


Figure 129. Time-height cross-section of σ_w at sodar (SOD) during IOP3. Legend represents m s^{-1} .

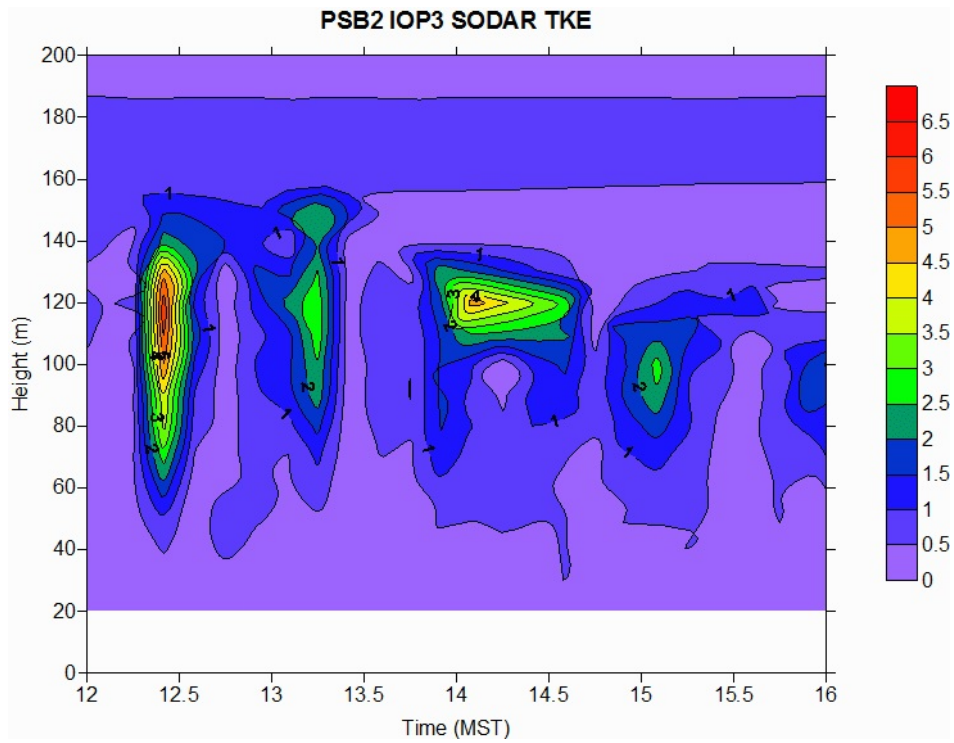


Figure 130. Time-height cross-section of TKE at sodar (SOD) during IOP3. Legend represents $\text{m}^2 \text{s}^{-2}$.

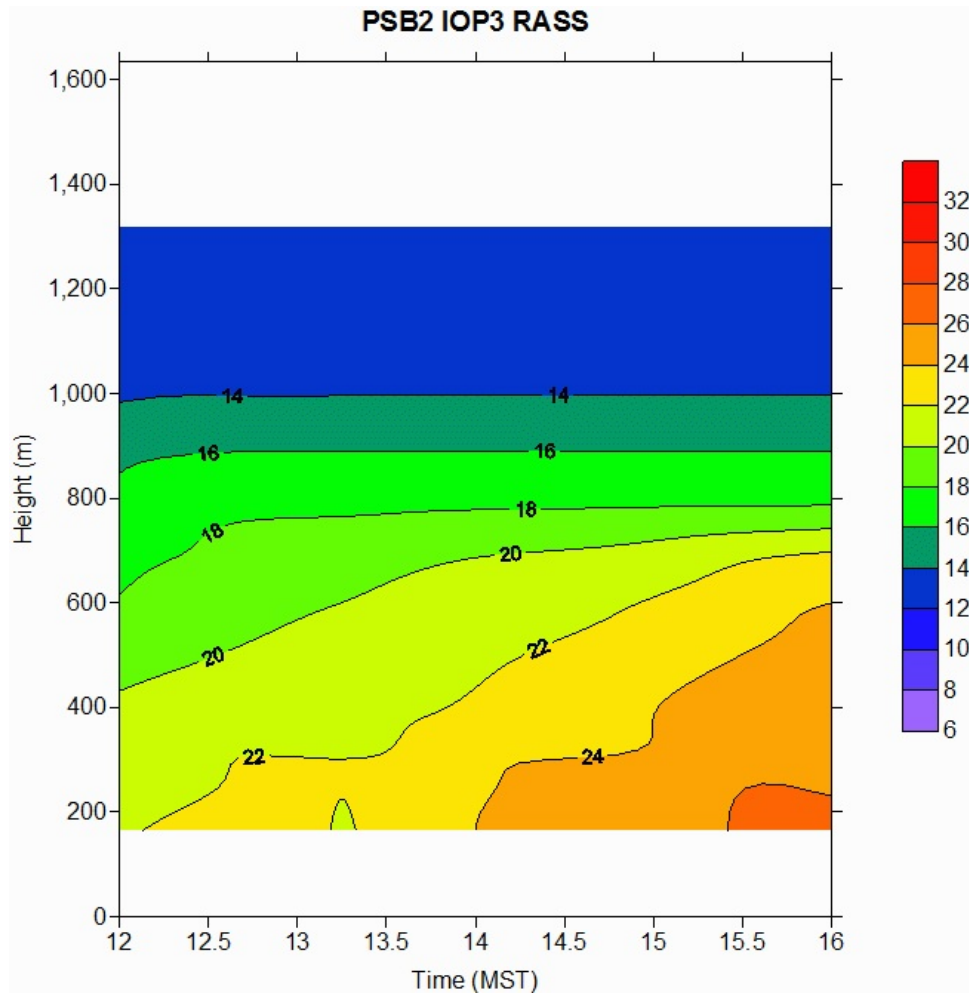


Figure 131. Time-height cross-section of virtual temperature at the RASS during IOP3. Temperatures are in degrees C.

Radiosonde Results

Pre and post-IOP radiosonde profiles of potential temperature and specific humidity for IOP4 are shown in Figs. 132 and 133. Both pre and post-test potential temperature profile suggest a mixing height of about 1900 m agl. The pre-test specific humidity profile suggests a mixing height between about 800-1000 m agl. The post-test specific humidity profile estimate of mixing height is roughly consistent with the potential temperature profile at about 1800 m agl.

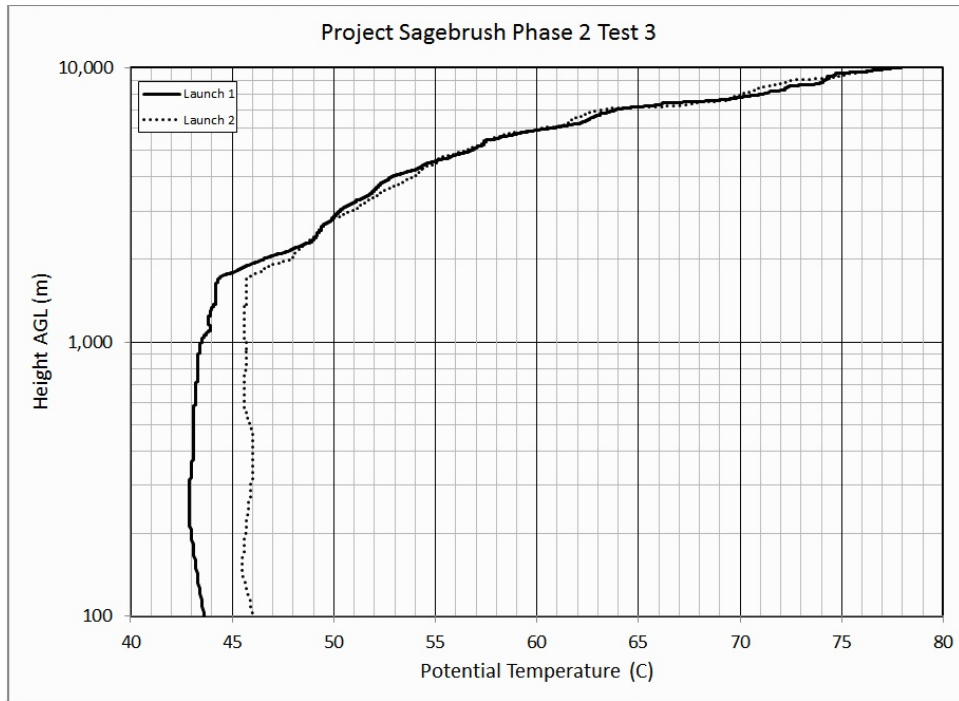


Figure 132. Potential temperature profile from radiosonde probe, IOP3. Pre-test launch bold, post-test launch dotted.

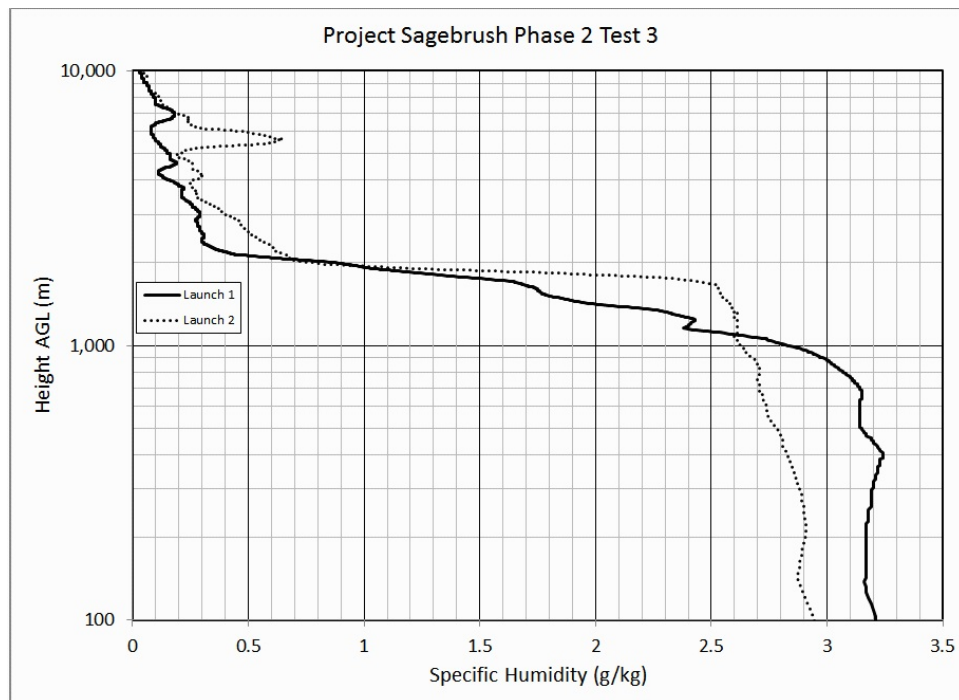


Figure 133. Specific humidity profile from radiosonde probe, IOP3. Pre-test launch bold, post-test launch dotted.

Bag Sampling Results

Figures 134 and 135 and Figures 136 and 137 show the 10-minute average normalized and actual, respectively, color-coded plan view concentration maps for IOP3 bag sampling at 1 m agl. Figures 138 and 139 and Figures 140 and 141 show the 10-minute average normalized and actual concentrations, respectively, along each of the arcs.

There were some 10-minute periods during which the plume was mostly over the 210° sampler array (e.g., bags 2, 10-12). However, it was more commonly the case that the western limb of the main plume was truncated at the edge of the sampler array. Typically about one-half of the plume was missing, especially on the 100 m arc. A few of the latter bag sampling intervals showed little or no plume truncation. Bags 10 and 11 show a bifurcation of the plume at 100 and 200 m. With few exceptions, the plume either missed the 800 m arc or concentrations were low. These observations are consistent with the observations of wind direction at GRI and COC (Figs. 119, 120; Table 20). Most of the truncated plumes along the western edge of the sampler array tended to exhibit a somewhat irregular gaussian morphology. It's difficult to say given the truncation but central, often composite peaks appeared to subtend a similar range of arc as in IOPs 1 and 2, again commonly with relatively sharp margins.

Figure 142 shows the vertical concentration profiles up to 25 m agl from the mobile tower located on the 100 m arc at 352° azimuth (red dot 2, Fig. 5). Most of the profiles exhibit a relatively uniform concentration with height but these are profiles with dominantly ambient background concentrations. Some of the remaining samples tend to show increasing concentration with height with maxima above 25 m. However, the measurements at 1420, 1430, and perhaps 1440 h suggest maxima at about 15-20 m agl.

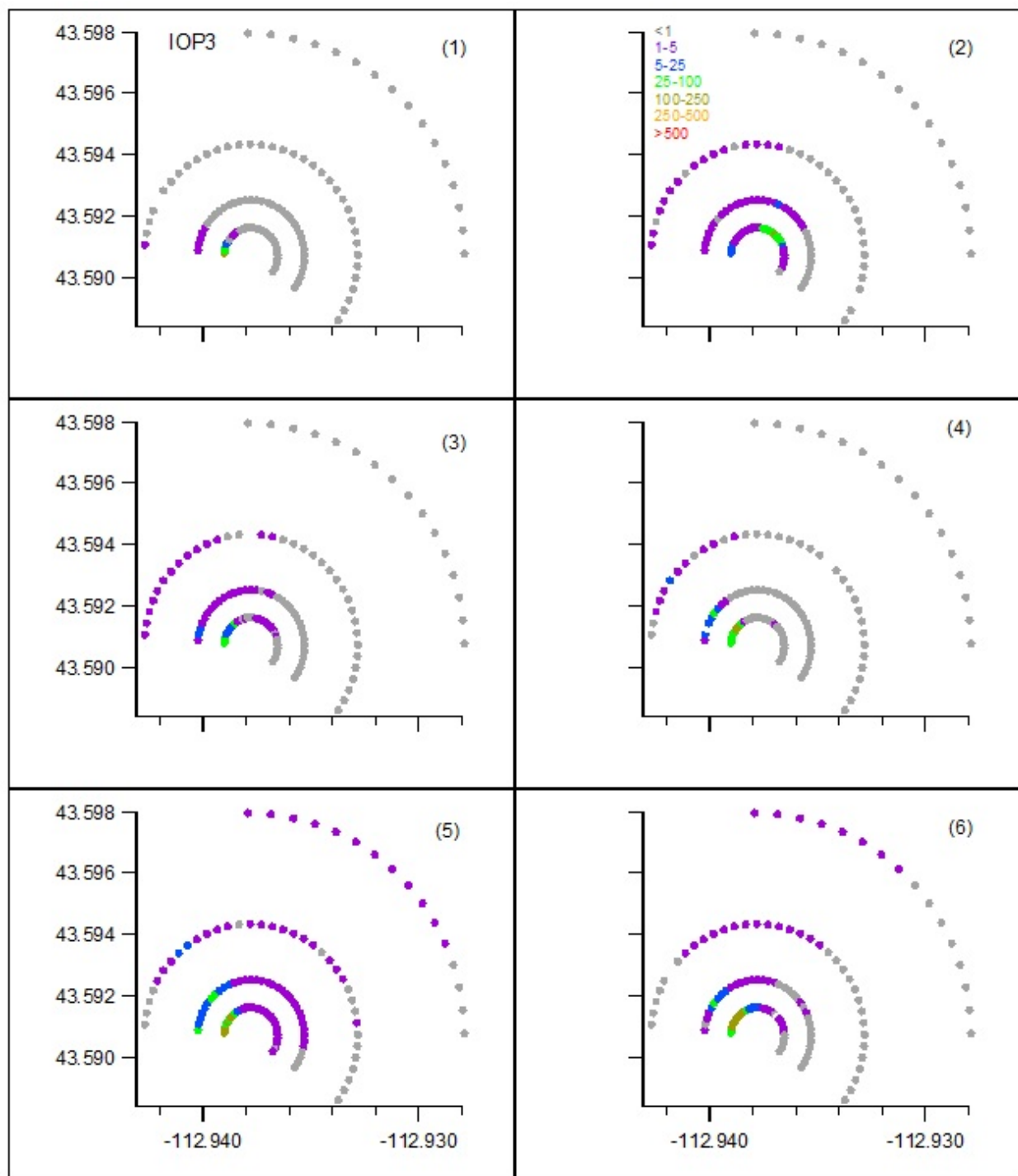


Figure 134. Color-coded normalized ($F^*\gamma/Q$ ppt s g⁻¹) concentrations at 1 m agl for bags 1-6 during IOP3. The number in () is bag number.

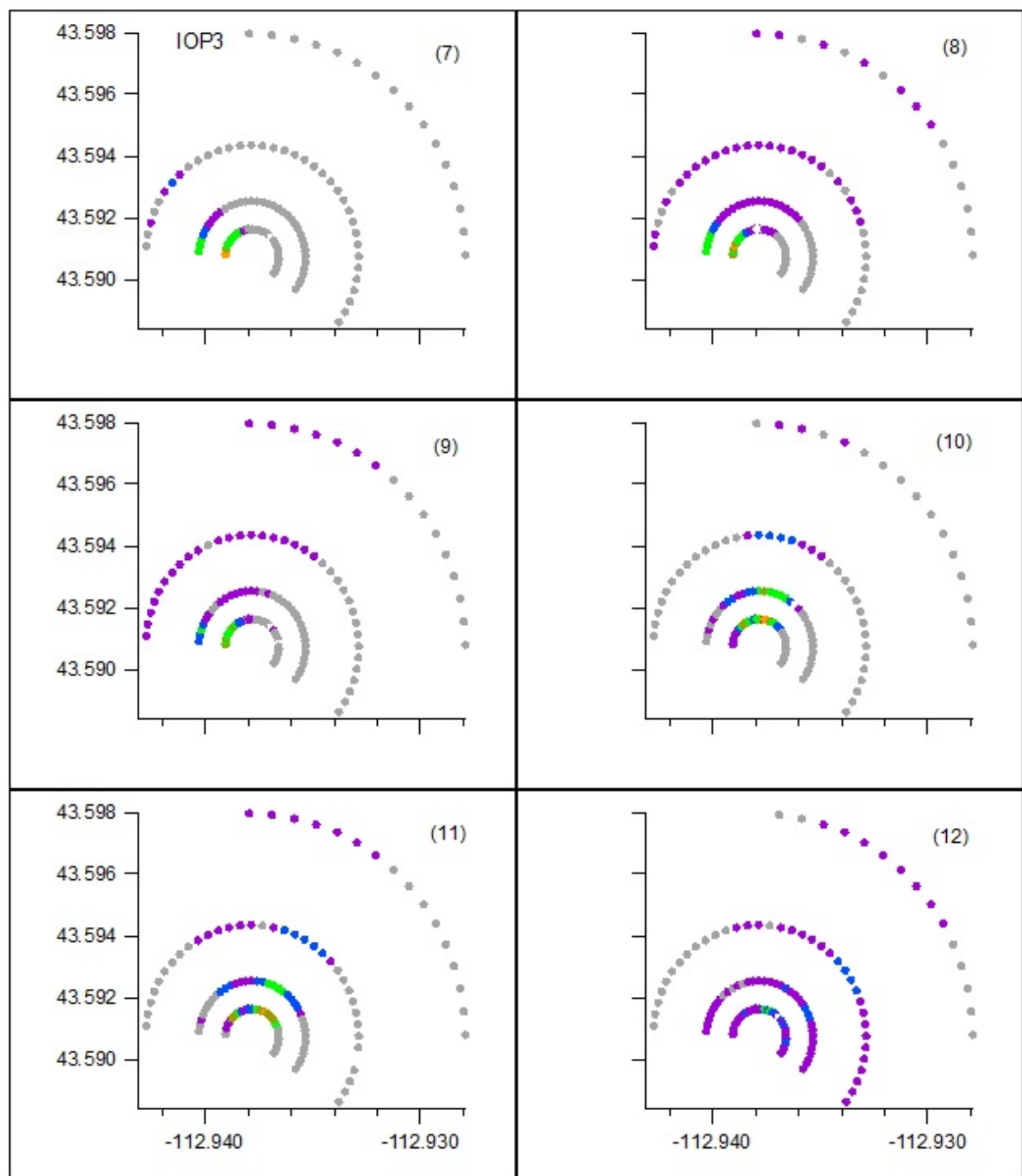


Figure 135. Color-coded normalized ($F^*\chi/Q$ ppt s g^{-1}) concentrations at 1 m agl for bags 7-12 during IOP3. The number in () is bag number.

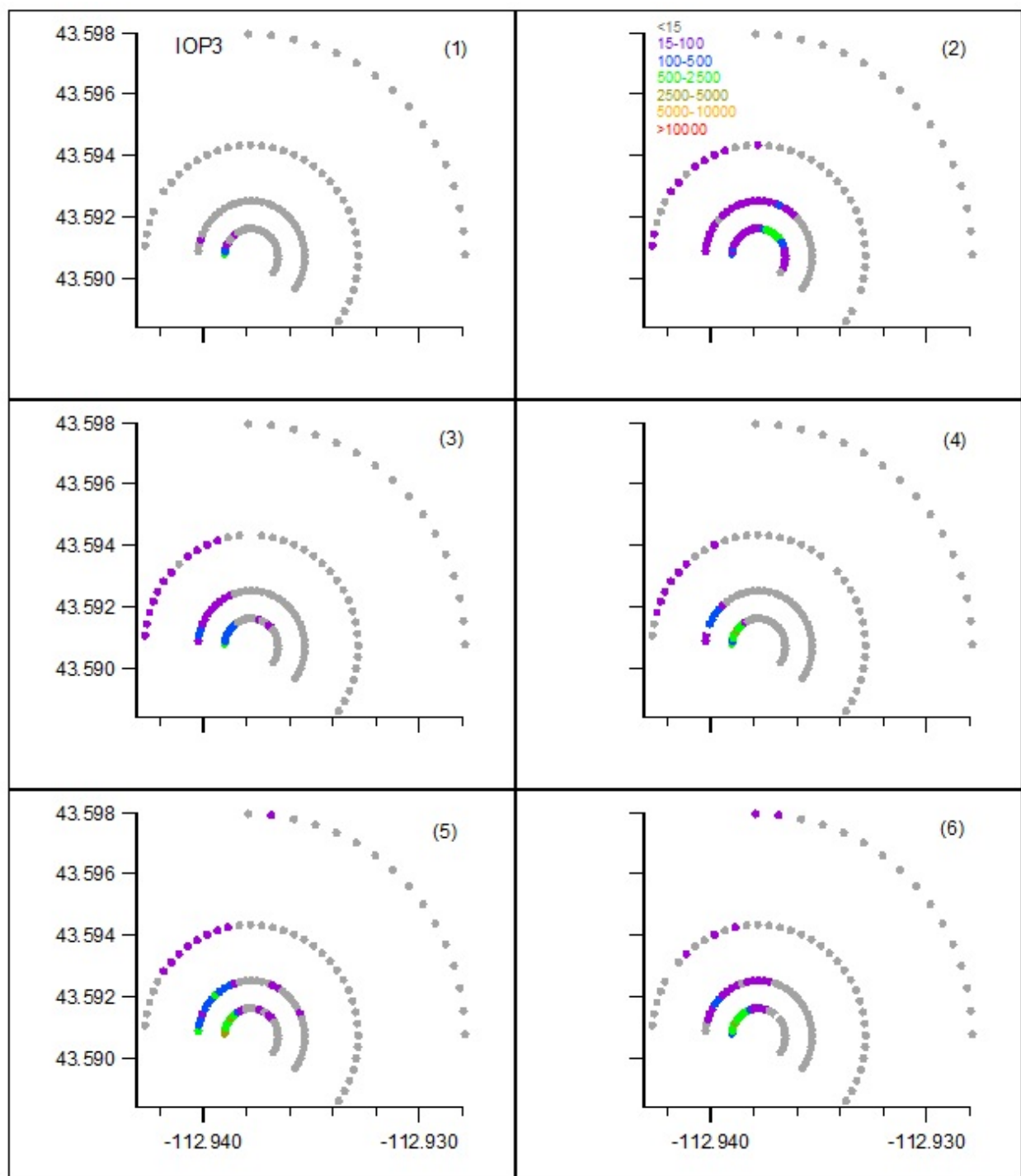


Figure 136. Color-coded measured SF_6 concentrations (ppt) at 1 m agl for bags 1-6 during IOP3. The number in () is bag number.

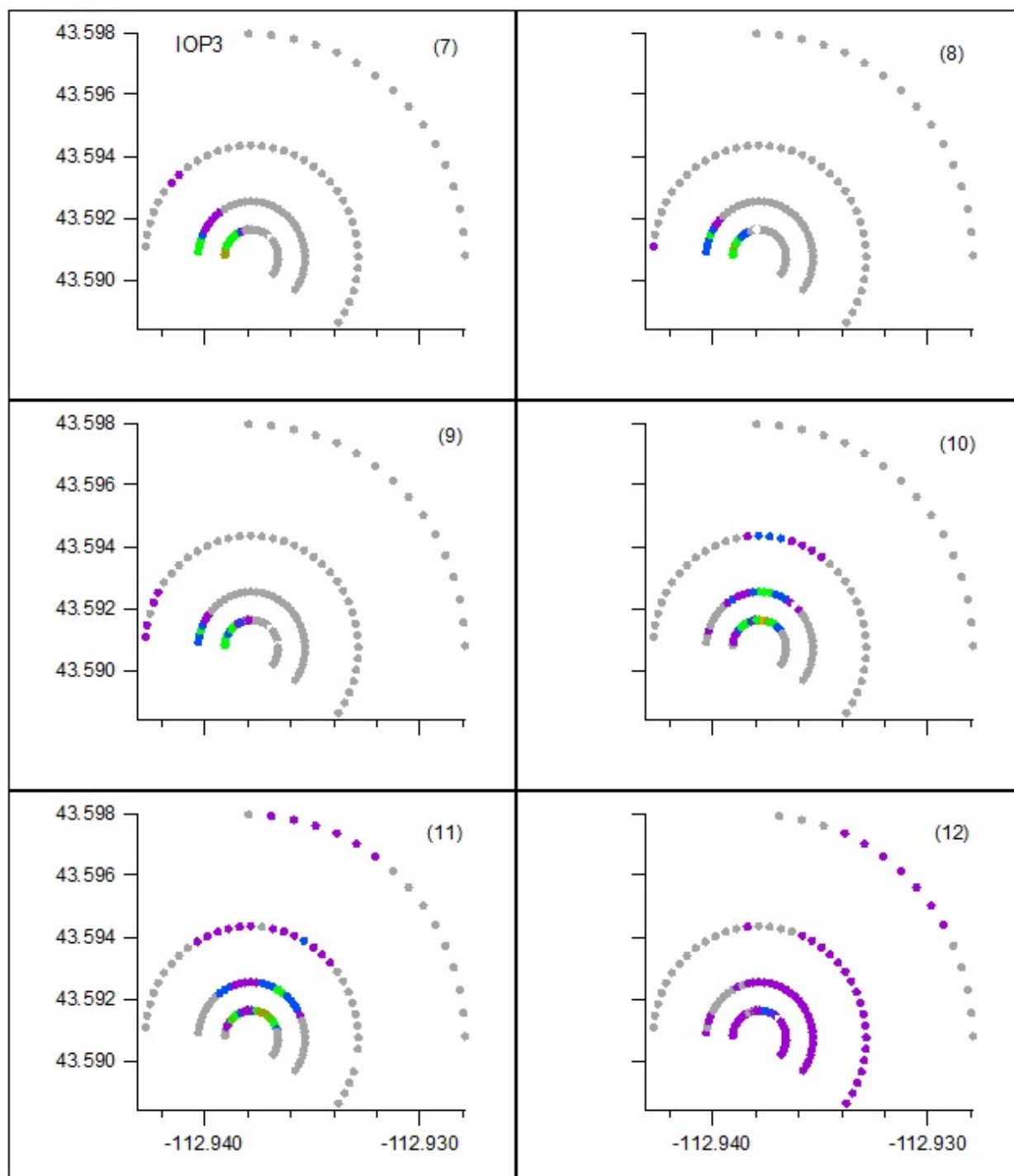


Figure 137. Color-coded measured SF_6 concentrations (ppt) at 1 m agl for bags 7-12 during IOP3. The number in () is bag number.

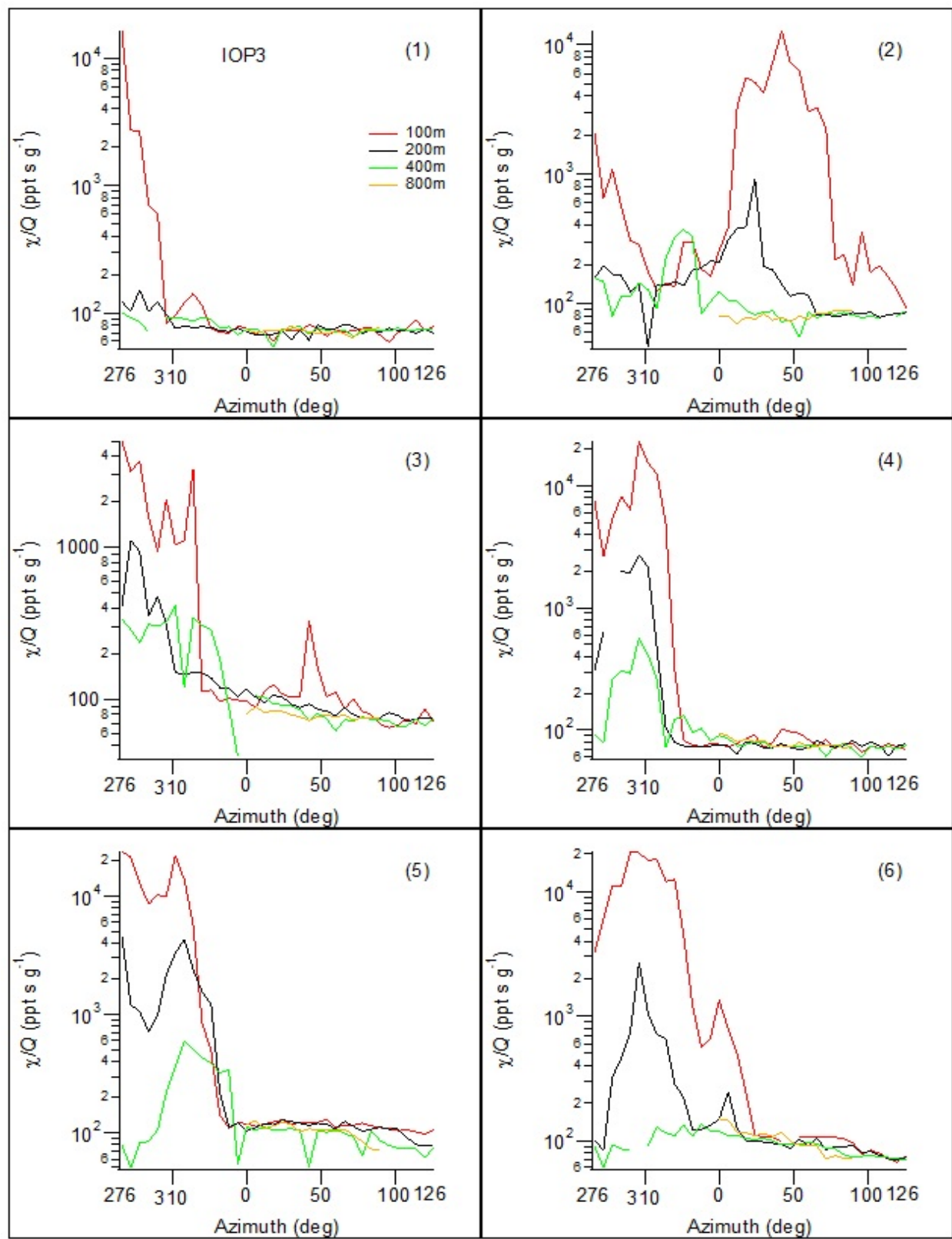


Figure 138. Cross-sections of normalized concentration along the arcs for bags 1-6 during IOP3.

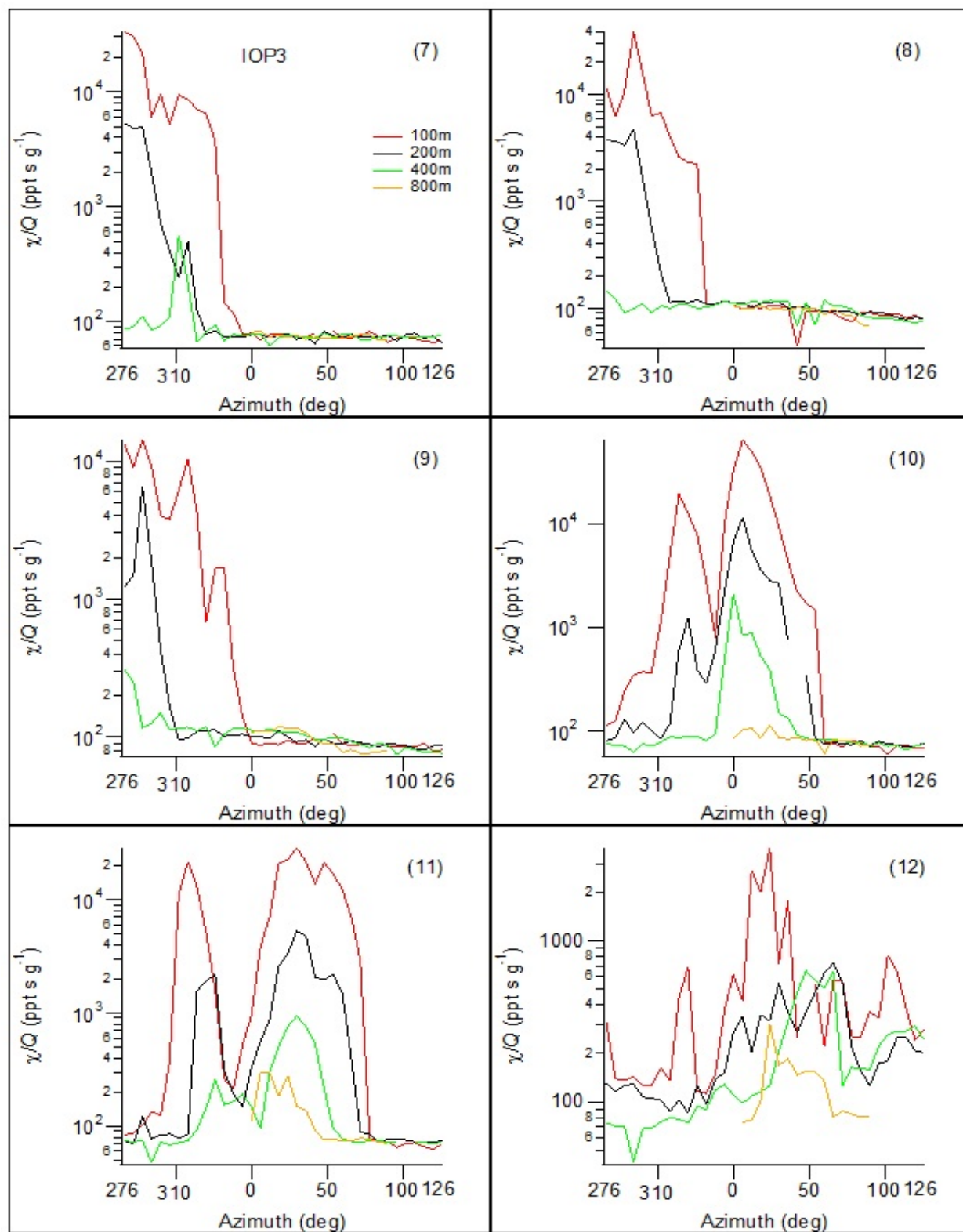


Figure 139. Cross-sections of normalized concentration along the arcs for bags 7-12 during IOP3.

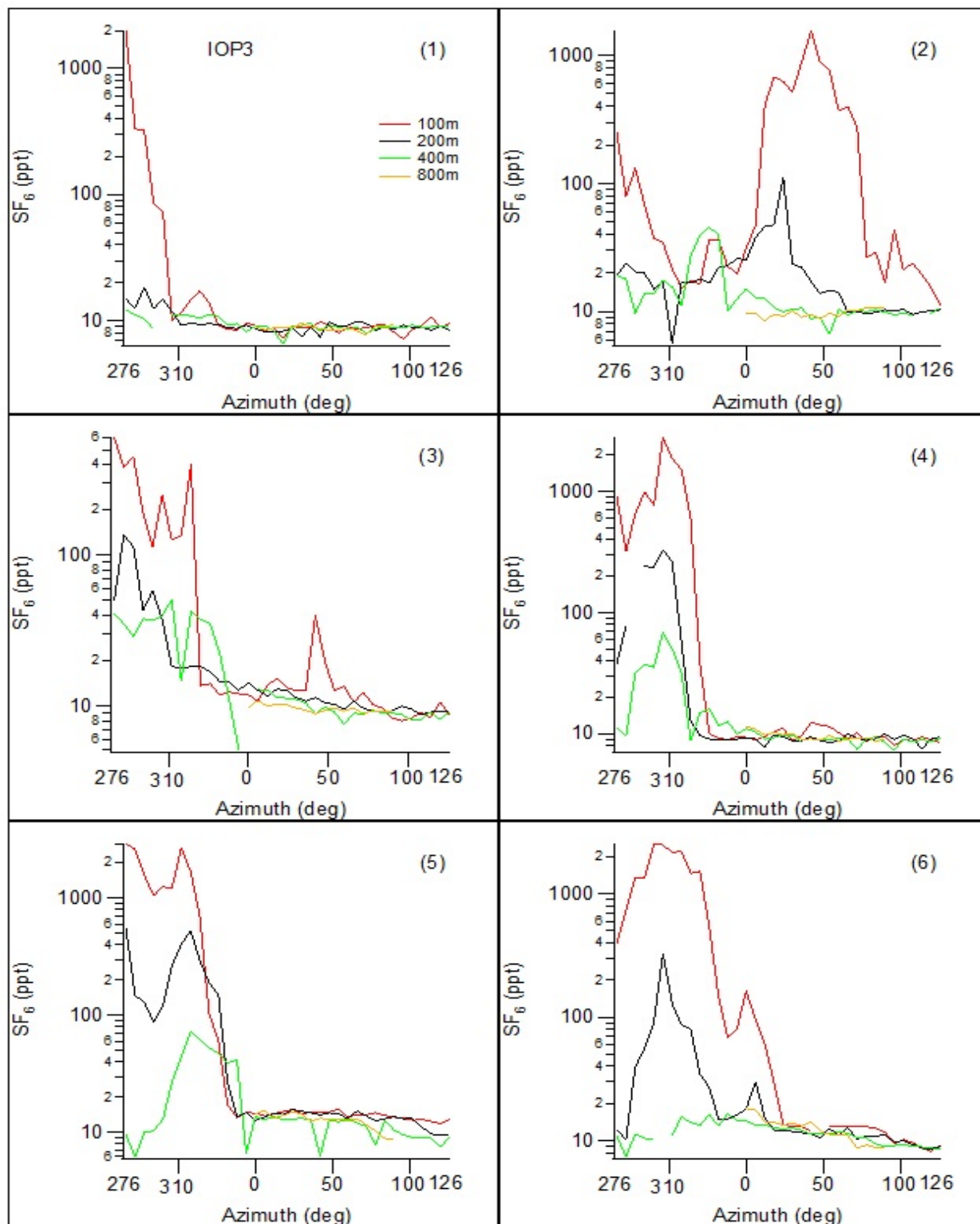


Figure 140. Cross-sections of measured SF_6 concentration along the arcs for bags 1-6 during IOP3.

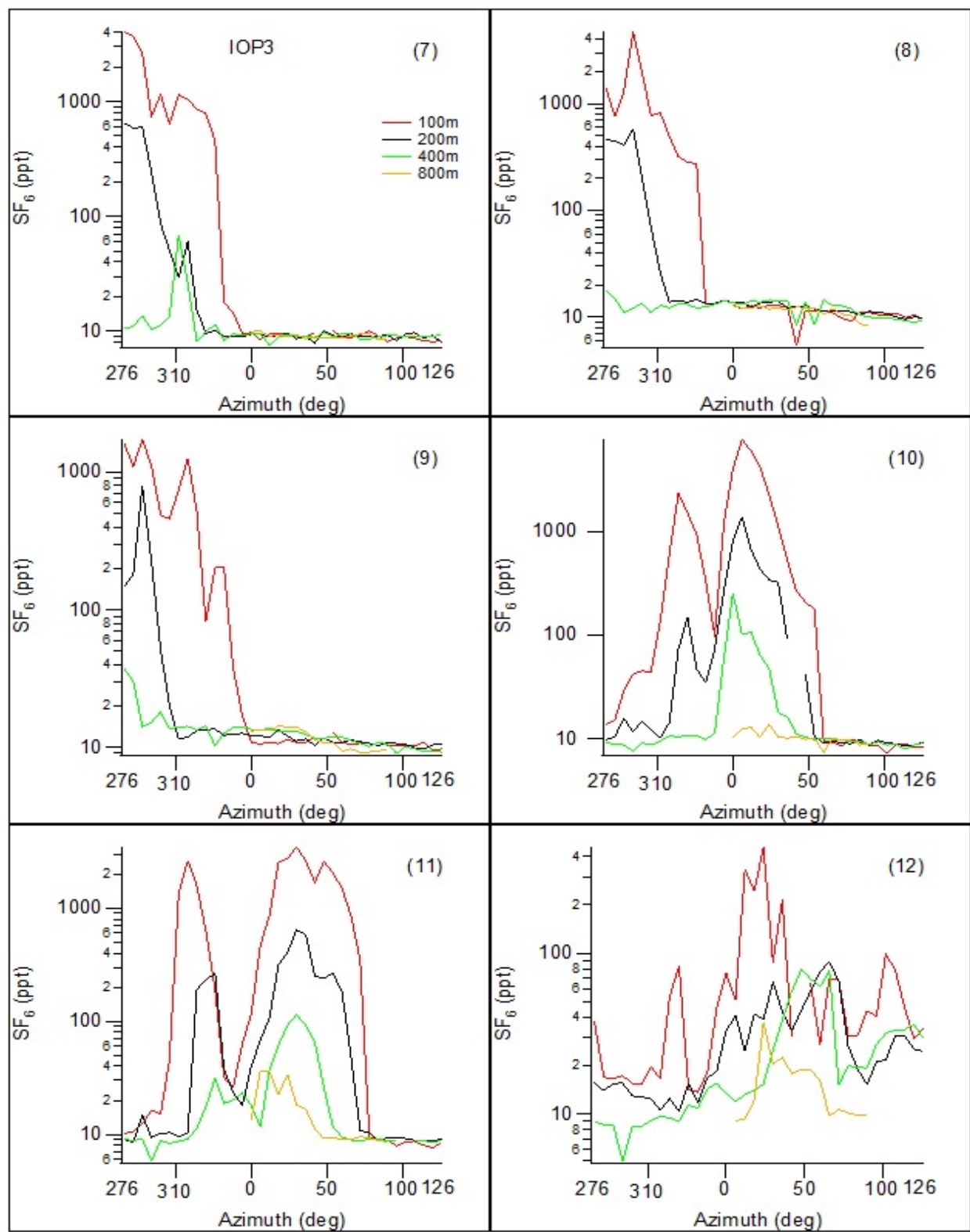


Figure 141. Cross-sections of measured SF_6 concentration along the arcs for bags 7-12 during IOP3.

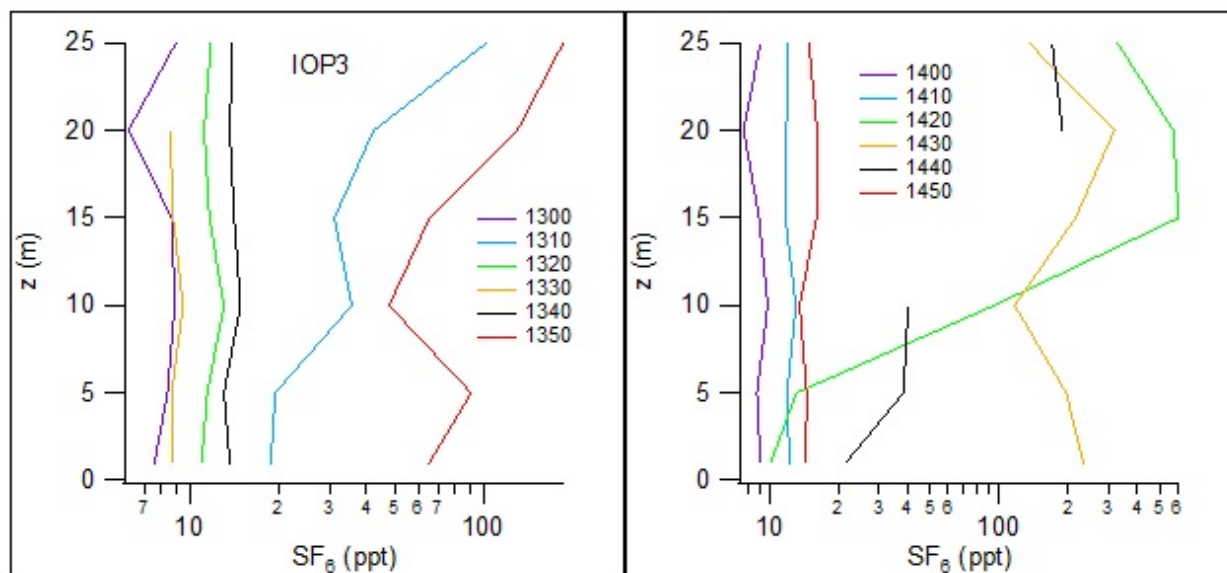


Figure 142. Vertical profiles of measured SF_6 concentration at the mobile tower during IOP3.

Fast Response Results

The locations of the fast response analyzers during IOP3 are shown in Fig. 143. The corresponding concentration time series are shown in Fig. 144. The color coding of the time series was described in the Introduction to this section.

At 342° azimuth, the analyzers were positioned near the eastern margin of the plume for much of the IOP. It is likely that this explains the relatively sparse and very intermittent time series measured by the fast response analyzers. Like IOPs 1 and 2, the measurements were again characterized by being highly variable and intermittent with often rapid increases to peak values followed by rapid drops in concentration back to background or near background concentrations. The character of the time series might be explained by the position of the analyzers at the edge of the main plume with peaks occurring in response to minor shifts in wind direction. However, the character of the time series was also consistent with IOPs 1 and 2. Thus the plume was probably relatively narrow at any given time and, with shifts in wind direction, resulted in the very intermittent time series observed at the edge of the overall plume.

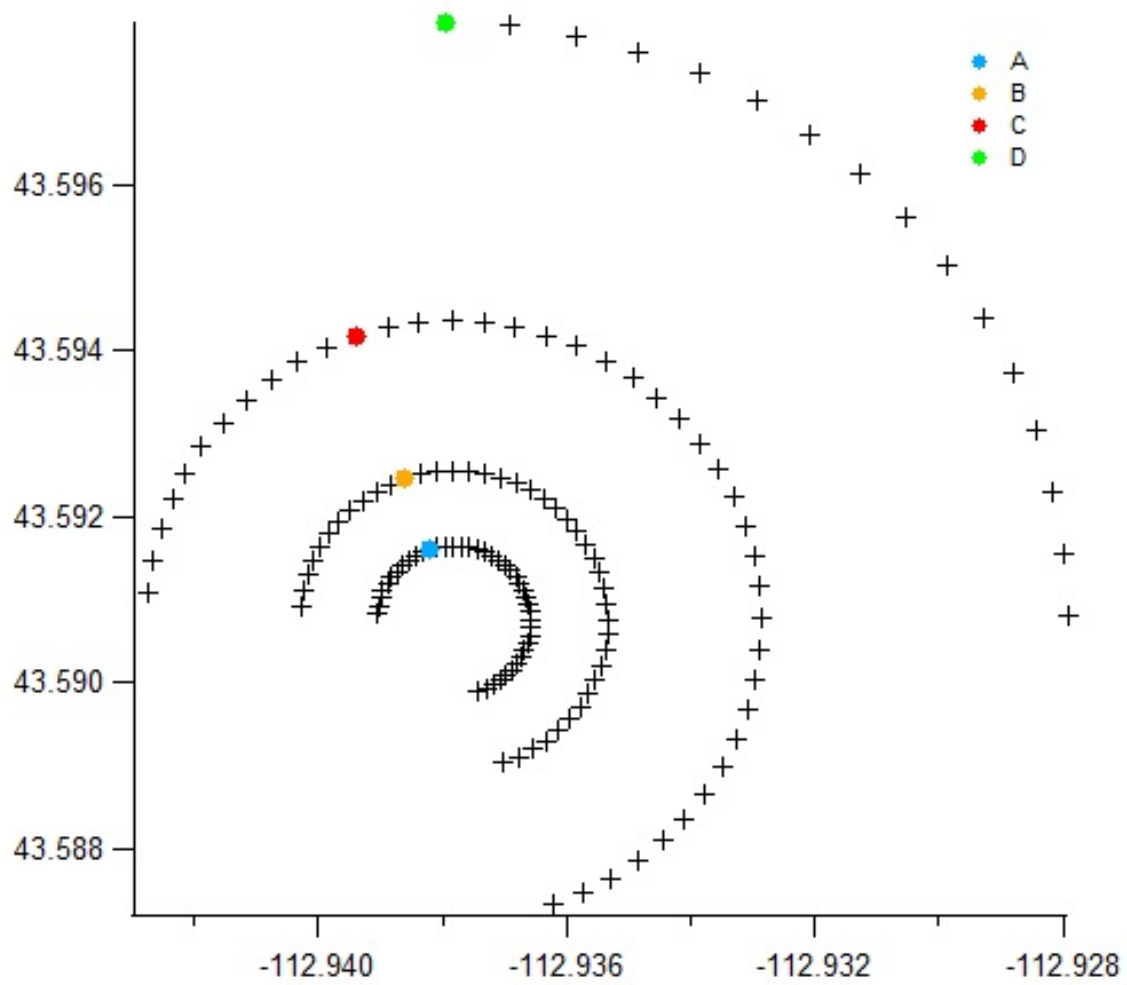


Figure 143. Locations of fast response analyzers during IOP3.

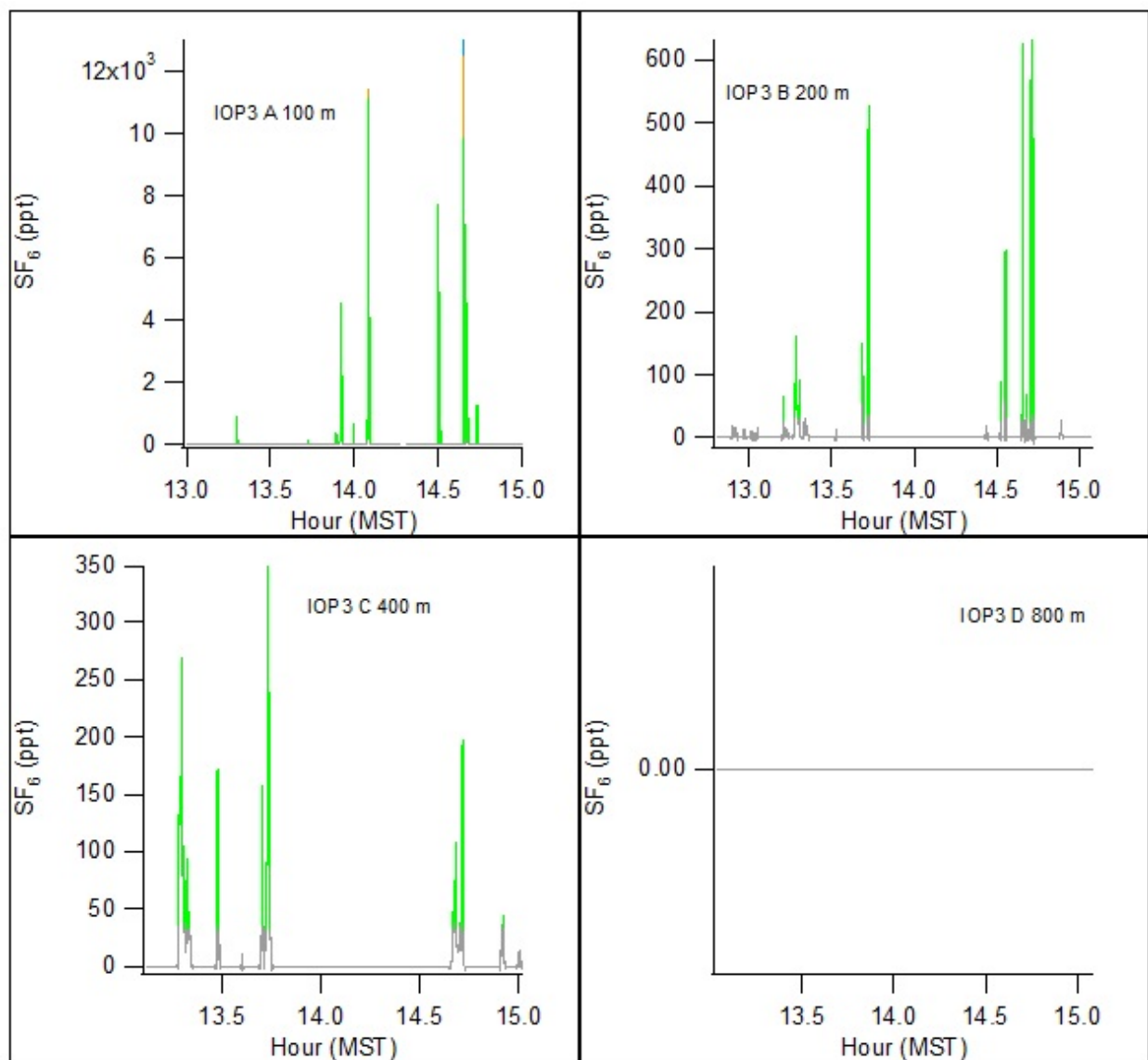


Figure 144. Fast response concentration time series during IOP3.

IOP 4

Date/Time and General Description

IOP4 was conducted on 05 August from 1230-1430 MST (1330-1530 MDT). Conditions were warm and dry with mostly sunny skies at the start of the test with cirrus clouds gradually building over the course of the test period. Winds were light, generally less than 3 m s^{-1} , and rather consistently northeasterly. Overall conditions were unstable but were the closest to achieving stationarity of any of the daytime IOPs. Estimates of stability based on traditional Pasquill-Gifford (P-G) schemes were mostly class A in the first hour and class C in the second hour (Fig. 145). Estimates of mean z/L from GRI ranged from -0.36 to -0.38 with a Ri_b of -1.25. Wind directions were such that the tracer plume missed the bag sampling array in whole or part throughout the measurement period. A summary of the meteorological conditions during IOP4 are shown in Table 21. The SF_6 release rate was 0.147 g s^{-1} (Table 2). Three of the fast response analyzers were located on the 100, 200, and 400 m arcs at the edge of the bag sampling array at approximately 276° azimuth. The fourth analyzer was located southwest of the release location at 400 m in the gap in the bag sampling array. The location of the fast response analyzers was motivated by the prevalence of northeast winds during the IOP.

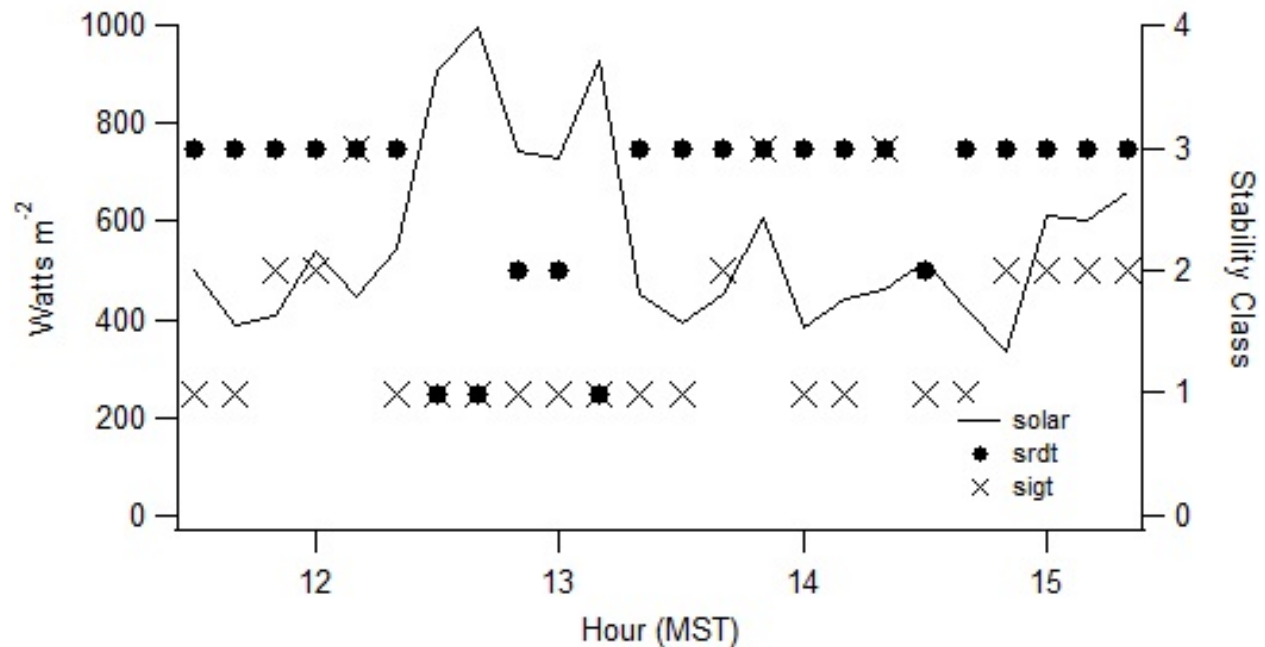


Figure 145. Incoming solar radiation and classification of stability conditions using the Pasquill-Gifford Solar Radiation Delta T (srdt) and σ_0 (sigt) methods (EPA 2000c) during IOP4. Classes A, B, C, and D are designated 1, 2, 3, and 4, respectively.

Table 21. Meteorological conditions during IOP4.

Bag	COC				GRI						GRI			Solar W m ⁻²
	U (m s ⁻¹)		WD (deg)		U (m s ⁻¹)		WD (deg)		σ_θ (deg)		L	L	degC	
	2m	10m	2m	10m	2m	10m	2m	10m	2m	10m	3.7m	9m	2m	
1	1.8	2.2	41.9	39.1	0.8	1.2	21.3	25.6	64.0	68.9	-4.4	-2.3	28.2	909.0
2	1.9	2.4	17.3	20.8	1.2	1.4	50.4	48.8	65.6	56.4	-1.7	-156.4	28.3	996.5
3	1.7	2.3	46.6	46.7	2.2	2.7	99.0	89.1	57.5	56.3	-12.0	-6.5	28.7	741.2
4	1.8	2.5	68.4	65.5	1.6	1.9	50.6	44.7	70.2	64.3	-11.2	-0.4	29.2	926.7
5	1.8	2.6	46.8	45.8	0.6	0.9	94.1	86.4	60.4	38.5	-4.6	-3.5	29.5	928.5
6	1.5	1.9	38.8	35.2	2.1	2.6	17.6	25.2	55.0	40.5	-17.4	-34.5	29.5	451.2
7	1.4	1.6	10.9	8.6	1.6	2.0	33.9	34.7	44.6	27.3	-2.2	-5.7	29.4	392.5
8	2.3	2.7	48.2	50.0	2.0	2.5	355.6	359.3	29.6	21.5	-7.5	-4.1	29.8	453.3
9	1.9	2.4	70.1	63.4	2.5	3.0	19.2	18.3	21.4	15.1	-9.6	-1.0	30.2	605.2
10	1.6	1.9	59.7	63.3	2.1	2.4	102.5	93.2	38.6	23.4	-34.2	-39.8	30.0	385.8
11	1.7	2.2	32.2	37.5	2.1	2.5	55.9	55.2	42.6	26.1	-13.6	-12.4	30.3	441.8
12	2.0	2.5	23.3	19.1	2.8	3.4	81.6	76.6	18.5	14.6	-4.8	-17.9	30.6	460.9
Avg. L											-10.27 -23.71			
z/L											-0.36 -0.38			
Ri _b											-1.25			

Wind Speed and Direction Quality Assurance

Figures 146-148 show wind speed and direction time series comparisons for a sequence of measurement heights during IOP4. In Fig. 146, the near surface measurement of U showed some variation with the largest differences relative to the other stations being associated with the 2 m cup anemometer at GRI. However, U was relatively constant at about 2 m s⁻¹ and, with the exception of a couple of excursions, wind directions were consistently northeasterly. No data was available from the G2 sonic site for IOP4. Although U was a little higher due to greater height above the surface, a similar pattern of observations held for the wind speed and direction measurements between 9 and 30 m agl (Fig. 147). Wind directions at SOD tended to be more northerly than the northeasterly directions prevalent at GRI and COC. There was good agreement between SOD and GRI for U at the 45 and 60 m levels (Fig. 148). The SOD measurement of wind direction again tended to be more northerly than northeasterly relative to GRI. There was no data available from SOD to allow any comparisons at the 160 m level. Other than the poor data recovery for SOD and PRO at 160 m agl, there is little evidence of a systematic measurement problem. Any of the observed variability or discrepancies are likely attributable to non-stationarity and horizontal inhomogeneity in the wind field.

Figure 149 shows time series measurements for cup anemometers and wind vanes only (excluding sonics) at all heights on the two towers during IOP4. Near surface measurements of U at GRI and COC were consistently about 2 m s⁻¹. Wind directions were consistently

northeasterly. The measured σ_0 were commonly 20-30° with magnitudes twice that during the first hour of the tracer measurements, especially at heights up to at least 15 m agl.

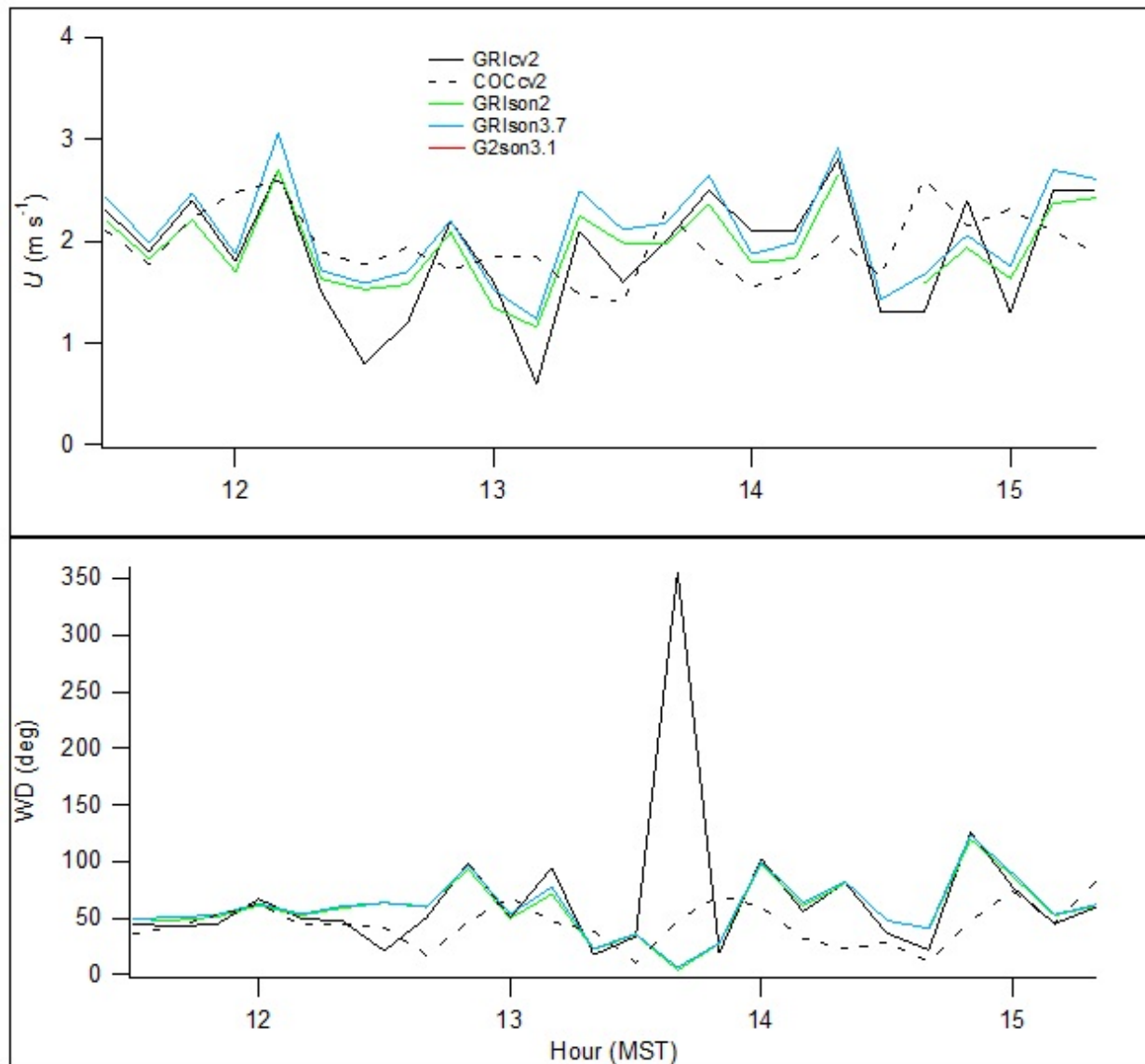


Figure 146. Time series of near surface wind speed and direction measurements during IOP4. In the legend, location is specified in upper case, the measurement type in lower case (cv = cup and vane, son = sonic), and the measurement height numerically.

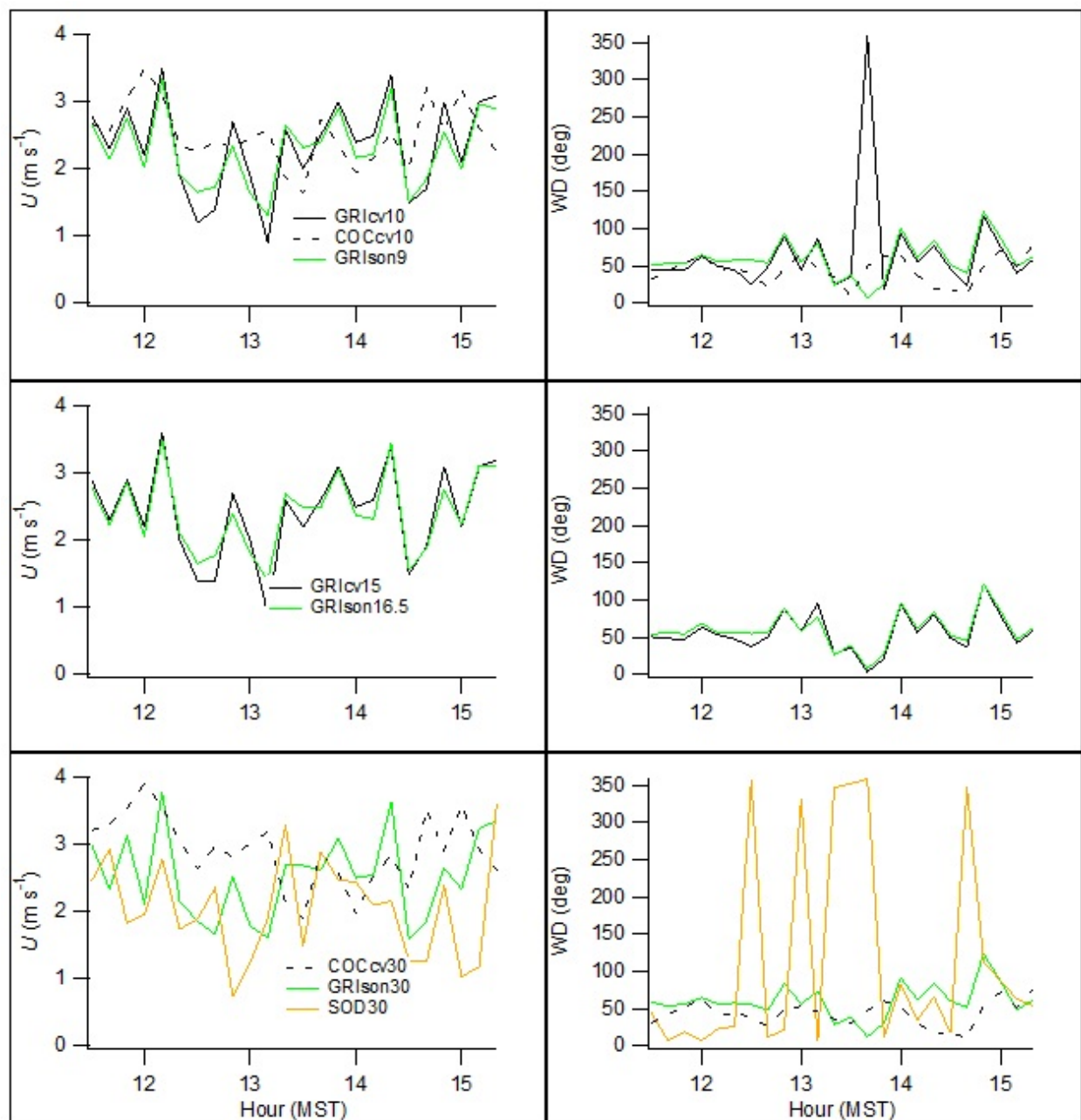


Figure 147. Time series of wind speed and direction measurements at heights between 9 and 30 m agl during IOP4. Legend notations described in caption of Fig. 146.

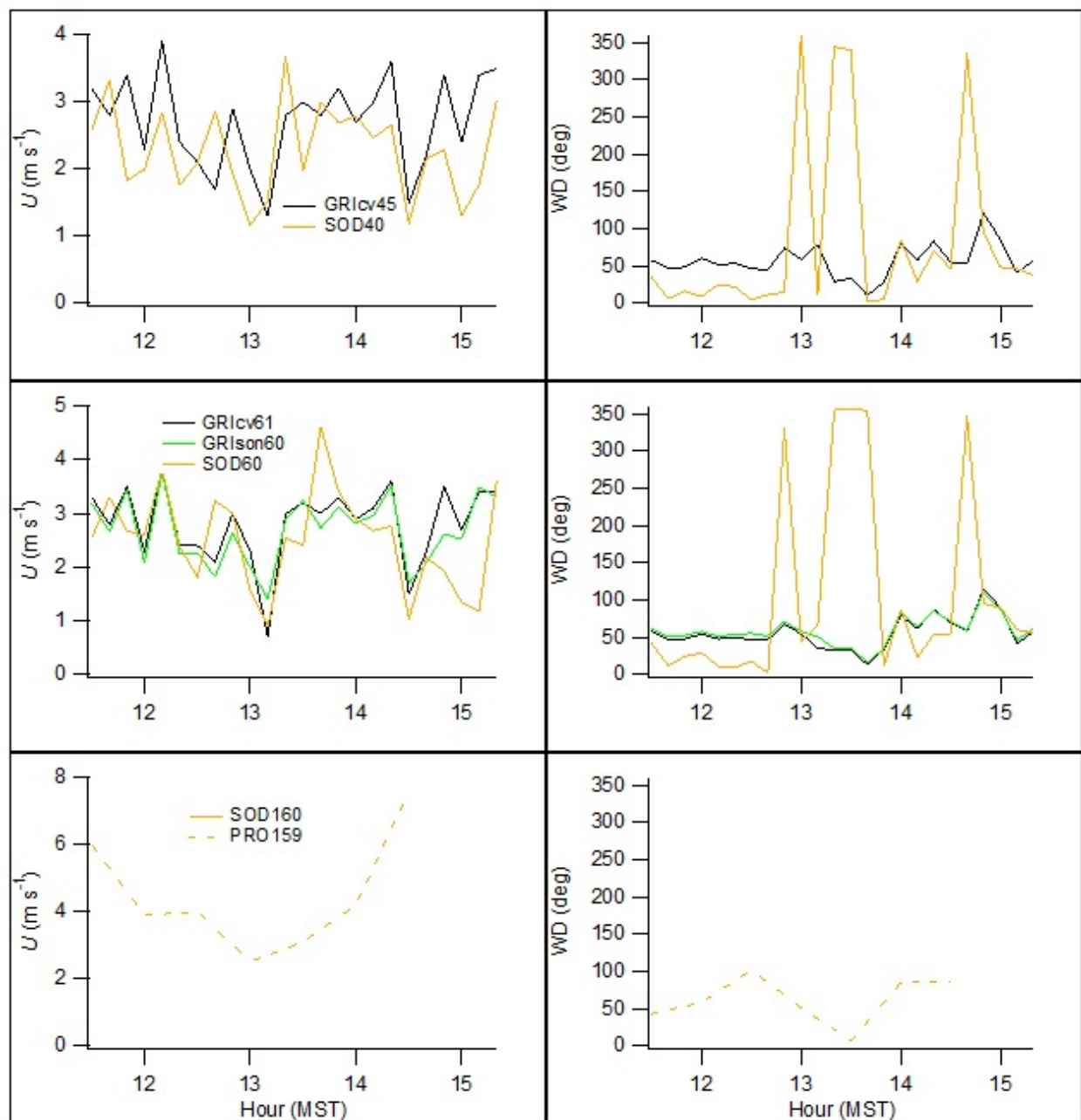


Figure 148. Time series of wind speed and direction measurements at heights above 30 m agl during IOP4. Legend notations described in caption of Fig. 146.

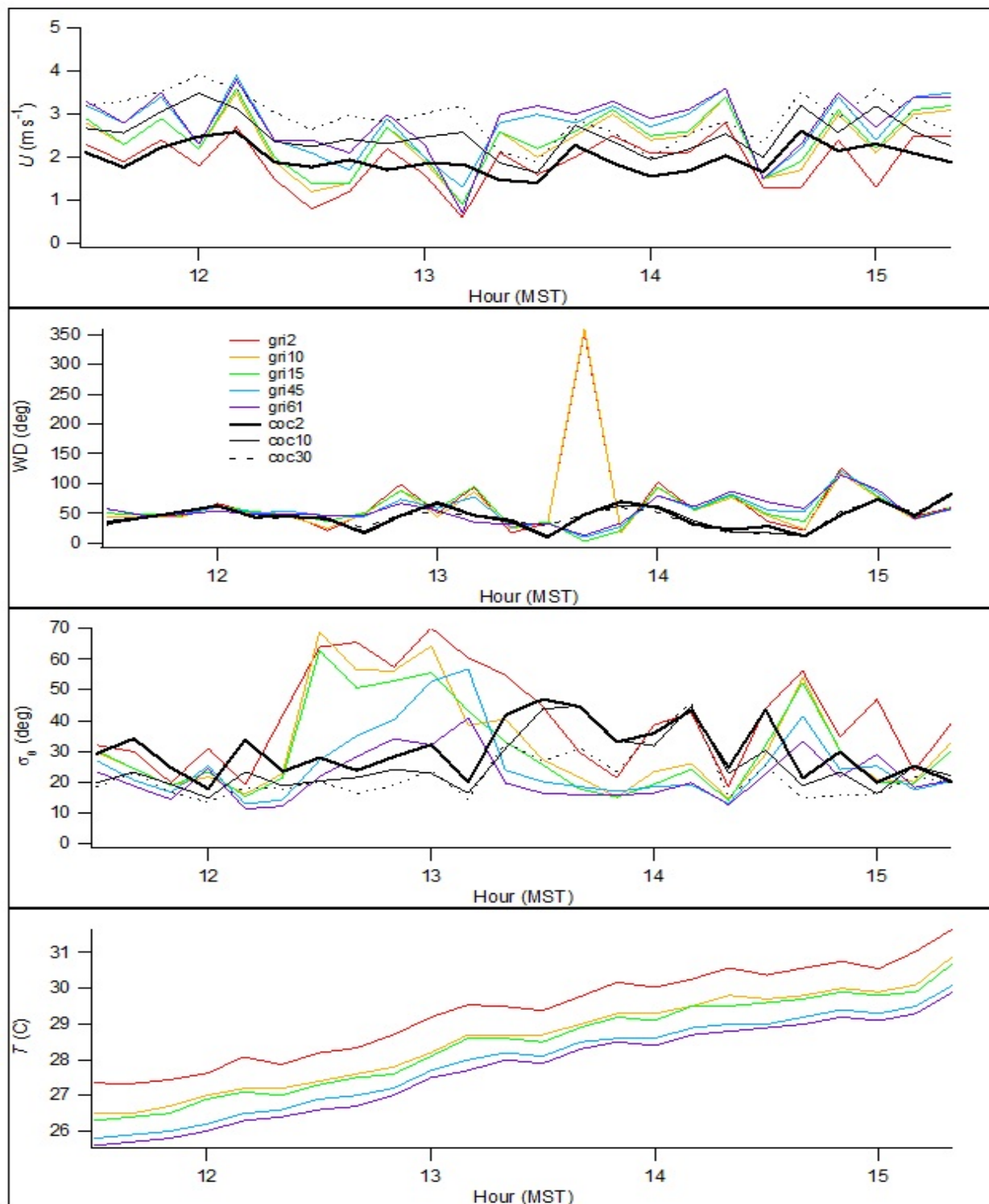


Figure 149. Time series from GRI and COC showing cup anemometer and wind vane measurements of U , wind direction, standard deviation of wind direction σ_0 , and temperature during IOP4. The locations are designated 'xxxxyy' where xxx = tower and yy = measurement height.

Turbulence

The loss of the G2 sonic for IOP4 restricts the comparison of near surface turbulence across sites (Fig. 150). The measurements on GRI are in close agreement with each other but vary with COC during the first hour of the tracer measurement period. During that period, the GRI measurements of σ_v/U , σ_w/U , and TKE exhibited a sustained excursion to higher magnitudes relative to COC. The magnitude of sensible heat flux $\langle wT \rangle$ was suppressed relative to the other daytime IOPs due to attenuation of solar input by cloudiness.

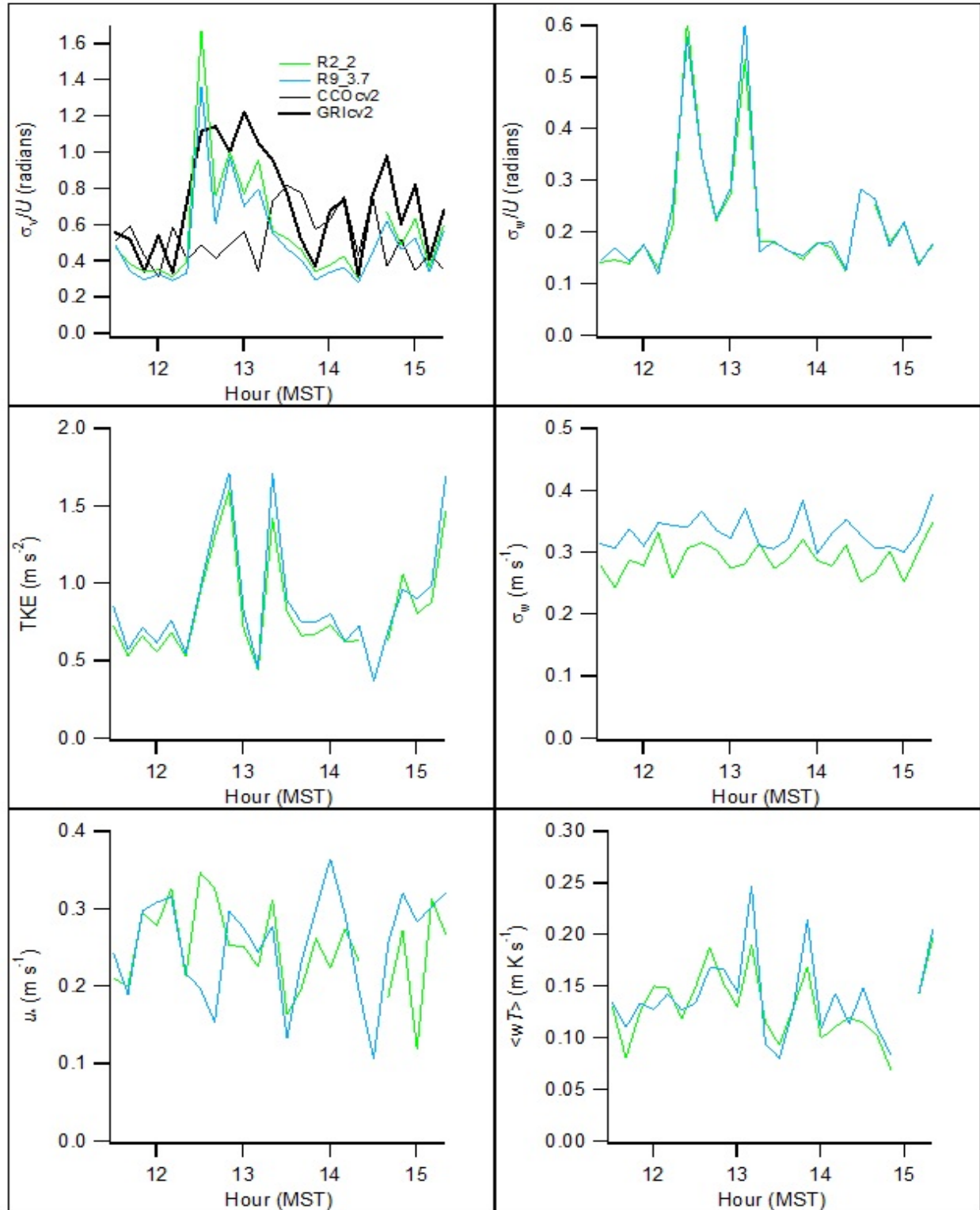


Figure 150. Time series of near surface turbulence (sonic) measurements during IOP4. The GRI and CCO are σ_θ wind vane measurements (cv) in degrees converted to radians for purposes of comparison. Notation before and after underscore designates location and height, respectively.

Wind and Turbulence Profiles

Figure 151 shows profiles of the non-sonic measurements at GRI and COC during IOP4. Wind directions varied but the variation was largely contained within the northeast quadrant. These measurements indicate that U increased slightly over the course of the IOP. The standard deviations of wind direction, σ_θ , were again large although they diminished somewhat in the second half of the IOP as U increased. Profiles were mostly well behaved with the exception of some kinks, mainly in the profiles of σ_θ .

Figures 152 and 153 show profiles of the sonic turbulence measurements at GRI during IOP4. Wind speeds and directions were similar to that seen in Fig. 151 with consistently northeast winds and a slight increase in U over the IOP. The σ_v/U and σ_w/U were large in magnitude during the first hour and then diminished during the second hour. Profiles were well behaved except for u_* and σ_w/U during the first hour.

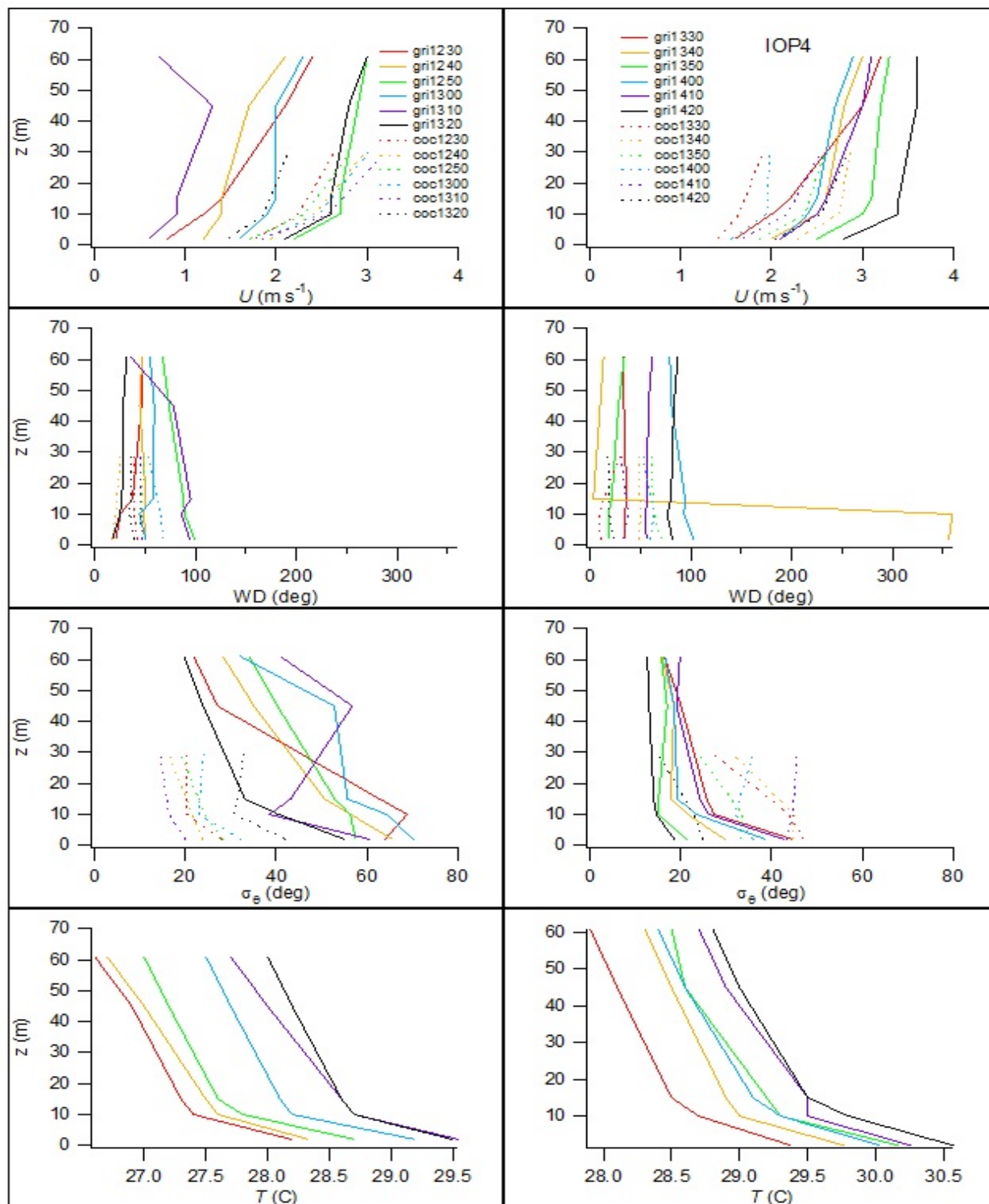


Figure 151. Profiles of U , wind direction, standard deviation of wind direction σ_θ , and aspirated temperature from cup anemometers and wind vanes during IOP4 at GRI and COC. Each profile is designated 'xxxhrmn' where xxx = tower and hrmn = start time of 10-minute interval.

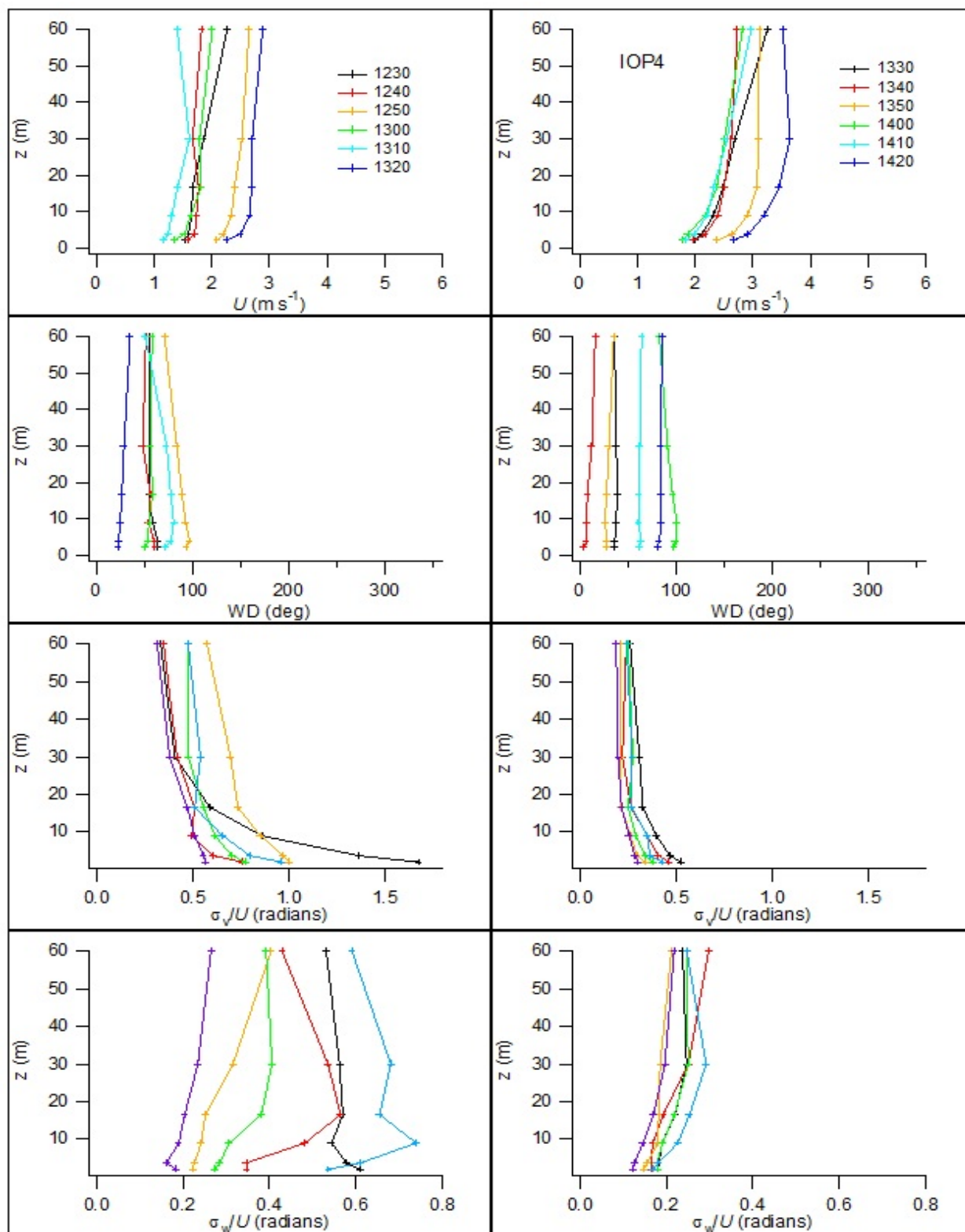


Figure 152. Profiles of U , wind direction, σ_v/U ($\sim\sigma_\theta$), and σ_w/U ($\sim\sigma_\phi$) from sonic anemometers at GRI during IOP4. The legend specifies the start time of the 10-minute interval (hrmn).

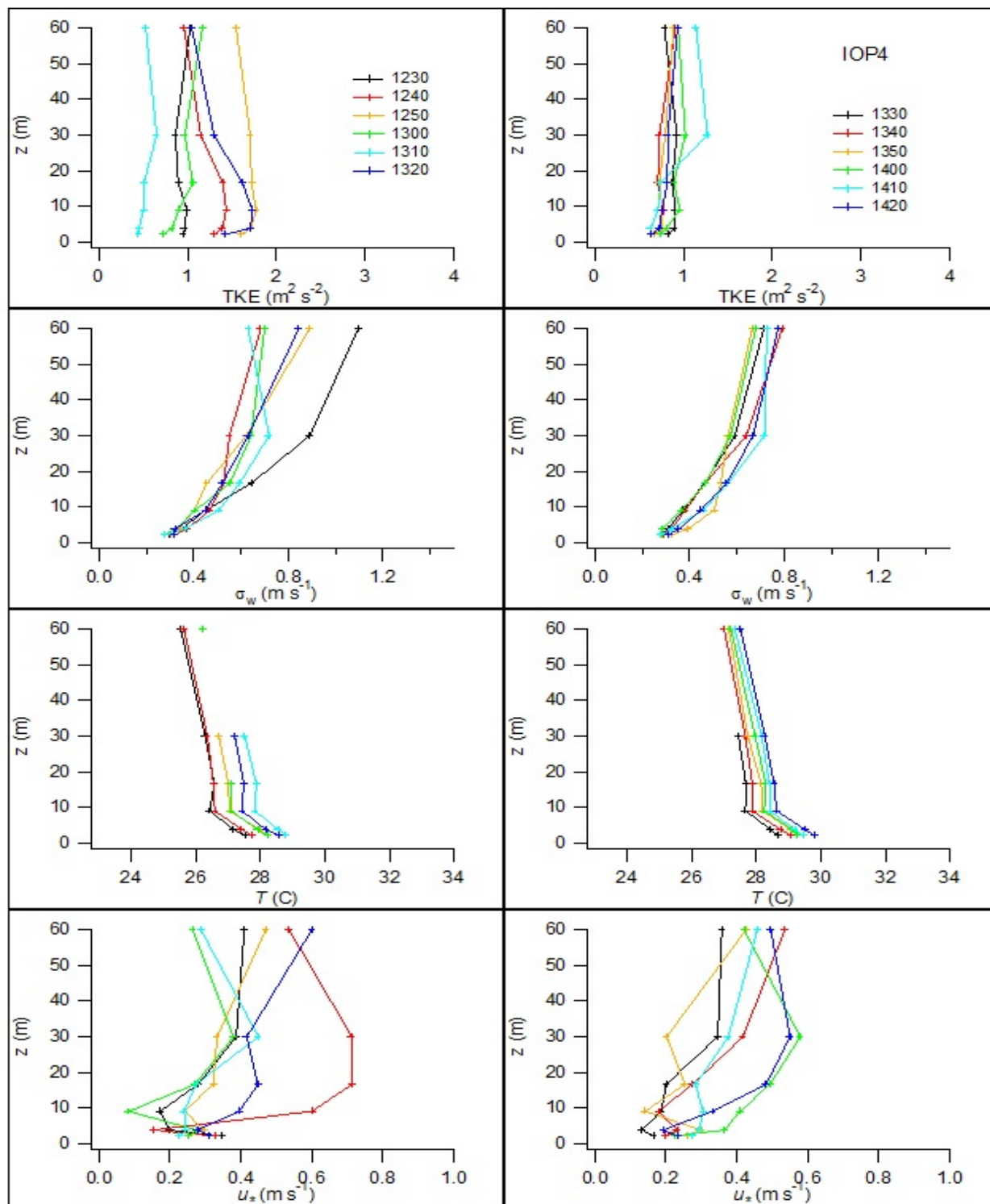


Figure 153. Profiles of turbulent kinetic energy (TKE), standard deviation in vertical wind speed σ_w , virtual temperature, and friction velocity u_* from sonic anemometers at GRI during IOP4. The legend specifies the start time of the 10-minute interval (hrmn).

Figures 154 and 155 show time-height representations of wind speed and direction for SOD and PRO, respectively, during IOP4. The U observed at SOD ranged mainly up to 4 m s^{-1} and were mainly from the north and northeast. That is entirely consistent with the observations at GRI (Figs. 151, 152). Data recovery at PRO was good. These showed generally east and northeast wind directions throughout the profiles with U mainly up to 6 m s^{-1} .

Figures 156 and 157 show SOD time-height representations of σ_w and TKE, respectively, during IOP4. The σ_w profiles are less distinctly episodic than the other daytime IOPs 1-3. Whatever periodic behavior was present, it was obscured below the levels measurable on GRI. The magnitudes of σ_w measured by sonic at GRI tended to be a tenth or two higher than those measured by SOD at comparable heights (Figs. 153, 156). The SOD TKE measurements exhibited pattern similar to that seen for σ_w . The overall magnitudes of TKE measured by GRI sonic (Fig. 153) were generally a few tenths greater than those measured by SOD (Fig. 157). The concentration of higher σ_w and TKE values at the upper levels might represent, in part, measurement artifacts near the top of the profiles. Figure 158 shows time-height temperature profiles from the RASS.

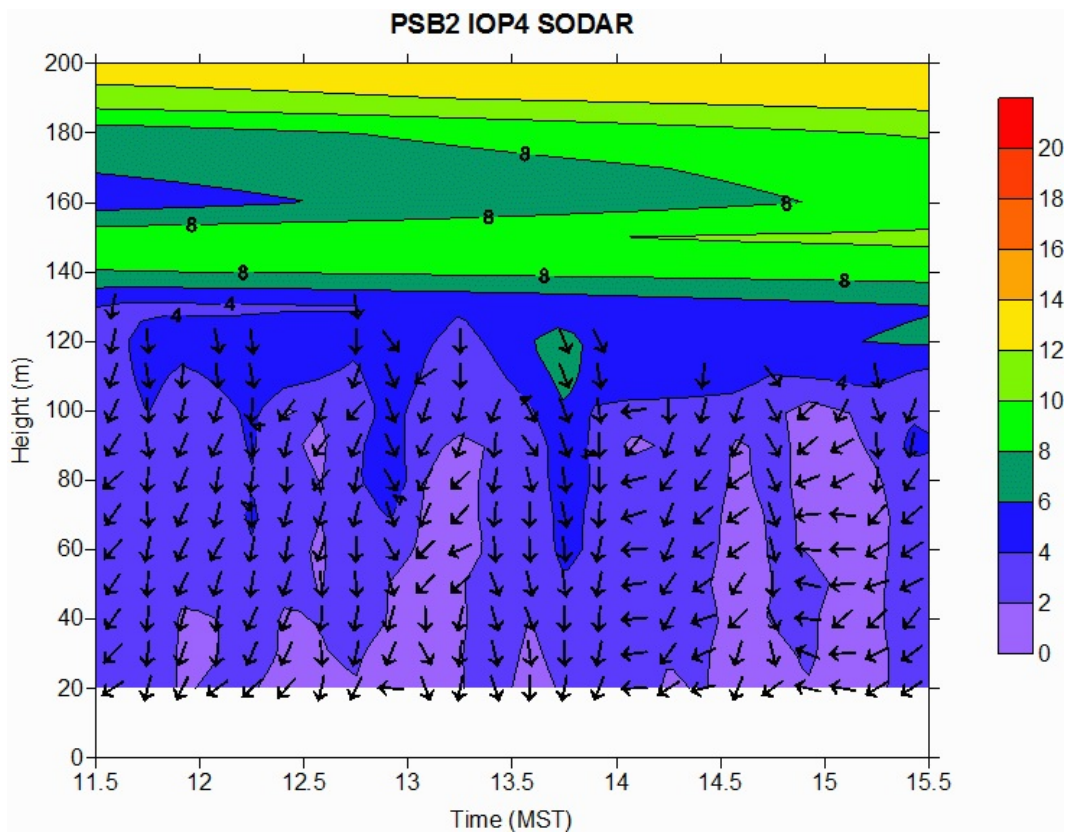


Figure 154. Time-height cross-section of wind speed and direction at sodar (SOD) during IOP4. Legend represents m s^{-1} .

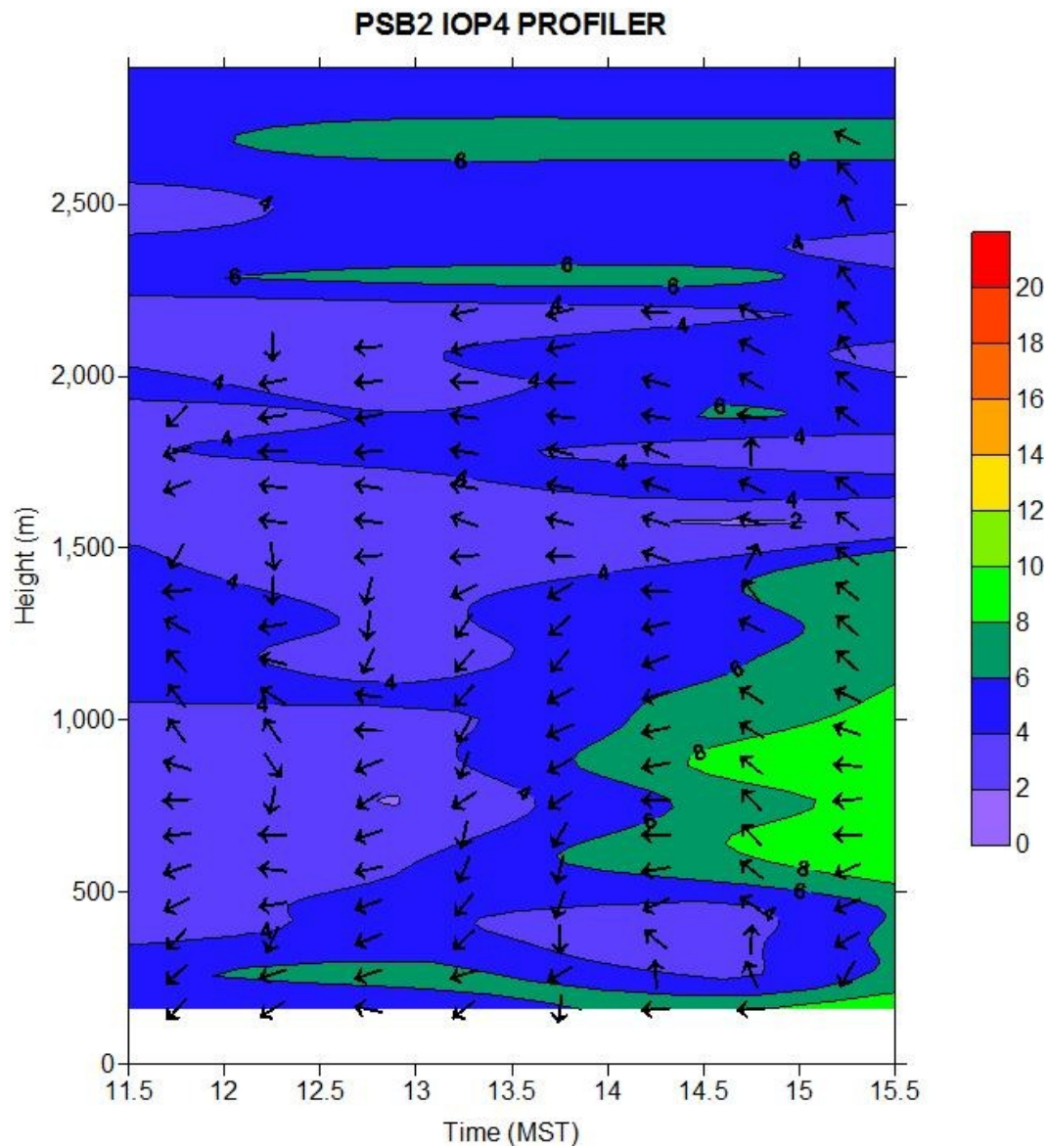


Figure 155. Time-height cross-section of wind speed and direction at wind profiler (PRO) during IOP4. Legend represents m s^{-1} .

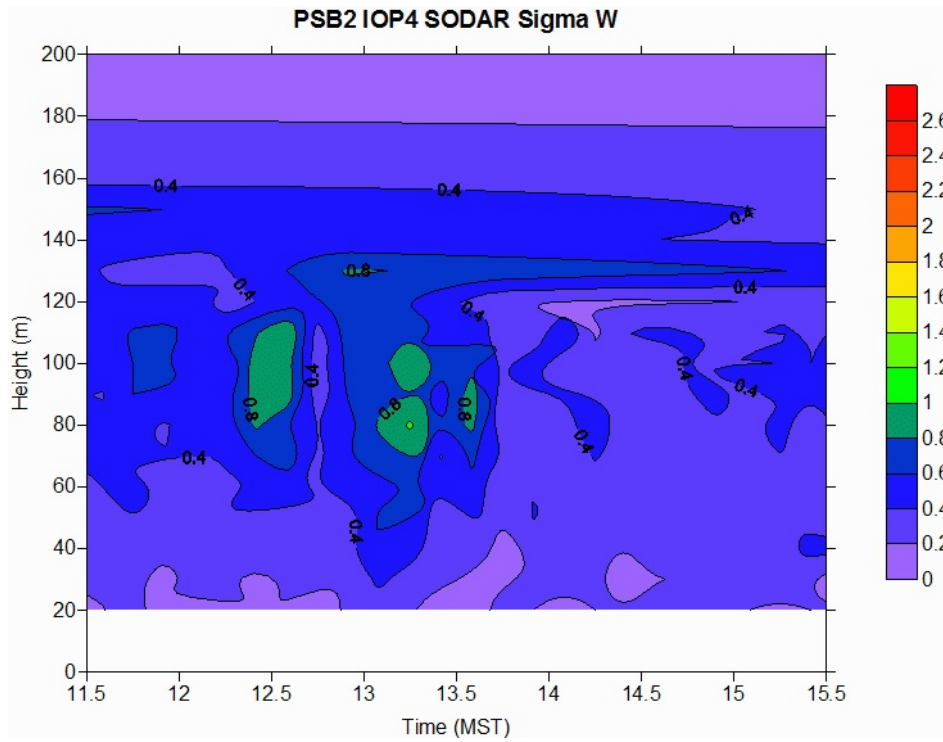


Figure 156. Time-height cross-section of σ_w at sodar (SOD) during IOP4. Legend represents m s^{-1} .

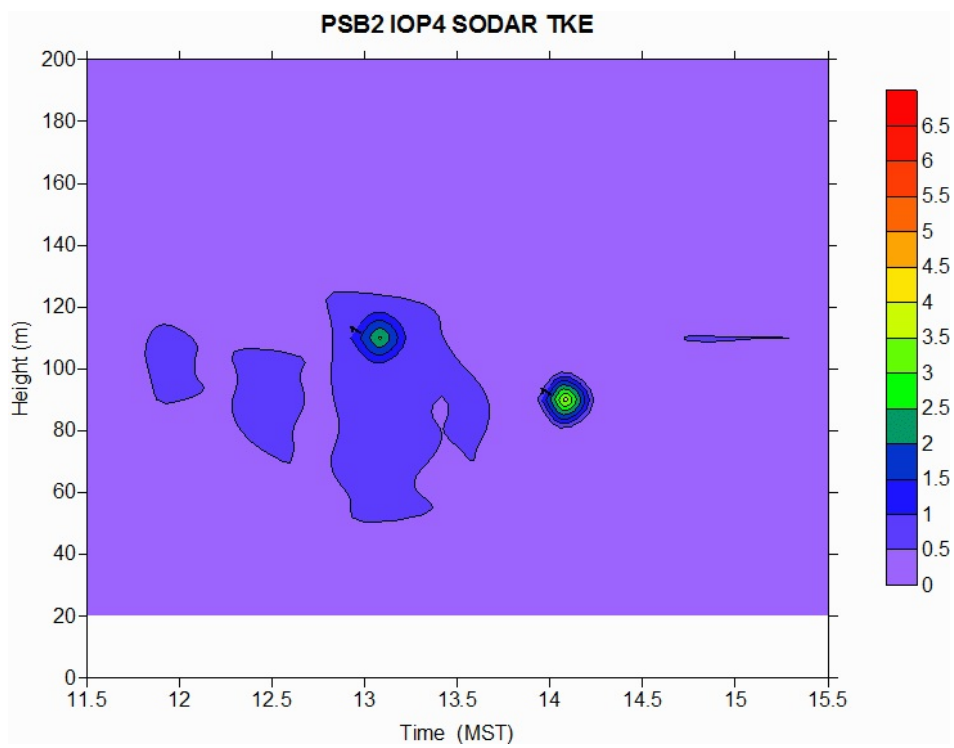


Figure 157. Time-height cross-section of TKE at sodar (SOD) during IOP4. Legend represents $\text{m}^2 \text{s}^{-2}$.

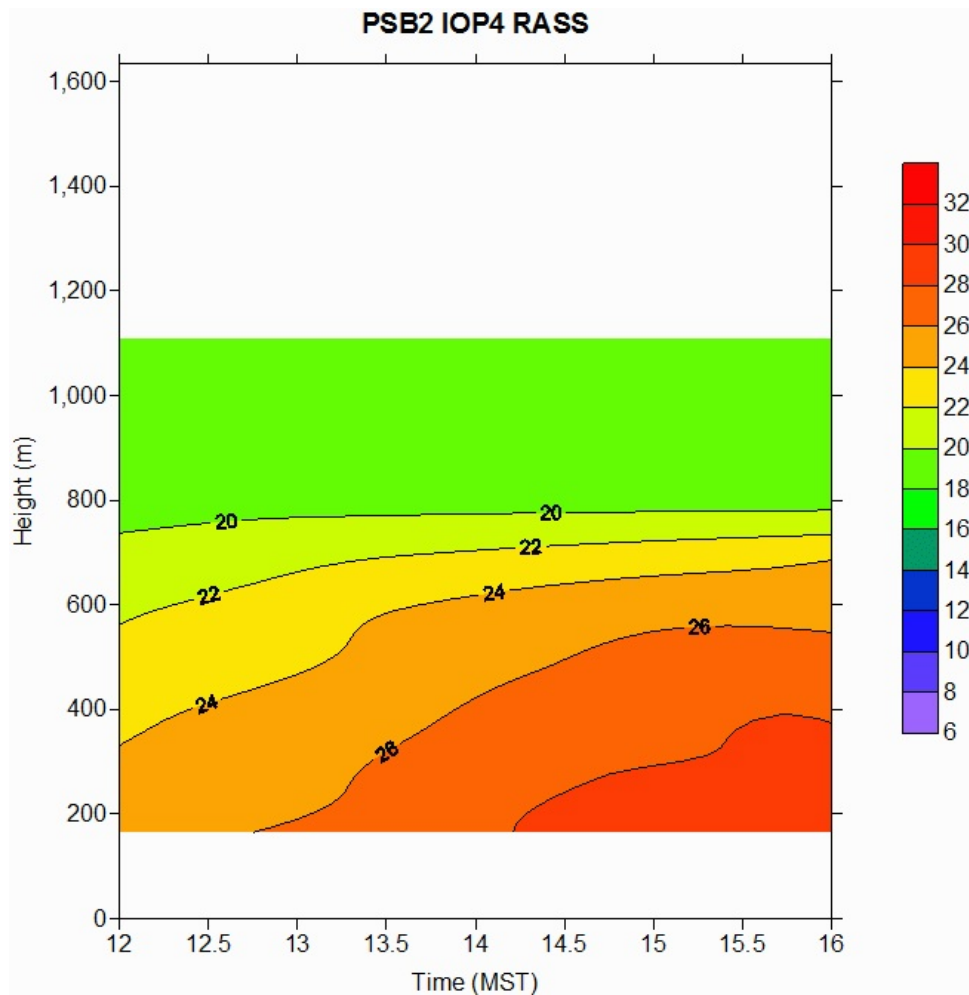


Figure 158. Time-height cross-section of virtual temperature at the RASS during IOP4. Temperatures are in degrees C.

Radisonde Results

Pre and post-IOP radiosonde profiles of potential temperature and specific humidity for IOP4 are shown in Figs. 159 and 160. For the post-test, both the potential temperature and specific humidity profiles suggest a mixing height of about 4000 m agl. The determination of the pre-test mixing height is much more ambiguous. There is no interval over which the potential temperature profile is approximately constant and the specific humidity profile suggests the presence of complex layering up to a height of about 4000 m. It is proposed to use the suggestion of a layer at about 700 m agl as a mixing height at the start of the test. These embedded layers were likely transient and probably breaking down rapidly over the course of the IOP. That said, there still appeared to be a relatively moist layer between about 2000-4000 m agl at the end of the test near the top of the mixing height.

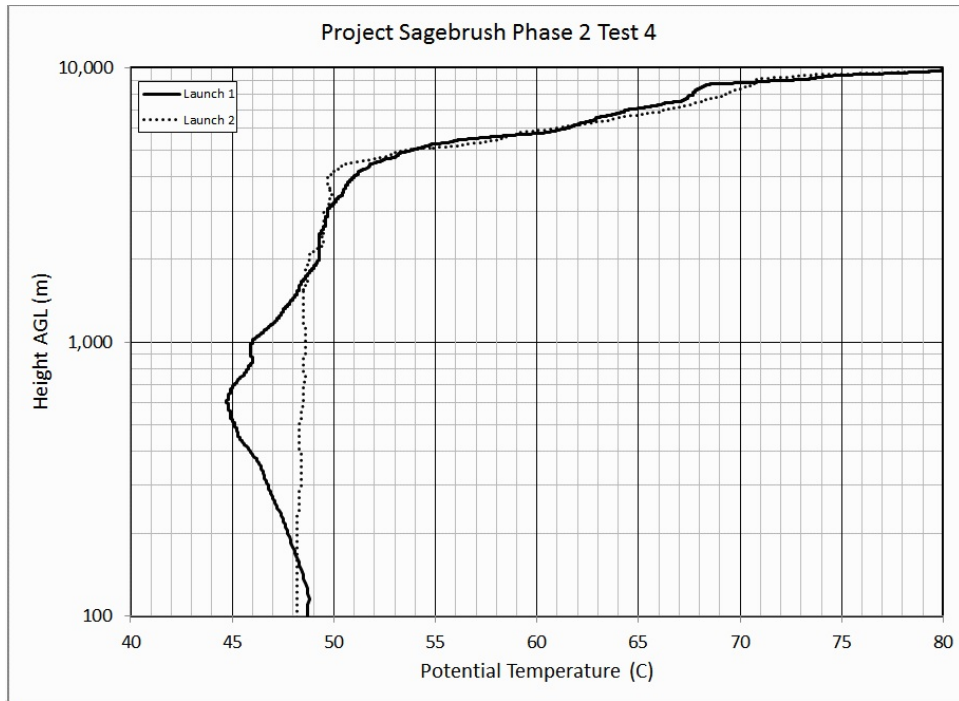


Figure 159. Potential temperature profile from radiosonde probe, IOP4. Pre-test launch bold, post-test launch dotted.

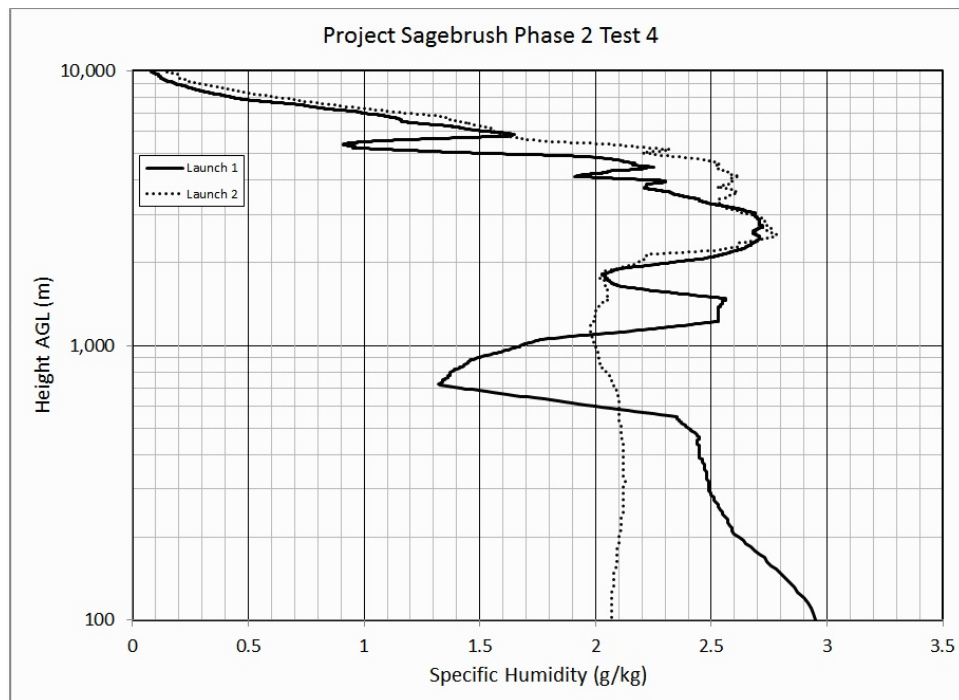


Figure 160. Specific humidity profile from radiosonde probe, IOP4. Pre-test launch bold, post-test launch dotted.

Bag Sampling Results

Figures 161 and 162 and Figures 163 and 164 show the 10-minute average normalized and actual, respectively, color-coded plan view concentration maps for IOP4 bag sampling at 1 m agl. Figures 165 and 166 and Figures 167 and 168 show the 10-minute average normalized and actual concentrations, respectively, along each of the arcs.

There were no 10-minute periods during which the plume was fully bounded within the 210° sampler array. In fact, it was common for the plume to either clip the western edge of the sampler array or sometimes miss it entirely, especially beyond the 100 m arc. The available data suggest that the plumes might have been relatively narrow compared to plumes in the other daytime IOPs. That is consistent with the generally lower σ_θ measured during IOP4. However, it is possible that larger portions of the plume were missing than is apparent, especially given the generally northeasterly winds measured at GRI and COC (Figs. 146, 147, 149; Table 21). Like IOPs 1-3, the margins of the plume tended to be sharp. There were only a very few samples on the 800 m arc that appear to have had concentrations slightly above the ambient background of about 9 ppt.

Figure 169 shows the vertical concentration profiles up to 25 m agl from the mobile tower located on the 100 m arc at 352° azimuth (red dot 2, Fig. 5). Only two profiles show concentrations consistently above ambient levels with maxima at about 15-20 m agl. A third profile shows a weak hit in only the 25 m sample (1320 h).

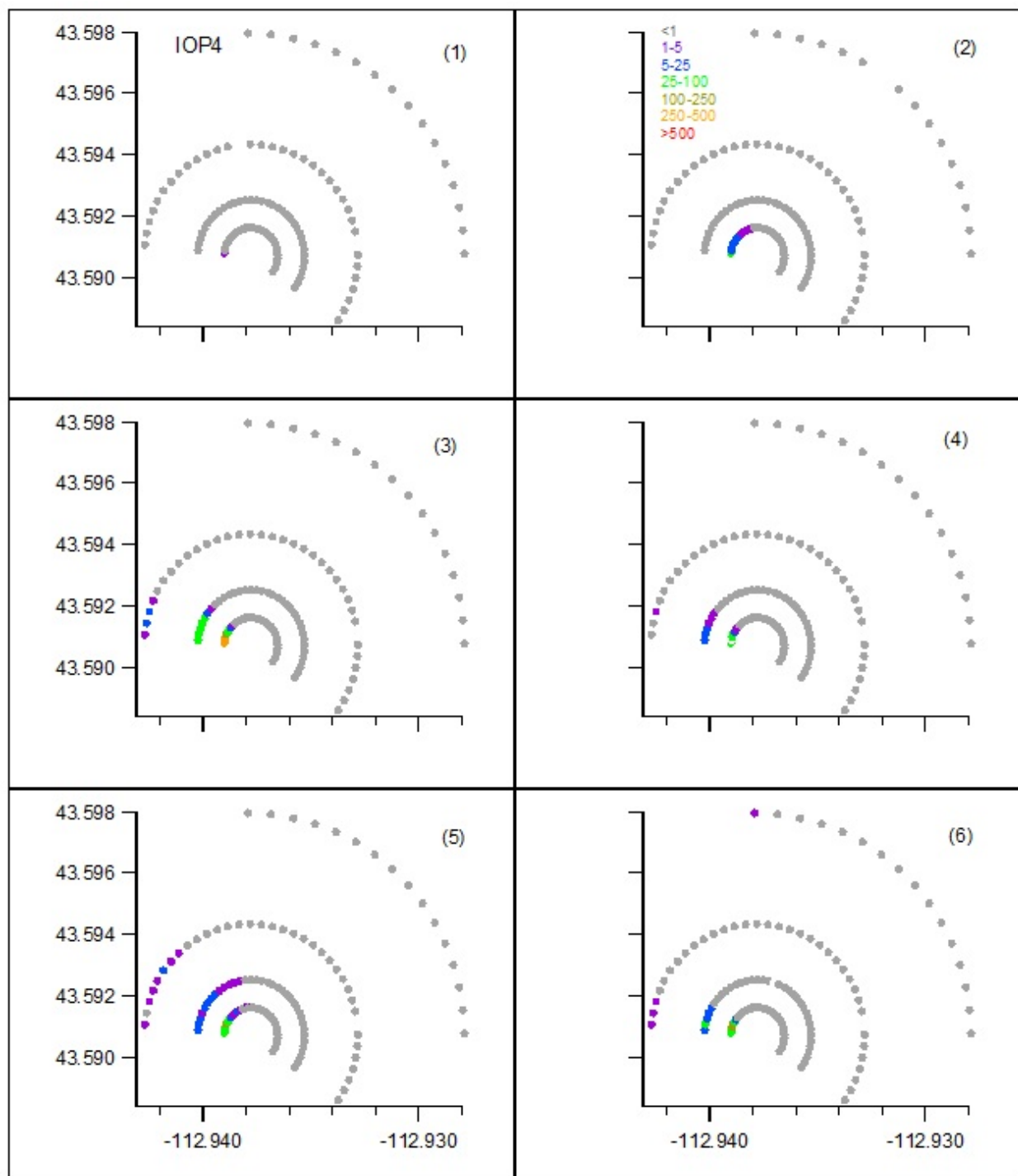


Figure 161. Color-coded normalized ($F^*\gamma/Q$ ppt s g^{-1}) concentrations at 1 m agl for bags 1-6 during IOP4. The number in () is bag number.

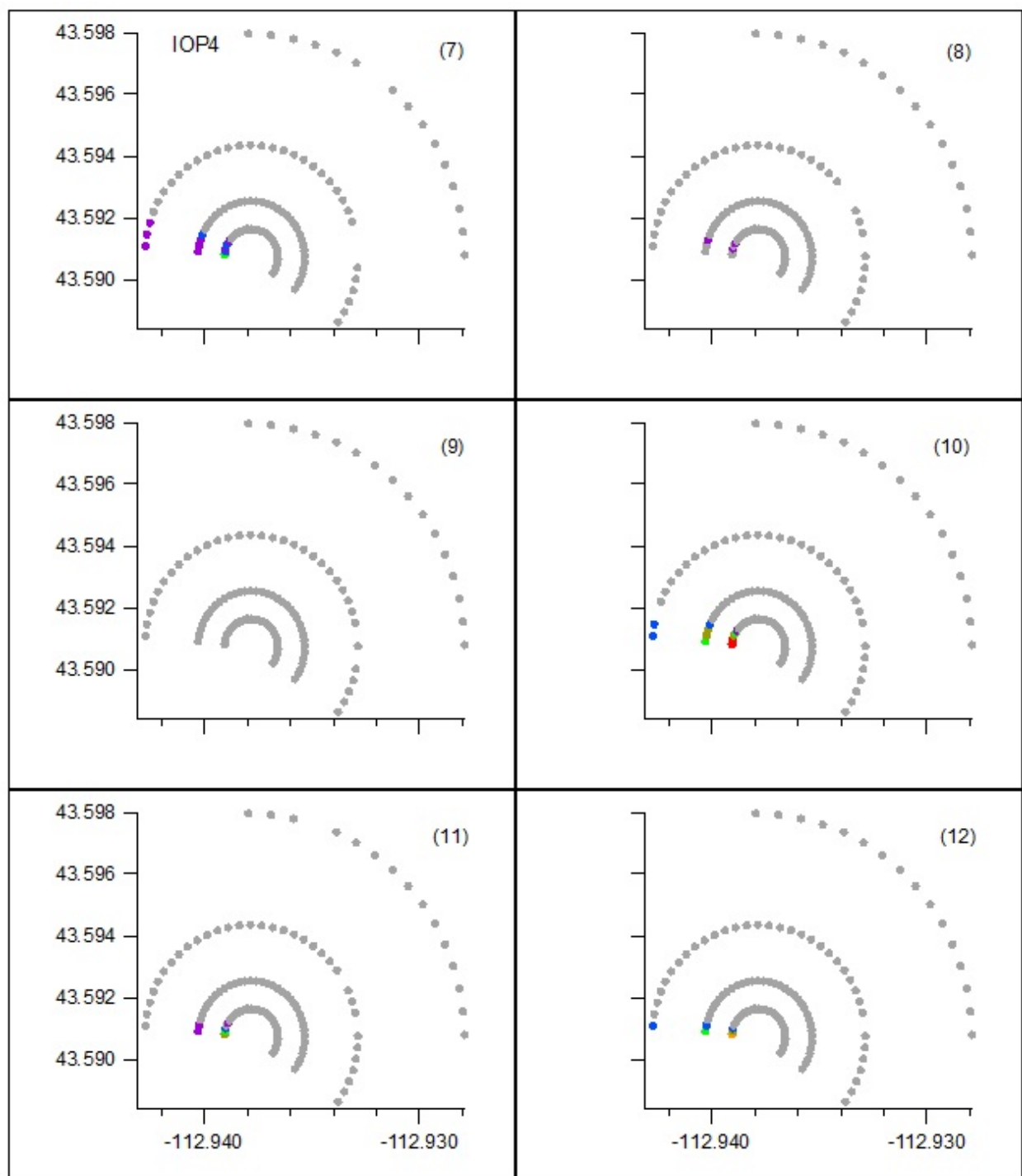


Figure 162. Color-coded normalized ($F^*\chi/Q$ ppt s g^{-1}) concentrations at 1 m agl for bags 7-12 during IOP4. The number in () is bag number.

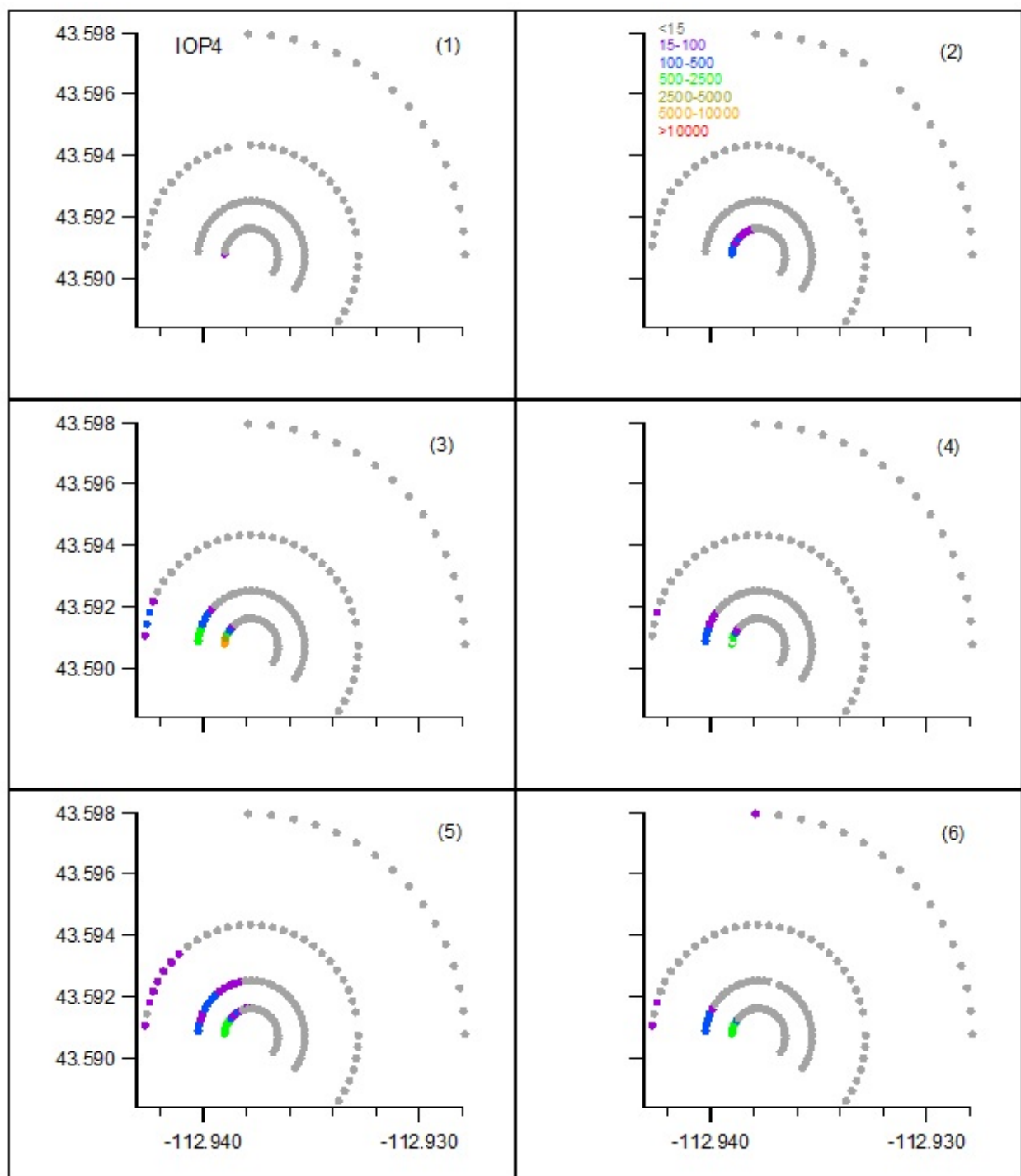


Figure 163. Color-coded measured SF_6 concentrations (ppt) at 1 m agl for bags 1-6 during IOP4. The number in () is bag number.

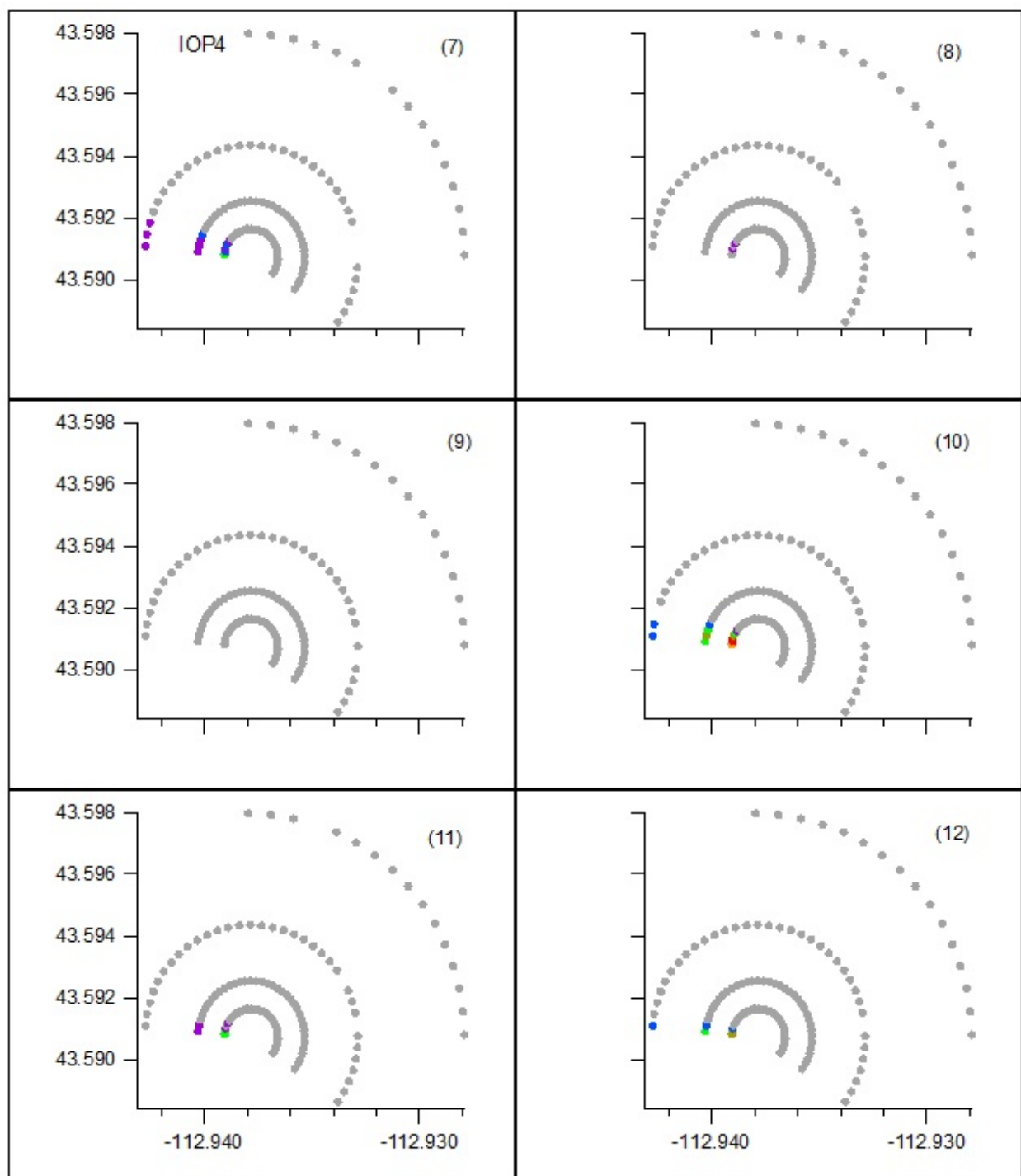


Figure 164. Color-coded measured SF_6 concentrations (ppt) at 1 m agl for bags 7-12 during IOP4. The number in () is bag number.

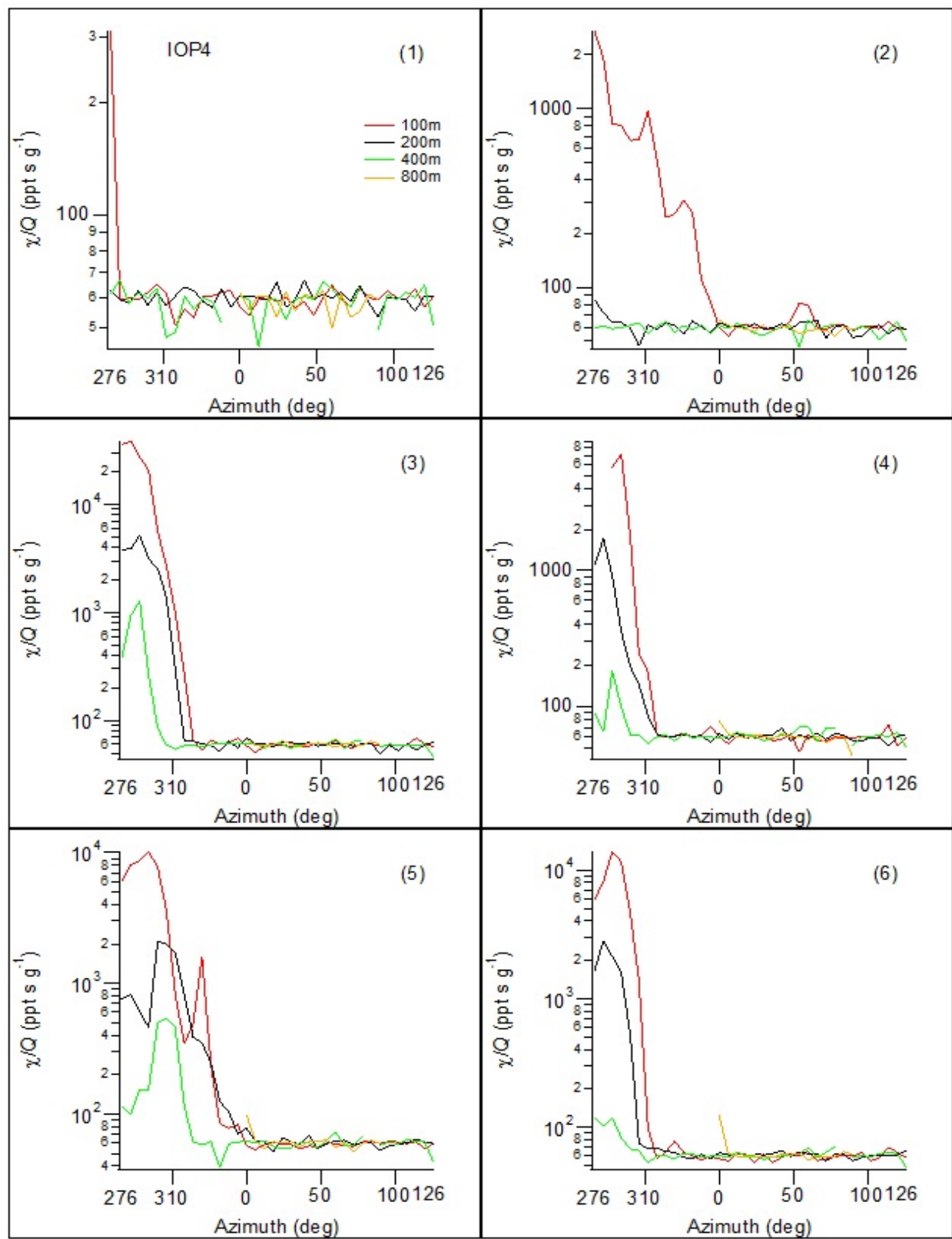


Figure 165. Cross-sections of normalized concentration along the arcs for bags 1-6 during IOP4.

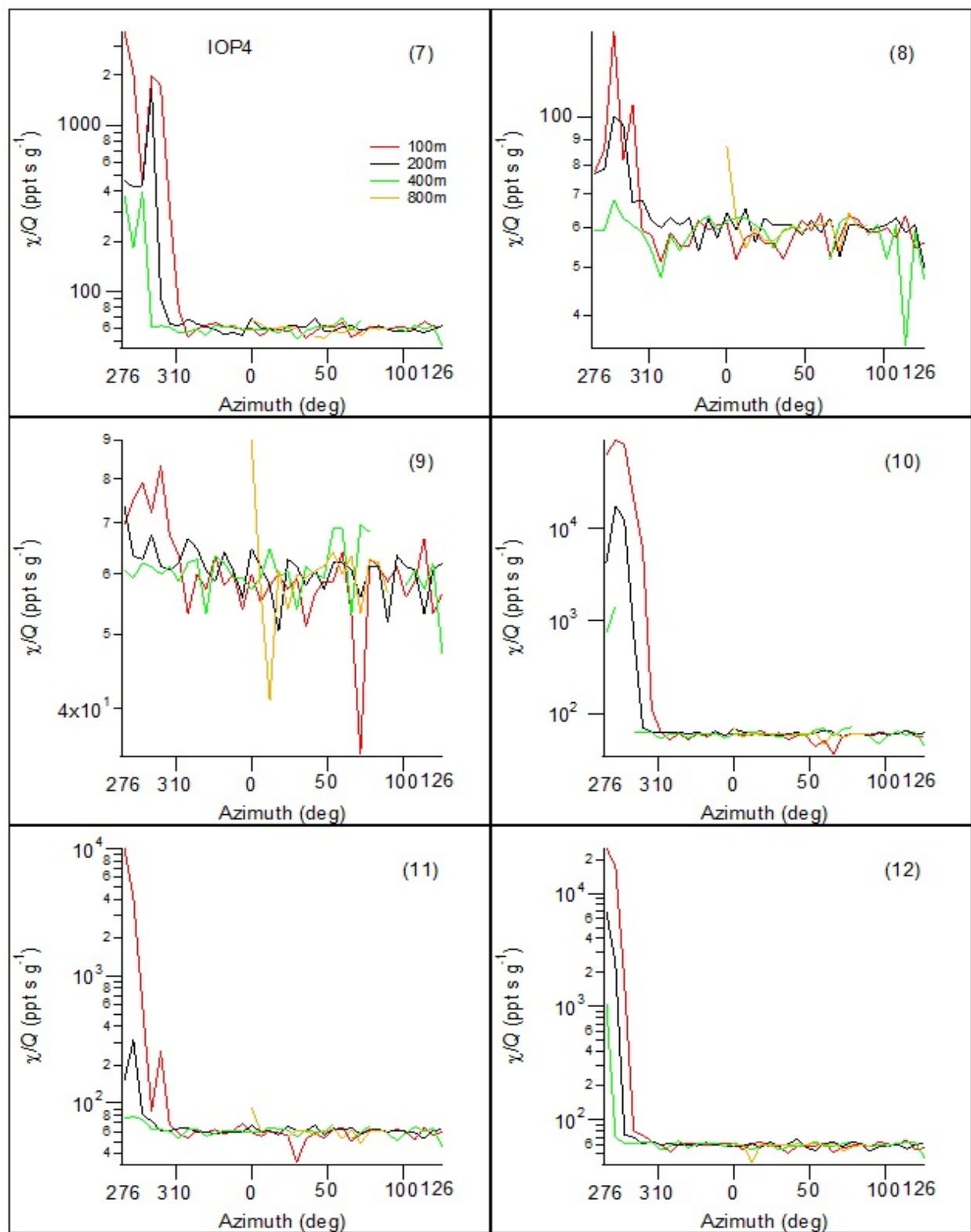


Figure 166. Cross-sections of normalized concentration along the arcs for bags 7-12 during IOP4.

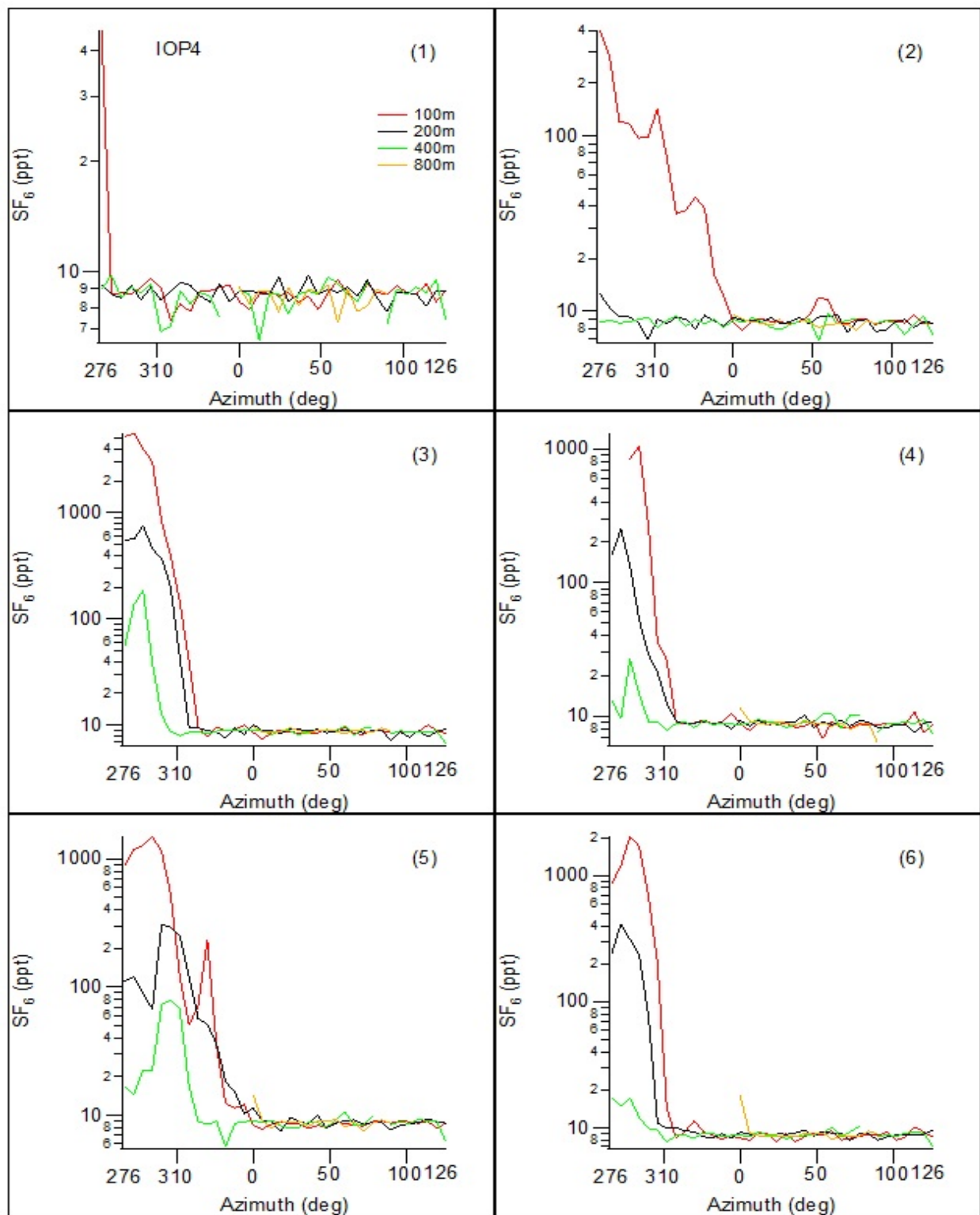


Figure 167. Cross-sections of measured SF_6 concentration along the arcs for bags 1-6 during IOP4.

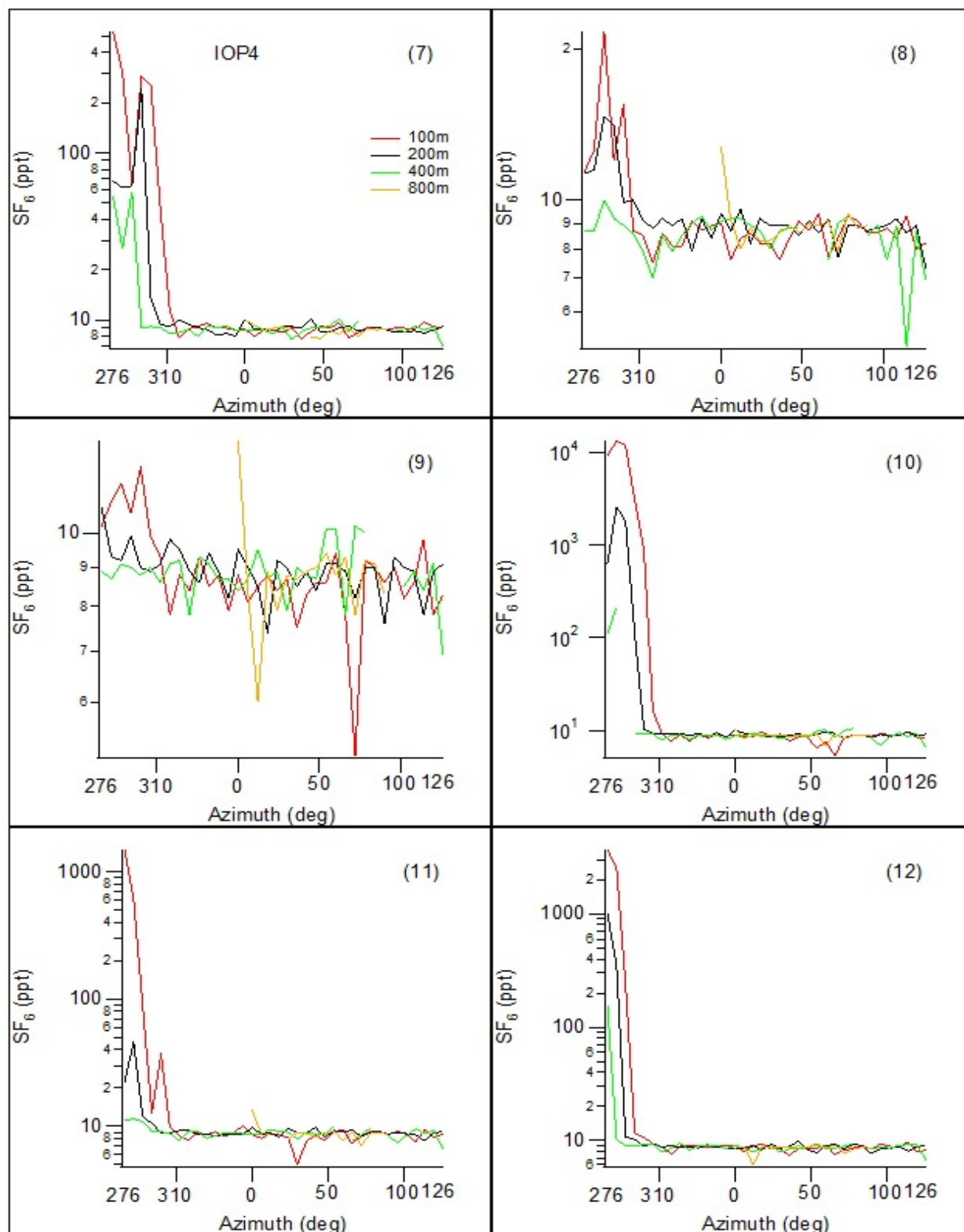


Figure 168. Cross-sections of measured SF_6 concentration along the arcs for bags 7-12 during IOP4.

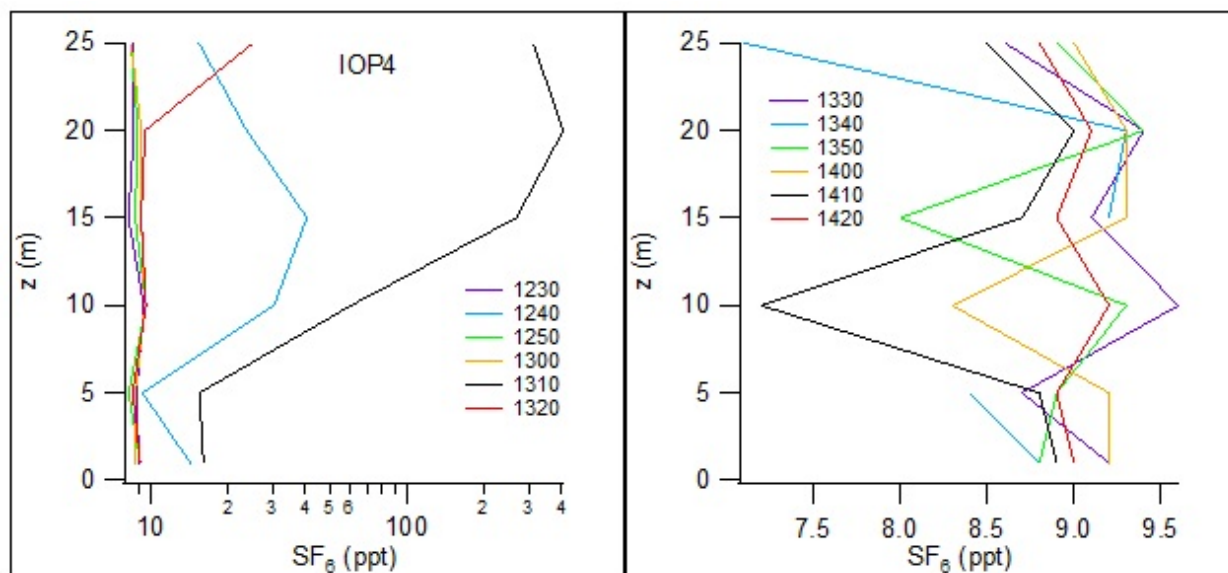


Figure 169. Vertical profiles of measured SF_6 concentration at the mobile tower during IOP4.

Fast Response Results

The locations of the fast response analyzers during IOP4 are shown in Fig. 170. The corresponding concentration time series are shown in Fig. 171. The color coding of the time series was described in the Introduction to this section.

Analyzers A, B, and C were positioned at the western end of the sampling array along the northern margin of the plume during the IOP. Analyzer D might have been positioned closer to the southern margin of the plume. Like the other daytime IOPs, the measurements were again characterized by being highly variable and intermittent with often rapid increases to peak values followed by abrupt drops in concentration back to background or near background concentrations. Again, this suggests a relatively narrow instantaneous plume at any given time with abrupt changes in concentration related to shifts in wind direction moving the plume back and forth across the sensor. The half hour gaps at A, B, and C with very little SF_6 measured from 1330-1400 h (bags 7-9) are consistent with the minimal SF_6 measured in the bag samplers (Figs. 162, 164, 166, 168).

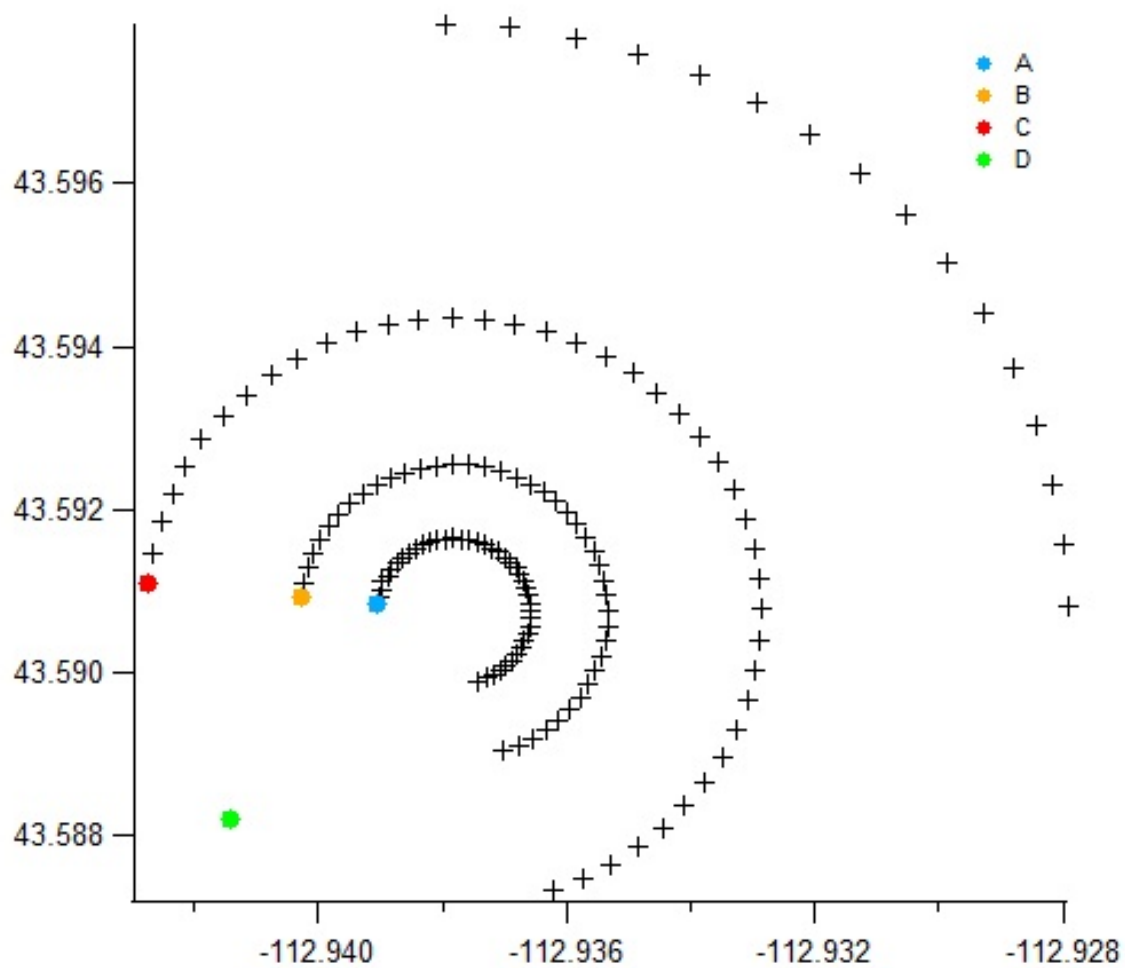


Figure 170. Locations of fast response analyzers during IOP4.

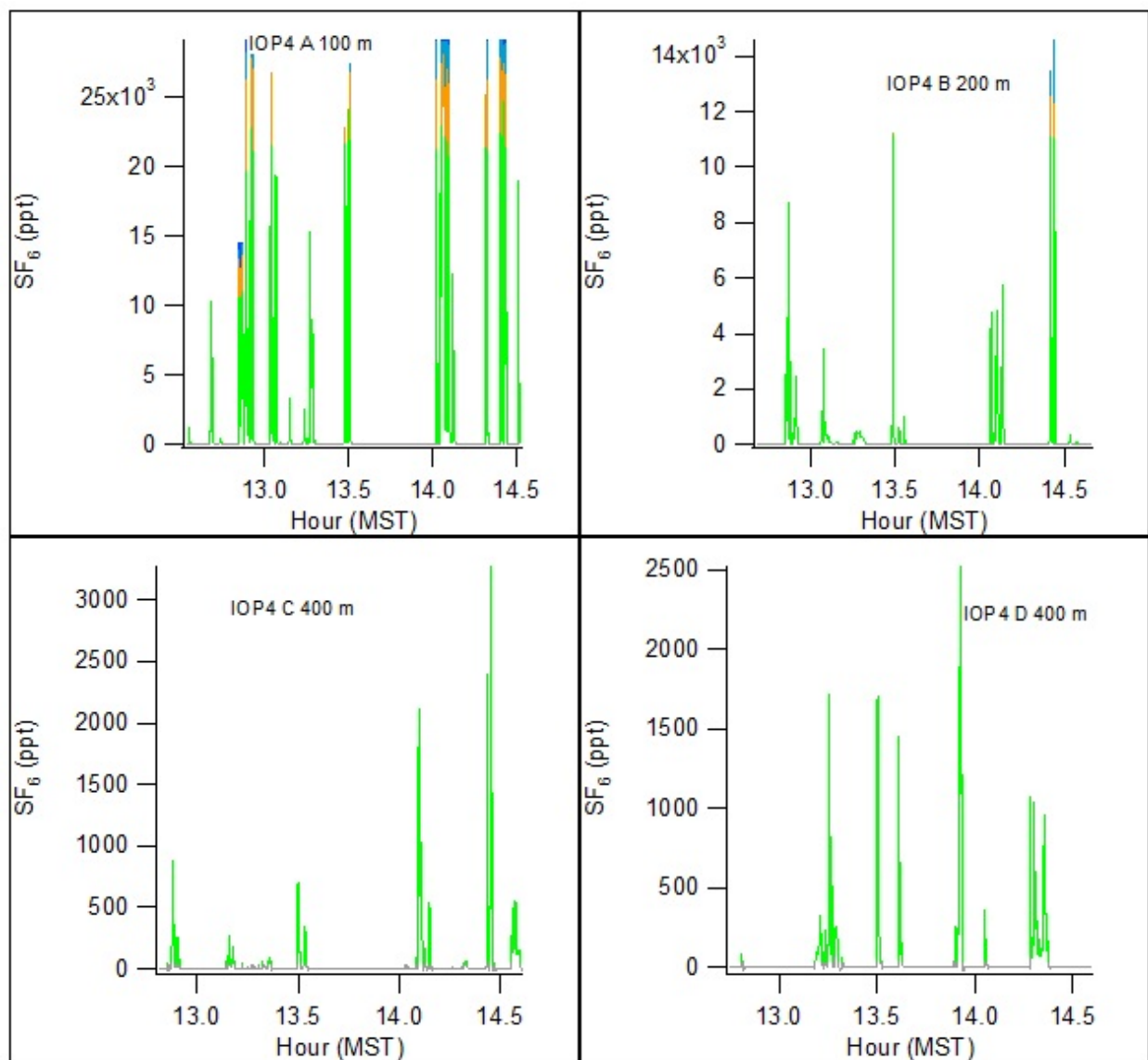


Figure 171. Fast response concentration time series during IOP4.

IOP 5

Date/Time and General Description

IOP5 was conducted on 13 October from 0400-0600 MST (0500-0700 MDT). Winds were very light, usually less than 1 m s^{-1} near the surface. Estimates of stability based on traditional Pasquill-Gifford (P-G) schemes were mainly classes E and F (Fig. 172). Estimates of mean z/L from GRI ranged from 0.85 to 4.34 with an Ri_b of 0.82 (Table 22). Wind directions were north-northwest within a few meters of the surface but often varied considerably in both time and space (Table 22; Figs. 173, 176). Above the lower few meters winds were generally north-northeast. A combination of wind direction and plume spread resulted in at least some portion of one or both limbs of the plume being truncated at the edge of the sampler array in all 10 min periods. This was most pronounced during the first hour of the IOP and for the 100 m arc. By the end of the first hour, essentially all samplers across the 210° of arc at 100 m arc measured concentrations well above ambient background levels. The plume tended to be better bounded by the 210° arc at the 200 and 400 m distances during the latter part of the IOP but they also exhibited some truncation. The plume often subtended 100-150 degrees of arc, more on the 100 m arc. The SF_6 release rate was 0.0147 g s^{-1} (Table 2). Fast response analyzers were at fixed locations on the 100 and 200 m arcs at the edge of the bag sampling array at 162° azimuth. The other two analyzers moved between several fixed locations on the 400 m arc during the IOP.

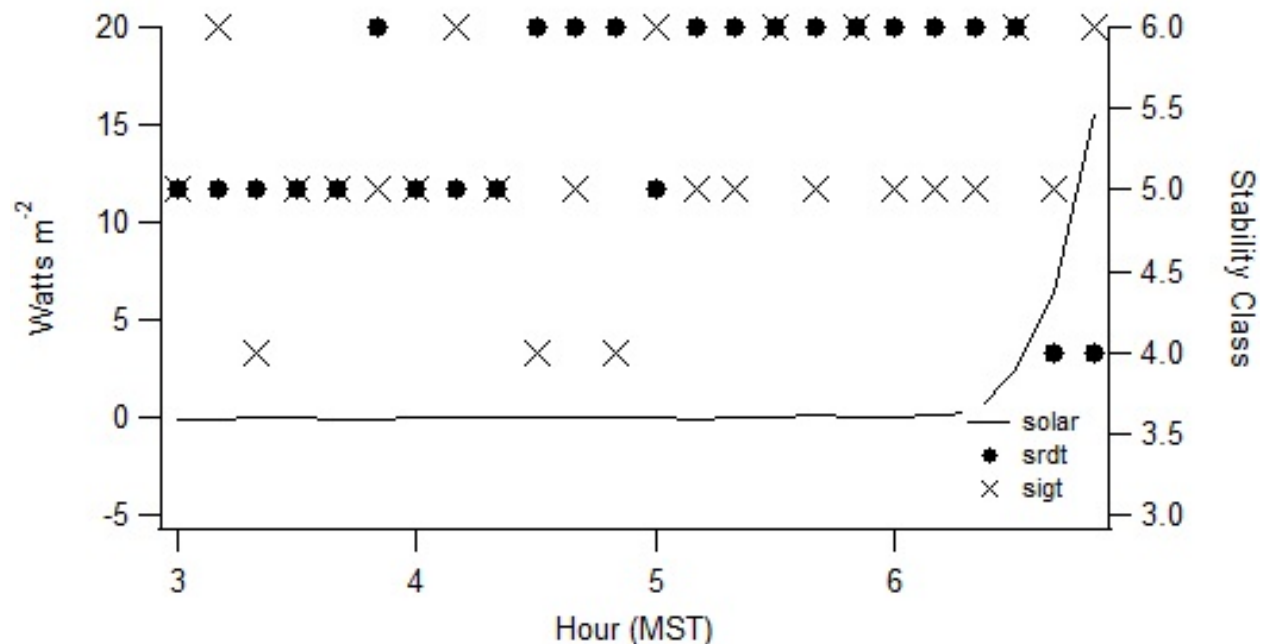


Figure 172. Incoming solar radiation and classification of stability conditions using the Pasquill-Gifford Solar Radiation Delta T (srdt) and σ_θ (sigt) methods (EPA 2000c) during IOP5. Classes D, E, and F, are designated 4, 5, and 6, respectively.

Table 22. Meteorological conditions during IOP5.

Bag	COC				GRI						GRI			Solar
	U (m s ⁻¹)		WD (deg)		U (m s ⁻¹)		WD (deg)		σ_θ (deg)		L	L	degC	W m ⁻²
	2m	10m	2m	10m	2m	10m	2m	10m	2m	10m	3.7m	9m	2m	
1	1.0	2.0	3.7	20.5	0.9	1.9	354.7	3.2	38.7	5.2	8.8	16.4	-2.9	0
2	0.8	1.7	359.2	29.6	0.8	1.8	341.3	7.8	14.9	2.6	1.6	5.8	-2.7	0
3	0.6	1.8	26.5	18.5	0.5	1.6	315.6	9.9	16.7	6.0	17.7	3.5	-2.8	0
4	0.5	1.2	13.5	7.0	0.4	0.8	256.8	1.2	17.2	9.9	58.4	NaN	-3.1	0
5	0.7	1.1	329.2	0.8	0.5	1.3	281.7	7.2	5.8	14.2	1.3	2.6	-3.0	0
6	0.9	1.6	320.6	359.1	0.3	1.2	249.3	34.2	29.2	8.4	12.0	7.3	-3.0	0
7	1.3	2.1	344.2	8.9	0.9	1.7	350.5	13.3	18.3	2.8	6.1	NaN	-2.8	0
8	0.6	1.8	352.8	18.9	0.9	1.7	13.2	24.7	18.9	5.7	NaN	-30.5	-2.8	-0.1
9	0.6	1.7	326.4	20.2	0.4	1.0	288.5	27.4	13.1	14.8	-5.1	5.1	-3.0	0
10	0.5	1.1	250.1	12.9	1.0	0.8	271.9	318.9	13.7	18.4	8.8	8.2	-2.9	0
11	0.6	1.0	274.5	1.9	1.0	1.3	298.3	325.0	7.0	4.4	0.5	-1.0	-3.5	0.1
12	0.4	1.1	193.9	46.8	1.0	1.9	321.6	342.8	6.0	1.7	6.0	3.5	-3.6	0
Avg. L											10.56	2.08		
z/L											0.85	4.34		
Ri _b												0.82		

Wind Speed and Direction Quality Assurance

Figures 173-175 show wind speed and direction time series comparisons for a sequence of measurement heights during IOP5. In Fig. 173, the near surface measurement of U showed some variation but mostly within a narrow range of 1 ± 0.5 m s⁻¹. Wind directions were mainly north-northwest within a few meters of the surface. However, by 9 m agl and above, wind directions were consistently north-northeast (Fig. 174). Wind directions were generally consistent between different locations and measurement types above 9 m, including the sodar (Figs. 174 and 175). Wind directions at COC were sometimes different compared to other sites. This particular phenomenon was commonly observed during the nighttime IOPs. Measured U at SOD varied somewhat from those for the cup or sonic anemometers but were roughly consistent in magnitude. On a very limited basis there was good agreement between the SOD and PRO measurements at 160 m agl. Other than the poor data recovery for SOD at 160 m agl, there is little evidence of a systematic measurement problem. The observed variability or discrepancies are likely primarily attributable to non-stationarity and horizontal inhomogeneity in the wind field.

The Brunt-Väisälä frequency N was relatively high throughout the plume measurement period except for a dip and rebound midway through the second hour in association with an uptick in U and a shift to more consistently northwesterly winds.

Figure 176 shows time series measurements for cup anemometers and wind vanes only (excluding sonics) at all heights on the GRI and COC towers during IOP5. Again, the near surface measurements of U at GRI and COC were low at about 1 m s^{-1} but the sometimes much larger U at heights above 30 m suggest a steep gradient. Wind directions near the surface were north-northwest but shifted to north-northeast within 10-15 m agl. The measured σ_θ near the surface exhibited considerable variation but were commonly $> 10^\circ$. Above that σ_θ were generally $< 5^\circ$. The temperature time series suggest a steep temperature gradient with a ΔT of about 5° C between 2 and 60 m.

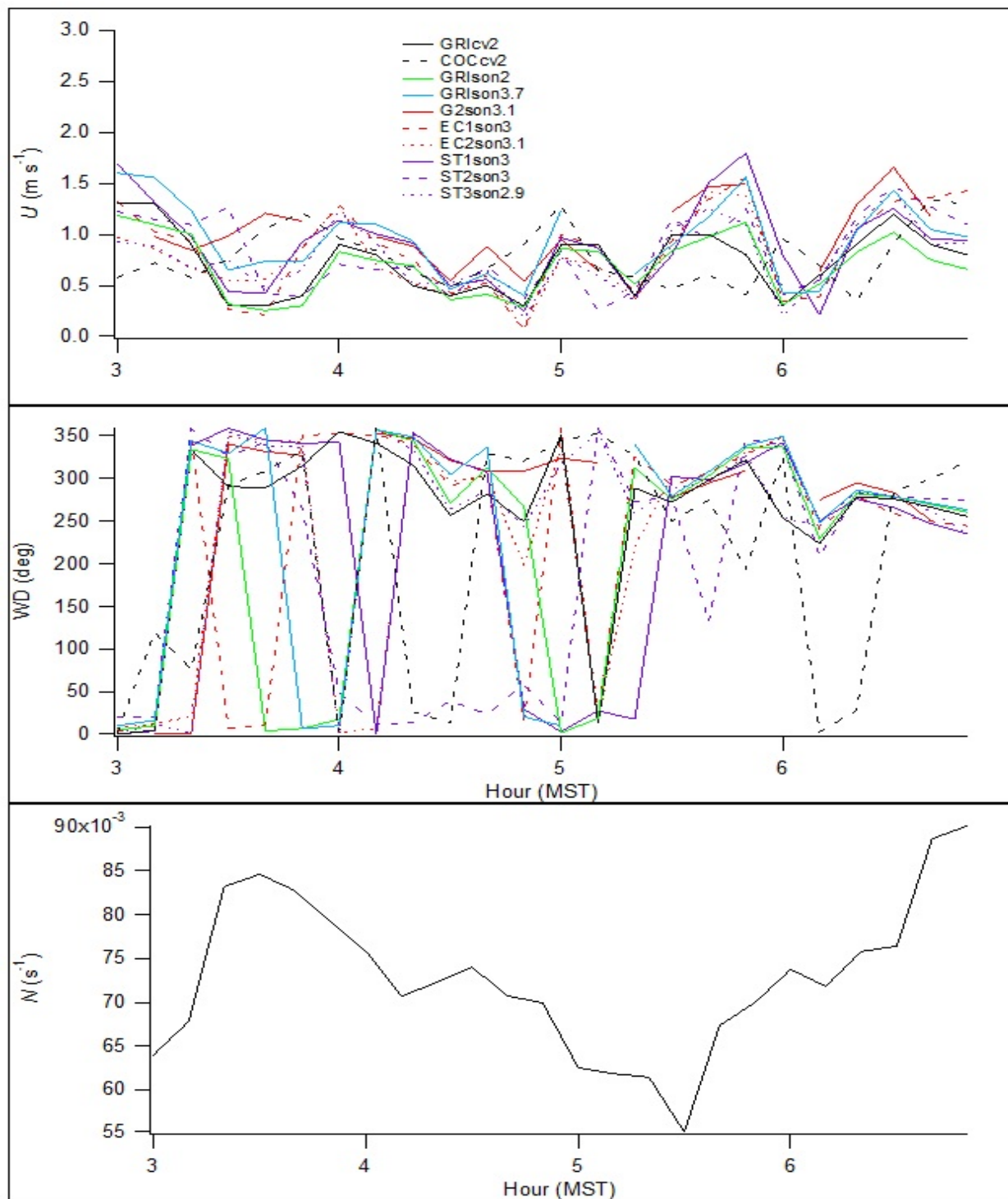


Figure 173. Time series of near surface wind speed and direction measurements and Brunt-Väisälä frequency N between 2 and 15 m agl during IOP5. In the legend, location is specified in upper case, the measurement type in lower case (cv = cup/vane, son = sonic), and the measurement height numerically.

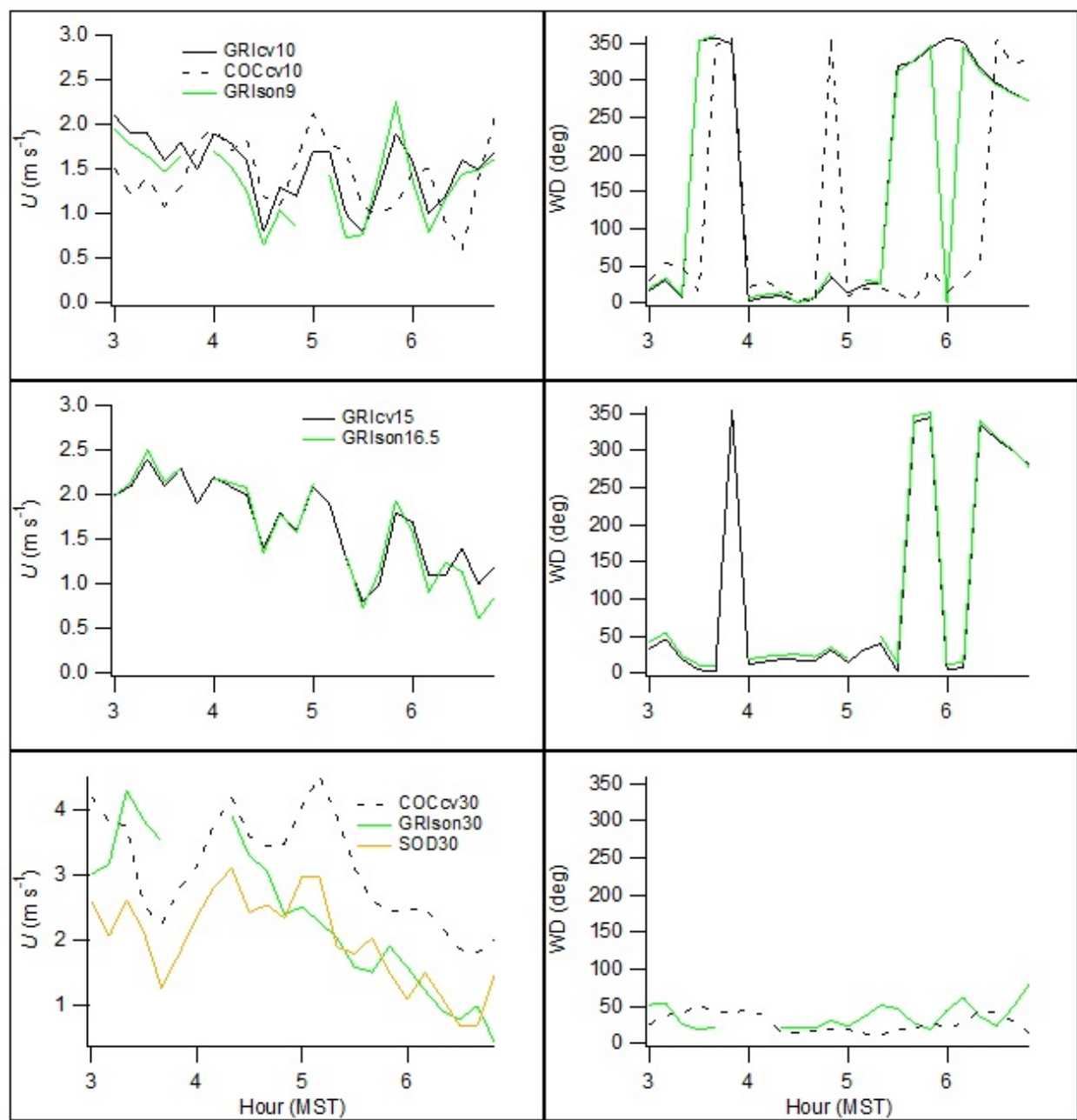


Figure 174. Time series of wind speed and direction measurements at heights between 9 and 30 m agl during IOP5. Legend notations described in caption of Fig. 173.

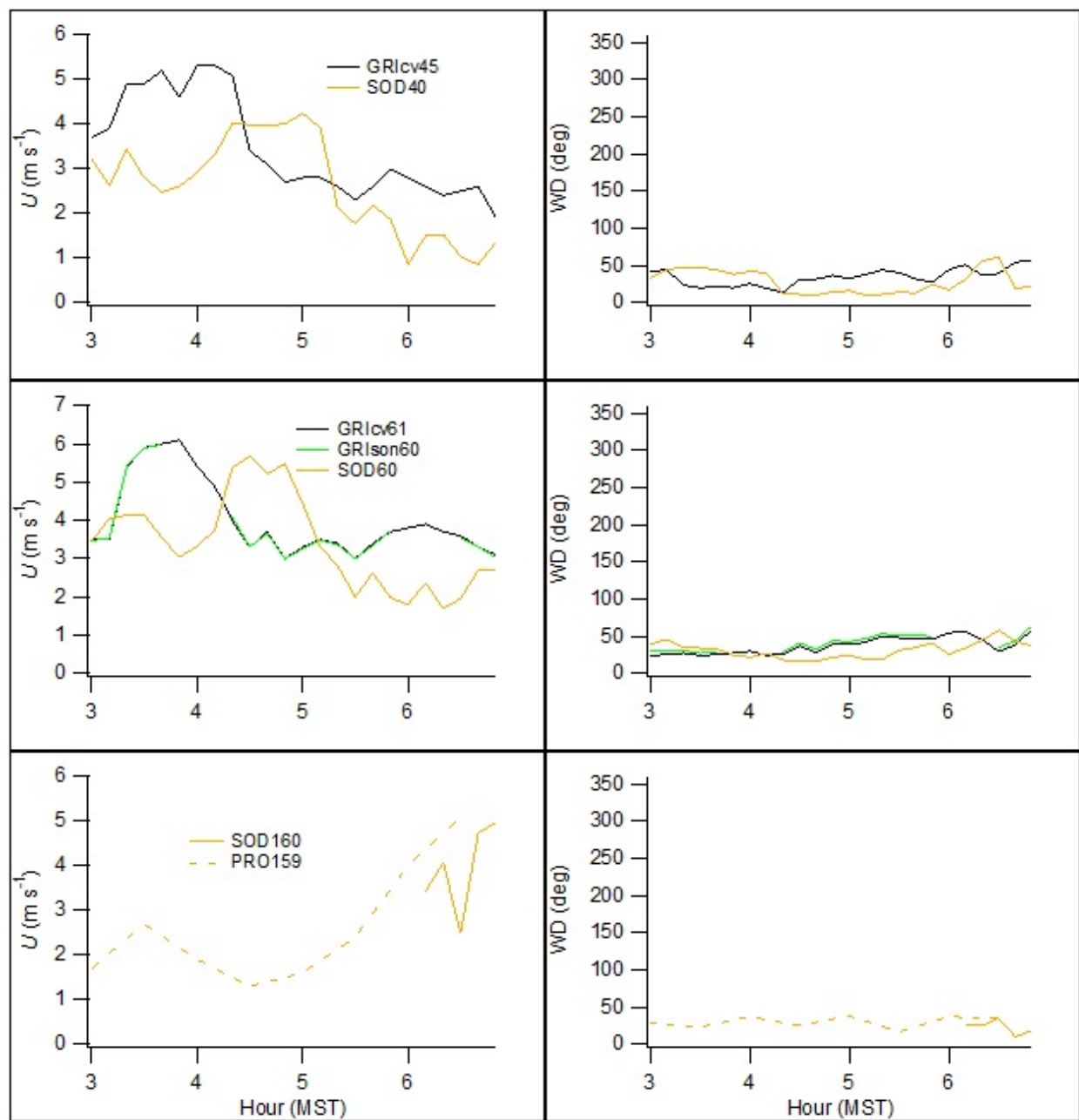


Figure 175. Time series of wind speed and direction measurements at heights above 30 m agl during IOP5. Legend notations described in caption of Fig. 173.

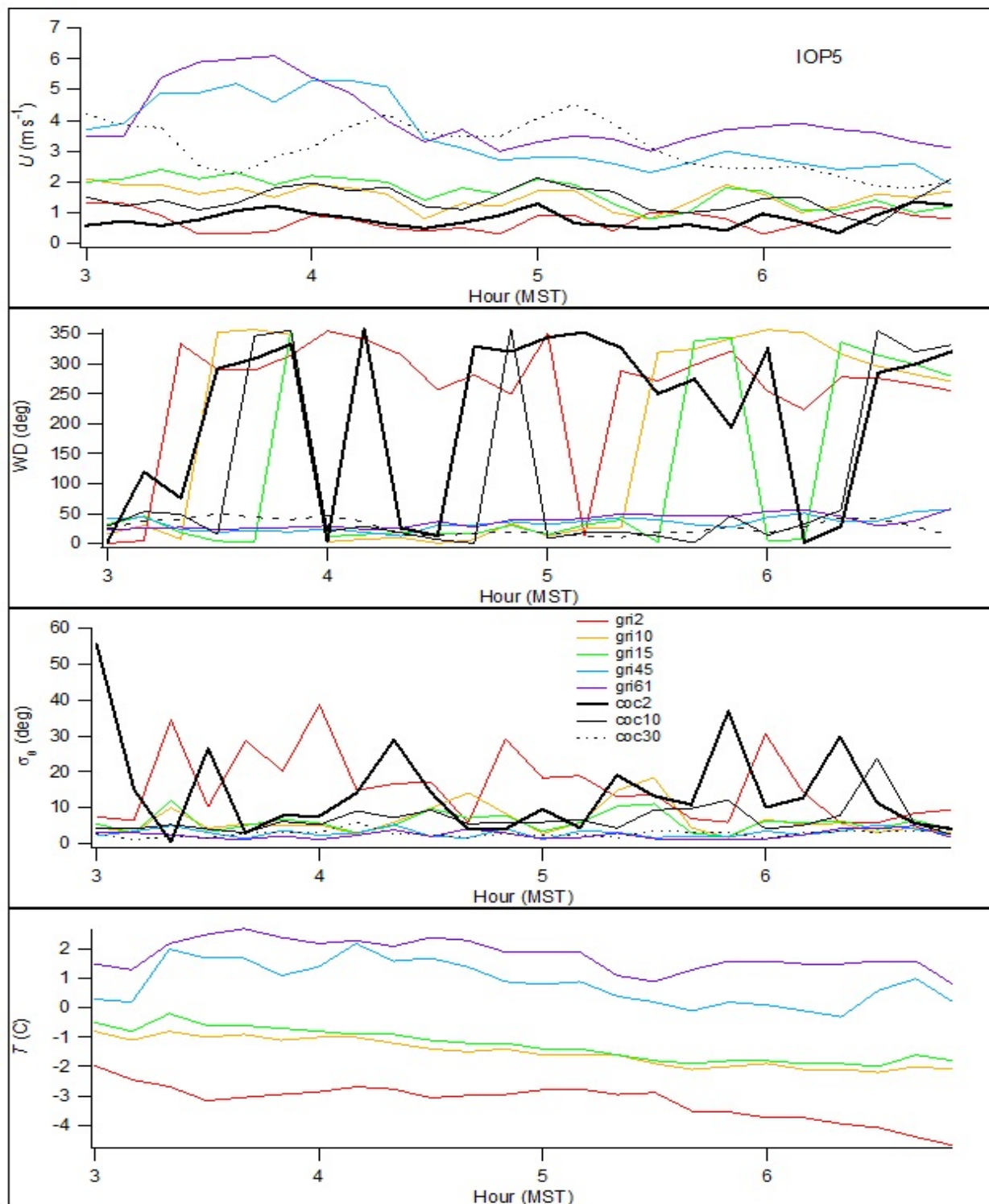


Figure 176. Time series from GRI and COC showing cup anemometer and wind vane measurements of U , wind direction, standard deviation of wind direction σ_θ , and temperature during IOP5. The locations are designated 'xxxxyy' where xxx = tower and yy = measurement height.

Turbulence

Near-surface turbulence measurements for IOP5 are shown in Fig. 177. The magnitudes of all the measurements of turbulence were very low but showed large variability in both space and over time. The variability in the measurements of σ_v/U and σ_w/U is likely due in significant part to the low U . The large variability was often expressed as some very large excursions from a more common magnitude. This might reflect the more intermittent nature of turbulence inherent to the stable boundary layer. Of particular note in this regard is station ST2, located to the west of the tracer sampling array a short distance southeast of a low hill (Figs. 2, 5). Large excursions were especially common in all of the parameters for ST2. Given its downwind location with respect to the near surface wind directions, it is possible that this subtle topographic feature further accentuated the nocturnal intermittency at that site. Any turbulence enhancements due to the low ridge or undulation to the northeast of the sampling array or the INTEC facility to the south were not as apparent. The ST1 station is located near the top of the low ridge visible to the left in Fig. 3. The σ_v/U (or σ_θ) are still large near the surface although much smaller than observed during the daytime IOPs. TKE, σ_w , and u_* were also much smaller than during the daytime IOPs, by an order of magnitude or more. The magnitude of the sensible heat flux was small and generally negative but there were a few positive excursions.

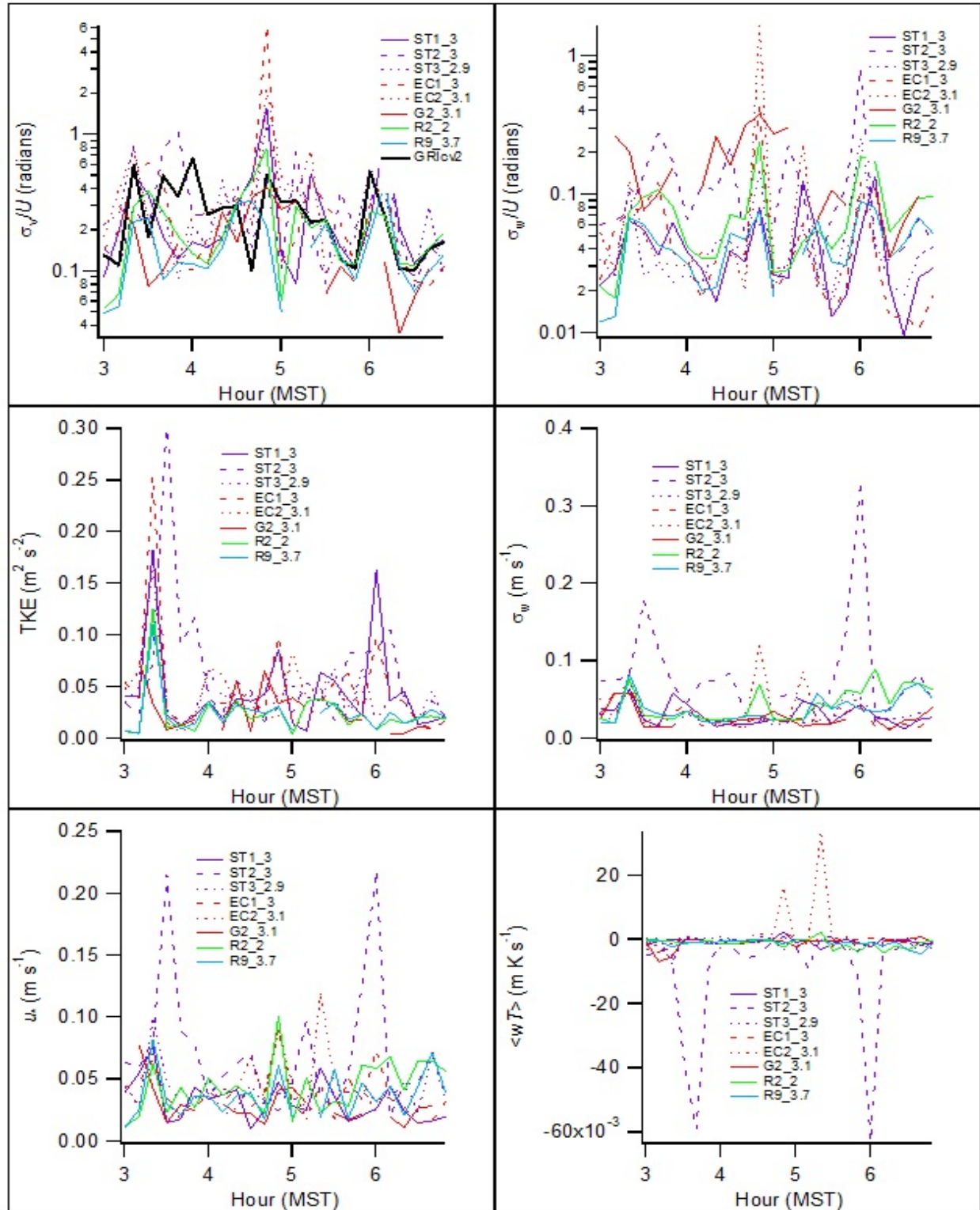


Figure 177. Time series of near surface turbulence (sonic) measurements during IOP5. The GRI and COC are σ_0 wind vane measurements (cv) in degrees converted to radians for purposes of comparison. Notation before and after underscore designates location and height, respectively.

Wind and Turbulence Profiles

Figure 178 shows profiles of the non-sonic measurements at GRI and COC during IOP5. There are two salient features of these profiles. First, there was a shallow northwesterly flow up to about 10 m in depth beneath a consistently north-northeast flow. The depth of this northwesterly flow increased to about 20 m in the latter half of the experiment. Second, there was a steep vertical gradient in U early in the experiment that gradually diminished with time. The temperature gradients were large throughout the experiment. The σ_θ were large near the surface in association with the shallow northwest flow but decreased rapidly upwards and decreased somewhat with time. Profiles were mostly well behaved excepting some minor irregularities within 10-20 m of the surface.

Figures 179 and 180 show profiles of the sonic turbulence measurements at GRI during IOP5. Wind speeds and directions were similar to that seen in Fig. 178. These also show a shallow north-northwest flow, beneath a north-northeast flow, that deepened in the latter part of the IOP and a steep gradient in U that gradually diminished with time. The σ_v/U and σ_w/U were large in magnitude with many irregularities near the surface, like σ_θ in Fig. 178, and then decreased rapidly upwards. TKE and σ_w were low throughout the IOP, especially during the second half of the IOP (Fig. 180). The virtual temperature gradients were large throughout the experiment, especially between the 2 and 3.7 m agl heights. The virtual temperature gradient was at a maximum during the first hour then gradually diminished during the second hour.

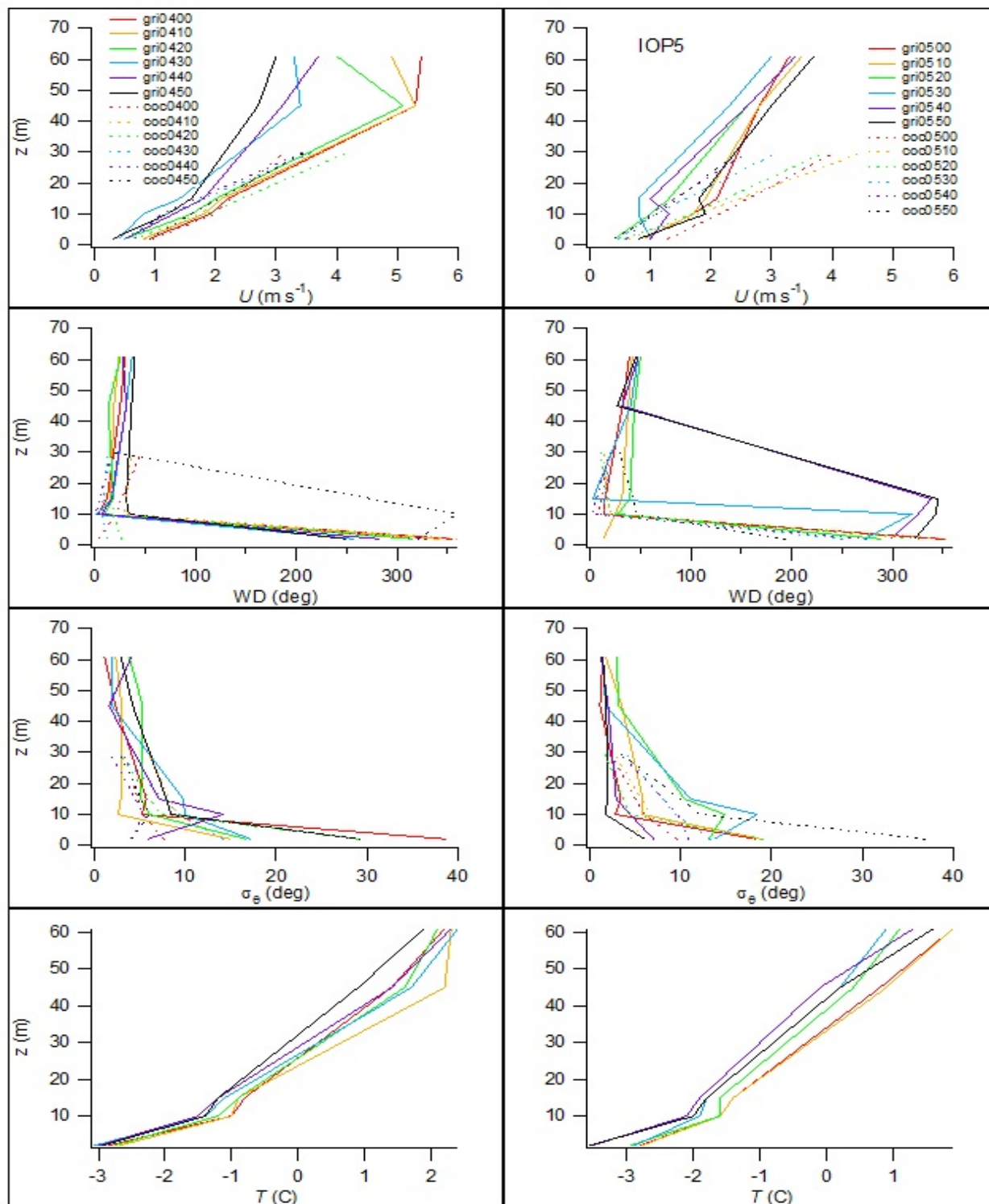


Figure 178. Profiles of U , wind direction, standard deviation of wind direction σ_θ , and aspirated temperature from cup anemometers and wind vanes during IOP5 at GRI and COC. Each profile is designated 'xxxhrmn' where xxx = tower and hrmn = start time of 10-minute interval.

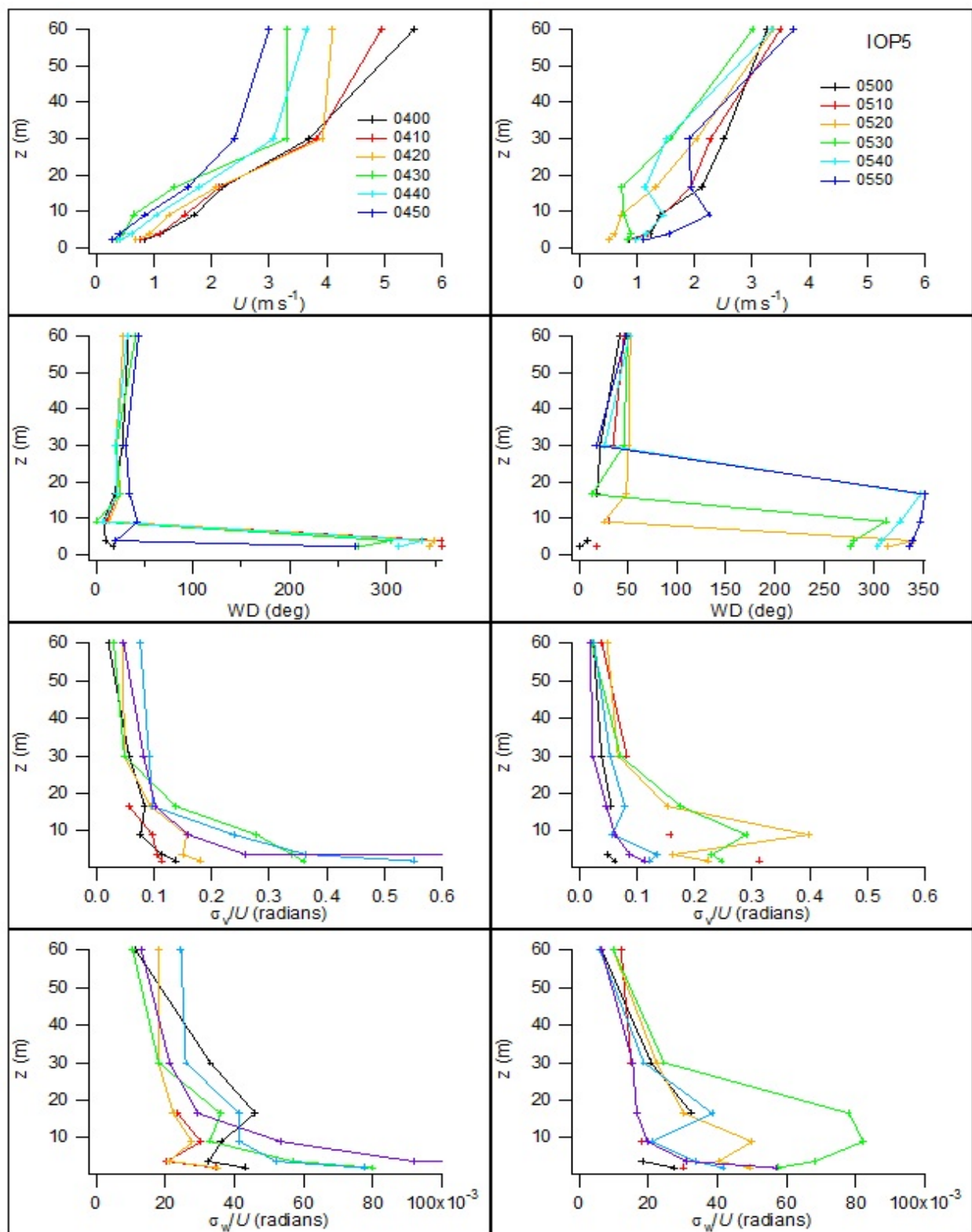


Figure 179. Profiles of U , wind direction, σ_v/U ($\sim\sigma_\theta$), and σ_w/U ($\sim\sigma_\phi$) from sonic anemometers at GRI during IOP5. The legend specifies the start time of the 10-minute interval (hrmn).

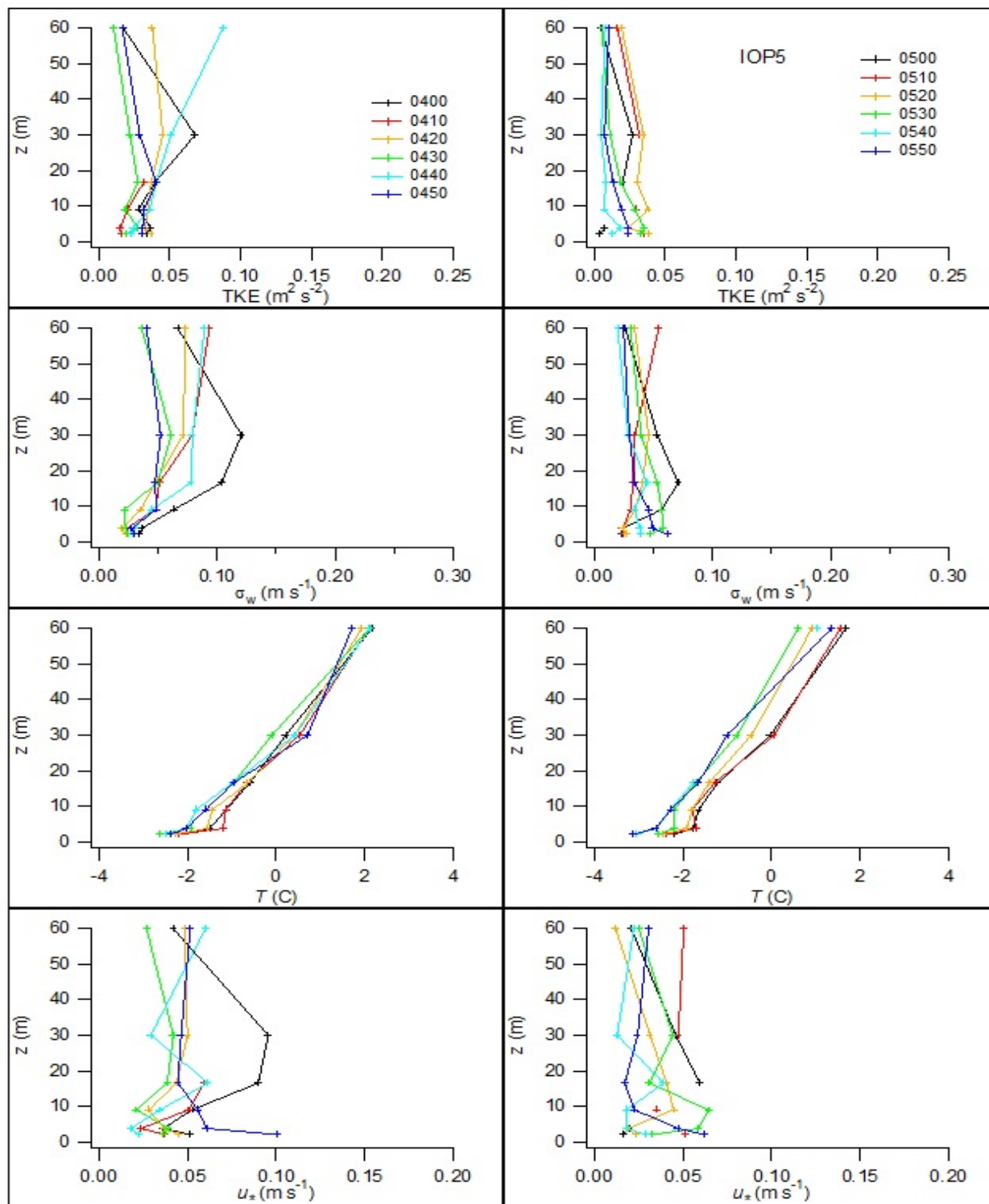


Figure 180. Profiles of turbulent kinetic energy (TKE), standard deviation in vertical wind speed σ_w , virtual temperature, and friction velocity u_* from sonic anemometers at GRI during IOP5. The legend specifies the start time of the 10-minute interval (hrmn).

Figures 181 and 182 show time-height representations of wind speed and direction for SOD and PRO, respectively, during IOP5. The wind directions and magnitudes of U in Fig. 181 are roughly consistent at the levels represented on GRI (Figs. 178, 179). At the upper levels of GRI U was also about $3\text{--}5\text{ m s}^{-1}$. There is a suggestion of a zone of higher U at about $100\text{--}120\text{ m}$ agl. This will be discussed later at greater length but it hints at the existence of a jet-like feature, something suggested by all of the SOD profiles of U and TKE during IOPs 5-7 (see especially IOP6 summary). The steep gradient in U at GRI would be consistent with this (Fig. 178). The lower level wind directions at PRO (Fig. 182) are consistent with the GRI and SOD measurements but it is possible the U are a little low. The zone of much higher U above about 2000 m agl shown in Fig. 182 is based on sparse consensus data but is somewhat consistent with the radiosonde results. The radiosonde results are not shown here but are available in the project database. These show a rapid increase in U from near the surface to about 15 m s^{-1} above 4 km agl. There is also a suggestion of a zone of somewhat lower U between about $400\text{--}600\text{ m}$ agl before U increases consistently above that. The pattern of wind directions was disrupted in that zone, shifting from northeasterly below to southwesterly above. A somewhat analogous pattern was seen in IOPs 6 and 7.

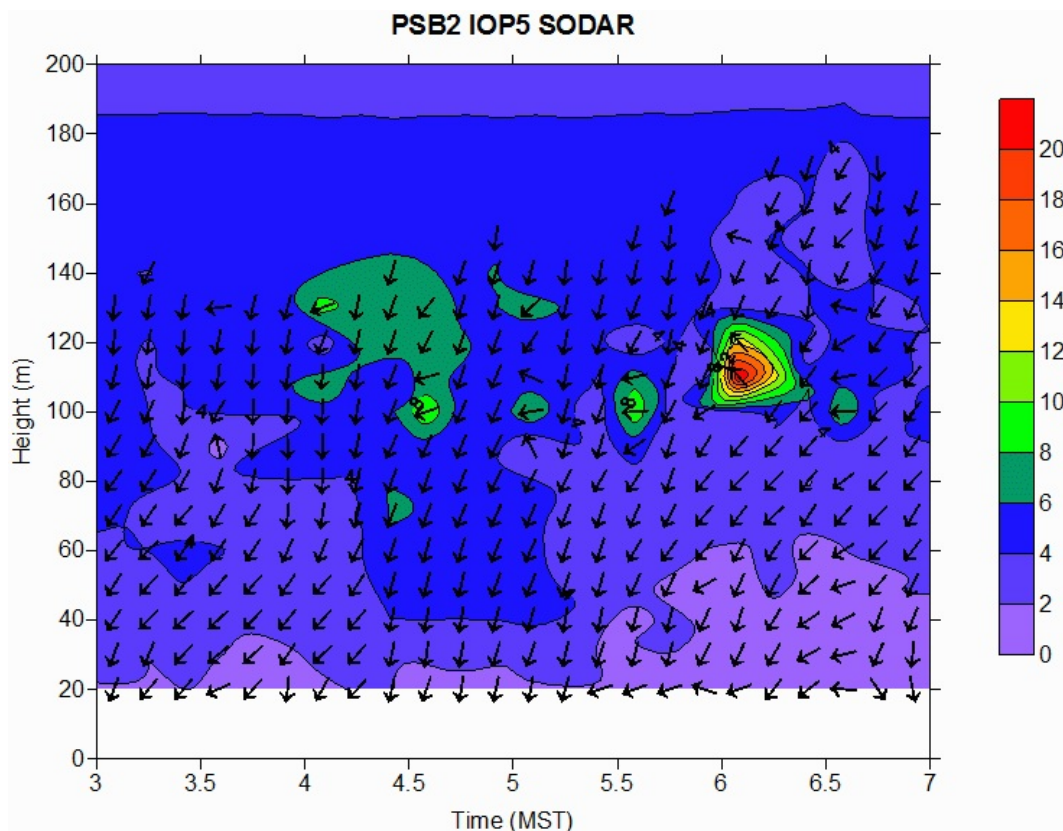


Figure 181. Time-height cross-section of wind speed and direction at sodar (SOD) during IOP5. Legend represents m s^{-1} .

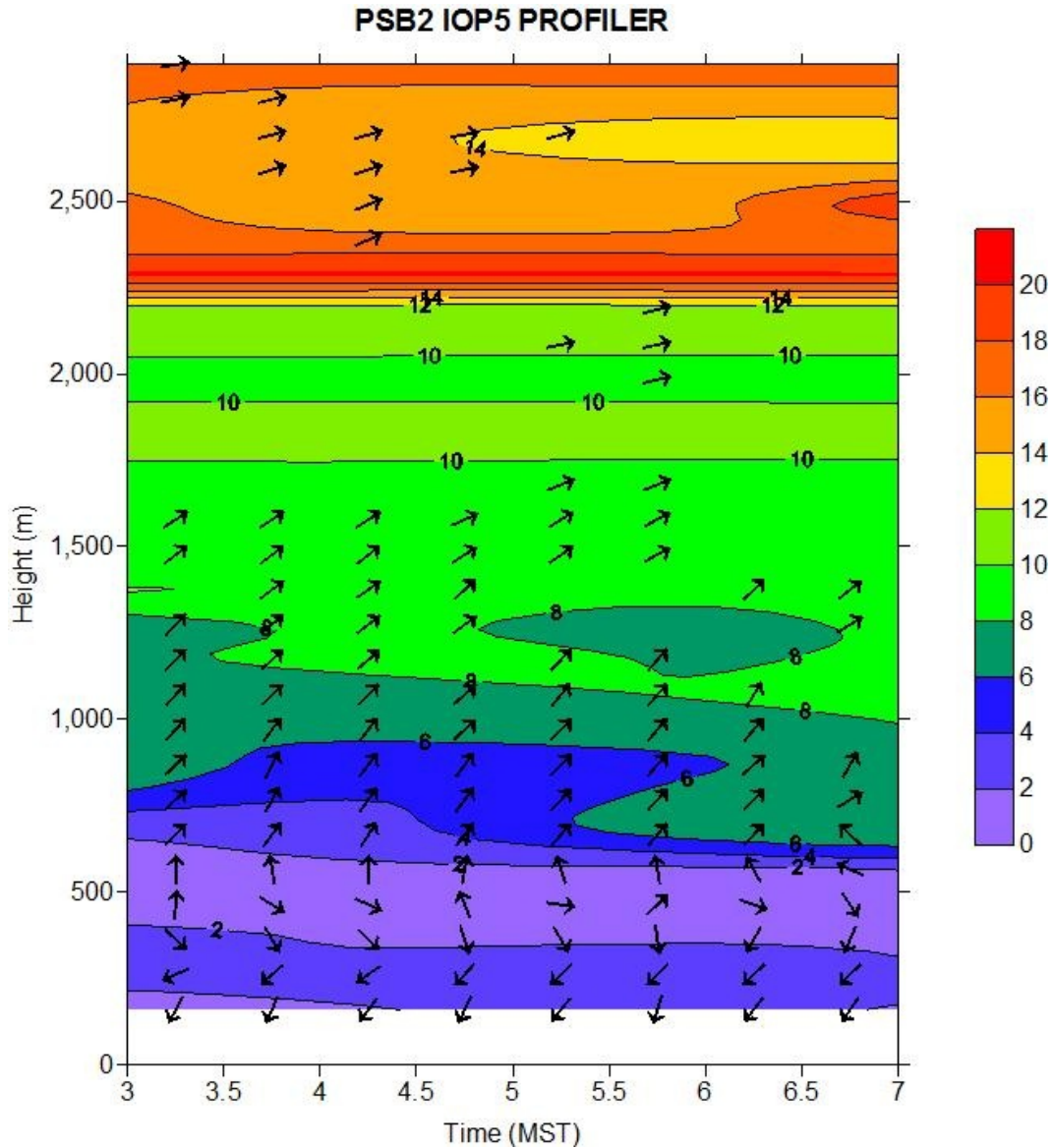


Figure 182. Time-height cross-section of wind speed and direction at wind profiler (PRO) during IOP5. Legend represents m s⁻¹.

Figures 183 and 184 show SOD time-height representations for σ_w and TKE respectively, during IOP5. The σ_w during the tracer measurement period were all very low. The σ_w anomaly near the surface late in the period shown is likely due to the initial effects of sunrise. TKE is low throughout the domain except for an anomalously high zone mainly 100-120 m agl. This is roughly consistent with the zone of higher U at the same levels (Fig. 181). Figure 185 shows time-height temperature profiles from the RASS.

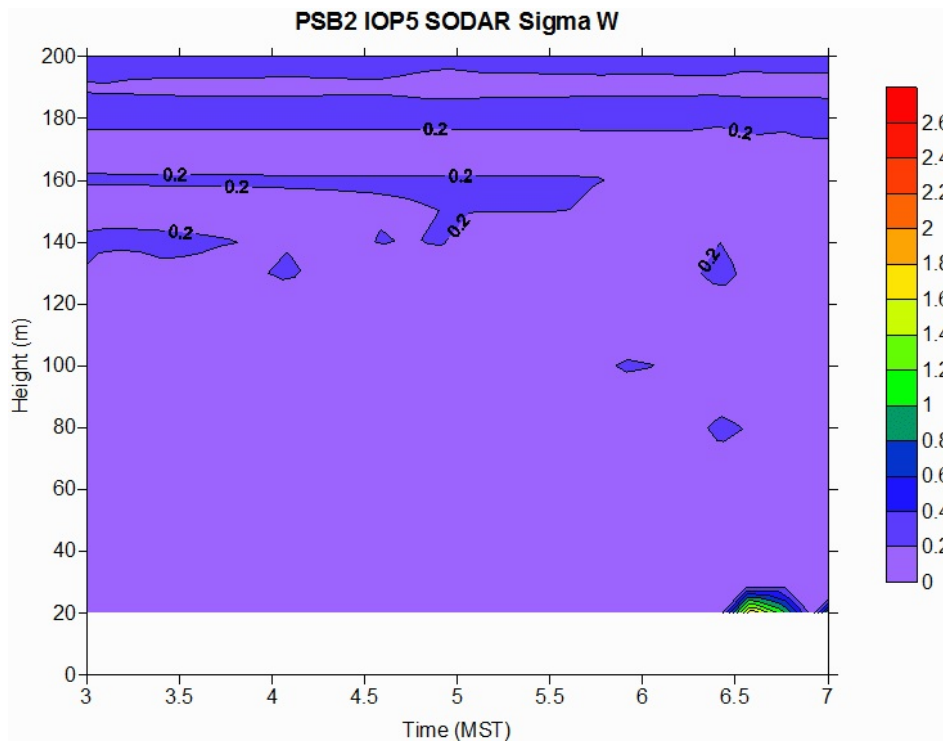


Figure 183. Time-height cross-section of σ_w at sodar (SOD) during IOP5. Legend represents m s^{-1} .

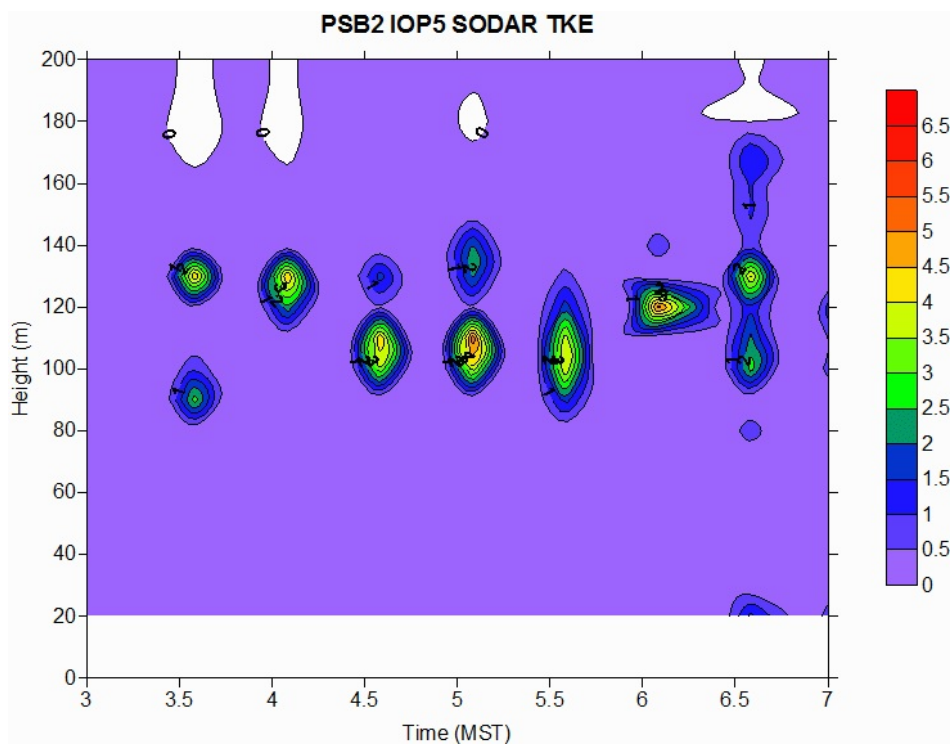


Figure 184. Time-height cross-section of TKE at sodar (SOD) during IOP5. Legend represents $\text{m}^2 \text{s}^{-2}$.

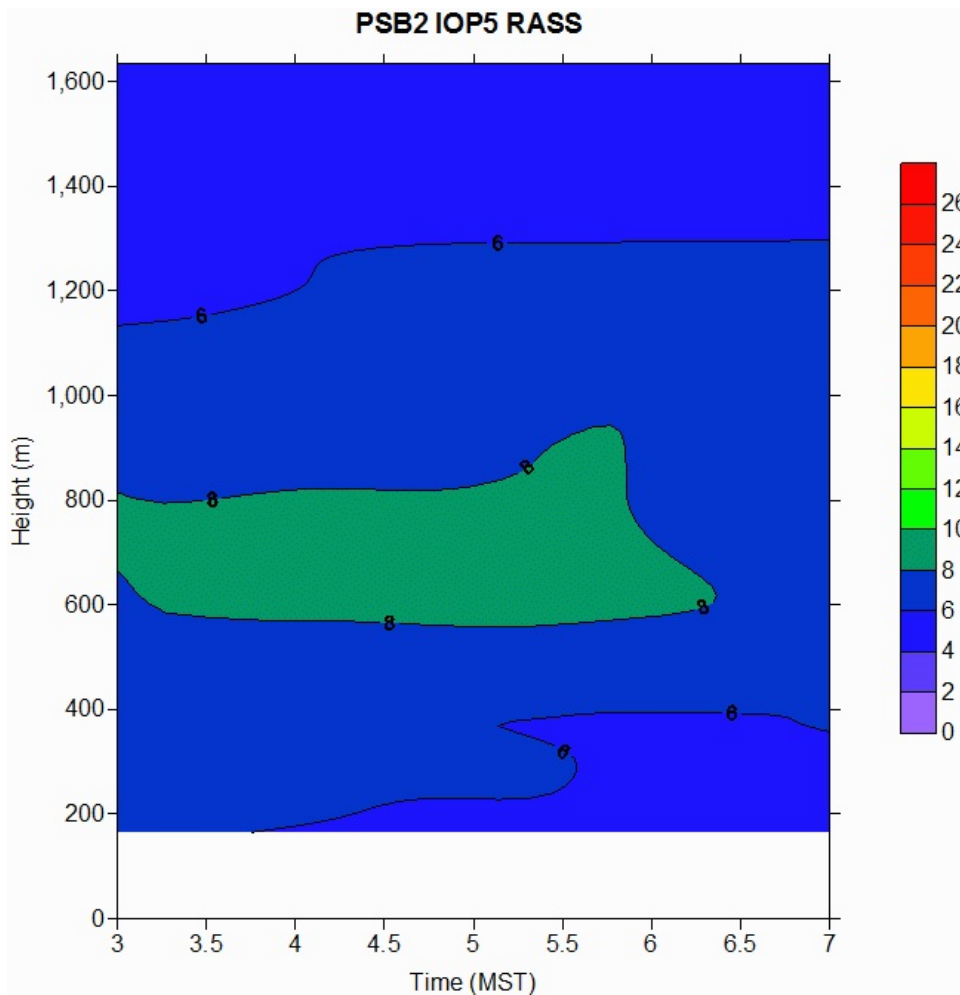


Figure 185. Time-height cross-section of virtual temperature at the RASS during IOP5. Temperatures are in degrees C.

Radiosonde Results

Pre and post-IOP radiosonde profiles of potential temperature and specific humidity for IOP5 are shown in Figs. 186 and 187. There is no constant potential temperature layer in Fig. 186 and it provides no basis for selecting a mixing height. The specific humidity profiles in Fig. 187 suggest some layering or structure to the boundary layer. However, there is no basis for an unambiguous selection of the boundary layer or a mixing depth. The ceilometer results suggest a boundary layer of a few hundred meters depth for about an hour overlapping the start of the tracer measurement period and then two layers after that for the remainder of the IOP (Table 23). The lower layer is at or near a minimum default value of 90 m (BL_Height1) with an upper layer of a few hundred meters (BL_Height2). The two lowermost layers suggested by the specific humidity profiles are approximately coincident with these ceilometer results.

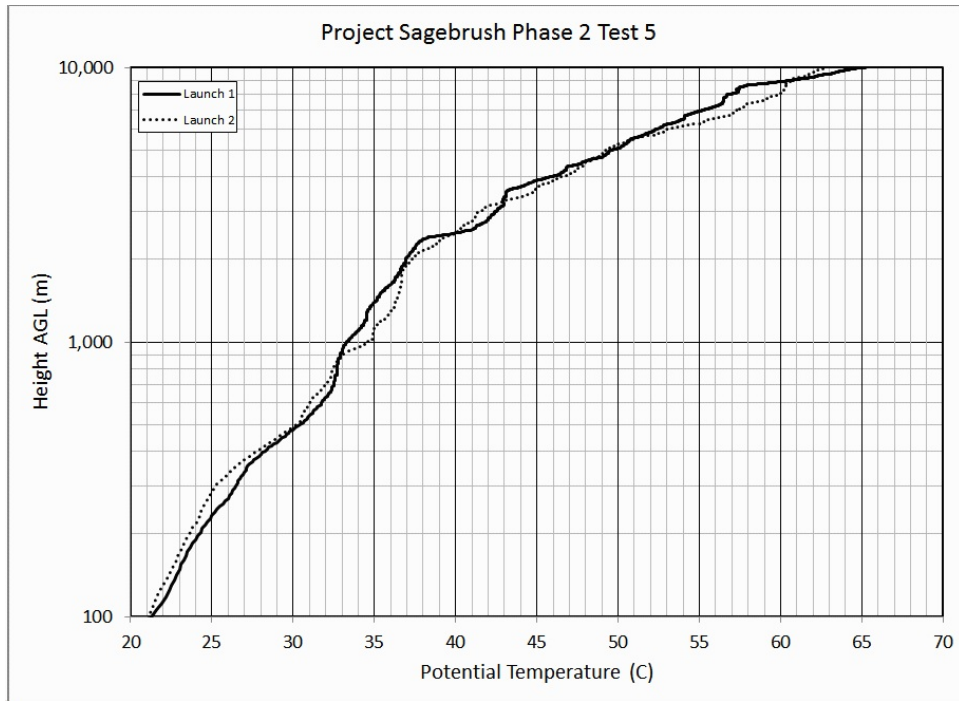


Figure 186. Potential temperature profile from radiosonde probe, IOP5. Pre-test launch bold, post-test launch dotted.

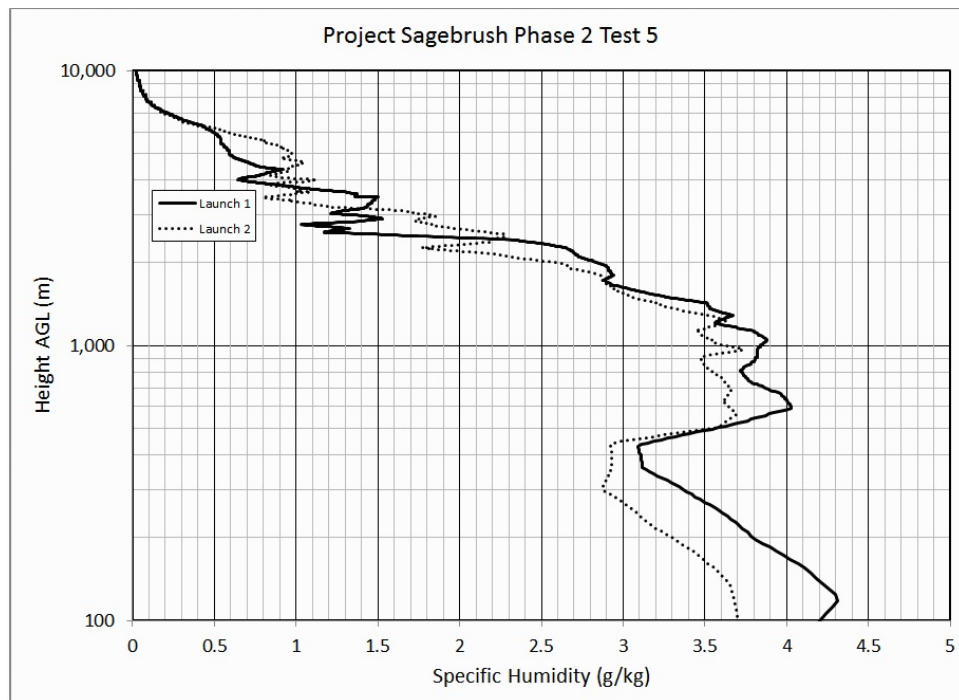


Figure 187. Specific humidity profile from radiosonde probe, IOP5. Pre-test launch bold, post-test launch dotted.

Table 23. Ceilometer estimates of boundary layer heights during IOP5.

Date	Time	BL	BL	BL	BL	BL	BL	Cloud	
(yyyymmdd)	(MST)	Height 1	Index 1	Height 2	Index 2	Height 3	Index 3	Status	Cloud 1
		(m)		(m)		(m)			(m)
20161013	3:05	90.00	2	385.25	1	-999.9	-999.9	0	-999.9
20161013	3:15	90.00	2	398.33	1	-999.9	-999.9	0	-999.9
20161013	3:25	90.00	2	396.00	1	-999.9	-999.9	0	-999.9
20161013	3:35	587.86	2	390.00	1	-999.9	-999.9	0	-999.9
20161013	3:45	630.75	3	-999.9	-999.9	-999.9	-999.9	0	-999.9
20161013	3:55	588.92	2	-999.9	-999.9	-999.9	-999.9	0	-999.9
20161013	4:05	584.25	2	-999.9	-999.9	-999.9	-999.9	0	-999.9
20161013	4:15	533.25	2	600.00	2	-999.9	-999.9	0	-999.9
20161013	4:25	342.67	2	600.00	2	-999.9	-999.9	0	-999.9
20161013	4:35	224.75	1	580.00	1	-999.9	-999.9	0	-999.9
20161013	4:45	90.00	3	-999.9	-999.9	-999.9	-999.9	0	-999.9
20161013	4:55	90.00	3	-999.9	-999.9	-999.9	-999.9	0	-999.9
20161013	5:05	90.00	2	434.50	1	-999.9	-999.9	0	-999.9
20161013	5:15	90.00	2	441.42	1	-999.9	-999.9	0	-999.9
20161013	5:25	90.00	2	450.00	1	-999.9	-999.9	0	-999.9
20161013	5:35	96.75	2	458.50	1	-999.9	-999.9	0	-999.9
20161013	5:45	100.00	2	472.33	1	-999.9	-999.9	0	-999.9
20161013	5:55	98.75	2	473.25	1	-999.9	-999.9	0	-999.9
20161013	6:05	90.00	2	470.00	2	-999.9	-999.9	0	-999.9
20161013	6:15	90.00	2	468.00	2	-999.9	-999.9	0	-999.9
20161013	6:25	90.00	2	471.25	2	-999.9	-999.9	0	-999.9
20161013	6:35	90.00	2	484	2	-999.9	-999.9	0	-999.9
20161013	6:45	90.00	2	480.75	2	-999.9	-999.9	0	-999.9
20161013	6:55	98.00	2	480	2	-999.9	-999.9	1	5172.63

Bag Sampling Results

Figures 188 and 189 and Figures 190 and 191 show the 10-minute average normalized and actual, respectively, color-coded plan view concentration maps for IOP5 bag sampling at 1 m agl. Figures 192 and 193 and Figures 194 and 195 show the 10-minute average normalized and actual concentrations, respectively, along each of the arcs.

The western limb of the plume was significantly truncated in bags 1-3. For the remainder of the IOP, the plume was mostly bounded within the 210° sampling arc although the western limb was still truncated to some degree. The degree of truncation decreased with downwind distance. In general, plume spreads were broad with often considerable variability across arcs, especially on the 100 m arc. Plume morphology on the 100 m arc was generally ill-defined with

tracer distributed across the array, sometimes with a better defined maximum peak. The flanks of the plume were often very ragged and irregular, especially during the second hour. The distributions on the 200 and 400 m arcs tended to be a little better behaved and sometimes developed peaks somewhat Gaussian in form. When that was the case, 100-150 degrees of arc were subtended by the plume.

There are two salient points about the plume measurements during IOP5 in these plots. First, the horizontal plume spread was much larger than that suggested by the measured σ_0 and much larger than expected by traditional dispersion schemes at nighttime. The degrees of arc intersected by the plume during IOP5 was similar to or sometimes much greater than the degrees of arc intersected during the daytime IOPs. This was the case in spite of the much larger daytime σ_0 relative to IOP5.

Second, the maximum normalized concentrations during IOP5 ranged upwards of one to two orders of magnitude greater than the maximum normalized daytime concentrations. For example, compare the cross-sections in Figs. 192 and 193 with some of the daytime IOPs (e.g., Figs. 84, 85, 111, 112). Also recall that the color-coded normalizations in the map views of Figs. 188 and 189 were suppressed by a factor of 10 relative to the daytime normalizations yet they feature an abundance of red and orange markers that are only sparsely present in the corresponding daytime plots (e.g., Figs. 80, 81, 107, 108).

The variability in the wind (Figs. 173, 176) and turbulence (Fig. 177) fields in time and space likely contributed to the significant plume spread and numerous irregularities in concentrations. The irregularities in concentration are consistent with the often large differences in collocated duplicate sampling that occurred during the nighttime IOPs. This was described in the bag sampling chapter. Recall that these large collocated differences were most acute on the 100 m arc and diminished downwind.

Figures 196 and 197 show the vertical concentration profiles at the four fixed towers and the mobile tower arranged by 10-min (bag) sampling period. Figures 198 and 199 show the temporal evolution of the vertical concentration profiles at each of the five towers. The most striking feature of these profiles is the extreme vertical concentration gradient with SF_6 concentrations dropping sharply from up to tens of thousands ppt to near ambient background concentrations above about 5-6 m agl in almost all cases. This is a third salient point. It is possible this is due, in part, to the suppression of vertical transport in a very stable atmosphere. However, a strong case can be made that this sharp cutoff is likely due in significant part to the shift in wind directions from mainly northwesterly below about 10 m to mainly north-northeasterly above that. That is, any tracer that made it above about 5-6 m was sheared off and transported toward the south-southwest, away from any tower measurement. Recall from Figs. 181 and 184 that a low level jet with a maximum near 100-120 m agl might have been present and embedded in the north-northeast flow above the northwesterly surface flow.

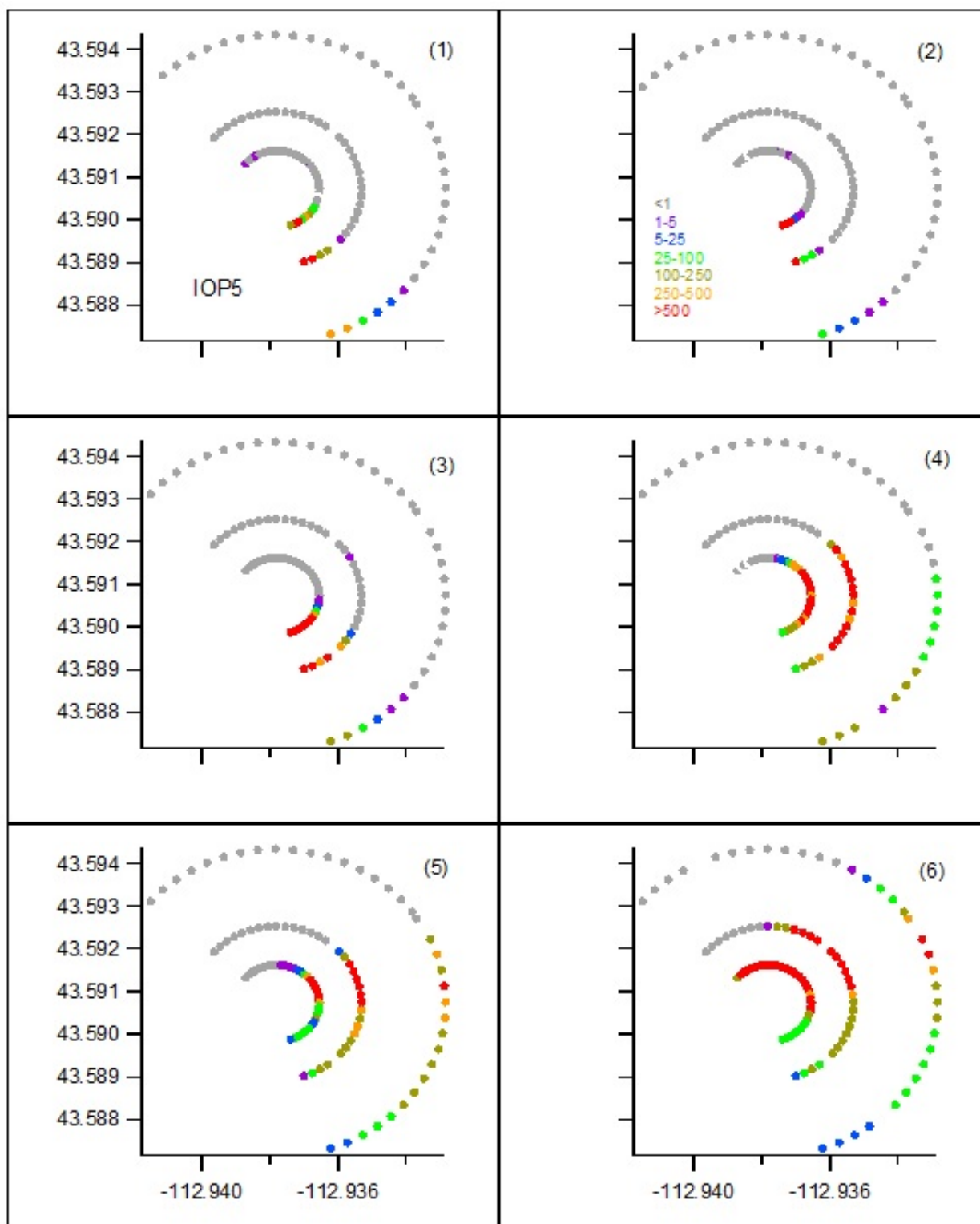


Figure 188. Color-coded normalized ($F^*\chi/Q$ ppt s g^{-1}) concentrations at 1 m agl for bags 1-6 during IOP5. The number in () is bag number.

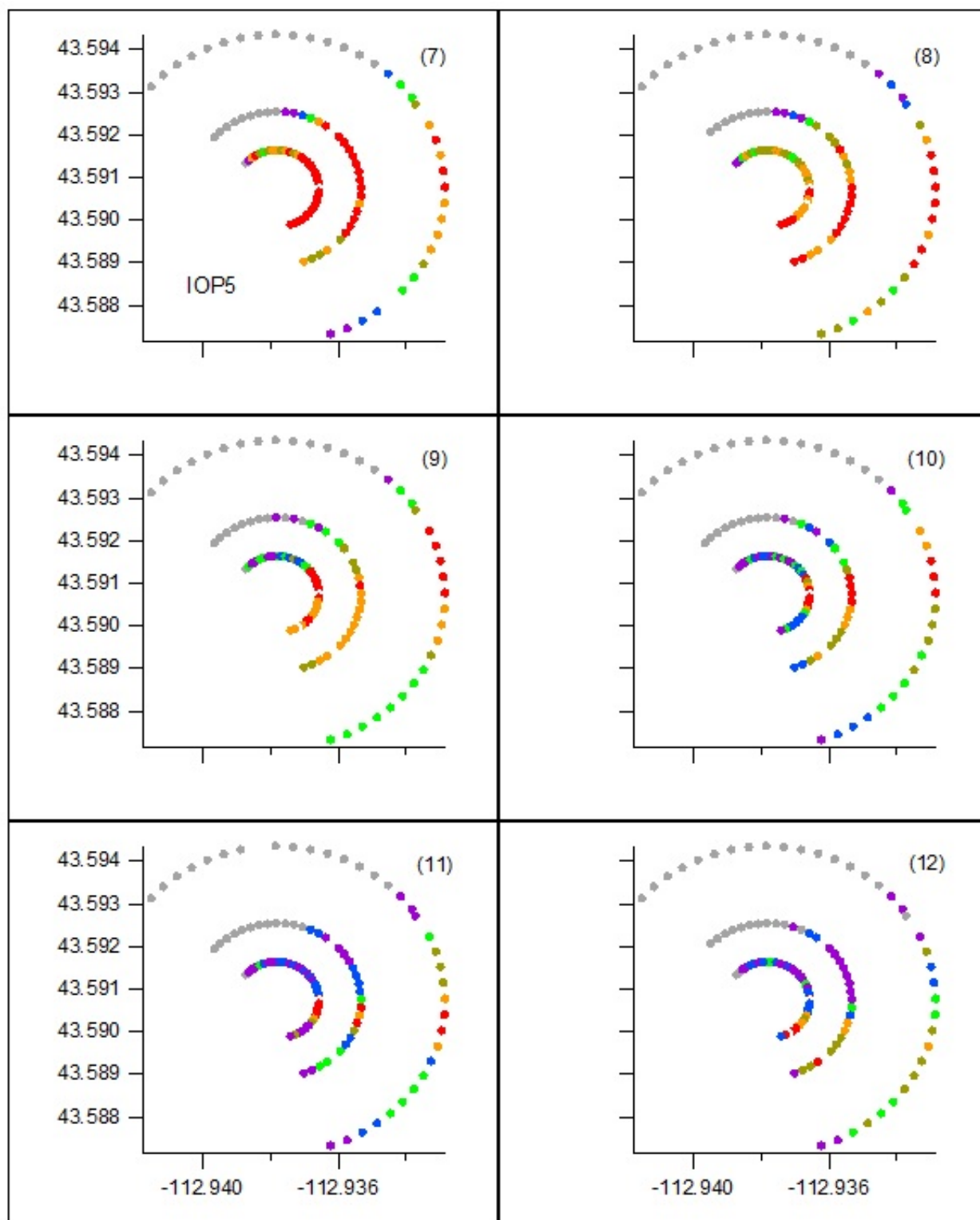


Figure 189. Color-coded normalized ($F^*\chi/Q$ ppt s g⁻¹) concentrations at 1 m agl for bags 7-12 during IOP5. The number in () is bag number.

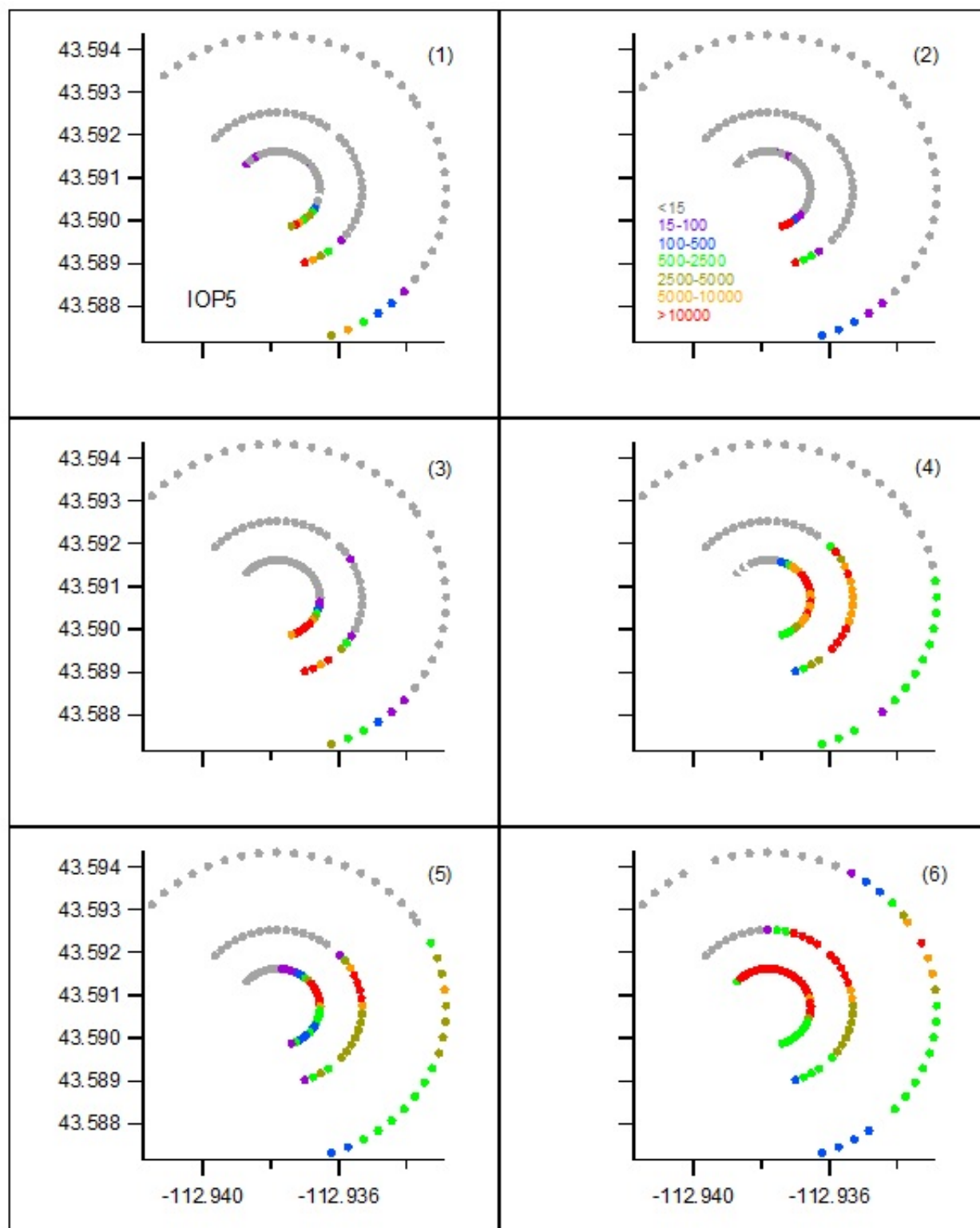


Figure 190. Color-coded measured SF_6 concentrations (ppt) at 1 m agl for bags 1-6 during IOP5. The number in () is bag number.

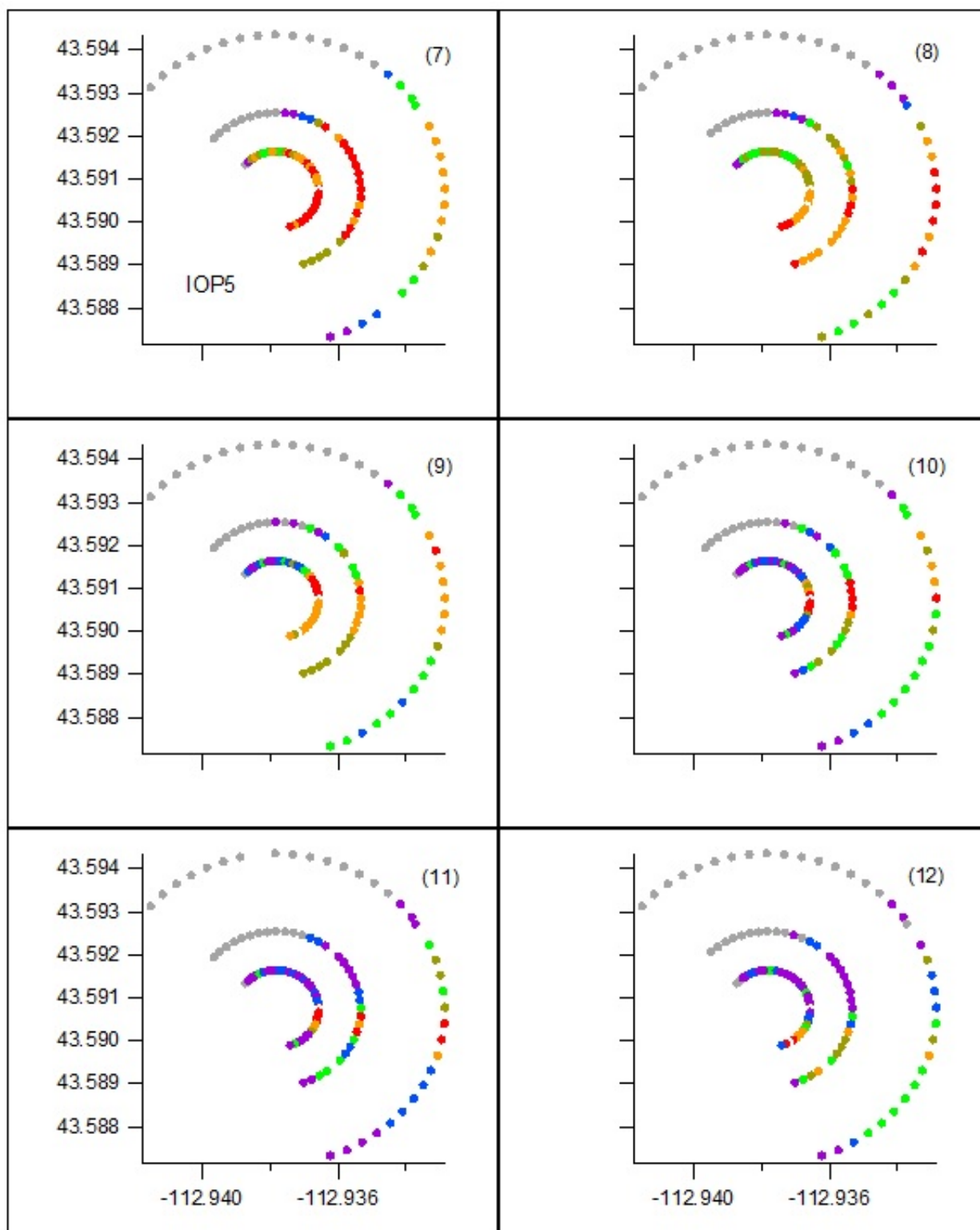


Figure 191. Color-coded measured SF_6 concentrations (ppt) at 1 m agl for bags 7-12 during IOP5. The number in () is bag number.

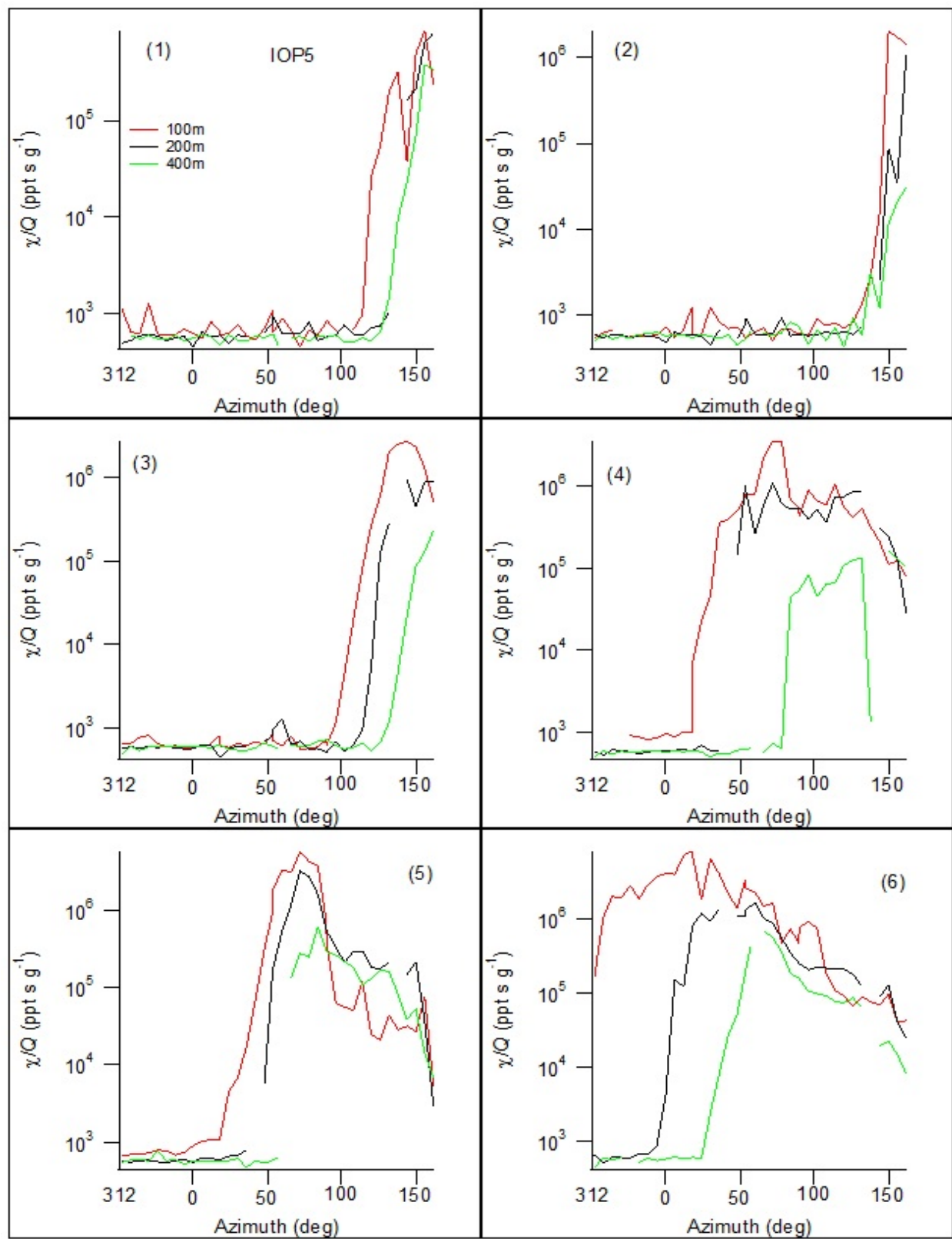


Figure 192. Cross-sections of normalized concentration along the arcs for bags 1-6 during IOP5.

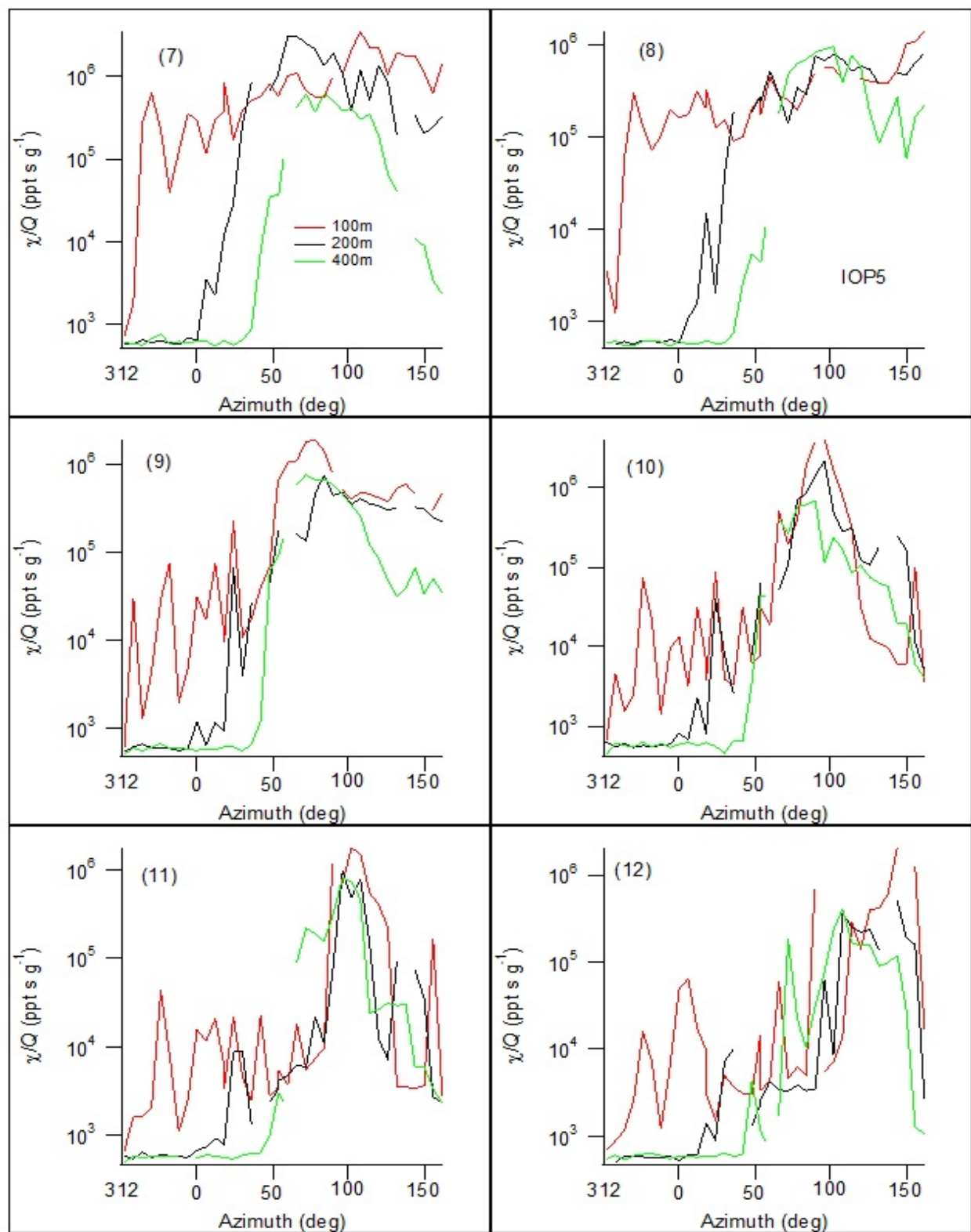


Figure 193. Cross-sections of normalized concentration along the arcs for bags 7-12 during IOP5.

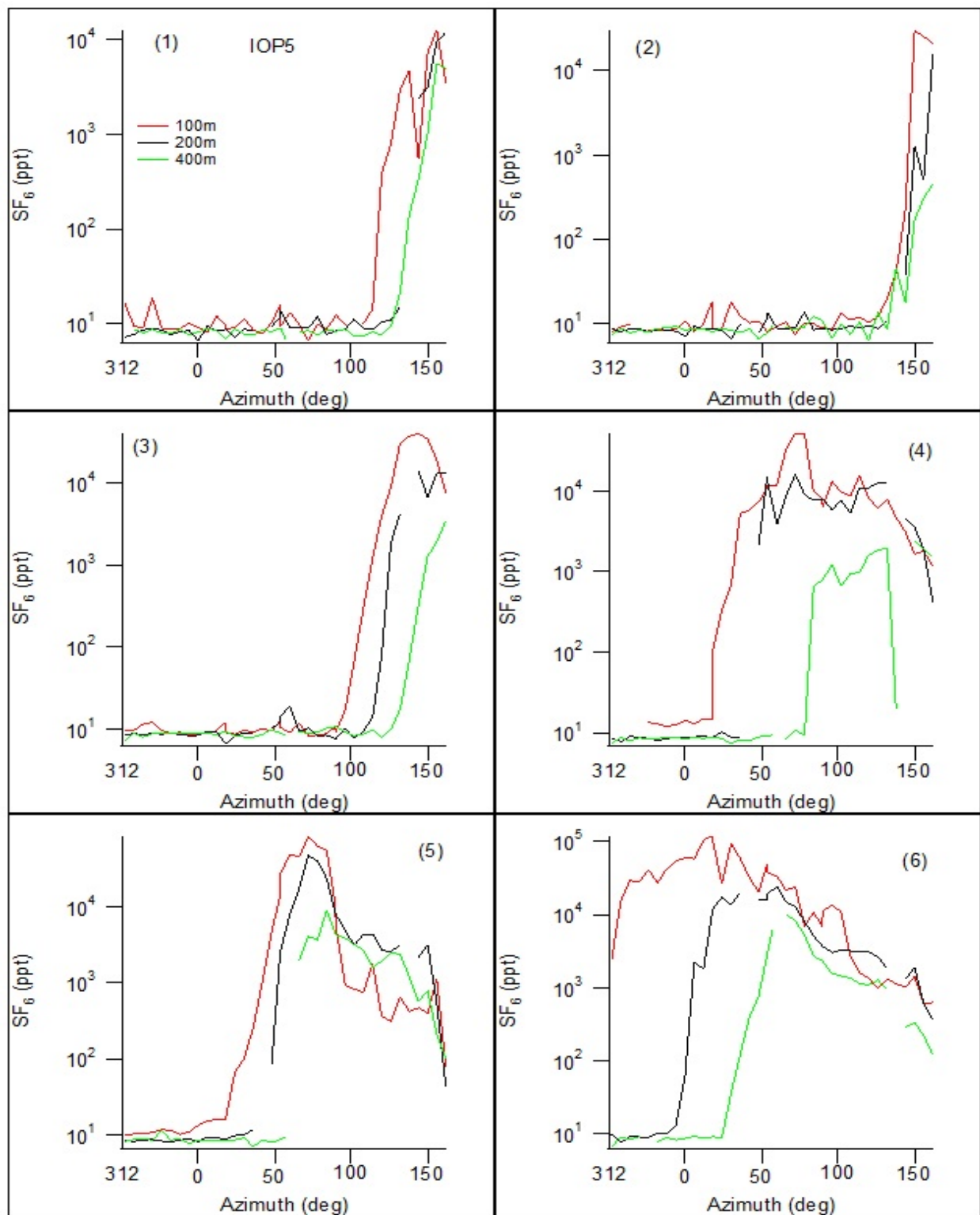


Figure 194. Cross-sections of measured SF_6 concentration along the arcs for bags 1-6 during IOP5.

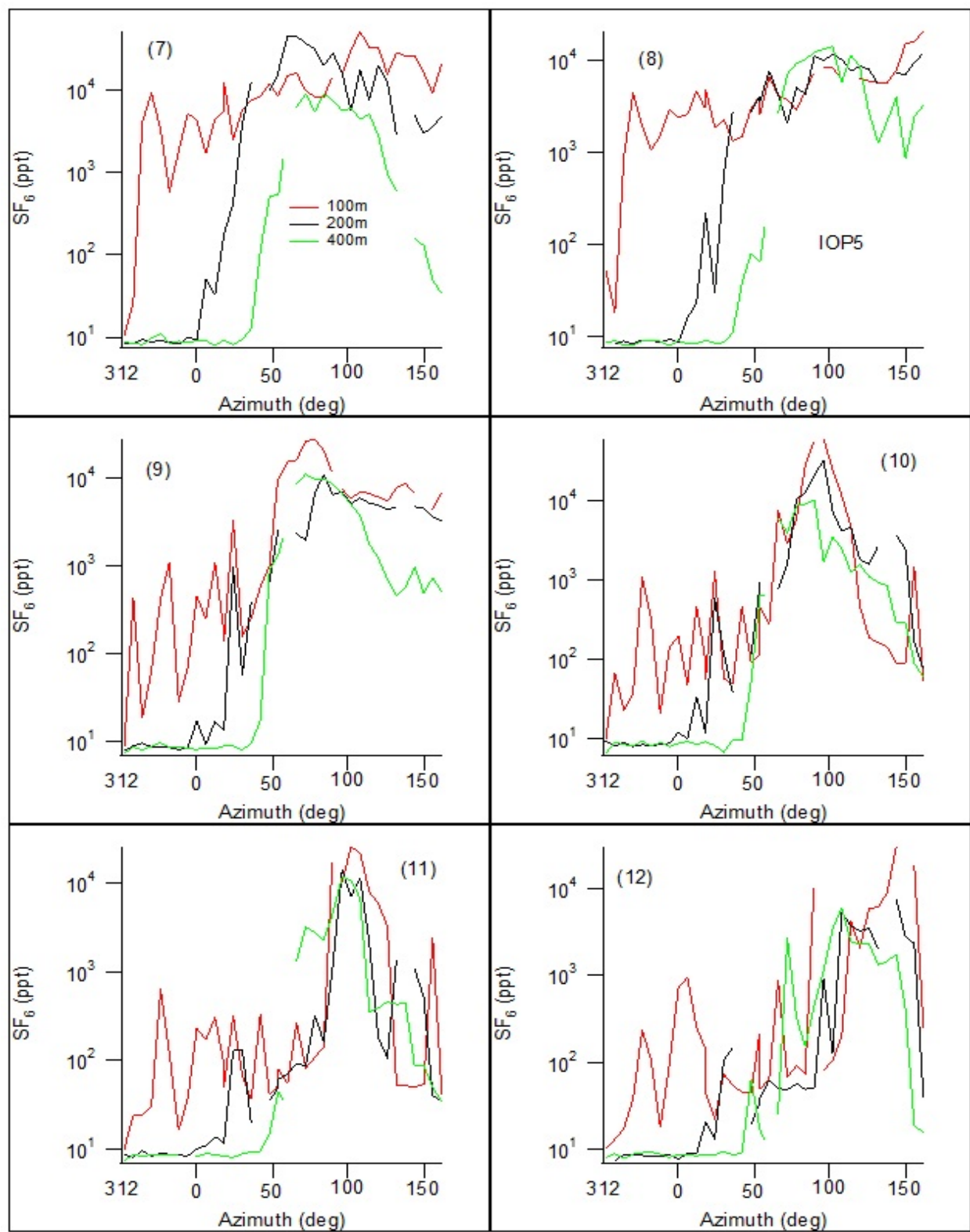


Figure 195. Cross-sections of measured SF_6 concentration along the arcs for bags 7-12 during IOP5.

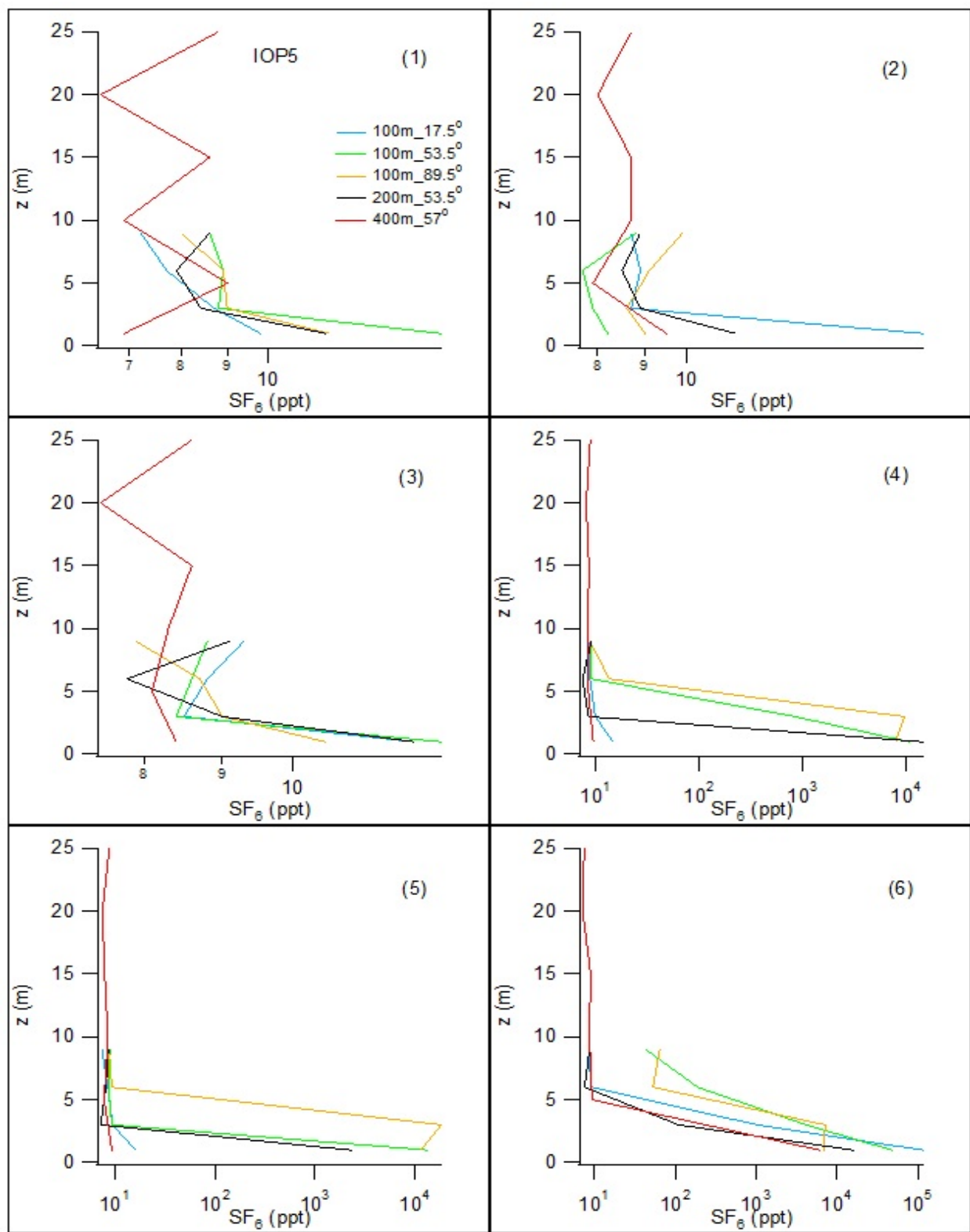


Figure 196. Vertical concentration profiles at the arc position given in the legend for (bags) 1-6 during IOP5.

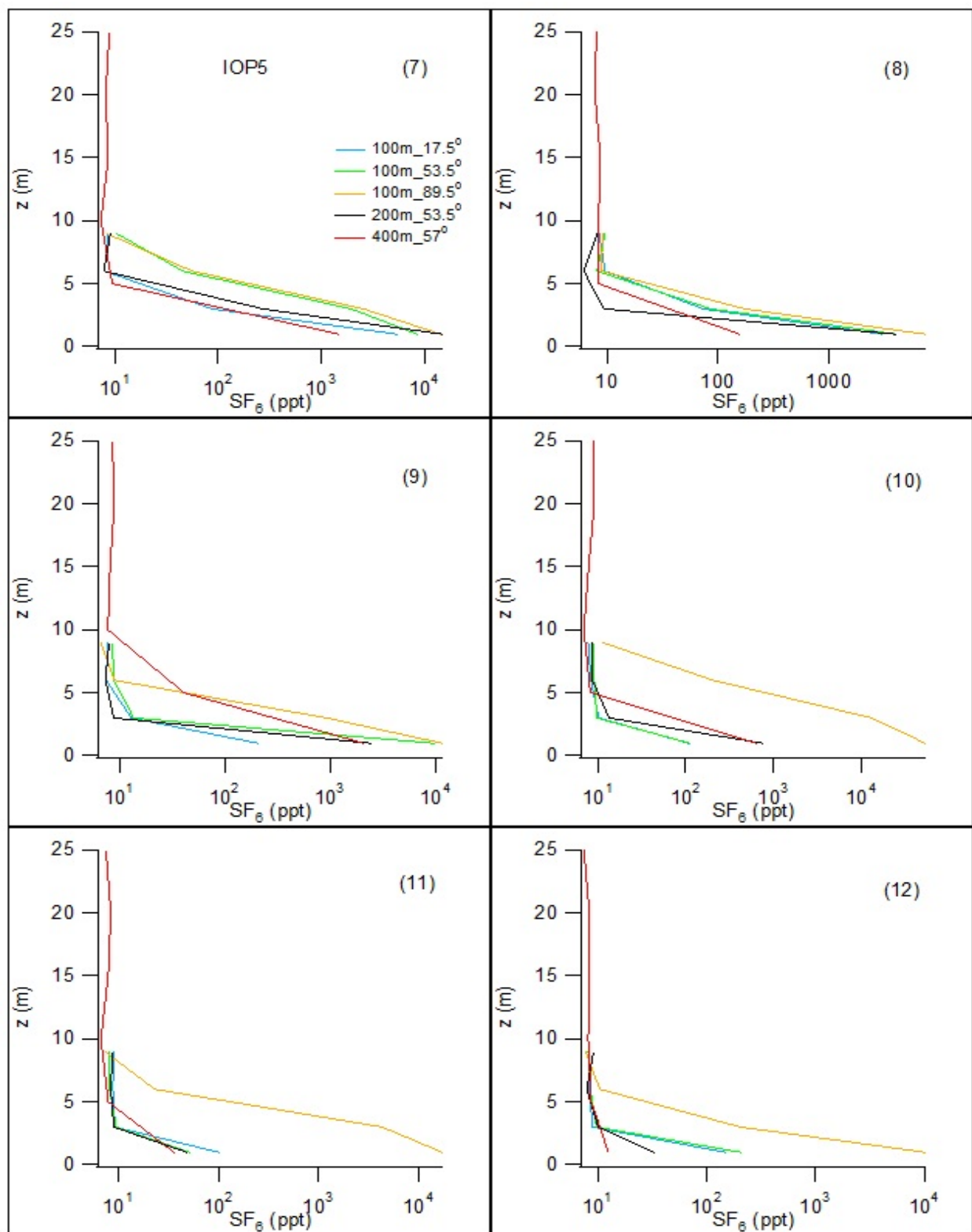


Figure 197. Vertical concentration profiles at the arc position given in the legend for (bags) 7-12 during IOP5.

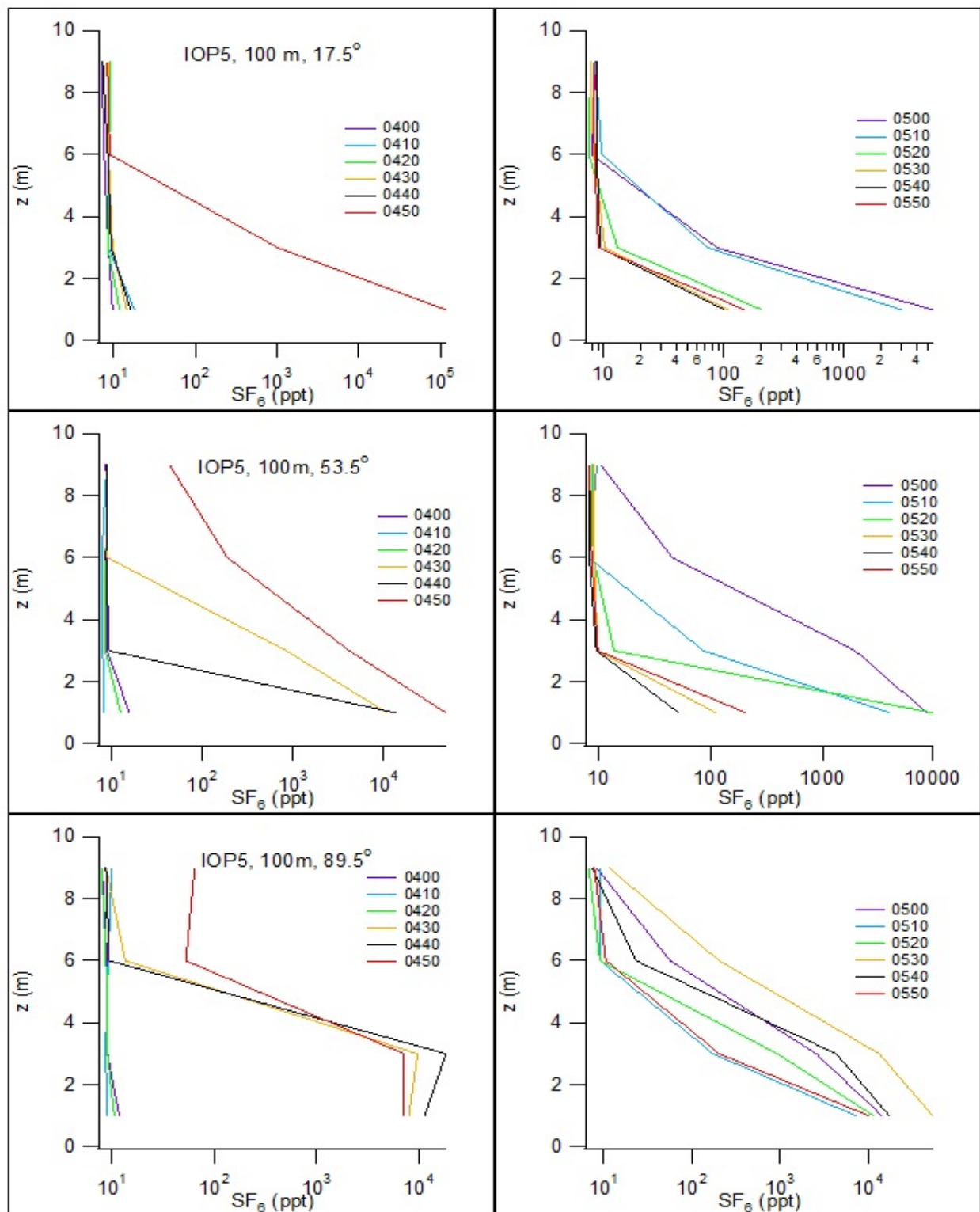


Figure 198. Vertical concentration profiles for the 100 m towers at the annotated arc position and times given in the legends during IOP5.

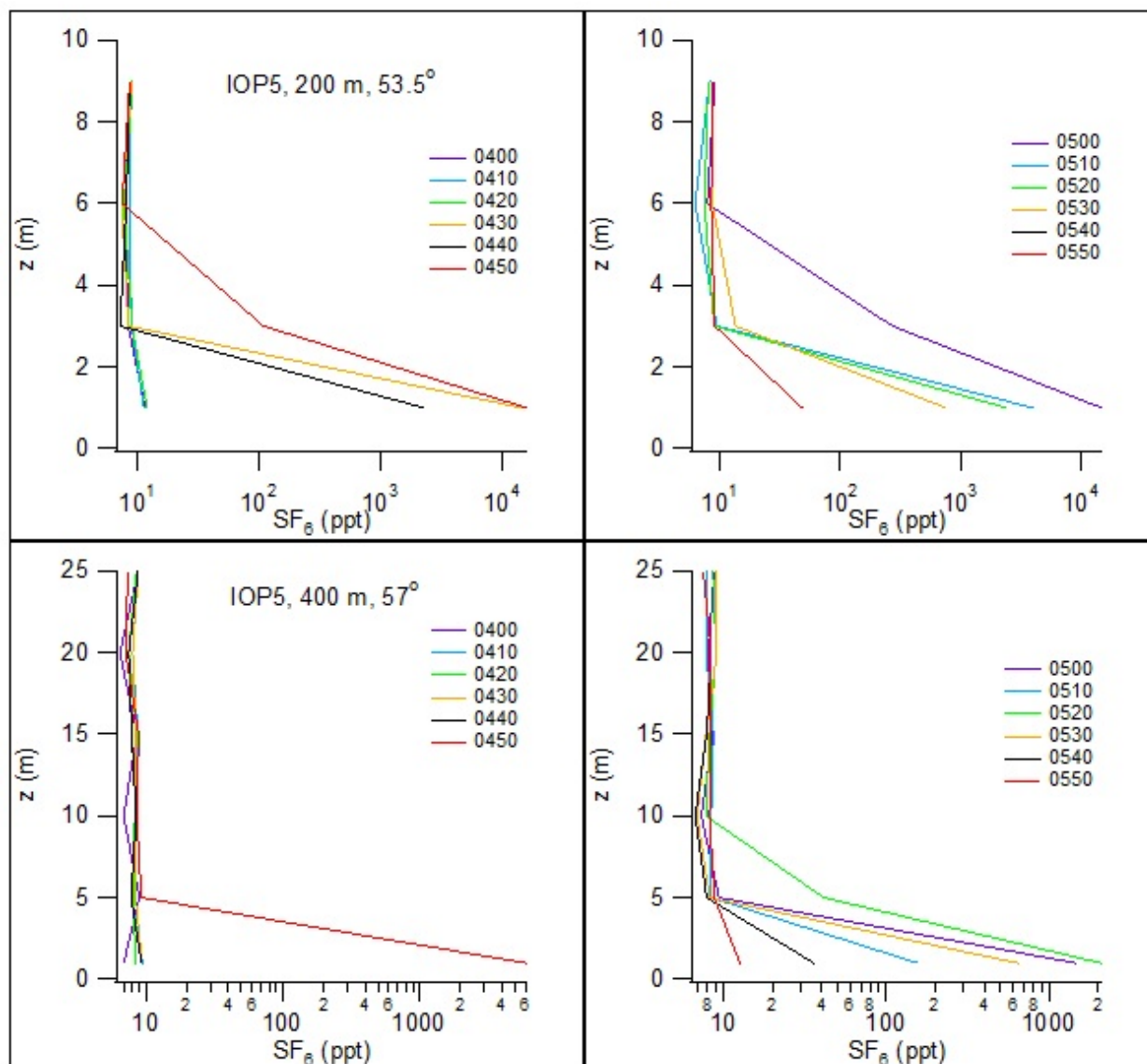


Figure 199. Vertical concentration profiles for the 200 m and mobile towers at the annotated arc position and times given in the legends during IOP5.

Fast Response Results

The locations of the fast response analyzers during IOP5 are shown in Fig. 200. The corresponding concentration time series are shown in Fig. 201. The color coding of the time series was described in the Introduction to this section. The time series records for periods of time with sampling at a fixed location in Fig. 201 are keyed by annotation with a corresponding annotation in Fig. 200. For example, the '1' for the C analyzer in Fig. 201 was located at location 'C1' in Fig. 200.

Like the daytime IOPs 1-4, the fast response measurements during IOP5 featured highly fluctuating signals alternating between very high peaks and concentrations at or near background. Abrupt shifts from background concentrations to railed values in excess of 30,000 ppt and back were common. However, the residence times of the sensor in the plume were often extended for longer periods of time than was usually the case for most of the daytime measurements. Thus, while residence times of the sensor in the plume were typically seconds to a few minutes for any one peak during the daytime IOPs, they were often well in excess of 10 min during IOP5. It is conjectured that the lesser σ_θ played a role in this. Restricted wind meander would reduce the frequency at which the plume was swept back and forth across the sensor, in and out of the plume, thus extending residence time in the plume. Thus there is a need

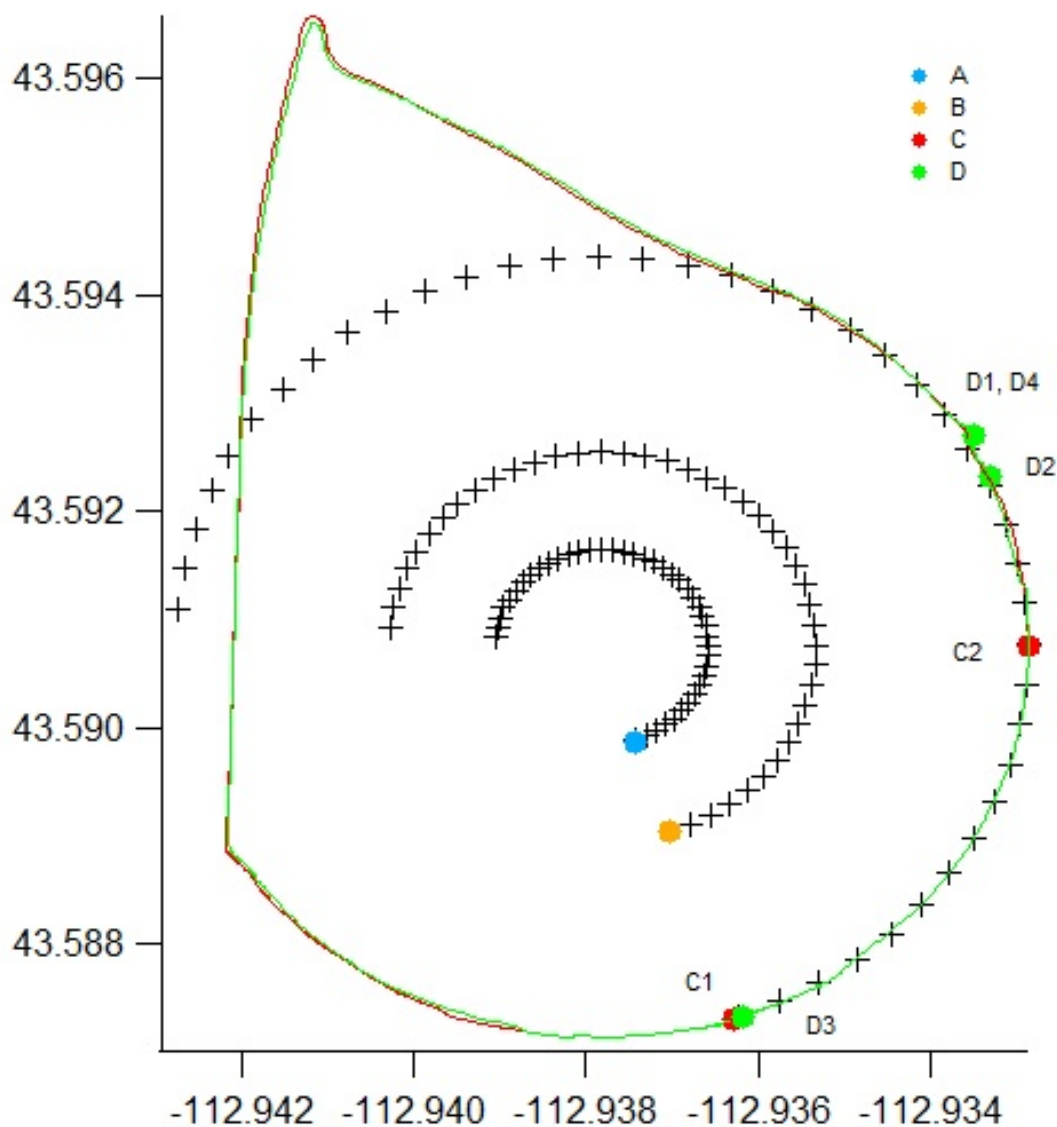


Figure 200. Locations of fast response analyzers during IOP5.

for an explanation that is consistent with both the long analyzer residence times in the plume and the very broad horizontal plume spreads observed in the bag sampling.

The plume rotated from mainly toward the southeast to more east and northeast late in the IOP. That accounts for the absence of SF_6 at analyzers A and B during the last half hour of the measurement period.

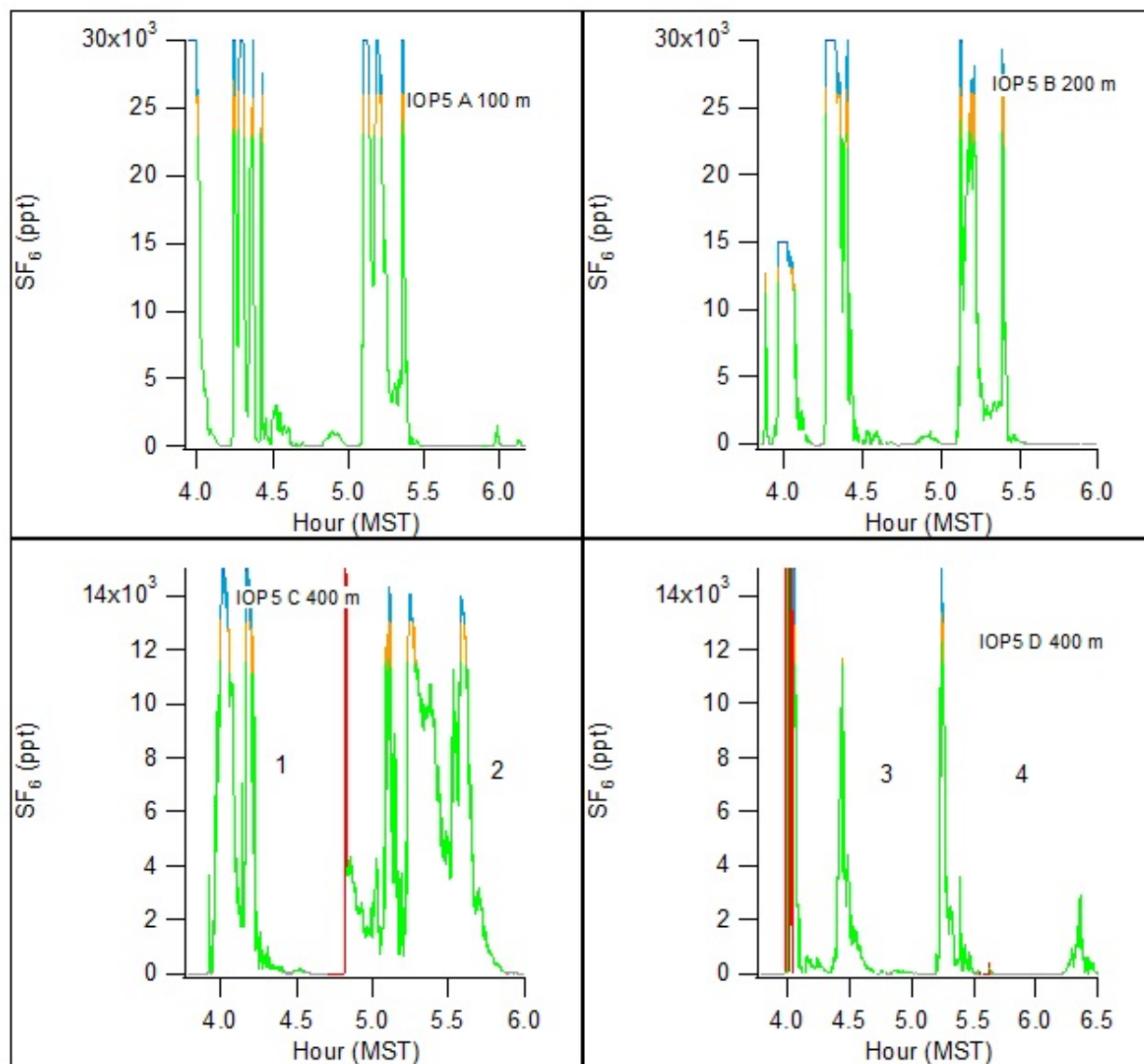


Figure 201. Fast response concentration time series during IOP5.

IOP 6

Date/Time and General Description

IOP6 was conducted on 20 October from 0400-0600 MST (0500-0700 MDT). Winds were very light, usually about 1 m s^{-1} near the surface. Estimates of stability based on traditional Pasquill-Gifford (P-G) schemes were mainly class E during the first hour and class F during the second hour (Fig. 202). Estimates of mean z/L from GRI ranged from 0.75 to 1.3 with an Ri_b of 0.19 (Table 24) making it the least stable of the nighttime IOPs. Wind directions were generally north-northwest within a few meters of the surface (Table 24; Figs. 203, 206). Above the lower few meters winds were generally north-northeast. Wind directions were similar to those in IOP5 with north-northwest winds in the lower few meters and northeasterly winds above. These directions resulted in the plume largely missing the 210° sampling arcs during the first hour and only the northern limb of the plume was sampled during the second hour. For this reason IOP6 was probably one of the least effective or useful tests during PSB2. The SF_6 release rate was 0.012 g s^{-1} (Table 2). Fast response analyzers were at fixed locations on the 100 and 200 m arcs at the edge of the bag sampling array at 162° azimuth. The analyzer on the 100 m arc moved late in the IOP to a due north position. Another analyzer was located at 162° azimuth on the 400 m arc before moving to a position to the northeast late in the IOP. The remaining analyzer moved frequently between several sites to the south of the release location.

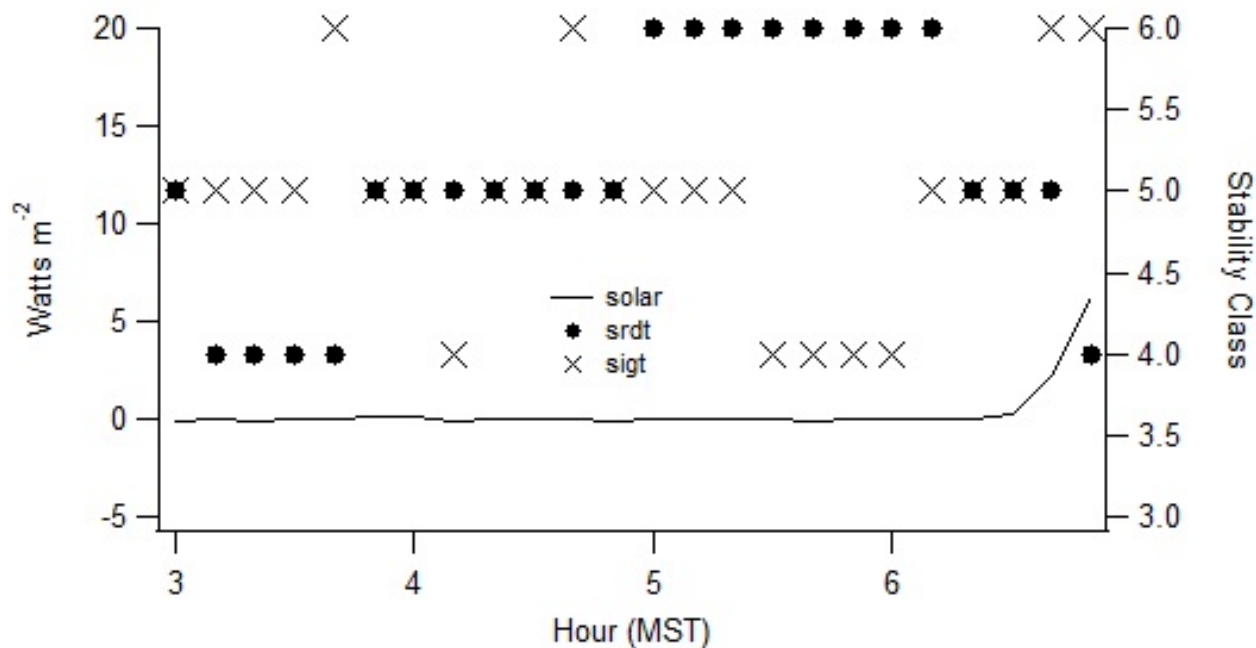


Figure 202. Incoming solar radiation and classification of stability conditions using the Pasquill-Gifford Solar Radiation Delta T (srdt) and σ_0 (sigt) methods (EPA 2000c) during IOP6. Classes D, E, and F are designated 4, 5, and 6, respectively.

Table 24. Meteorological conditions during IOP6.

Bag	COC				GRI						GRI			Solar
	U (m s ⁻¹)		WD (deg)		U (m s ⁻¹)		WD (deg)		σ_θ (deg)		L	L	degC	W m ⁻²
	2m	10m	2m	10m	2m	10m	2m	10m	2m	10m	3.7m	9m	2m	
1	1.0	1.8	352.1	27.8	1.0	1.9	7.4	26.6	7.4	4.8	7.0	17.3	-3.1	0.1
2	1.2	2.2	351.8	21.6	1.3	2.1	359.3	13.9	14.5	10.0	16.8	21.6	-3.0	-0.1
3	1.0	2.1	23.9	23.8	1.0	1.9	10.0	19.3	9.4	4.4	6.7	9.5	-3.1	0.0
4	1.1	2.2	5.9	26.4	1.2	2.3	358.5	10.1	9.4	4.4	3.9	8.6	-3.4	0.0
5	1.1	2.2	344.1	4.6	1.0	2.3	341.3	3.0	10.0	2.4	4.5	5.7	-3.6	0.0
6	0.6	1.5	17.3	23.5	0.8	2.0	334.7	2.8	9.0	4.0	3.5	10.8	-3.6	-0.1
7	1.0	1.6	12.5	30.2	0.6	1.6	325.9	3.8	16.5	6.2	NaN	8.4	-3.3	0.0
8	1.0	1.7	355.1	12.5	0.8	1.5	338.9	10.0	16.2	6.3	6.9	15.1	-3.1	0.0
9	0.9	1.6	2.4	21.8	1.0	1.7	10.2	22.7	11.4	6.3	9.4	11.9	-2.9	0.0
10	1.2	2.0	351.7	13.1	0.8	1.6	356.5	22.0	19.5	8.9	9.1	7.3	-2.9	0.0
11	1.1	2.3	347.5	4.2	0.8	1.5	358.3	20.5	16.6	8.0	5.9	16.3	-2.8	-0.1
12	0.9	1.9	334.4	4.7	1.0	1.4	16.4	28.4	10.9	7.7	2.2	12.2	-2.8	0.0
Avg. L											6.9	12.06		
z/L											1.3	0.75		
Ri _b												0.19		

Wind Speed and Direction Quality Assurance

Figures 203-205 show wind speed and direction time series comparisons for a sequence of measurement heights during IOP6. In Fig. 203, the near surface measurement of U showed some variation but mostly within a narrow range of 1 ± 0.5 m s⁻¹. Wind directions were distinctly north-northwest within a few meters of the surface and, with the possible exception of COC, were roughly consistent between stations. However, by 9 m agl and above, wind directions were consistently north-northeast (Fig. 204). Wind directions were very consistent between different locations and measurement types above 9 m, including the sodar (Figs. 204 and 205). Wind directions at COC were sometimes different compared to other sites. This particular phenomenon was commonly observed during the nighttime IOPs. Measured U at SOD varied somewhat lower than those for the cup or sonic anemometers but were roughly consistent in magnitude. The wind speed and direction measurements for SOD and PRO at 160 m agl showed clear differences, especially a low U bias at PRO. Other than that there is little evidence of a systematic measurement problem. The observed variability or discrepancies are likely primarily attributable to non-stationarity and inhomogeneity in the wind field.

The Brunt-Väisälä frequency N during IOP6 was the lowest of all the nighttime tests. One possible reason for this is the strength of a low-level jet that appears to have increased turbulence and modified the temperature gradient. IOPs 5 and 7 also exhibited some evidence for

the presence of a low-level jet but it was less consistent or well defined. This will be discussed in more detail later.

Figure 206 shows time series measurements for cup anemometers and wind vanes only (excluding sonics) at all heights on the GRI and COC towers during IOP6. Again, the near surface measurements of U were low at about 1 m s^{-1} but the sometimes much larger U at heights above 30 m suggest a steep gradient. Wind directions near the surface were north-northwest but shifted to north-northeast by 10 m agl. The measured σ_θ near the surface ranged upwards to near 20° but decreased upward and were mostly $< 5^\circ$ above the 2 m level. The temperature time series suggest a steep temperature gradient with a ΔT of about $4\text{-}5^\circ \text{ C}$ between the 2 and 60 m levels on GRI.

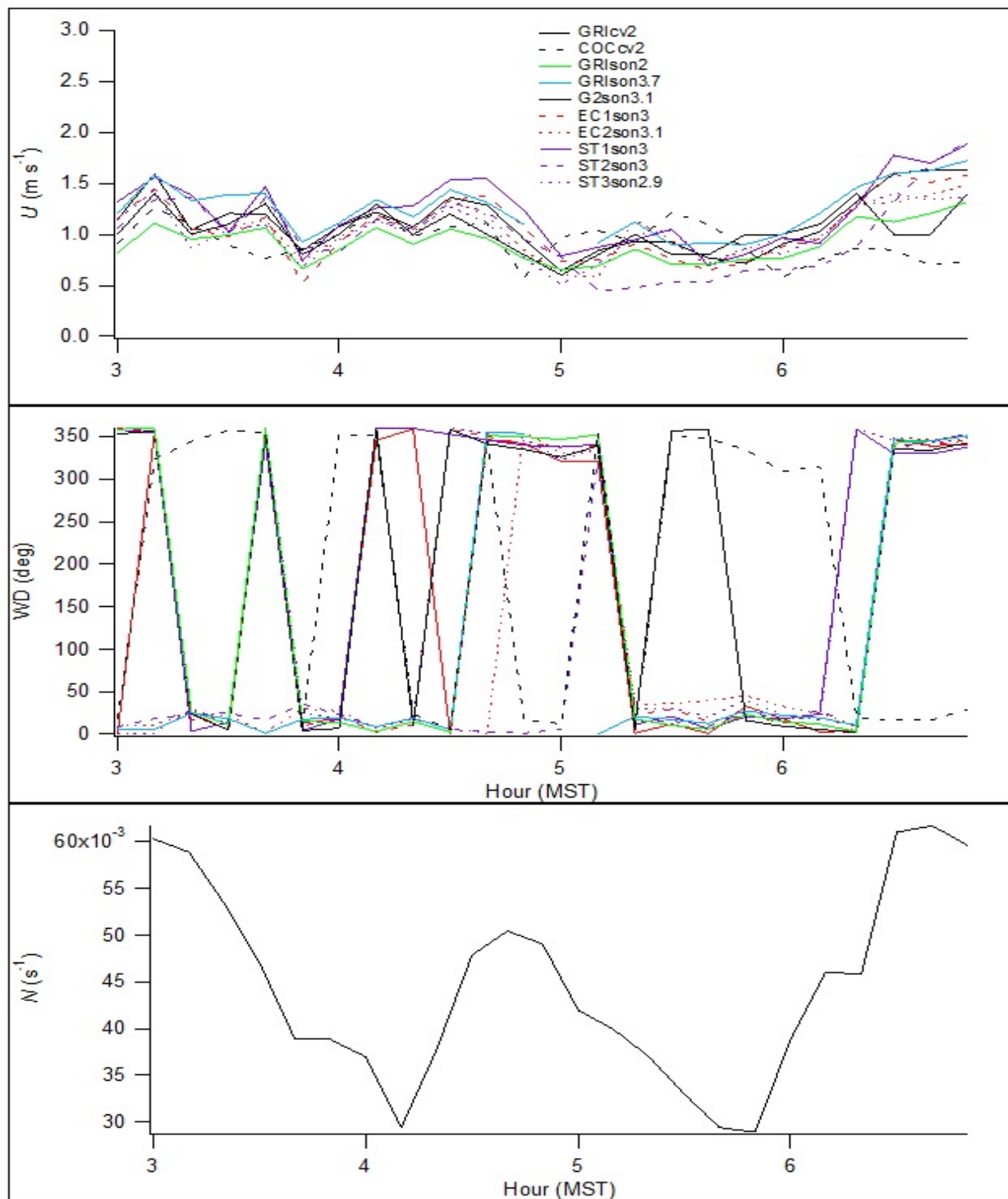


Figure 203. Time series of near surface wind speed and direction measurements and Brunt-Väisälä frequency N between 2 and 15 m agl during IOP6. In the legend, location is specified in upper case, the measurement type in lower case (cv = cup/vane, son = sonic), and the measurement height numerically.

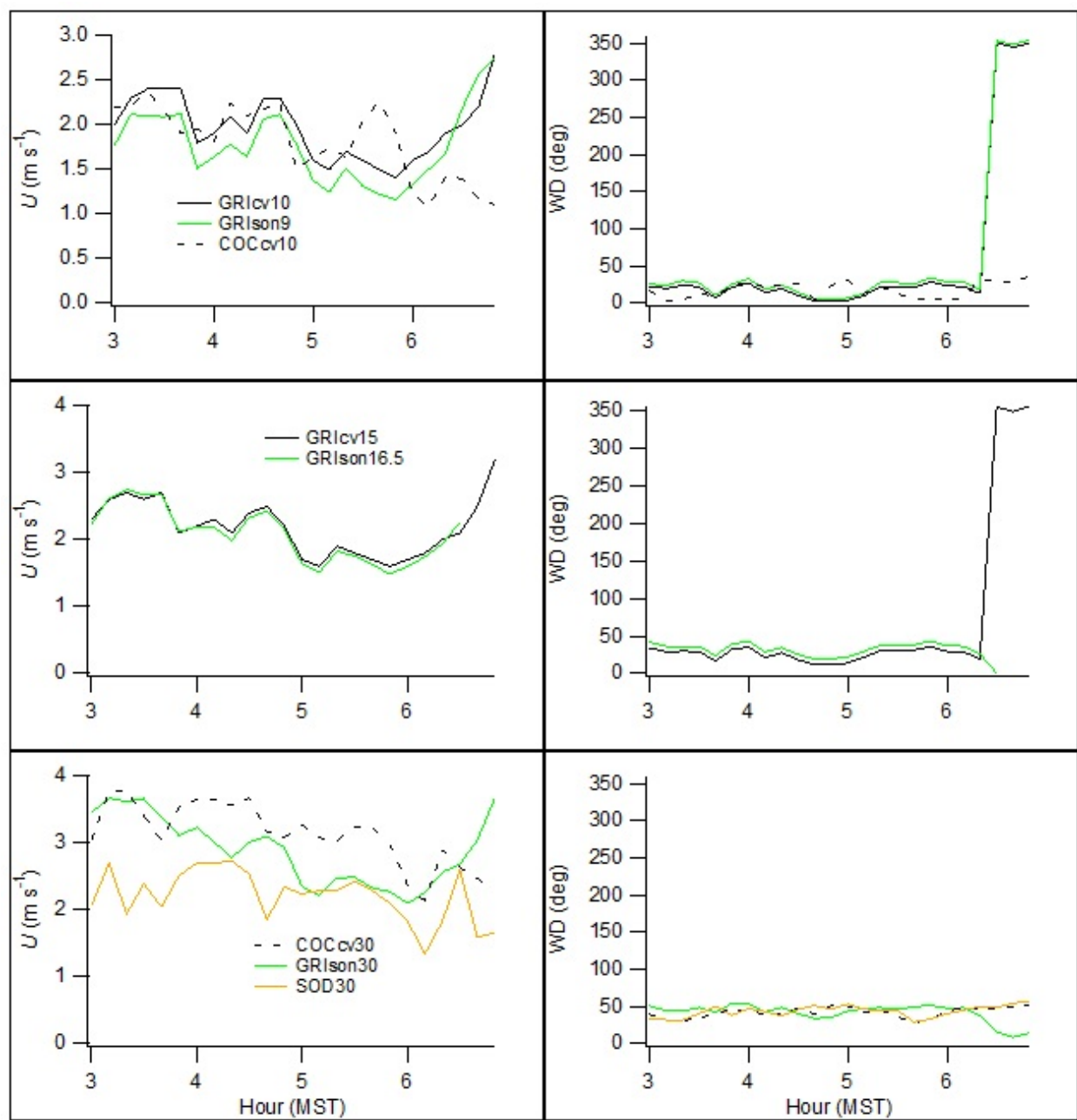


Figure 204. Time series of wind speed and direction measurements at heights between 9 and 30 m agl during IOP6. Legend notations described in caption of Fig. 203.

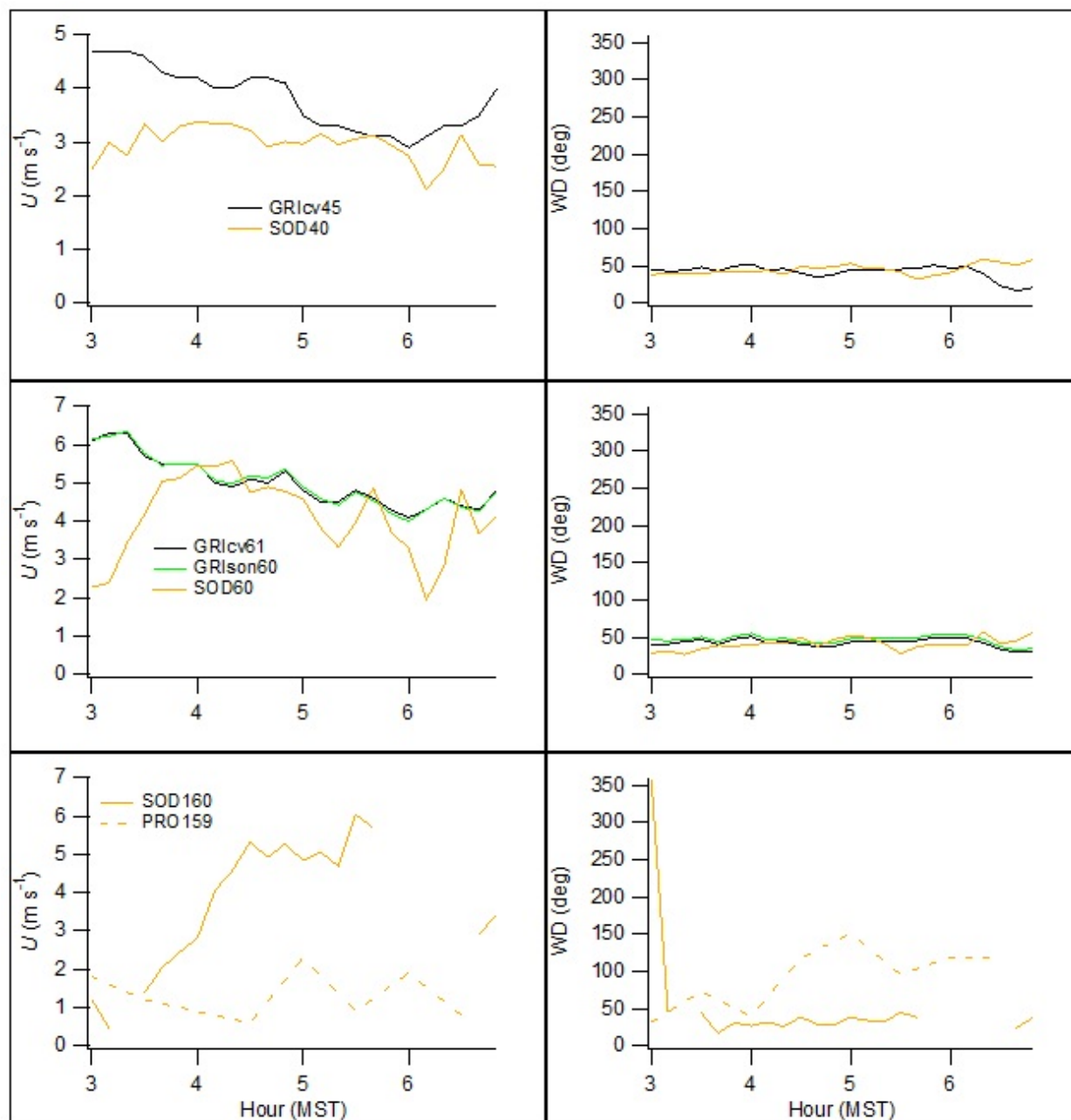


Figure 205. Time series of wind speed and direction measurements at heights above 30 m agl during IOP6. Legend notations described in caption of Fig. 203.

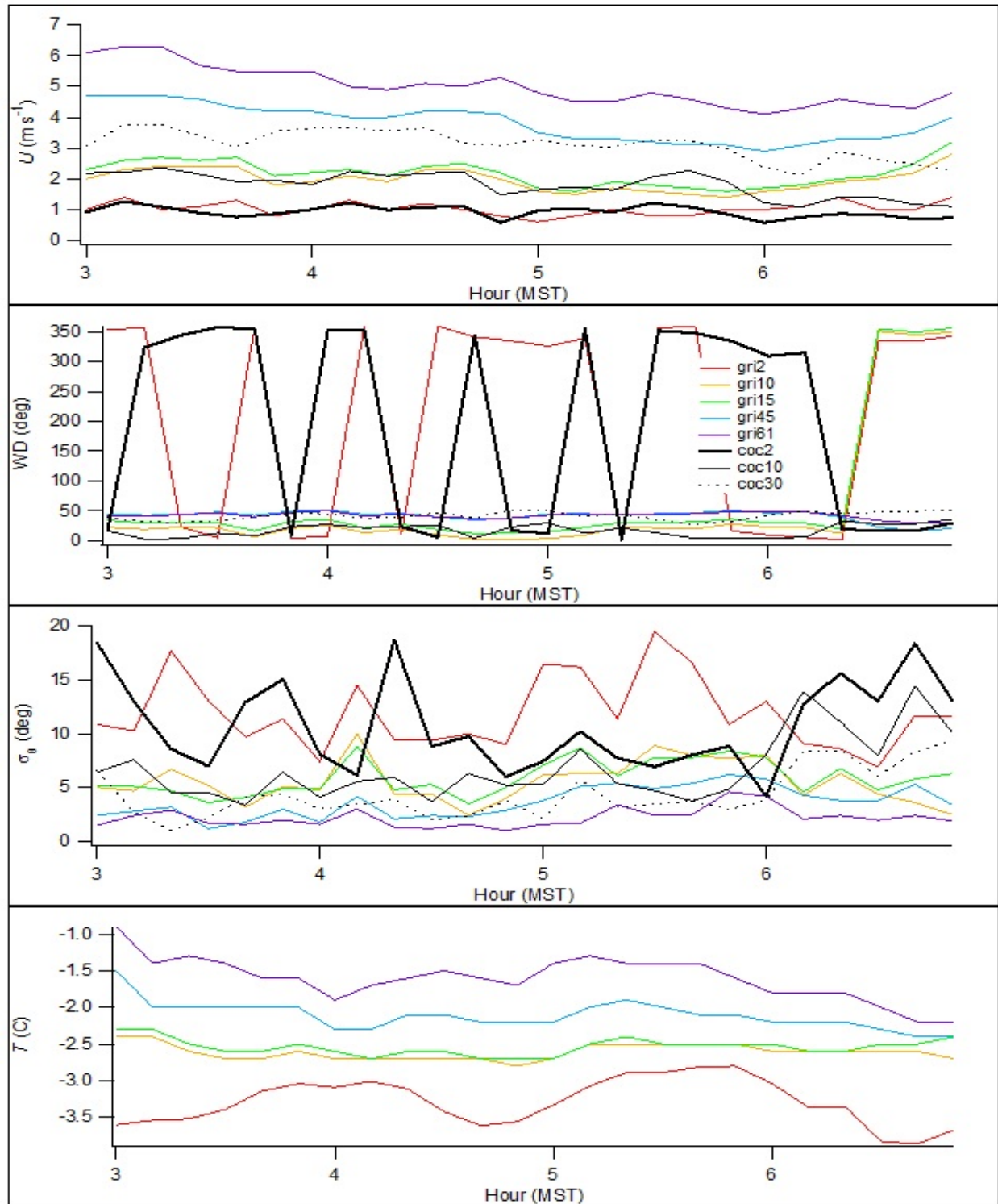


Figure 206. Time series from GRI and COC showing cup anemometer and wind vane measurements of U , wind direction, standard deviation of wind direction σ_θ , and temperature during IOP6. The locations are designated 'xxxxyy' where xxx = tower and yy = measurement height.

Turbulence

Near-surface turbulence measurements for IOP6 are shown in Fig. 207. The magnitudes of all the measurements of turbulence were very low but showed large variability in both space and over time. The variability in the measurements of σ_v/U and σ_w/U is likely due in significant part to the low U . The large variability was often expressed as some very large turbulent excursions from a more common magnitude. This might reflect the more intermittent nature of turbulence inherent to the stable boundary layer. Of particular note in this regard is station ST2, located to the west of the tracer sampling array a short distance southeast of a low hill (Fig. 5). Similar to IOP5, large excursions were especially common in all of the parameters for ST2 during IOP6. Given its downwind location with respect to the near surface wind directions, it is possible that this subtle topographic feature further accentuated the nocturnal intermittency at that site. Any turbulence enhancements due to the low ridge to the northeast of the sampling array or the INTEC facility to the south were not as apparent. This low ridge is visible to the left in the distance in Fig. 3 and the ST1 station is located near the top of the ridge. The σ_v/U (or σ_θ) were still large near the surface although much smaller than observed during the daytime IOPs. TKE, σ_w , and u_* were also much smaller than during the daytime IOPs, by an order of magnitude or more. The sensible heat flux was consistently negative and small but without the large excursions measured during IOP5.

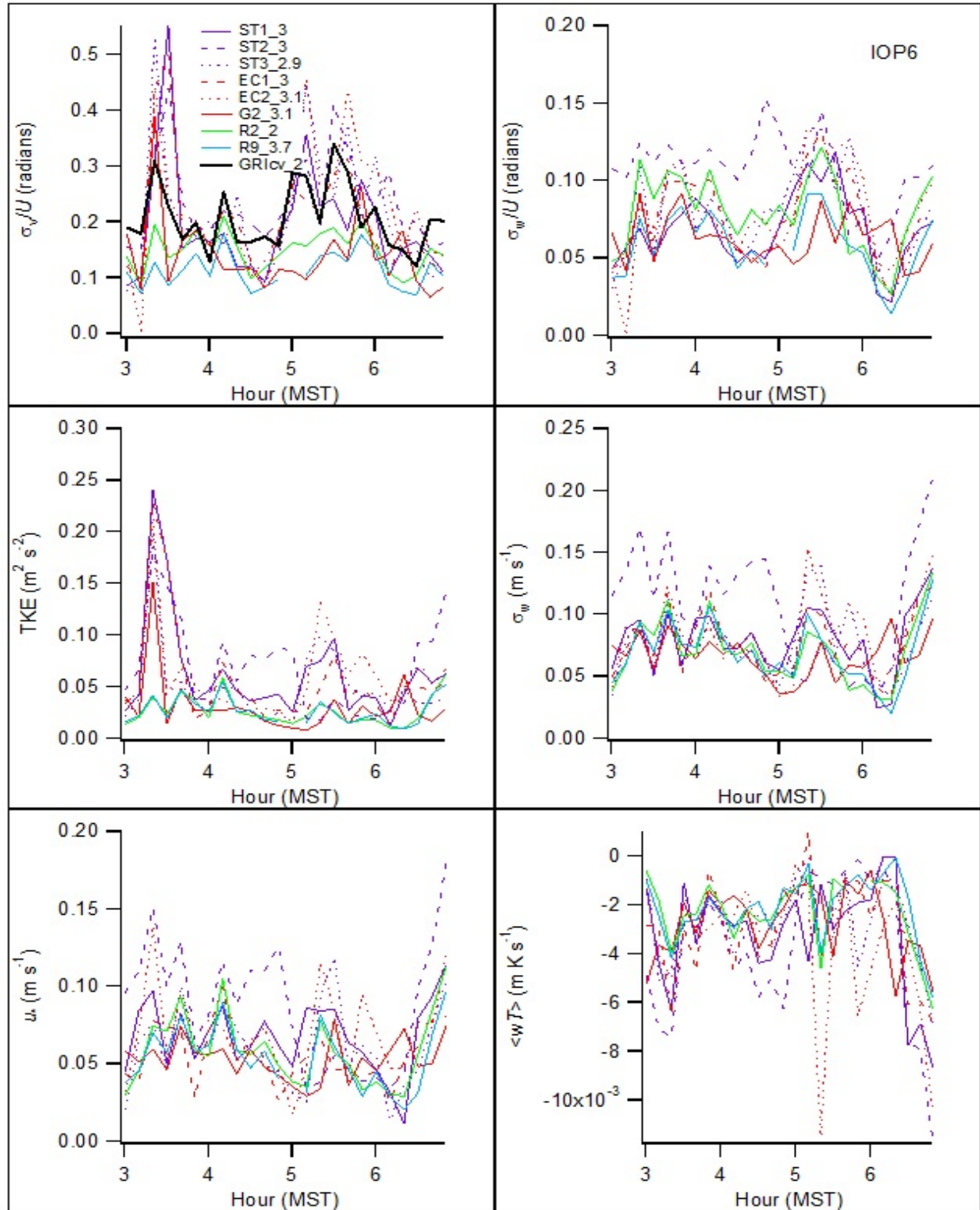


Figure 207. Time series of near surface turbulence (sonic) measurements during IOP6. The GRI and COC are σ_0 wind vane measurements (cv) in degrees converted to radians for purposes of comparison. Notation before and after underscore designates location and height, respectively.

Wind and Turbulence Profiles

Figure 208 shows profiles of the non-sonic measurements at GRI and COC during IOP6. There are two salient features of these profiles. First, there was a shallow north-northwest flow below 10 m beneath a consistently north-northeast flow. Second, there was a steep gradient in U during the first hour that diminished slightly during the second hour. This was also observed during IOP5. The temperature gradients were large throughout the experiment but much less than the other nighttime IOPs. The σ_θ were large near the surface in association with the shallow northwest flow but decreased rapidly upwards and decreased somewhat with time. Profiles were mostly well behaved excepting some minor irregularities near 10 m agl.

Figures 209 and 210 show profiles of the sonic turbulence measurements at GRI during IOP6. Wind speeds and directions were similar to that seen in Fig. 208. These also show a shallow north-northwest flow beneath a north-northeast flow and a steep gradient in U that gradually diminished with time. There were irregularities in σ_v/U and σ_w/U below 10 m, like σ_θ in Fig. 208, with magnitudes rapidly decreasing upwards. TKE and σ_w were low throughout the IOP but were generally higher than the other nighttime IOPs. There are maxima at about 30 m agl with the height of the maxima increasing with time (Fig. 210). The overall virtual temperature gradients were much smaller than during IOP5 but there still was a steeper gradient between the 2 and 3.7 m agl heights (compare Figs. 210 and 180).

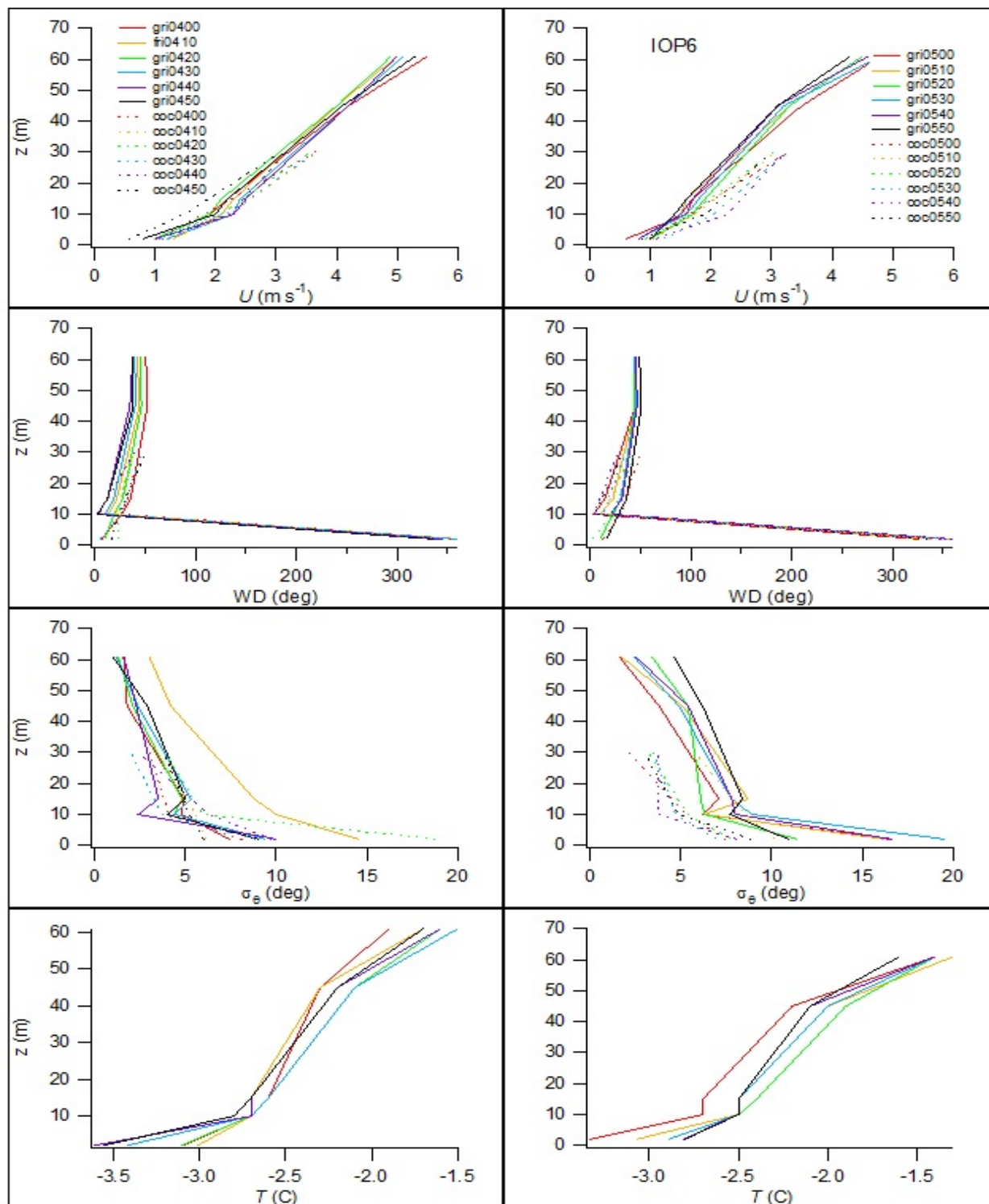


Figure 208. Profiles of U , wind direction, standard deviation of wind direction σ_θ , and aspirated temperature from cup anemometers and wind vanes during IOP6 at GRI and COC. Each profile is designated 'xxxhrmn' where xxx = tower and hrmn = start time of 10-minute interval.

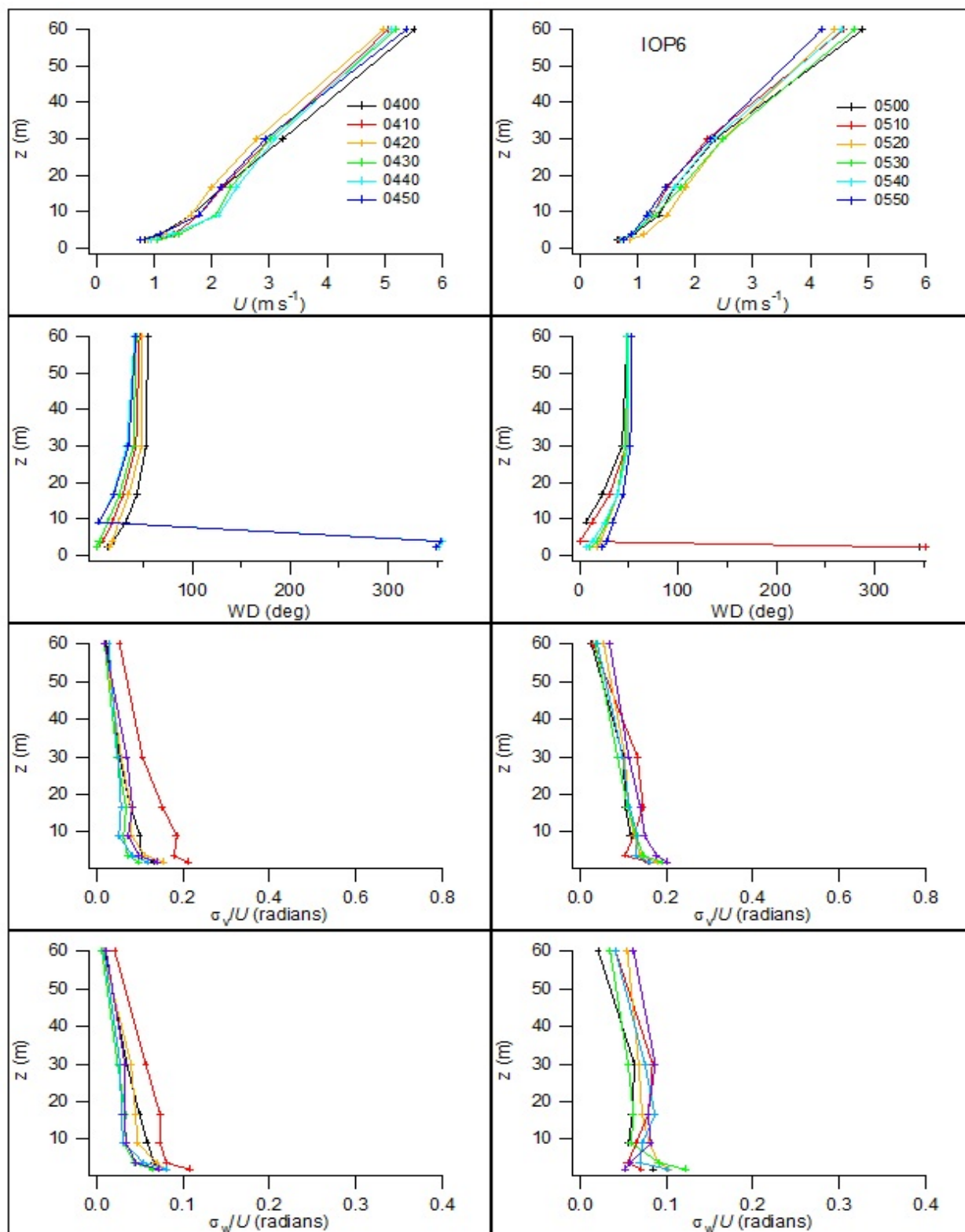


Figure 209. Profiles of U , wind direction, σ_v/U ($\sim\sigma_\theta$), and σ_w/U ($\sim\sigma_\phi$) from sonic anemometers at GRI during IOP6. The legend specifies the start time of the 10-minute interval (hrmn).

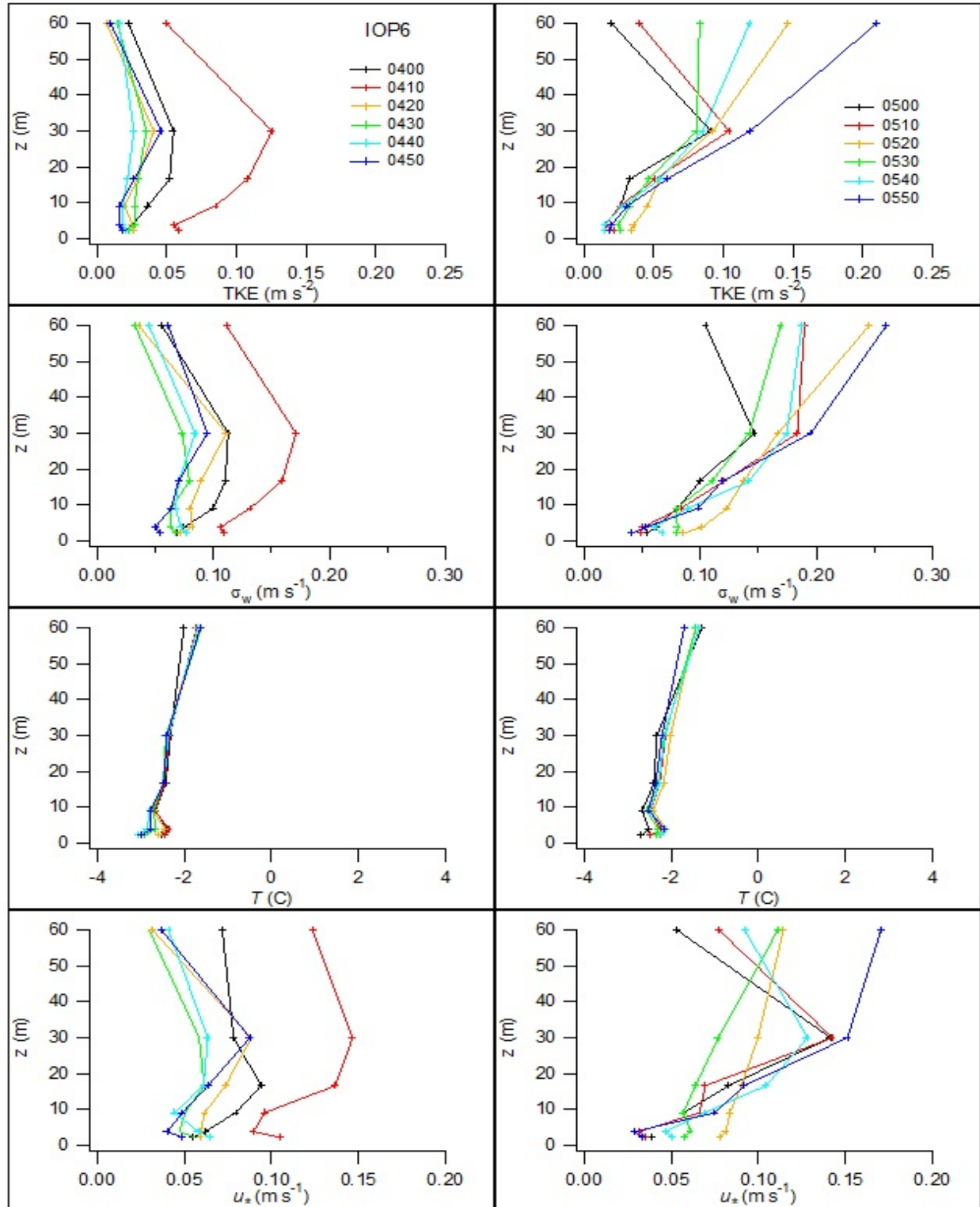


Figure 210. Profiles of turbulent kinetic energy (TKE), standard deviation in vertical wind speed σ_w , virtual temperature, and friction velocity u_* from sonic anemometers at GRI during IOP6. The legend specifies the start time of the 10-minute interval (hrmn).

Figure 211 shows a time-height representation of wind speed and direction during IOP6 for SOD. The wind directions and magnitudes of U in Fig. 211 are roughly consistent at the levels represented on GRI (Figs. 208, 209). At the upper levels of GRI, U was also about 5 m s^{-1} , roughly the same as those shown in Fig. 211. The slight decrease in U at the upper levels of GRI after 0500 h is also consistent with the results shown in Fig. 211. Like IOP5, there was a zone of higher U at about 100-120 m agl. Unlike IOP5, this appears to have begun closer to 70 m agl before lifting to 100-120 m agl by about 0500 h. This jet-like feature was embedded in a northeast flow and is better defined here than in IOPs 5 and 7. Figure 212 shows that this jet-like structure begins to develop as early as 0300 h at about 40-50 m agl then gradually strengthens and lifts to about 100-120 m agl over the course of the test. The steep gradient in U at GRI would be consistent with the presence of this jet (Fig. 208). The data from PRO (Fig. 213) do not provide direct evidence in support of the low level jet. Wind speeds are low in these profiles up to about 600 m agl through a zone characterized by highly variable wind directions. Above that U began to increase with consistently southwesterly wind directions. Thus might be interpreted as indirect evidence of a zone from about 159-600 m agl that represents a transition from the low level jet, in a northeasterly flow near the surface, to the southwest winds aloft. A somewhat analogous pattern was seen in IOPs 5 and 7. The PRO U might be biased a little low and there is almost no data passing consensus above 1300 m to provide a reliable basis for contouring.

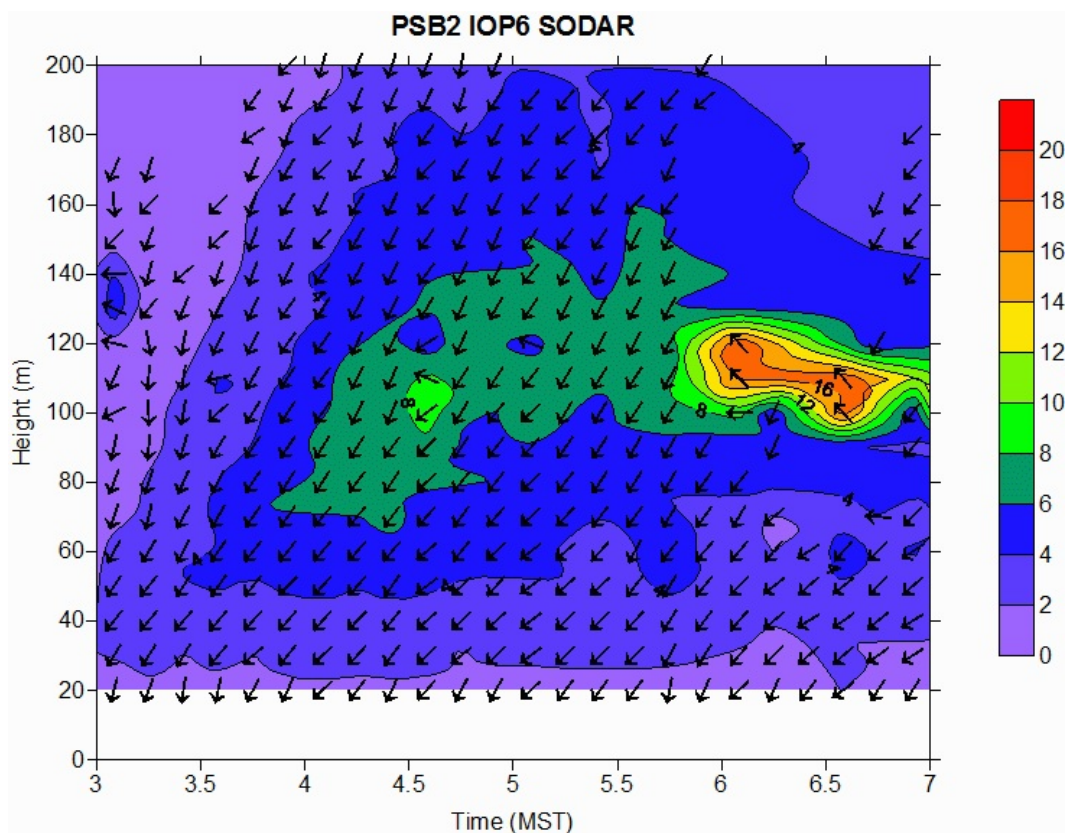


Figure 211. Time-height cross-section of wind speed and direction at sodar (SOD) during IOP6. Legend represents m s^{-1} .

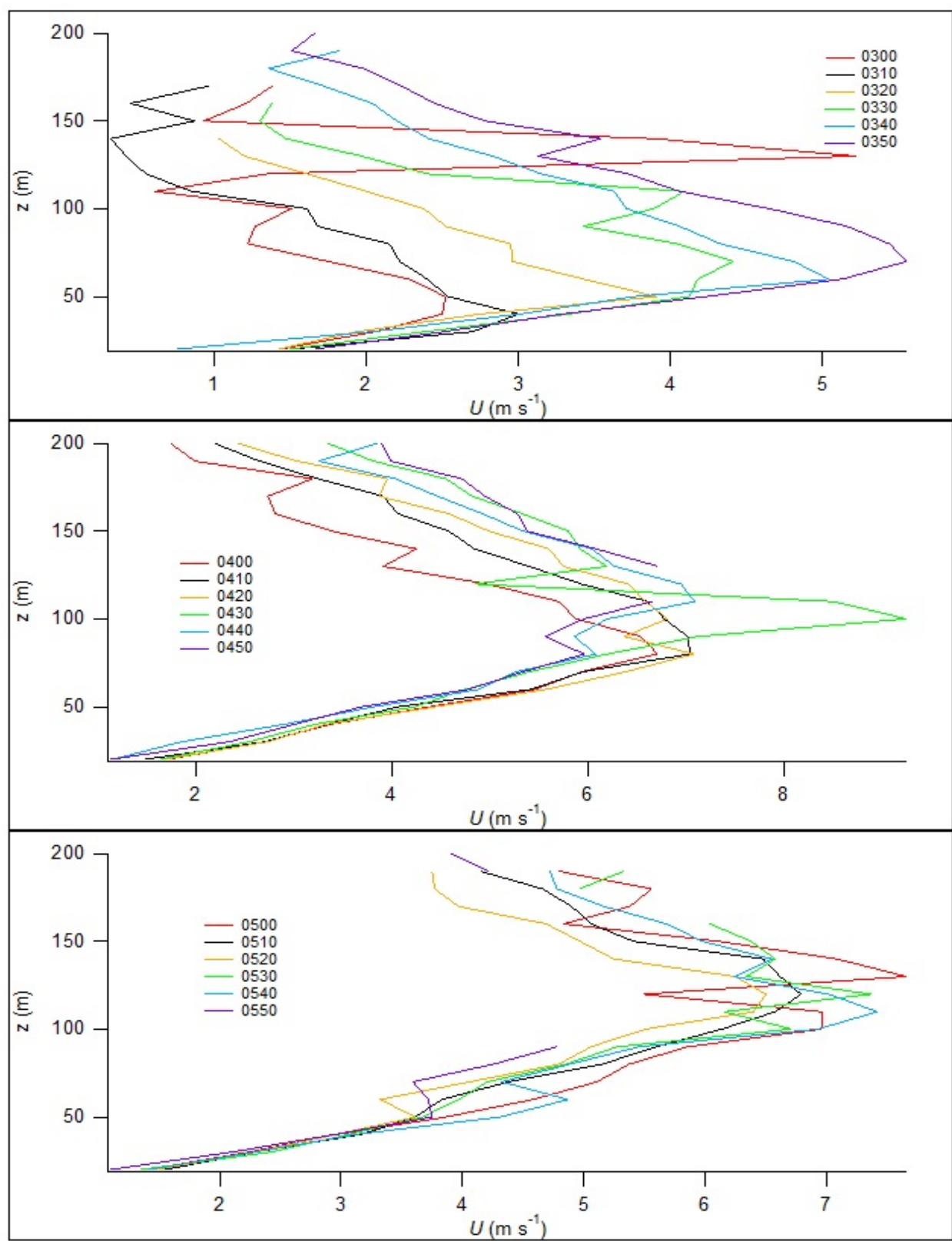


Figure 212. Profiles of low-level jet 0300 to 0600 h during IOP6.

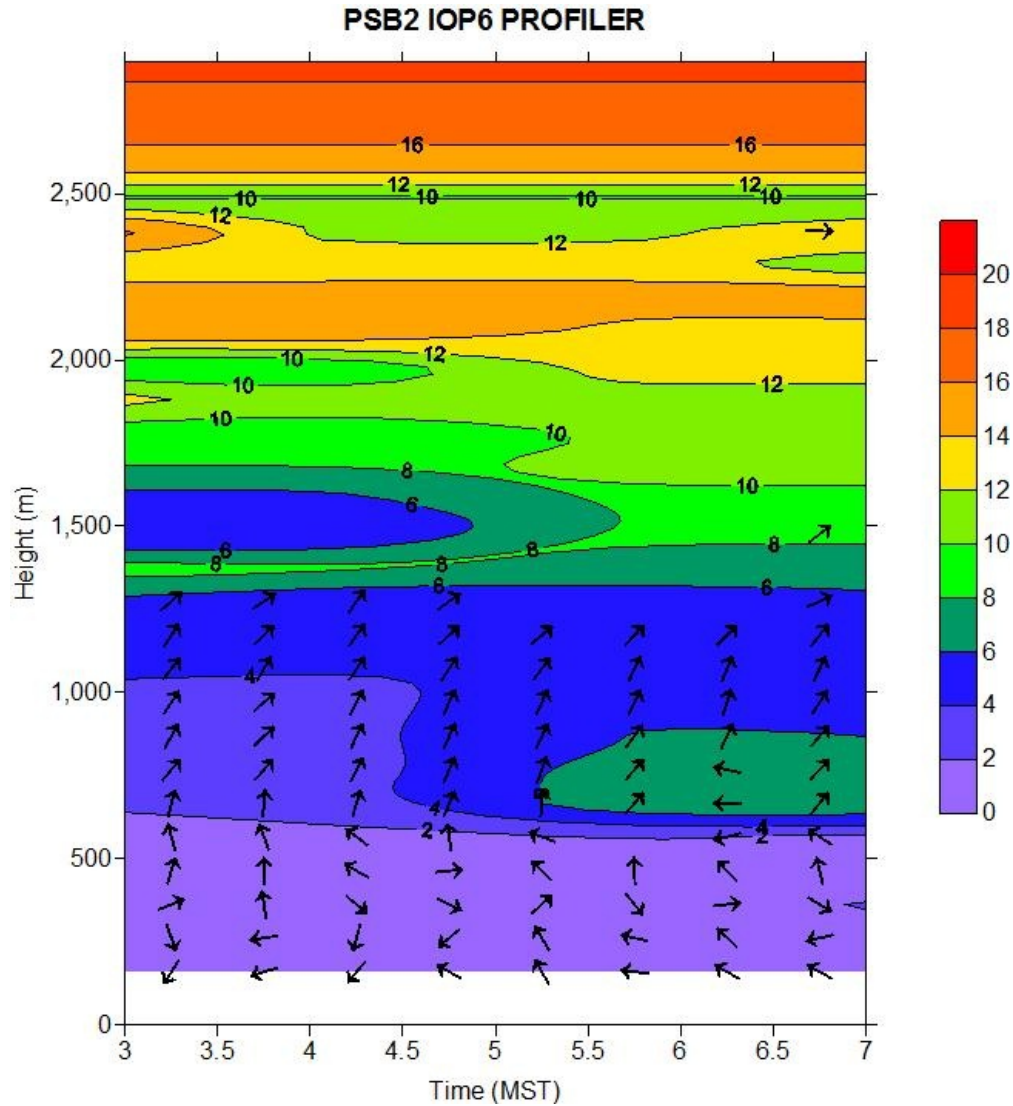


Figure 213. Time-height cross-section of wind speed and direction at wind profiler (PRO) during IOP6. Legend represents m s^{-1} .

Figures 214 and 215 show SOD time-height representations of σ_w and TKE, respectively, during IOP6. The σ_w during the tracer measurement period were all very low. TKE was low throughout the domain except, again, for the suggestion of a zone of higher TKE from about 100-120 m agl. This is roughly consistent with the zone of higher U at the same levels (Figs. 211, 212). It is also consistent with the distinct increase in TKE at the upper levels of GRI over the course of the test (Fig. 210), suggesting that the upper levels of GRI were being affected by turbulence generated by the jet. Figure 216 shows time-height temperature profiles from the RASS. As a conjecture, the reduced temperature gradient and often higher turbulence levels in the upper part of the vertical profiles in IOP6, compared to the other nighttime IOPs, might have been due to the effects of enhanced mixing resulting from the turbulence generated at the jet-like feature. This would also suppress N .

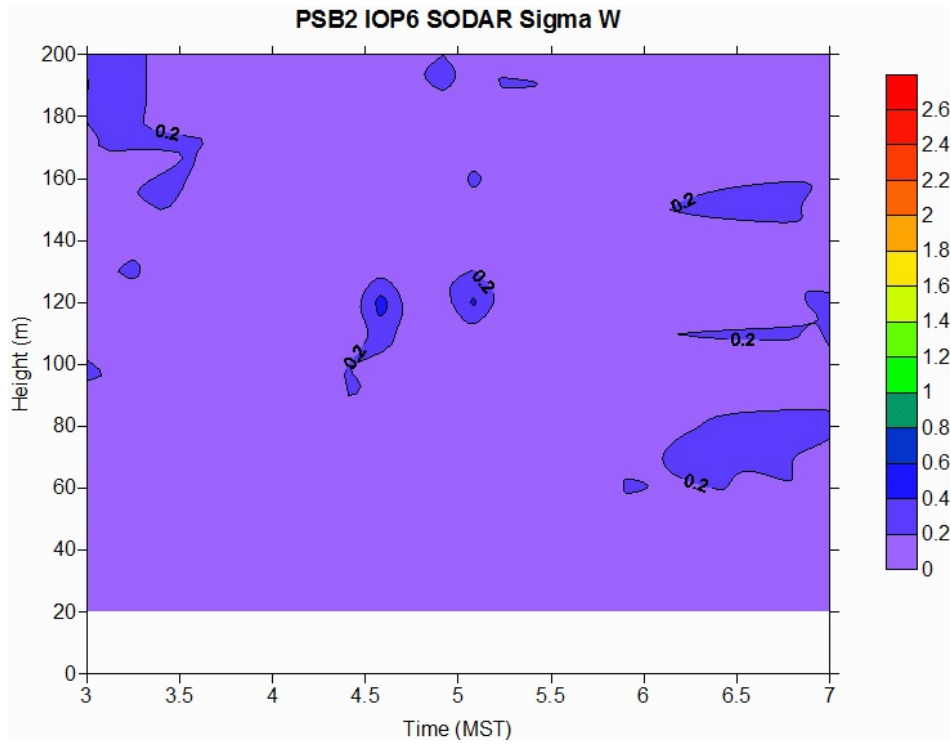


Figure 214. Time-height cross-section of σ_w at sodar (SOD) during IOP6. Legend represents m s^{-1} .

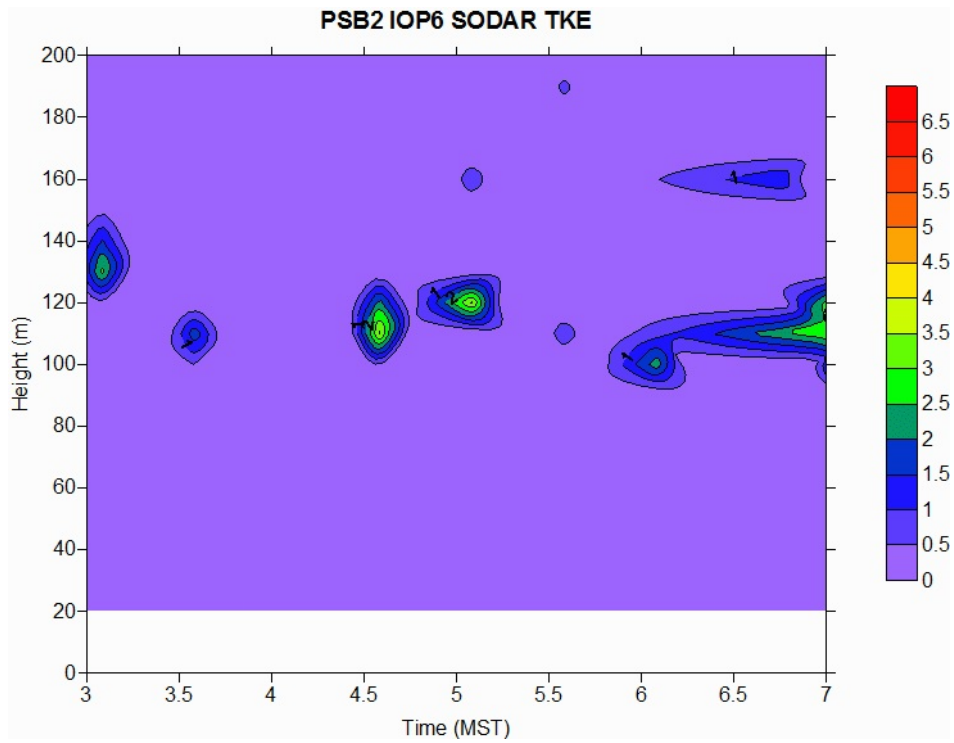


Figure 215. Time-height cross-section of TKE at sodar (SOD) during IOP6. Legend represents $\text{m}^2 \text{s}^{-2}$.

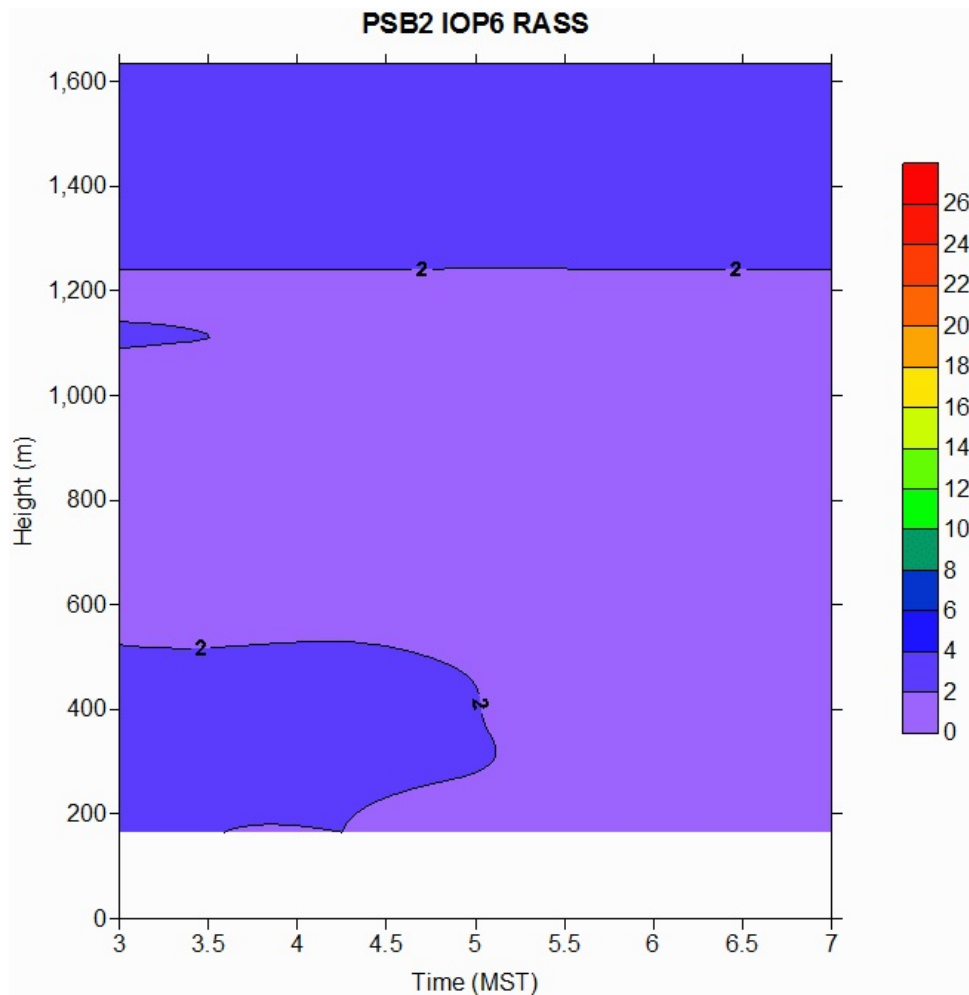


Figure 216. Time-height cross-section of virtual temperature at the RASS during IOP6. Temperatures are in degrees C.

Radiosonde Results

Pre and post-IOP radiosonde profiles of potential temperature and specific humidity for IOP6 are shown in Figs. 217 and 218. Data from the post-IOP launch is mostly missing. There is no constant potential temperature layer in Fig. 217 and it provides no basis for selecting a mixing height. The specific humidity profiles in Fig. 218 suggest some layering or structure to the boundary layer with a distinct feature at 1000 m agl. However, there is no basis for an unambiguous selection of the boundary layer or a mixing depth. The ceilometer results suggest a lower layer near 100 m (BL_Height1) and an upper layer near 500 m (BL_Height2) (Table 25). Neither of these heights is consistent with any features in the radiosonde profiles.

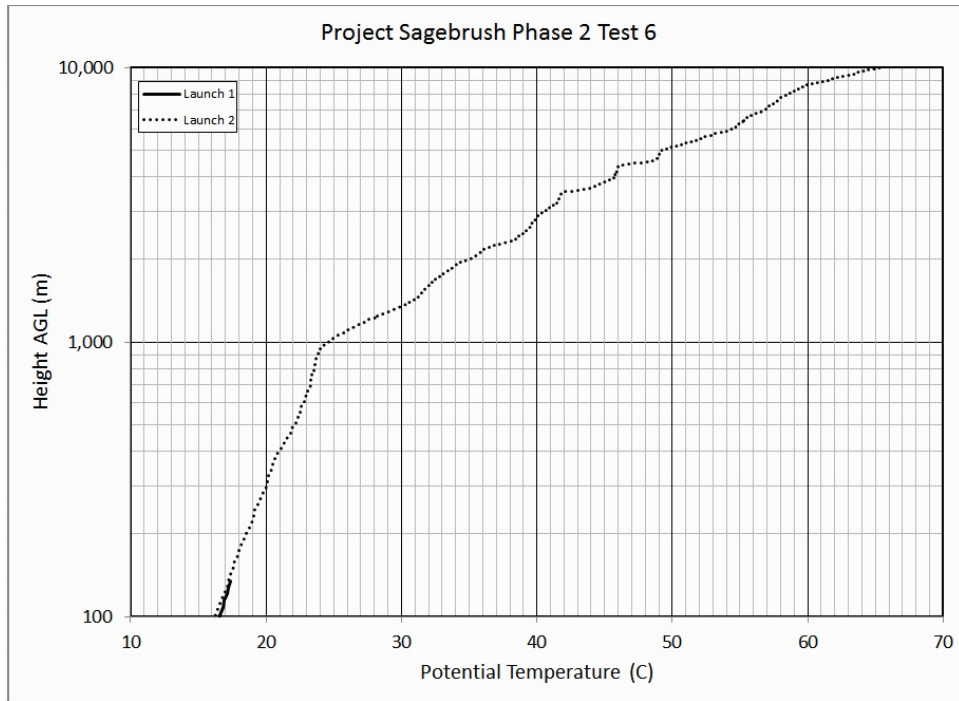


Figure 217. Potential temperature profile from radiosonde probe, IOP6. Pre-test launch bold, post-test launch dotted.

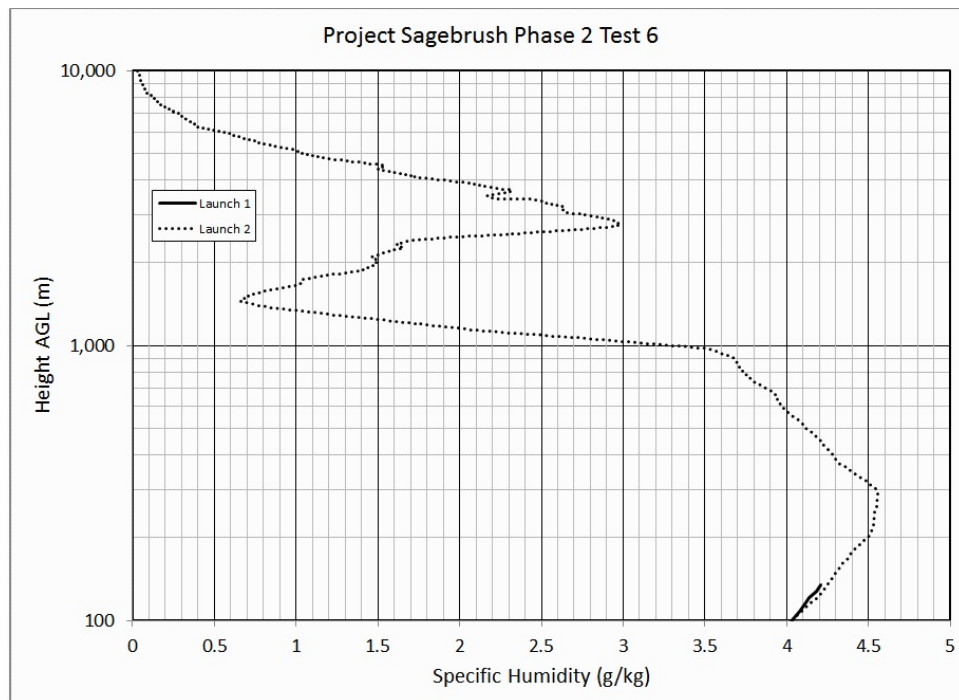


Figure 218. Specific humidity profile from radiosonde probe, IOP6. Pre-test launch bold, post-test launch dotted.

Table 25. Ceilometer estimates of boundary layer heights during IOP6.

Date	Time	BL Height 1 (m)	BL Index 1	BL Height 2 (m)	BL Index 2	BL Height 3 (m)	BL Index 3	Cloud Status	Cloud 1 (m)
(yyyymmdd)	(MST)								
20161020	3:05	100.00	3	-999.9	-999.9	-999.9	-999.9	1	5,913.71
20161020	3:15	97.50	2	493.89	1	-999.9	-999.9	1	5,718.09
20161020	3:25	90.50	2	474.75	1	-999.9	-999.9	1	5,617.89
20161020	3:35	100.00	2	503.17	2	-999.9	-999.9	1	5,590.50
20161020	3:45	100.50	3	542.62	2	-999.9	-999.9	1	5,462.48
20161020	3:55	110.00	3	-999.9	-999.9	-999.9	-999.9	1	4,839.28
20161020	4:05	120.00	3	-999.9	-999.9	-999.9	-999.9	1	5,120.83
20161020	4:15	104.75	3	-999.9	-999.9	-999.9	-999.9	1	4,965.43
20161020	4:25	103.75	3	3,960.00	1	-999.9	-999.9	1	4,666.08
20161020	4:35	100.00	3	-999.9	-999.9	-999.9	-999.9	0	-999.9
20161020	4:45	100.00	3	3,950.94	1	-999.9	-999.9	1	3,977.75
20161020	4:55	98.00	3	-999.9	-999.9	-999.9	-999.9	1	3,983.08
20161020	5:05	90.00	2	580.00	2	-999.9	-999.9	1	3,982.95
20161020	5:15	95.50	3	580.00	2	-999.9	-999.9	1	3,971.90
20161020	5:25	101.50	3	3,959.58	1	-999.9	-999.9	1	3,850.45
20161020	5:35	109.33	2	684.00	2	3,931.08	2	1	3,785.28
20161020	5:45	102.00	2	589.75	1	3,878.83	2	1	3,773.03
20161020	5:55	110.00	2	517.50	2	3,836.11	1	1	3,722.94
20161020	6:05	103.33	2	486.25	2	-999.9	-999.9	0	-999.9
20161020	6:15	95.00	2	474.00	2	-999.9	-999.9	0	-999.9
20161020	6:25	92.00	2	460.50	2	-999.9	-999.9	0	-999.9
20161020	6:35	100.00	2	460.00	2	-999.9	-999.9	1	4,398.00
20161020	6:45	91.00	2	473.50	2	-999.9	-999.9	0	-999.9
20161020	6:55	90.00	2	475.67	2	-999.9	-999.9	0	-999.9

Bag Sampling Results

Figures 219 and 220 and Figures 221 and 222 show the 10-min average normalized and actual, respectively, color-coded plan view concentration maps for IOP6 bag sampling at 1 m agl. Figures 223 and 224 and Figures 225 and 226 show the 10-min average normalized and actual concentrations, respectively, along each of the arcs. Figures 227 and 228 show the vertical concentration profiles at the four fixed towers and the mobile tower arranged by 10-min (bag) sampling period.

Unfortunately, the meteorology was such that the plume largely missed the 210° arc sampling array during IOP6. This was especially the case during the first hour. However, even during the second hour of sampling, only the northern edge of the plume was measured and it is

likely most of the plume was missing for all 10-min averaging periods. Only ambient background concentrations were measured at the towers. For these reasons it is difficult to say much about the bag sampling results except to say this IOP was not effective for analyzing plume dispersion.

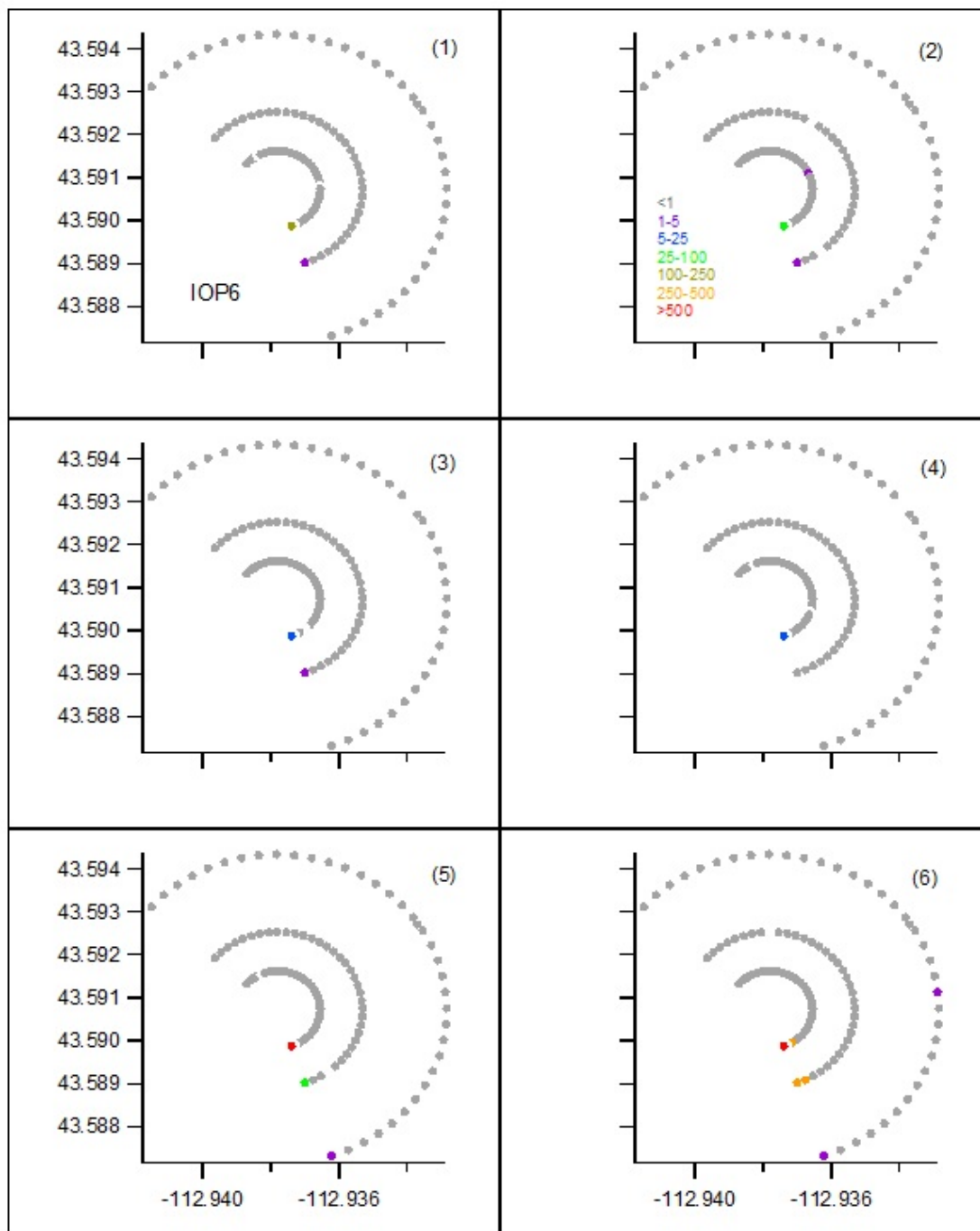


Figure 219. Color-coded normalized ($F \cdot \chi / Q$ ppt s g^{-1}) concentrations at 1 m agl for bags 1-6 during IOP6. The number in () is bag number.

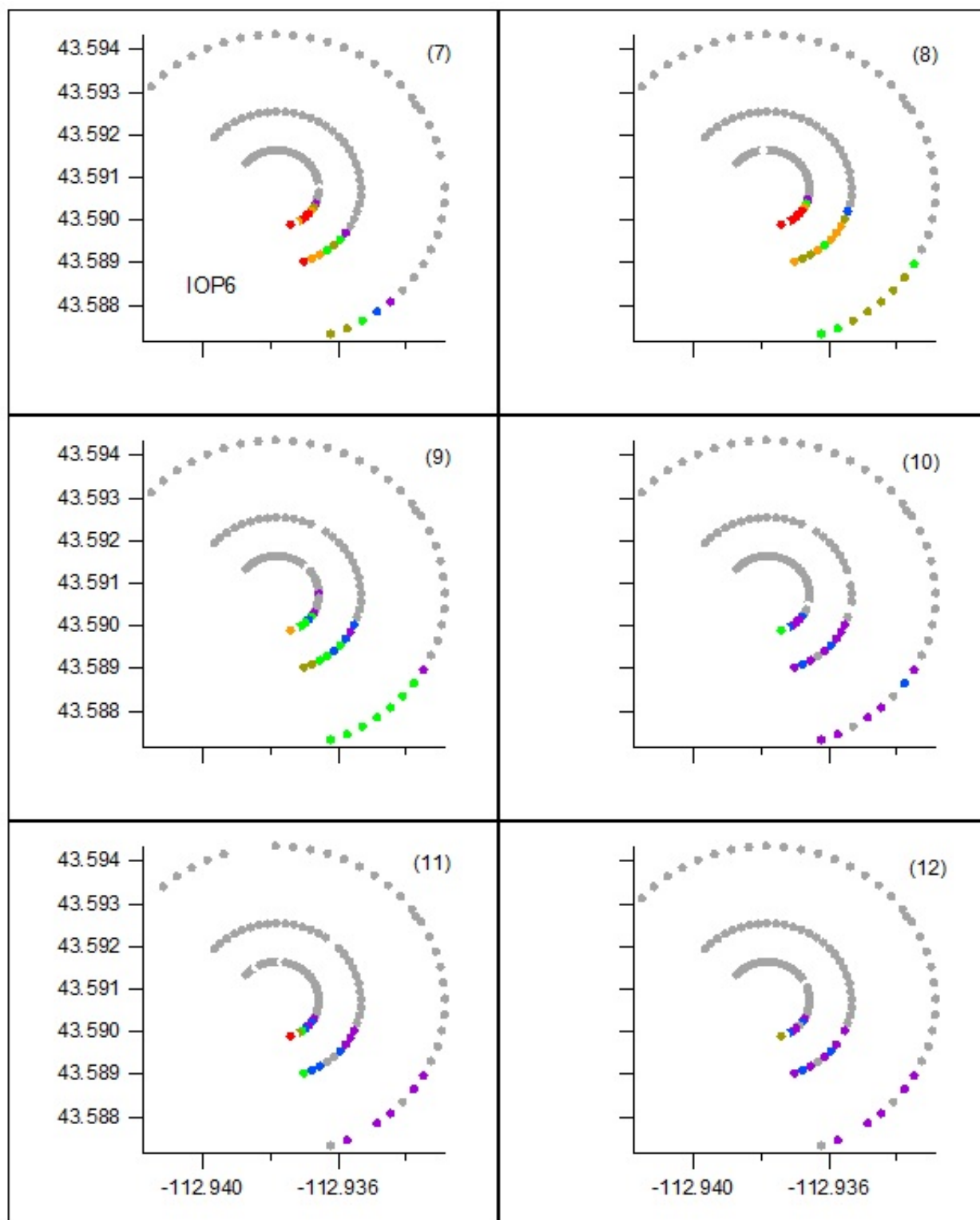


Figure 220. Color-coded normalized ($F^*\chi/Q$ ppt s g^{-1}) concentrations at 1 m agl for bags 7-12 during IOP6. The number in () is bag number.

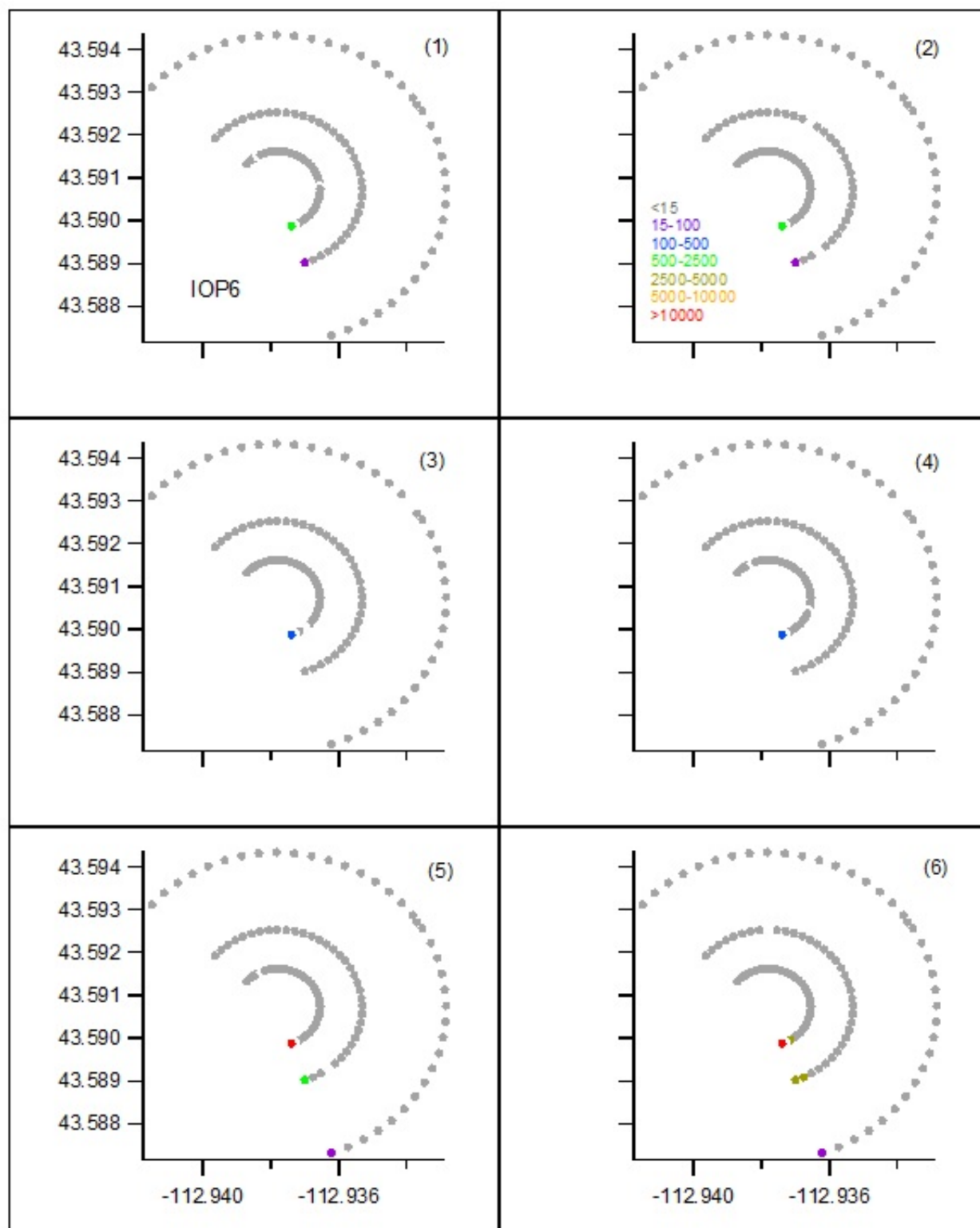


Figure 221. Color-coded measured SF₆ concentrations (ppt) at 1 m agl for bags 1-6 during IOP6. The number in () is bag number.

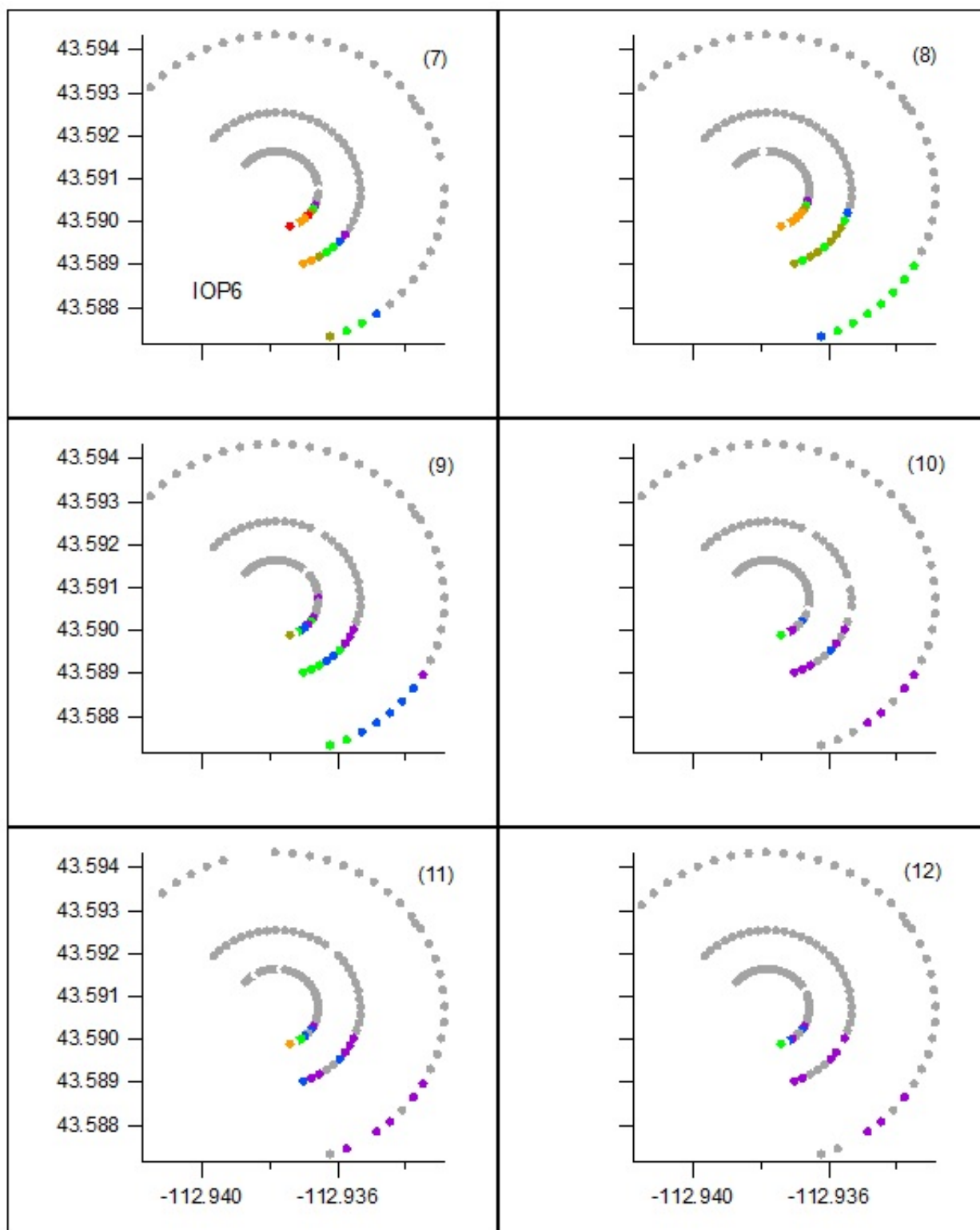


Figure 222. Color-coded measured SF_6 concentrations (ppt) at 1 m agl for bags 7-12 during IOP6. The number in () is bag number.

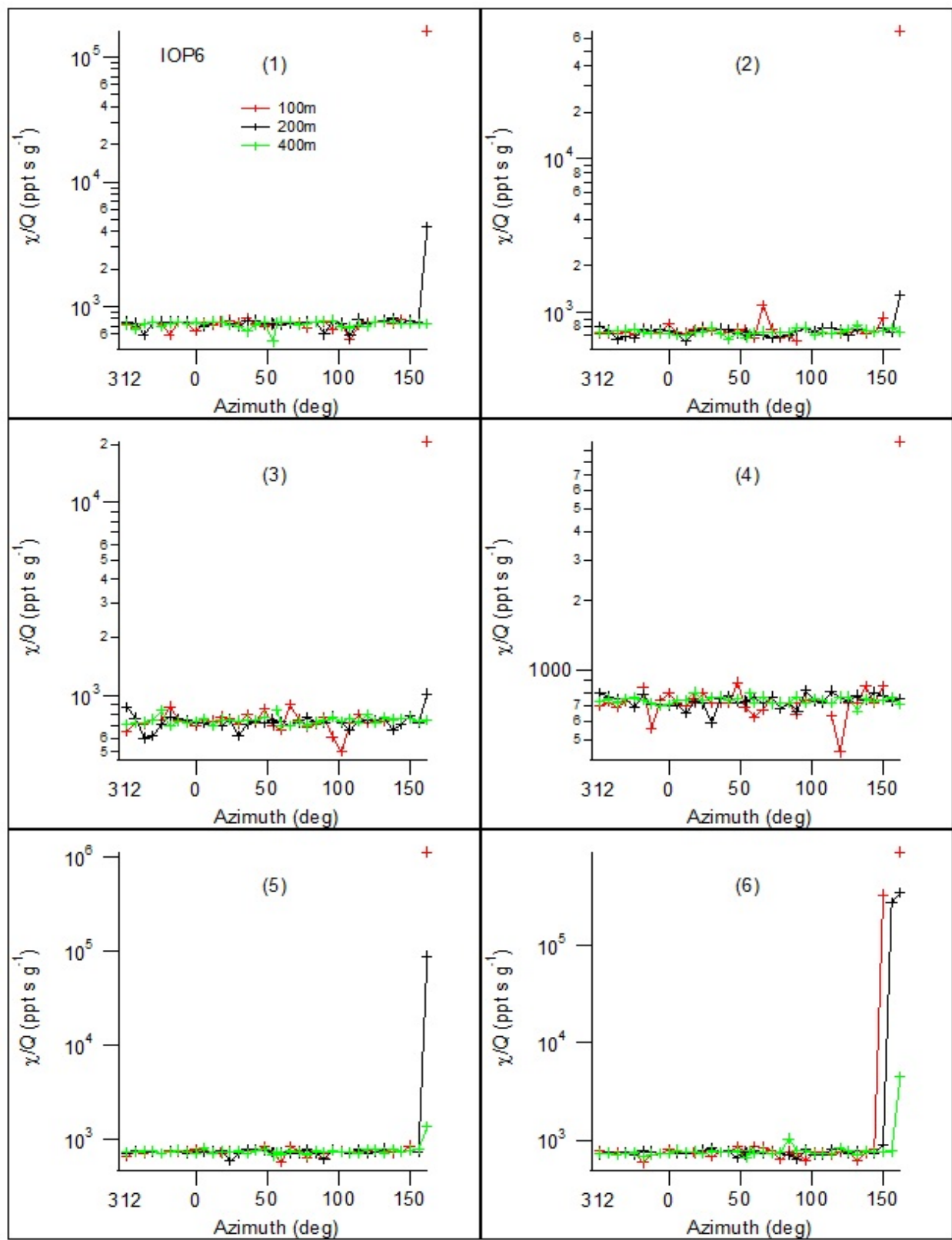


Figure 223. Cross-sections of normalized concentration along the arcs for bags 1-6 during IOP6.

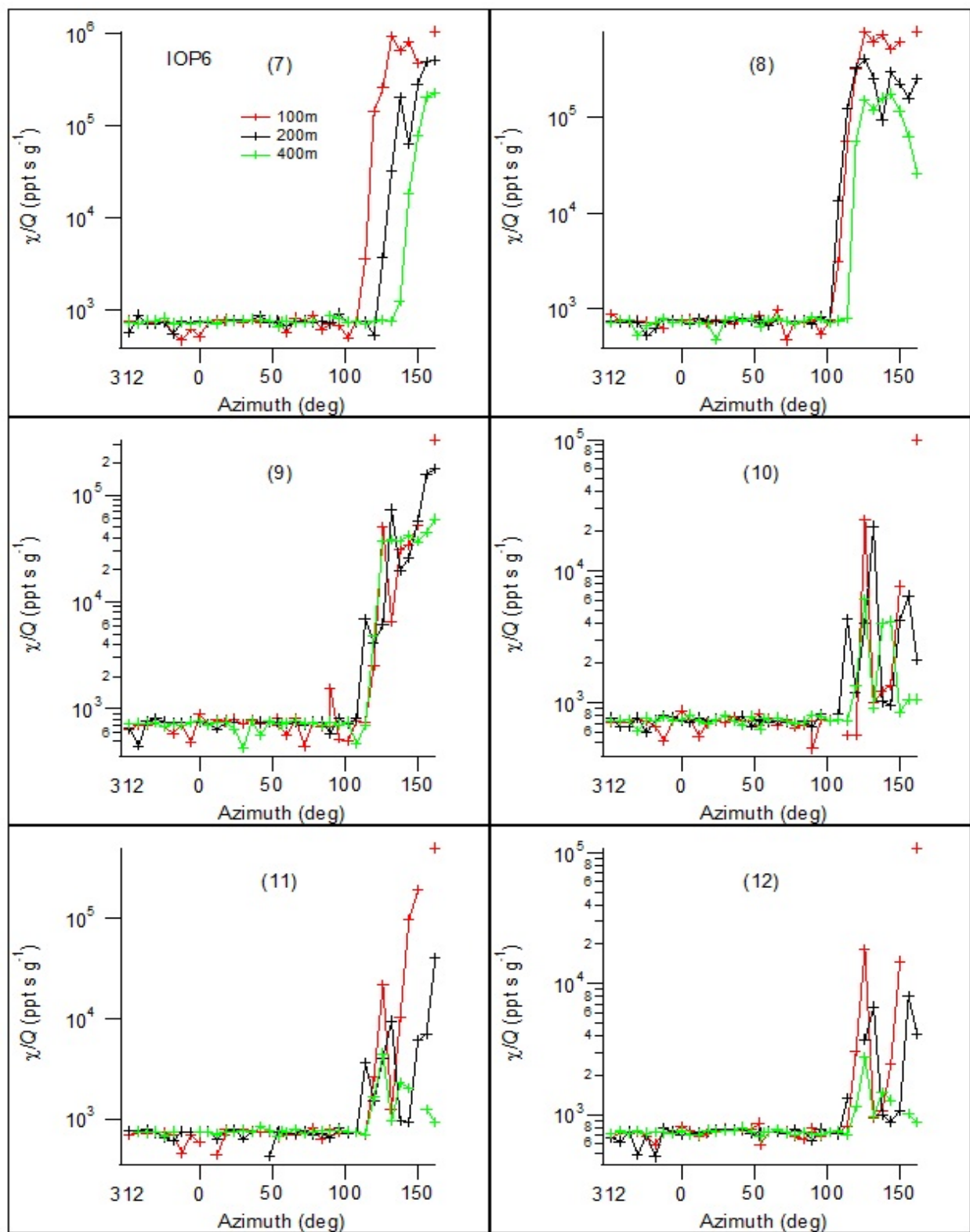


Figure 224. Cross-sections of normalized concentration along the arcs for bags 7-12 during IOP6.

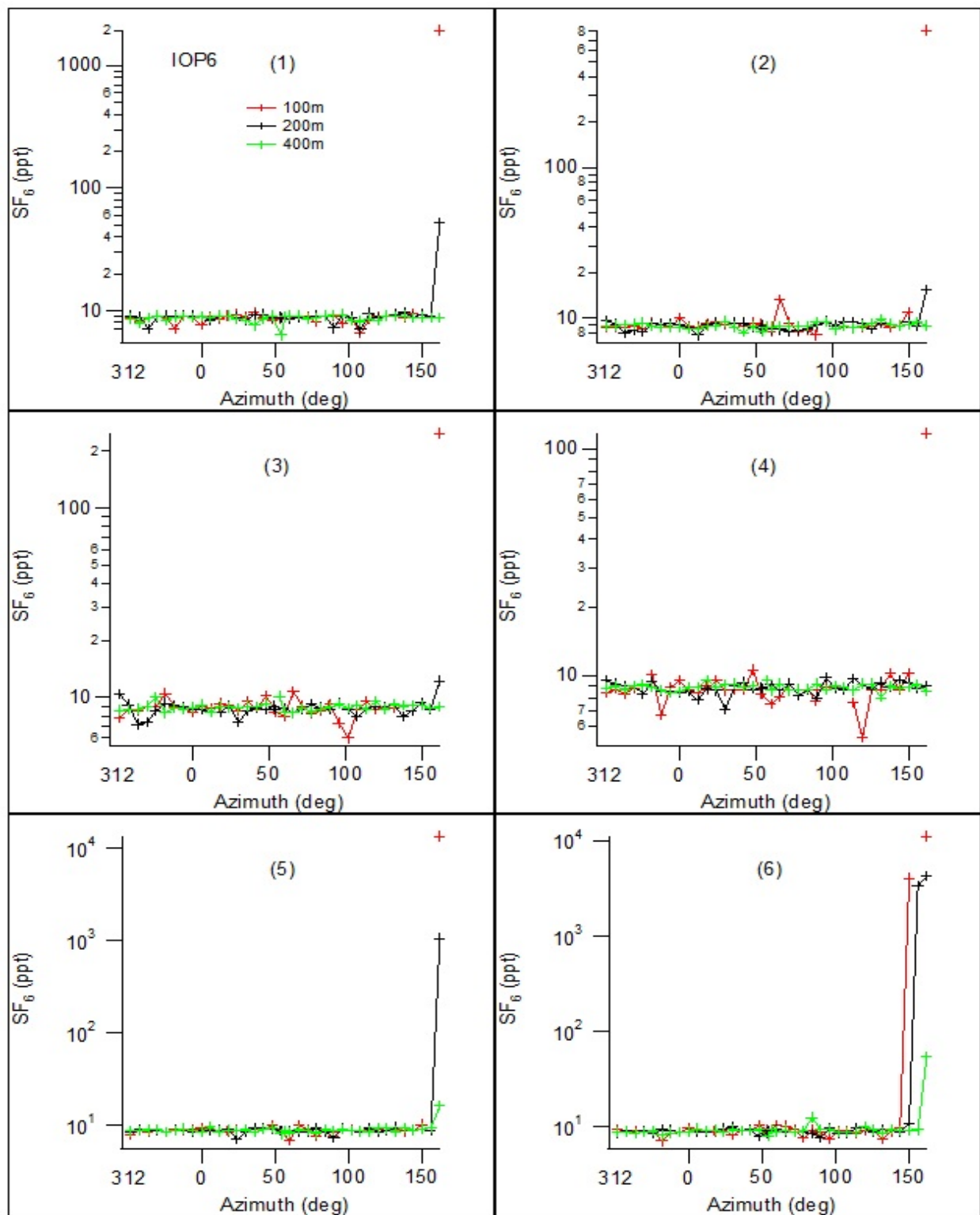


Figure 225. Cross-sections of measured SF_6 concentration along the arcs for bags 1-6 during IOP6.

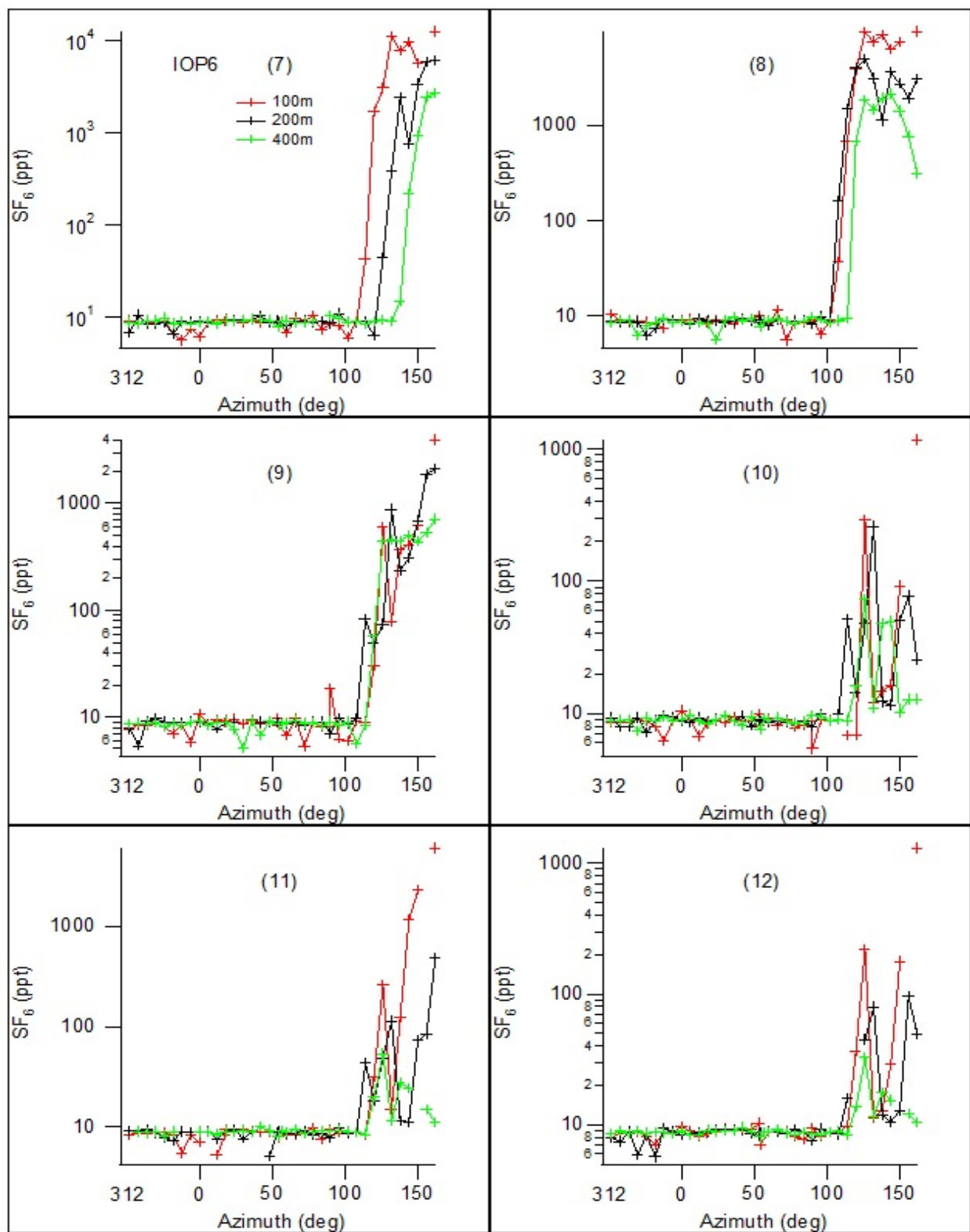


Figure 226. Cross-sections of measured SF_6 concentration along the arcs for bags 7-12 during IOP6.

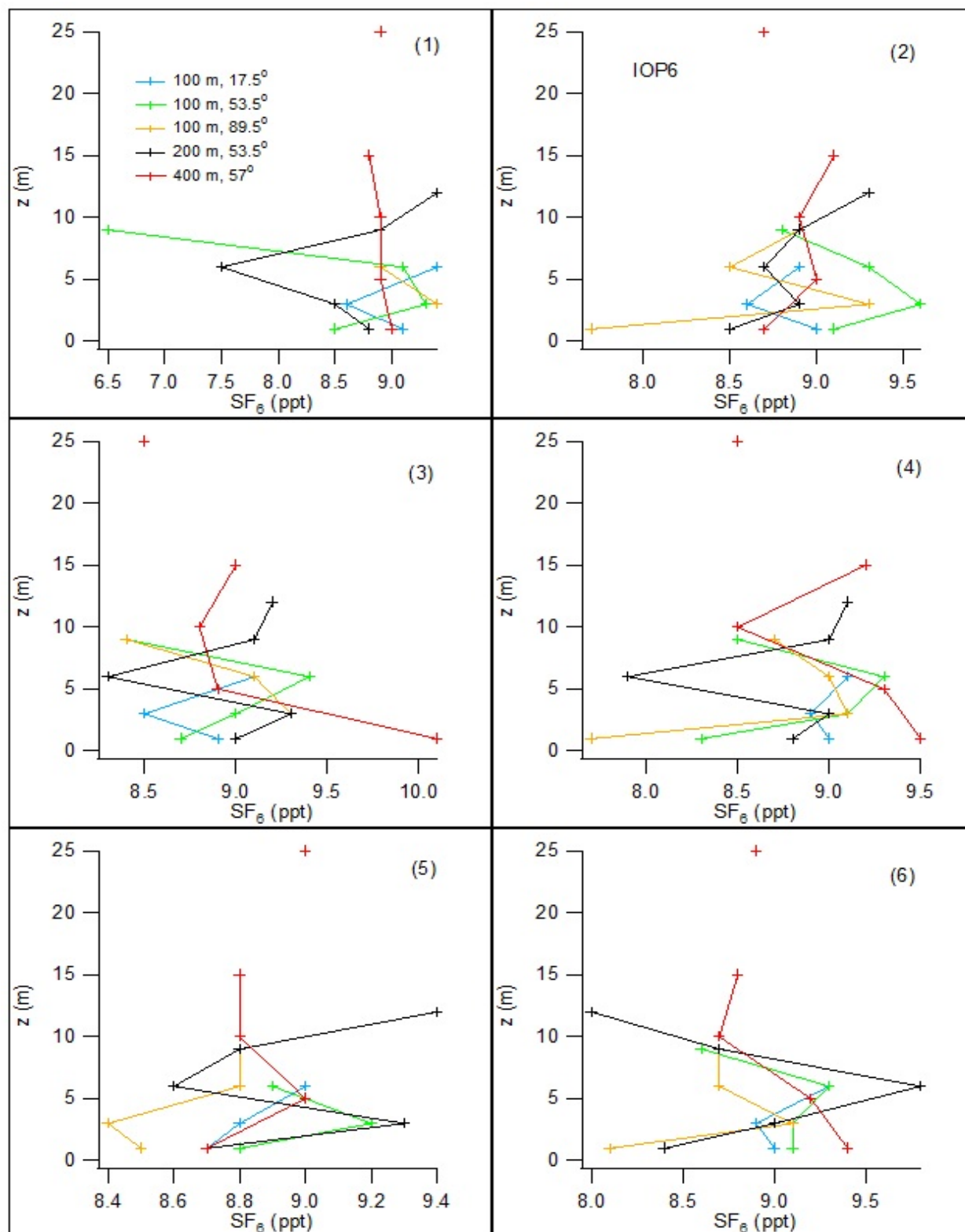


Figure 227. Vertical concentration profiles at the arc position given in the legend for (bags) 1-6 during IOP6. All concentrations were at or near background.

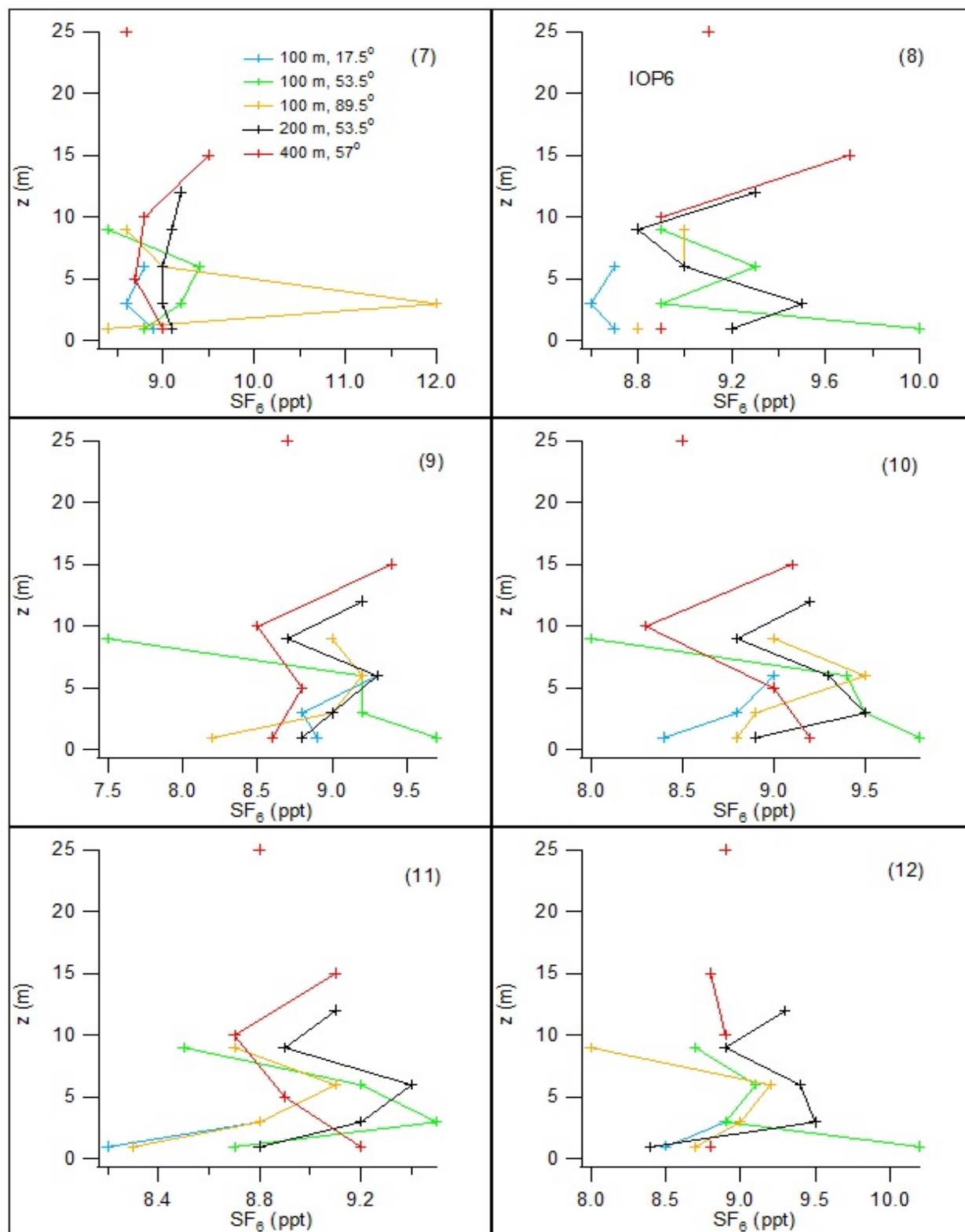


Figure 228. Vertical concentration profiles at the arc position given in the legend for (bags) 7-12 during IOP6. All concentrations were at or near background.

Fast Response Results

The locations of the fast response analyzers during IOP6 are shown in Fig. 229. The corresponding concentration time series are shown in Fig. 230. The color coding of the time series was described in the Introduction to this section. The time series records for periods of time with sampling at a fixed location in Fig. 230 are keyed by annotation with a corresponding annotation in Fig. 229. For example, the '1' for the D analyzer in Fig. 230 was located at location 'D1' in Fig. 229.

The fast response analyzers were mainly located to the south of the release, probably along the eastern margin of the plume. The character of the fast response measurements during IOP6 resembled that seen for IOPs 5 and 7. When present, the concentrations were highly fluctuating and alternated between very high peaks and concentrations at or near background. Also like IOPs 5 and 7, the residence times of the sensor in the plume for a given peak were generally much longer than during the daytime IOPs. The potential significance of that is

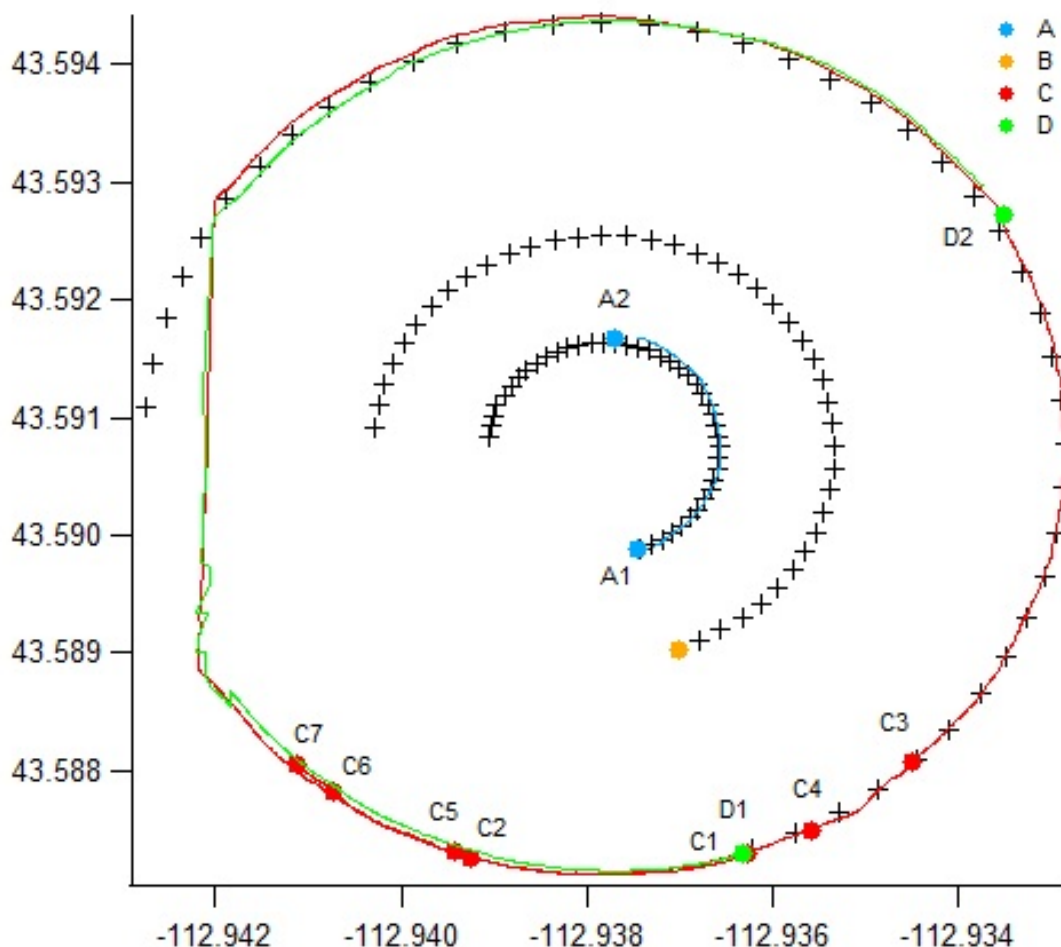


Figure 229. Locations of fast response analyzers during IOP6.

discussed elsewhere. Plume intercepts associated with times when an analyzer was mobile showed as abrupt, sharp spikes (red traces, analyzer C).

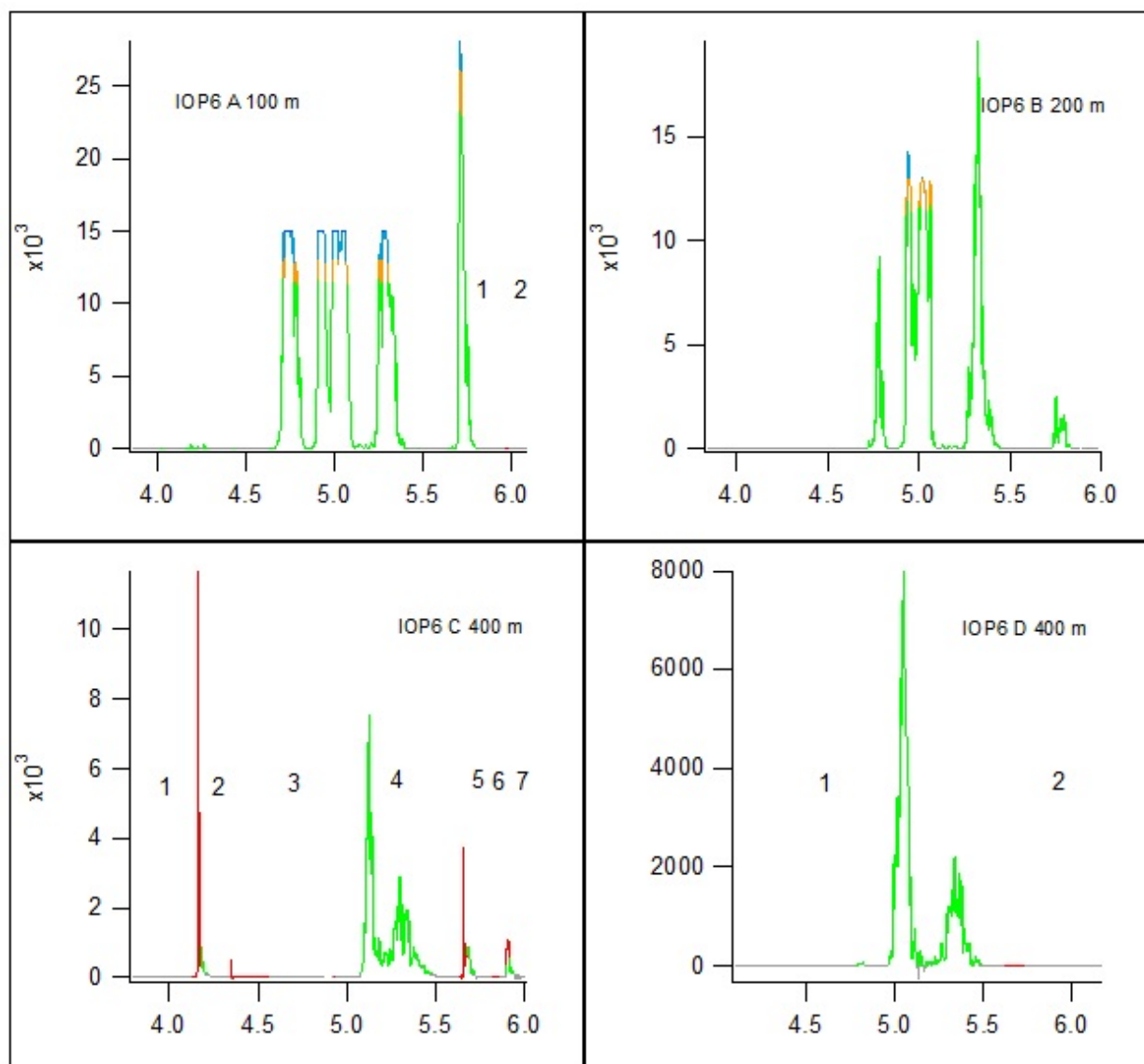


Figure 230. Fast response concentration time series during IOP6.

IOP 7

Date/Time and General Description

IOP7 was conducted on 21 October from 0400-0600 MST (0500-0700 MDT). Estimates of stability based on traditional Pasquill-Gifford (P-G) schemes were mainly class F, especially using the SRDT method, but some 10-min periods fell into classes D or E (Fig. 231). Estimates of mean z/L from GRI ranged from 2.69 to 1.96 with a Ri_b of 1.13 (Table 26). In aggregate, the z/L and Ri_b results suggest that IOP7 had the most stable atmosphere and lightest winds of all of the IOPs. Winds were mostly less than 1 m s^{-1} near the surface and highly variable in direction in both space and time, especially during the first hour of the IOP (Table 26; Figs. 232, 235). After 0500 h the near surface wind directions organized around west-northwest. Wind directions above the surface varied with time and height and ranged from consistently northeast aloft to northeast (early) or northwest (late) at lower levels. The plume often subtended 50-100 degrees of arc, more on the 100 m arc. A combination of wind direction and the large horizontal plume spread resulted in at least some portion of one or both limbs of the plume being truncated at the edge of the sampler array in all 10-min periods. Truncation was most common or severe during the first hour and on the 100 m arc. While truncation decreased with downwind distance, it was also common on the 200 and 400 m arcs as well. There were a few 10-min periods where above background tracer concentrations were measured at almost every bag sampler on all arcs. The SF_6 release rate was 0.012 g s^{-1} (Table 2). Fast response analyzers were at fixed locations on the 100 and 200 m arcs at the edge of the bag sampling array at 162° azimuth. The analyzer on the

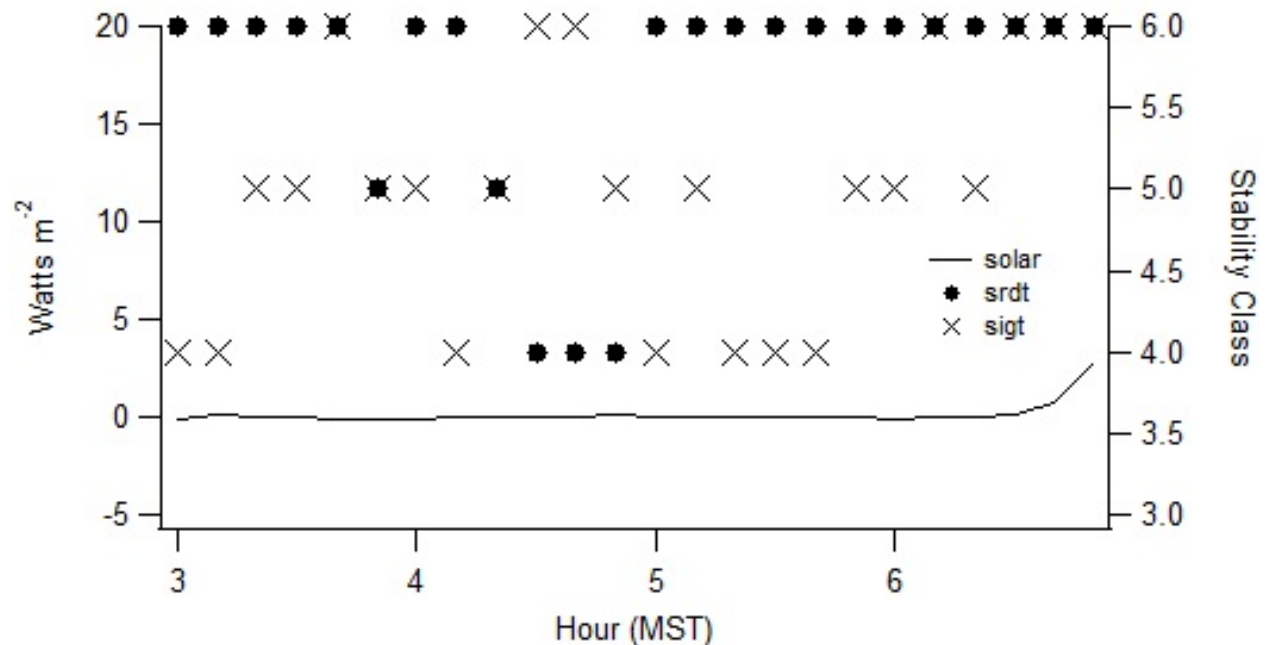


Figure 231. Incoming solar radiation and classification of stability conditions using the Pasquill-Gifford Solar Radiation Delta T (srdt) and σ_0 (sigt) methods (EPA 2000c) during IOP7. Classes D, E, and F are designated 4, 5, and 6, respectively.

Table 26. Meteorological conditions during IOP7.

Bag	COC				GRI						GRI			Solar
	U (m s ⁻¹)		WD (deg)		U (m s ⁻¹)		WD (deg)		σ_θ (deg)		L	L	degC	W m ⁻²
	2m	10m	2m	10m	2m	10m	2m	10m	2m	10m	3.7m	9m	2m	
1	0.5	0.4	192.1	86.5	0.5	1.2	248.0	62.6	8.6	4.5	14.1	NaN	-3.2	-0.1
2	0.7	0.5	319.3	58.4	0.6	1.2	210.3	82.9	14.7	11.7	3.7	7.1	-3.3	0.0
3	0.9	0.9	10.8	39.0	0.5	1.8	78.3	61.7	43.1	6.2	4.5	4.4	-2.8	0.0
4	0.8	0.8	10.8	47.4	1.0	2.6	17.3	39.7	8.3	2.8	1.5	1.6	-2.9	0.0
5	0.1	1.0	0.9	63.1	0.8	2.8	350.5	34.8	14.3	2.6	2.2	1.2	-3.3	0.0
6	0.4	1.7	51.0	72.6	0.6	2.0	310.0	30.0	8.8	4.9	3.4	1.7	-3.2	0.1
7	0.3	1.9	62.6	68.4	1.0	0.7	232.9	16.4	9.0	8.1	2.6	10.0	-3.5	0.0
8	0.6	1.7	125.5	83.3	0.8	0.7	232.6	29.1	8.5	14.2	1.6	8.0	-3.8	0.0
9	0.2	1.8	117.6	66.0	0.5	1.0	271.6	13.1	13.3	8.4	4.8	7.9	-3.1	0.0
10	1.2	2.0	27.7	41.3	1.0	0.7	275.7	346.0	7.3	7.9	0.7	3.2	-3.3	0.0
11	1.2	2.5	25.5	38.5	1.1	1.1	283.3	324.4	7.1	7.8	0.3	NaN	-3.8	0.0
12	0.8	2.5	0.2	36.7	1.0	1.4	276.5	308.6	8.4	7.3	0.6	0.9	-4.2	0.0
Avg. L											3.34	4.6		
z/L											2.69	1.96		
Ri _b													1.13	

200 m arc moved to a northeast position late in the IOP. The other two analyzers each moved several times during the IOP along the 400 m arc. They operated at fixed locations to the northeast for much of the IOP.

Overall, IOP7 had some resemblance to IOP5 but was likely less affected by the shift in wind directions and shearing off of the plume at a low height. Much more SF₆ was measured at heights above 5 m than during IOP5. As a consequence, IOP7 is probably the single best nighttime test.

Wind Speed and Direction Quality Assurance

Figures 232-234 show wind speed and direction time series comparisons for a sequence of measurement heights during IOP7. In Fig. 232, the near surface measurement of U showed some variation but was mostly less than 1 m s⁻¹ for most of the tracer measurement period before increasing slightly to 1 m s⁻¹ or a little more late in the period. Wind directions were highly variable until past the midway point of the measurement period when the directions became more organized from the west-northwest. An exception to this was the 2 m wind direction at COC. This organization probably explains the better defined plumes seen in the second hour (see Bag Sampling Results below). Above the surface, the wind direction was from the northeast until after 0500 h at which time it switched to northwest. By 30 m agl and above, wind directions were consistently from the northeast throughout the IOP (Fig. 234). Wind directions were mostly

consistent between different locations and measurement types above 9 m (Figs. 233 and 234). Measured U at SOD appeared to have been biased a little low with respect to the cup or sonic anemometers. Almost no SOD data was recovered from the 160 m level so there is no basis for comparison between the SOD and PRO measurements. The 2 and 10 m wind direction measurements at COC vary from their peers at each height. However, this does not seem unreasonable given the numerous other examples of spatial inhomogeneity observed during IOP7. The observed variability or discrepancies are likely attributable primarily to non-stationarity and spatial inhomogeneity in the wind field. Other than the poor data recovery for SOD at 160 m agl, there is little evidence of any serious, systematic measurement problem.

The Brunt-Väisälä frequency N during IOP7 was the most consistently high of all the nighttime tests and consistent with the observed steep temperature gradients.

Figure 235 shows time series measurements for cup anemometers and wind vanes only (excluding sonics) at all heights on the GRI and COC towers during IOP7. Again, the near surface measurements of U at GRI and COC were low at mostly 1 m s^{-1} or less but the sometimes much larger U at heights above 30 m suggest a steep vertical gradient. Wind directions at 2 m on COC and GRI varied significantly over time and with each other. By about 0500 h, 2 m wind directions at GRI began to organize at west-northwest and the 10 and 15 m wind directions followed a short time later. However, COC at 2 m still showed considerable variation and did not shift to a more westerly wind direction until the end of the measurement period. Wind directions at 30 m and above were from the northeast throughout the IOP. The measured σ_θ at 2 m on GRI exhibited large variations in the first half hour of the measurement period but then settled to being generally $< 10^\circ$. The σ_θ at 2 m on COC varied considerably throughout the IOP. Above 2 m the σ_θ were generally $< 5\text{-}10^\circ$. The temperature time series suggest a steep temperature gradient with a ΔT of $4\text{-}6^\circ \text{ C}$ between 2 and 60 m agl.

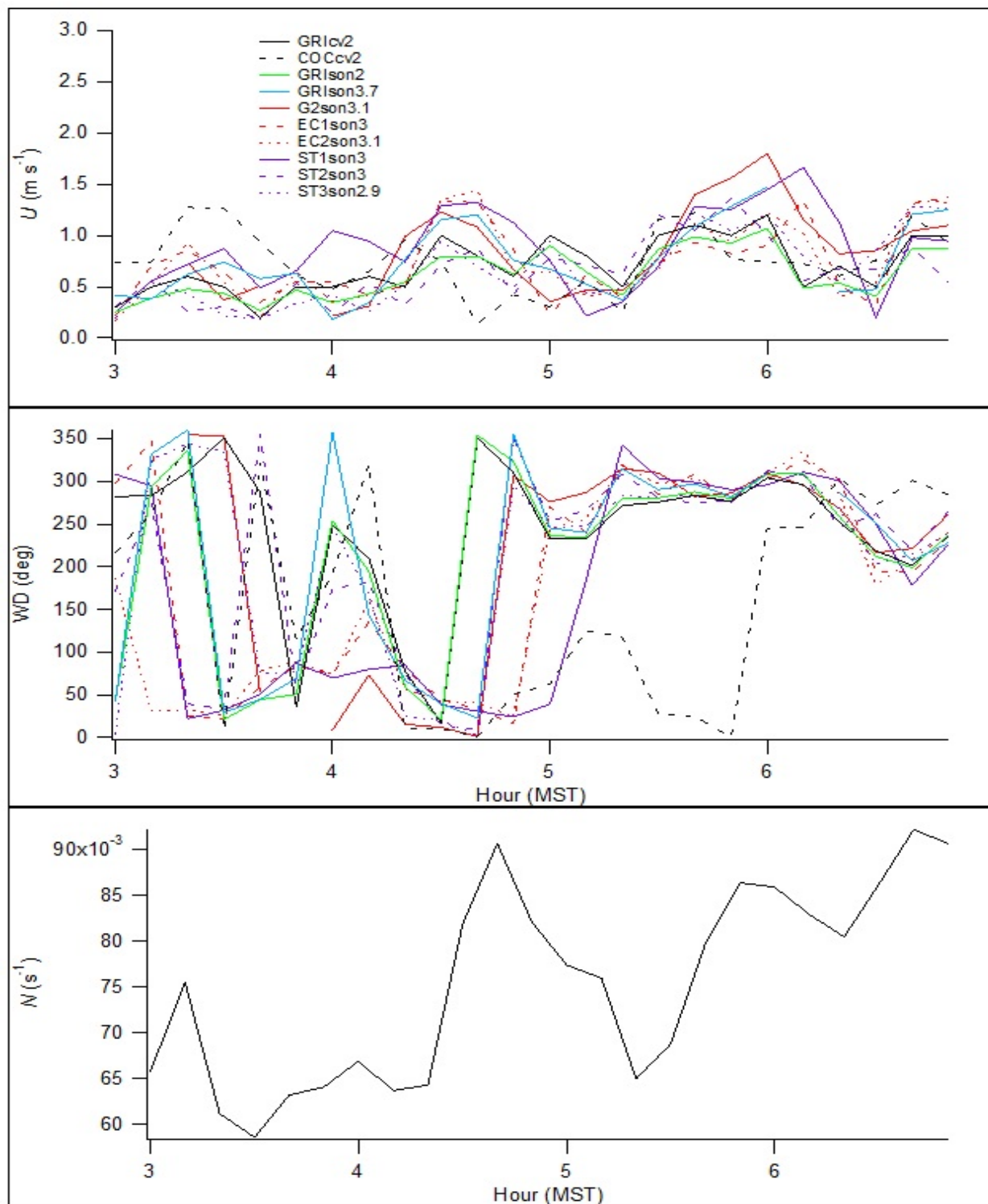


Figure 232. Time series of near surface wind speed and direction measurements and Brunt-Väisälä frequency N between 2 and 15 m agl during IOP7. In the legend, location is specified in upper case, the measurement type in lower case (cv = cup/vane, son = sonic), and the measurement height numerically.

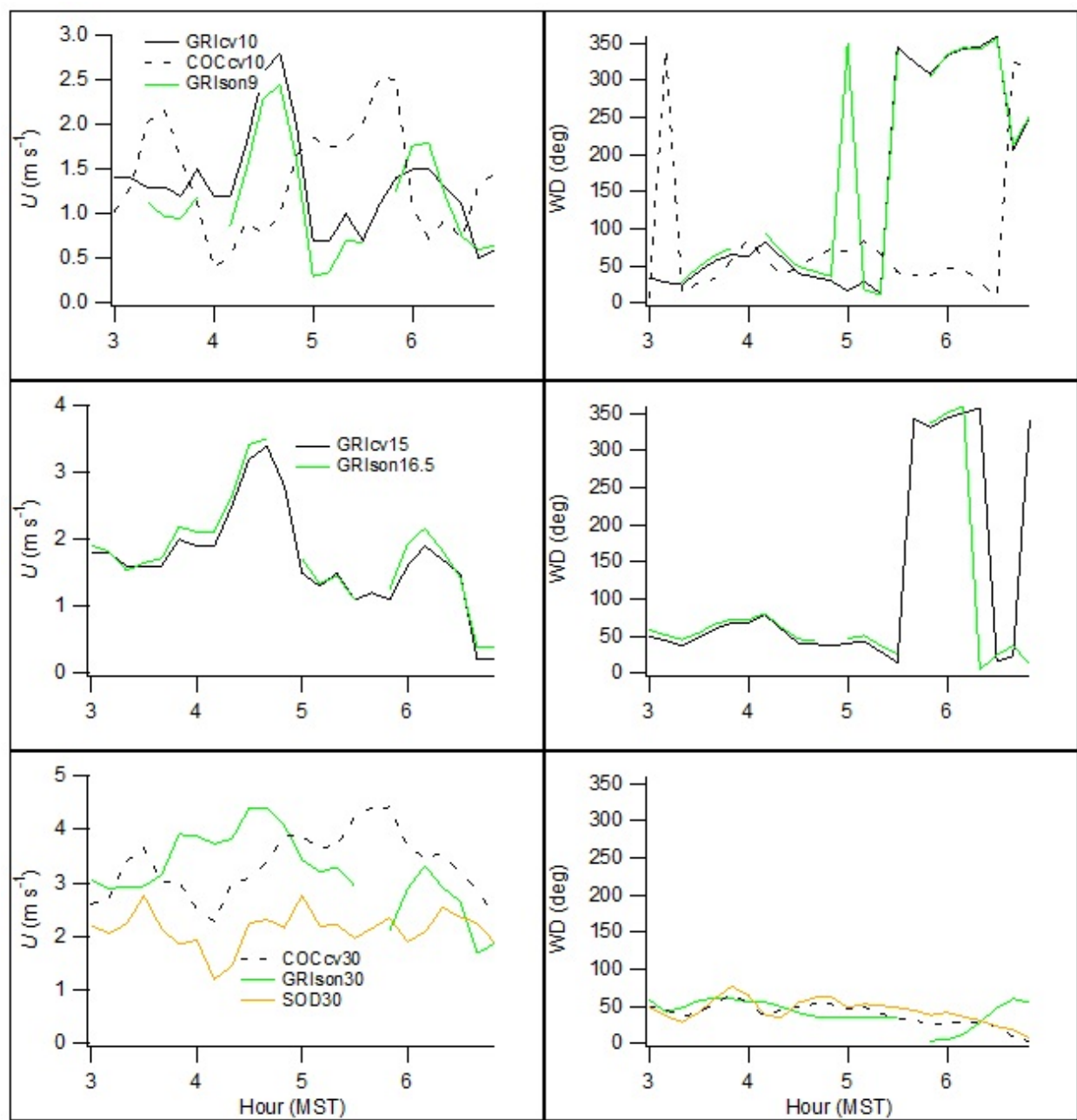


Figure 233. Time series of wind speed and direction measurements at heights between 9 and 30 m agl during IOP7. Legend notations described in caption of Fig. 232.

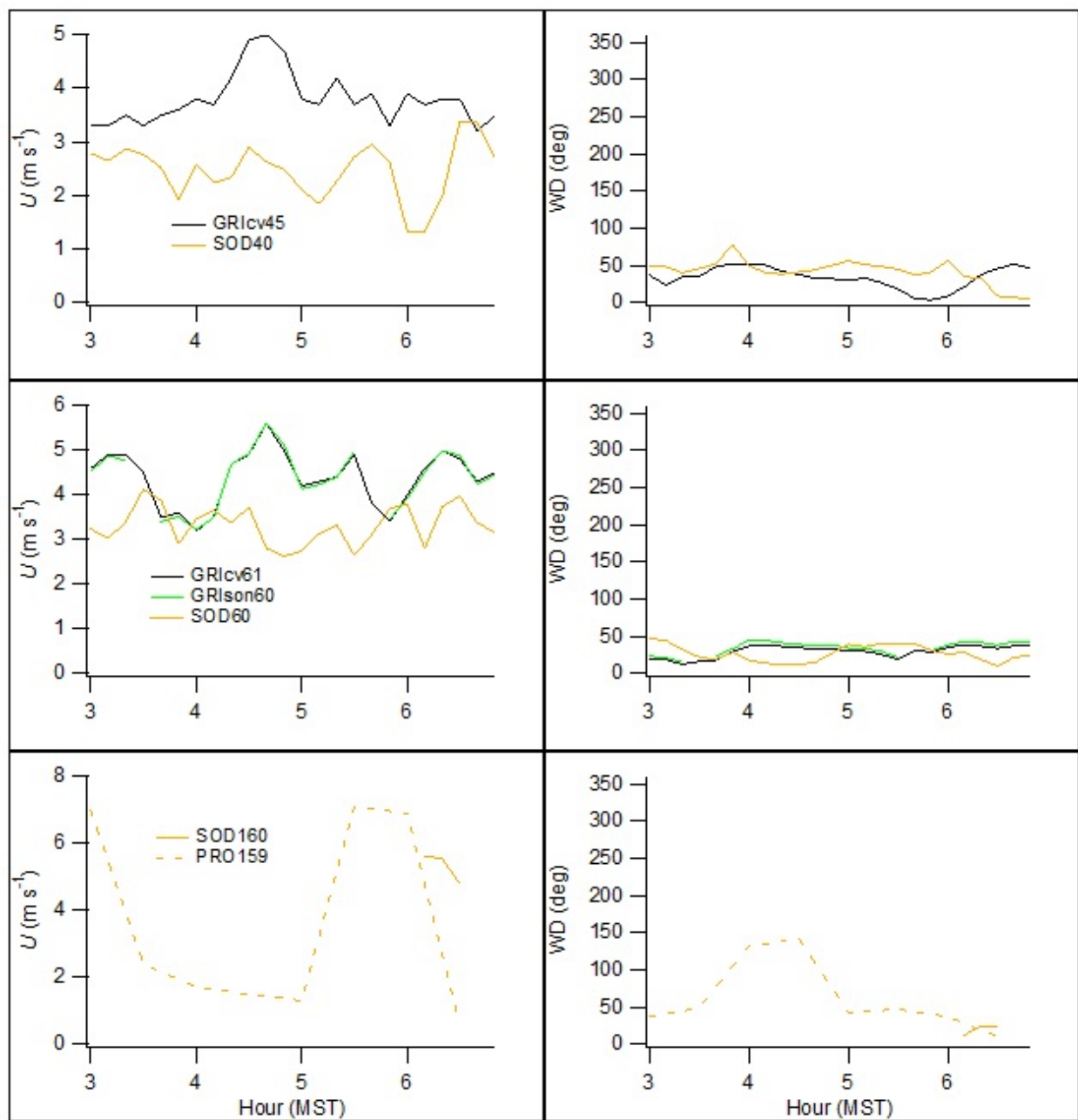


Figure 234. Time series of wind speed and direction measurements at heights above 30 m agl during IOP7. Legend notations described in caption of Fig. 232.

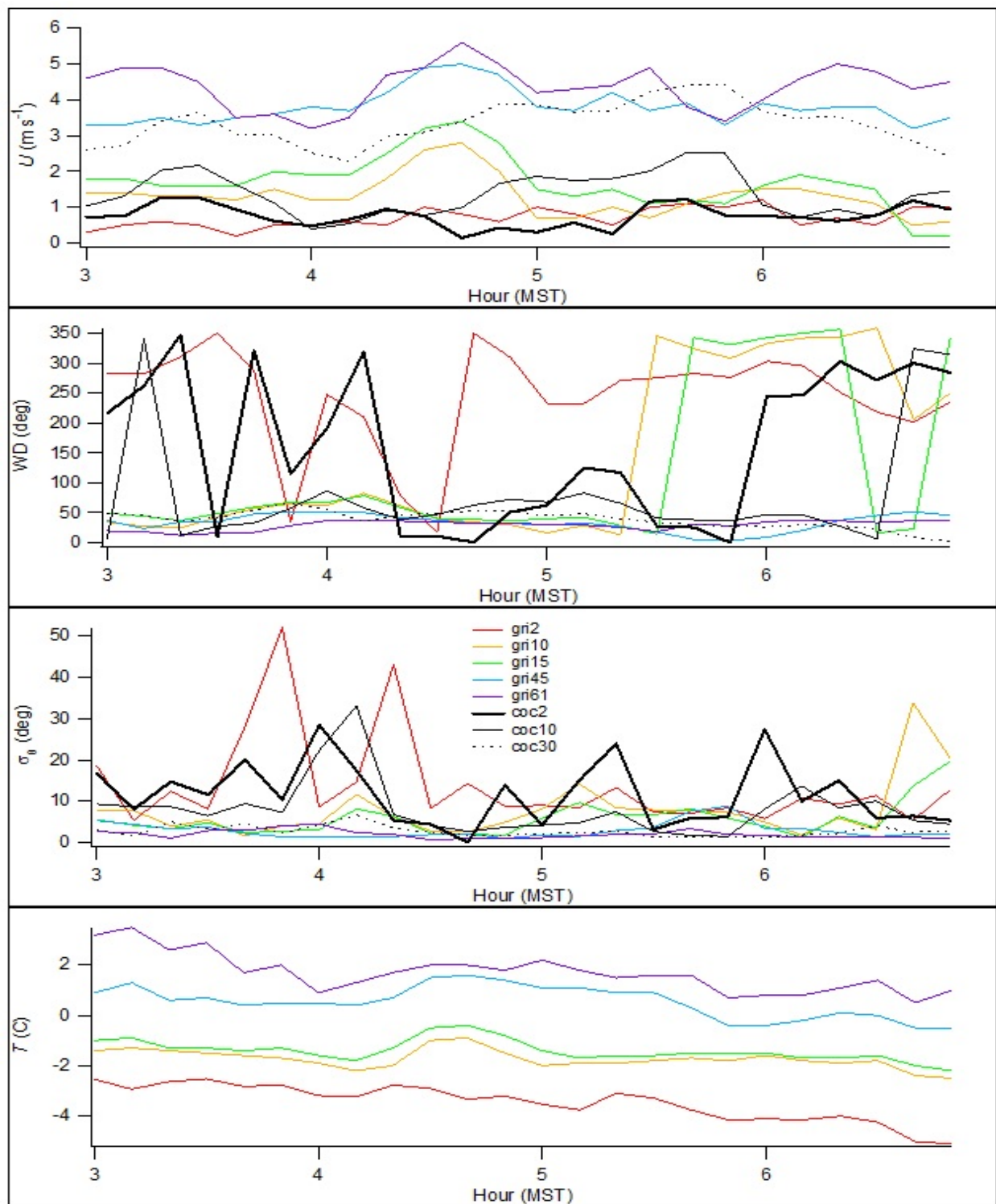


Figure 235. Time series from GRI and COC showing cup anemometer and wind vane measurements of U , wind direction, standard deviation of wind direction σ_θ , and temperature during IOP7. The locations are designated 'xxxxy' where xxx = tower and yy = measurement height.

Turbulence

Near-surface turbulence measurements for IOP7 are shown in Fig. 236. The magnitudes of all the measurements of turbulence were very low but showed large, irregular variability in both space and over time. The TKE, σ_w , and u_* were smaller still than those measured during IOPs 5 and 6 and much smaller than during the daytime IOPs. The measurements of σ_v/U and σ_w/U exhibited large variations and often very large excursions from more baseline values. These were likely due in significant part to the very low U . TKE, σ_w , and u_* also exhibited large variability although the variability was not quite as significant and the intermittent turbulent excursions were not as extreme. The excursions might reflect the more intermittent nature of turbulence inherent to the stable boundary layer. In IOPs 5 and 6, station ST2 stood out as having the strongest association with turbulence intermittency. The wind directions during IOP7 varied somewhat from those of IOPs 5 and 6 and this is perhaps expressed in the more varied set of stations exhibiting strong turbulence intermittency. ST2 is still represented but its most significant event occurred just after tracer sampling was completed at 0600 h. Other sites showing some large excursions include ST1, ST3, EC1, and EC2. Given the observed wind directions, there is not a ready unifying explanation based on topographical factors to explain these observations. The magnitude of the sensible heat flux was small and generally negative but with some much larger negative spikes and a few smaller positive spikes.

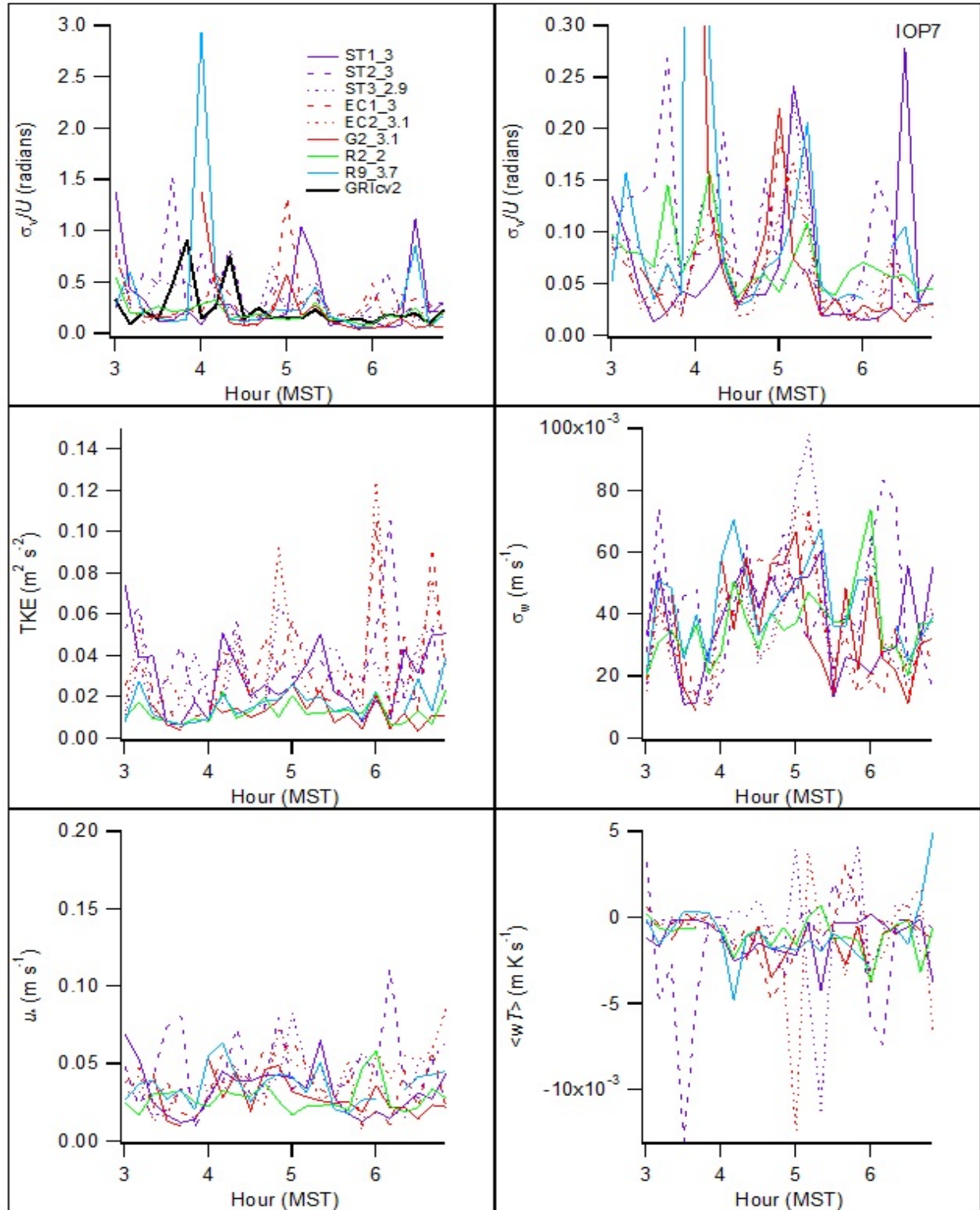


Figure 236. Time series of near surface turbulence (sonic) measurements during IOP7. The GRI and COC are σ_0 wind vane measurements (cv) in degrees converted to radians for purposes of comparison. Notation before and after underscore designates location and height, respectively.

Wind and Turbulence Profiles

Figure 237 shows profiles of the non-sonic measurements at GRI and COC during IOP7. These show smooth, steep gradients in U during the first hour at both GRI and COC. However, in the second hour, the gradient relaxes slightly and there are distinct irregularities in the GRI profiles of U below 15 m and a break in gradient at 45 m. Meanwhile, the COC profiles remain smooth. This is consistent with the earlier observation of the wind direction shifts occurring at GRI in the second hour that were delayed at COC (Fig. 235). The GRI wind directions at 2 m ranged from northeast to northwest in the first hour before shifting to west-northwest in the second hour. During the first hour all wind directions at 10 m and above were from the northeast. During the second hour the height of the shift from northwest to northeast winds began to increase. In contrast, wind directions at COC were commonly from the northeast at all heights for most of the IOP. The σ_θ were large near the surface during the first hour, decreasing sharply in the second hour. The temperature gradients ranged upwards to 5-6 degrees C between 2 and 60 m agl throughout the IOP.

Figures 238 and 239 show profiles of the sonic turbulence measurements at GRI during IOP7. Wind speeds and directions were similar to that seen in Fig. 237 for GRI. These also show west-northwest and northeast wind directions below 10 m in the first hour becoming uniformly northeasterly above that. During the second hour the height of the shift from northwest winds at the surface to northeast winds aloft lifted. A notable feature of the σ_v/U and σ_w/U profiles were sharp deviations for some 10-min intervals at the 3.7 and 9 m heights before decreasing rapidly upward to very low values. TKE, σ_w , and u_* showed similar deviations in profile for some 10-min periods throughout the 2 h tracer measurement period, mainly at the 9 and 16.5 m levels. The increase in turbulence at that level might be linked to the shift in wind directions from west-northwest below to northeast above. The virtual temperature gradients were large throughout the experiment with irregularities in the profiles common below 10 m.

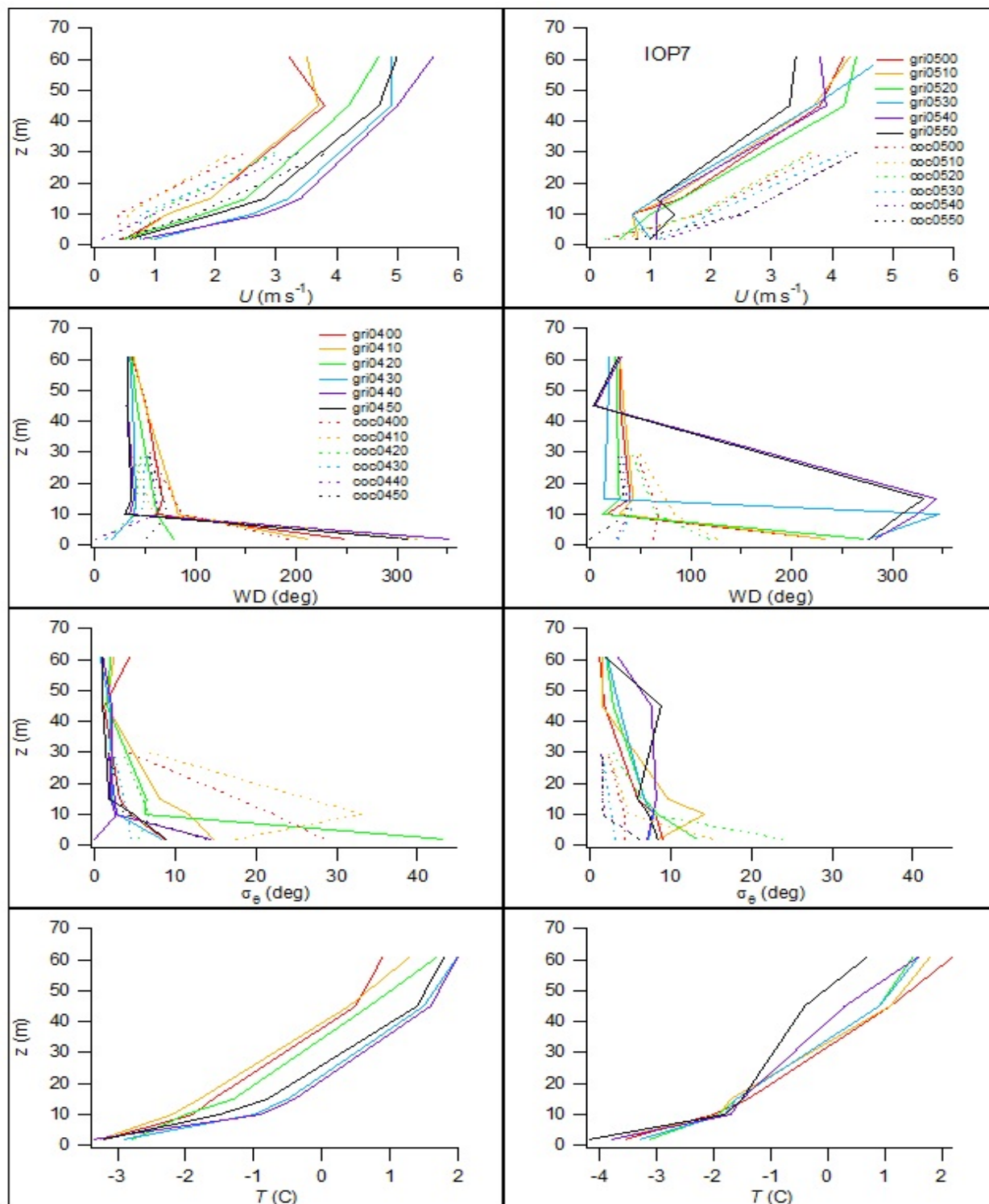


Figure 237. Profiles of U , wind direction, standard deviation of wind direction σ_θ , and aspirated temperature from cup anemometers and wind vanes during IOP7 at GRI and COC. Each profile is designated 'xxxhrmn' where xxx = tower and hrmn = start time of 10-minute interval.

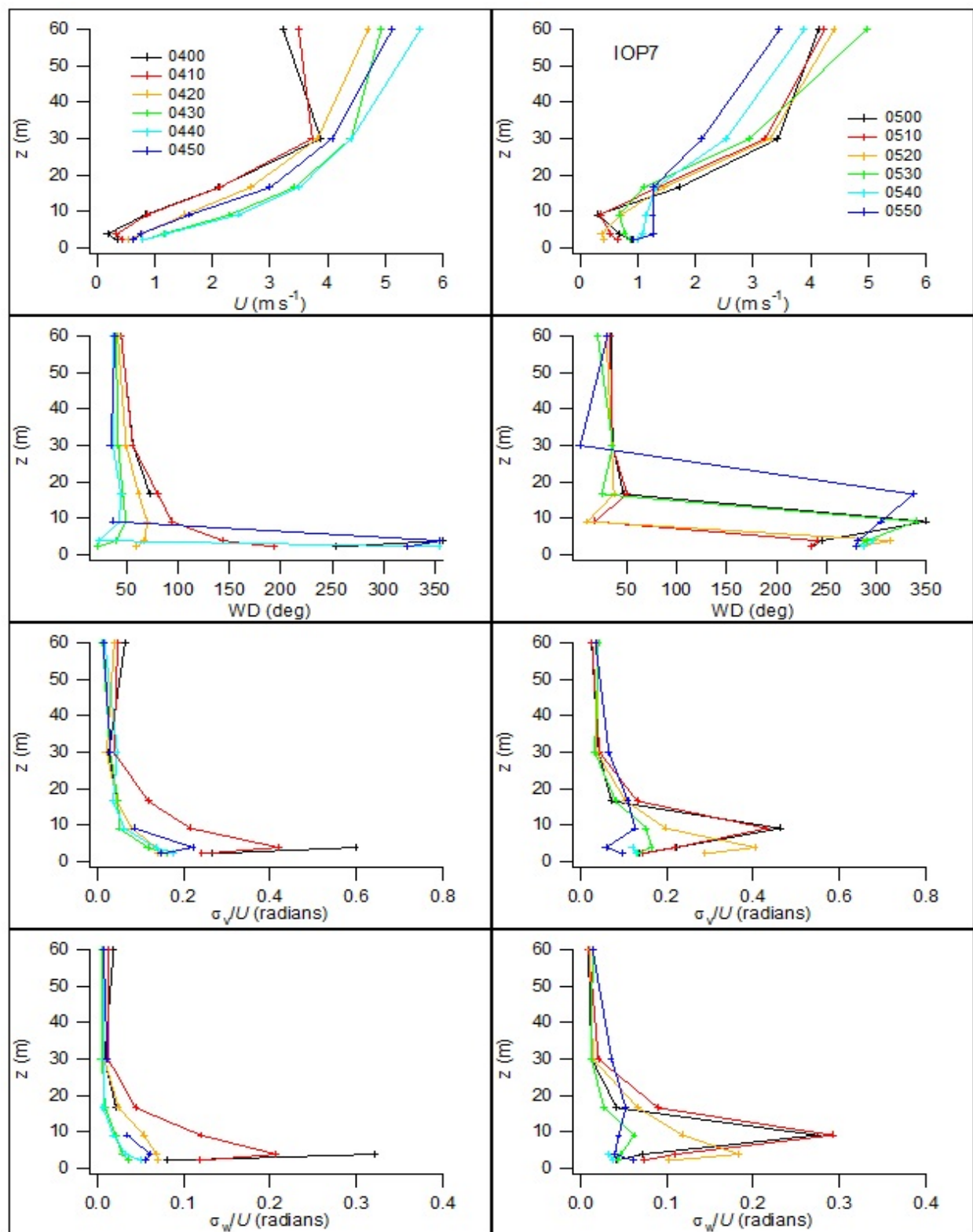


Figure 238. Profiles of U , wind direction, σ_v/U ($\sim\sigma_\theta$), and σ_w/U ($\sim\sigma_\phi$) from sonic anemometers at GRI during IOP7. The legend specifies the start time of the 10-min interval (hrmn).

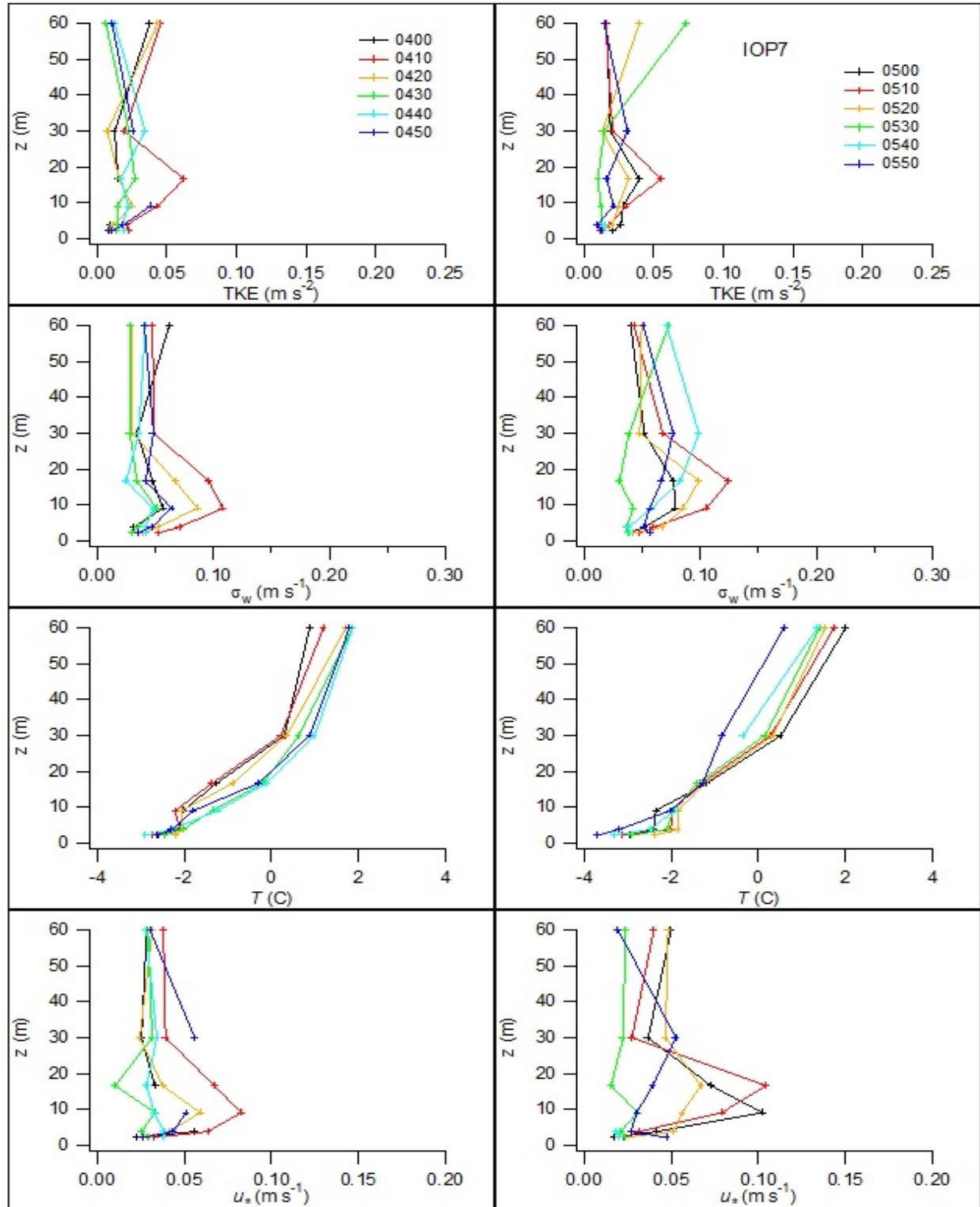


Figure 239. Profiles of turbulent kinetic energy (TKE), standard deviation in vertical wind speed σ_w , virtual temperature, and friction velocity u_* from sonic anemometers at GRI during IOP7. The legend specifies the start time of the 10-min interval (hrmn).

Figures 240 and 241 show time-height representations of wind speed and direction for SOD and PRO, respectively, during IOP7. The northeast wind directions in Fig. 240 are consistent with the wind directions on GRI (Figs. 237, 238) but the magnitudes of U at the upper levels of GRI tended to range a little higher at about $4\text{--}5\text{ m s}^{-1}$. Again, there is a suggestion of a zone of higher U at about $100\text{--}120\text{ m agl}$. This might be partly attributable to measurement anomalies near the top of the profiles but many of the higher U are not at the top of the profiles. This hints at the presence of a jet-like feature embedded in northeast winds at about $100\text{--}120\text{ m agl}$ as was also described in the summaries for IOPs 5 and 6. Figure 241 suggests the presence of a zone up to about 500 m agl is characterized by light winds with variable directions. At 500 m there is a hint of a decrease in U before U again increased upwards with southwesterly winds. A somewhat analogous pattern was seen in IOPs 5 and 6. The low level U appear to be biased a little low relative to the observed U at SOD, at least during the first half of the test. The zone of much higher U above about 2000 m agl in Fig. 241 is consistent with the radiosonde results (not shown, see project database).

Figures 242 and 243 show SOD time-height representations for σ_w and TKE, respectively, during IOP7. The σ_w during the tracer measurement period were generally very low. Values were slightly elevated around $100\text{--}120\text{ m agl}$, possibly in association with the hypothesized jet, and there was a distinct anomaly near the surface from about 0540 to 0600 h of

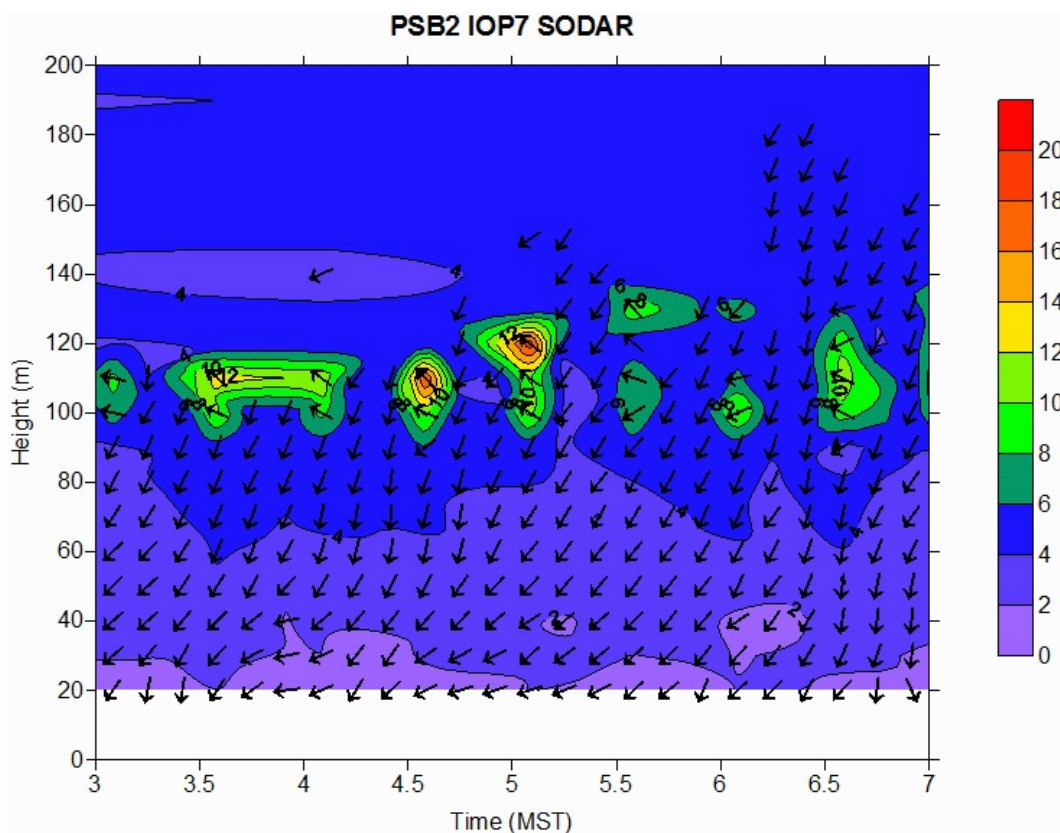


Figure 240. Time-height cross-section of wind speed and direction at sodar (SOD) during IOP7. Legend represents m s^{-1} .

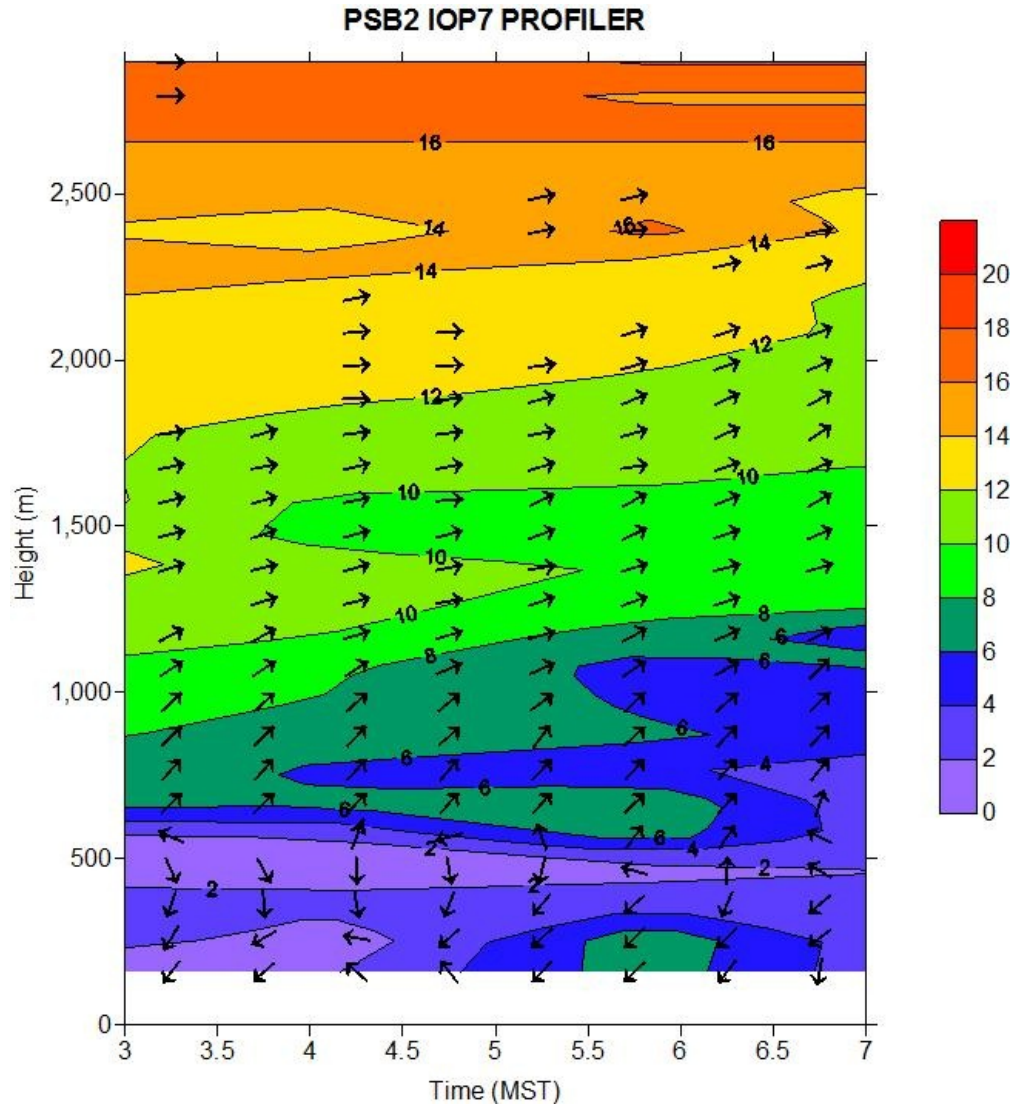


Figure 241. Time-height cross-section of wind speed and direction at wind profiler (PRO) during IOP7. Legend represents m s^{-1} .

unknown origin. That would be ahead of sunrise. TKE is low throughout the domain except for a distinct band of higher values between 100-120 m agl. This is again consistent with the zone of higher U at the same levels (Fig. 240). Figure 244 shows time-height temperature profiles from the RASS.

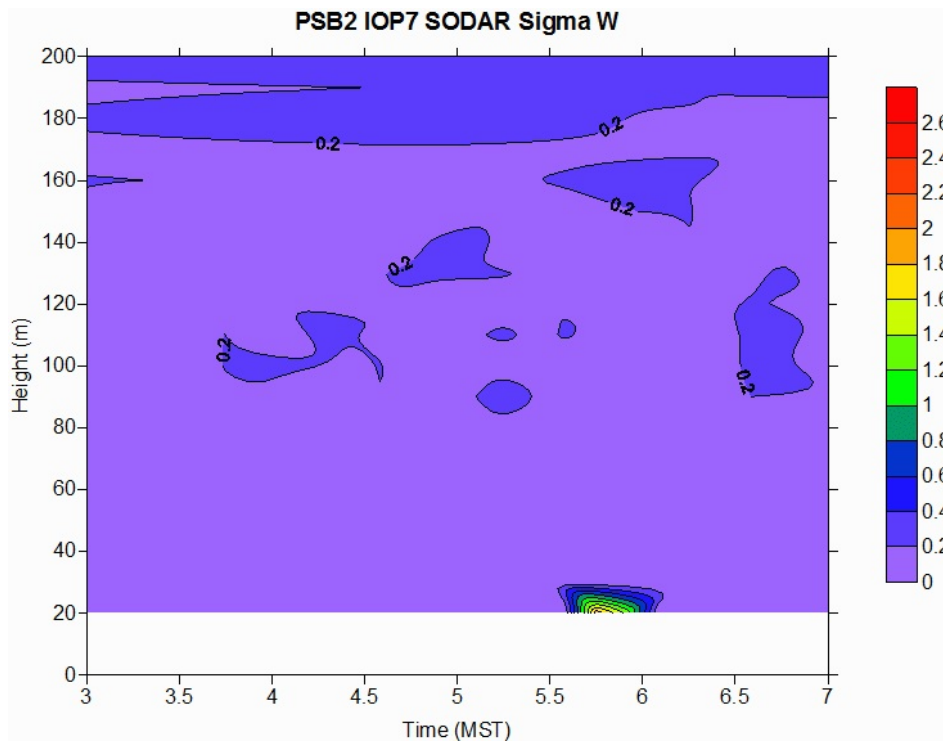


Figure 242. Time-height cross-section of σ_w at sodar (SOD) during IOP7. Legend represents m s^{-1} .

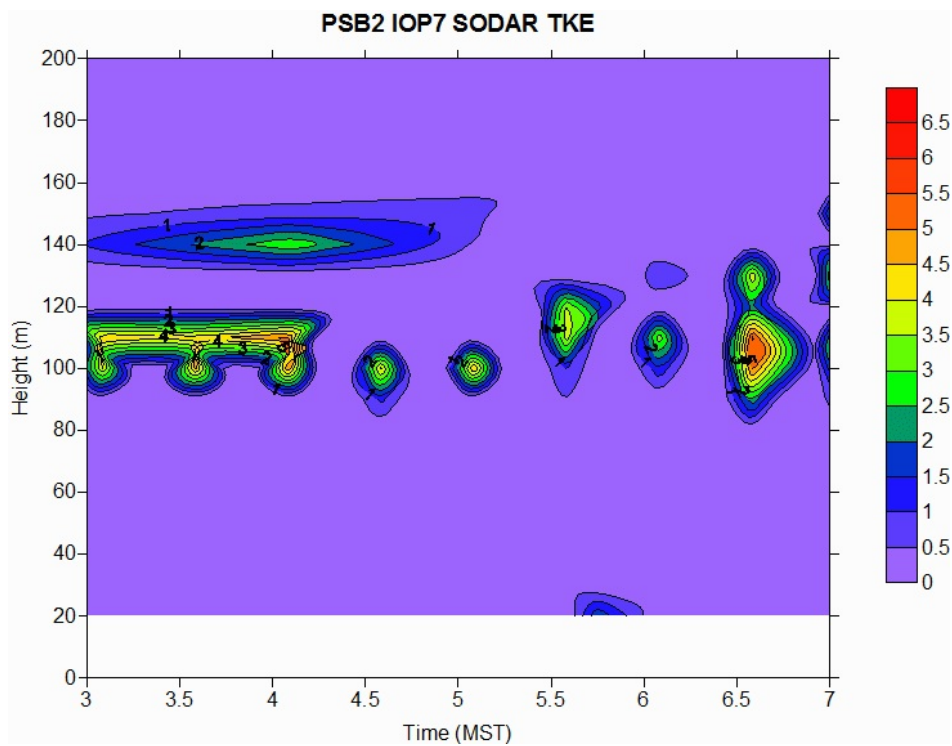


Figure 243. Time-height cross-section of TKE at sodar (SOD) during IOP7. Legend represents $\text{m}^2 \text{s}^{-2}$.

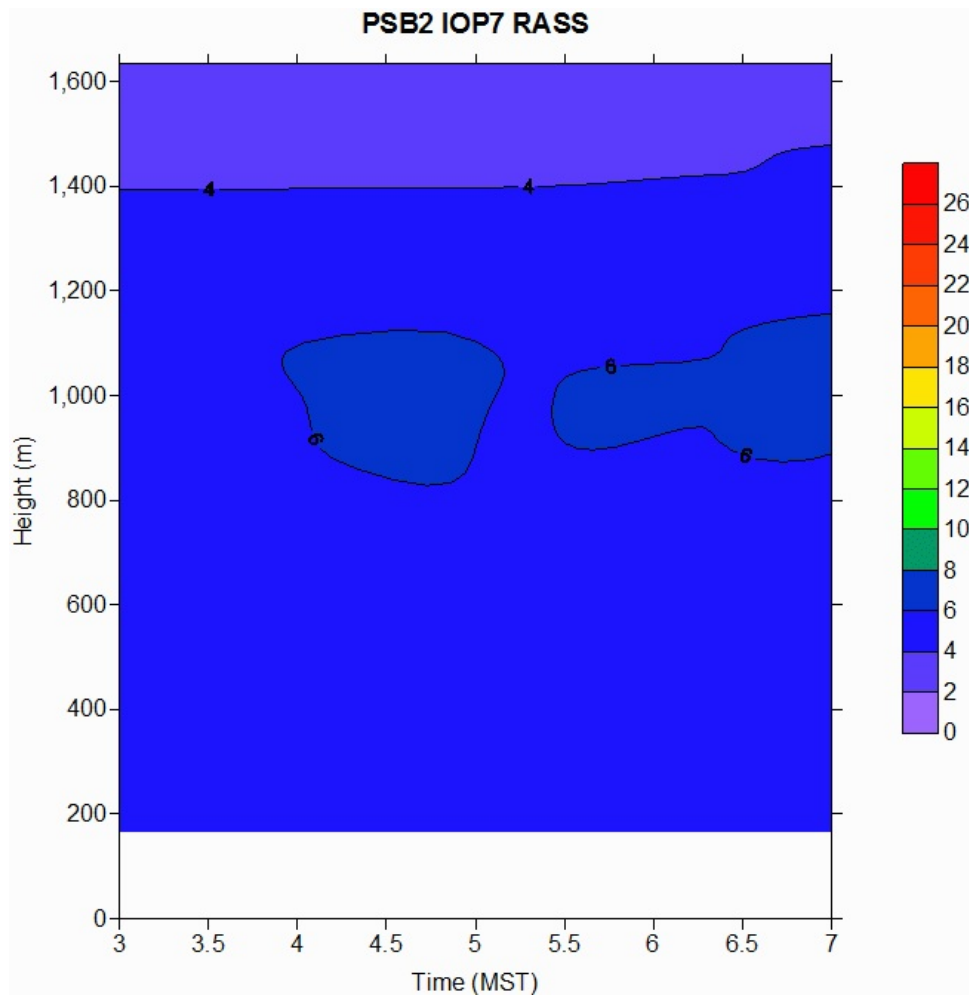


Figure 244. Time-height cross-section of virtual temperature at the RASS during IOP7. Temperatures are in degrees C.

Radiosonde Results

Pre and post-IOP radiosonde profiles of potential temperature and specific humidity for IOP7 are shown in Figs. 245 and 246. There is no constant potential temperature layer in Fig. 245 and it provides no basis for selecting a mixing height. Similar to IOPs 5 and 6, the specific humidity profiles in Fig. 246 suggest some layering or structure to the boundary layer. There are prominent breaks in the profiles of specific humidity at about 1000 and 1200 m. However, there is no basis for an unambiguous selection of the boundary layer depth. Data recovery by the ceilometer results was very sparse and does not provide much basis for interpretation (Table 27).

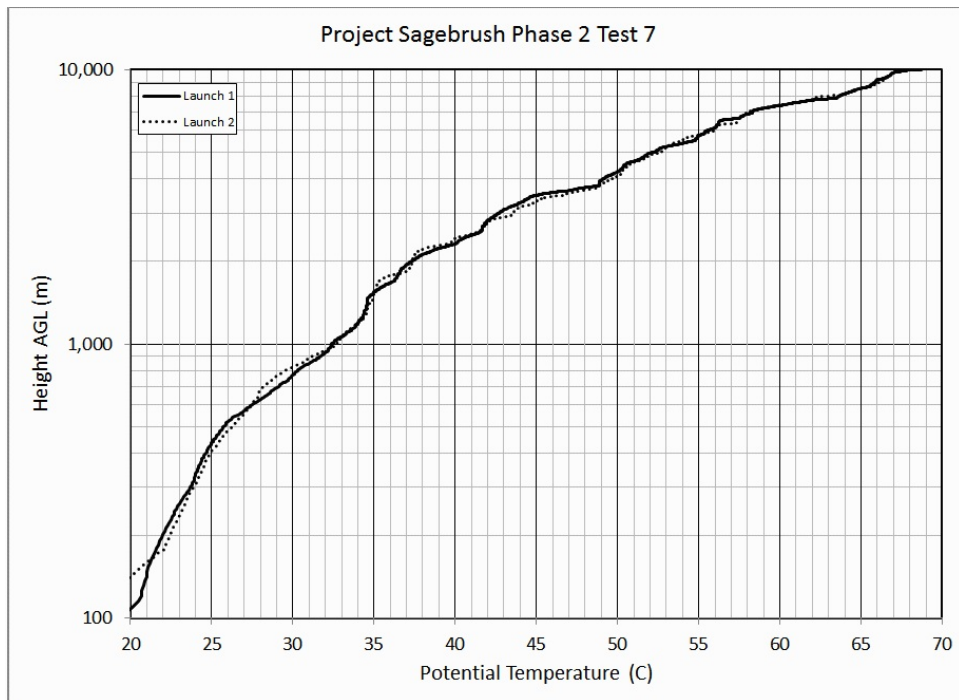


Figure 245. Potential temperature profile from radiosonde probe, IOP7. Pre-test launch bold, post-test launch dotted.

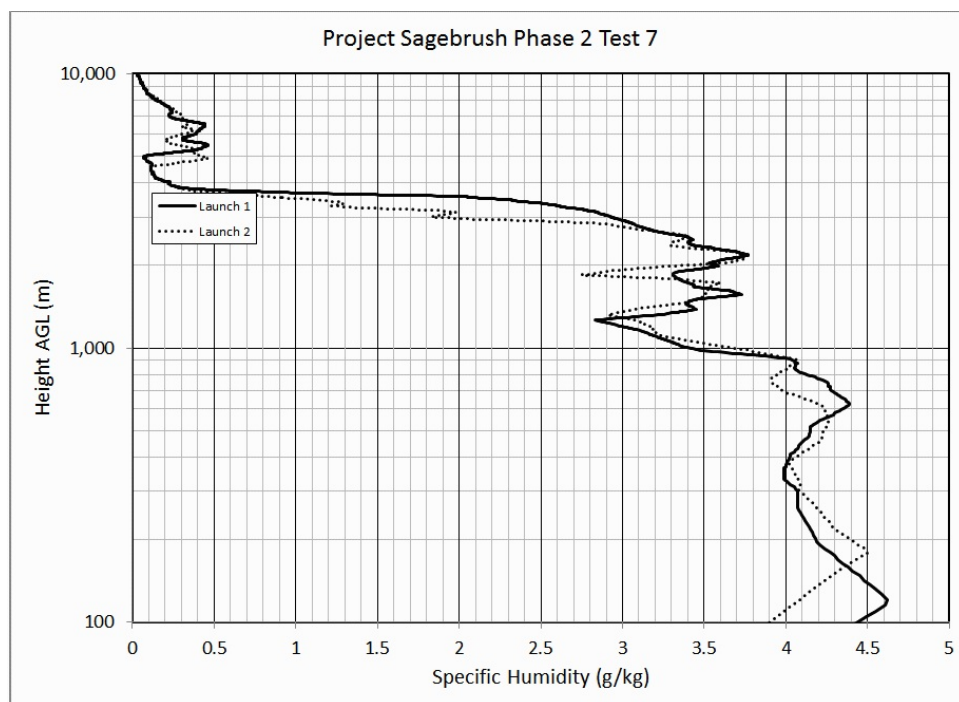


Figure 246. Specific humidity profile from radiosonde probe, IOP7. Pre-test launch bold, post-test launch dotted.

Table 27. Ceilometer estimates of boundary layer heights during IOP7.

Date	Time	BL	BL	BL	BL	BL	BL	Cloud	
(yyyymmdd)	(MST)	Height 1	Index 1	Height 2	Index 2	Height 3	Index 3	Status	Cloud 1
		(m)		(m)		(m)			(m)
20161021	3:05	-999.9	-999.9	-999.9	-999.9	-999.9	-999.9	0	-999.9
20161021	3:15	-999.9	-999.9	-999.9	-999.9	-999.9	-999.9	0	-999.9
20161021	3:25	-999.9	-999.9	-999.9	-999.9	-999.9	-999.9	0	-999.9
20161021	3:35	-999.9	-999.9	-999.9	-999.9	-999.9	-999.9	0	-999.9
20161021	3:45	-999.9	-999.9	-999.9	-999.9	-999.9	-999.9	0	-999.9
20161021	3:55	570.00	1.5	-999.9	-999.9	-999.9	-999.9	0	-999.9
20161021	4:05	570.33	2	-999.9	-999.9	-999.9	-999.9	0	-999.9
20161021	4:15	590.00	1.5	-999.9	-999.9	-999.9	-999.9	0	-999.9
20161021	4:25	-999.9	-999.9	-999.9	-999.9	-999.9	-999.9	0	-999.9
20161021	4:35	-999.9	-999.9	-999.9	-999.9	-999.9	-999.9	0	-999.9
20161021	4:45	-999.9	-999.9	-999.9	-999.9	-999.9	-999.9	0	-999.9
20161021	4:55	-999.9	-999.9	-999.9	-999.9	-999.9	-999.9	0	-999.9
20161021	5:05	-999.9	-999.9	-999.9	-999.9	-999.9	-999.9	0	-999.9
20161021	5:15	-999.9	-999.9	-999.9	-999.9	-999.9	-999.9	0	-999.9
20161021	5:25	573.00	2	-999.9	-999.9	-999.9	-999.9	0	-999.9
20161021	5:35	580.00	1	-999.9	-999.9	-999.9	-999.9	0	-999.9
20161021	5:45	591.50	2	-999.9	-999.9	-999.9	-999.9	0	-999.9
20161021	5:55	600.00	1	-999.9	-999.9	-999.9	-999.9	0	-999.9
20161021	6:05	584.81	2	-999.9	-999.9	-999.9	-999.9	0	-999.9
20161021	6:15	592.67	2	-999.9	-999.9	-999.9	-999.9	0	-999.9
20161021	6:25	590.00	1	-999.9	-999.9	-999.9	-999.9	0	-999.9
20161021	6:35	-999.9	-999.9	-999.9	-999.9	-999.9	-999.9	0	-999.9
20161021	6:45	-999.9	-999.9	-999.9	-999.9	-999.9	-999.9	0	-999.9
20161021	6:55	-999.9	-999.9	-999.9	-999.9	-999.9	-999.9	0	-999.9

Bag Sampling Results

Figures 247 and 248 and Figures 249 and 250 show the 10-min average normalized and actual, respectively, color-coded plan view concentration maps for IOP7 bag sampling at 1 m agl. Figures 251 and 252 and Figures 253 and 254 show the 10-min average normalized and actual concentrations, respectively, along each of the arcs.

IOP7 resembled IOP5 with both having very large horizontal plume spreads. However, unlike IOP5 during which bags 1-3 showed marked plume truncation, the plume was mostly bounded within the 210° sampling arcs for all 10-minute sampling periods. To be clear, plume truncation was definitely a factor but there were fewer instances of loss of major parts of the plume than during IOP5. One or both limbs of the plume showed some evidence of truncation at

the edge of the sampler array in all 10-min periods. Truncation was most common or severe during the first hour and on the 100 m arc. Essentially all 10-min average bag samples on the 100 m arc measured concentrations at least somewhat greater than ambient background levels. While truncation decreased with downwind distance, it was also common on the 200 and 400 m arcs as well. There were a few 10-min periods where above background tracer concentrations were measured at almost every bag sampler on all arcs.

The greater plume truncation during the first hour can be explained by recalling that the wind directions were in flux and clearly non-stationary during the first hour of measurements. Furthermore, the magnitude and variation of σ_θ were their greatest, especially on GRI (e.g., Figs, 232, 235, 236; Table 26).

The structure of the plumes was generally ill-defined on the 100 m arc during the first hour. Plume morphology on the 200 and 400 m arcs in the first hour sometimes approximated Gaussian but that was not always the case. In contrast, the plumes tended to have much better defined, approximately Gaussian forms during the second hour, even at the 100 m arc. There was generally a prominent, central, Gaussian-like peak over about 50-60 degrees of arc, sometimes more, that tended to narrow downwind. However, this was bounded by broad, ragged, irregular flanks featuring considerable variability, especially on the 100 m arc. Again, the better organized plumes of the second hour can probably be linked to the consolidation of wind directions from mainly the west-northwest past the midway point of the measurement period. An exception to this was the 2 m wind direction at COC.

The two salient points made about the IOP5 plume measurements also apply to the IOP7 measurements. First, the horizontal plume spread, while generally less than during IOP5, was still much larger than that suggested by the measured σ_θ . The degrees of arc subtended by the plume during IOP7 was often similar to the degrees of arc intersected during the daytime IOPs. This was the case in spite of the much larger daytime σ_θ relative to IOP7. These IOP5 and IOP7 results suggest a breakdown of the traditionally understood link between horizontal plume dispersion and the magnitude of σ_θ in stable, low wind speed, nighttime conditions.

Second, the maximum normalized concentrations during IOP7 ranged up to two orders of magnitude greater than the maximum normalized daytime concentrations. This is clearly shown in the cross-sections in Figs. 251 and 252 (compare Figs. 84, 85, 111, 112). Also recall that the color-coded normalizations in the map views of Figs. 247 and 248 were suppressed by a factor of 10 relative to the daytime normalizations yet they feature an abundance of red and orange markers that are only sparsely present in the corresponding daytime plots. This was also the case for IOP5.

The variability in the wind (Figs. 232, 235; Table 26) and turbulence (Fig. 236) fields in time and space likely contributed to the significant plume spread and numerous irregularities in concentrations. The irregularities in concentration are consistent with the often large differences in collocated duplicate sampling that occurred during the nighttime IOPs. This was described in

the bag sampling chapter. Recall that these large collocated differences were most acute on the 100 m arc and diminished downwind.

Figures 255 and 256 show the vertical concentration profiles at the four fixed towers and the mobile tower arranged by 10-min (bag) sampling period. Figures 257 and 258 show the temporal evolution of the vertical concentration profiles at each of the five towers. A striking feature of these profiles is the extreme vertical concentration gradient during the first hour with SF₆ concentrations dropping sharply from several thousand ppt at 1 m to near ambient background concentrations within 5-10 m of the surface. Something similar to this was observed during IOP5 except it persisted for the whole IOP. As noted in the IOP5 summary, it is possible this is due, in part, to the suppression of vertical transport in a very stable atmosphere. However, a strong case can be made that this sharp cutoff is likely due in significant part to the shift to northeast winds above about 10 m. That is, any tracer that made it above about 10 m during the first hour was sheared off and transported toward the southwest, away from any tower measurement.

However, unlike IOP5, the second hour of IOP7 featured vertical concentration profiles with tracer concentrations greater than ambient background up to 15-20 m agl. Recall that the height of the shift to northeast wind directions was increasing through the second hour from about 10 m to something closer to 15-20 m (Figs. 237, 238). This would suggest that it was less likely that the top of the plume was being sheared off and that the plume was probably mainly contained within the more westerly flow near the surface during the second hour.

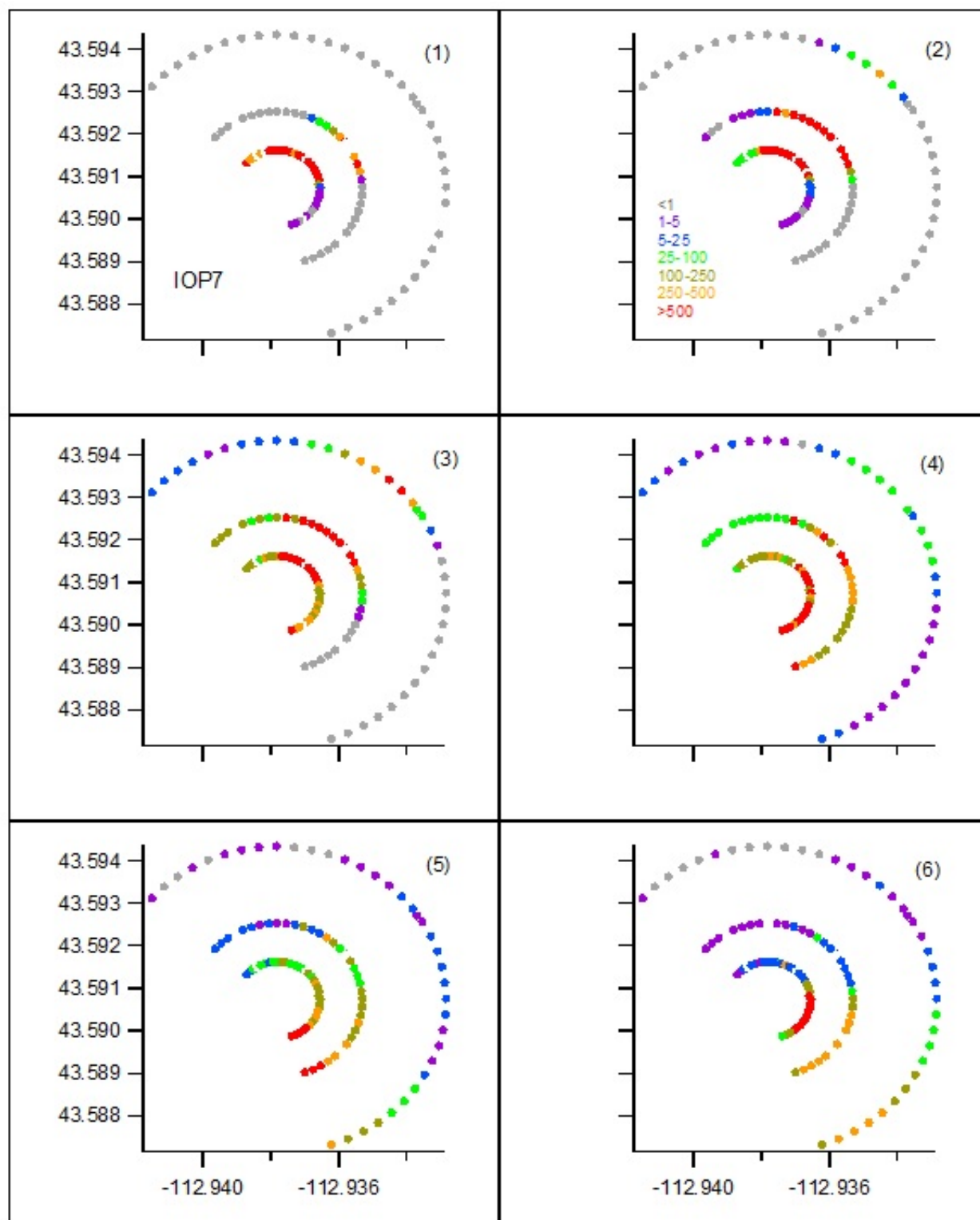


Figure 247. Color-coded normalized ($F^*\chi/Q$ ppt s g^{-1}) concentrations at 1 m agl for bags 1-6 during IOP7. The number in () is bag number.

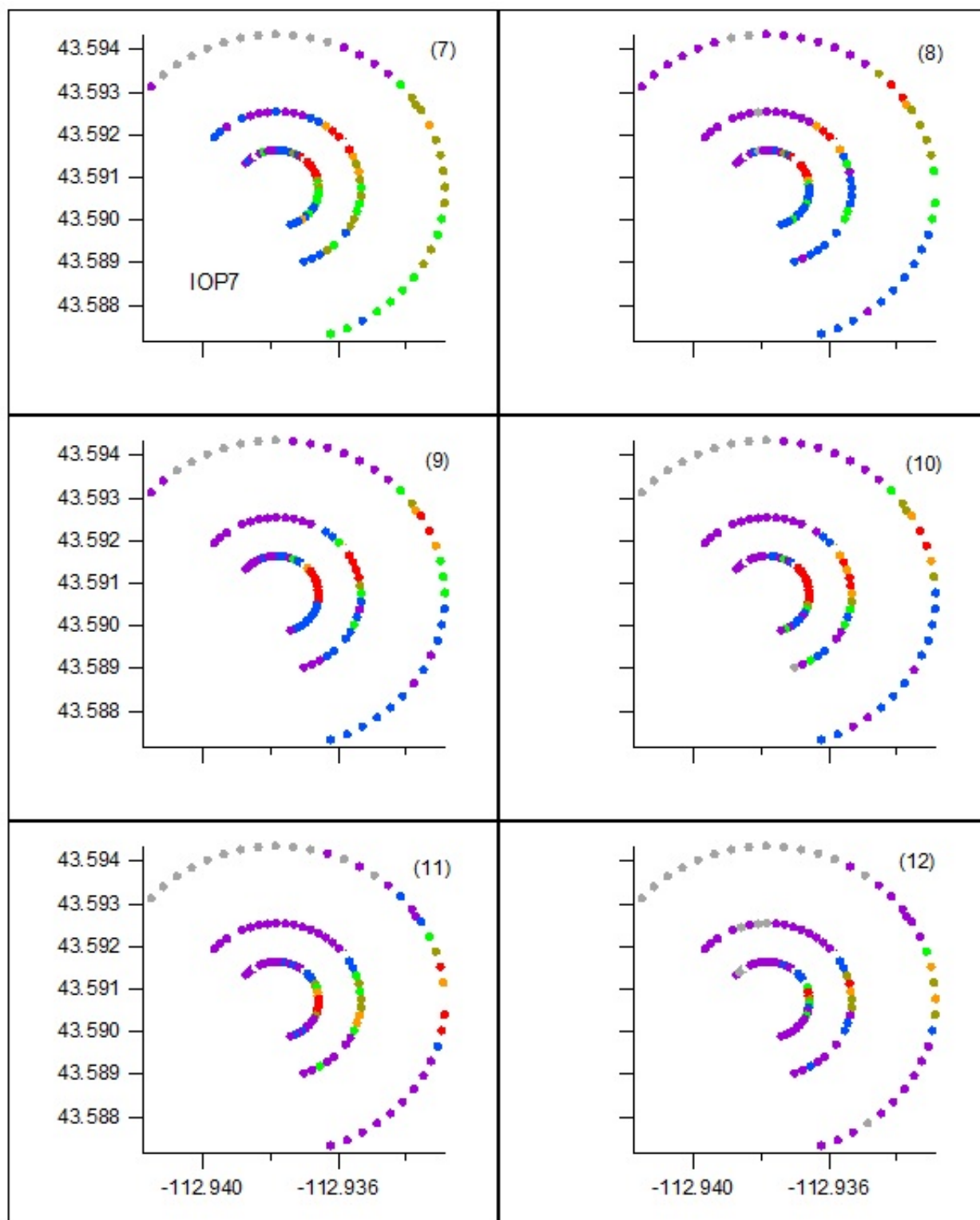


Figure 248. Color-coded normalized ($F^*\chi/Q$ ppt s g^{-1}) concentrations at 1 m agl for bags 7-12 during IOP7. The number in () is bag number.

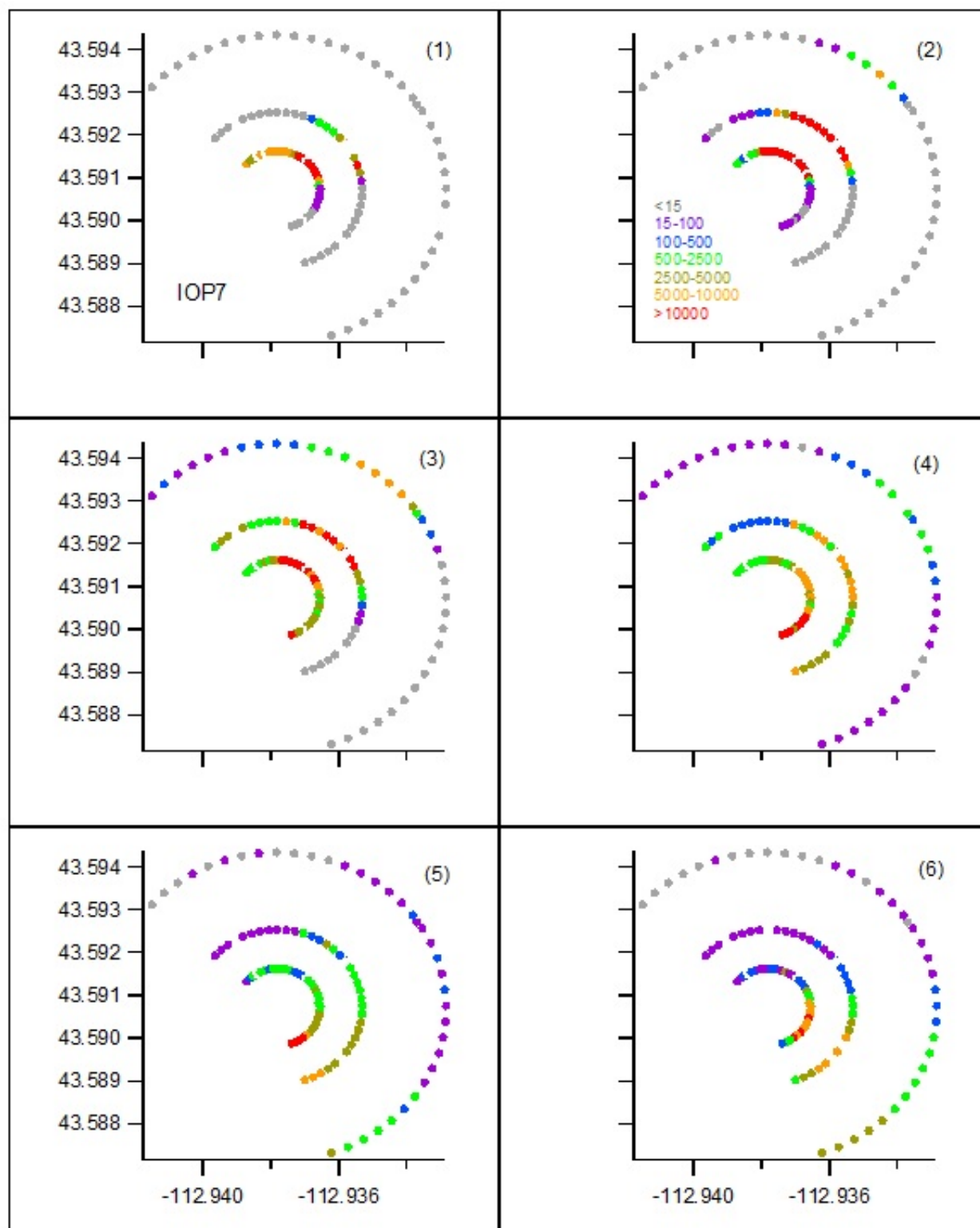


Figure 249. Color-coded measured SF_6 concentrations (ppt) at 1 m agl for bags 1-6 during IOP7. The number in () is bag number.

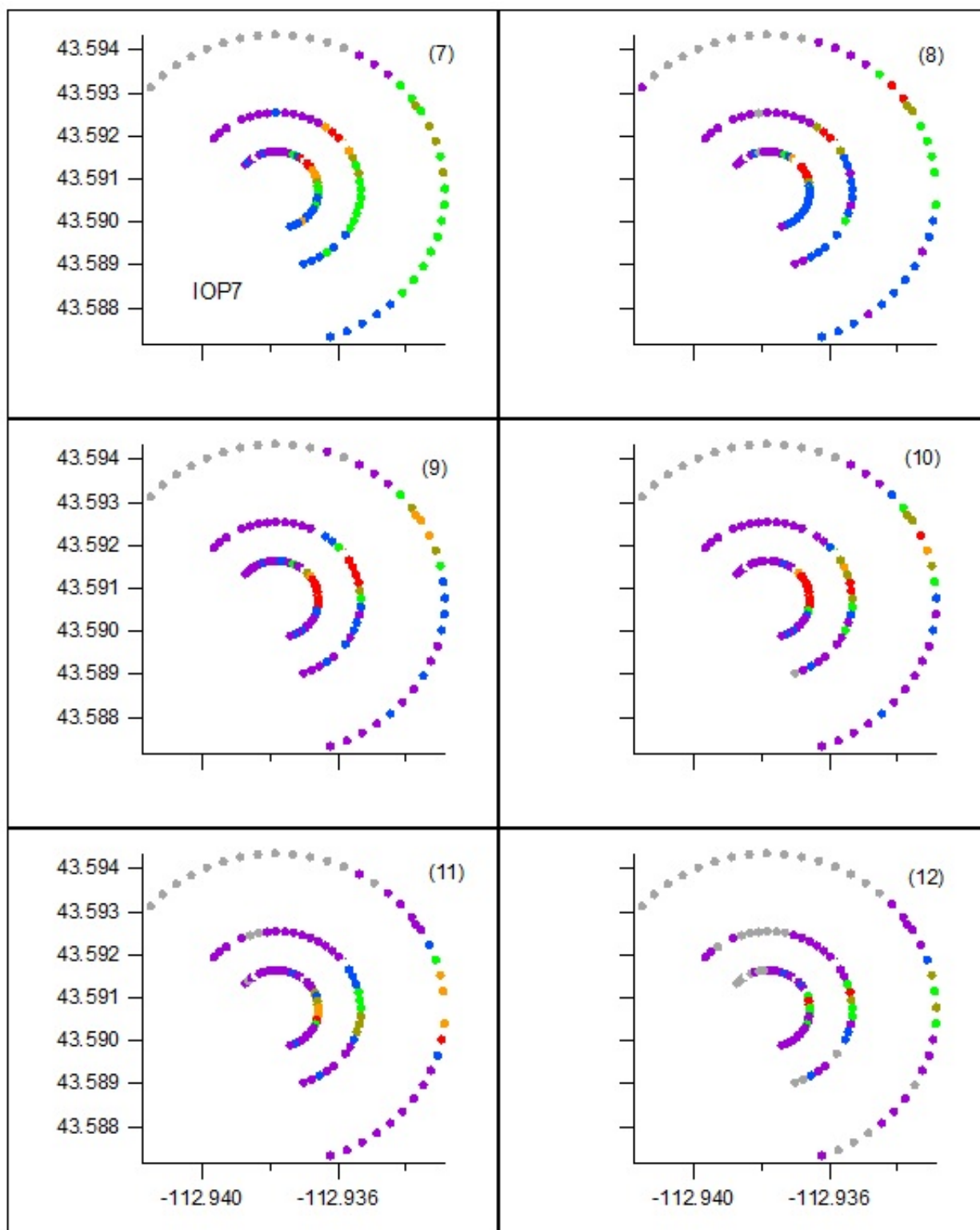


Figure 250. Color-coded measured SF_6 concentrations (ppt) at 1 m agl for bags 7-12 during IOP7. The number in () is bag number.

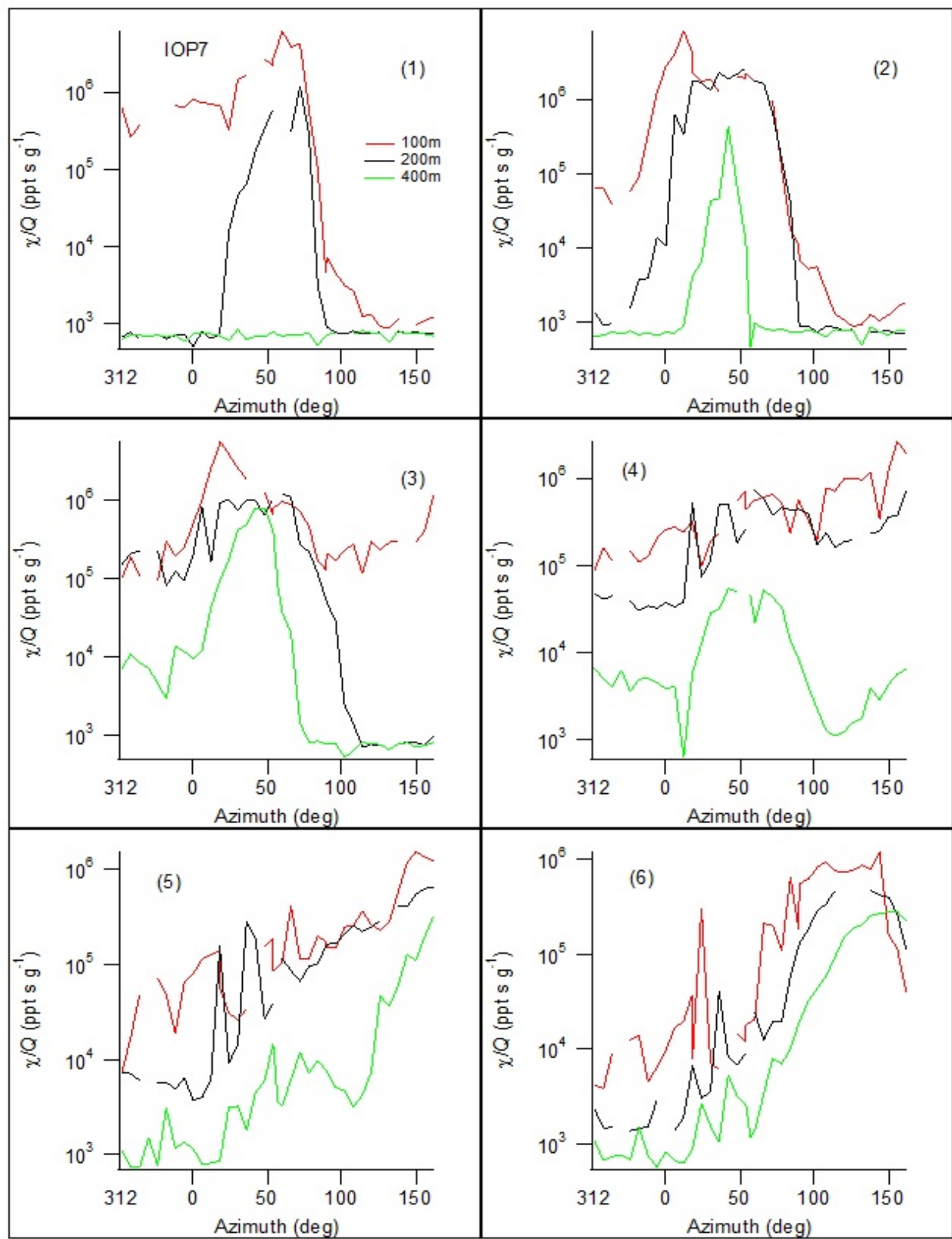


Figure 251. Cross-sections of normalized concentration along the arcs for bags 1-6 during IOP7.

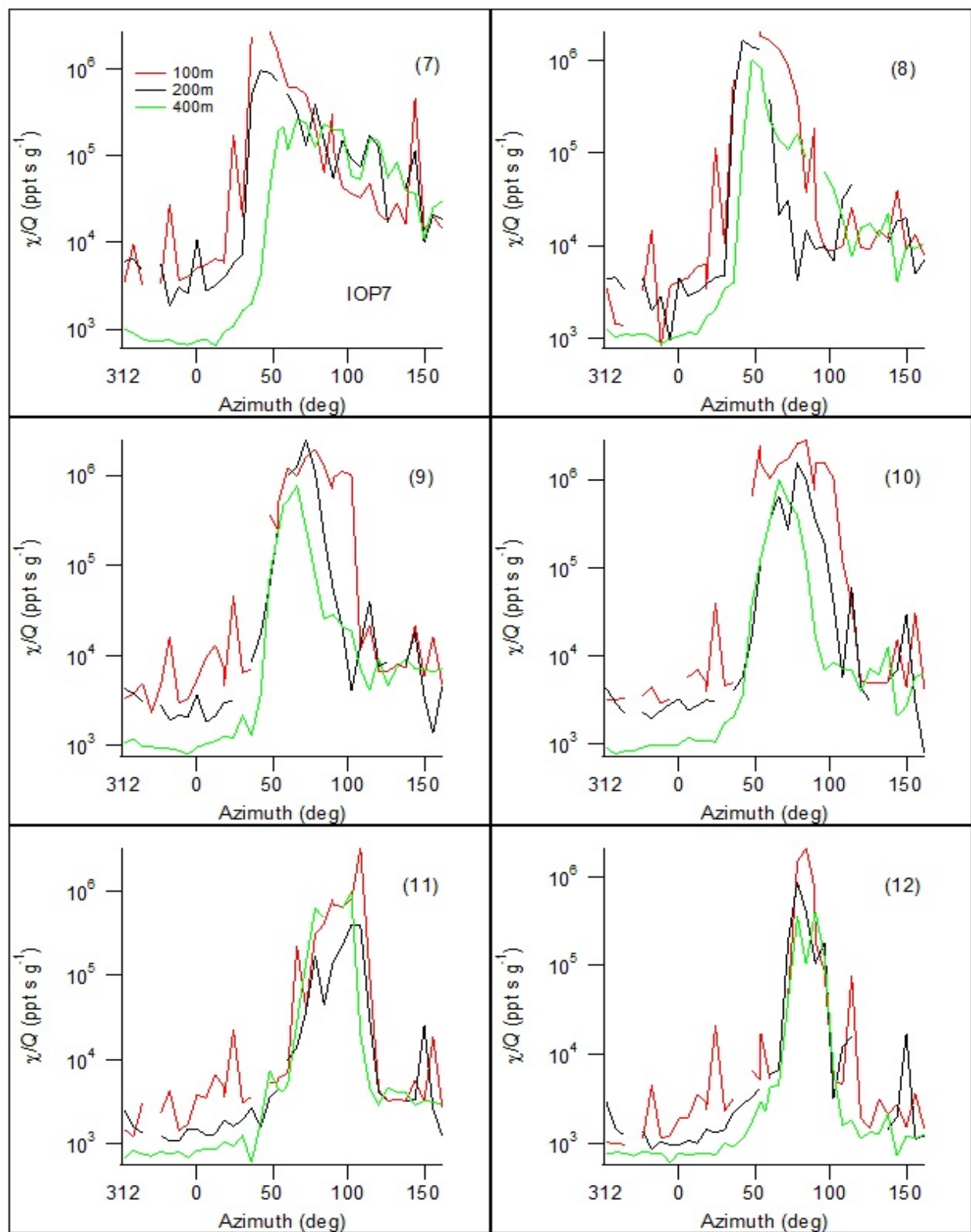


Figure 252. Cross-sections of normalized concentration along the arcs for bags 7-12 during IOP7.

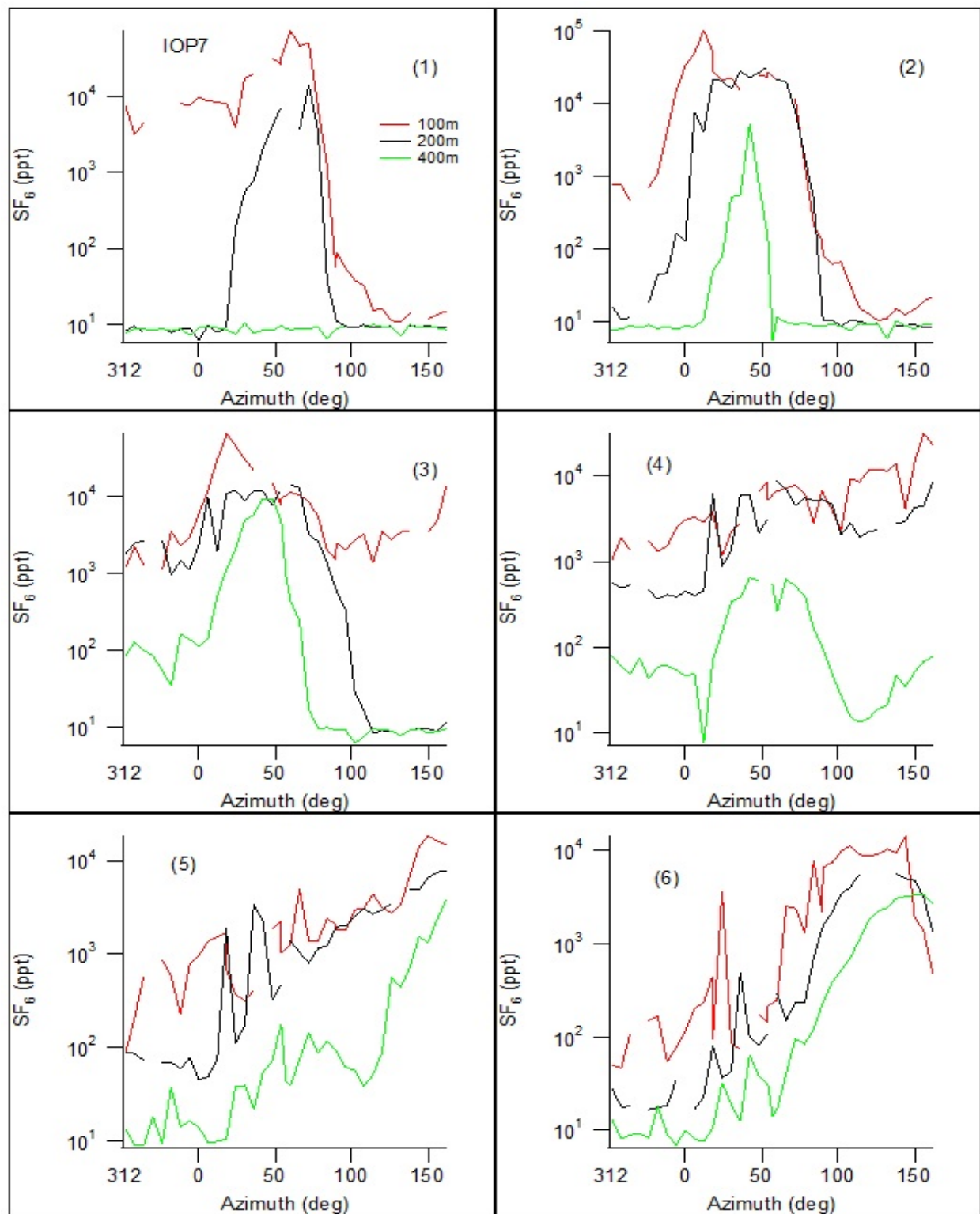


Figure 253. Cross-sections of measured SF_6 concentration along the arcs for bags 1-6 during IOP7.

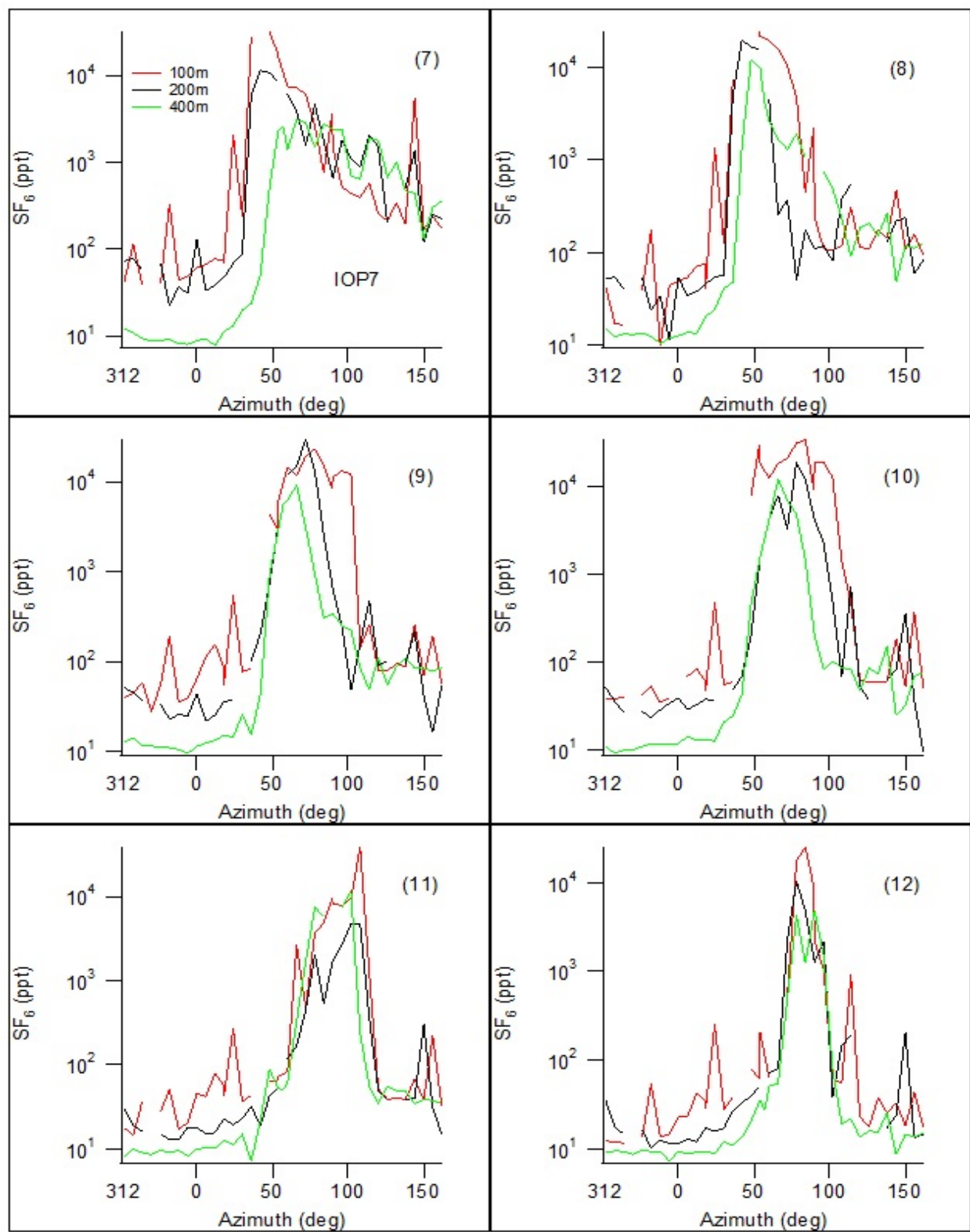


Figure 254. Cross-sections of measured SF_6 concentration along the arcs for bags 7-12 during IOP7.

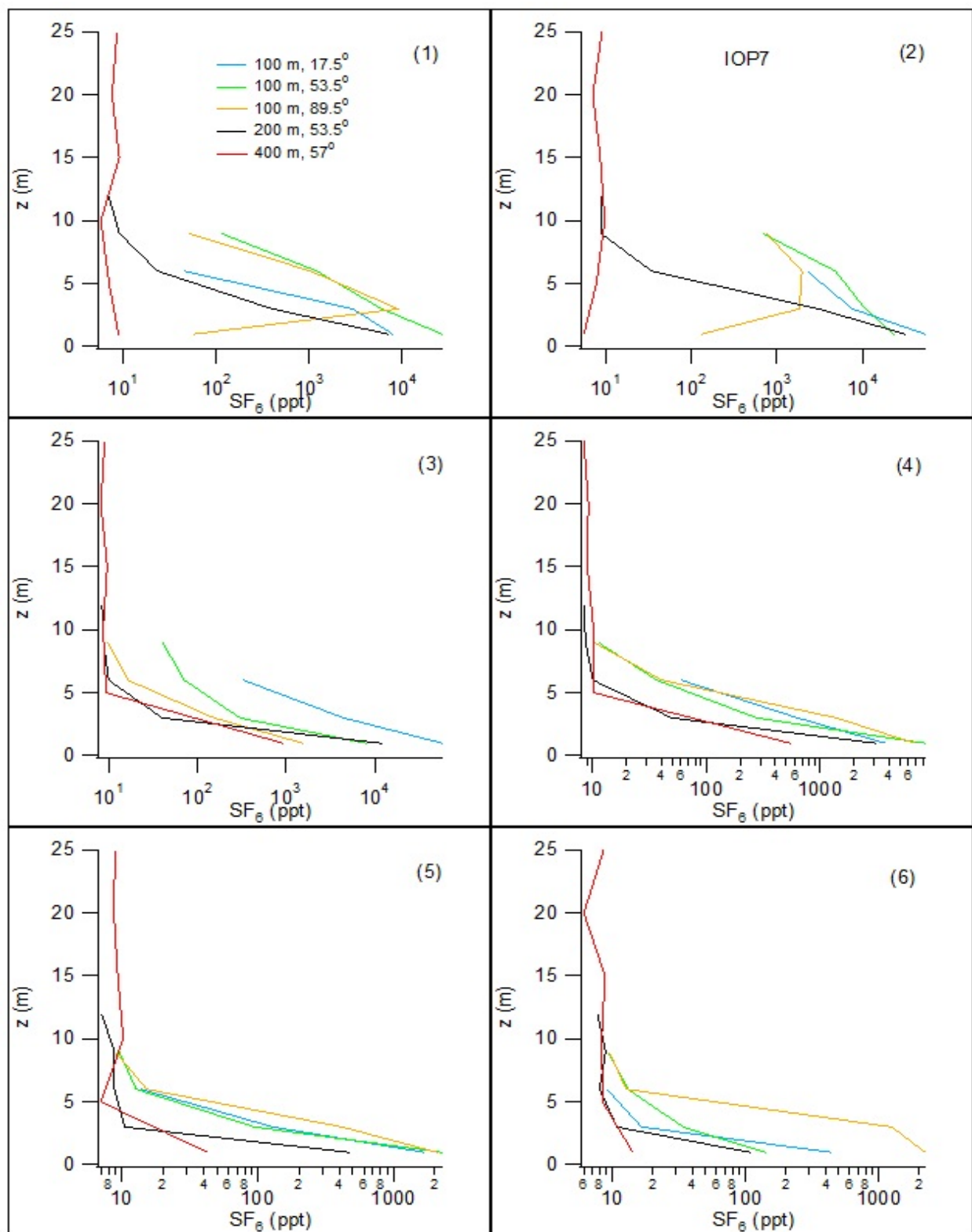


Figure 255. Vertical concentration profiles at the arc position given in the legend for (bags) 1-6 during IOP7.

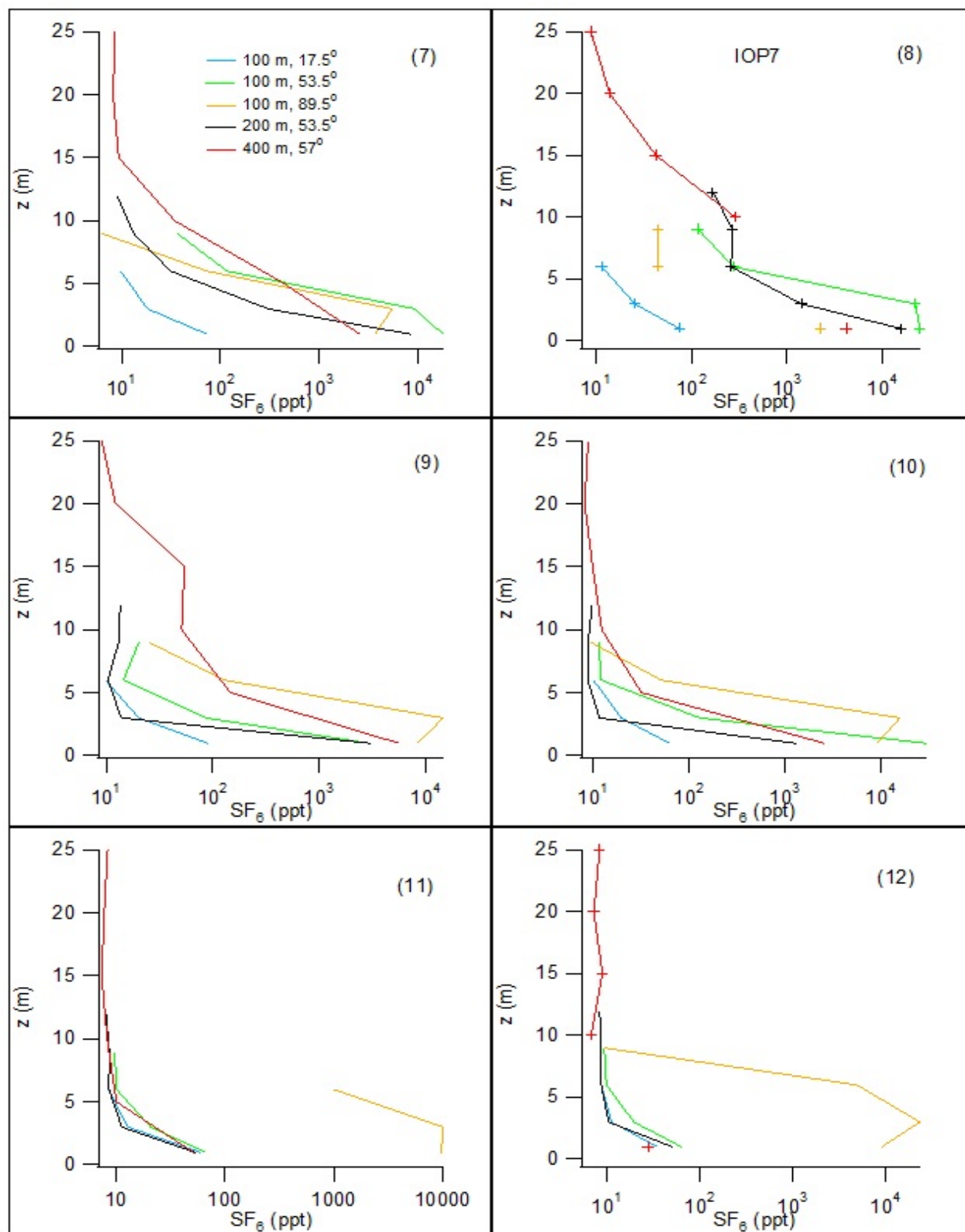


Figure 256. Vertical concentration profiles at the arc position given in the legend for (bags) 7-12 during IOP7.

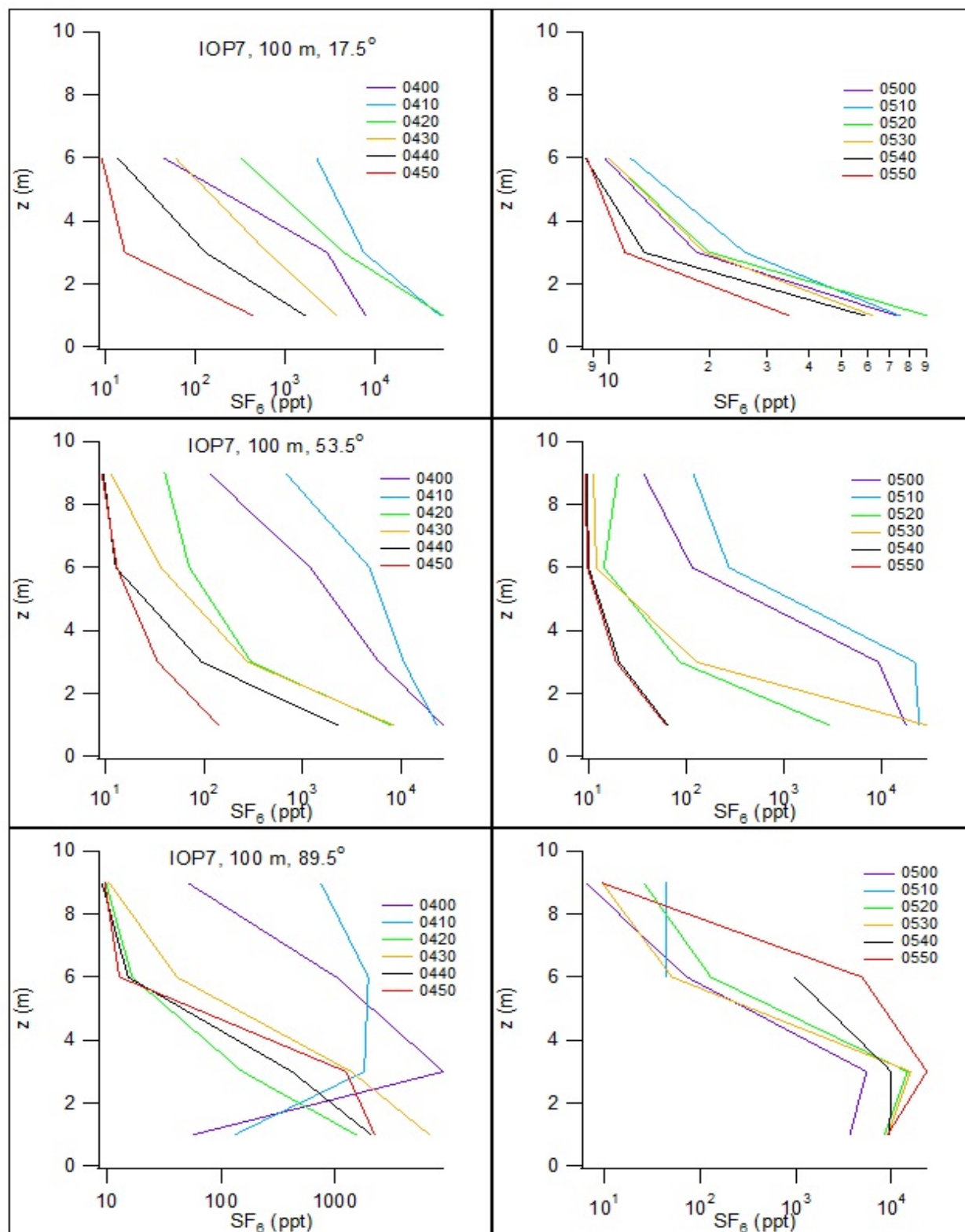


Figure 257. Vertical concentration profiles at the arc position given in the legend for (bags) 1-6 during IOP7.

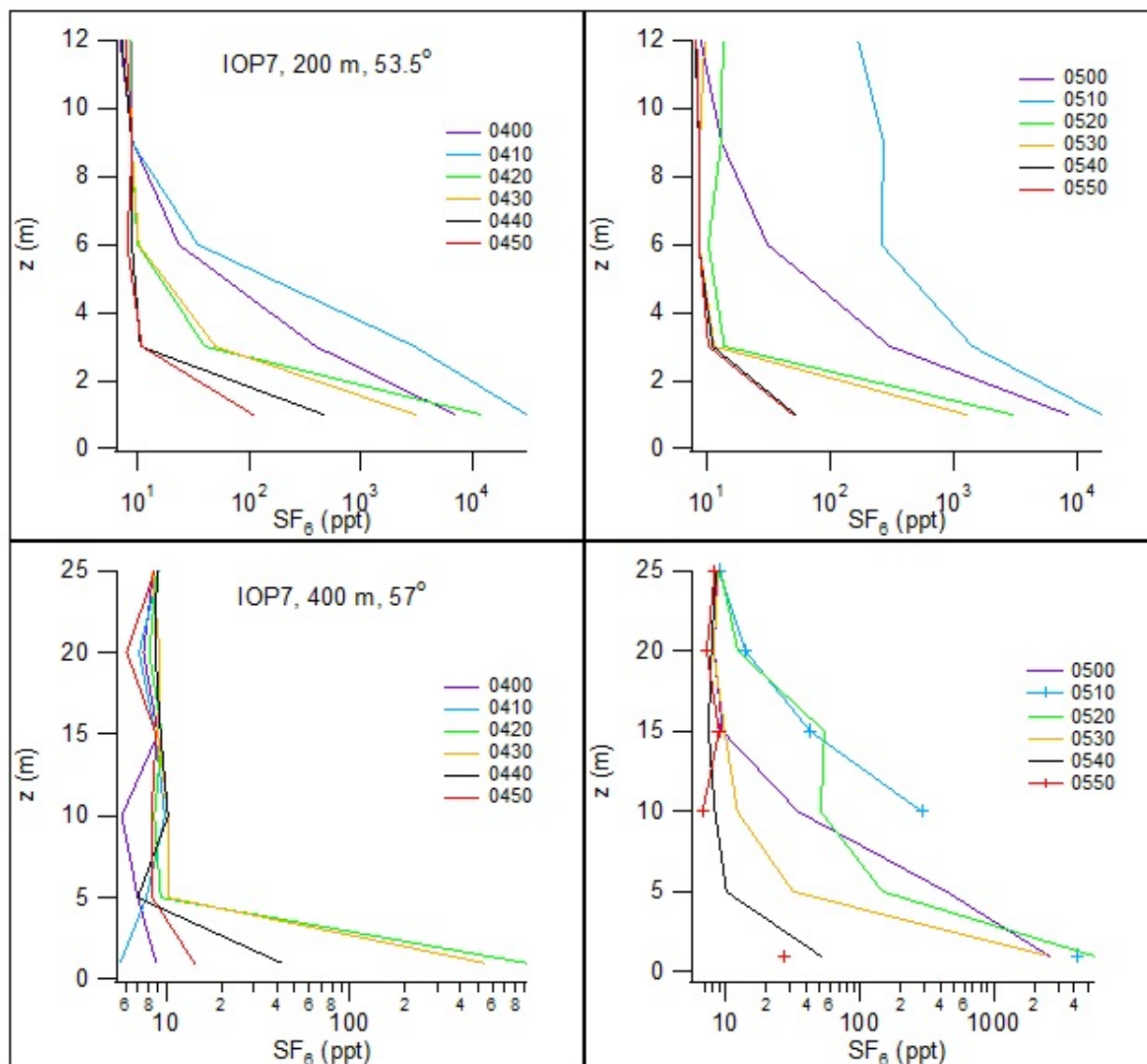


Figure 258. Vertical concentration profiles for the 200 m and mobile towers at the annotated arc position and times given in the legends during IOP7.

Fast Response Results

The locations of the fast response analyzers during IOP7 are shown in Fig. 259. The corresponding concentration time series are shown in Fig. 260. The color coding of the time series was described in the Introduction to this section. The time series records for periods of time with sampling at a fixed location in Fig. 260 are keyed by annotation with a corresponding annotation in Fig. 259. For example, the '1' for the B analyzer in Fig. 260 was located at location 'B1' in Fig. 259.

Perhaps the most striking feature of the fast response concentration time series during IOP7 was the persistence with which the sensors were in the plume. All four analyzers had a period of about a half hour where they were continuously in the plume when located at fixed locations. Analyzer stations A, B1, and D2 to the southeast of the release were continuously in the plume from about 0430-0500 h. There was considerable variation within these continuous peaks but the concentrations did not return to background as was typical of the time series for other IOPs. Fixed station C6 was continuously in the plume to the northeast of the release during the next half hour. Recall that wind directions largely consolidated from the west during the second hour. These observations are also consistent with the bag sampling results (Figs. 247-254). Note also the sharp, very thin peaks associated with the mobile sampling (red traces) suggesting very narrow plumes.

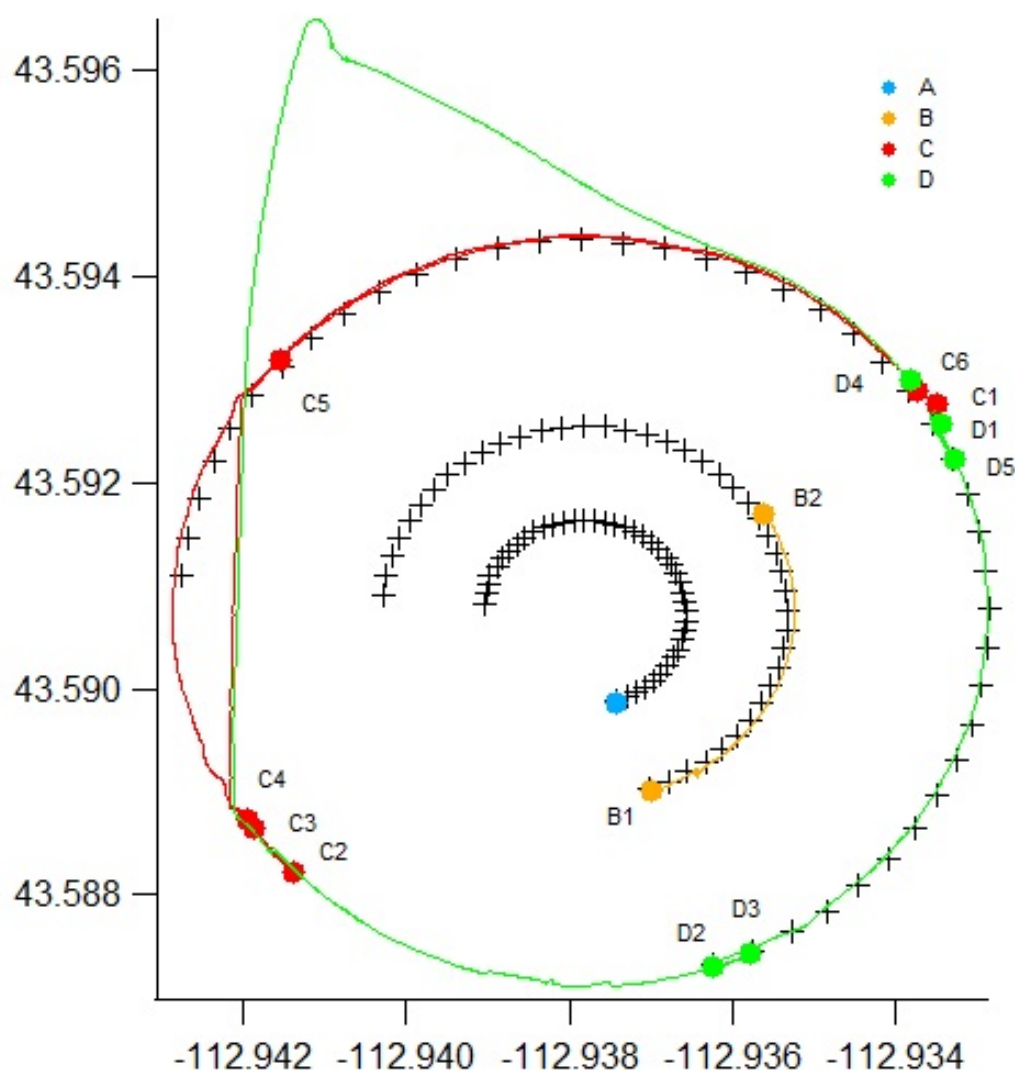


Figure 259. Locations of fast response analyzers during IOP7.

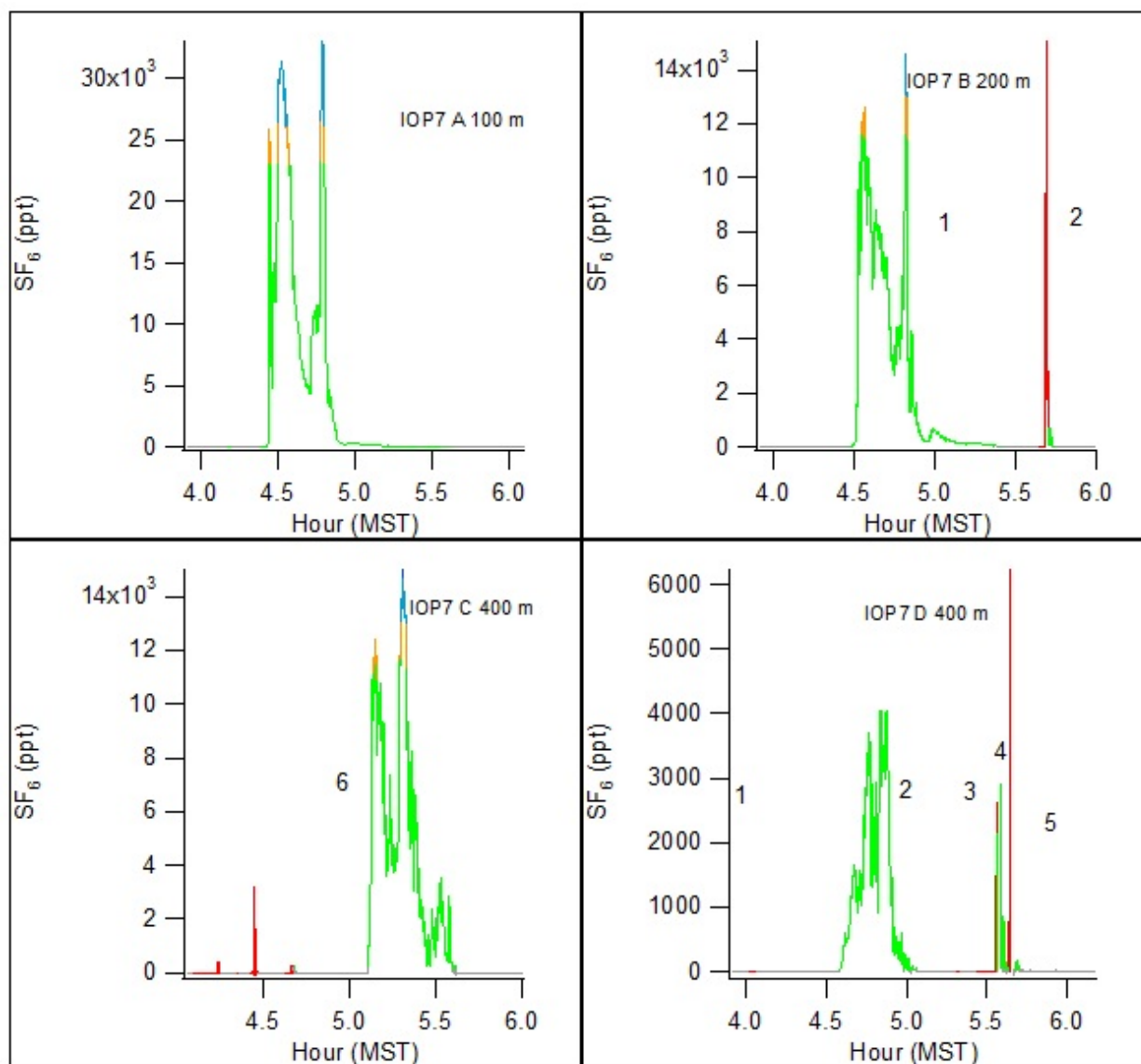


Figure 260. Fast response concentration time series during IOP7.

IOP 8

Date/Time and General Description

IOP8 was conducted on 26 October from 1830-2030 MST (1930-2130 MDT). The earlier nighttime start was an attempt to conduct the tracer release during a more reliably southwest flow such that the plume would be more likely to be bounded within the 210° sampling arcs. Estimates of stability based on traditional Pasquill-Gifford (P-G) schemes were mainly class D but included some class E and a few class F (Fig. 261). Estimates of mean z/L from GRI ranged from 0.5 to 1.57 with a Ri_b of 0.51 (Table 28). In aggregate, results suggest that IOP8 had the least stable atmosphere of all of the nighttime IOPs. Due to the timing, it is likely that the atmosphere was still in something more like a transition state than the other nighttime IOPs. Wind speeds were mostly 1-2 m s^{-1} near the surface (Table 28; Figs. 262, 265). Wind directions exhibited significant variability, both in time and across the study area. During the first hour, wind directions on GRI were out of the southwest, as desired, but then shifted to a more generally northerly direction during the second hour. In contrast, wind directions at COC during the first hour tended to be more easterly during the first hour, shifted to mostly south and southwest near the end of the first hour, then shifted back to northeasterly at the end of the IOP. Wind directions above the surface tended to be much more consistent with near surface winds than seen for the other nighttime IOPs. The tracer measurements indicate that the plume was transported to the northeast and bounded by the 210° sampling arcs during the first hour. That was consistent with the wind directions at GRI. However, late in the first hour, the shift to more northerly wind directions at GRI resulted in the plume being transported mainly to the southeast

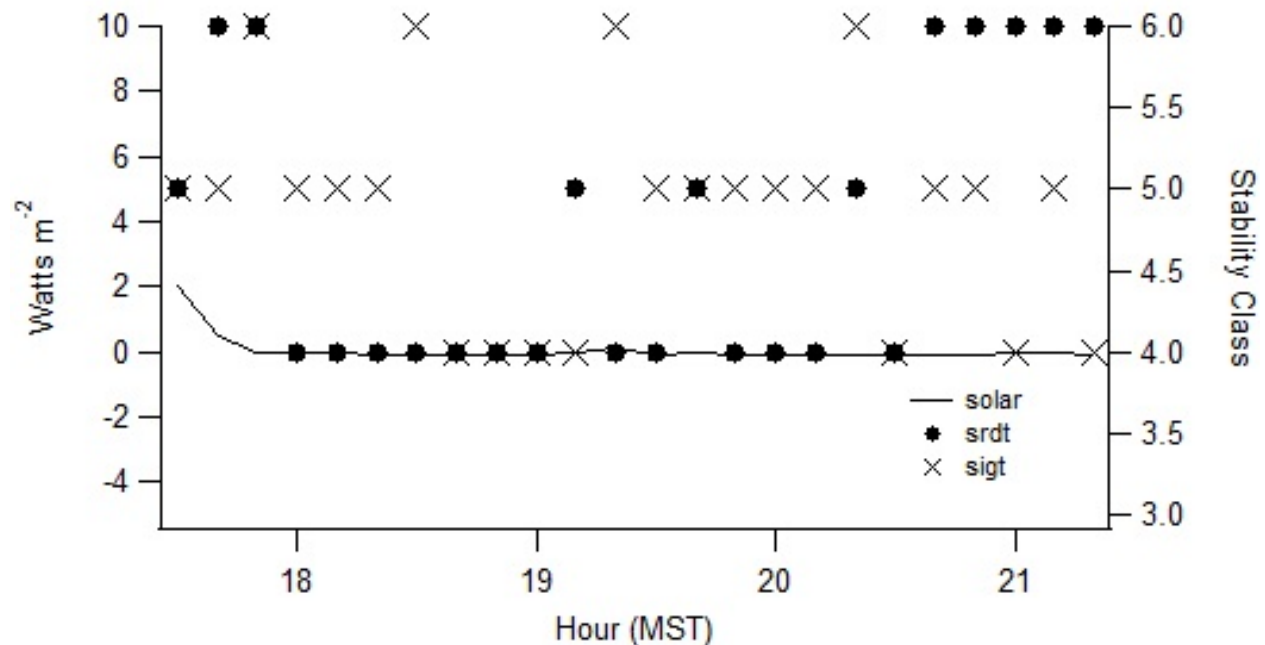


Figure 261. Incoming solar radiation and classification of stability conditions using the Pasquill-Gifford Solar Radiation Delta T (srdt) and σ_0 (sigt) methods (EPA 2000c) during IOP8. Classes D, E, and F are designated 4, 5, and 6, respectively.

Table 28. Meteorological conditions during IOP8.

Bag	COC				GRI						GRI			Solar
	U (m s ⁻¹)		WD (deg)		U (m s ⁻¹)		WD (deg)		σ_θ (deg)		L	L	degC	W m ⁻²
	2m	10m	2m	10m	2m	10m	2m	10m	2m	10m	3.7m	9m	2m	
1	1.1	2.2	45.4	45.3	1.2	2.0	226.2	192.5	13.6	19.1	6.4	5.6	12.0	-0.1
2	1.3	1.9	74.8	81.9	1.9	2.9	247.6	229.8	8.0	9.0	4.8	8.1	11.5	-0.1
3	1.4	2.3	129.0	138.2	1.4	2.9	248.4	246.4	12.0	9.4	7.4	-15.4	11.2	-0.1
4	1.7	2.9	149.0	147.6	1.5	2.4	231.7	239.8	10.3	8.4	2.2	13.3	12.1	-0.1
5	1.4	3.2	162.4	153.0	1.0	1.9	208.4	238.7	28.2	9.8	4.8	-5.3	11.6	0
6	1.5	3.2	172.6	161.5	1.5	2.6	58.9	58.6	16.7	40.5	12.7	19.8	10.0	0.1
7	1.3	2.7	211.6	178.8	0.8	2.2	359.7	45.4	21.3	4.7	5.9	5.2	9.6	-0.1
8	1.4	2.6	249.7	213.9	0.9	2.2	347.3	36.0	15.6	6.2	1.1	0.9	9.6	0
9	1.5	3.1	254.3	239.3	1.8	2.9	4.6	27.6	7.3	6.8	NaN	2.0	9.9	-0.1
10	1.4	2.8	234.3	230.2	1.9	3.4	0.5	13.7	8.2	4.7	6.0	11.2	8.8	-0.1
11	1.0	1.8	141.2	208.9	0.7	2.1	14.4	7.3	39.3	14.7	8.5	114.5	8.3	-0.1
12	1.0	2.3	52.6	50.3	1.0	1.9	341.2	15.4	71.8	30.2	3.2	55.7	8.2	-0.1
Avg. L											5.74	17.97		
z/L											1.57	0.5		
Ri _b												0.51		

with significant truncation of the plume west of the 162° sampler during the second hour. The plume patterns appear to have been roughly consistent with the observations of wind direction at GRI but inconsistent with those at COC. The first hour provides some relatively ideal cases for plume analysis but the plume truncation during the second hour complicates any analysis. The SF₆ release rate was 0.0119 g s⁻¹ (Table 2). All four of the fast response analyzers moved several times over the course of the IOP on the 100, 200, and 400 m arcs.

Wind Speed and Direction Quality Assurance

Figures 262-264 show wind speed and direction time series comparisons for a sequence of measurement heights during IOP8. In Fig. 262, the near surface measurement of U showed some variation but 1-2 m s⁻¹ was common for most of the tracer measurement period. Wind directions were highly variable in space and time. Most stations showed south-southwest winds for most of the first hour then shifted to northerly during the second hour. The wind direction at 2 m on COC was a distinct outlier. Wind directions at higher levels tended to be roughly consistent with the near surface wind directions at the same stations (Figs. 263 and 264). Again, wind directions at COC were distinctly different than those on GRI but the 30 m SOD wind measurements were consistent with the 30 m COC wind measurements in both speed and direction. These results suggest a somewhat different wind regime to the east beyond the 400 m arc. The differences between SOD and GRI persisted at the 45 and 60 m levels. There was good

data recovery for both the SOD and PRO measurements at 160 m. The mean of the wind directions at PRO were similar to the mean from a much less variable set of observations of wind direction at SOD. Beyond a large spike in U at PRO prior to the tracer measurement period, U at PRO exhibited a low bias with respect to SOD. It's not clear if the discrepancies in wind direction between GRI and the surface sonics on the one hand, and COC and SOD on the other hand, reflect a real difference in wind regime or perhaps a systemic measurement artifact. However, it does not seem unreasonable to believe it is due to spatial inhomogeneity in the wind field given the routine observations of such variability in the nighttime IOPs.

The Brunt-Väisälä frequency N began low during IOP8 but consistently increased over the course of the test to values similar to those observed during IOPs 5 and 7. That would be consistent with the more transitional character of this IOP.

Figure 265 shows time series measurements for cup anemometers and wind vanes only (excluding sonics) at all heights on the GRI and COC towers during IOP8. Again, the near surface measurements of U at GRI and COC were mostly 1-2 m s⁻¹ and, with some exceptions, evidence of steep gradients in U is limited. Wind directions on COC and GRI varied significantly between the sites at all height. The measured σ_θ at 2 m on GRI were generally < 15° except for some large deviations near the end of the first hour of tracer measurements and then again near the end. A large deviation in σ_θ at 2 m on COC was also observed late in the IOP. These deviations coincided with the wind direction shifts already described and affected some of the levels above 2 m. The σ_θ were generally < 10° above 2 m with the exceptions noted. The temperature time series suggest there was a steep gradient between the 2 and 10 m levels then the near absence of a vertical gradient in temperature above that until late in the IOP. By the end of the IOP the ΔT ranged up to 6° C between 2 and 60 m agl.

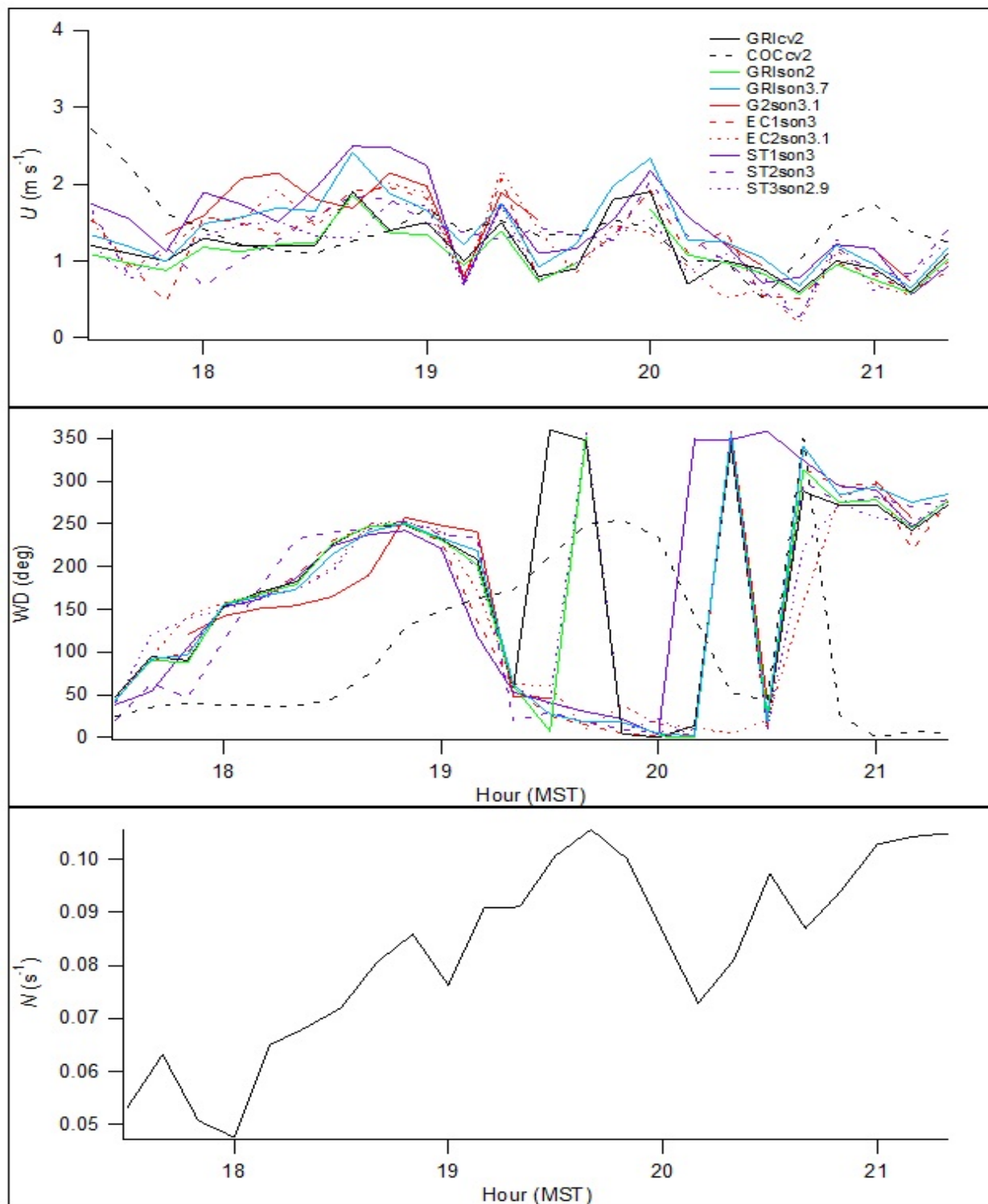


Figure 262. Time series of near surface wind speed and direction measurements and Brunt-Väisälä frequency N between 2 and 15 m agl during IOP8. In the legend, location is specified in upper case, the measurement type in lower case (cv = cup/vane, son = sonic), and the measurement height numerically.

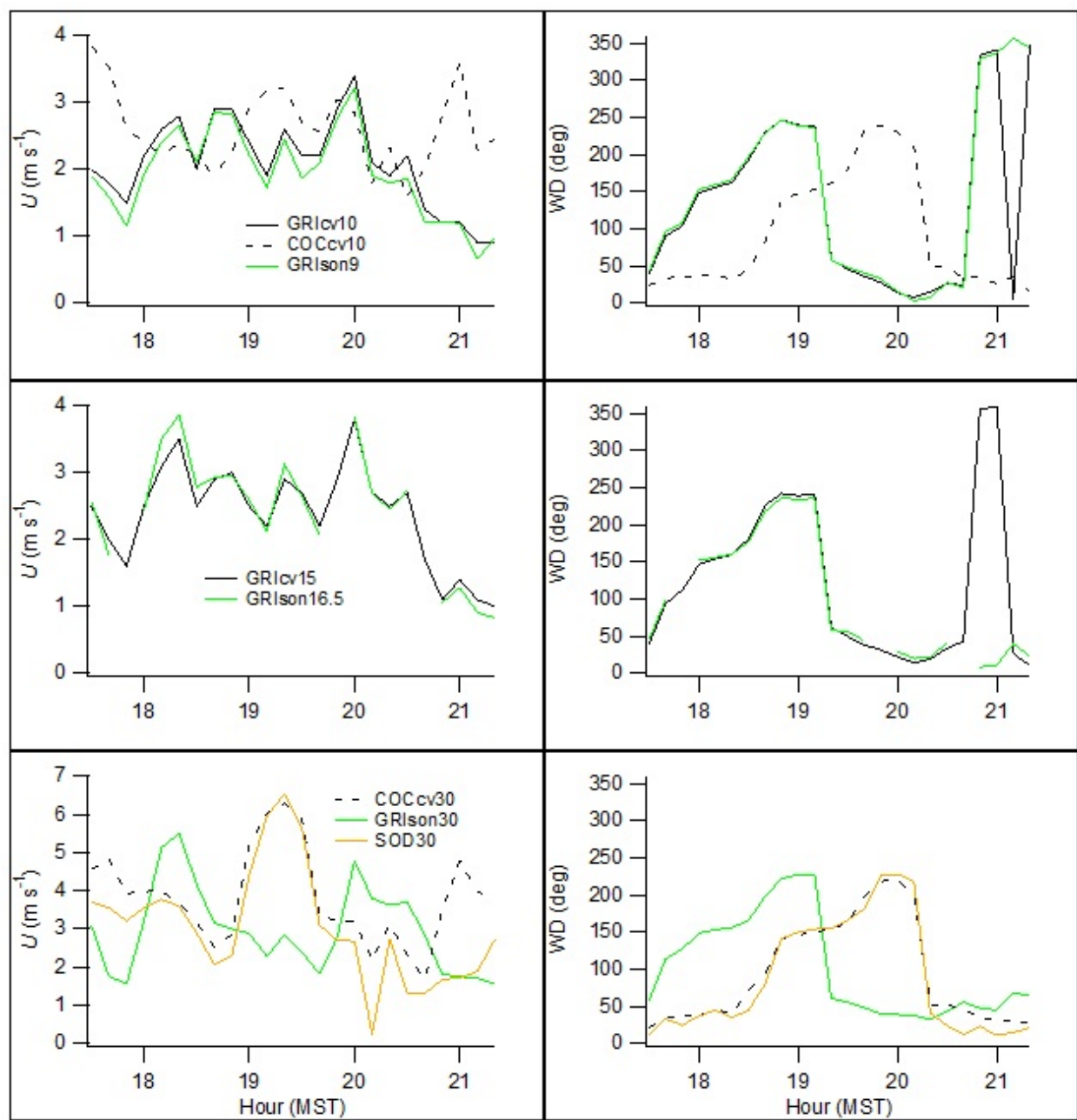


Figure 263. Time series of wind speed and direction measurements at heights between 9 and 30 m agl during IOP8. Legend notations described in caption of Fig. 262.

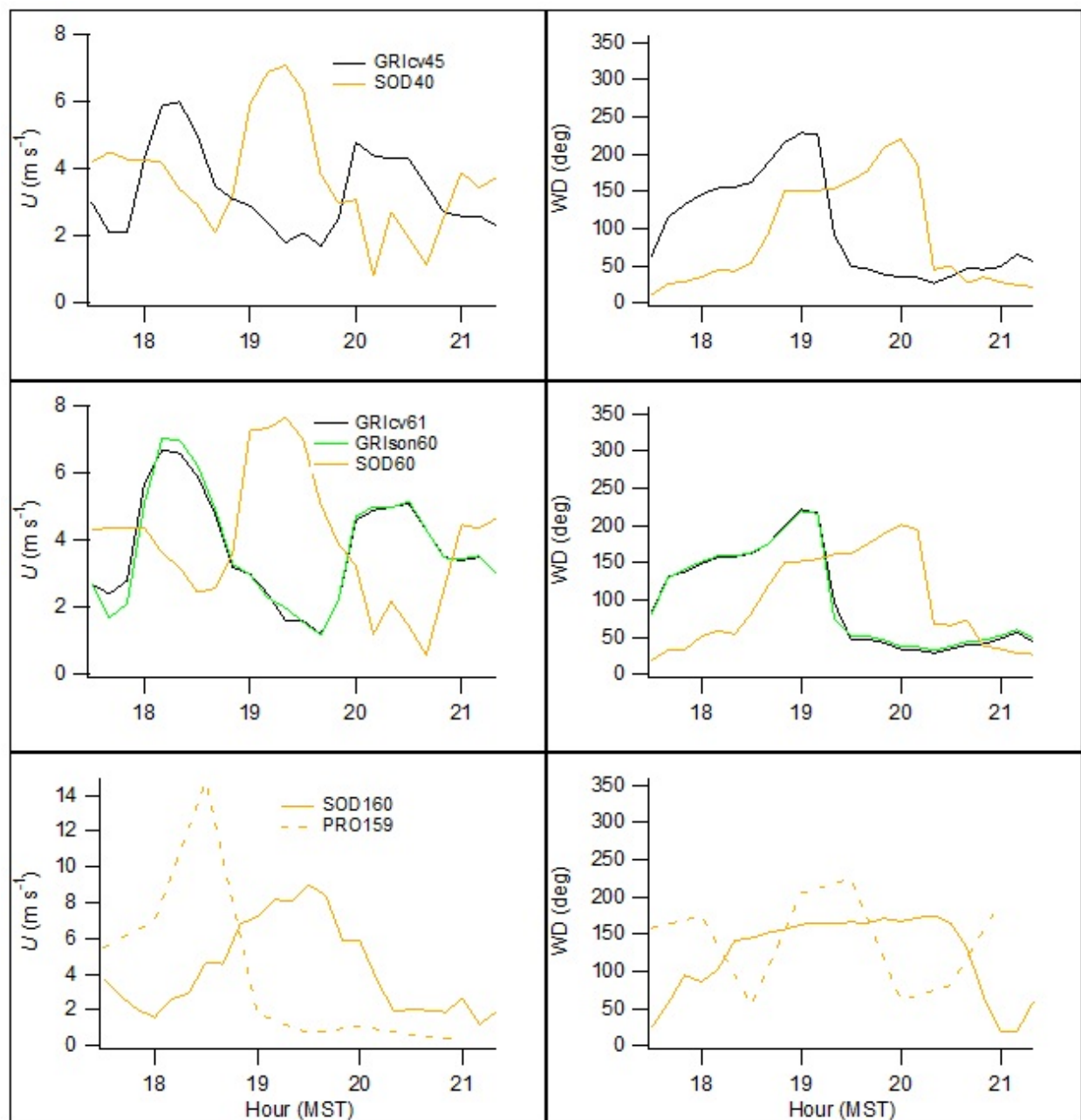


Figure 264. Time series of wind speed and direction measurements at heights above 30 m agl during IOP8. Legend notations described in caption of Fig. 262.

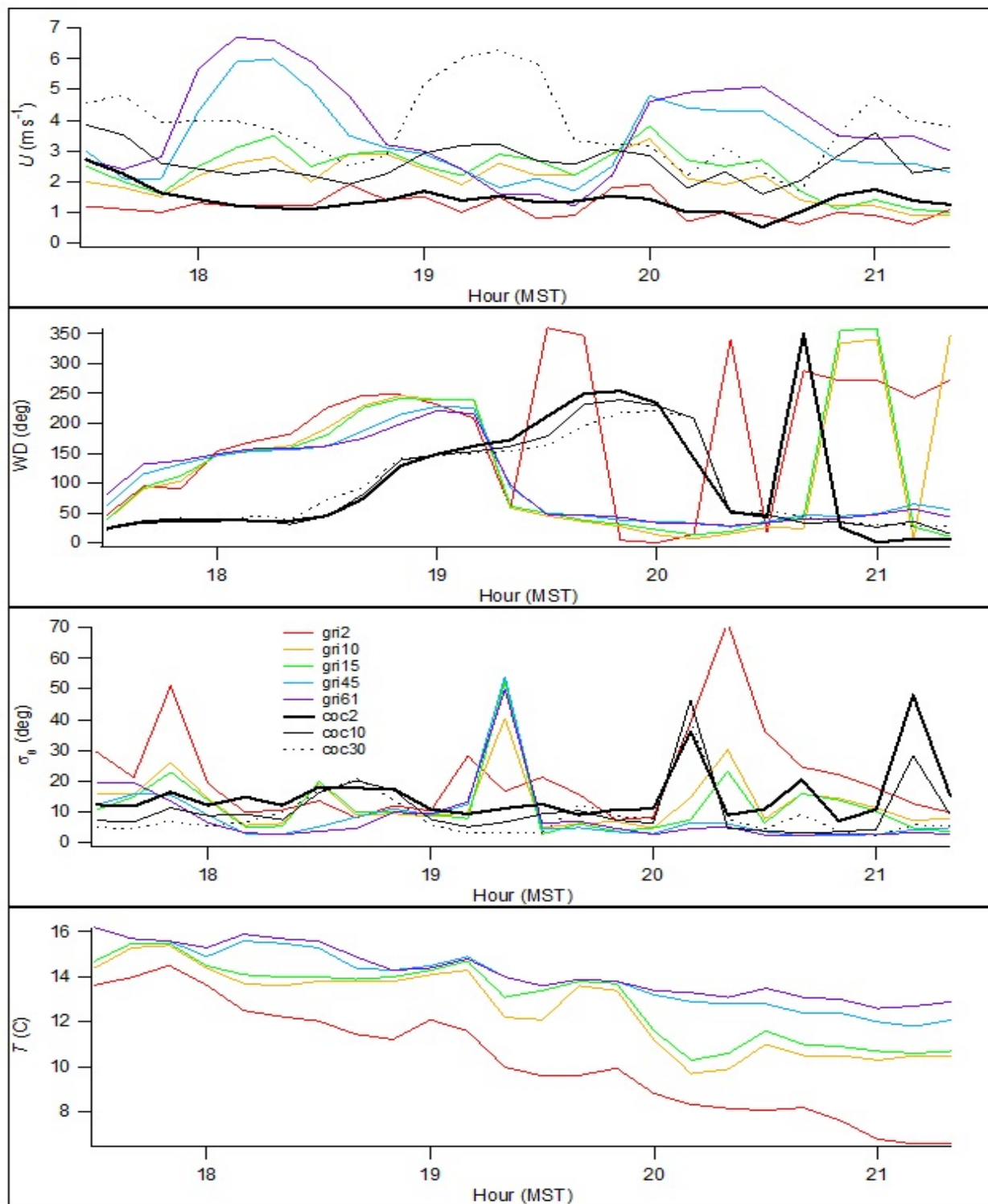


Figure 265. Time series from GRI and COC showing cup anemometer and wind vane measurements of U , wind direction, standard deviation of wind direction σ_θ , and temperature during IOP8. The locations are designated 'xxxy' where xxx = tower and yy = measurement height.

Turbulence

Near-surface turbulence measurements for IOP8 are shown in Fig. 266. The magnitudes of all the measurements of turbulence were low but markedly higher than those measured during the other nighttime IOPs. There were some large, irregular excursions but these occurred much less often than during the other nighttime IOPs. Stations ST1, EC1, and EC2 showed the largest excursions. The timing of the spike just after 1900 h is shortly ahead of the shift in wind direction. The magnitudes of σ_w and u_* decreased over the course of the IOP. The magnitude of the sensible heat flux was small and generally negative with the magnitude tending to decrease toward zero with time.

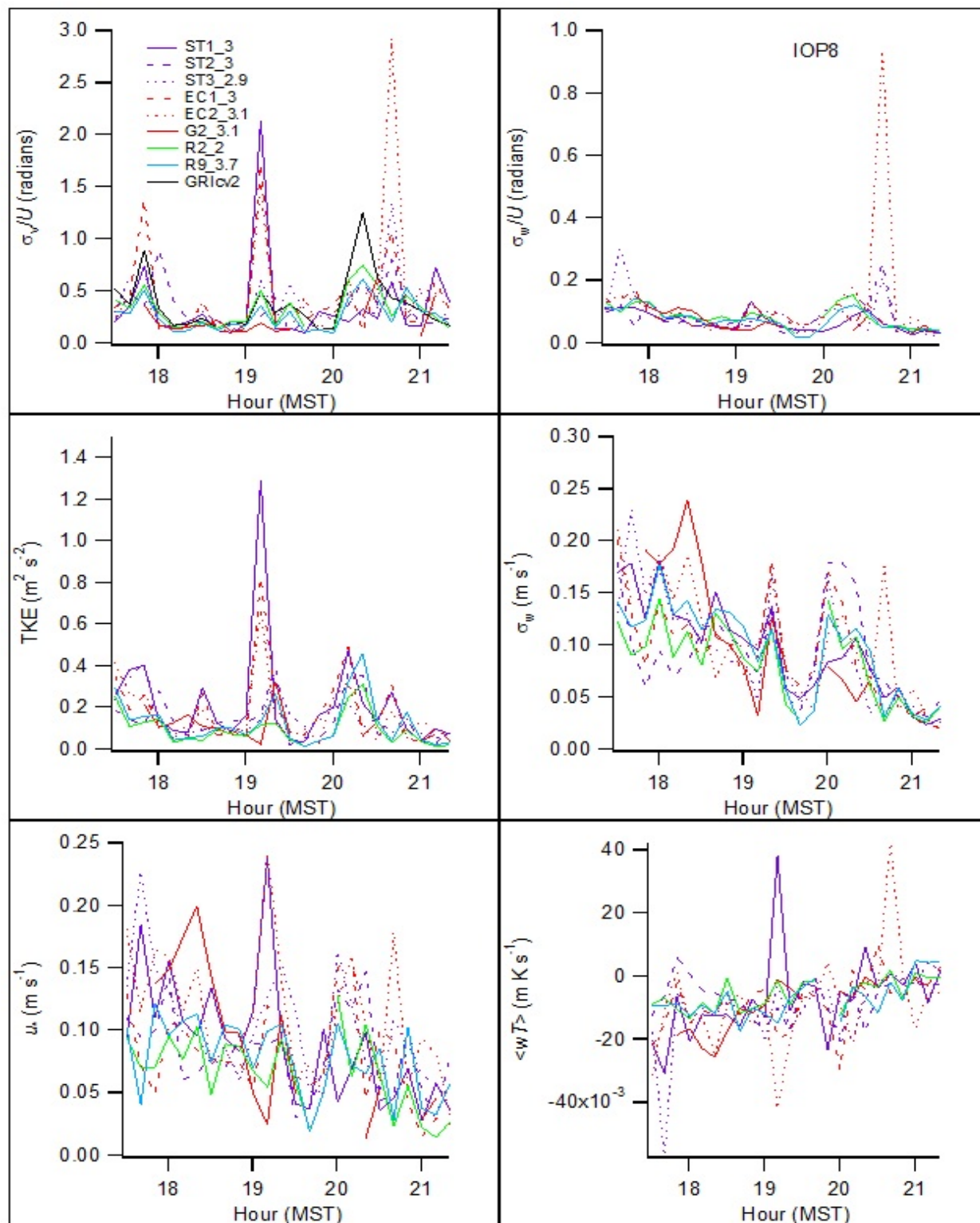


Figure 266. Time series of near surface turbulence (sonic) measurements during IOP8. The GRI and COC are σ_0 wind vane measurements (cv) in degrees converted to radians for purposes of comparison. Notation before and after underscore designates location and height, respectively.

Wind and Turbulence Profiles

Figure 267 shows profiles of the non-sonic measurements at GRI and COC during IOP8. Profiles of U at GRI mostly show increasing U with height. However, there are four 10-min periods from 1920 to 2000 h that suggest jet-like profiles with maxima at 15 m. These do not appear to be present at COC. Wind directions at GRI were mostly uniform with height excepting a transition period at the start of the second hour when winds shifted from generally southwesterly to generally northerly. Wind directions at COC are also mostly uniform with height although from much different directions than at GRI. The σ_θ were commonly less than about 10° in most profiles and relatively uniform with height except for some excursions to much larger values in a few profiles. These occurred mainly at the 2, 10, and 15 m levels and coincided with periods of wind direction shifts. The temperature gradients were large between and 2 and 10 m and then small above that until near the end of the IOP.

Figures 268 and 269 show profiles of the sonic turbulence measurements at GRI during IOP8. Wind speeds and directions were similar to that seen in Fig. 267 for GRI. There are several profiles that also hint at a jet-like feature with a maximum near 16.5 m agl. Wind direction shifts in Fig. 268 are consistent with those shown in Fig. 267. The σ_v/U and σ_w/U values are relatively small with profiles that tended to be relatively uniform with height except for some higher values near the surface. TKE was small and relatively uniform with height excepting for a few 10-min periods near the end of each hour of the IOP. Again, these were periods featuring wind direction shifts. The virtual temperature gradients were also large up to 9 or 16.5 m and then much smaller above that.

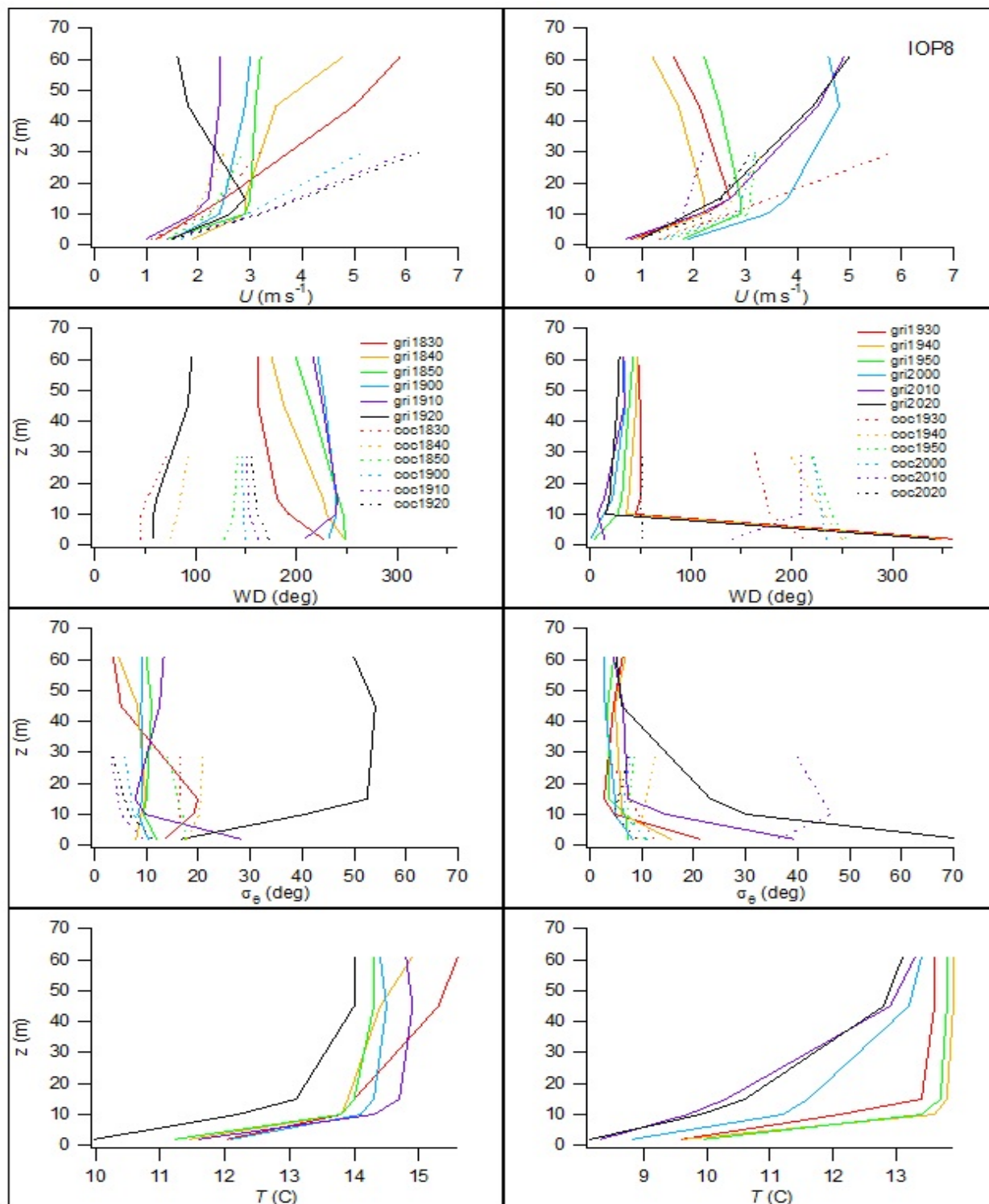


Figure 267. Profiles of U , wind direction, standard deviation of wind direction σ_θ , and aspirated temperature from cup anemometers and wind vanes during IOP8 at GRI and COC. Each profile is designated 'xxxhrmn' where xxx = tower and hrmn = start time of 10-minute interval.

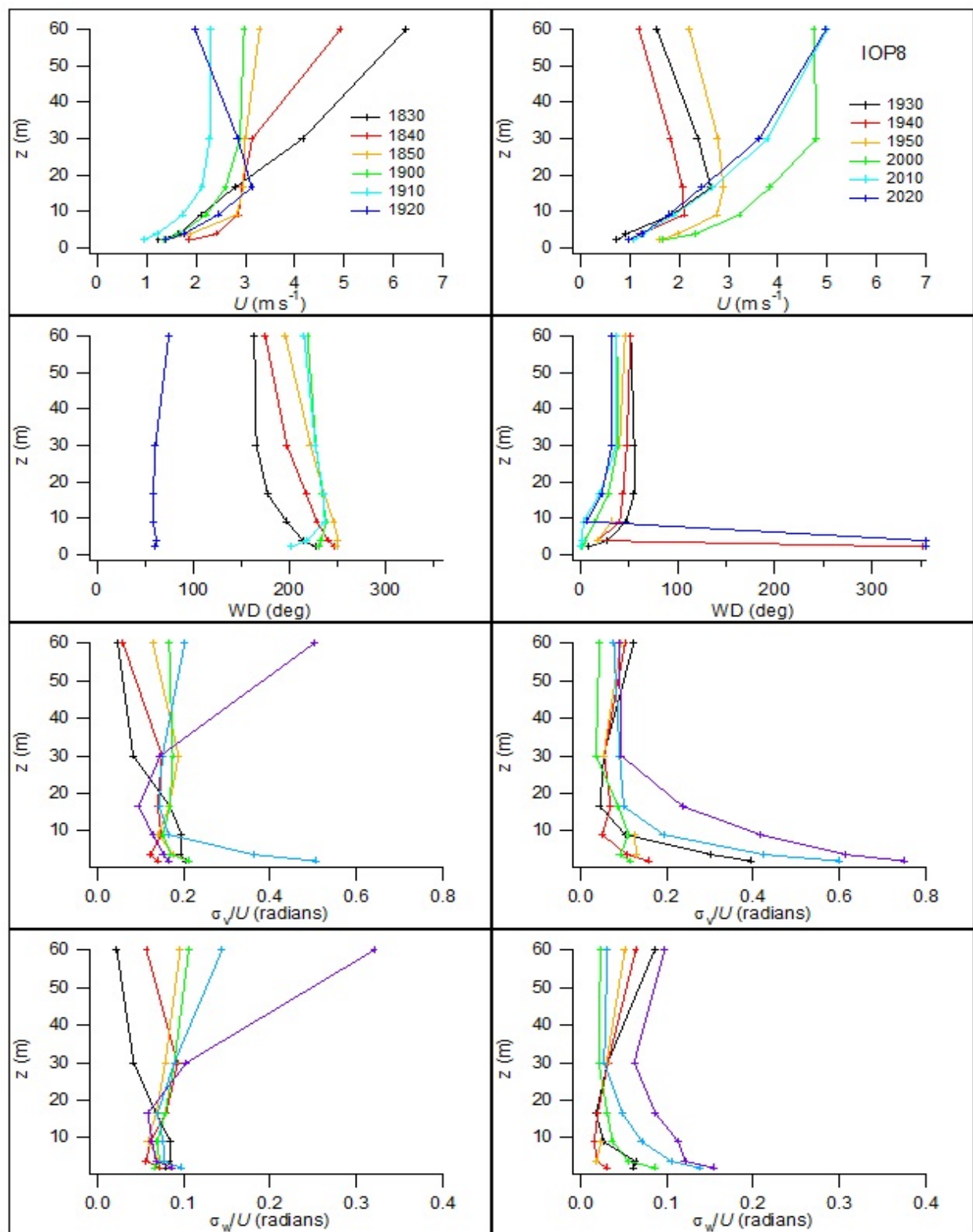


Figure 268. Profiles of U , wind direction, σ_v/U ($\sim \sigma_\theta$), and σ_w/U ($\sim \sigma_\phi$) from sonic anemometers at GRI during IOP8. The legend specifies the start time of the 10-min interval (hrmn).

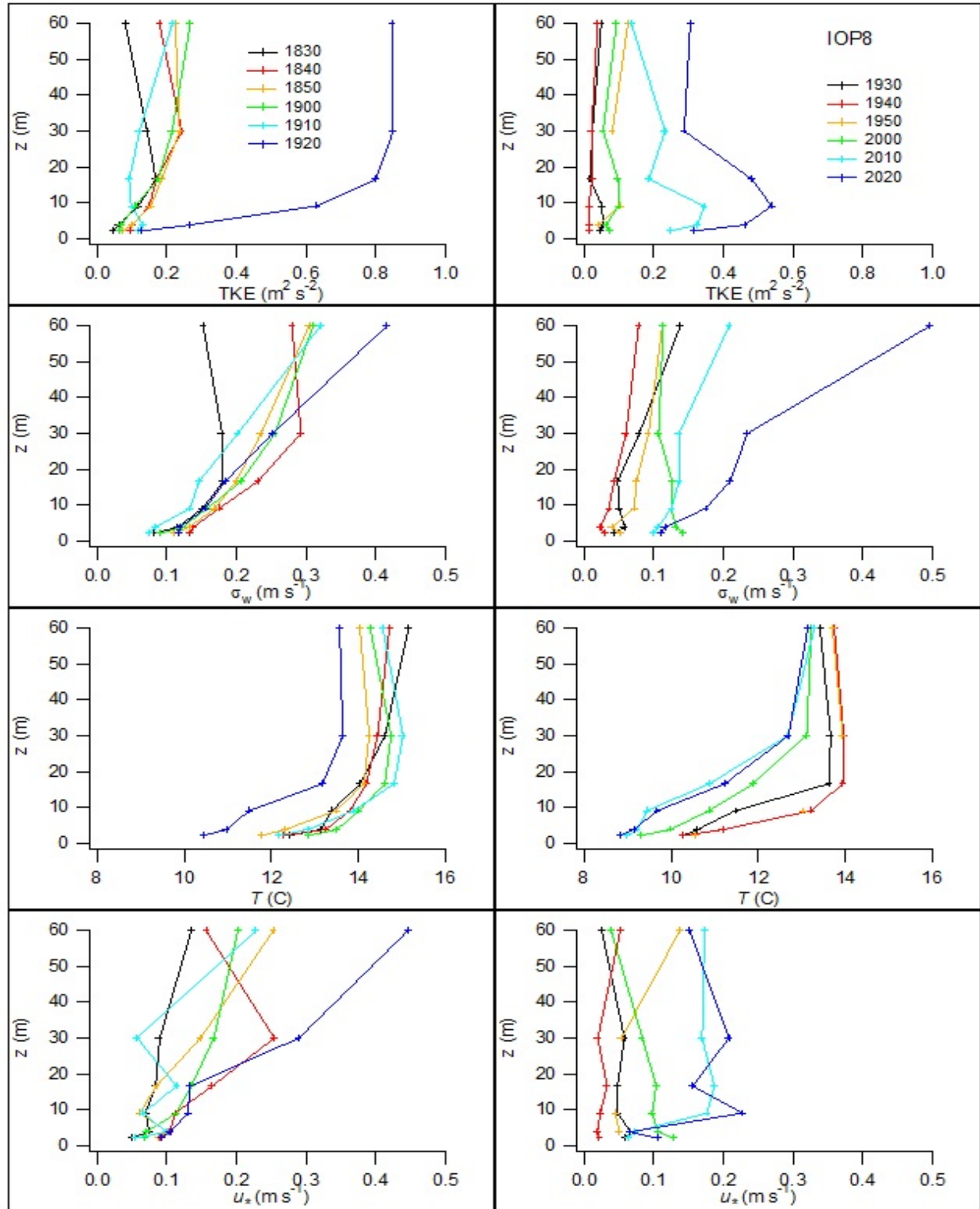


Figure 269. Profiles of turbulent kinetic energy (TKE), standard deviation in vertical wind speed σ_w , virtual temperature, and friction velocity u_* from sonic anemometers at GRI during IOP8. The legend specifies the start time of the 10-min interval (hrmn).

The wind field measured by SOD and PRO were much different during IOP8 than the previous nighttime IOPs. These are shown in the time-height representations in Figs. 270 and 271, respectively. The wind directions measured at SOD were generally consistent with those measured at COC and often differed with respect to wind direction measurements at GRI (Figs. 267, 268). A similar observation was made in the comparison of wind directions across the study area (Fig. 263) suggesting that COC and SOD were in a somewhat different wind regime than GRI. The increase in U at SOD midway through the test was also consistent with a similar increase at COC (Fig. 267). SOD recoveries were very good and showed strong evidence of the variation of wind direction with height outside of the time period with higher U from about 1850 to 2010 h. Figure 271 shows a zone of higher U near the surface early on lifting to about 500 m by midway through the test. Wind directions were generally southerly up to about 1700 m except near the surface and/or in lighter U . Above 1700 m, Fig. 271 suggests winds shifted to southwest and increased to over 15 m s^{-1} . That would be somewhat higher than indicated by the radiosonde data (not shown, see project database). Except for the maximum in U near 15 m agl, there is no evidence for a jet-like feature like that seen in IOPs 5-7.

Figures 272 and 273 show SOD time-height representations for σ_w and TKE, respectively, during IOP8. The measured σ_w were mostly low but higher than the other nighttime IOPs, especially before 1900 h. This probably reflects residual daytime turbulence decaying into

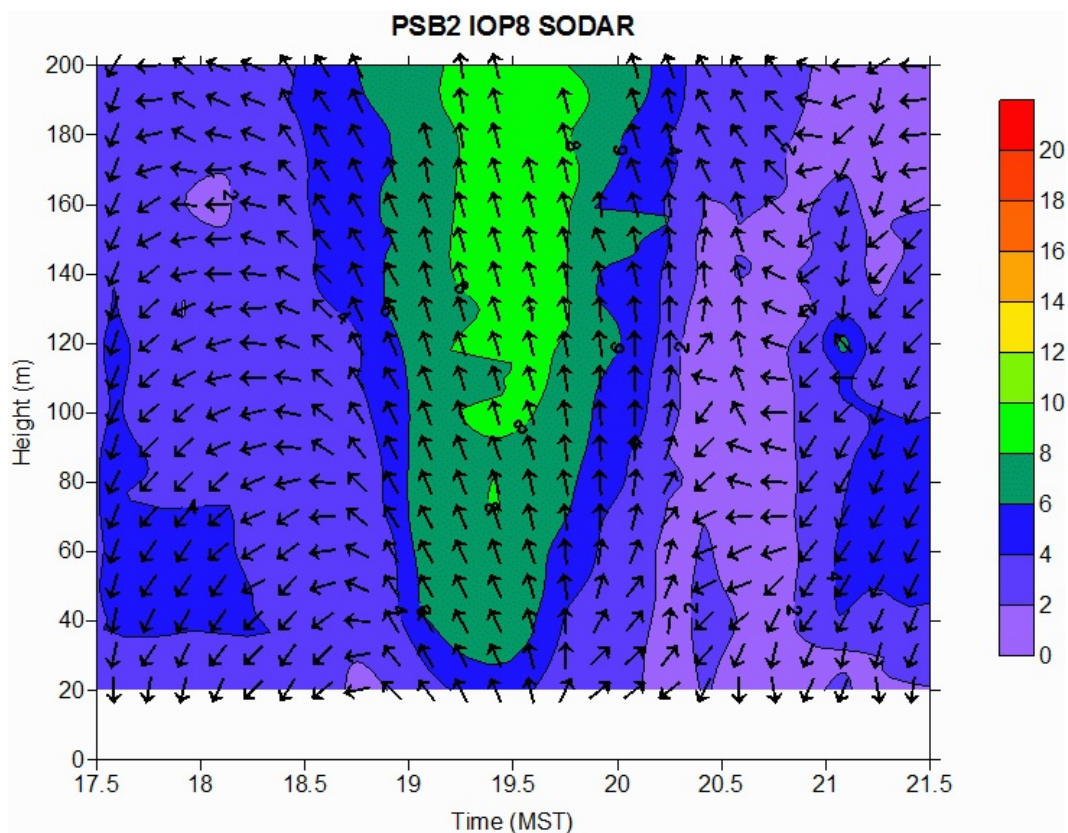


Figure 270. Time-height cross-section of wind speed and direction at sodar (SOD) during IOP8. Legend represents m s^{-1} .

transition. The σ_w anomaly near the start of the period probably represents the end of the daytime turbulence regime near sunset. There is a similar TKE anomaly at the start of the period but it is otherwise low except for an unexplained anomaly after 2100 h at about 120 m agl. Figure 274 shows time-height temperature profiles from the RASS.

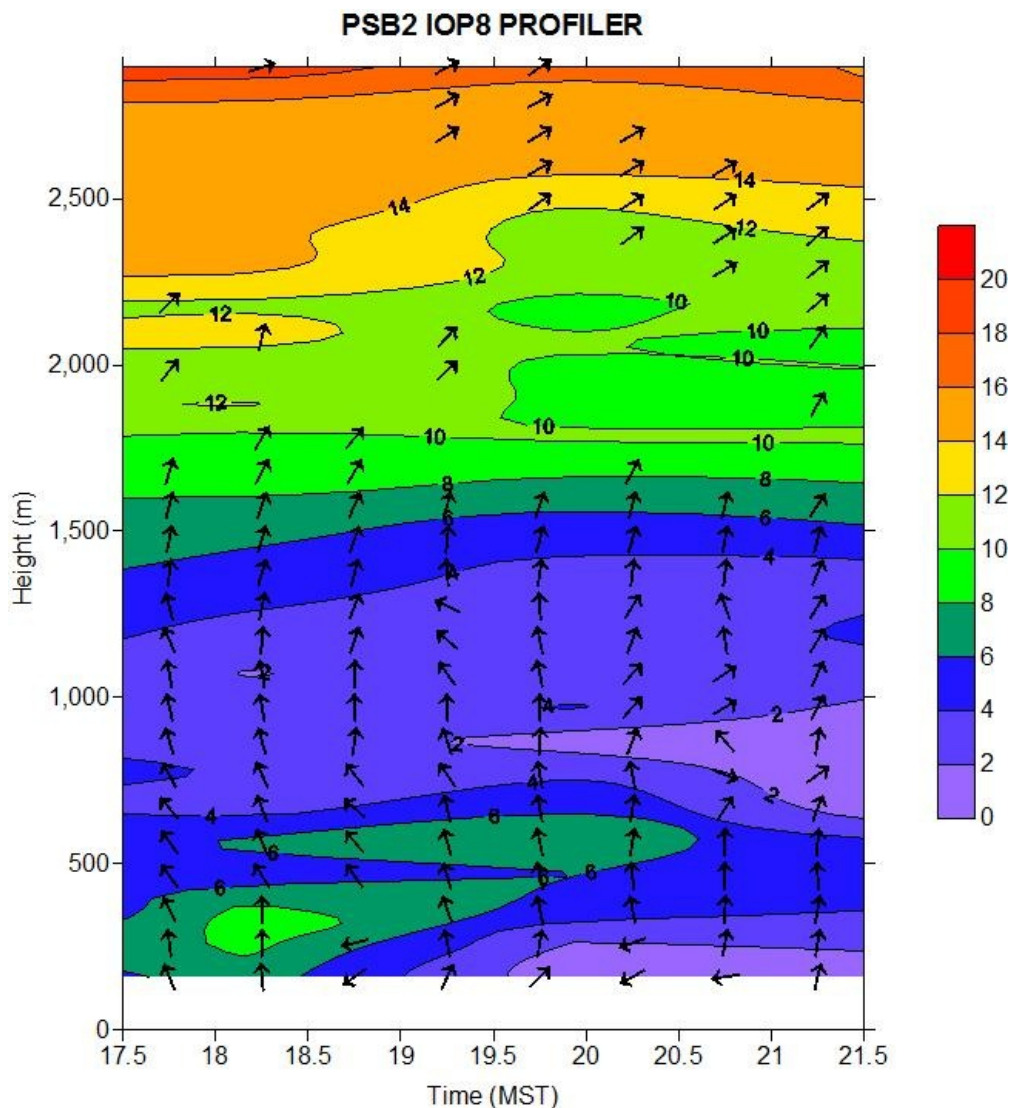


Figure 271. Time-height cross-section of wind speed and direction at wind profiler (PRO) during IOP8. Legend represents m s^{-1} .

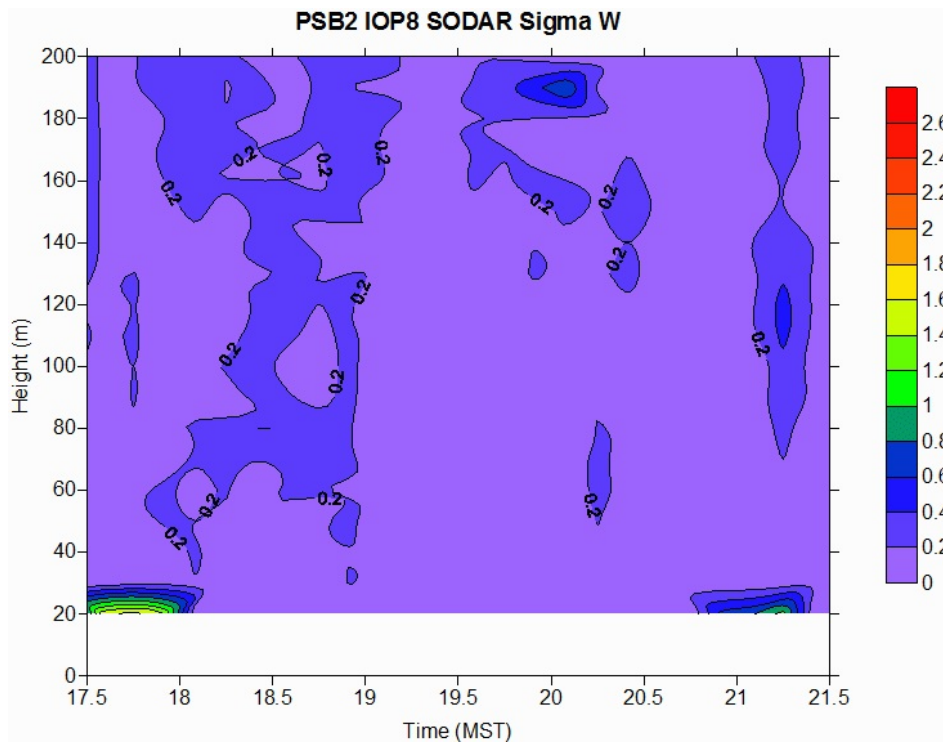


Figure 272. Time-height cross-section of σ_w at sodar (SOD) during IOP8. Legend represents m s^{-1} .

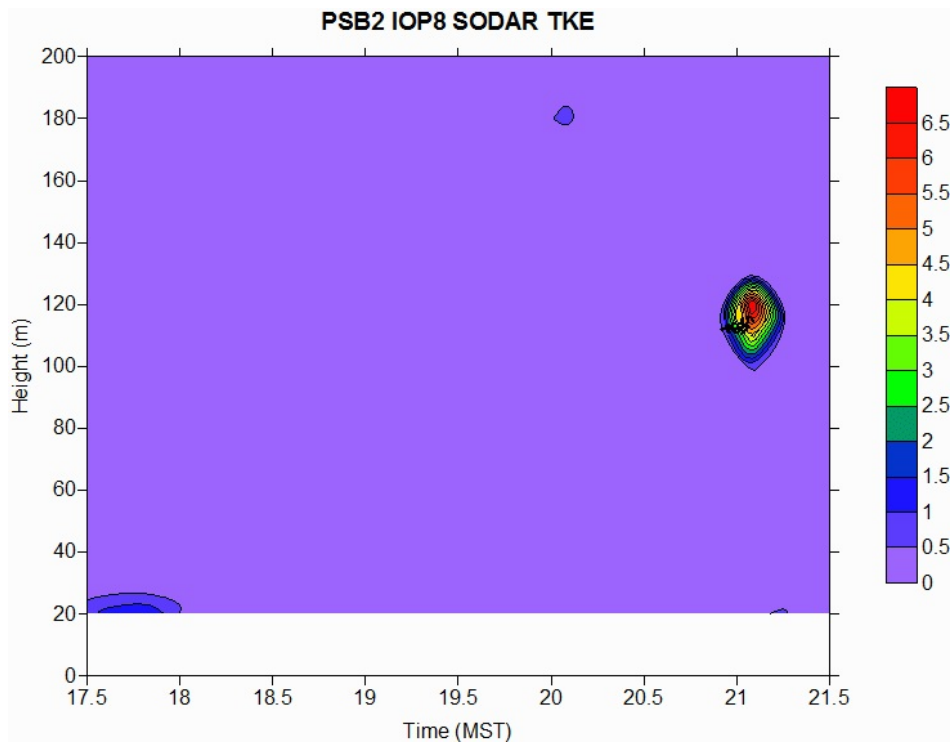


Figure 273. Time-height cross-section of TKE at sodar (SOD) during IOP8. Legend represents $\text{m}^2 \text{s}^{-2}$.

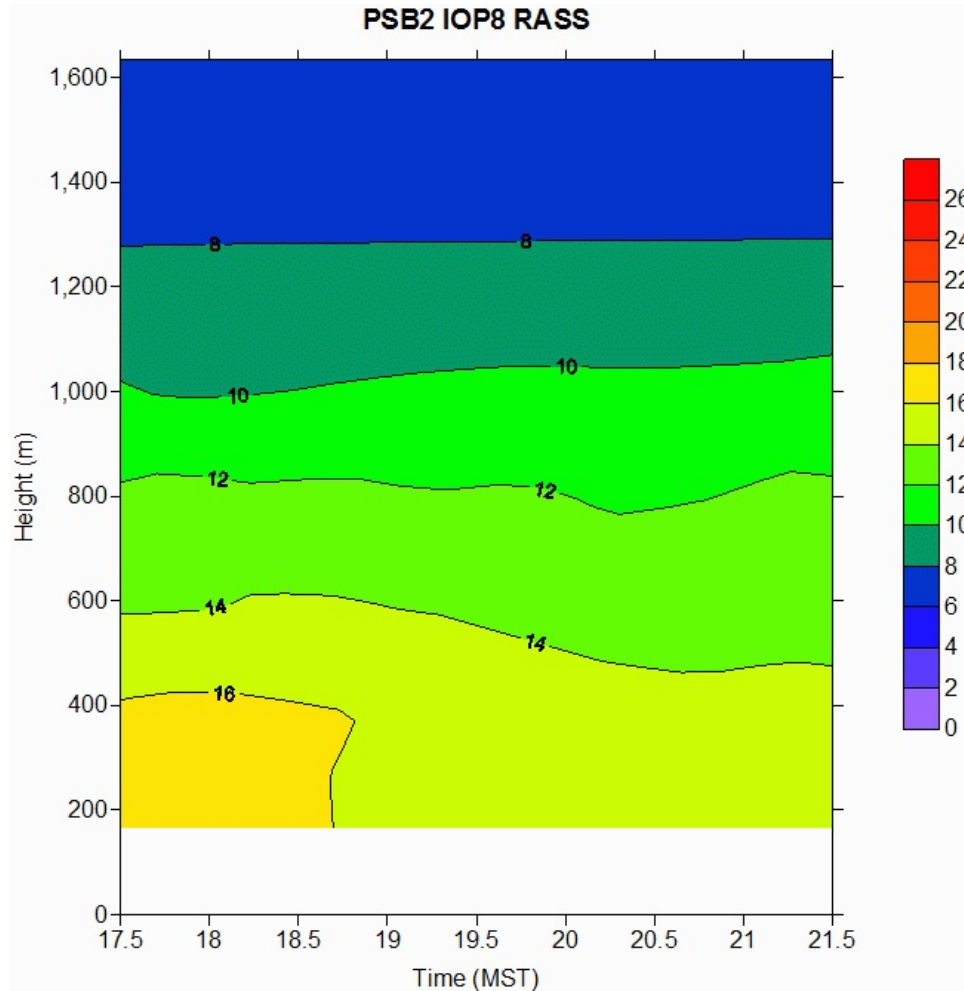


Figure 274. Time-height cross-section of virtual temperature at the RASS during IOP8. Temperatures are in degrees C.

Radiosonde Results

Pre and post-IOP radiosonde profiles of potential temperature and specific humidity for IOP8 are shown in Figs. 275 and 276. Unlike the other nighttime IOPs, there is an approximation of a constant potential temperature layer in Fig. 275. While not fully convincing, it appears better defined in the pre-IOP launch but both the pre and post launches suggest a major boundary at just above 1000 m agl. It is somewhat ambiguous but the specific humidity profiles in Fig. 276 potentially provide some corroboration. There was no data recovery by the ceilometer during IOP8.

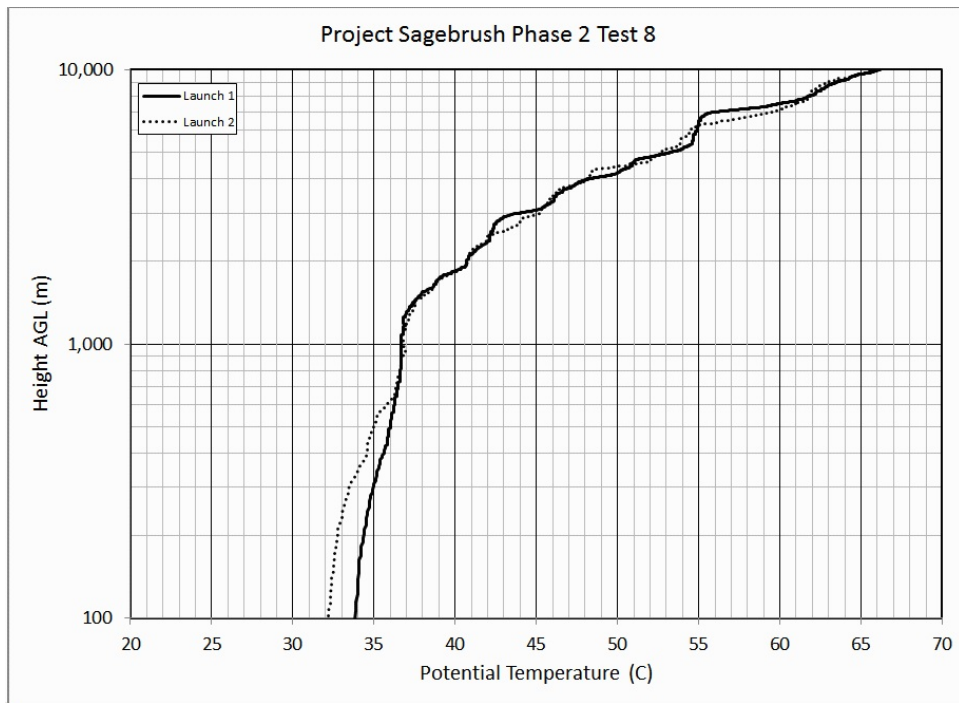


Figure 275. Potential temperature profile from radiosonde probe, IOP8. Pre-test launch bold, post-test launch dotted.

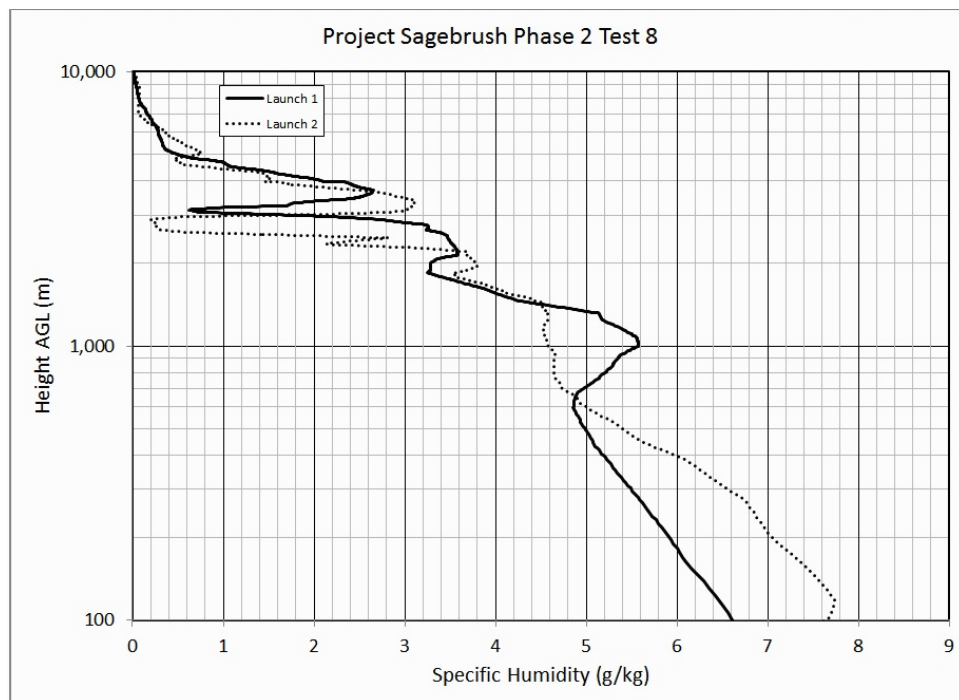


Figure 276. Specific humidity profile from radiosonde probe, IOP8. Pre-test launch bold, post-test launch dotted.

Bag Sampling Results

Figures 277 and 278 and Figures 279 and 280 show the 10-min average normalized and actual, respectively, color-coded plan view concentration maps for IOP8 bag sampling at 1 m agl. Figures 281 and 282 and Figures 283 and 284 show the 10-min average normalized and actual concentrations, respectively, along each of the arcs.

The plume was advected toward the northeast and was well-bounded by the sampling arcs during the first hour of IOP8. Near the end of the first hour the wind directions shifted resulting in the plume being transported mainly toward the south-southeast. As a consequence, all of the profiles showed evidence of significant truncation west of the ends of the arcs at 162° during the second hour. This plume behavior was consistent with the wind directions observed at GRI but not at COC. Most of the plumes tended to have a fairly well defined central, Gaussian-like peak on all arcs. During the first hour, the central peaks intersected at least 50-60 degrees of arc along the 100 m arc upwards to about 100 degrees. It was somewhat less on the 200 and 400 m arcs. The available data for the second hour suggest a similar picture. Relative to the other nighttime IOPs, the central peaks tended to be more prominent and consistently defined with less overall concentration variability on the flanks. The flank variability was especially limited during the first hour but somewhat more common during the second hour. Overall, the horizontal dispersion during IOP8 was similar to or somewhat less than the other IOPs that exhibited relatively lesser truncation (e.g., IOPs 1, 2, 5, and 7).

The measured σ_y for IOP8 were greater than the daytime IOPs but less than the more stable IOPs such as IOPs 5 and 7.

Like IOPs 5 and 7, the maximum normalized concentrations during IOP8 ranged up to two orders of magnitude greater than the maximum normalized daytime concentrations. This is clearly shown in the cross-sections in Figs. 281 and 282 (compare Figs. 84, 85, 111, 112). Also recall that the color-coded normalizations in the map views of Figs. 277 and 278 were suppressed by a factor of 10 relative to the daytime normalizations yet they feature an abundance of red and orange markers that are only sparsely present in the corresponding daytime plots. This was also the case for IOP8.

Figures 285 and 286 show the vertical concentration profiles at the four fixed towers and the mobile tower arranged by 10-min (bag) sampling period. Figures 287 and 288 show the temporal evolution of the vertical concentration profiles at each of the five towers. During the first hour, when the plume was advected mainly toward the northeast, the plume was measured at least weakly on all towers, even at 400 m. In some cases the maximum concentrations were measured at the surface and in other cases the maximum concentration was above the 1 m level, usually at 3 m agl. Concentrations reached background or very near background levels by 15-20 m agl in all profiles. During the second hour, with the shift in wind directions, concentrations were much lower in the vertical profiles with maxima usually less than 20-30 ppt. Maximum concentrations were at the 1 m level in almost all cases. All concentrations on the 400 m tower

were at or near background levels and nothing above background concentrations was measured above 3 m agl.

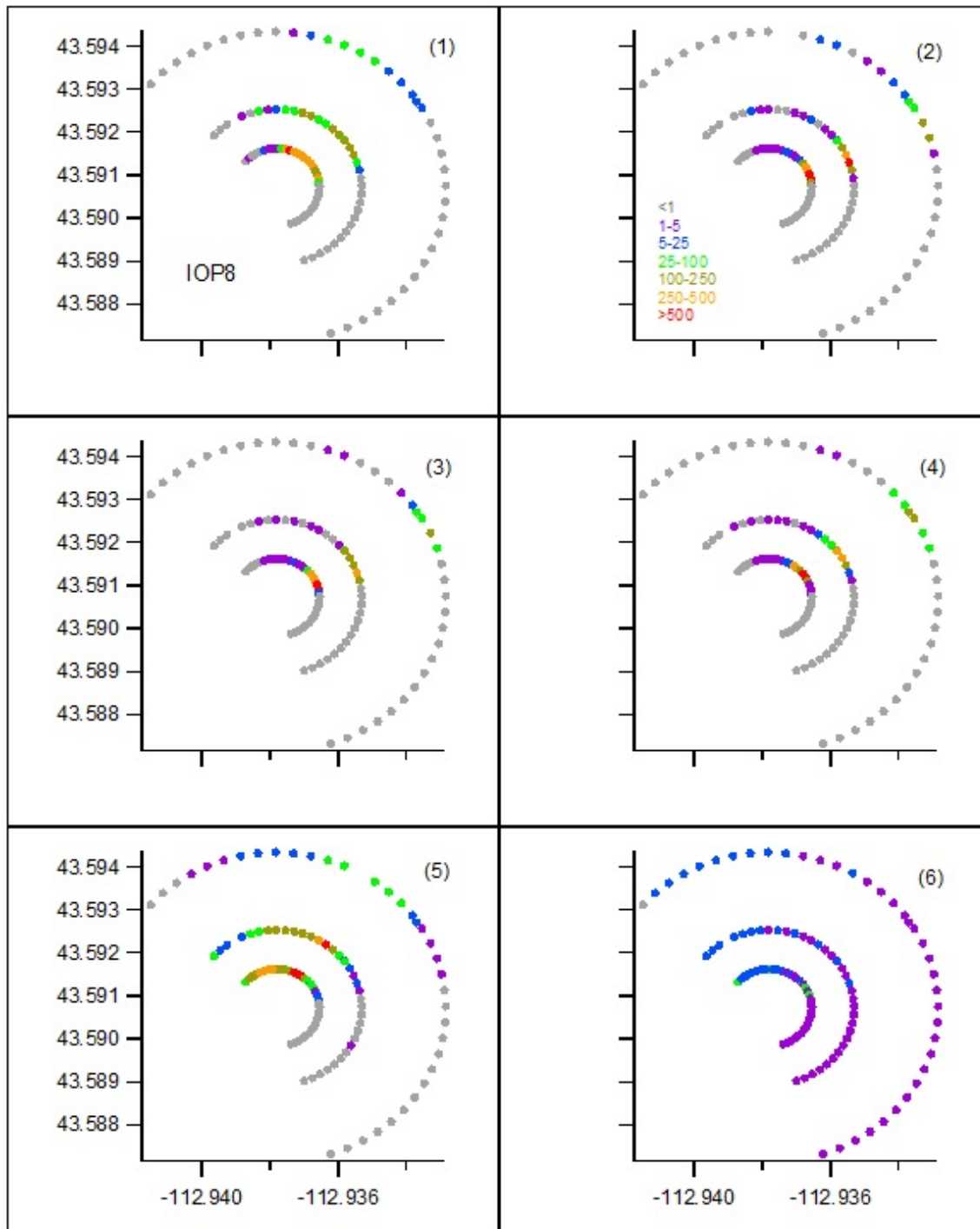


Figure 277. Color-coded normalized ($F^*\gamma/Q$ ppt s g⁻¹) concentrations at 1 m agl for bags 1-6 during IOP8. The number in () is bag number.

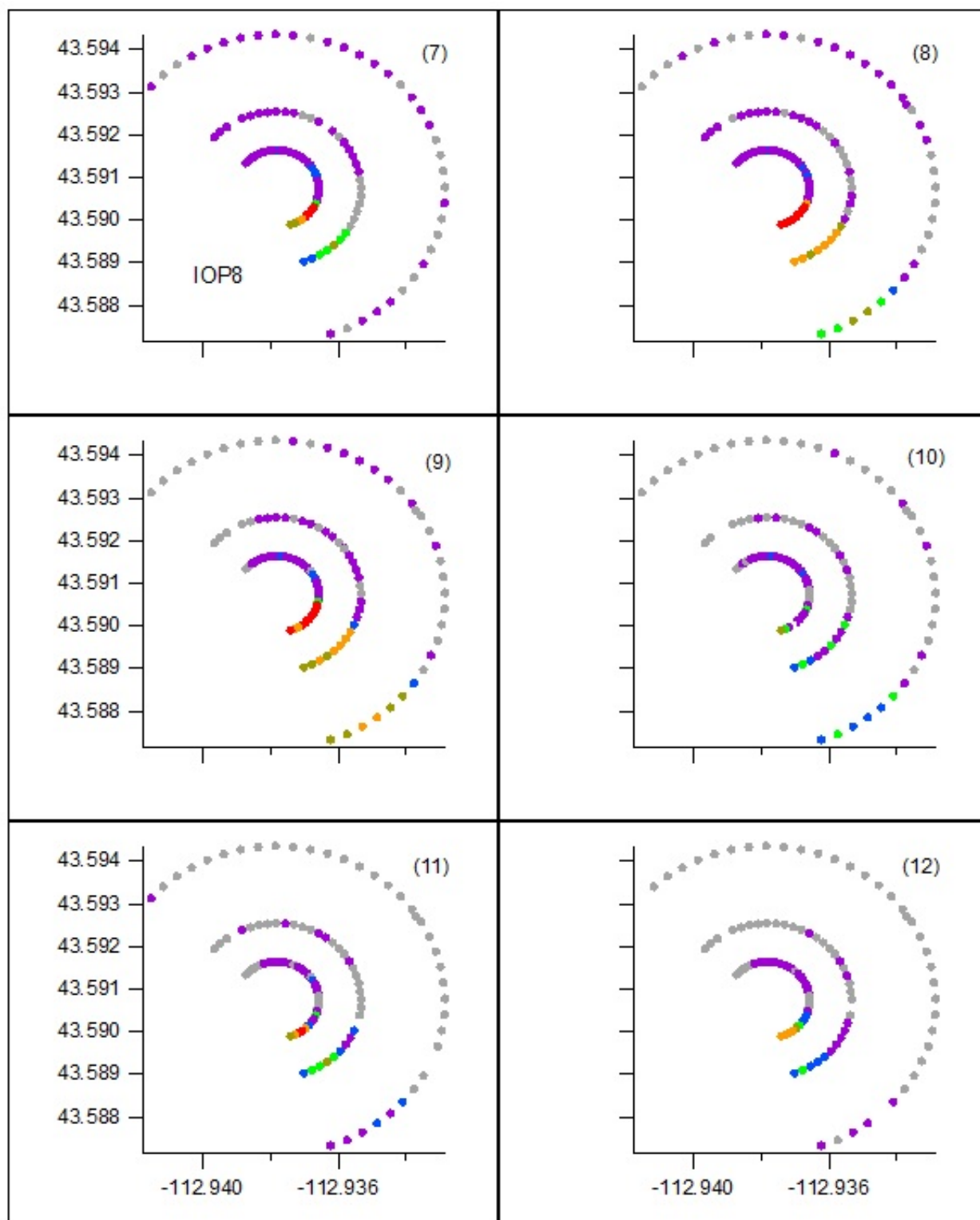


Figure 278. Color-coded normalized ($F^*\chi/Q$ ppt s g^{-1}) concentrations at 1 m agl for bags 7-12 during IOP8. The number in () is bag number.

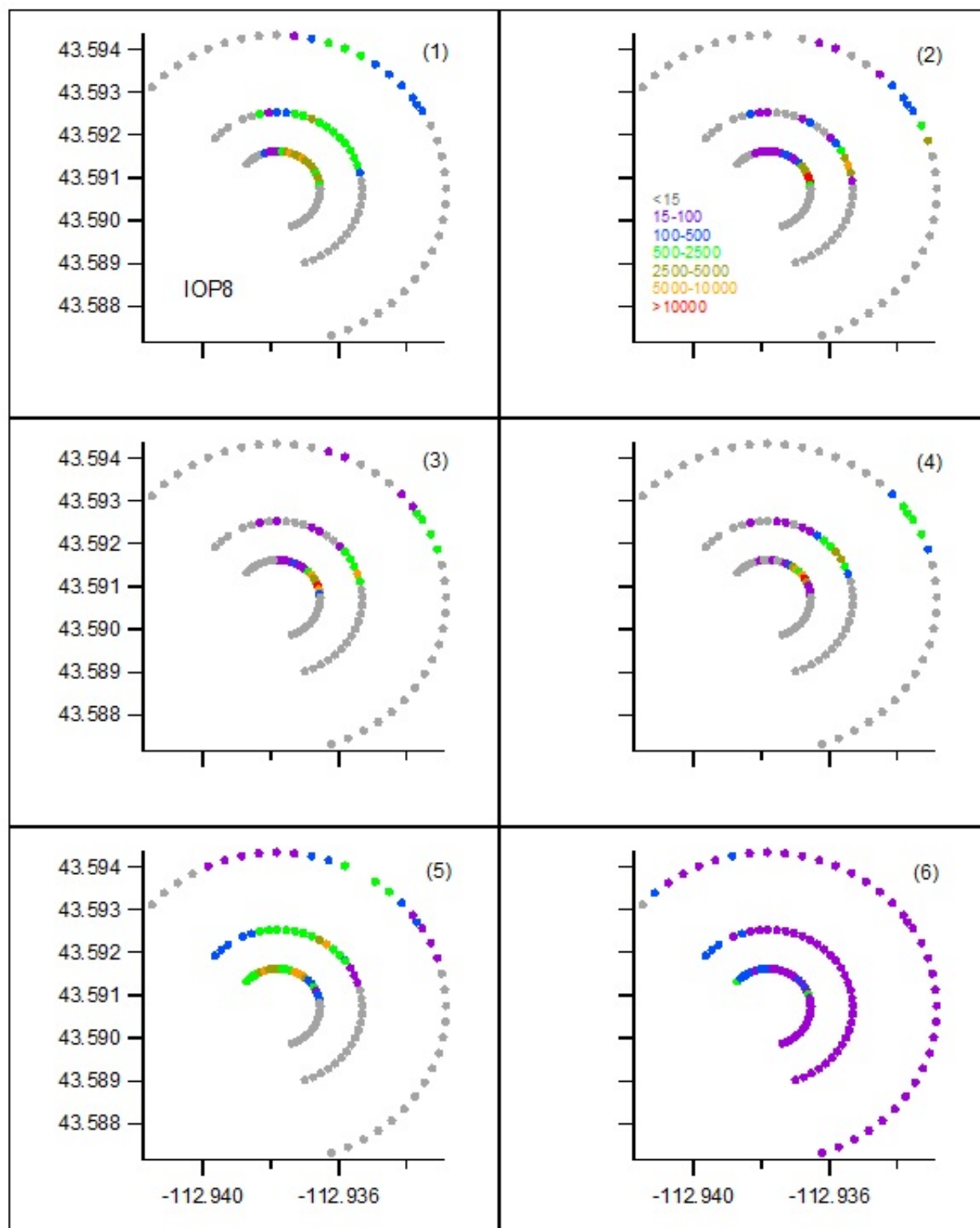


Figure 279. Color-coded measured SF₆ concentrations (ppt) at 1 m agl for bags 1-6 during IOP8. The number in () is bag number.

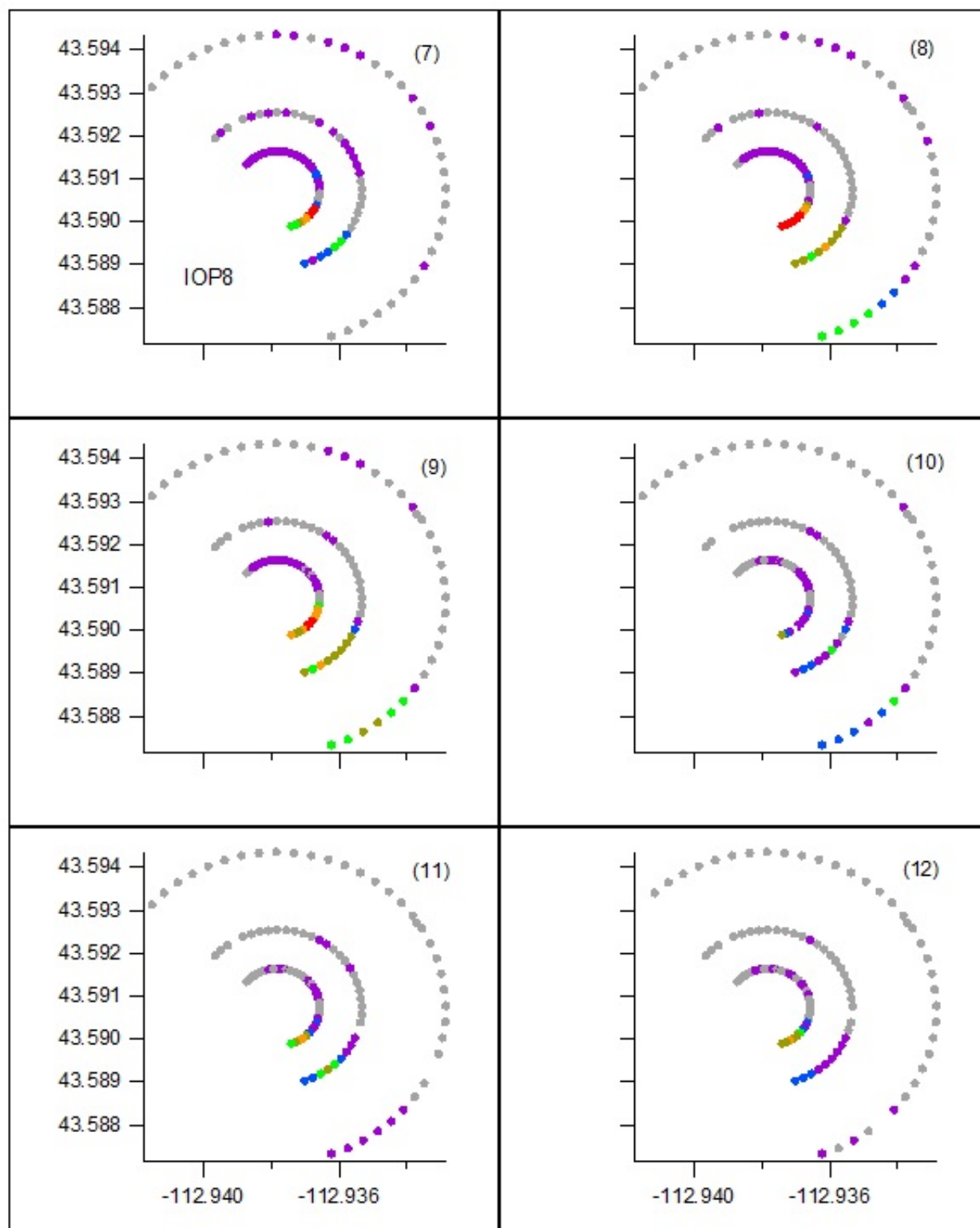


Figure 280. Color-coded measured SF_6 concentrations (ppt) at 1 m agl for bags 7-12 during IOP8. The number in () is bag number.

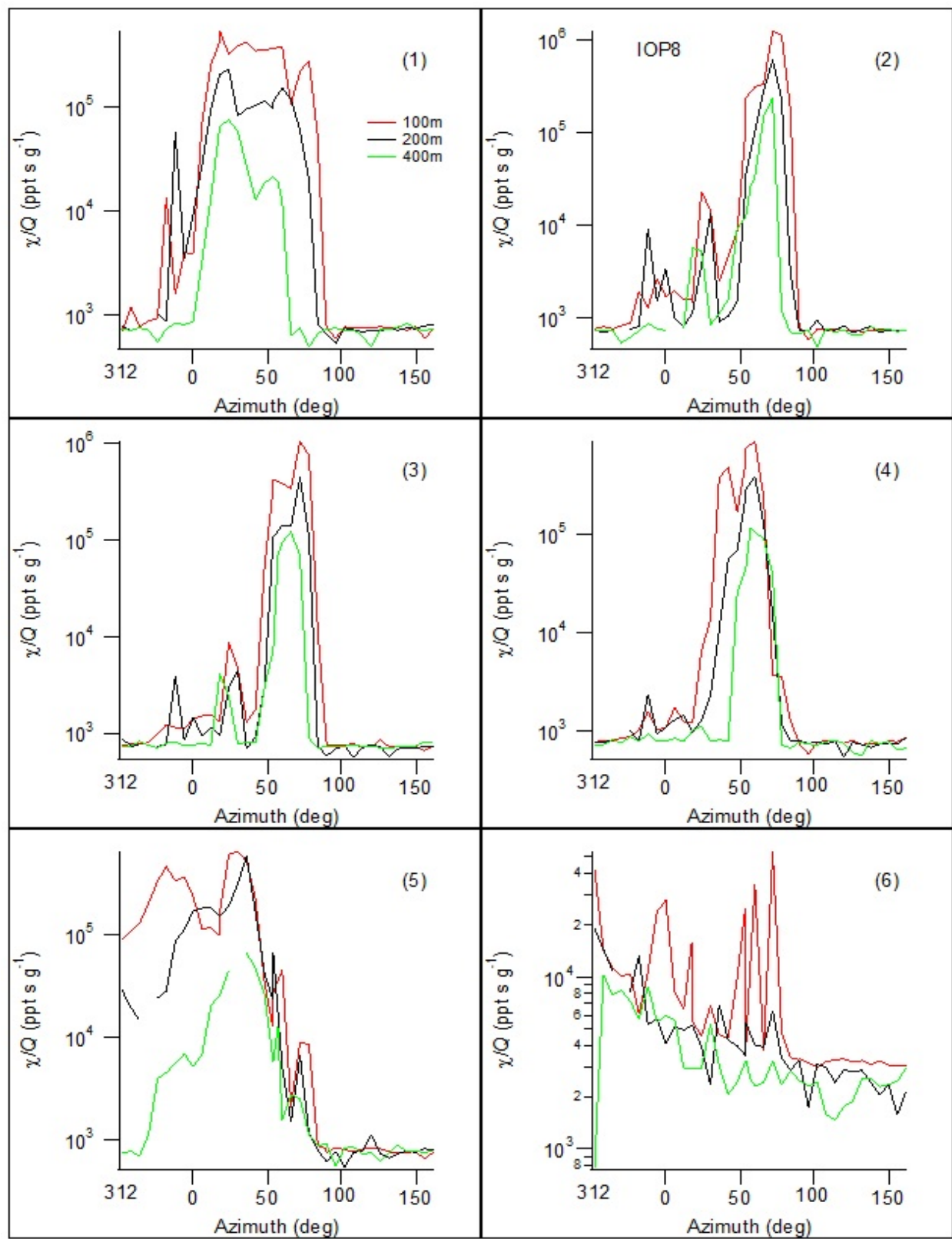


Figure 281. Cross-sections of normalized concentration along the arcs for bags 1-6 during IOP8.

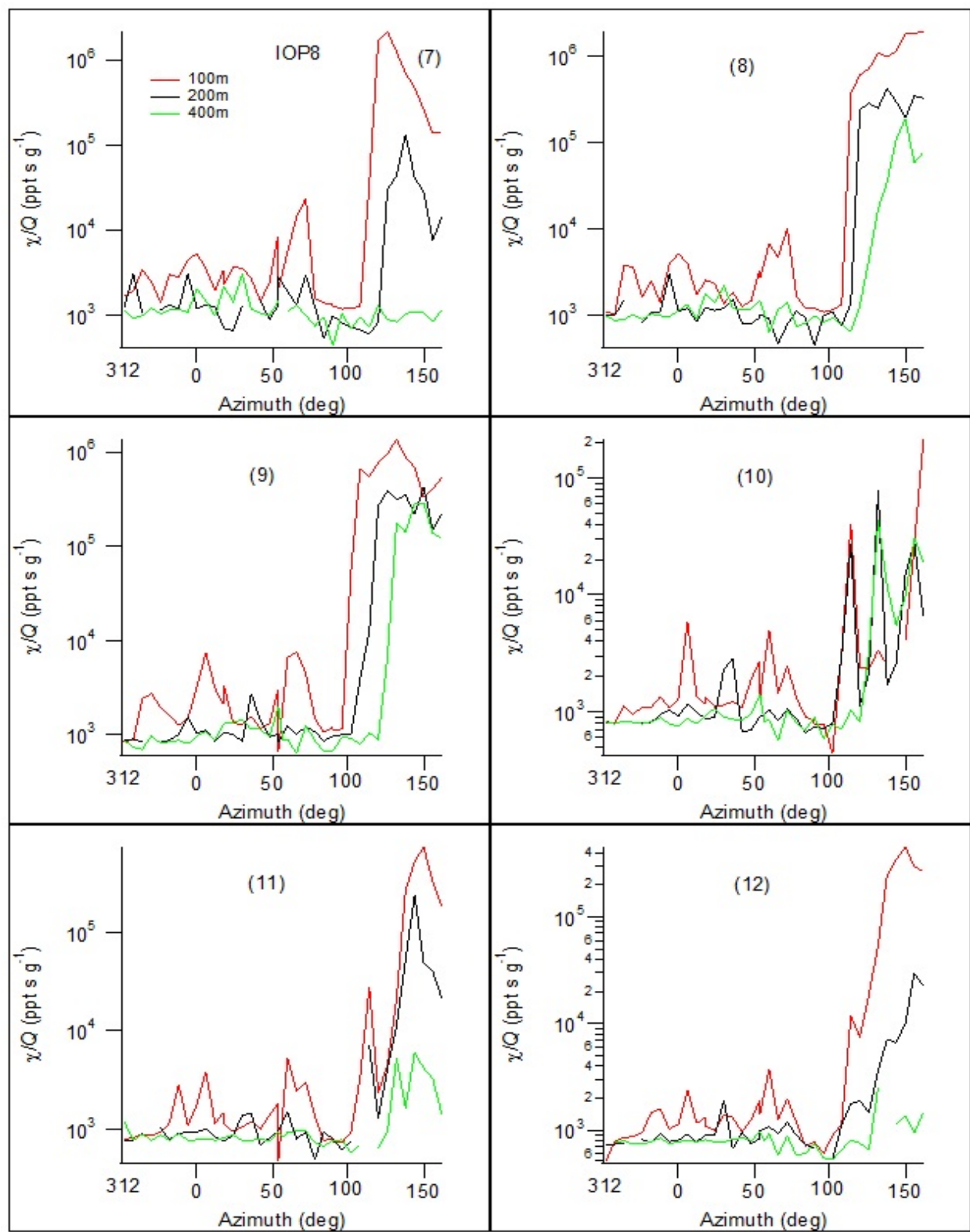


Figure 282. Cross-sections of normalized concentration along the arcs for bags 7-12 during IOP8.

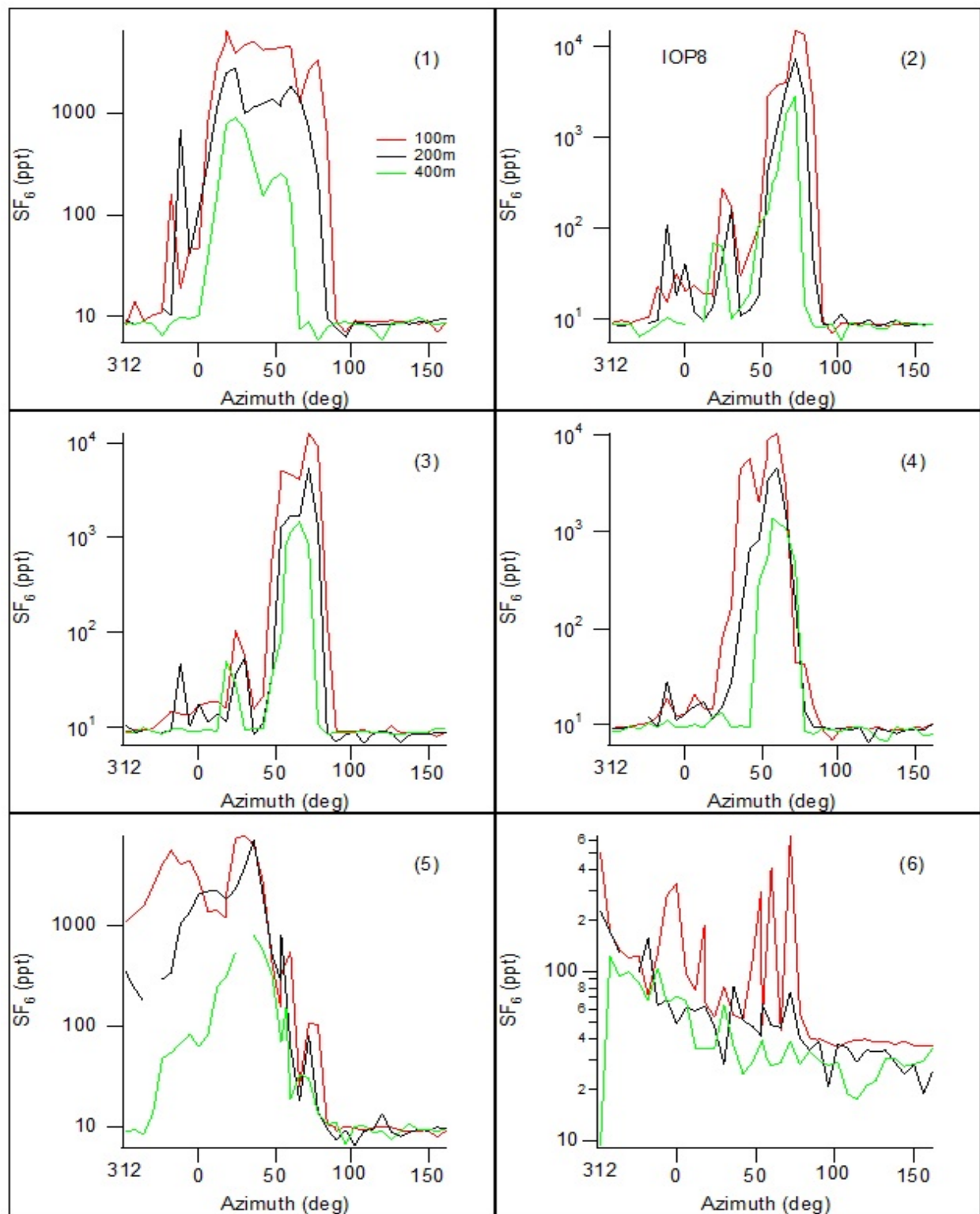


Figure 283. Cross-sections of measured SF_6 concentration along the arcs for bags 1-6 during IOP8.

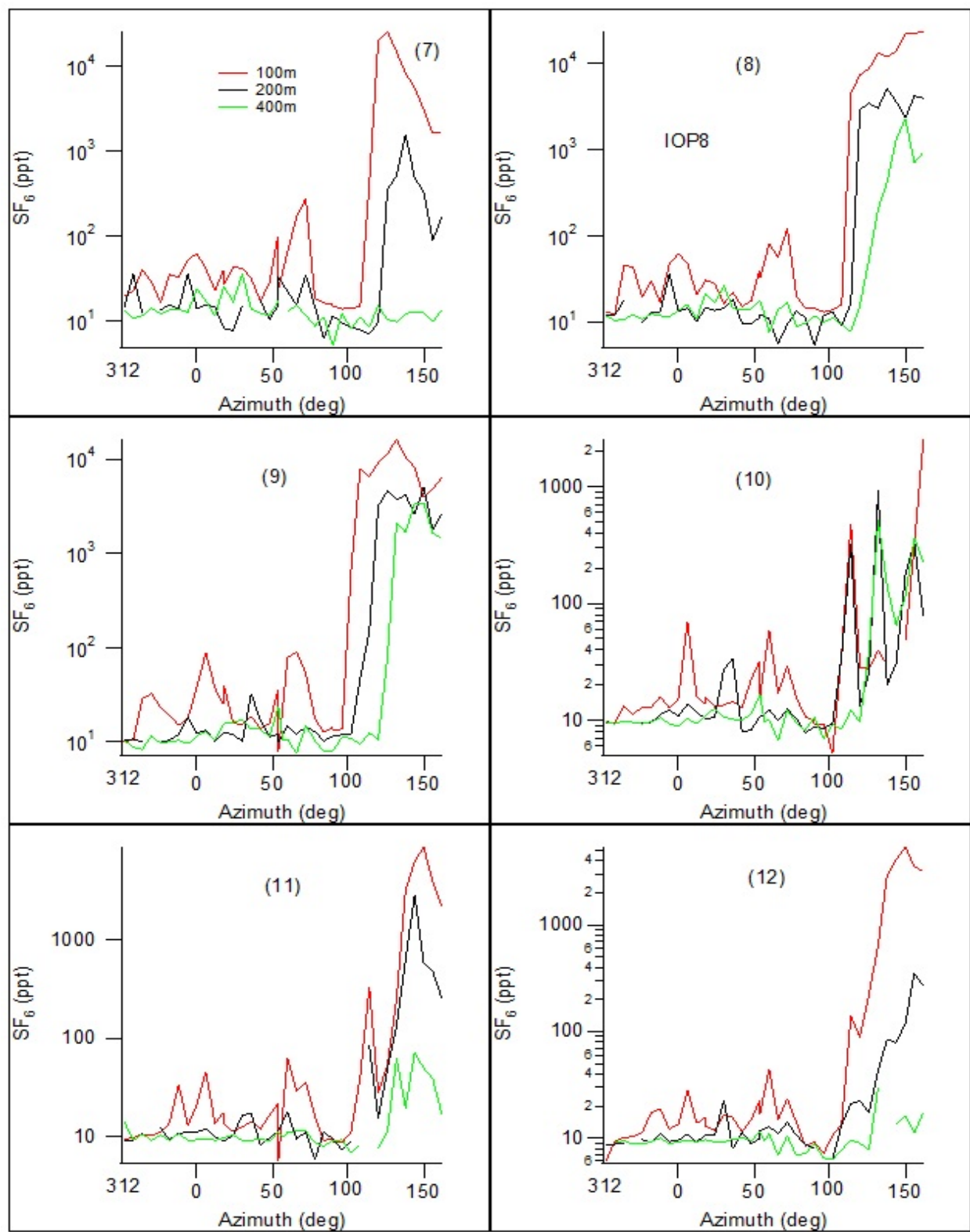


Figure 284. Cross-sections of measured SF_6 concentration along the arcs for bags 7-12 during IOP8.

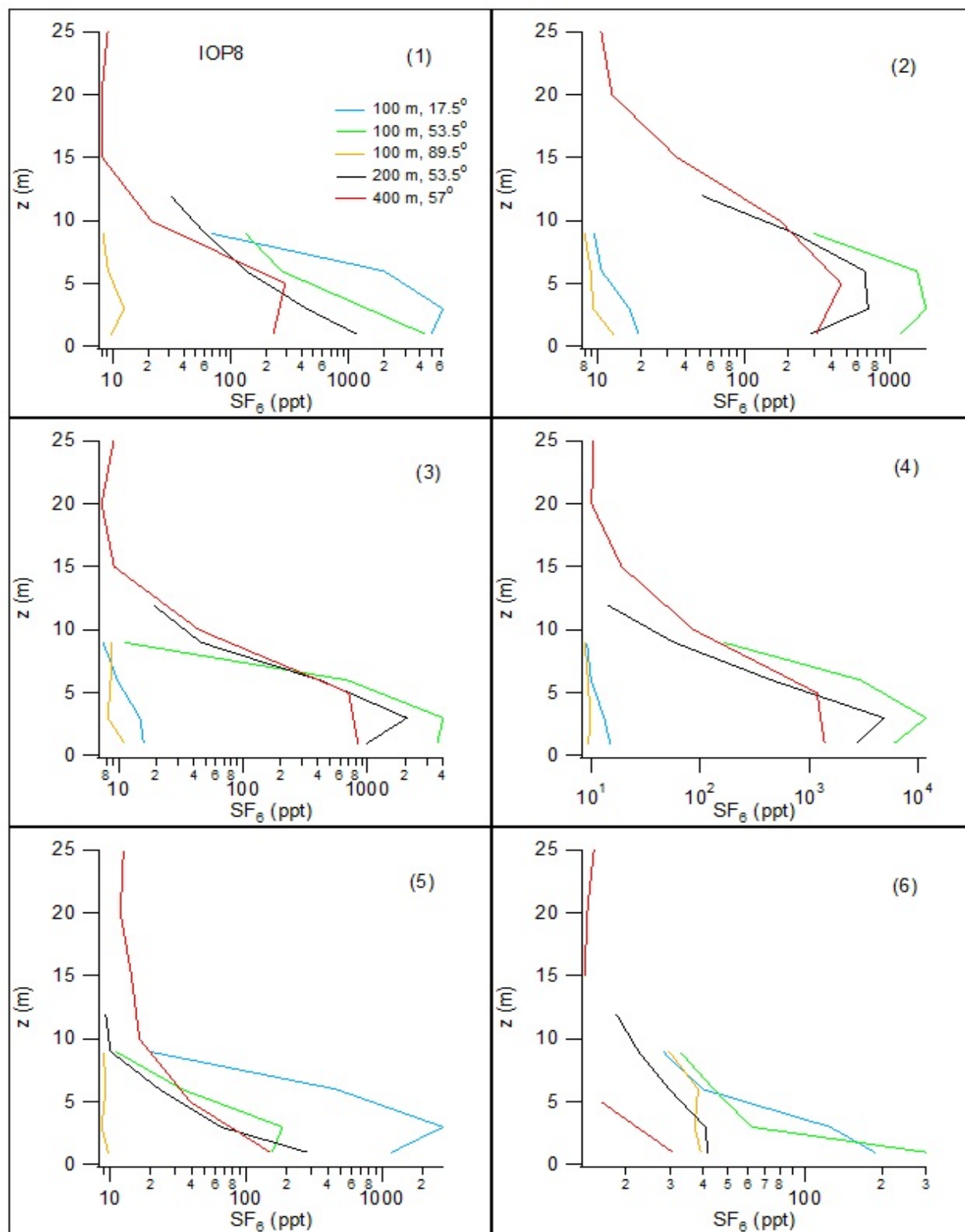


Figure 285. Vertical concentration profiles at the arc position given in the legend for (bags) 1-6 during IOP8.

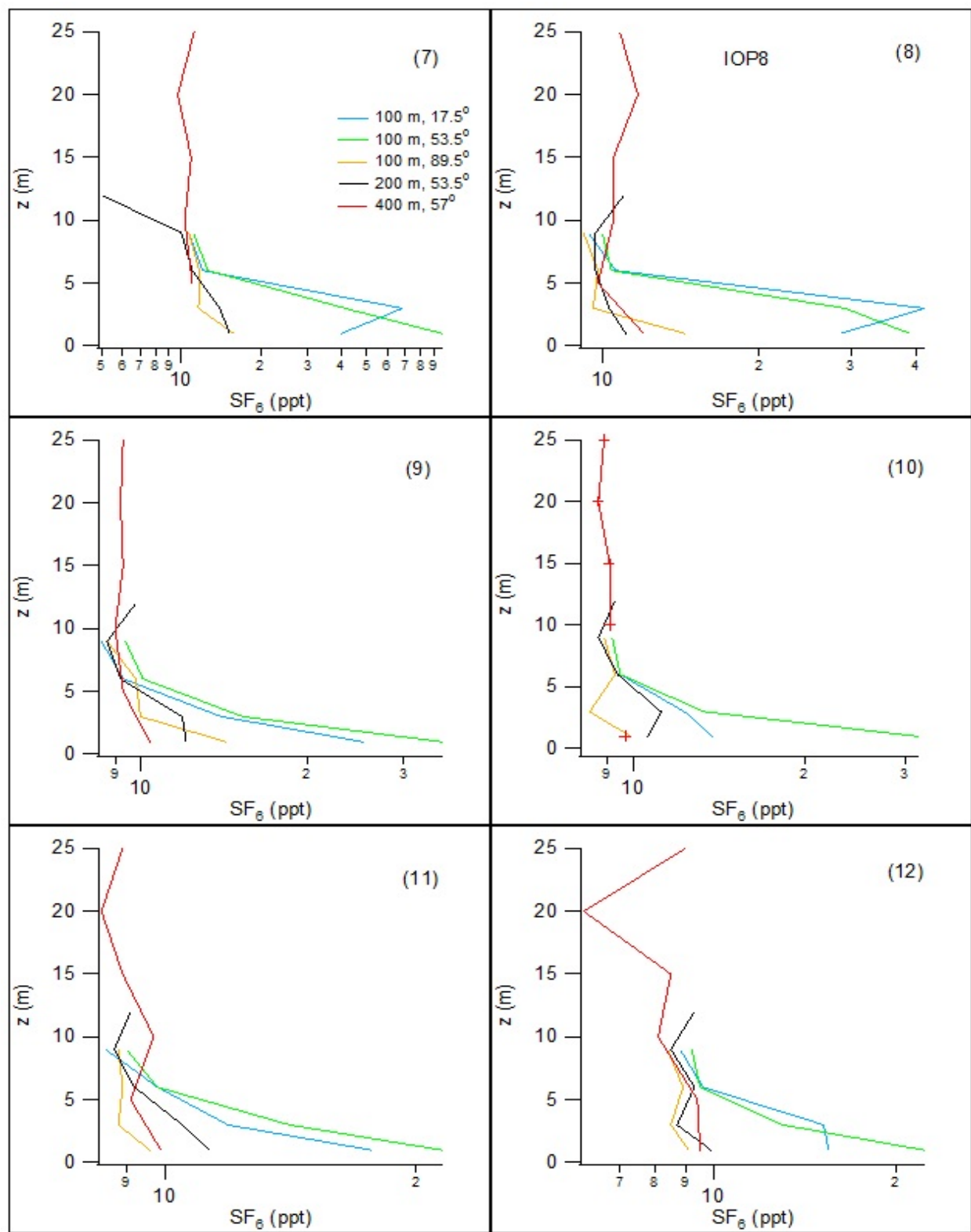


Figure 286. Vertical concentration profiles at the arc position given in the legend for (bags) 7-12 during IOP8.

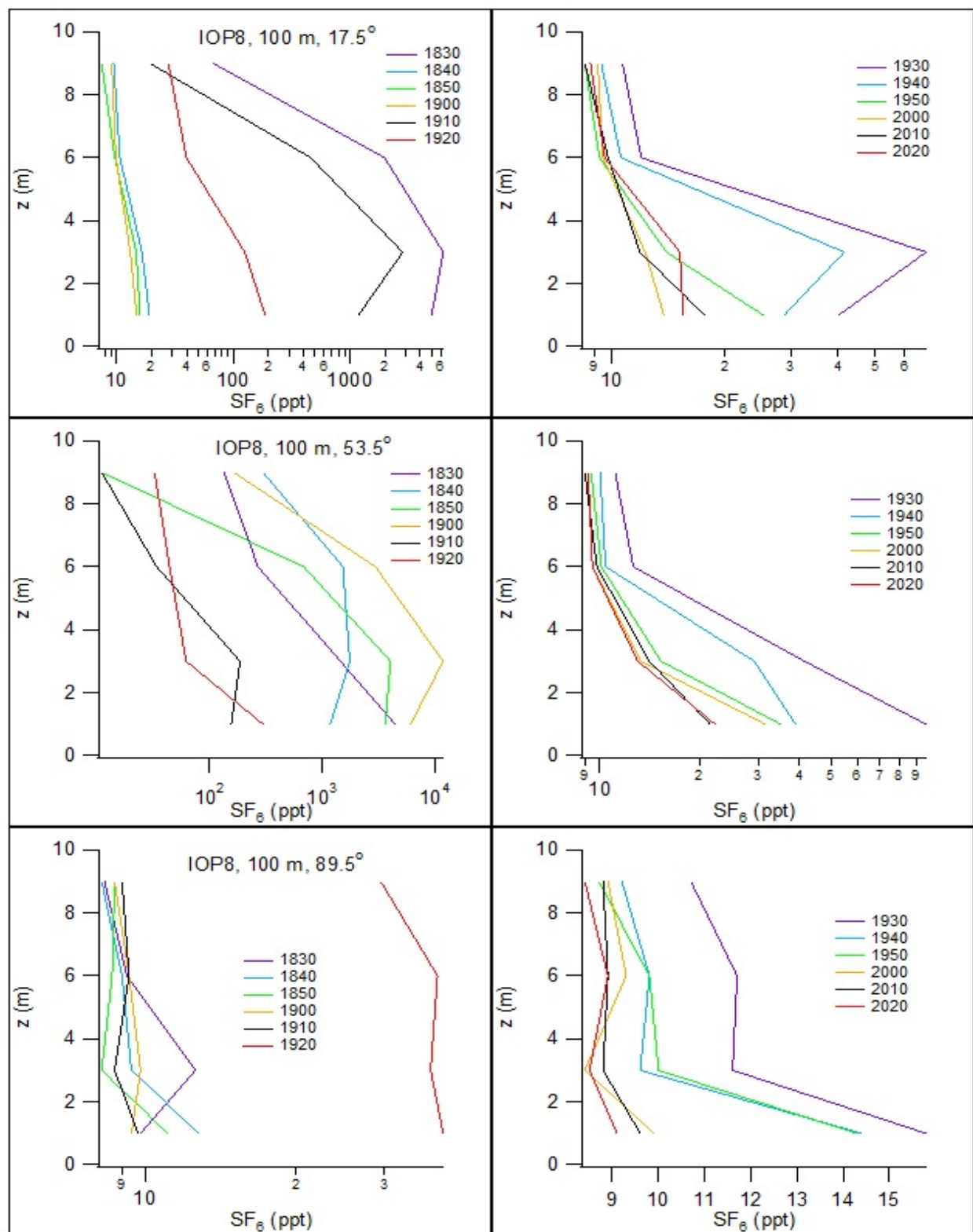


Figure 287. Vertical concentration profiles for the 100 m towers at the annotated arc position and times given in the legend during IOP8.

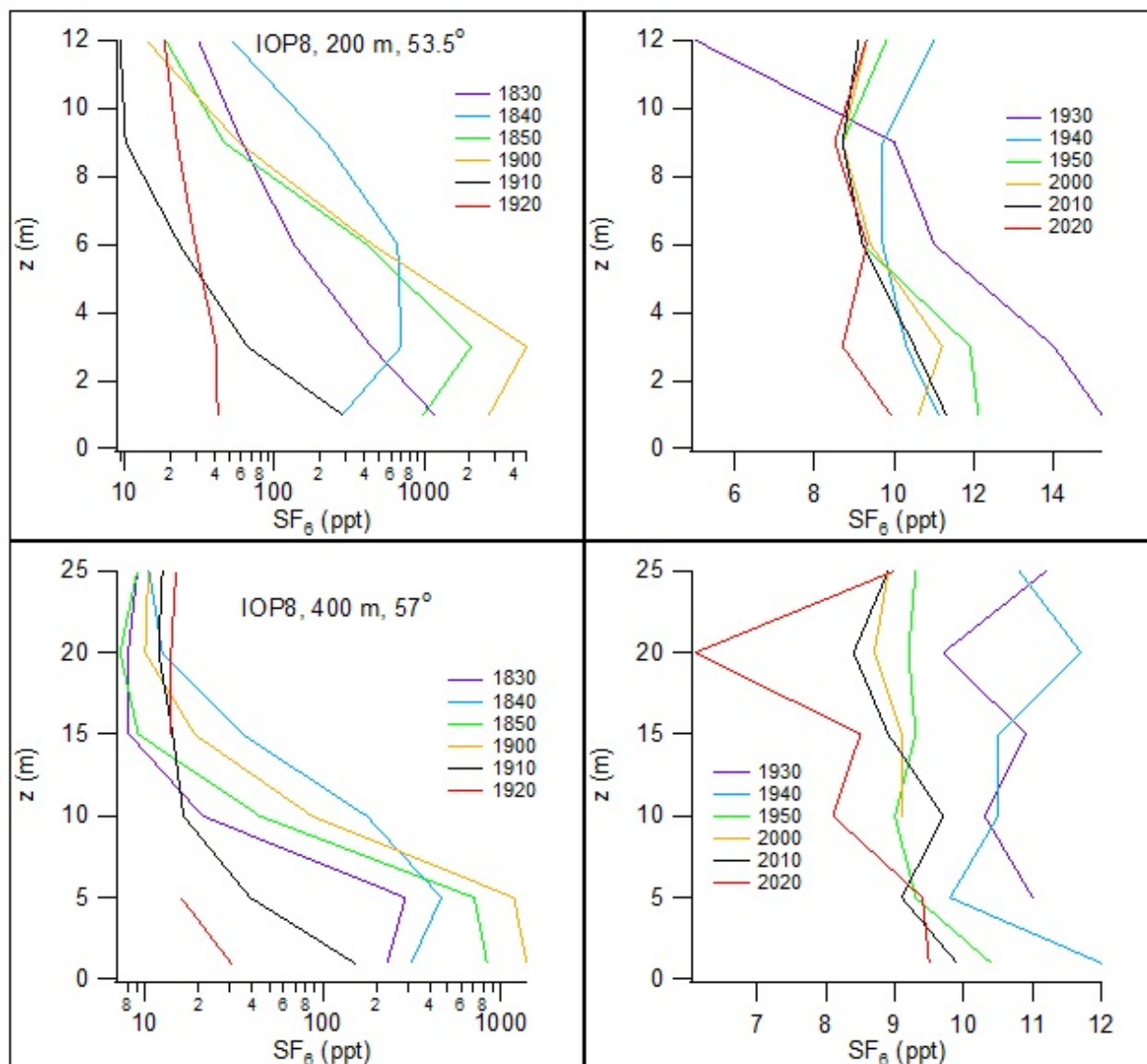


Figure 288. Vertical concentration profiles for the 200 m and mobile towers at the annotated arc position and times given in the legends during IOP8.

Fast Response Results

The locations of the fast response analyzers during IOP8 are shown in Fig. 289. The corresponding concentration time series are shown in Fig. 290. The color coding of the time series was described in the Introduction to this section. Due to the frequency of moves by all of the analyzers, the fixed location sites in Fig. 289 have not been keyed to their respective time series in Fig. 290.

The frequency of analyzer movement complicates an interpretation of the fast response concentration time series. Nevertheless, it is clear that they were again characterized by highly fluctuating signals with rapid shifts between very high peaks and concentrations at or near background. The peaks were often brief, no more than a few minutes, and the fluctuations abrupt. This was particularly the case for when the analyzers were mobile (red traces) and the peaks were characteristically very sharp spikes. The short plume transect times would suggest that the individual plume elements were very narrow.

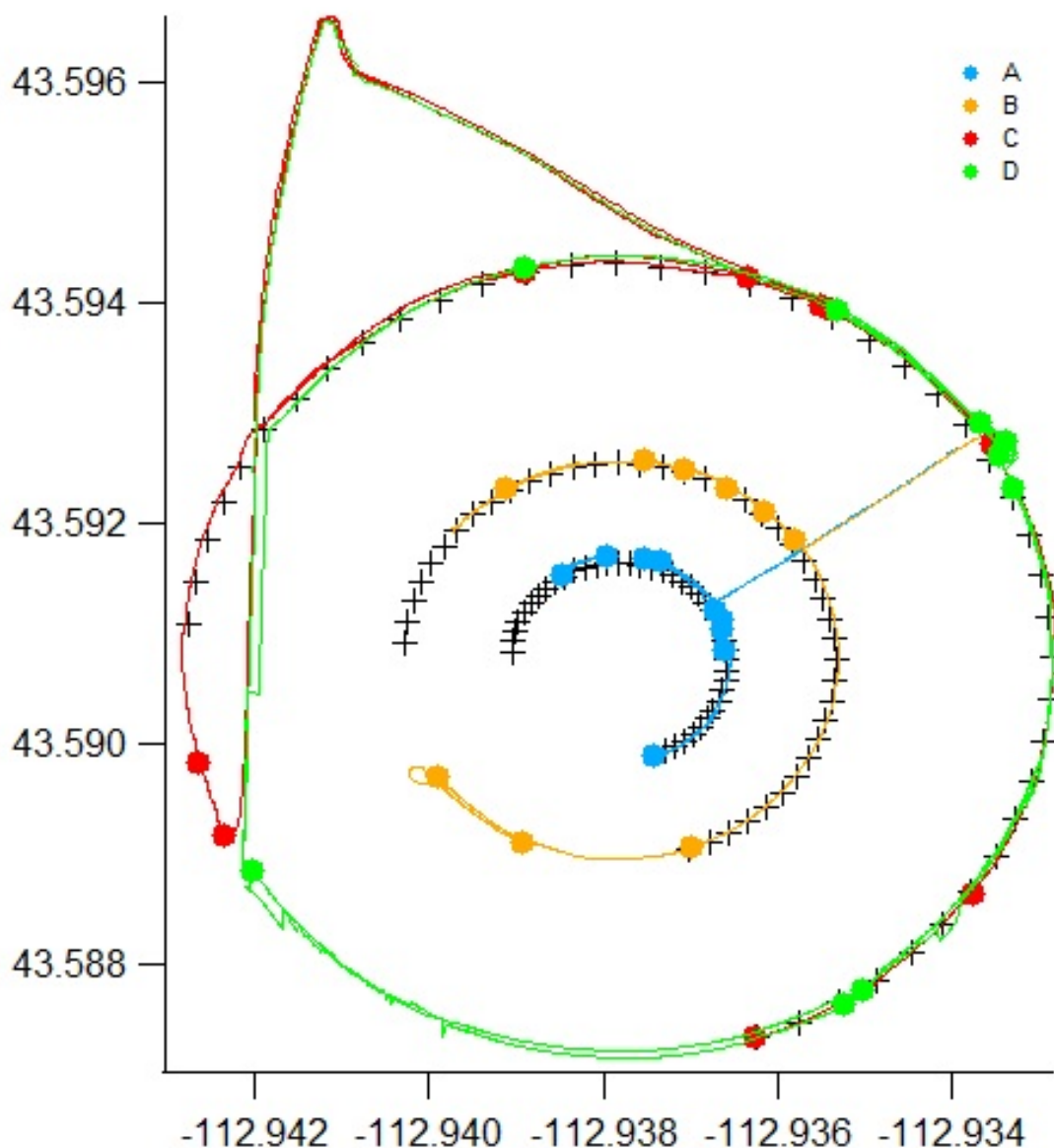


Figure 289. Locations of fast response analyzers during IOP8.

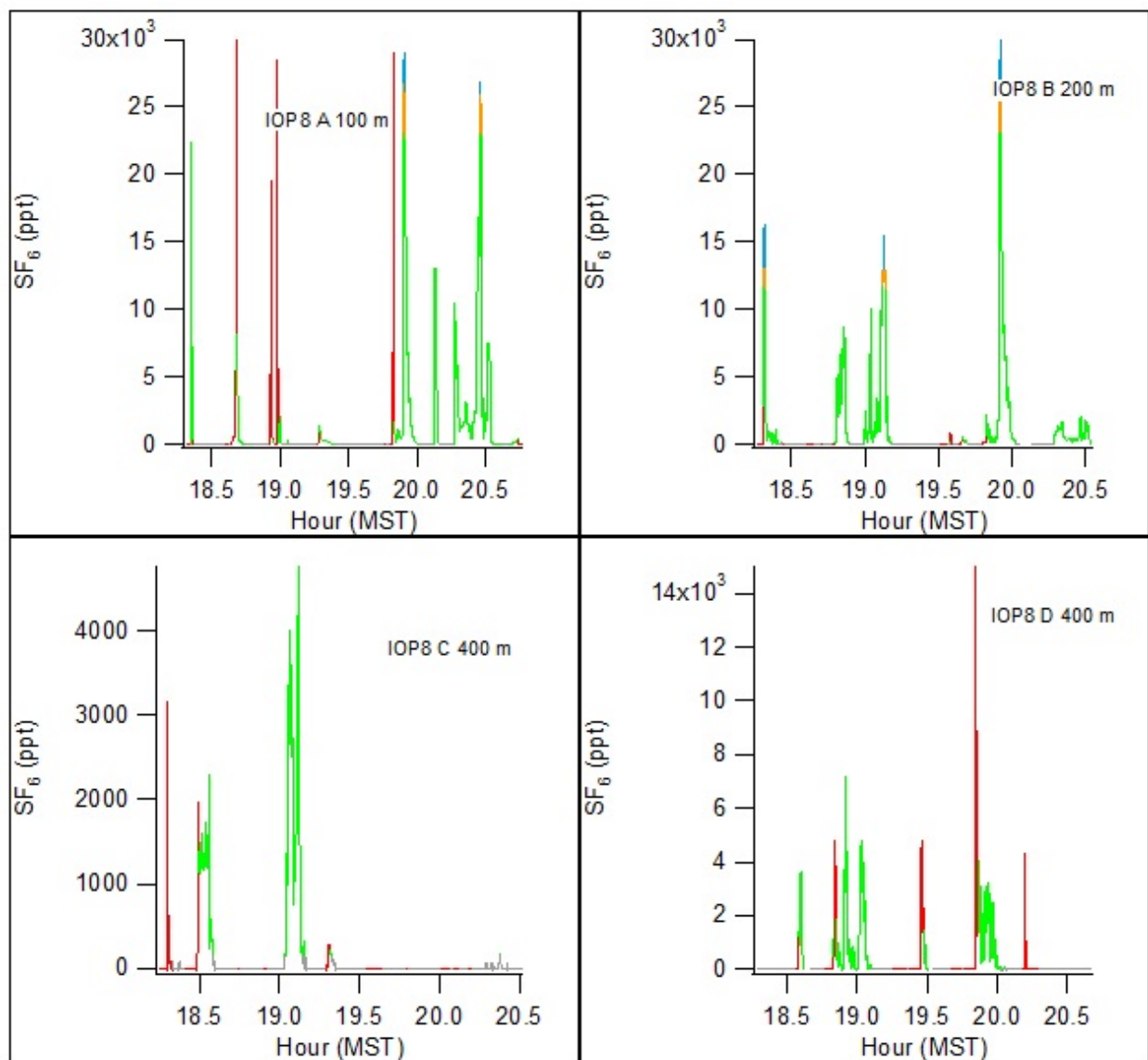


Figure 290. Fast response concentration time series during IOP8.

This page intentionally left blank.

Preliminary Discussion

The combination of higher resolution (10 min) time-averaged bag sampling, fast response tracer sampling, and the extensive meteorological measurements of turbulence and vertical profiles provides a unique data set that offers insights into plume dispersion in light wind conditions. This is especially the case for the nighttime tests.

One of the most salient features of the data is what it says about the uncertainty in plume concentration measurements. The sometimes very large differences observed in the field duplicate sampling raised this issue. There was considerable follow up testing to determine whether these differences were a measurement artifact or accurately represented the concentration field (see Bag Sampling chapter). The weight of evidence suggests it is likely that the latter is the case and the large differences were real.

The magnitude of these differences is a function of distance and time of day. The field duplicate results for PSB2 shown in Table 12 make this point. To further develop this picture, the means for $|\%RPD|$ with one standard deviation error bars for the 10 min average data are shown for PSB1 daytime, PSB2 daytime, and PSB2 nighttime in Fig. 291a. It shows a clear pattern of decreasing average $|\%RPD|$ and uncertainty with distance and significantly larger $|\%RPD|$ at night (about two times higher). Figure 291b shows that increasing averaging times only moderately reduces the uncertainty.

The daytime $|\%RPD|$ appears to asymptotic to about 7-8% in the downwind limit. The distance result would be an expected consequence of (1) increased mixing and smoothing of concentration gradients in the plume and (2) plume broadening so that meander and being in and out of the plume would diminish in importance with downwind distance. However, that alone does not fully explain these results.

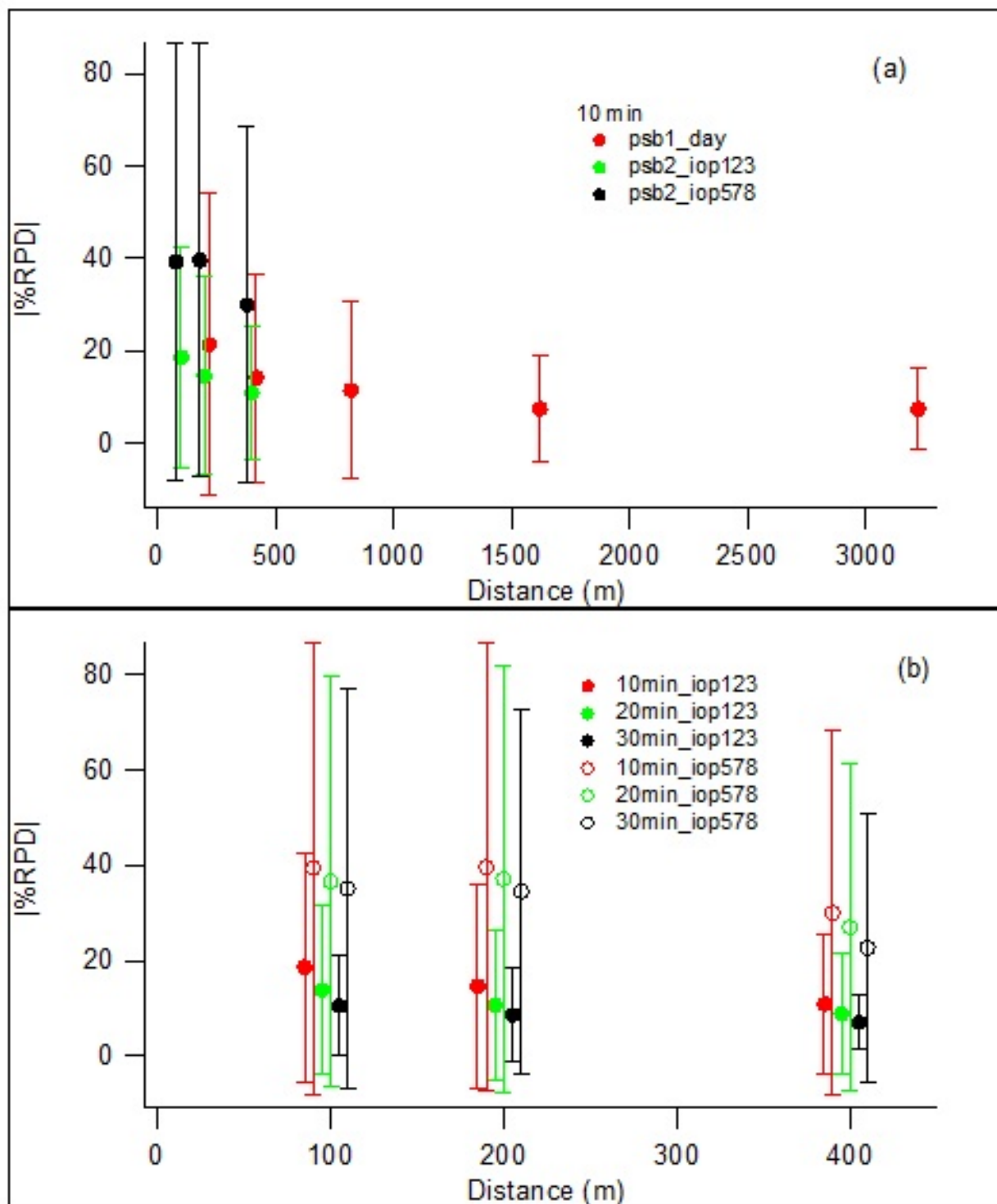


Figure 291. Mean absolute values of field duplicate %RPD with standard deviations by distance for (a) PSB1 daytime, PSB2 daytime, and PSB2 nighttime and (b) PSB2 10, 20, and 30 min results. IOPs 4 and 6 have been omitted to minimize the effects of including ambient background samples. Error bars slightly offset to avoid overwrite.

There are several other lines of evidence to consider in this discussion. First, the bag sampling results indicated that the nighttime plumes typically subtended similar ranges of arc as the daytime plumes. The edges of the daytime plumes were characterized by sharp boundaries with smooth transitions to ambient, background concentrations. The margins of the nighttime plumes often featured a very ragged, irregular pattern of concentration sub-peaks or ramps before the complete transition to background.

Second, the daytime fast response results at fixed location sites were characterized by large peaks of short duration, often less than a minute or two for any given peak, with abrupt rises from and back to baseline. The σ_θ were large (Figs. 68, 95, 122, 149) and the character of the fast response time series can be attributed to the rapid sweeping of a relatively narrow plume across the analyzer. In contrast, the nighttime fast response results at fixed locations often featured a much smaller number of large peaks but with durations in the plume of up to a half hour. The σ_θ were much smaller than during the daytime (Figs. 176, 206, 235, 265) and it appears as if once the plume arrived at the analyzer, it was much less likely to sweep past the analyzer and move on. The fast response analyzers were more often mobile during the nighttime IOPs. When they intercepted and moved through the plume, their residence time in the plume was often very short as indicated by the sharp concentration spikes associated with these intercepts (e.g., Figs. 230, 260, 290). That would mean that the nighttime plumes were also narrow but more likely to remain fixed in one direction. Anecdotally, there were instances during nighttime IOPs when vans with analyzers on the 400 m arc were parked adjacent to each other with one analyzer measuring background concentrations and one analyzer measuring very high concentrations. So the plume edges at night could be very sharp.

An explanation is then necessary that accommodates the following stable, low U nighttime observations for a continuous release:

- The often large RPD associated with field duplicate field duplicate bag sampling (Fig. 291). There were sometimes very large time-averaged concentration differences across a short separation (~ 1 m).
- The fast response analyzers indicated the stable boundary layer plumes were narrow (red spikes on mobile traverses) but exhibited some constancy in wind direction with little meander as shown by the often long plume residence times in fixed sampling (Figs. 201, 230, 260).
- The bag sampling provides overwhelming evidence that the effective horizontal plume spread in the stable boundary layer was very large and comparable to daytime in many respects.
- The nighttime arc cross-sections often featured a prominent, central set of peak(s), crudely Gaussian in form, subtending 50-80 degrees or more of arc flanked by extended, very irregular plume margins or ramps.

- Plume meander occurred at low U during both the daytime and nighttime IOPs. However, IOPs 1-4 (day) were characterized by high frequency shifts in wind direction and IOPs 5-8 (night) were characterized by limited shifts in wind direction on short time scales punctuated by larger, episodic shifts in wind direction.

This set of observations would suggest that the nighttime plumes were comprised of an ensemble of narrow plume filaments or elements across a limited range of arc, each with individually minimal meander or horizontal spread. This would explain the abrupt changes in concentration over short distances and the sustained residence time of the plume at a certain wind direction. Then episodic shifts in wind direction redirected the ensemble of plume elements to account for the large effective plume spreads over the extended duration of the continuous release.

A third line of evidence to consider is the turbulence measurements with respect to nighttime plume variability. It is possible that turbulent bursts from above the near surface could have had the effect of injecting clean parcels of air from aloft down to where the tracer measurements were being made. These could either displace or dilute plume parcels. There is limited direct evidence of this but the nighttime time series of σ_ϕ , TKE, and σ_w (Figs. 177, 207, 236, 266) typically exhibited more variability and spikes than corresponding daytime time series (Figs. 69, 96, 123, 150). Figures 292 and 293 show fluctuation intensities (standard deviation/mean of 10-min records) for TKE and σ_w , respectively, for each IOP. These certainly suggest that the turbulent fluctuation intensity levels were greater during the nighttime IOPs and might have played a role in the observed concentration variability. It's beyond the scope of this discussion to pursue this topic in detail here.

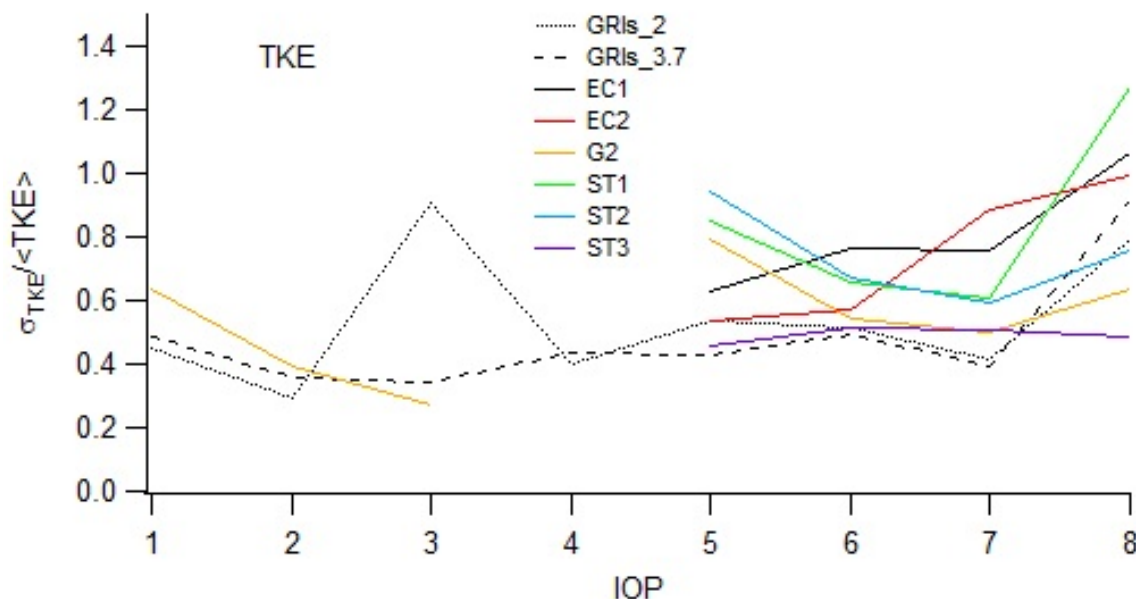


Figure 292. TKE fluctuation intensity ($\sigma_{\text{TKE}} / \langle \text{TKE} \rangle$) for 10-min records at the near surface sonic anemometers.

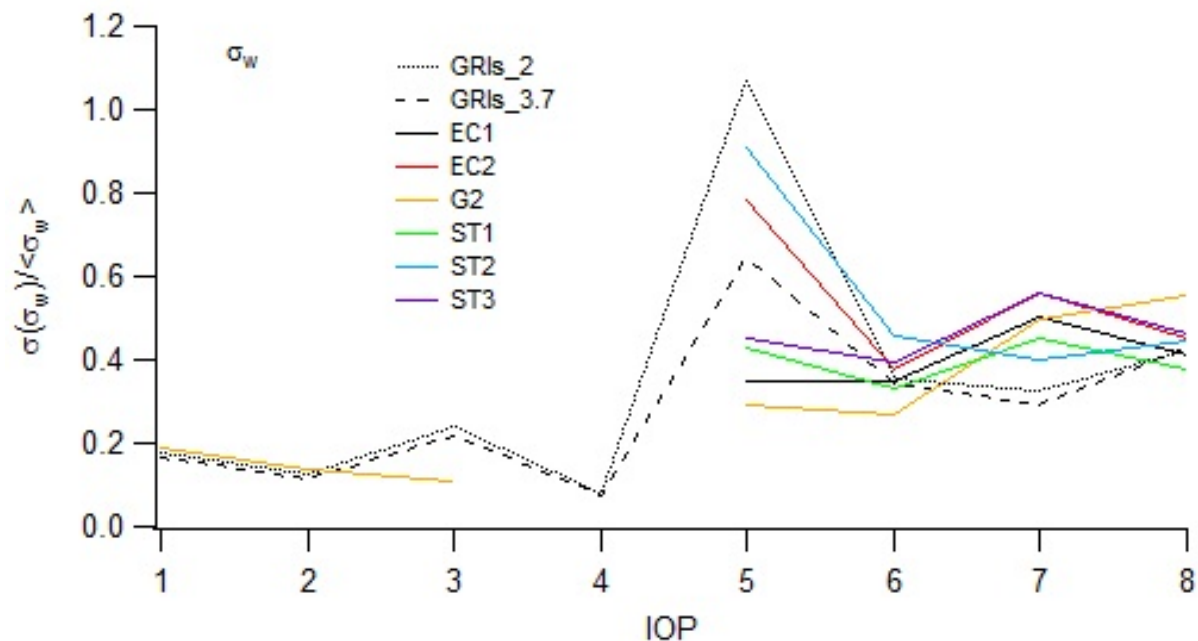


Figure 293. σ_w fluctuation intensity ($\sigma(\sigma_w)/\langle \sigma_w \rangle$) for 10-min records at the near surface sonic anemometers.

It's an open question as to how features such as the hypothetical low-level jet might have contributed to this. There is strong evidence for the presence of a low-level jet during IOP6. This can be seen most clearly in the sodar data. The vertical turbulence profiles on GRI also show distinct increases in turbulence at higher profile levels, the gradient in U at the upper levels is still steep, and the sharply reduced temperature gradients could reflect enhanced mixing. Similar data from IOPs 5 and 7 also hint at this possibility but it is much less convincing and well defined.

The PRO data for IOPs 5-7 suggest a transition zone in wind directions from northeast to southwest above about 500 m. The hypothetical jet was embedded in the lower levels of the northeast flow. It is speculated that this zone could also have been a source of shear and turbulence.

The results for N in Fig. 294 indicate that IOP7 was the most stable and IOP6 the least stable of the nighttime IOPs. There is also a suggestion that southwest to northwest wind directions at GRI during IOPs 5, 7, and 8 tended to associate with higher N and lower U . Any pattern is less clear for COC.

Observations from PSB2 have consequences with regard to how to account for uncertainties in plume modeling, especially with respect to light wind conditions in the very stable boundary layer. The data indicate that the concentration at any given place and time is best represented by a probability distribution, and one with fat tails at that, rather than a single

discrete concentration. This is not a novel idea but few data sets show it with such clarity. The data also show this is exacerbated at nighttime.

Discussion about uncertainty in plume concentrations is often framed in terms of concentration fluctuation intensity, peak:mean ratio, intermittency, and probability distributions. However, most data sets do not provide a complete basis for such an analysis. Even the PSB2 data is limited in this regard due to the frequent occurrence of railing and loss of the uppermost concentrations in the fast response analyzers. It is the field duplicate bag sampling that really highlights this issue.

The PSB2 data make it clear that there could be adverse consequences to not adequately representing the uncertainties. These would be present during the day and worst at night and closer to the source of a continuous release. Relatively small shifts in location could have big effects. They also raise other questions. It is well known that toxic effects are enhanced by high concentration fluctuation intensities compared to the same average but with a more uniform concentration and low fluctuation intensity (Ride, 1984). The fast response analyzer time series for both the day and night IOPs featured large, abrupt changes in concentration. For the daytime IOPs, the frequency of plume meander was sufficient to create mean values that usually led to well-defined, time-averaged Gaussian cross-sections. However, the means largely represented a lot of zeros with intermittent periods with high concentrations. The net effect was that differences between collocated field duplicates were relatively minimal.

However, for the nighttime IOPs, two factors complicate an evaluation of potential health consequences. One is that the normalized concentrations were up to two orders of magnitude greater than the daytime. This would further magnify the effects of any concentration variability. The other is that any given location reached by the plume is more likely to remain within the plume for extended periods of time resulting in relatively minimal concentration variation with an apparent narrow-tailed distribution. Yet PSB2 shows that this can provide a false picture of the concentration variability with small changes in location potentially yielding much different results and a much fatter tailed distribution. Thus the duration of the release and averaging period at any given location could have a major effect on uncertainty.

A common feature of the nighttime IOPs was how the observations of wind direction, in particular, often varied significantly between GRI and COC. In fact, it almost appeared as if there were sometimes two wind direction regimes across the study area. Wind directions at GRI and the horizontal array of sonic anemometers were usually roughly consistent with each other while COC and SOD, to the east of the outermost nighttime sampling arc, were more likely to be consistent with each other. The significance of this is not clear and the actual plume patterns tended to be most consistent with GRI. Whether the situation featuring such horizontal variability on this scale in very stable, low U conditions is unique to the Grid 3 study area or a common occurrence in other real world settings is not known.

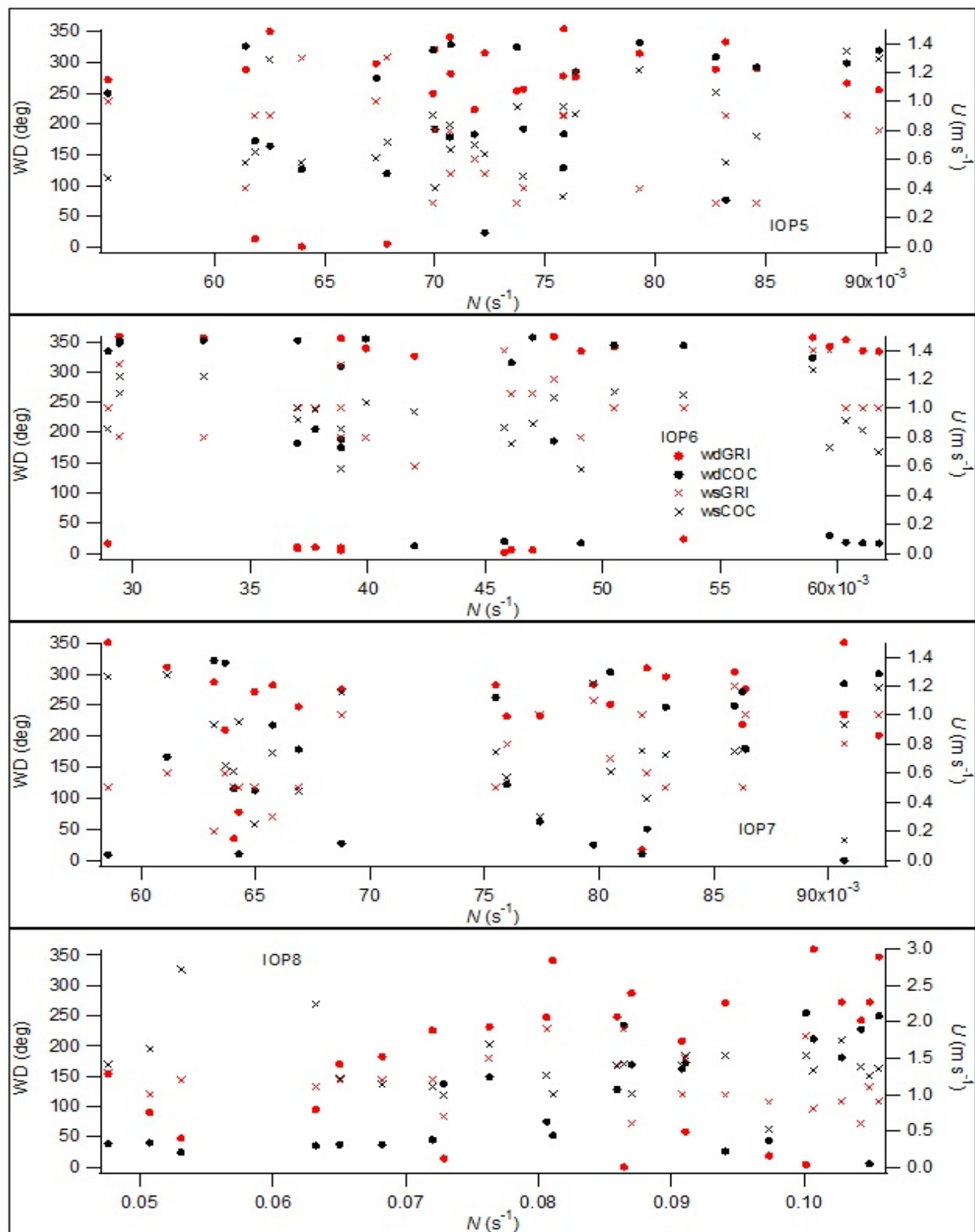


Figure 294. Ten-minute average 2 m wind speed and direction at GRI and COC as a function of Brunt-Väisälä frequency N .

This page is intentionally left blank.

REFERENCES

- ANSI/ANS-3.11, 2005. *Determining Meteorological Information at Nuclear Facilities*. American Nuclear Society, La Grange Park, IL, 31 pp.
- ANSI/ANS-3.2, 2006. *Administrative Controls and Quality Control Assurance for the Operational Phase of Nuclear Power Plants*. American Nuclear Society, La Grange Park, IL, 37 pp.
- Aubinet, M., A. Grelle, and others, 2000. Estimates of the annual net carbon and water exchange of forests: the EUROFLUX methodology. *Advances Ecological Res.*, **30**, 113-175.
- Benner, R.L., and B. Lamb, 1985: A Fast Response Continuous Analyzer for Halogenated Atmospheric Tracers. *J. Atmos. Oceanic Technol.*, **2**, 582-589.
- Carter, R.G., 2003. *ARLFRD ATGAS Software Operator's Manual*. NOAA Air Resources Laboratory Field Research Division, Idaho Falls, ID, 26 pp.
- Clawson, K.L., R.G. Carter, and others, 2004. *URBAN 2000 SF₆ Atmospheric Tracer Field Tests*. NOAA Tech. Memo OAR ARL-253, Air Resources Laboratory, Idaho Falls, ID.
- Clawson, K.L., R.G. Carter, and others, 2005. *Joint Urban 2003 (JU03) SF₆ Atmospheric Tracer Field Tests*. NOAA Tech. Memo OAR ARL-254, Air Resources Laboratory, Idaho Falls, ID.
- Clawson, K.L., R.M. Eckman, and others, 2007. *Climatography of the Idaho National Laboratory*, 3rd edition. NOAA Tech. Memo OAR ARL-259, Air Resources Laboratory, Idaho Falls, ID.
- Clawson, K.L., R.M. Eckman, and others, 2009. *Roadside Sound Barrier Tracer Study 2008*. NOAA Tech. Memo OAR ARL-260, NOAA Air Resources Laboratory, Idaho Falls, ID, 212 pp.
- DOD, 2002. *Department of Defense Quality Systems Manual for Environmental Laboratories*, Final Version 2. U.S. Department of Defense, Environmental Data Quality Workgroup, Department of the Navy, Lead Service, 167 pp.
- DOE, 2004. DOE/EH0173T Chapter 4, *Environmental Regulatory Guide for Radiological Effluent Monitoring and Environmental Surveillance*. U.S. Department of Energy, Office of Air, Water and Radiation Protection Policy & Guidance, 16 pp.
- DOE, 2005. DOE Order 151.1C, *Comprehensive Emergency Management System*, U.S. Department of Energy, Office of Emergency Operations. Washington, D.C., 90 pp.

EPA, 2000a. *Guidance for Data Quality Assessment-Practical Methods for Data Analysis*. U.S. Environmental Protection Agency, QA/G-9, EPA/600/R-96/084.

EPA, 2000b. *Quality Systems. National Environmental Laboratory Accreditation Conference (NELAC)*. U.S. Environmental Protection Agency, QA/G-9, EPA/600/R-00/084, NTIS PB2001-104049.

EPA, 2000c. *Meteorological Monitoring Guidance for Regulatory Modeling Applications*. U.S. Environmental Protection Agency, EPA-454/R-99-005, 171 pp.

EPA, 2004. *Revised Assessment of Detection and Quantitation Approaches*. U.S. Environmental Protection Agency, EPA-821-B-04-005, Engineering and Analysis Division, Office of Science and Technology, Office of Water (4303T).

Finn, D., K. L. Clawson, R. G. Carter, J. D. Rich, R. M. Eckman, S. G. Perry, V. Isakov, and D. K. Heist, 2010. Tracer studies to characterize the effects of roadside noise barriers on near-road pollutant dispersion under varying atmospheric stability conditions. *Atmos. Environ.*, **44**, 204–214.

Finn, D., K.L. Clawson, R.M. Eckman, R.G. Carter, J.D. Rich, T.W. Strong, S.A. Beard, B.R. Reese, D. Davis, H. Liu, E. Russell, Z. Gao, S. Brooks, 2015: *Project Sagebrush Phase 1*, NOAA Technical Memorandum OAR ARL-268 , Air Resources Laboratory, Idaho Falls, Idaho, pp 338. doi:10.7289/V5VX0DHV

Foken, T., Leuning, R., Oncley, S., Mauder, M., & Aubinet, M., 2012. Corrections and Data Quality Control. In M. Aubinet, T. Vesala, & D. Papale (Eds.), *Eddy Covariance* (pp. 85–131). Springer Netherlands.

Garodz, L. J., and K. L. Clawson, 1991: *Vortex Characteristics of C5A/B, C141B, and C130E aircraft applicable to ATC terminal flight operations, tower fly-by data*. NOAA/ERL/ARLFRD, Idaho Falls, Idaho, 250 pp.

Garodz, L. J., and K. L. Clawson, 1993: *Volume 1, Vortex Wake Characteristics of B757-200 and B767-200 Aircraft Using the Tower Fly-By Technique. Volume 2, Appendices*. NOAA/ERL/ARLFRD, Idaho Falls, ID.

International Organization on Standardization (ISO), 1990: General Requirements for the Competence of Calibration and Testing Laboratories. *ISO/IEC Guide 25-1990*. 3 pp.

Keith, L.H., W. Crummett, J. Deegan, R.A. Libby, J.K. Taylor, and G. Wentler, 1983. Principles of Environmental Analysis. *Analytical Chemistry*, **55**, 2210-2218.

Sagendorf, J. F. and C. R. Dickson, 1974. *Diffusion under low windspeed, inversion conditions*. NOAA Tech. Memo ERL ARL-52, Air Resources Laboratory, Idaho Falls, ID.

Start, G. E., J. F. Sagendorf, G. R. Ackermann, J. H. Cate, N. F. Hukari, and C. R. Dickson. 1984. *Idaho Field Experiment 1981, Volume II: Measurement data*, NUREG/CR-3488 Vol 2.

Willis, G. E. and N. Hukari. 1984. Laboratory modeling of buoyant stack emissions in the convective boundary layer. *Fourth Joint Conference on Applications of Air Pollution Meteorology*, October 16-19 1984, Portland, OR, pp. 24-25

Vickers, D., and L. Mahrt, 1997. Quality control and flux sampling problems for tower and aircraft data. *J. Atmos. Oceanic Technol.*, **14**, 512-526.

This page left intentionally blank.